ESCAMPIG 2024

9- 13 JULY 2024, BRNO, CZECH REPUBLIC

26th Europhysics Conference on Atomic and Molecular Physics of Ionized Gases

BOOK OF ABSTRACTS

MUNI SCI Department of Plasma Physics and Technology

CEPLANT

escampig2024@physics.muni.cz

ESCAMPIG 2024 organized by

Department of Plasma Physics and Technology and CEPLANT

Faculty of Science

Masaryk University

In collaboration with Jednota českých matematiků a fyziků

Local Organizing Committee

Chairman: Zdeněk Bonaventura (MUNI)

Co-chairman: Tomáš Hoder (MUNI)

Bohumila Tesaříková (MUNI)

František Krčma (BUT)

Ondřej Jašek (MUNI)

Pavel Dvořák (MUNI)

Realization/Support

Eliška Vrzalová (MUNI)

Anežka Winklerová (MUNI)

Pavel Kunovský (MUNI)

Monika Stupavská (MUNI)

Tereza Schmidtová (MUNI)

Radka Kunovská (MUNI)

Jan Vondra (JČMF)

International Scientific Committee

Chairman: Carlos Pintassilgo (Portugal)

Ronny Brandenburg (Germany)

Claudiu Costin (Romania)

Aranka Derszi (Hungary)

Anatoly Filippov (Russia)

Victor Herrero (Spain)

Nikola Škoro (Serbia)

Tiberiu Minea (France)

Eugen Stamate (Denmark)

Francesco Taccogna (Italy)

František Krčma (Czech Republic)

Erik Wagenaars (United Kingdom)

Edited by Ondřej Jašek

Postconference edition, Updated 11.9. 2024, Brno

ESCAMPIG 2024 supported by

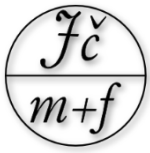

escampig2024.physics.muni.cz/#supporters

Table of Content

About Escampig Conference	4
Conference program overview	5
Conference Workshops	6
Social Events	7
Detailed Program, Tuesday July 9th	8
Detailed Program, Wednesday July 10th	8
Poster Session 1, Wednesday July 10th	26
Detailed Program, Thursday July 11th	182
Poster Session 2, Thursday July 11th	213
Detailed Program, Friday July 12th	364
Detailed Program, Saturday July 13th	383
Conference participants and Author Index	399
ESCAMPIG 2024 Participation statistics	404
Conference photo	405
Best Poster Prizes	406
Escampig Herald	407
Sponsors	420

About ESCAMPIG Conference

The history of the ESCAMPIG conference dates back to 1973, when the first ESCAMPIG conference was held in Versailles. Since 1974, the ESCAMPIG conference has been held every two years, with the exception of 2020, when the event was postponed for two years due to the pandemic. The community of conference participants increased since the first conference and settled at a stable value of around 200 participants, leading experts worldwide focusing on atomic and molecular processes in ionized gases, basic and applied plasma research, diagnostic methods, plasma-surface interactions, plasma sources, and technologies. During half a century of ESCAMPIG history, this conference has been organized in many countries of Western and Eastern Europe. In 2024, ESCAMPIG will be held in the Czech Republic for the first time in history.

Dear Participants,
On behalf of the Local Organization Committee and the Realization/Support team, I would like to extend our heartfelt thanks for your participation in ESCAMPIG 2024!
The friendly and enthusiastic atmosphere that, I believe, we all experienced during the conference is a testament to the vitality of the ESCAMPIG community. The significant number of young researchers attending is also a very promising sign for the future of the field. Let's hope we will have plenty of opportunities to meet and exchange ideas at events to come. It was our great pleasure to host you at ESCAMPIG 2024!

Zdenek Bonaventura, Chairman of LOC

1973	Versailles	France
1974	Innsbruck	Austria
1976	Bratislava	Czechoslovakia
1978	Essen	West-Germany (F.R.G.)
1980	Dubrovnik	Yugoslavia
1982	Oxford	United Kingdom
1984	Bari	Italy
1986	Greifswald	East-Germany (G.D.R.)
1988	Lisbon	Portugal
1990	Orléans	France
1992	St. Petersburg	Russia
1994	Noordwijkerhout	The Netherlands
1996	Poprad	Slovak Republic
1998	Malahide	Ireland
2000	Lillafüred	Hungary
2002	Grenoble	France
2004	Constanta	Romania
2006	Lecce	Italy
2008	Granada	Spain
2010	Novi Sad	Serbia
2012	Viana do Castelo	Portugal
2014	Greifswald	Germany
2016	Bratislava	Slovakia
2018	Glasgow	United Kingdom
2022	Paris	France
2024	**Brno**	**Czech Republic**

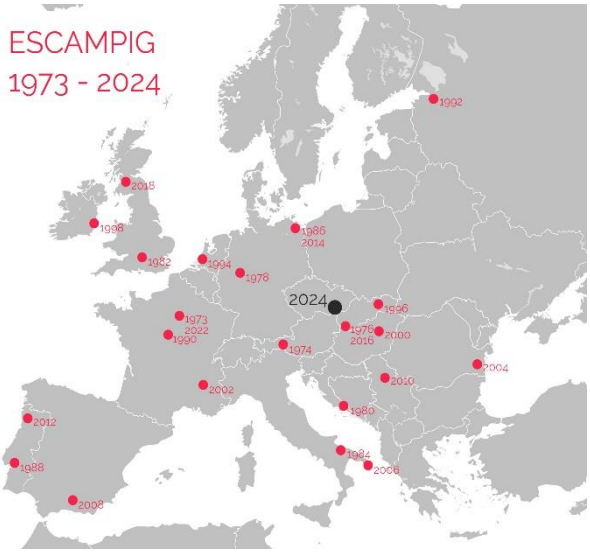

Conference Program Overview

Tuesday July 9		Wednesday July 10		Thursday July 11		Friday July 12		Saturday July 13	
		8:20	OPENING						
		8:35	H. Kersten	8:30	G. D. Stancu			8:30	J. Országh
		9:20	M. Puač	9:15	C. Vitelaru	9:15	L. Vialetto	9:15	F. Cichocki
		9:50	F. Sobczuk	9:50	Y. Guo	9:45	M. Baeva	9:45	Crookes Prize **X.Tu**
		10:10	O. Tarvainen	10:05	C.L. da Silva	10:05	Z. Kozáková		
		10:30	Coffee Break	10:30	Coffee Break	10:30	Coffee Break	10:30	Coffee Break
		11:00	P. Bruggeman	11:00	K. Kutasi	11:00	L.L. Alves	11:00	J. de Urquijo
		11:45	A. Stancampiano	11:45	M. Jimenez Redondo	11:45	A. Gómez-Ramírez	11:20	F.J. Morales-Calero
		12:15	V. Guerra	12:15	M. Rutigliano	12:15	C. Ionita	11:40	A. Cobos-Luque
		12:35	E. Wagenaars	12:35	J. Teunissen	12:35	T. Osawa	12:00	Q. Delavière-Delion
		12:55	Lunch	13:10	Lunch	12:55	Lunch	12:20	CLOSING
								12:50	
		14:30	Poster Session 1	14:30	Poster Session 2	14:30	Excursions		
16:30	Registration	16:30	Coffee Break	16:30	Coffee Break			**LEGEND**	
		17:00	A. Nelson, V. Guerra, M.Becker, M. Kushner	17:00	A. Dogariu	17:00	Lab tour MUNI	General Invited Talk	
18:00	**Welcome Party**			17:30	A. Gerakis			Topical Invited Talk	
				18:00	P. Dvořák	18:00	Garden Party MUNI	Oral Presentation	
		19:00		18:30	J.-P. van Helden	19:00		Hot Topic Talk	
				19:00				Workshops	
				20:00	**Conference dinner**			IUPAP Early Career Prize	
21:30				1:00		21:30			

Workshop 1

Predictive and practical simulations of plasma systems and plasma processes

Chairman: Adam Obrusník (MUNI, PlasmaSolve, Czech Republic)

This topical workshop explores the evolution of plasma modeling and simulation over the past 10-20 years, highlighting both success stories and challenges. It features four renowned speakers from the field of low- temperature plasma, each with distinct primary expertise: calculating fundamental data for models, engineering plasma chemistry, modeling of industrial low-pressure systems, and elucidating new plasma mechanisms. The workshop will commence with each expert sharing their insights and experiences regarding plasma process simulation and their future outlook on the topic. This will be followed by a panel discussion, during which the audience, facilitated by the moderator, is encouraged to pose questions related to the workshop's theme. The workshop will be moderated by Adam Obrusník who is a researcher dedicated to the development of plasma models for various applications, such as material deposition and plasma catalysis but also an entrepreneur who operates a company providing simulation solutions to diverse industries utilizing plasma.

SPEAKERS

Anna Nelson (United Kingom), Vasco Guerra (Portugal), Marcus Becker (Germany), Mark J. Kushner (USA)

Workshop 2

Advancements in non-equilibrium plasma laser diagnostics

Chairman: Gabi Daniel Stancu (CentraleSupélec, France)

Non-equilibrium plasmas are complex reactive environments driven by multiphysics interactions that are employed or studied to meet numerous societal goals. Given the high intricacy of these systems, laser diagnostics remain essential to the advancement of plasma knowledge and engineering. Their exceptional features enable probing with high sensitivity, selectivity, spatial and temporal resolutions crucial plasma parameters such as nonequilibrium temperatures, densities of key reactive species, velocity and flux distributions and fields. The workshop will expose recent progresses achieved in advanced laser diagnostics for the investigation of non-equilibrium plasmas. Fundamental properties of non-equilibrium plasmas are tackled here by resonant or non-resonant, single or multiphoton and multi-wave techniques, including cavities and ultrashort lasers with wavelengths from ultraviolet to the THz spectroscopic domain. Principles, challenges, examples of studies of non-equilibrium plasmas and perspectives will be addressed.

SPEAKERS

Jean-Pierre van Helden (Germany) - Atomic oxygen measurements with THz absorption spectroscopy, ps- TALIF, and CRDS: A comparison
Alexandros Gerakis (Luxembourg) –Non-resonant four wave mixing diagnostics for the determination of nonequilibrium in plasmas
Pavel Dvořák (Czech Republic) - LIF studies of hydride dissociation in electric discharges
Arthur Dogariu (USA) - Non-equilibrium thermometry in gases and plasmas using hybrid CARS

EXCURSIONS

Friday July 12th, 2024

ŠPILBERK CASTLE

Špilberk Castle has dominated Brno's skyline since the mid-13th century. Historically, it served not only as a symbol of safety and protection but also, at times, inspired fear and represented oppression for the city's citizens. A sightseeing tour of the castle includes the Casemates prison, historical fortifications, and a lookout tower.

BRNO UNDERGROUND

Water tanks Žlutý kopec: Mysterious underground cathedrals from the years 1874, 1894, and 1917 Two brick and one concrete water tank, unparalleled in Europe, whose visit will take your breath away! This Brno "must-see" is located under the unassuming grassy area of a revitalized park on Žlutý kopec and offers an experience akin to that of another world from a long-lost civilizations. Three colossal underground tanks are a unique architectural monument and a testament to exceptional technical industrial architecture in its pristine form.

VILLA TUGENDHAT

Villa Tugendhat, designed by the renowned German architect Ludwig Mies van der Rohe, was constructed in 1929–1930. It quickly became an icon of modern architecture in Europe, particularly noted for its revolutionary approach to space and the use of industrial building materials. The villa's history is as captivating as its cultural significance. In 2001, Villa Tugendhat was inscribed on the UNESCO World Heritage List, cementing its status as a pivotal work of architecture.

SOCIAL EVENTS

WELCOME RECEPTION/PARTY

Tuesday July 9th, 2024

The welcome reception will take place at the conference venue on Tuesday, July 9, from 6 p.m. The reception will feature a performance by the University Folk Song and Dance Ensemble Poľana Brno, along with their folk dance school.

CONFERENCE DINNER

Thursday July 11th, 2024

The conference dinner will take place at the Brewery House Poupě (Dominikánská 342, Brno) on Thursday, July 11, 2024, at 8 p.m. A buffet-style dinner offering a wide selection, including non-alcoholic beverages, beer, and wine, is planned. This dinner is included in the conference fee.

GARDENPARTY AND LABTOURS

Friday July 12th, 2024 from 5 p.m.

The garden party will be held on Friday, July 12, from 6 p.m. at the Botanic Garden of Masaryk University (Kotlářská 2, Brno). A BBQ-style dinner will be available, including soft drinks, beer, and wine. Guests will have the opportunity to visit the greenhouses of the Botanic Garden. Additionally, lab tours at the Department of Plasma Physics and Technology will be possible prior to the Garden Party.

ACCOMPANYING PERSONS

Optional programs for accompanying persons will be prepared and could additionally be arranged with the LOC upon request.

Detailed conference program Tuesday 9th, 2024

16:30	REGISTRATION
18:00	Welcome Party
21:30	

Detailed conference program Wednesday 10th, 2024

8:00	REGISTRATION		
8:20	OPENING - Carlos Pintassilgo, Zdeněk Bonaventura		
	Morning Session Chairman: Ronny Brandenburg		
8:35	General invited	H. Kersten	On the combination of common and non-conventional probe diagnostics for process plasmas
9:20	Topical invited	M. Puač	Nature of radiofrequency breakdown in argon viewed through electron energy distribution functions modeled by the Monte Carlo technique
9:50	Oral	F. Sobczuk	Enhancing Low-Temperature Plasma Diagnostics: Ultra-High Resolution Spectroscopy with Signal Amplification
10:10		O. Tarvainen	Space charge compensation of pulsed high-current negative and positive hydrogen ion beams
10:30	Coffee Break		
	Midday Session Chairman: Nikola Škoro		
11:00	General invited	P. Bruggeman	Plasma-liquid interactions: overview and perspectives
11:45	Topical invited	A. Stancampiano	Plasma in interaction with water droplets
12:15	Hot topic	V. Guerra	Deep Learning for Low-Temperature Oxygen-Based Plasmas Modelling
12:35		E. Wagenaars	Formation of O and H radicals in an atmospheric-pressure nanosecond pulsed discharge in helium with water vapour admixtures
12:55	Lunch		
14:30	Poster Session 1		
16:30	Coffee Break		
17:00	Workshop 1	A. Nelson, V. Guerra, M. Becker, M. Kushner	Predictive and practical simulations of plasma systems and plasma processes **(Panel discussion)**
19:00			

On the combination of common and non-conventional probe diagnostics for process plasmas

H. Kersten(*)[1], F. Schlichting[2], D. Zuhayra[1], M. Klette[1], L. Hansen[1], T. Trottenberg[1]

[1] *Institute for Experimental and Applied Physics, PlasmaTechnology, University of Kiel, Kiel, Germany*

[2] *Technical Faculty, University of Kiel, Kiel, Germany*

(*) kersten@physik.uni-kiel.de

The wide range and ever-growing applications of plasma processes in research and industry require an equally improved diversity and accessibility of suitable plasma diagnostic methods. In the present study, diagnostics of electrons and ions in plasmas and fluxes of charged and neutral species toward plasma-facing surfaces by non-optical methods will be reviewed and discussed.
To further enhance the determination of different fluxes of species, their energies, and behavior influencing the surface processes, custom-built combinations of plasma process diagnostics have been developed. For example, we present a retarding field energy analyzer where a passive thermal probe substitutes the collector. By doing so, we can determine the energy distribution of the charged ions, their energy flux density at a certain potential, and the power deposited onto a substrate. Another advantage is that the thermal probe can even measure the power deposited by incoming (fast) neutrals and by other contributions (radiation, chemical reactions, film condensation) when the grids suppress the ions.

The focus of this general invited talk (review) is laid on the fundamentals of conventional probe-based plasma diagnostic methods as Langmuir probes (LPs), Faraday cups (FCs) and retarding field analyzers (RFA), but as well as on the principles of non-conventional diagnostics as calorimetric and force probes (CPs, FPs) [1]. These rather simple methods are useful tools for the measurement of overall, not species resolved, ion and neutral fluxes toward surfaces, see Fig. 1.

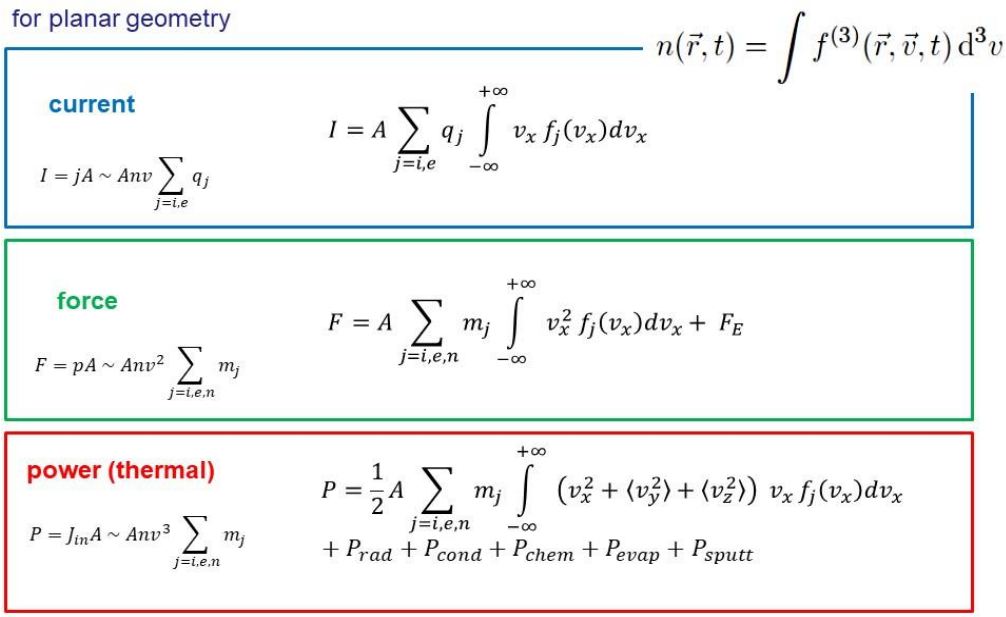

Fig. 1: Moments of the VDF of involved species result in particle flux (current), momentum flux (force) and energy flux (power). In addition, other phenomena can also contribute to the integral fluxes.

For example, RFAs provide overall ion energy distribution functions, whereas CPs and FPs can even deliver information about fluxes of fast neutrals and other contributions which are not related to charge carriers (Fig. 1). Although many of these diagnostics have their roots in the beginnings of plasma research, they were gradually refined to match the requirements of plasma environments in industry, such as rf-discharges, reactive plasmas, dusty plasmas, and atmospheric pressure plasmas. Examples for "non-conventional" diagnostics, which are also applicable in plasma processes, are the determination of the total energy fluxes from plasma to substrate by calorimetric probes [2,3] and the measurement of momentum transfer due to sputtered particles or changes of plasma pressure by force probes [4,5].

Of particular interest is the combination of different types of probes, e.g. retarding field analyzer (RFA) and passive thermal probe (PTP). With a retarding field energy analyzer, one can obtain the ion energy distribution in a plasma by measuring the current at the collector depending on the applied discriminator voltage at the scan grid. A passive thermal probe determines the energy flux density coming from a process plasma by measuring the temperature change of a dummy substrate. The PTP serves as collector, in front of which three centrally aligned grids are operated as the retarding field system [6]. By doing so, we can determine the energy distribution of the charged ions, their energy flux density at a certain potential, and their power deposited onto a substrate. An advantage is that the thermal probe replacing the collector can even measure the power deposited by incoming (fast) neutrals, by the background gas and by other phenomena when the grids keep away the ions. Hence, the ion energy distribution (IED) can be determined regarding the energy exchange of the neutral background gas with the ions extracted from the plasma source. Combining these two powerful diagnostics yields information they neither can deliver on their own. The probe has been tested in three different plasma environments: ion beam source, magnetron sputtering and radio frequency discharge plasma. In Fig. 2 a typical measurement for HiPIMS sputtering of a carbon target in an argon atmosphere is shown. Although the ion current (and also the energy influx by the ions) vanishes above the discriminator voltage of about +20 V which corresponds to the plasma potential, there is still a remarkable energy influx which originates from other contributions like fast neutrals (from the target and due to charge exchange collisions) and carbon thin film condensation at the PTP collector (substrate).

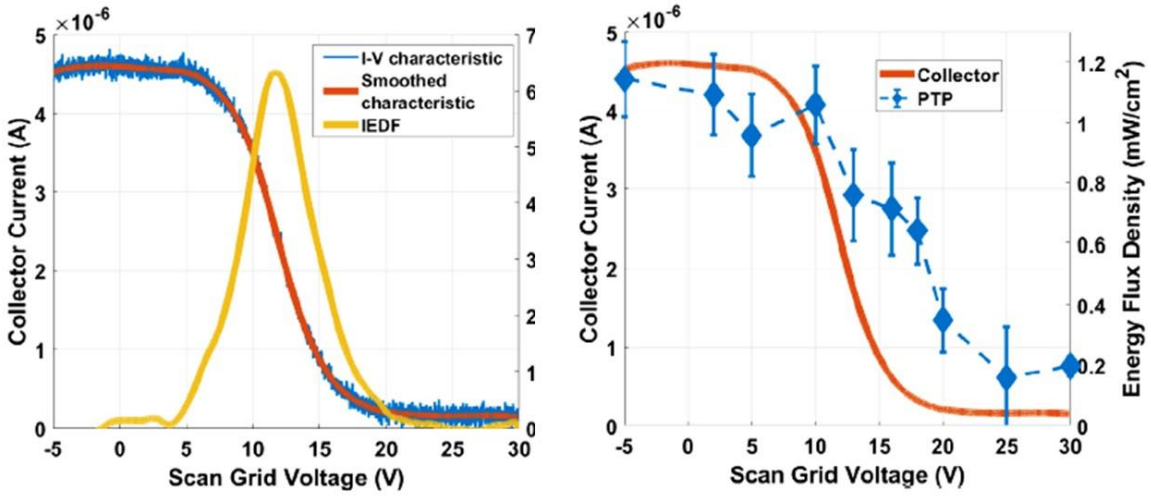

Fig. 2: I-V characteristic of the collector and the derived IEDF measured in a HiPIMS system (left) and comparison of the collector current due to the ions with the integral energy influx (right).
The working gas is Ar at 0,36 Pa and the C target was operated at 800 W.
The combined sensor (RFA + PTP) was placed in the substrate region.

Another example for an advanced probe diagnostic is the combination of a quartz crystal microbalance (QCM) with an interferometric force probe (FP) [6,7]. In the experiment, an aluminum target was sputtered by an ion beam of 1200 eV. The sputtered atoms are deposited either onto a "simple" QCM or onto a FP where the probe is the QCM. The incoming – either sticking or reflecting – species transfer their momentum and contribute to the thin film growth (Fig. 3). The probe (substrate) was scanned around the target in order to observe the angular dependence of ion beam sputtering. The transfer of momentum due to sticking, e.g. film forming particles (at small angles) is about factor 1 and, therefore, smaller compared to larger angles where more reflection (and less deposition) occurs with a momentum transfer of about factor 2. The angular dependence of the deposition rate is vice versa.

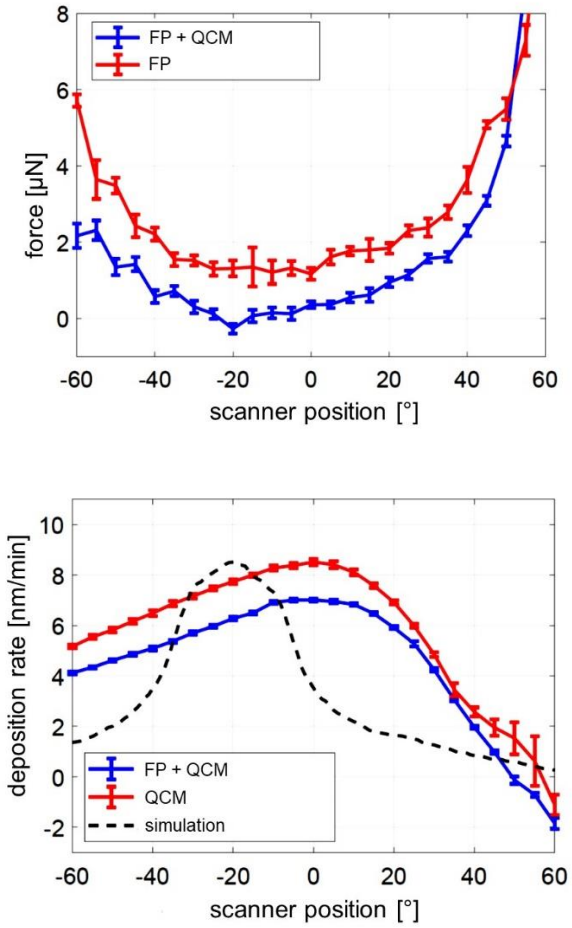

Fig. 3: Measured force (top) and deposition rate (bottom) by "only" the force probe and by the combined FP + QCM in dependence on the angle of the ejected Al atoms which is related to the sputtering angle.

The current trend in the miniaturization of sensors, adopted from the manufacturing of MEMS, will allow more and more measurements with high spatial resolution in miniaturized plasma sources, like plasma jets or micro discharges [8], respectively.

[1] J. Benedikt, H. Kersten, A. Piel, *Plasma Sources Sci. Technol*. **30** (2021) 033001.
[2] H. Kersten, H. Deutsch, H. Steffen, G.M.W. Kroesen, R. Hippler, *Vacuum* **63** (2001) 385-431.
[3] S. Gauter, F. Haase, and H. Kersten, *Thin Solid Films* **669** (2019) 8-18.
[4] T. Trottenberg, A. Spethmann, H. Kersten, *Eur. Phys. J. Techn. Instrum*. **5** (2018) 3.
[5] M. Klette, M. Maas, T. Trottenberg, H. Kersten, *J. Vac. Sci. Technol. A*, **38** (2020) 033013.
[6] F. Schlichting, H. Kersten, *Eur. Phys. J. Techn. Instrum*. **10** (2023) 19.
[7] M. Weise, S. Seeger, K. Harbauer, S. Welzel, K. Ellmer, *J. Appl. Phys.* **122** (2017) 044503.
[8] L. Hansen, N. Kohlmann, U. Schürmann, et.al., *Plasma Sources Sci. Technol.* **31** (2022) 035013.

Nature of radiofrequency breakdown in argon viewed through electron energy distribution functions modeled by the Monte Carlo technique

Marija Puač[1] and Zoran Lj Petrović[2,3]

[1] *Institute of Physics, University of Belgrade, 11080 Zemun, Serbia*

[2] *Serbian Academy of Science and Arts, 11001 Belgarde, Serbia*

[3]*Department of Electrical Engineering Ulster University,*

(*) *smarija@ipb.ac.rs*

This paper investigates radiofrequency breakdown in argon by analyzing the electron energy distribution functions obtained from a Monte Carlo code. Energy gain is determined by the external AC field and applied frequency of 13.56 MHz while losses are due to many collisions between electrons and the background gas and electrons and infinite parallel electrodes. Two points on the breakdown voltage curve with the same breakdown pressure of 0.2 Torr and different voltages of 94 V and 447 V highlighted the need of increasing the number of electron – background gas collisions to maintain the discharge, which led to increase of pressure, hence the double valued nature of rf breakdown voltage curve. On the other hand, presence of Ramseur minimum in the cross section for elastic scattering is responsible for fast collapse of EEDF peak for some combinations of breakdown voltage and breakdown pressure.

Radiofrequency (RF) breakdown has been analyzed in our recent papers [1], [2] as well as the role of attachment process in oxygen gas on the breakdown curve as the loss mechanism in the gas volume between two electrodes [3]. Now we have employed Monte Carlo code to investigate electron energy distribution functions (EEDFs). Background gas is argon and the applied frequency is 13.56 MHz. Electron dynamics is defined only by the external AC field and electron-gas molecule collisions. When electron reaches one of the electrodes it is being deleted from the simulation.

In Fig. 1 we have presented EEDFs along the breakdown voltage curve. As expected, mean energies are higher at high voltages (left-hand side of the curve). Electrons can also gain more energy from the AC filed along their path uninterrupted with collisions, due to small pressures (background gas density). At the same time, there is a difference between EEDF sampled at different times in one period of AC field (lines in various colors in the same plot). When the AC field passes through zero, the EEDF has its maximum peak value because electrons gain small amounts of energy from the field and the low energy electrons are dominant. At the AC field maximum EEDF has the longest "tail", electrons gain more energy, as expected. Right-hand side of the breakdown voltage curve has almost uniform EEDF over time period (from zero to 2π). Electrons mean energy has small deviation from the mean value. It is because the energy gain from the AC field gets "interrupted" by numerous collisions and EEDF doesn't change much over one period.

Double valued nature of RF breakdown voltage curve [1] can be analyzed by focusing on the energy balance. Fig. 2 shows the differences between two breakdown points that have the same breakdown pressure of 0.2 Torr and different voltages of 94 V and 447 V (plots A and D from Fig. 1). In Fig. 2a there is comparison of mean energies. Minimum values of both energy plots are similar but maximum energies and means are quite different. Mean value for point A is around 20 eV while for D point is around 8 eV. We know that pressure is the same and it can be assumed that electrons experience the same number of collisions with background gas in both points (assuming that the collision frequency is not strongly dependent on the energy). Hence losses in the gas volume do not play a deciding role in energy balances for those two points. It is very likely that the high voltage in the second ('upper') curve is due to the high voltage that pushed electrons towards the electrode and thus increased the losses at

same point allowed electron to gain enough energy to ionize before colliding with the electrode. That allowed for achieving selfsustained conditions again for the same pressure.

The main difference is in energy that electron can obtain from the field between two collisions, presented in Fig. 2b. At the higher voltage that energy is around 1.5 eV while at lower voltage that energy drops almost 100 times. It means that electron needs to experience 100 times more elastic collisions to acquire enough energy to perform ionization, compared to the electron at 447 V. As both points are in region of low pressures and small number of collisions with the background gas, we can conclude that higher voltage point has more efficient ionizations.

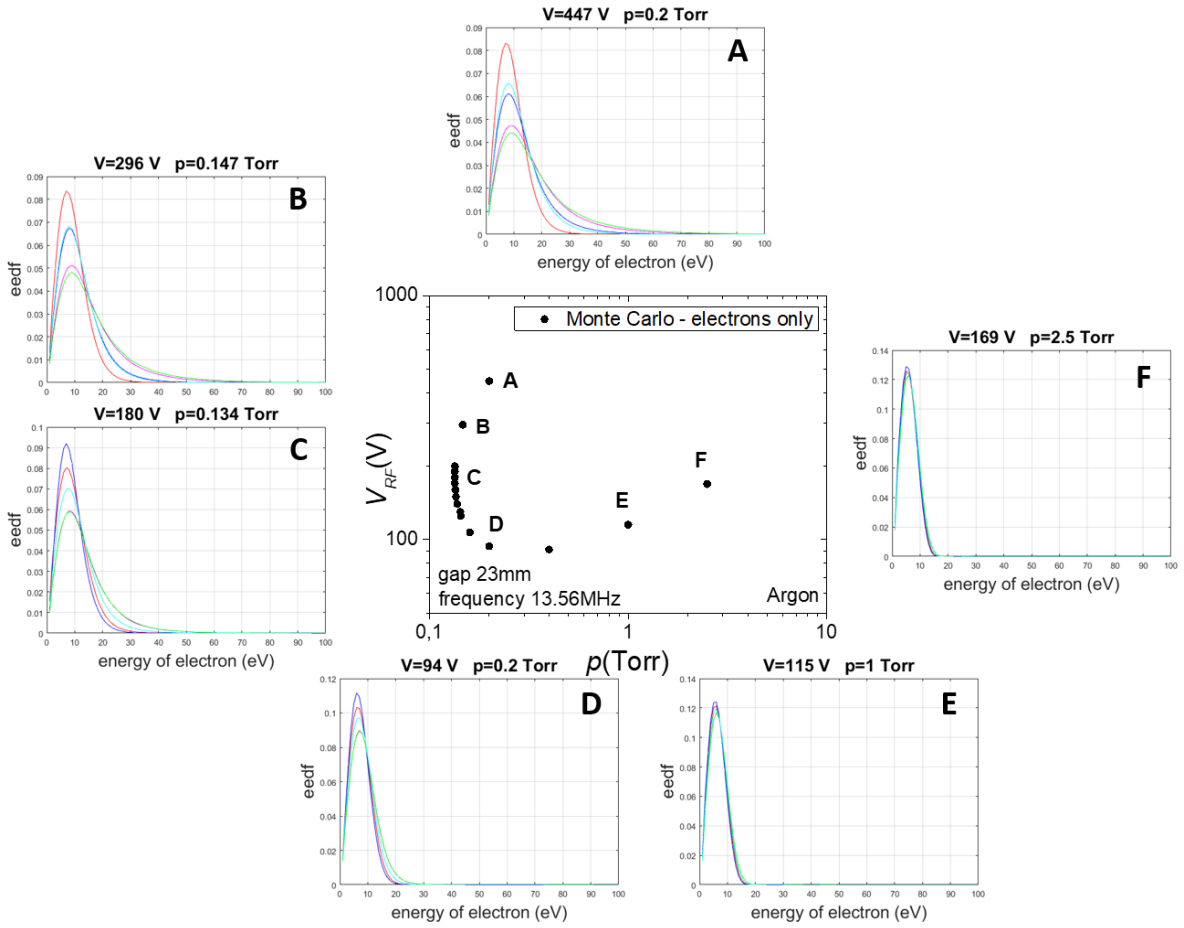

Fig. 1: Electron energy distribution functions (EEDFs) along breakdown voltage curve. Different lines at the same plot represent EEDF sampled at different times (from zero to 2 π). Background gas is argon, frequency is 13.56 MHz and gap is 23 mm.

How the EEDFs are linked to the number of collisions can be seen in Fig. 3. In Fig. 3a EEDFs in the volume of the gas over one half period of time for the already mentioned points A and D from Fig. 1 are presented. We can see that at higher voltage there is a narrow peak with long tail that indicates presence of high energy electrons. At lower voltage peak is wider and tail is much shorter than at 447 V. Both peaks are slightly delayed compared to the field minima at π/2 which is a consequence of the inability of energy to relax at applied frequency of 13.56 MHz. Also, the difference in time necessary for the peak to form and to diminish can be observed. To investigate this peak "cycle" we have presented relaxation of 95% EEDF peak value over half period of time in Fig. 3b with applied AC filed in light blue colored line. Value of 95% of the peak is chosen to avoid statistical fluctuations that the 100% of the peak has. Fig. 3c shows number of elastic collisions. As can be seen in Figure 3b, there is a steep slope that characterizes peak decline, which is more pronounced at the higher voltage. Decline in EEDF

means that electrons obtain energy fast which is in a good agreement with the peak in number of elastic collisions. Peak in the number of collisions (Fig. 3c) has to be a consequence of the peak in argon cross section set. That leads to a conclusion that at point A after the EEDF peak, the majority of the electrons have the energy that corresponds to the energy of the Ramseur minimum and at the same time they gain energy fast.

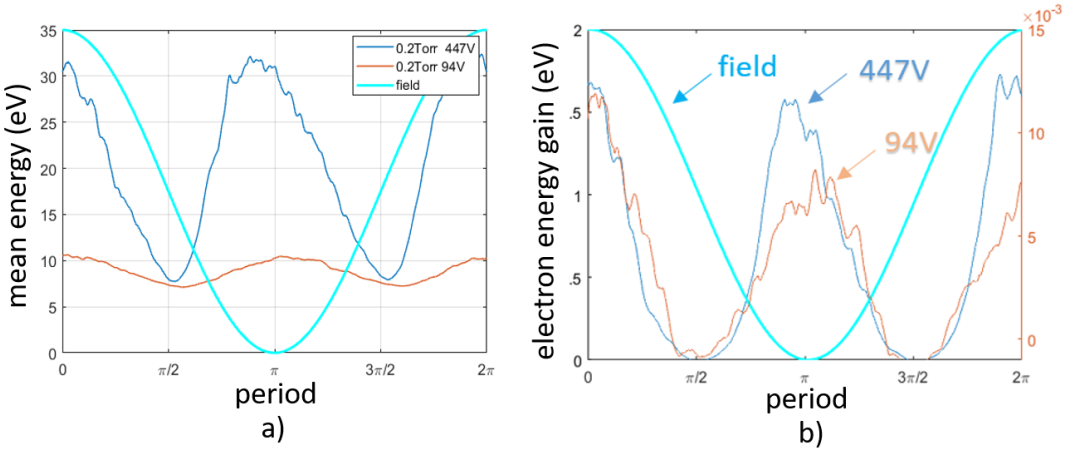

Fig. 2: a) mean energies for point A and D from Fig. 1, b) Gain of energy transferred from AC field to the electron between two collisions for points A and D (Fig. 1) with the same breakdown pressure of 0.2 Torr and different voltages: 447 V and 94 V. Background gas is argon, frequency is 13.56 MHz and gap is 23 mm.

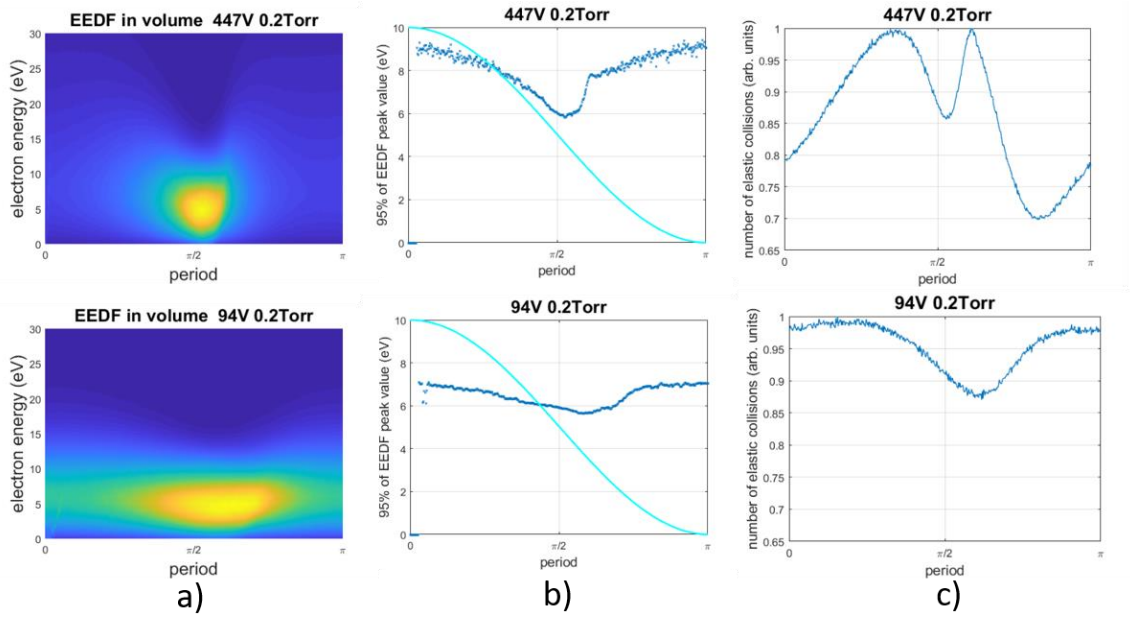

Fig. 3: a) EEDF over half period of time in 2D plots for points A and D (Fig. 1) with the same breakdown pressure of 0.2 Torr and different voltages: 447 V and 94 V. b) Relaxation of the 95% EEDF peak value over one half period for the same points as in Fig. 3a. Light blue line presenting applied AC filed. c) Number of elastic collisions over one half of the period. All features do not present values but only how their shape is changing over half period of time (all are normalized to have maximum at 1). Background gas is argon, frequency is 13.56 MHz and gap is 23 mm.

The moment when discharge induced by the applied AC field ignites, as we know, is a balance of electron production via ionization and losses at electrode surfaces by absorption. Behind rough counting of electron number over time [1, 2] there is a neat energy balance that needs to be fulfilled. When voltage

breakdown curve moves towards high voltages and low pressures, number of collisions with the background gas decreases, breakdown voltage has a steep rise in its value and the amount of energy that electron can get from the AC field between two collisions has a steep growth as well. Rapid increase in electron energy is restricted by the point where electron crosses the gap between two electrodes too fast with insufficient number of collisions to perform ionization and they are being absorbed by the electrode, no matter how high their energy is. At that point, increase in number of collisions is required to randomize electron movement and to increase probability for them to experience ionization before they reach the electrode. Their portions of energy gained from the AC field between two collisions are being reduced but still big enough to overcome ionization threshold before they are lost at the electrode.

Acknowledgments: This research was supported by the Science Fund of the Republic of Serbia, 7739780, APPerTAin-BIOM project and MSTDI-451-03-68/2022-14/200024. Zoran Lj Petrović is grateful to the SASA project F155.

References:

[1] Savić M, Radmilovic-Radjenovic M., Šuvakov M., Marjanović S., Marić D., Petrović Z. Lj, *IEEE T Plasma Sci*. **39** (2011) 2556.
[2] Puač M., Marić D., Radmilović-Radjenović M., Šuvakova M., Petrović Z. LJ, *Plasma Sources Sci. Technol*. **27** (2018) 075013.
[3] Puač M., Đorđević A., Petrović Z. Lj. *European Physical Journal D:* **74** (2020) 74:72.

Enhancing Low-Temperature Plasma Diagnostics: Ultra-High Resolution Spectroscopy with Signal Amplification

Franciszek Sobczuk[1*], Krzysztof Dzierżęga[1], Wojciech Talik[1], Robin Flaugère[2]

[1] *Marian Smoluchowski Institute of Physics, Jagiellonian University, Poland*

[2] *GREMI, UMR 7344, Université d'Orléans/CNRS, F-18020, Bourges Cedex, France*

[(*)] franciszek.sobczuk@uj.edu.pl

The application of laser light scattering technique for low-temperature plasma diagnostics offers a reliable means to determine critical plasma parameters such as temperature and particle concentrations. This method involves analyzing the scattering signal, which encompasses contributions from Thomson, Rayleigh, and Mie scattering processes — reflecting interactions with free electrons, atoms and ions, and dust particles respectively. However, distinguishing between these contributions necessitates ultra-high spectral resolving power ($\mathcal{R} > 10^5$) spectroscopy, a challenge due to the extremely low intensity of scattered light within the apparatus's solid angle. With scattered light pulses often falling below 0.1 fJ within their 6 ns duration, the signal-to-noise ratio (SNR) drops to an exceptionally low level.

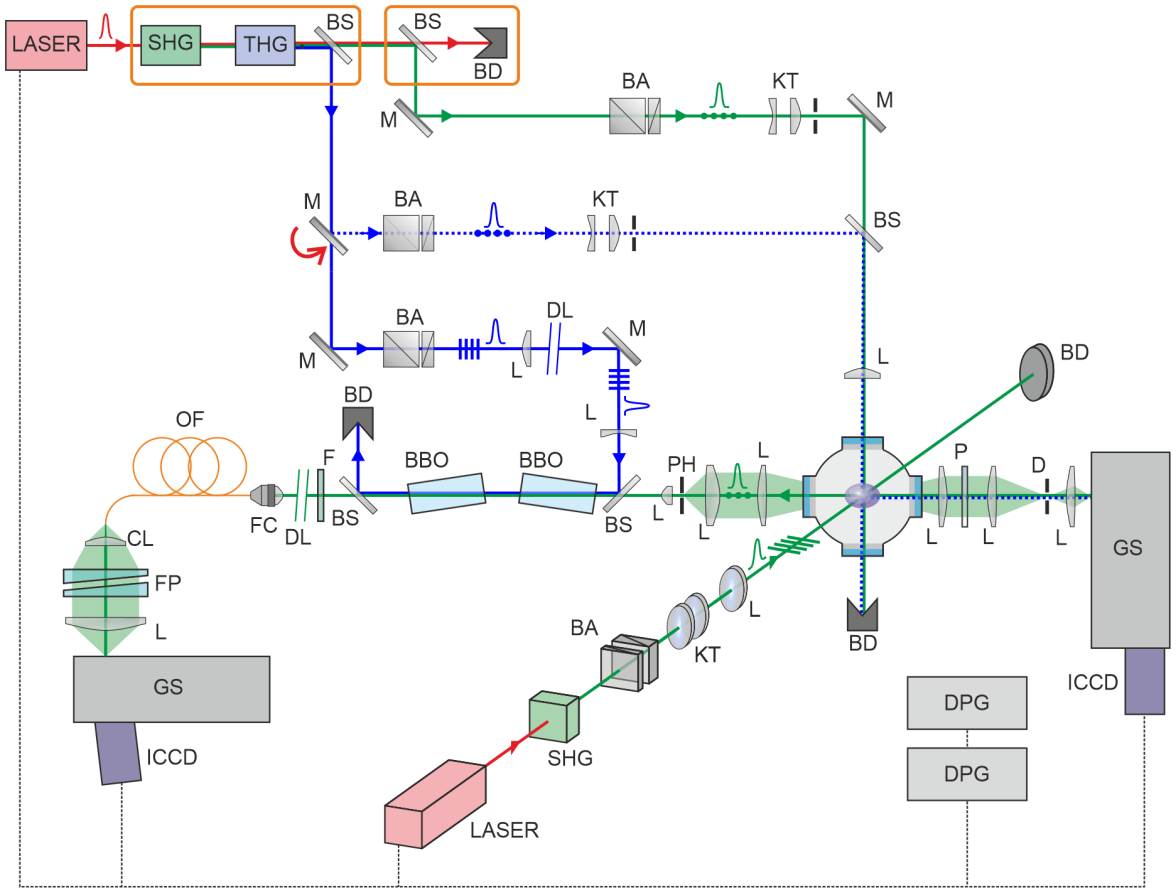

Fig. 1: Scheme of the experimental setup. SHG — 2nd harmonic generator, THG — 3rd harmonic generator, M — mirror, BA — beam attenuator, BS — dichroic mirror, DL — delay line, KT — telescope, L — lens, CL — cylindrical lens, BD — beam dump, D — diaphragm, PH — pinhole, FC — fiber coupler, OF — optical fiber, FP — Fabry-Pérot etalon, GS — grating spectrometer, BBO — beta-barium-borate crystal. The laser at the bottom of the picture generates the plasma in the vacuum chamber. The laser at the top generates the probe beam. The ICCD camera on the right side collects the scattered light in a standard way (using grating spectrometer as a spectrum analyzer). The camera on the left side collects the scattered light amplified by the OPA system and analyzed with a high spectral resolving power by a FP etalon.

To address this issue, we employ a high-finesse ($\mathcal{F}$ > 100) Fabry-Perot (FP) etalon as a spectrum analyzer integrating it with an optical parametric amplifier (OPA). Positioned in front of the FP etalon, this OPA boosts the analyzed light by a factor of approximately 5000, resulting in a 50-fold enhancement of SNR and reducing measurement times from hours to minutes.

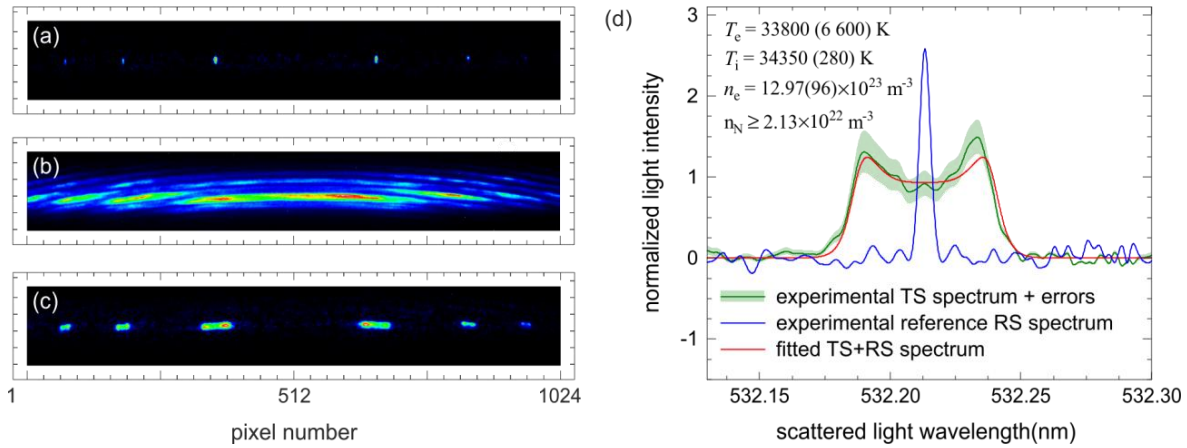

Fig. 2: Interferograms of light scattered on the reference gas (a), light emitted by the laser-induced plasma (b), light scattered on this plasma (c). Example spectrum of the light scattered on the nitrogen plasma (d). This spectrum was used to infer plasma parameters: electron concentration n_e, electron temperature T_e, ion temperature T_i and to estimate concentration n_N of neutral atoms.

During my presentation I will show details of the design of the combined setup for ultrahigh resolution spectroscopy with amplification of weak signals. It is based on the optical parametric amplifier pumped by the 3rd harmonic of Nd:YAG pulsed nanosecond laser and the FP etalon equipped with a grating spectrometer used as a narrow-banded filter. I will present example of laser light scattering spectra registered using this setup. Next, I will consider main limitations of the presented technique. Especially, I will describe the spontaneous parametric down conversion (SPDC) process, which produces majority of the apparatus noise. In principle, it should be possible to obtain near one-photon accuracy of light detection using OPA setup. I will show how it could be possible to approach this quantum-mechanical limitation.

Space charge compensation of pulsed high-current H^- and H^+ ion beams

O Tarvainen(*)[1], B. John[2], R. Abel[1], D. Morris[1], A. Garcia Sosa[1], E. Flannigan[1], A. Letchford[1], D. Emerson[2], D. Faircloth[1]

[1] *UK Research and Innovation, STFC Rutherford Appleton Laboratory, ISIS, Didcot, OX11 0QX, UK*
[2] *UK Research and Innovation, STFC Daresbury Laboratory, Warrington, WA4 4AD, UK*
(*) olli.tarvainen@stfc.ac.uk

Pulsed high-current hydrogen ion beams (H^- and H^+) are used in many large scale accelerator facilities for discovery science and applications, such as high energy particle physics (e.g. at CERN) and spallation neutron production (e.g. at ISIS). The 10-100 mA current / 0.1-10 ms pulses / $10-100$ keV energy beams are produced by plasma ion sources, and transported through a Low Energy Beam Transport (LEBT) section before further acceleration. The pulse repetition rate is 1-100 Hz depending on the accelerator facility. The LEBT section, which is typically 1-3 m long, consists of ion optical focusing elements, e.g. solenoid magnets. The focusing is required for matching the beam into the subsequent accelerator, in particular, for counteracting the repulsive space charge force between the beam particles.

Space Charge Compensation (SCC) is a process that lowers the space charge of the ion beam. The SCC occurs when the H^- or H^+ beam ionises the background gas and traps either positive ions or electrons to the beam potential forming a peculiar "beam-plasma". Significant amount of the beam is lost during the SCC build-up at the beginning of each beam pulse because the beam optics are set to optimise the beam transport at steady-state following the SCC transient. Thus, it is desirable to minimise the SCC time. The beam loss is demonstrated in Fig. 1(a) showing an example of the (normalised) LEBT beam current and the beam current transported through a Radio-Frequency Quadrupole (RFQ) accelerator at the Front End Test Stand (FETS) at ISIS. Unlike the LEBT beam pulse, the RFQ beam current pulse is not square. The initial transient of 75 µs is empirically attributed to poor space charge compensation.

The SCC time τ can be estimated [1] by considering the final SCC degree η, often assumed ~0.9 for high-current beams, the beamline gas density n_{H_2}, the energy-dependent ionisation cross section $\sigma(E_b)$ of the reaction $H^+ + H_2 \rightarrow H^- + H_2^+ + e$ (for H^- beam) or $H^+ + H_2 \rightarrow H^+ + H_2^+ + e$ (for H^+ beam), and the beam velocity v_b:

$$\tau = \frac{\eta}{n_{H_2}\sigma(E_b)v_b}. \quad (1)$$

The beam energy and, hence, the cross section of the beam-induced ionisation are set by the accelerator design, which means that the minimising the SCC time requires increasing the beamline gas pressure. Alternatively, heavier gas with larger ionisation cross section can be injected into the beamline [1]. However, in the case of H^- beam the increased gas pressure or heavy gas injection would lead to increased electron detachment rate or "stripping losses" in $H^- + H_2 \rightarrow H_{\text{fast}} + H_2 + 2e$. The apparent simplicity of the SCC by beam-induced ionisation of the background gas is deceiving. There are no reported cross sections for the H^- induced ionisation of H_2 at relevant energies, which dictates using the H^+ cross section for modelling. The SCC time of H^- beam tends to be overestimated by Eq. 1 as; in the case of Fig. 1 the H^- beam energy in the LEBT is 65 keV and the average beamline gas pressure along the beam path approximately 4×10^{-6} mbar. With σ of 2.2×10^{-20} m^2 [2] the predicted SCC time is 130 µs, which is significantly longer than the experimentally observed 75 µs.

As the SCC process is crucial for the LEBT but cannot be predicted precisely with a simple model, we have launched a campaign to better understand the mechanism. This involves development of bespoke diagnostics for the beam-induced low-density plasma, and a comparative study of H^+ and H^- beams with experiments and Particle-In-Cell (PIC) simulations. The purpose of the comparison is to resolve the uncertainty arising from the use of H^+ ionisation cross section for the H^--driven reaction, and to probe the relevance of different compensating particles (electrons for H^+ and positive ions for H^-) on the SCC dynamics and degree. Furthermore, in the H^- case it is conceivable that the electron impact ionisation, i.e. $e + H_2 \rightarrow H_2^+ + 2e$, affects the SCC time as the electrons liberated by the beam-driven ionisation are propelled to energies corresponding to the beam potential (10-100 eV order of magnitude). Figure 1(b) shows a time-resolved measurement of the beam-induced light emission (obtained

with a Multi-Pixel Photon Counter diode) exhibiting a peak that matches the SCC time determined from the RFQ beam current. The transient is presumably due to initially low SCC degree resulting in high beam potential, which then tapers off towards the equilibrium SCC degree and low beam potential. Figure 1(c) demonstrates that the magnitude of the light emission transient depends on the LEBT beam current, which implies that the beam potential and the electron impact reactions are relevant for the beam-induced light emission. We are currently commissioning a Retarding Field Analyser (RFA) [3] to correlate the beam transport and light emission signals with the dynamics of the beam potential through time-resolved measurement of the energy distribution of the electrons repelled by the H^- beam.

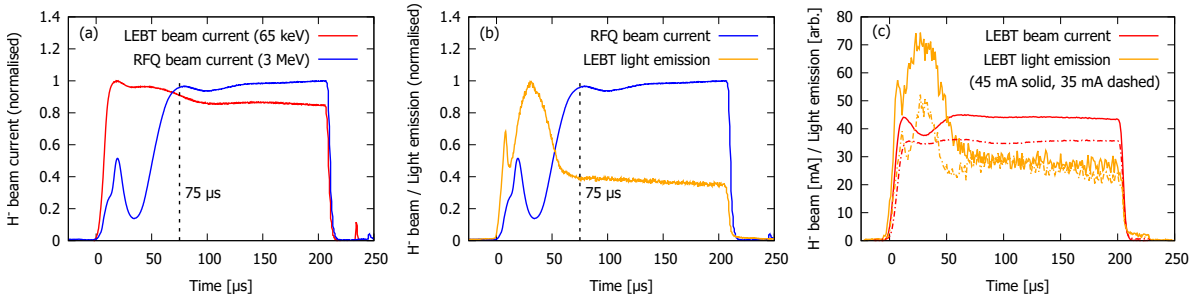

Fig. 1: An example of the space charge compensation. (a) H^- beam pulses in the FETS LEBT and after the RFQ, (b) a comparison of the RFQ beam pulse and LEBT beam-induced light emission, and (c) the effect of the LEBT beam current on the dynamics of the beam-induced light emission.

Figure 2 shows initial PIC simulation results of H^- SCC with PICLas code [4]. The ratio of compensating H_2^+ ions and beam H^- ions in the simulation domain vs. time is plotted for (a) different H_2 pressures (at $0.35\,\mathrm{T}$), (b) different axial magnetic fields (at $1 \times 10^{-5}\,\mathrm{mbar}$), and (c) w/wo including the electron impact ionisation and H^- detachment reactions and corresponding electron energy distributions [2] ($1 \times 10^{-5}\,\mathrm{mbar}$, $0.35\,\mathrm{T}$). When the given ratio is one, the beam potential is zero. The simulation correctly reproduces the neutral gas density dependence of the SCC time and suggests that the previously overlooked LEBT magnetic field could affect the SCC time and final degree. Finally, the PIC simulation implies that the electron impact ionisation has only a small effect on the SCC dynamics, which contradicts the qualitative explanation offered for the light emission transient. The following steps with the PIC simulations include a comparison of the SCC process with H^- and H^+ beams and implementation of wavelength-resolved light emission as an output. Finally, we are exploring the possibility of minimising the SCC time with an external plasma generator producing the compensating particles before the beam pulse. The required plasma density is on the order of $10^8\,\mathrm{cm}^{-3}$, which is attainable with various plasma generator types at relevant H_2 pressures. The effect of the "pre-generated" plasma on the SCC dynamics will be studied first with PICLas simulations and, if found promising, later with experiments.

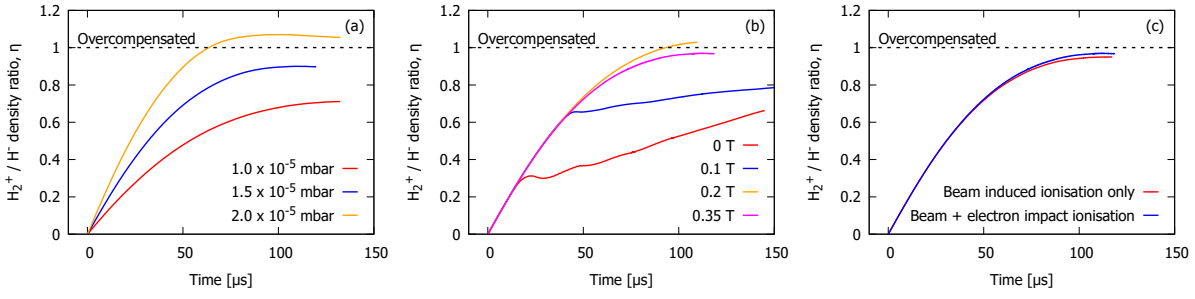

Fig. 2: An example of the PIC simulations of H^- beam SCC. The ratio of compensating H_2^+ ions and beam H^- ions vs. time at (a) different H_2 pressures, (b) axial magnetic fields, and (c) w/wo electron impact ionisation.

[1] C. A. Valerio-Lizarraga *et al.*, Phys. Rev. Accel. Beams **18**, 080101 (2015).
[2] M. E. Rudd, Nuclear Tracks and Radiation Measurements, **16**, pp. 213-218, (1989).
[3] D. Winklehner *et al.*, Rev. Sci. Instrum. **85(2)**:02A739, (2014).
[4] Fasoulas, S. *et al.*, Physics of Fluids, 2019, 31(7): 072006.

Plasma-liquid interactions: overview and perspectives

Peter J. Bruggeman[1*]

[1] *Department of Mechanical Engineering, University of Minnesota, Minneapolis MN 55455, USA*

[(*)] pbruggem@umn.edu

The interaction of liquids with low temperature atmospheric pressure plasmas has been investigated intensively due to its large potential in many applications including plasma-aided decomposition of recalcitrant organic pollutants in water, plasma medicine and material synthesis [1]. These applications leverage the unique ability of plasmas to deliver large fluxes of highly reactive plasma species to liquids. The strong coupling between the plasma and the liquid phase can lead to huge changes in the local plasma properties in the vicinity of the liquid phase while significantly enhancing the complexity of the underpinning processes. This coupling does not only impact the transport of reactive species into the liquid phase, the driving force behind many applications, but can also impact plasma dynamics, stability, and kinetics.

In this presentation, we will report experimental studies on the impact of evaporation on the electron kinetics near the plasma-liquid interface and the development and suppression of plasma instabilities in the presence of a liquid electrode [2]. We will further explore plasma-enabled liquid phase chemistry and show that we can develop quantitative models to describe plasma-induced redox reactions for selected molecules, interactions with biological matter and the synthesis of gold nanoparticles [3,4,5]. We will extend these case studies to currently unexplored liquid phase reactions, highlight some areas that require further research and provide a perspective for opportunities in the field.

Acknowledgement: This work was partially supported by the US Department of Energy, Office of Science, Office of Fusion Energy Sciences, General Plasma Science program, under Award Number DE-SC-0020232 and DE-SC-0024480, the National Science Foundation under Award Number PHY 2020695, and CBET-2318493 and the Army Research Office under Grant Number W911NF-23-1-0377 and W911NF-20-1-0105.

References:

[1] P.J. Bruggeman, R.R. Frontiera, U.R. Kortshagen, et al *J. Appl. Phys.* **129** (2021) 200902
[2] Y. Yue, P. Bruggeman *Plasma Sources Sci. Technol.* **31** (2022) 124004
[3] Y. Yue, S. Exarhos, J. Nam, et al *Plasma Sources Sci. Technol.* **31** (2022) 125008
[4] T. Srivastava, S. Chaudhuri, C. Rich, et al, *J. Chem. Phys*. (accepted)
[5]A. Moldgy, G. Nayak, H.A. Aboubakr, et al, *J. Phys. D: Appl. Phys.* **53** (43) (2020) 434004

Plasma in interaction with water droplets

Augusto Stancampiano(*)[1], Alexandre Devos[1], Pradeep Murugesan[1], Sébastien Dozias[1], Julien Lemaire[1], Pablo Escot-Bocanegra[1], Eric Robert[1]

[1] *GREMI – CNRS/Université d'Orléans, Orléans, France*

(*) augusto.stancampiano@univ-orleans.fr

Cold plasma at atmospheric pressure in or above water is widely studied nowadays for its application in several fields like medicine, agriculture or for the treatment of wastewater. The effects of plasma treated water are due to the creation, inside the water, of reactive oxygen and nitrogen species (RONS) during the plasma treatment. The formation of RONS and therefore the efficiency of plasma system is somewhat limited by the interface between plasma and liquid phases.
The combination of plasma and micrometric droplets (ie. aerosol and spray) could greatly improve the performances of plasma-water systems [1]. Anyway, one of the key point in the study of multiphase plasmas is the understanding of the complex physical and chemical processes occurring during the interaction between plasma and droplets [2]. In order to study those physicochemical aspects, we consider one single water micro droplet trapped in an acoustic levitator exposed to a microplasma. A pin-to-pin tungsten electrodes configuration, connected to a custom high voltage pulse generator (developed by the GREMI) creates a cold atmospheric plasma discharge pathing through or around the droplet (Figure 1). To be able to observe the path of the plasma and the morphology of the droplet we used a double shutter camera coupled with a pulsed laser allowing to take an image of the droplet hit by the plasma as well as follow the droplet evolution at different instants after the interaction.
The study investigate the effect of different parameters, like the size or the conductivity of the water or the voltage delivered to the high-voltage electrode. The obtained results provide new insight on the interaction between plasma and water droplets and encourage the development of new optimized plasma-aerosol devices in the field of agriculture or medicine.

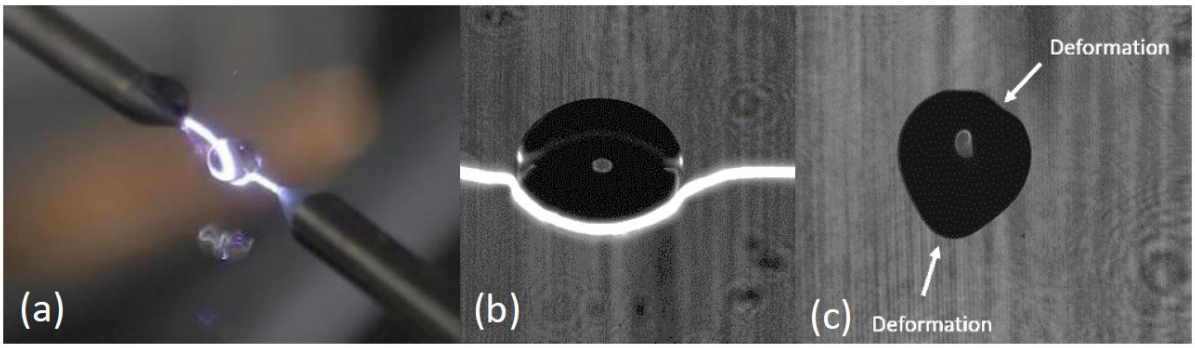

Fig. 1: Photography (a) and high-resolution acquisition (b) of the microplasma droplet interaction between two electrodes, droplet deformation after microplasma droplet interaction.

Acknowledgements: National founded project PLASMASOL - ANR-23-CE04-0003

[1] N. S. L. Chew, K. S. Wong, W. S. Chang, C. W. Ooi, L. Y. Yeo, et M. K. Tan, « Nanoscale plasma-activated aerosol generation for in situ surface pathogen disinfection », *Microsyst. Nanoeng.*, vol. 8, p. 41, 2022, doi: 10.1038/s41378-022-00373-3.

[2] A. Stancampiano *et al.*, « Plasma and Aerosols: Challenges, Opportunities and Perspectives », *Appl. Sci.*, vol. 9, nº 18, Art. nº 18, janv. 2019, doi: 10.3390/app9183861.

Deep Learning for Low-Temperature Oxygen-Based Plasmas Modelling

M Valente[1], M Gonçalves[1], T C Dias[1], R Ventura[2], V Guerra[(*)1]

[1] *Instituto de Plasmas e Fusão Nuclear, Instituto Superior Técnico, Universidade de Lisboa, Avenida Rovisco Pais, Lisboa 1049-001, Portugal*

[2] *Instituto de Sistemas e Robótica, Instituto Superior Técnico, Universidade de Lisboa, Avenida Rovisco Pais, Lisboa 1049-001, Portugal*
[(*)] *vguerra@tecnico.ulisboa.pt*

Low-temperature plasmas (LTPs) are versatile in their applications, finding uses in areas ranging from plasma medicine to CO_2 conversion for *in-situ* resource utilisation [1,2]. While experimental studies provide valuable physical parameters for these systems, a comprehensive understanding of LTPs necessitates a synergy of experimental and modelling efforts. Models can access crucial information unattainable by experiments alone. However, plasma simulations, while essential, can often be computationally intensive [3]. Surrogate models mitigate this limitation by offering quick approximations of complex systems, crucial for optimisation, real-time decision-making, and analysing large-scale problems [4]. Conversely, accurate modelling of LTPs presents challenges due to the complex plasma chemistry and uncertainties in input parameters. A key aspect of LTP modelling is developing an accurate kinetic scheme, which involves identifying relevant reactions and determining their rate coefficients. This task is complicated by the limited available knowledge of rate coefficients [5], often derived through time-consuming trial-and-error methods.

In this work, we apply deep learning to tackle both the modelling and parameter recovery challenges in plasma physics, illustrating the benefits of merging physical insights with machine learning to improve the accuracy and efficiency of models. The system under study is an oxygen plasma created by a DC glow discharge at gas pressures of $p = 0.2 - 10$ Torr and discharge currents of $I = 10 - 40$ mA. The reason for this choice is twofold. On the one hand, this system exhibits a high degree of complexity, as its properties depend on the interplay between electron, vibration, chemical, ion and surface kinetics. On the other hand, a detailed reaction mechanism was recently developed [3], providing an ideal test bed for the proposed novel approaches.

Surrogate models can be designed to predict steady-state species concentrations, temperature, and transport coefficients as a function of the reactor's relevant operating conditions. Since data collection can be costly, encoding prior physics knowledge into the neural network (NN) can be helpful as it amplifies the available information. Modern physics-informed machine learning methods include a penalty term in the loss function, discouraging deviations from physical constraints and efficiently guiding the model toward the correct solution [6]. However, these models do not guarantee that, after training, the outputs for unseen inputs will satisfy such constraints. Here, we propose a novel approach for integrating physical information into the deep learning model. Our method involves projecting the model's predictions onto a manifold defined by the constraint $g(x, y) = 0$, where x is the model's input, y is the model's output and $g(x, y)$ is a vector-valued constraint function that is zero if, and only if, those physical laws are satisfied. To that aim, through sequential quadratic programming, we formulate the projection operation as a constrained optimisation problem

$$minimise\ ||p - f(x;\Theta)||_W^2\ , \quad s.t.\ g(x,p) = 0 \qquad (1)$$

where W is a symmetric positive definite weighting matrix, i.e. $||v||_W^2 = v^T W v$, $f(x;\Theta)$ is the machine learning parametric model and Θ is the model parameter vector [7]. This projection is pivotal in guiding the network to adhere to the physical laws governing plasma behaviour, enhancing the model's accuracy and minimising the dataset's training size. We have developed a surrogate model to the reaction mechanism developed in [3]. The physical laws included in the constraint function are the ideal gas law, the quasi-neutrality condition, and the relation between the discharge current and electron density. Fig. 1 compares the NN modelling and target simulation values of the concentration of ground state positive ions O_2^+, denoted as O2(+, X), as a function of pressure and for $I = 30$ mA. It evidences the method's

ability to improve the pressure-related trend, yielding predictions that closely match those observed in the simulation. The mean error in predicting this species is reduced from 1.2% to 0.5%. Moreover, this technique reduces the error of compliance with physical laws to below 0.50% of its original value, ensuring adherence to the imposed physical laws.

We carried out an additional study to extend the use of deep NNs to automate the prediction of a selected set of rate coefficients within this oxygen-based plasma scheme. Our framework comprises data generation using the LoKI-B+C modules [8] of the LisbOn KInetics (LoKI) simulation tool, data processing, architecture search, and hyperparameter tuning. This deep learning model is trained on artificial data generated by LoKI-B+C with sampled reaction rate coefficients around their established reference values. The aim is for the model to accurately recover these coefficients. The NN, receiving the steady-state densities of species as input, under various experimental conditions, learns to inversely map the simulations, thereby determining the reaction rate coefficients. We consider the prediction of seven rate coefficients based on heavy-species densities under diverse pressure and current conditions. The model effectively predicts rate coefficients with a mean relative error of 2.00% across predictions, showcasing its reliability as a proof-of-concept.

Future work will broaden the scope of the study to include more reactions, rate coefficients, and plasma systems and operating conditions. This expansion will also incorporate experimental data and explore diverse chemistries (*e.g.* CO_2, CH_4, N_2-H_2) and plasma-surface interactions, enriching the model's applicability and accuracy.

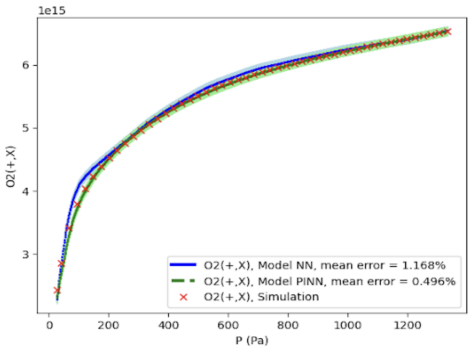

Fig. 1: Comparison between NN predictions and simulation values of the concentration of O_2^+ as a function of pressure, for a reactor radius of 12 mm and $I = 30$ mA, before projecting the model's predictions and after projecting the model's predictions.

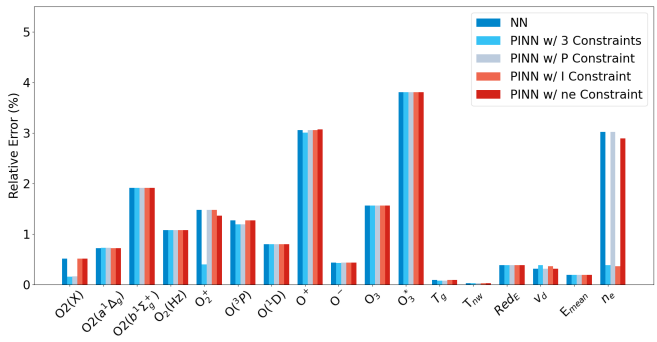

Fig. 2: For each output, comparison of the relative errors of the standard NN model; NN with each of the physical constraints applied individually; and NN with the three constraints applied simultaneously.

This work was partially supported by the Portuguese FCT-Fundação para a Ciência e a Tecnologia, under funding to IPFN (DOI: 10.54499/LA/P/0061/2020, 10.54499/UIDB/50010/2020, 10.54499/UIDP/50010/2020, and 10.54499/PTDC/FIS-PLA/1616/2021); and to LARSyS (DOI: 10.54499/LA/P/0083/2020, 10.54499/UIDP/50009/2020 and 10.54499/UIDB/50009/2020).

[1] V. Guerra *et al* (2022). Journal of Applied Physics, 132(7), 070902.
[2] M. Laroussi *et al* (2021), IEEE Trans. Rad. Plasma Med. Sci. 6(2), 127-157
[3] T. C. Dias *et al* (2023). Plasma Sources Science and Technology, 32(8), 084003.
[4] P.W. Hatfield *et al* 2021 Nature 593 351–361.
[5] M. Hanicinec *et al* (2023). Journal of Physics D: Applied Physics, 56(37), 374001.
[6] M. Raissi *et al* 2019 Journal of Computational Physics 378 686-707.
[7] J. Nocedal and S.J. Wright 2006 Numerical Optimization Springer.
[8] A. Tejero-del-Caz *et al* (2019). Plasma Sources Science and Technology, 28(4), 043001

Formation of O and H radicals in an atmospheric-pressure nanosecond pulsed discharge in helium with water vapour admixtures

A. Brisset[1], M. Bieniek[2], L. Invernizzi[3], J. Walsh[4], M. Hasan[5], E. Wagenaars[4*]

[1] *EM2C, CNRS, CentraleSupélec, Université Paris Saclay, Gif-sur-Yvette, France*

[2] *The University of Antwerp, Department of Chemistry, Campus Drie Eiken, Wilrijk, Belgium*

[3] *Laboratoire des Sciences des Procédés et des Matériaux, LSPM, CNRS, Université Sorbonne Paris Nord, Villetaneuse, France*

[4] *York Plasma Institute, School of Physics, Engineering and Technology, University of York, York, UK*

[5] *Department of Electrical Engineering and Electronics, University of Liverpool, Liverpool, UK*

(*) erik.wagenaars@york.ac.uk

1 Introduction

Plasma-produced O-, H- and N-species that have a high oxidative power and play major roles in biological functions are extensively studied for applications. In particular, plasmas containing water vapour are studied for the production of reactive species such as OH, H_2O_2, HO_2 [1]. Even though the plasma chemistry is complex and not fully understood, it is clear that atomic oxygen and hydrogen radicals play a crucial role in these plasmas.

The aim of this work was to investigate the kinetics of reactive O and H radicals in a fast pulsed discharge (rise rate ~80 V/ns) generated at atmospheric pressure in humid Helium (up to 0.25% H_2O). O and H densities are obtained experimentally by ps-TALIF (Two-photon Absorption Laser Induced Fluorescence) and are combined with 1D fluid modelling to investigate the reaction mechanisms for O and H production.

2 Methodology

The plasma has a pin-to-pin electrode geometry with a gap of 2.2 mm. A discharge in Helium with a water vapour content of 0.1% – 0.25% is created through a positive high-voltage nanosecond pulse to one of the pins. The pulse has a voltage of about 2 kV, 35 ns rise time (10-90%) and 90 ns duration FWHM. The energy dissipated in the discharge is 90 μJ and the repetition rate is 5 kHz.

TALIF is used to measure the densities of O and H radicals. Details of this method can be found in [2].

The 1D plasma fluid model used is based on a system of differential equations: continuity of the flux density of electrons, electron energy, ions, and neutral species, and Poisson's equation. Full details can be found in [2].

3 Results

The results of the TALIF experiments and the 1D fluid modelling are presented in figures 1 and 2. Figure 1 shows the temporal evolution of the O density from both the experiment and the model for H_2O admixtures of 0.1% and 0.25%. Figure 2 shows the equivalent H densities.

The model and experiment have a reasonable agreement, within a factor of 2 for both densities. From both figures it is clear that the main production of O and H occurs after the voltage pulse has finished. For 0.1% water, the O density builds up over ~1-2 ms to a value of approximately $2\text{x}10^{16}$ cm^{-3}. From 10-100 ms, the O density decays again. For 0.25% water content the O density is enhanced by roughly 40%. In the experiments, the peak in O density occurs earlier, at about 0.3 ms. This is not reproduced in the modelling.

The situation for H is similar, for both water admixtures there is a rapid increase in H density in the early pulse afterglow (<1 ms). Densities of the order of $0.2–1.0\text{x}10^{16}$ cm^{-3} are observed, with the densities for 0.25% water being 50-100% higher than 0.1% water.

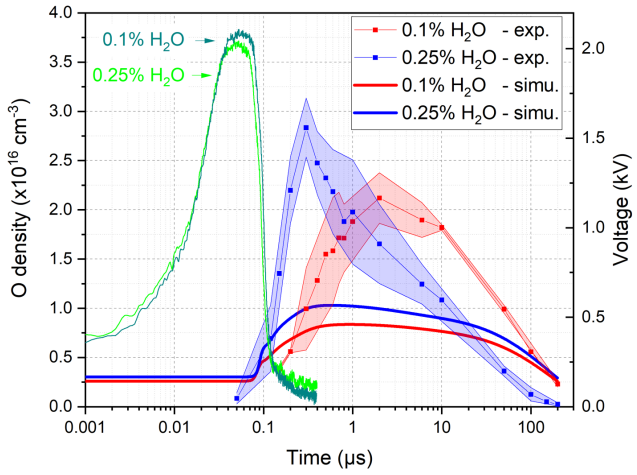

Figure 1: Temporal evolution of O density for 0.1% and 0.25% water admixture. Both modelling and experimental results are presented [2].

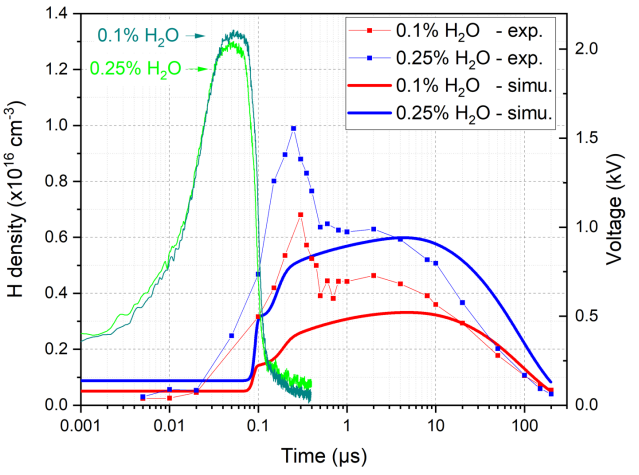

Figure 1: Temporal evolution of H density for 0.1% and 0.25% water admixture. Both modelling and experimental results are presented [2].

4 Discussion and conclusion

The delay of the production of O and H relative to the voltage pulse is surprising since it is often assumed that the dominant production mechanism is direct electron-impact dissociation. Analysis of the reaction pathways from the modelling show that there is a distinct change in reaction mechanisms during the discharge cycle. During the voltage pulse O is predominantly produced through electron-impact dissociation of O_2. For H, the dominant mechanism is electron-impact dissociation of H_2O. However, most of the O and H radicals are produced in the early afterglow (up to 1 μs) through recombination processes of O_2^+ and H_2^+. It can therefore be concluded that not only the discharge itself, but also the (early) afterglow of pulsed discharges need to be considered when studying O and H-based plasma chemistries.

Acknowledgments

The authors acknowledge the support of the Engineering and Physical Science Research Council (Project No EP/S026584/1 and EP/S025790/1).

References

[1] A. Brisset, A.R. Gibson, S. Schröter, K. Niemi, J.-P. Booth, T. Gans, D. O'Connell, E. Wagenaars, *J. Phys. D: Appl. Phys.* **54** (2021) 285201.

[2] A. Brisset, M. Bieniek, L. Invernizzi, M. Hasan, J. Walsh, K. Niemi, E. Wagenaars, *Plasma Sources Sci. Technol.* **32** (2023) 065004.

POSTER SESSION 1, Wednesday, July 10, 14:30-16:30

P1-T1-01 S. Raskar; H. Telfah; and **I. V. Adamovich**; *Measurements of Excited Metastable Species and Associative Ionization in a Heated Nonequilibrium Flow Plasma Reactor*

P1-T1-02 J. Suijker; **B. Bagheri**; *The reaction mechanisms between atomic oxygen and water using high-level quantum mechanical calculations*

P1-T1-03 K. Lemishko; **S. Mohr**; A Nelson; J Tennyson; *Machine learning estimator for electron impact ionisation fragmentation patterns*

P1-T2-04 **S.K. Kodanova**; M.K. Issanova; T.S. Ramazanov; *Investigation of the Coulomb Logarithm for transport coefficients in warm dense matter*

P1-T3-05 **A. Pikalev**; X. Chen; V. Guerra; G .Zhang; M. C. M. van de Sanden; *Insights into CO_2 conversion with plasma-electrolysis synergy*

P1-T3-06 **Y. Inagaki**; Y. R. Hayashi; N. Shirai; S. Takakusagi; and K. Sasaki; *Direct conversion of benzene to phenol in plasma-irradiated aqueous solution*

P1-T3-07 **J. Gans**; Q. Shen; A. Hughes; C. van Deursen; W. Bongers; F. Peeters; M.C.M van de Sanden; *Nitrogen fixation: Synergy between microwave plasma and catalyst*

P1-T3-08 **V. Kudrle**; T. Vaněčková; O. Jašek; Z. Bonaventura; R. Brunovský; Z. Navrátil; P. Slavíček; *Possibilities of plasma conversion of CO_2 and H_2/H_2O to CH_4 at extraterrestrial conditions*

P1-T4-09 A.S. Stodolna; T.W. Mechielsen; **K. Papamichou**; S. Oostrom; V. Navarro Paredes; M. van de Kerkhof; *Studying the interaction of scanner materials with EUV-generated plasma*

P1-T4-10 **J. Pawlat**; K. Wolny-Koladka; P. Terebun; M. Kwiatkowski; D. Zarzeczny; M. Zdaniewicz; S. Bodziacki; *Processing of diatomaceous earth after beer filtration process with non equilibrium plasma*

P1-T4-11 **A. Saito**; T. Nozaki; T. Miyazaki; Y. Inagaki; K. Sasaki; *Distribution of radicals in plasma catalysis for CO_2 methanation using an atmospheric pressure plasma jet*

P1-T4-12 **M.S. Benilov**; *Ionization layer with collision-free atoms at the edge of partially to fully ionized plasmas*

P1-T4-13 **C. Cro**; H. Kaufmann; N. Almeida; P. Almeida; M. Benilov; *Phenomenological description of vacuum breakdown and detailed modelling of cathode spots*

P1-T4-14 **D. Zarzeczny**; J. Pawłat; P. Terebun; M. Kwiatkowski; A. Starek-Wójcicka; M. Krajewska; E. Grządka; B. Chudzik; *The impact of plasma treatment using the GlidArc generator on apple juice in a stationary and flow system*

P1-T4-15 **D. F. N. Santos**; N. A. Almeida; L. G. Benilova; M. S. Benilov; *Modelling non-equilibrium near-cathode plasma at layers ignition of high-pressure arcs on refractory cathodes*

P1-T4-16 **P. Viegas**; A. Filipe; J. Silveira; T. C. Dias; A. S. Morillo-Candas; O. Guaitella; V. Guerra; *Surface recombination in Pyrex in CO_2 DC glow discharges*

P1-T5-17 **W. Khan**; P. Dvorak; *Concentration and rotational temperature of N_2 ions in RF plasma jet measured by LIF*

P1-T5-18 A.D. Pajdarova; M. Farahani; **T. Kozak**; J. Capek; *Reverse discharge in bipolar HiPIMS and its dependence on magnetic field geometry*

P1-T5-19 **F.J. Arellano**; M. Kusaba; S. Wu; R. Yoshida; S. Hamaguchi; *Machine learning prediction of the electron density and the electron energy distribution function from the optical emission spectra*

P1-T5-20 **A. Meindl**; C.K. Kiefer; R. Antunes; A. Hecimovic; U. Fantz; *Investigation of Stark broadening in plasma conversion reactors by means of high resolution optical emission spectroscopy*

P1-T5-21 **C. Pascual-Fort**; A. Brisset; N De Oliveira; N. Minesi; C..O Laux; G..D Stancu; *Spatial characterization of N(4S) in a microwave plasma jet at atmospheric pressure by fs-TALIF*

P1-T5-22 M. Krbal; **D. Prokop**; L. Kuthanova; S. Kadlec; T. Hoder; *Breakdown with solid insulation flashover in naturally occurring gases; SF_6; and its alternatives*

P1-T5-23 **D.J. Schreuder**; G. Mattausch; B. Zimmermann; E. von Hauff; *Optical Emission Spectroscopy of an Electron Beam Sustained Hybrid Discharge of Nitrogen at 1 mbar*

P1-T5-24 **D. Maletic**; N. Selakovic; D. Popovic; S. Milosevic; G. Malovic; Z Lj Petrovic; *Mass spectrometry measurements of the capillary single electrode helium plasma jet*

P1-T5-25 **D. Sadi**; E. Baratte; T. Silva ; O. Guaitella; *Ro-vibrational temperatures of CO(X) deduced from emission of third positive and angstrom system of CO in CO_2 glow discharge*

P1-T5-26 **E. Maťaš**; M. Neogrady; L. Moravsky; S. Matejcik; *Quantitative analysis of NO_2 generated in Atmospheric Pressure Plasma Jet using Ion Mobility Spectrometry*

P1-T5-27 **G. F. Alfaro**; M. N.Shneider; A. Gerakis; *Coherent scattering from ponderomotive-driven density perturbations for plasma diagnostics*

P1-T5-28 **G. Kreyder**; D. Stefas; L. Invernizzi; G. Lombardi; K. Gazeli; S. Prasanna; S.M. Starikovskaia; *Nitrogen atoms ps-TALIF in atmospheric pressure*

P1-T5-29 **P. Hartmann**; J. Carmona-Reyes; L.Y. Luo; L. Matthews; T. Hyde; *Mapping the field around a Langmuir probe with charged dust particles*

P1-T5-30 **J. Hnilica**; K. Bernatova; P. Klein; Z. Hubicka; M. Cada; P. Vasina; *Time and energy-resolved mass spectrometry study of the HiPIMS discharge operated in Ar and Ar-N_2 atmospheres*

P1-T5-31 G. Tetard; A. Michau; **S. Prasanna**; P. Brault; K. Hassouni; *Self consistent simulation of dust formation and dynamic in non-equilibrium RF Ar-acetylene plasma*

P1-T5-32 **K. Jurik**; M. Stastny; P. Drexler; K. Mrozek; A. Obrusnik; *Analysis of a radiofrequency-driven resonant plasma source*

P1-T5-33 **K. Sasaki**; K. Fushimi; N. Shirai; *Measurement of negative ion density in streamer discharge in air by transient cavity ringdown spectroscopy*

P1-T6-34 **M. D. Acciarri**; ***C. Moore***; S. D. Baalrud; *Particle in Cell Simulations and Correlation Heating*

P1-T6-35 **H. Akashi**; K. Mizuno; T. Yoshinaga; *Optimization of Null Collision Method in Monte Carlo Model*

P1-T6-36 F. Taccogna; **A. Panarese**; P. Minelli; F. Cichocki; *Particle-in-Cell modeling of SPIDER negative ion source*

P1-T6-37 **A. Popoli**; G. Pierotti; F. Ragazzi; A. Cristofolini; *Development of an efficient plasma global model in MATLAB*

P1-T6-38 T. C. Dias; V. Guerra; **C. D. Pintassilgo**; *Electron kinetics in AC electric fields: testing the limitations of the HF approximation in the two-term Boltzmann equation*

P1-T6-39 T. C. Dias; **V. Guerra**; *Are local field and local energy approximations appropriate for nanosecond discharges?*

P1-T6-40 **C. H. Moore**; A.K. Jindal; R. Martinez; A. Padgett; *Comparison of 2D and 3D PIC-DSMC Simulations of Pin-to-Plane Breakdown Through a Thin-Film Dielectric Coated Electrode*

P1-T6-41 **D. Nikic**; A. Fierro; C.H. Moore; J.M. Lehr; *Simulations of centimeter-scale, atmospheric pressure, positive streamer discharges using EMPIRE-PIC*

P1-T6-42 **D. Eremin**; L. Vogelhuber; J. Kallaehn; K. Koehn; D. Krueger; L. Xu; R.P. Brinkmann; *Nonadiabatic energization of electrons in spokes observed in magnetrons with a nonuniform magnetic field*

P1-T6-43 T. M. Santos; **E. Calvo**; J. P.L. Monteiro; P. Sa; M. J. Pinheiro; *Towards Sustainable Space Exploration: Assessing Hall Thrusters for CubeSat Missions*

P1-T6-44 T. M. Santos; **E. Calvo**; J. P.L. Monteiro; P. Sa; M. J. Pinheiro; *Design and Validation of a Low-Power Hall Thruster for CubeSats: A Scaling Laws Approach*

P1-T6-45 **E. Litch**; H. Lee; S. K. Nam; M. J. Kushner; *Pulsed Low Bias Frequencies for High Aspect Ratio Plasma Etching*

P1-T6-46 **F. Taccogna**; P. Minelli; F Cichocki; *Particle-in-Cell modeling of needle-to-plate ns-pulse spark discharge*

P1-T6-47 **G. Huebner**; N. Schoeneweihs; D. Filla; S. Wilczek; T. Mussenbrock; I. Korolov; *The effect of gas pressure on plasma dynamics in surface dielectric barrier discharges driven by nanosecond voltage pulses*

P1-T6-48 **G. Fubiani**; F. Gaboriau; L. Garrigues; *PIC-MCC modelling of the dynamics of rotating spokes in a Penning discharge*

P1-T6-49 **I. Tsonev**; O. Biondo; A. Bogaerts; *Simulation of a pulsed CO_2 plasma based on a six-temperature energy approach*

P1-T6-50 **J. Skacel**; P. Parodi; G. Gangemi; F. Bariselli; T. Magin; Z. Bonaventura; *Simulation of Space Platform Charging in Very Low Earth Orbit with Particle Methods*

P1-T6-51 D. Simoes; J. Martins; S. Baghel; J. P. Booth; D. R.. Ferreira; O Guaitella; L. Marques; N. Pinhao; C. D. Pintassilgo; **L. L. Alves**; *Plasma-surface coupled modelling of ammonia production in DC discharges*

P1-T6-52 **A. Malagon-Romero**; J. Teunissen; *Towards efficient data-driven numerical models for streamer discharges*

P1-T6-53 **R. Almeida**; P. Almeida; G. Naidis; M. Benilov; *Dynamics of Breakdown along a Dielectric Surface in Air at 1 atm*

P1-T6-54 **J. P. Booth**; S. Zhang; and G. A. Curley*; Oxygen atom kinetics in pulsed Radiofrequency Capacitively-coupled plasmas at intermediate pressures*

P1-T6-55 S. Zhang; A. Alvarez Laguna; N. Lequette and **J. P. Booth**; *Modelling for RF-CCPs at Intermediate Pressure: Doubts on Drift-Diffusion Models*

P1-T7-56 **A. U. Utegenov**; Ye. Yerlanuly; Zh. Onaybergenov; A. Abdrakhmanov; S.A. Orazbayev; T.S. Ramazanov; *Characterization of nanomaterials obtained in DC glow discharge plasma of Ar-C_2H_2*

P1-T7-57 **T. Miyazaki**; K. Sasaki; N. Shirai*; Influence of gas temperature and neutral particle density on self-organized luminous patterns in atmospheric-pressure DC glow discharge*

P1-T8-58 **A. Robledo-Martinez**; L. A. Garcia-Villarreal; C. Gonzalez-Armendariz; J. M. Basurto; *Lightning discharges in a Jovian atmosphere*

P1-T9-59 **A. Derzsi**; R. Masheyeva; F. Beckfeld; J. Schulze; Z. Donko; *Determination of the effective secondary electron emission coefficient for low-pressure RF discharges based on pixel-based similarity of spatio-temporal excitation map images*

P1-T9-60 **Z. Donko**; B. Z. Bentz; P. Hartmann; A. Derzsi*; Electron density measurements and calculations in a helium capacitively-coupled radio-frequency plasma*

P1-T9-61 **E. Juengling**; S. Wilczek; T. Mussenbrock; M. Boeke; A. von Keudell; *Plasma sheath tailoring by a magnetic field for three-dimensional plasma etching*

P1-T9-62 **G. Saab** ;C..Lahoud; S..Youssef; M..Mikikian*; Fluid simulation of a CCRF dusty plasma using COMSOL: First stage under dust-free conditions*

P1-T9-63 **J. Thiel**; Ts. V. Tsankov; U. Czarnetzki; *Multidimensional effects in low-pressure discharges*

P1-T9-64 **M. Matasova**; M. Klas; P. Cermak; S. Matejcik; *Statistical analysis of microgap vacuum breakdown mechanisms for palladium electrodes in pulsed electric fields*

P1-T9-65 **T.W. Mechielsen;** A.S. Stodolna; P. Van der Walle; C.J Meekens; H. Lensen; *A novel low-temperature hydrogen plasma source for EUV lithography applications*

P1-T10-66 **A. Takacova**; T. Orriere; G. Gomit; T. Hoder; *Investigation of a liquid droplet affected by an electrical charge injection*

P1-T10-67 J. Haton; **A. Belinger**; S. Dap; L. Stafford and N. Naude; *Memory effect of a diffuse dielectric barrier discharge obtained in air: surface and volume mechanisms*

P1-T10-68 **P. Bilek**; G. Arora; P. Hoffer; V. Prukner; M. Simek; *Radially and axially resolved optical emission observed during the initial phase of nanosecond discharge in liquid water*

P1-T10-69 **C. Bajon**; E. Barrate; D. Sadi; O. Guaitella; A. Belinger; S. Dap; T. Hoder; N. Naude; *CO_2 and CO vibrational excitation in Townsend and filamentary DBD at atmospheric pressure: in situ FTIR measurements*

P1-T10-70 **J. Cech**; P. Stahel; D. Trunec; R. Hornak; L. Prokes; P. Rudolf; B. Marsalek; E. Marsalkova; P. Lukes; Z. Machala; *CaviPlasma: The properties of energy-efficient plasma source for the treatment of liquids on the scale of cubic metres per hour*

P1-T10-71 **C. K. Kiefer**; R. Antunes; A. Hecimovic; A. Meindl; U. Fantz; *CO_2 dissociation using a lab-scale microwave plasma torch: an investigation of industrially relevant parameters*

P1-T10-72 **D. Aceto**; P. R. Rotondo; M. Ambrico; G. Dilecce; F. Faretra; R. M. De Miccolis Angelini; P. F. Ambrico; *Atmospheric Pressure: Low Temperature Plasma applications for decontamination of agrifood products*

P1-T10-73 S. Marin-Meana; M. Oliva-Ramirez; **M.C. Garcia**; J. Cotrino; A.R. Gonzalez-Elipe; A. Gomez-Ramirez; *Optical emission spectroscopy characterization of a novel atmospheric pressure argon-ammonia gliding arc*

P1-T10-74 **E. Benova**; P. Marinova; T. Bogdanov; Y. Todorova; M. Kirilova; I. Yotinov; I. Schneider; Y. Topalova; *Toxicity reduction of landfill leachate by direct plasma treatment*

P1-T11-75 **A. Ashirbek**; Ye. Ussenov; M. Dosbolayev; M. Gabdullin; T. Ramazanov; *Impact of convective flow on filaments in narrow gap DBD*

P1-T11-76 **L. Alomari**; T. Orriere; R. Bellanger; B. Teychene; E. Moreau; *Investigation of the liquid velocity gradient induced by a plasma dielectric barrier discharge and its impact on reactive species generation*

P1-T11-77 **N. Bente**; H. Piquet; N. Merbahi; E. Bru; *Thermal modelling of an atmospheric pressure cylindrical DBD reactor for NO_x removal*

P1-T12-78 **S. J. Shetty**; S. Atikukke; M. Veis; T. Roch; P. Veis; *Studies of the self-absorption of boron doublet at 249 nm for an accurate Cf-LIBS analysis of diboride thin layers*

Measurements of Excited Metastable Species and Associative Ionization in a Heated Nonequilibrium Plasma Flow Reactor

S. Raskar, H. Telfah, and I.V. Adamovich(*)

[1] *Department of Mechanical and Aerospace Engineering, Ohio State University, Columbus, OH 43210*

(*) adamovich.1@osu.edu

Time-resolved, absolute number densities of metastable nitrogen molecules, $N_2(A^3\Sigma_u^+,v=0,1)$, and molecular ions, N_2^+, as well as the gas temperature, are measured in nitrogen and N_2-NO mixtures in a heated plasma flow reactor with optical access for laser diagnostics, at the pressure of P=100 Torr and temperatures of T=300-1000 K. The gas mixture in the reactor is excited by the ns pulse discharge bursts operated at a high pulse repetition rate, up to 100 kHz, generating a diffuse plasma with well-defined boundaries. The measurements are made by the cw Tunable Diode Laser Absorption Spectroscopy (TDLAS) and pulse UV Cavity Ring Down Spectroscopy (CRDS). The results illustrate the generation and decay of $N_2(A)$, a precursor for metastable excited atoms, during the discharge burst. Time-resolved N_2^+ measurements in the afterglow exhibit its transient rise with a subsequent decay, indicating the effect of associative ionization of excited species accumulated during the discharge burst. Since $N_2(A)$ decays significantly during the discharge burst, due to the accumulation of N atoms [1], this suggests that the excited species resulting in the associative ionization are the metastable N atoms generated during the $N_2(A)$ quenching by the ground state nitrogen atoms, e.g.

$$N_2(A^3\Sigma_u^+) + N \rightarrow N_2\left(X^1\Sigma_g^+\right) + N(\,^2P,\,^2D)\,, \tag{1}$$

$$N(^2P) + N(^2P) \rightarrow N_2^+ + e^-. \tag{2}$$

Future work will focus on the direct measurements of the excited atoms by the vacuum UV absorption spectroscopy, and of NO^+ ions by mid-IR, cw Cavity Ring Down Spectroscopy.

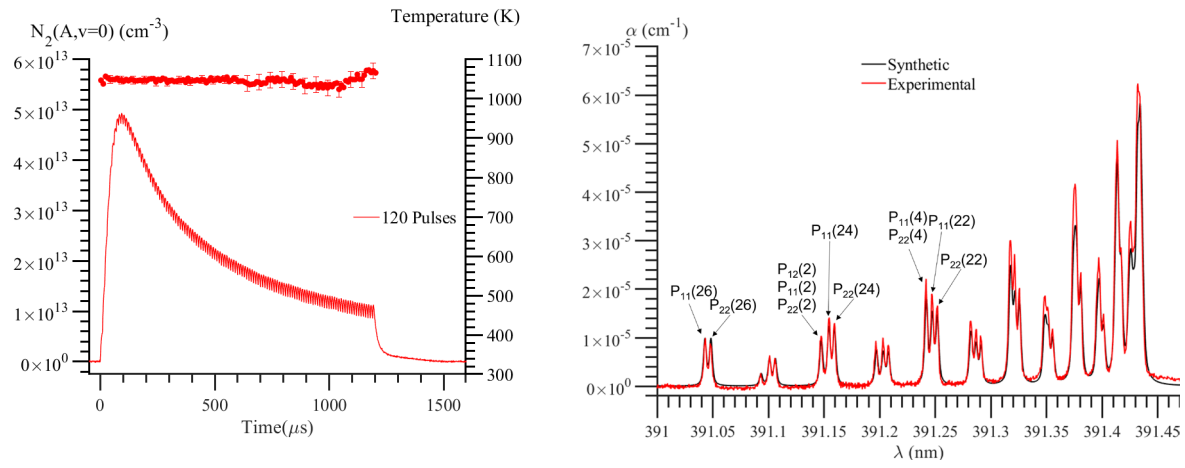

Fig. 1: **Left:** $N_2(A^3\Sigma_u^+,v=0)$ population during a 120-pulse burst (pulse repetition rate 100 kHz, burst repetition rate 10 Hz) and gas temperature, inferred from the $P_{11}(26)$ and $R_{23}(4)$ rotational line ratio in the $N_2(B^3\Pi_g, v = 2 \leftarrow A^3\Sigma_u^+,v = 0)$ band. **Right:** CRDS spectrum of $N_2^+(B^2\Sigma_u^+, v=0 \leftarrow X^2\Sigma_g^+,v=0)$ band at the furnace temperature of T=1000 K. Nitrogen, P=100 Torr, 15 μs after a 60-pulse discharge burst, pulse repetition rate 100 kHz.

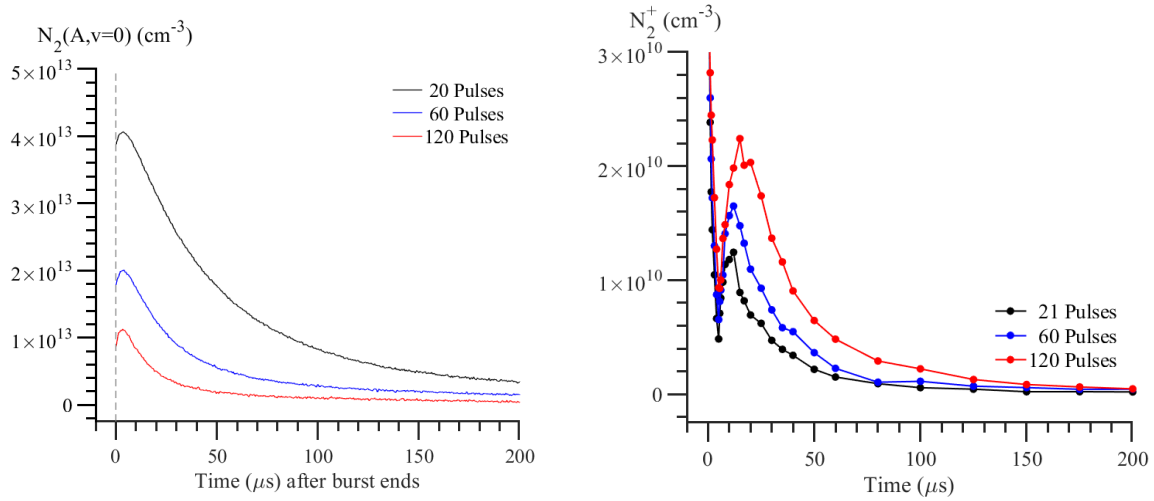

Fig. 2: Time-resolved time-resolved $N_2(A^3\Sigma_u^+,v=0)$ population **(left)** and N_2^+ number density inferred from the CRDS data **(right)** after 21, 60, and 120-pulse discharge bursts, at the conditions of Fig. 1.

[1] X. Yang, E.R. Jans, C. Richards, S. Raskar, D. van den Bekerom, K. Wu, and I.V. Adamovich, *Plasma Sources Science and Technology* **31** (2022) 015017

The reaction mechanisms between atomic oxygen and water using high-level quantum mechanical calculations

Jos Suijker[1], Behnaz Bagheri[(*)1,2]

[1]*Department of Applied Physics & Science Education, Technical University of Eindhoven, the Netherlands.*

[2] *Institute for Complex Molecular Systems, Eindhoven, the Netherlands.*

[(*)] b.bagheri@tue.nl

Electric gas discharge plasmas generated in oxygen containing gas mixtures, such as air or oxygen admixed with noble gases, produce atomic oxygen in either the ground triplet state, $O(^3P)$, or the excited singlet state, $O(^1D)$ [1-3]. In contact with humidity or with aqueous solutions, oxygen atoms may undergo reactions with water molecules, or may dissolve in solutions and undergo reactions in the liquid phase [4-8]. These reactions are crucial for plasma processing of liquids and biological molecules for diverse applications in health and environmental remediation. In addition, these reactions are broadly involved in environmental and atmospheric chemistry.

Despite their significance, the detailed reaction mechanisms involving oxygen atoms in the presence of water are not completely understood. Yusupov *et al.* [9] investigated the interaction of atomic oxygen with liquid water using ReaxFF molecular dynamics simulations wherein abstraction of a hydrogen atom from a water molecule was predicted with subsequent formation of two OH radicals. Verlackt *et al.* [10] predicted the formation of oxywater as a result of interaction of singlet states oxygen atoms with water using density functional tight binding (DFTB)-based molecular dynamics simulations which was stable for 10 ps of simulation time. Xu *et al.* [11] predicted the formation of oxywater as the intermediate product in the interaction between singlet state oxygen atom and water using density functional theory (DFT)-based molecular dynamics simulations. This was followed by the generation of hydrogen peroxide as the final product.

The past controversial outcomes motivated us to explore the reaction mechanisms between oxygen atoms and water molecules using high-level quantum mechanical calculations. The results will be presented in this talk.

[1] Jaffke, T., Meinke, M., Hashemi, R., Christophorou, L.G. and Illenberger, E., 1992. Dissociative electron attachment to singlet oxygen. *Chemical physics letters*, *193*(1-3), pp.62-68.

[2] Peyrous, R., 1990. The effect of relative humidity on ozone production by corona discharge in oxygen or air–a numerical simulation–part II: air.

[3] Schröter, S., Wijaikhum, A., Gibson, A.R., West, A., Davies, H.L., Minesi, N., Dedrick, J., Wagenaars, E., De Oliveira, N., Nahon, L. and Kushner, M.J., 2018. Chemical kinetics in an atmospheric pressure helium plasma containing humidity. *Physical Chemistry Chemical Physics*, *20*(37), pp.24263-24286.

[4] Benedikt, J., Hefny, M.M., Shaw, A., Buckley, B.R., Iza, F., Schäkermann, S. and Bandow, J.E., 2018. The fate of plasma-generated oxygen atoms in aqueous solutions: non-equilibrium atmospheric pressure plasmas as an efficient source of atomic $O_{(aq)}$. *Physical Chemistry Chemical Physics*, *20*(17), pp.12037-12042.

[5] Hefny, M.M., Pattyn, C., Lukes, P. and Benedikt, J., 2016. Atmospheric plasma generates oxygen atoms as oxidizing species in aqueous solutions. *Journal of Physics D: Applied Physics*, *49*(40), p.404002.

[6] Jirásek, V. and Lukeš, P., 2019. Formation of reactive chlorine species in saline solution treated by non-equilibrium atmospheric pressure He/O_2 plasma jet. *Plasma Sources Science and Technology*, *28*(3), p.035015.

[7] Gorbanev, Y., Golda, J., Schulz-von der Gathen, V. and Bogaerts, A., 2019. Applications of the COST plasma jet: More than a reference standard. *Plasma*, *2*(3), pp.316-327.

[8] Myers, B., Barnat, E. and Stapelmann, K., 2021. Atomic oxygen density determination in the effluent of the COST reference source using in situ effective lifetime measurements in the presence of a liquid interface. *Journal of Physics D: Applied Physics*, *54*(45), p.455202.

[9] Yusupov, M., Neyts, E.C., Simon, P., Berdiyorov, G., Snoeckx, R., Van Duin, A.C.T. and Bogaerts, A., 2013. Reactive molecular dynamics simulations of oxygen species in a liquid water layer of interest for plasma medicine. *Journal of Physics D: Applied Physics*, *47*(2), p.025205.

[10] Verlackt, C.C.W., Neyts, E.C. and Bogaerts, A., 2017. Atomic scale behavior of oxygen-based radicals in water. *Journal of Physics D: Applied Physics*, *50*(11), p.11LT01.

[11] Xu, S., Jirasek, V. and Lukes, P., 2020. Molecular dynamics simulations of singlet oxygen atoms reactions with water leading to hydrogen peroxide. *Journal of Physics D: Applied Physics*, *53*(27), p.275204.

Machine learning estimator for electron impact ionisation fragmentation patterns

K M Lemishko[1], S Mohr[(*)1], A Nelson[1], J Tennyson[2]

[1] *Quantemol Ltd, 320 City Rd, London EC1V 2NZ, United Kingdom*
[2] *Department of Physics Astronomy, University College London, Gower St., London WC1E 6BT, United Kingdom*
[(*)] s.mohr@quantemol.com

There are many measurements and calculations of total electron impact ionisation cross sections. However, it is often desirable to know the cross sections of the dissociation products resulting from ionisation. Partial ionisation cross sections can be derived from the total ionisation cross section by multiplying it by branching ratios for the production of distinct fragments. Branching ratios, in turn, can be inferred from ionisation mass spectrometry data, assuming that the ratios of charged fragments resulting from electron impact ionisation align with the observed fragments in the mass spectra at the energy where the spectrum was obtained [1].

Unfortunately, the required mass spectrometry data are not always readily available. A viable approach to generate reasonable mass spectra estimations for species lacking experimental data on fragmentation patterns is to use existing mass spectrometry data to train a machine learning model. Machine learning has been previously used in plasma modelling, including for estimation of rate coefficients of heavy species collisions [2] and prediction of total ionisation cross sections [3, 4].

We have developed a machine learning regression model to estimate ionisation mass spectra for the subsequent inference of electron impact ionisation fragmentation patterns. The model was trained on over 6500 instances of mass spectra of species with molecular masses up to 300 Da obtained from the NIST WebBook [5]. The model features included data describing readily available general properties of species, along with data characterising species atoms and bonds, extracted using the RDKit open-source tool [6]. The final prediction algorithm is a voting regressor that combines three optimised machine learning regressors: a random forest regressor [7], a gradient-boosted trees regressor [8], and a multilayer perceptron regressor [9] (Fig. 1).

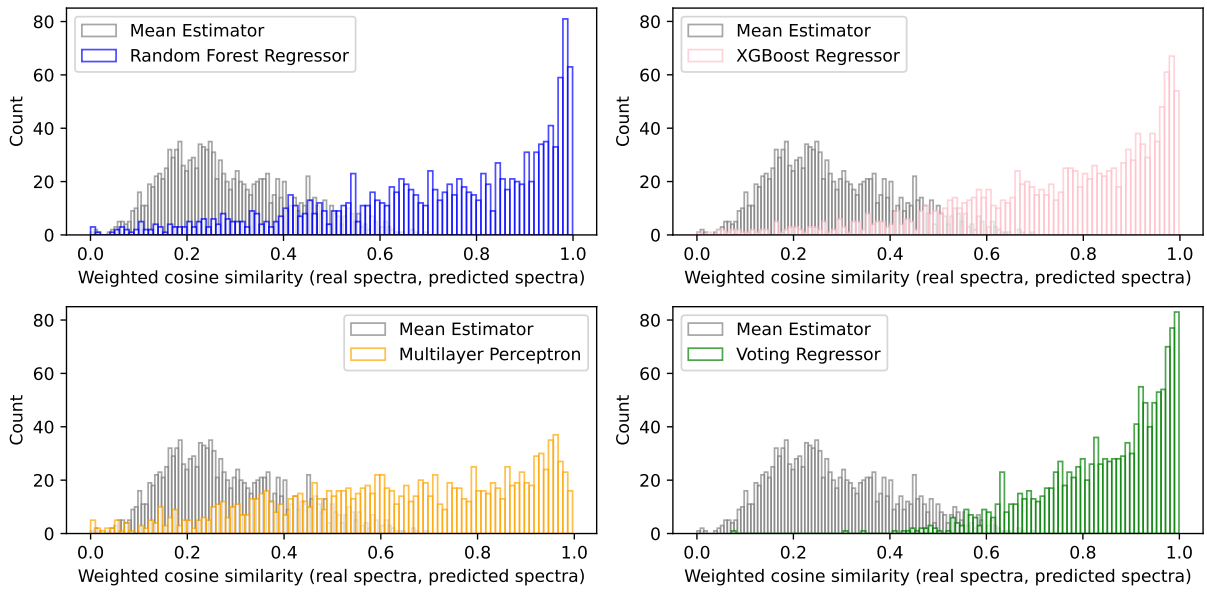

Fig. 1: Comparison of distributions of real and predicted spectra similarities obtained with various machine learning models and the mean estimator for test species.

As a metric of model accuracy, we have used weighted cosine similarity of real and predicted spectra vectors, defined as:

$$cosine\_similarity(y_{\text{real}}, y_{\text{pred}}) = \frac{\sum_{i=0}^{m_{\max}-1} y_{\text{real}}[i] \cdot y_{\text{pred}}[i]}{\sqrt{\sum_{i=0}^{m_{\max}-1} (y_{\text{real}}[i])^2} \cdot \sqrt{\sum_{i=0}^{m_{\max}-1} (y_{\text{pred}}[i])^2}}, \quad (1)$$

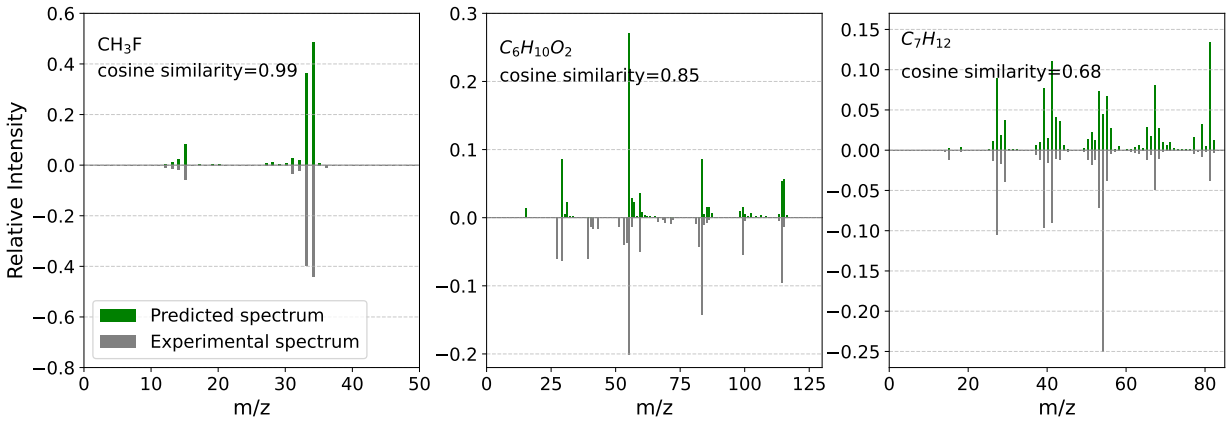

Fig. 2: Examples of real and predicted spectra with different values of cosine similarity

Fig. 2 presents examples of various predicted spectra alongside their corresponding experimental spectra for varying values of cosine similarity. An evaluation of the final prediction algorithm was performed on a dataset containing over 1300 test mass spectra. It was found that for around 70% of the test species, the similarity between the predicted and experimental spectra exceeded 80%. These results demonstrate that the developed machine learning approach can estimate ionisation mass spectra with a reasonable degree of accuracy.

[1] T. D. Mark, *Beiträge aus der Plasmaphysik* **22, 3** (1982) 257–294.
[2] M. Hanicinec, S. Mohr, J. Tennyson, *J. Phys. D: Appl. Phys.* **56** (2023) 374001 (24pp).
[3] L. Zhong, *J. Appl. Phys.* **125** (2019) 183302.
[4] A. L. Harris, J. Nepomuceno, *preprint* (2023).
[5] W.E. Wallace, *Gaithersburg, MD: National Institute of Standards and Technology* (2016) 20899.
[6] RDKit: Open-Source Cheminformatics, *http://www.rdkit.org*
[7] T.K. Ho, *Proceedings of 3rd international conference on document analysis and recognition* **1** (1995) 278—282.
[8] T. Chen, C. Guestrin, *Proceedings of the 22nd ACM SIGKDD International Conference on Knowledge Discovery and Data Mining* (2016) 785–794.
[9] S. Haykin, *Prentice Hall PTR* (1994)

Investigation of the Coulomb Logarithm for transport coefficients in warm dense matter

S.K. Kodanova(*)[1], M.K. Issanova[1], T.S. Ramazanov[1]

[1] *IETP, Al-Farabi Kazakh National University, Almaty 050040, Kazakhstan*

(*) kodanova@physics.kz

A perspective approach for the theoretical study of the dynamic and transport characteristics of dense plasma of inertial confinement fusion (ICF) is the pair collision approximation. When modeling the dynamic and transport characteristics of a dense ICF plasma, two approaches can be used. One of the is to calculate transport coefficients determined on the basis of particle scattering cross sections. In the second approach, a kinetic equation is solved, the collision integral of which contains a logarithmic divergent integral over the impact parameters, which is replaced by the Coulomb logarithm. The Coulomb logarithm is one of the fundamental parameters of plasma, which plays a decisive role in the study of transport and dynamic properties of plasma [1].

Whereas the Coulomb logarithm value is used in many plasma related studies and plays a key role in understanding the transport processes and behavior of plasma in various applications. Coulomb collisional processes in plasmas occur in many scenarios, ranging from particle and energy transport (e.g., self-diffusion, thermal diffusion, viscosity, thermal conduction, stopping power, temperature relaxation, and electrical conductivity) to wave damping, particulate drag, wake formation, and others. Central to the description of such processes is the Coulomb logarithm [2], which is usually defined as

$$\lambda = \ln \frac{b_{max}}{b_{\min}} \tag{1}$$

Here b_{max} and $b_{\min}$ are the maximum and minimum impact parameters, respectively. Most formulas describing energy transfer contain a Coulomb logarithm, in which the cutoff parameter is usually estimated from these values of the maximum and minimum collision parameters. The screening length (Debye length) is taken as the upper limit of integration b_{max}, since starting from distances of the order of the r_D, the particles are considered not to interact and do not scatter on each other. In reality, charged particles located at large distances from a certain scattering center are exposed to a large number of other scattering centers. Therefore, in plasma, even at moderate densities, it is necessary to take into account the effects caused by the interaction of a large number of particles, the so-called collective effects. Elimination of divergence at the lower limit is also carried out by choosing a finite value of the $b_{\min}$ that corresponds to a physically reasonable mechanism for eliminating close collisions:

$$b_{\min} = b_{\perp} = \frac{|q_1 q_2|}{m\upsilon^2} \tag{2}$$

Since any error in this term appears only within this logarithm and is usually accepted that it does not affect the result obtained by this formula. But this statement becomes unfair in the case when the argument is small, for example, in the case of dense plasma. Therefore, due to the long-range nature of the Coulomb interaction, the influence of density on plasma properties turns out to be more significant. In this area, which requires more precise formulation, it is desirable that all parameters be precisely defined. Therefore, to ensure the accuracy of results in plasma research, it is recommended to take into account important factors such as electronic screening, quantum mechanical effects, correlations between particles, etc [3-4]. In this regard, the Coulomb logarithm has been studied in many publications [5-7] and various approximations have often been used, taking into account screening by both electrons and ions, also based on the analysis of the obtained results of numerical modeling and experimental data [8], which are applicable for a specific problem and for different ranges of plasma parameters.

A study of dense nonideal semiclassical plasma has shown that taking into account quantum effects is important in a weakly coupled plasma, that is, for coupling parameters less than unity. At the same time, in the limit of weak coupling, quantum effects become insignificant. The discrepancy in the

Coulomb logarithm is due to the neglect of correlation: in a plasma, the collective effect of the surrounding plasma introduces Debye screening, which limits the interaction region.

The quantum mechanical approximation uses various approaches. In the Born approximation, it is mainly used at high velocities of incident particles or at large impact parameters [9]. In many works, the transport cross section for particle scattering in the quantum mechanical approximation is based on the calculation of scattering phases with different interaction potentials [10-12]. Another effect associated with the replacement of Maxwell-Boltzmann statistics with Fermi-Dirac statistics in the quantum approximation, i.e. at high densities or at low temperatures, which can be found in the article [13-14].

In this regard, to show the criterion for the applicability of various approximations: either the classical or quantum mechanical description used in the calculations of scattering cross sections is relevant and depends on the nature of the study. Here we limited ourselves to considering the electron-ion contributions to the transfer processes, and taking into account the contribution of the electron-electron interaction in the following works. In this work, the problem is considered in two cases: 1) when the quantum mechanical approximation is applicable to particle collisions and 2) when the collision process is quasi-classical. Comparisons are made of the electron-ion scattering cross section and, accordingly, the Coulomb logarithm in various degeneracy parameters and densities using classical theory and quantum mechanical theory.

In this work, we considered taking into account quantum mechanical effects during scattering and their influence on collision integrals and, accordingly, on the Coulomb logarithm, calculated on the basis of collision integrals. The obtained results are compared and the degeneracy parameters and density parameters at which the value of the Coulomb logarithm exactly coincides with each other within an error of 1% are shown. Calculations were carried out using classical and quantum mechanical theory.

Therefore, the analysis of these methods in classical and quantum plasma is of great interest. In this work, we consider comparisons of the results of two approximations when calculating the scattering cross section and Coulomb logarithms for different values of plasma parameters.

[1] A. Filippov, A. Starostin, and V. Gryaznov, Zhurnal Eksperimental'noi i Teoreticheskoi Fiziki **153**, 514 (2018).
[2] L. Spitzer, Physics of Fully Ionized Gases (N.Y. Interscience, 1962) p. 586.
[3] E. Bésuelle, R. R. E. Salomaa, and D. Teychenné, Phys. Rev.E **60**, 2260 (1999).
[4] C.-K. Li and R.D. Petrasso, Phys. Rev. Lett. **70**, 3063 (1993).
[5] C.A. Ordonez and M.I. Molina, Phys. Plasmas **1**, 2515 (1994).
[6] T.S. Ramazanov and S.K. Kodanova, Phys. Plasmas **8**, 5049 (2001).
[7] J.R. Correa, Y. Chang, and C. A. Ordonez, Phys. Plasmas **12**, 084505 (2005).
[8] N.A. Tahir and et al., Phys. Rev. STAB. **17**, 041003 (2014).
[9] F.Sigener, S. Arndt, R. Redmer etc., Physics A **152** (1988).
[10] T.S. Ramazanov, S.K. Kodanova, M.M.Nurusheva, M.K. Issanova, Physics of Plasmas **28(9)**, 092702 (2021).
[11] T.S. Ramazanov, M.K. Issanova, Y.K. Aldakul, S.K. Kodanova, Physics of Plasmas **29(11)**, 112706 (2022).
[12] T.S. Ramazanov, S.K. Kodanova, M.K. Issanova, B.Z. Kenzhegulov, Contrib. Plasma Phys., e202300127 (2024).
[13] L.G. Stanton and M.S. Murillo, Physical Review E **93**, 043203(2016).
[14] Sh. Rightley, S.D. Baalrud, Physical Review E **103**, 063206 (2021).

Insights into CO_2 conversion with plasma-electrolysis synergy

Aleksandr Pikalev [1,2], Xingyu Chen [1,3,4], Vasco Guerra [2], Guanjun Zhang [4], Mauritius C.M. van de Sanden[(*)1,3]

[1] *Dutch Institute for Fundamental Energy Research (DIFFER), Eindhoven 5612AJ, NL.*

[2] *Instituto de Plasmas e Fusão Nuclear, Instituto Superior Técnico, Lisboa 1049-001, Portugal.*

[3] *Eindhoven Institute for Renewable Energy Systems (EIRES), and Department of Applied Physics, Eindhoven University of Technology, Eindhoven 5600 MB, NL.*

[4] *School of Electrical Engineering, Xi'an Jiaotong University, 710049 Xi'an, China.*

[(*)] m.c.m.vandesanden@differ.nl

In-situ resource utilization (ISRU) is vital for the human colonization of Mars, in order to be self-sufficient for food and energy production [1]. The Martian atmosphere consists of CO_2 (95.9%), Ar (1.9%) and N_2 (1.9%). This CO_2 abundance can provide a feedstock for direct conversion into O_2 and CO, which can be used for life support and energy conversion respectively.

Amongst the CO_2 conversion and oxygen production technologies, the most promising is the combination of non-thermal plasmas and solid oxide electrolyte cell (SOEC) with an oxygen separation membrane. Although the CO_2 splitting can be performed at the SOEC surface, it requires high temperatures (typically 700-900°C) to break the stable carbon-oxygen double bonds electrochemically. The non-thermal plasma provides a highly-chemical-activated environment favorable for CO_2 dissociation, while the SOEC can separate the O_2 from the plasma environment, limiting the backward reaction of CO combing with O_2 to form CO_2. The plasma-SOEC synergy effects have been reported [2,3], but no detailed investigations of the plasma-SOEC performance enhancement have been conducted.

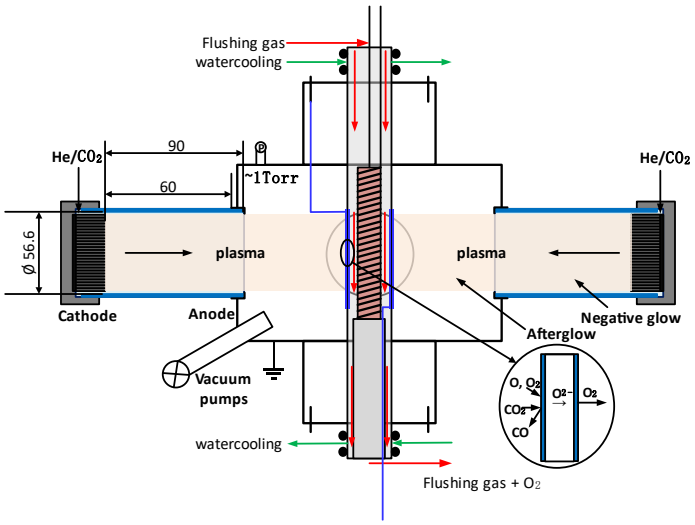

Fig. 1: The scheme of the SOEC integration into the BABE reactor.

To elucidate the kinetics behind the plasma-SOEC synergy, we investigate the plasma-SOEC interactions in the BAri Brush Electrode (BABE) reactor [4] with four DC glow discharges and the afterglow region between their ring anodes. The tubular SOEC consisting of yttria-stabilized zirconia (YSZ) electrolyte and lanthanum strontium manganite (LSM) electrodes is situated in the afterglow region. The scheme of the setup is shown in fig. 1. We investigate several essential factors, including plasma parameters, SOEC working temperatures and bias, and their effects on the catalytic process,

aiming to reach a higher oxygen permeation whilst limiting SOEC working temperature. The CO_2 conversion is studied for He(80%)-CO_2(20%) gas mixture with the pressure of 1 Torr. The plasma conditions are investigated in the discharge region by means of optical emission spectroscopy and in the afterglow region using a Langmuir probe. The dissociation products are determined by mass-spectrometry.

The oxygen pumping experiments demonstrate that the glow discharge can enhance the oxygen transport at the low SOEC working temperatures (350-650°C). At 298W discharge power and 10 sccm feed gas flow, the oxygen permeation can be enhanced from ~0.07mln/min to ~0.6mln/min. Simultaneously, the oxygen separation enhances the CO_2 conversion from 87.1% to 89.7%. The OES shows that the oxygen pumping out of the afterglow region also reduces the intensities of the atomic oxygen lines in the discharge region. In our conditions, the plasma-induced enhancement of the oxygen permeation grows with increasing plasma power, reaching saturation at ~300W. The results are compared with the experiments with He-O_2 and pure He experiments [5].

This work was partially supported by the European Space Agency under Project I-2021-03399. IPFN activities were funded by FCT (Fundação para a Ciência e a Tecnologia) under projects UIDB/50010/2020, UIDP/50010/2020, LA/P/0061/202 and PTDC/FIS-PLA/1616/2021 (https://doi.org/10.54499/UIDB/50010/2020) (https://doi.org/10.54499/UIDP/50010/2020) (https://doi.org/10.54499/LA/P/0061/2020) (https://doi.org/10.54499/PTDC/FIS-PLA/1616/2021). The authors are thankful to Ashley Hughes for critical reading of the abstract.

[1] V. Guerra et al. *J. Appl. Phys.* **132** (2022) 070902.

[2] A. Pandiyan et al. *J. CO_2 Utilization* **57** (2022) 101904.

[3] F. Buck et al. *J. Industrial and Engineering Chem.* **104** (2021) 1–7.

[4] S. Ratynskaia, G. Dilecce, and P. Tolias *J. Plasma Phys.* **81** (2015) 345810202.

[5] X. Chen et al. *ICPIG XXXV*, Egmond aan Zee, The Netherlands, 2023, 132.

Direct conversion of benzene to phenol in plasma-irradiated aqueous solution

Y. Inagaki[1], Y. R. Hayashi[1], N. Shirai[1], S. Takakusagi[2], and K. Sasaki[1]

[1] *Faculty of Engineering, Hokkaido University, Kita 13, Nishi 8, Kita-ku, Sapporo 060-8628, Japan*

[2] *Institute for Catalysis, Hokkaido University, Kita 21, Nishi 10, Kita-ku Sapporo 060-0810, Japan*

inagaki@eng.hokudai.ac.jp

Phenol is a fundamental chemical and is widely used in chemical industry [1]. Most of phenol is industrially produced by the Cumene process, which requires tree-step reactions with a low production yield. This work focuses on the phenol production using a new chemical process that utilizes active species induced by plasma-liquid interaction. Phenol was produced by adding benzene into water that was irradiated with an atmospheric-pressure air plasma. We optimized the discharge method and the experimental conditions. We measured the optical absorption spectrum of the aqueous solution, and investigated the temporal variations of the concentrations of benzene and phenol.

Figure 1 shows the experimental setup for irradiating a plasma to water. A stainless-steel nozzle electrode was inserted into an alumina tube for electrical isolation. The distance between the tops of the alumina tube and the stainless-steel electrode was 1 mm. Air was bubbled from the nozzle into an NaCl solution (30 ml, 0.1%) at a flow rate of 70 ml/min. A ballast resistor of 50 kΩ was inserted between the nozzle electrode and a dc power supply. A dc voltage was applied between the nozzle electrode and the solution to generate an atmospheric-pressure dc discharge in the bubble. The voltage of the dc power supply was 0.6-1.5 kV, and the current was 13 mA. The duration of the plasma irradiation was 5 min. Immediately after stopping the discharge, benzene with a volume of 62 µl was mixed into the plasma-irradiated water, and the solution was kept in a hermetic glass bottle. The solution pipetted from the hermetic glass bottle was then diluted with an equal volume of water, and we measured the optical absorption spectrum of the solution.

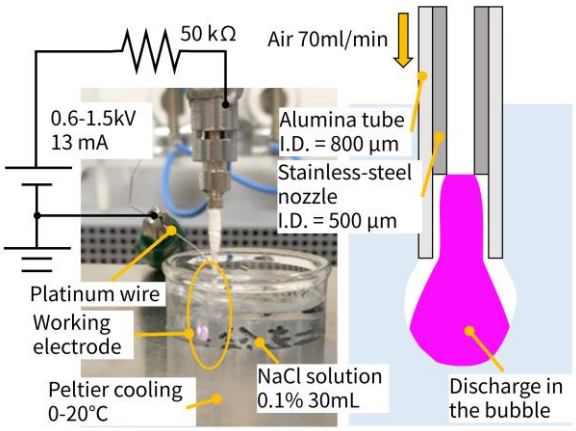

Fig. 1 Photograph of the experimental setup and the details of the working electrode.

Figure 2 shows optical absorption spectrum of the plasma-irradiated water at 7 days after adding benzene. Four absorption peaks observed in the range of 240-260 nm were attributed to benzene, while the absorption in the range of 270-280 nm was attributed to phenol. We fitted the absorption spectrum by adopting the following equation,

$$\begin{pmatrix} \left.\frac{\mathrm{d}A(\lambda)}{\mathrm{d}\lambda}\right|_{\lambda_1} \\ \left.\frac{\mathrm{d}A(\lambda)}{\mathrm{d}\lambda}\right|_{\lambda_2} \end{pmatrix} = \begin{pmatrix} \left.\frac{\mathrm{d}\epsilon_1(\lambda)}{\mathrm{d}\lambda}\right|_{\lambda_1} & \left.\frac{\mathrm{d}\epsilon_2(\lambda)}{\mathrm{d}\lambda}\right|_{\lambda_1} \\ \left.\frac{\mathrm{d}\epsilon_1(\lambda)}{\mathrm{d}\lambda}\right|_{\lambda_2} & \left.\frac{\mathrm{d}\epsilon_2(\lambda)}{\mathrm{d}\lambda}\right|_{\lambda_2} \end{pmatrix} \begin{pmatrix} c_1 \\ c_2 \end{pmatrix} l,$$

where l is the optical path length, λ is the wavelength (λ_1 = 261 nm, λ_2 = 279 nm), c_1 and c_2 are the concentrations of benzene and phenol, respectively, $A(\lambda)$ is the measured absorption spectrum, and $\epsilon_1(\lambda)$ and $\epsilon_2(\lambda)$ are the absorption coefficient of benzene and phenol, respectively. The absorbance spectra of benzene and phenol obtained by the fitting are shown in figure 2 together with the residue. The concentrations of benzene and phenol were deduced from the absorbance to be 2.5 and 0.27 mM, respectively. In the residue spectrum, the broad peak around 280 nm and the tail at wavelengths longer than 330 nm are attributable to pyrocatechol, hydroquinone, and nitrophenol. Figure 3 shows the temporal variations in the concentrations of benzene and phenol. We observed a relatively steep increase in the phenol concentration in the first few hours. After that, we observed gradual increase for a week. The production yield, which is defined by $-\Delta[\mathrm{Phenol}]/\Delta[\mathrm{Benzene}]$, was 0.013 at 7 days after adding benzene into plasma-irradiated water.

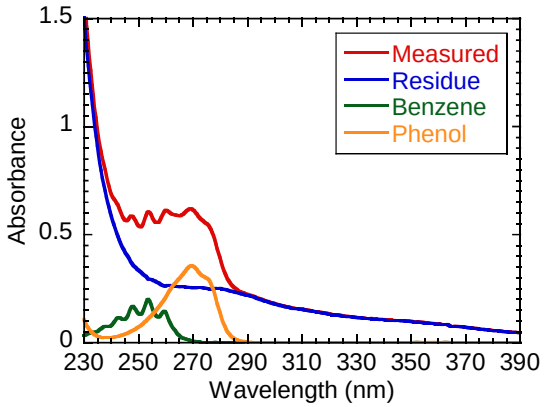

Fig. 2 Absorption spectrum of the plasma-irradiated water at 7 days after adding benzene. The fitted absorbance of benzene and phenol are shown together with the residue.

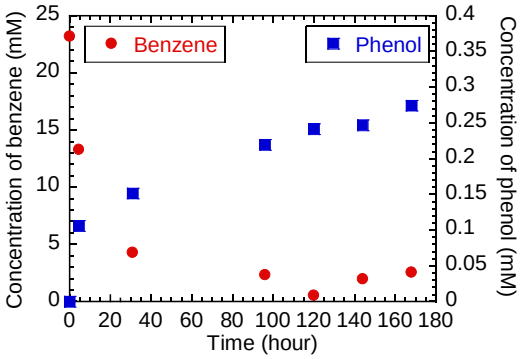

Fig. 3 Concentration of benzene and phenol in the plasma-treated water at various times after adding benzene.

The gradual increase in the phenol concentration shown in figure 3 indicates that the benzene-phenol conversion is driven by long-lived chemical species induced in the plasma-irradiated water. In plasma-irradiated water, $OH^{\cdot}$ and $HO_2^{\cdot}$ are produced from H_2O_2 and NO_2^- via the following reactions [2,3]:

$$\begin{aligned} NO_2^- + H_2O_2 + H^+ &\rightarrow ONOOH + H_2O, \\ ONOOH &\rightleftarrows OH^{\cdot} + NO_2, \\ OH^{\cdot} + H_2O_2 &\rightarrow HO_2^{\cdot} + H_2O, \\ HO_2^{\cdot} + H_2O_2 &\rightarrow O_2 + OH^{\cdot} + H_2O, \\ ONOOH + H_2O_2 &\rightarrow HO_2NO_2 + H_2O, \\ HO_2NO_2 &\rightleftarrows HO_2^{\cdot} + NO_2. \end{aligned}$$

In addition, iron ions were also observed in the plasma-irradiated water, which were thought to be eluted from the stainless-steel electrode. The following reaction, known as the Fenton reaction, is also a possible route for the formation of $OH^{\cdot}$:

$$H_2O_2 + Fe^{2+} \rightarrow OH^{\cdot} + OH^- + Fe^{3+}.$$

It is reported in some papers that benzene is converted to phenol with the help of $OH^{\cdot}$ or $HO_2^{\cdot}$ [4,5]. We speculate that $OH^{\cdot}$ and/or $HO_2^{\cdot}$ produced by the above reactions contribute to the production of phenol in the present experiment.

References

[1] R. J. Schmidt, Applied Catalysis A: General **280**, 89 (2005).
[2] K. Ikuse and S. Hamaguchi, Jpn. J. Appl. Phys. **61**, 076002 (2022).
[3] S. Ikawa, A. Tani, Y. Nakashima and K. Kitano, J. Phys. D: Appl. Phys. **49**, 425401 (2016).
[4] X.-M. Pan, M. N. Schuchmann and C. Von Sonntag, J. Chem. Soc., Perkin Trans. **2**, 289 (1993).
[5] K. Hirose, K. Ohkubo and S. Fukuzumi, Chemistry – A European Journal **22**, 12904 (2016).

Nitrogen fixation: Synergy between microwave plasma and catalyst

Jonas Gans(*)[1], Qinghao Shen[1], Ashely Hughes[1], Cas van Deursen[1], Waldo Bongers[1], Floran Peeters[2], M.C.M van de Sanden[1,3]

[1] *Dutch Institute for Fundamental Energy Research (DIFFER), Eindhoven, 5612 AJ, The Netherlands*

[2] *Leyden Jar Company, Eindhoven, 5657 EB, The Netherlands*

[3] *Eindhoven University of Technology, Eindhoven, 5612 AZ, The Netherlands*

(*) j.gans@differ.nl

Nitrogen fixation, the foundation of fertiliser production, currently relies on the energy-intensive Haber-Bosch process, contributing significantly to global energy consumption (2%) [1,2]. New greener technologies are urgently required to sustainably feed the world's growing population [3]. In this work, the synergy of electrically driven microwave plasma and heterogeneous catalyst was investigated. Using air as feedgas, nitrogen fixation is achieved by the formation of NO_x (i.e. NO, NO_2, and less significantly also N_2O_4), directly through the plasma process and through interactions of plasma activated species with catalyst surfaces. WO_3 and Al_2O_3 pellets were used as catalysts in a post-plasma packed-bed configuration. The produced NO_x densities were quantitatively measured using gas-phase Fourier Transform Infrared (FTIR) spectroscopy. Parameter studies were carried out actively varying gas flowrate, pressure, microwave power, catalyst material and catalyst temperature. The energy cost of the reactor was improved beyond the 0D modelling limitation of the plasma process (2.61 MJ/mol), reaching 2.17 MJ/mol (figure 1). Measurements show that the NO_2/NO ratio correlates with the reactor performance, with higher ratios resulting in higher efficiencies. This is attributed to an oxygen donating effect of the catalyst, which enhances NO production and its further oxidation to NO_2. In this work, it was demonstrated that heterogenous post-plasma catalyst can significantly enhance microwave plasma's energy efficiencies for NO_x production.

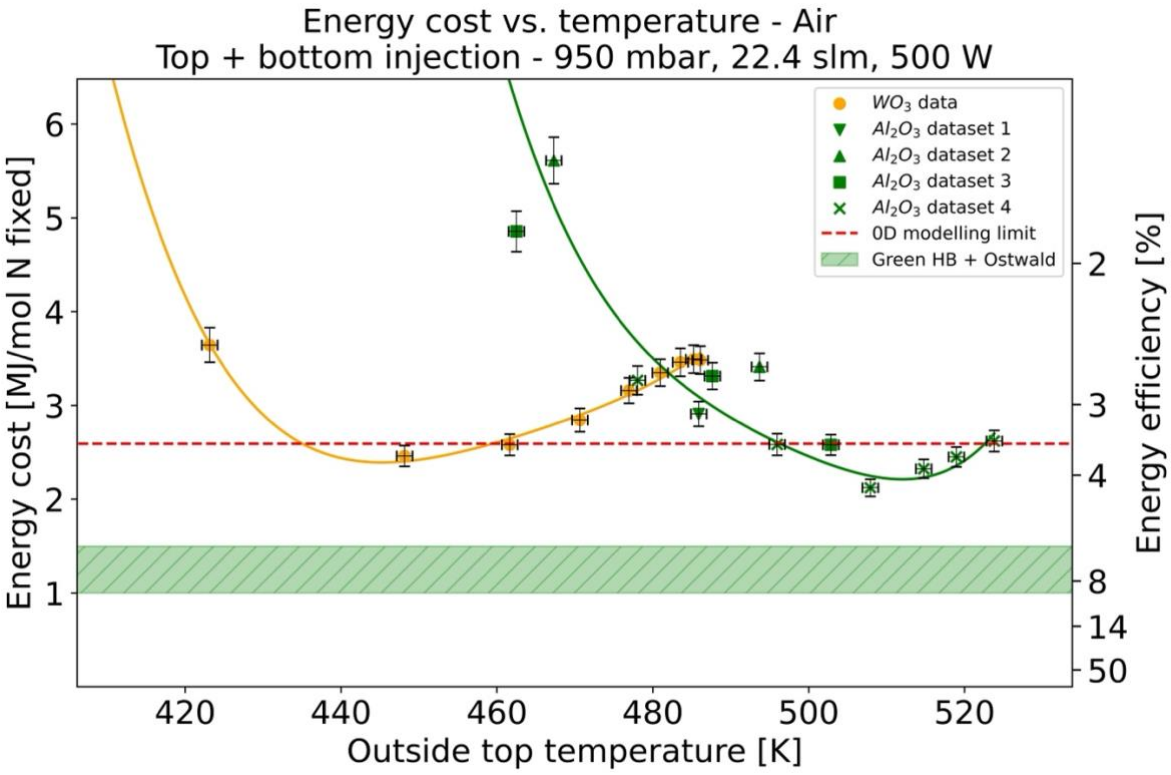

Figure 1: Reactor energy cost vs. outside top catalyst bed temperature at 950 mbar, 22.4 slm and 500 W operating condition for WO_3 and Al_2O_3 catalyst pellets.

References:

[1] W.Z. Wang, B. Patil, S. Heijkers, V. Hessel, A. Bogaerts, *Chemsuschem* **10** (2017) 2145–2157.

[2] O. S. Bahnamiri, C. Verheyen, R. Snyders, A. Bogaerts, N. Britun, *Plasma Sources Science and Technology* **30** (2021) 065007.

[3] S. Van Alphen, V. Vermeiren, T. Butterworth, D. C. M. van den Bekerom, G. J. Van Rooij, A. Bogaerts, *The Journal of Physical Chemistry C* **124** (2019) 1765–1779.

Acknowledgment:

This project is financially supported by ARC CBBC.

Possibilities of plasma conversion of CO_2 and H_2/H_2O to CH_4 at extraterrestrial conditions

V. Kudrle(*), T. Vaněčková, O. Jašek, Z. Bonaventura,
R. Brunovský, Z. Navrátil, P. Slavíček

Department of Plasma Physics and Technology, Faculty of Science, Masaryk University, Brno, Czechia

(*) kudrle@sci.muni.cz

Manned mission to Mars is a promising but risky step in future space exploration. The amount of rocket fuel needed for a return of such mission back to Earth is one of many complications. It is nearly impossible to carry all needed fuel from the mission start due to an exponential nature of Tsiolkovsky equation. On-site production from the local sources (CO_2 atmosphere, surface and subsurface water ice) seems a necessity.

We investigate the possibilities of simple plasma-based conversion process as an alternative to a classical catalytic chemistry. Intended plasma chemistry is based on Sabatier reaction and water shift reaction [1]. Plasma conversion of CO_2 was already a topic of many experimental and modelling studies, e.g. [2] and [3].

Schematic drawing of the experimental set-up is shown in Fig.1. Surface wave driven (2.45 GHz surfatron) microwave discharge is operated at conditions similar to Mars surface (300 K, 600 Pa). Working gas is a mixture of CO_2 with H_2 or H_2O. Optical emission spectroscopy is used for the plasma diagnostics while MS and FTIR are used to determine chemical composition of the outflowing gas.

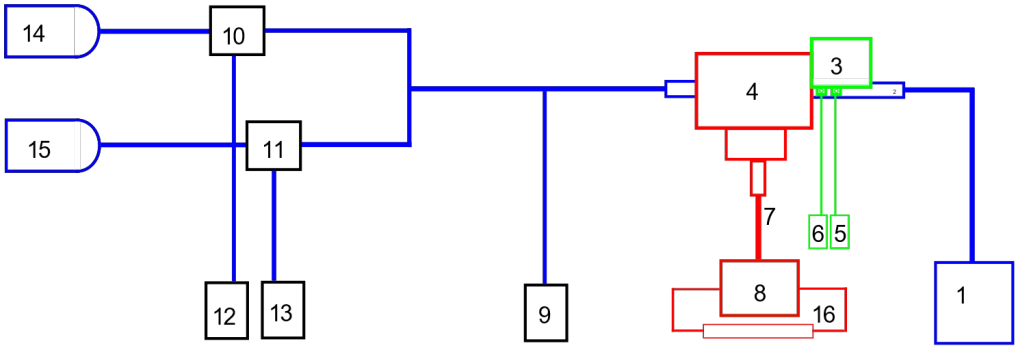

Fig. 1: Experimental setup: 1 – vacuum pump, 2 – fused silica discharge tube of 8 mm diameter, 3 – optical cable holder with micrometric screw, 4 – surfatron launcher, 5 – spectrometer JY Triax 550, 6 – low-res spectrometer Avantes, 7 – coaxial cable, 8 – Sairem solid state microwave generator, 9 – capacitive pressure gauge 10, 11 – flow controllers Bronkhorst 12, 13 – display units, 14 – CO_2 bottle, 15 – H_2 bottle, 16 – cooling water circuit

Plasma appearance in different gas mixtures is shown in Fig.2. Image analysis of such photographs can provide e.g. dependence of plasma length on gas flows, as in Fig.3.

a) b) c)

Fig. 2: Discharge appearance at P = 50 W, for several gas flows a) H_2 ~ 100 sccm, b) H_2 ~ 50 sccm, CO_2 ~ 50 sccm, c) CO_2 ~ 100 sccm.

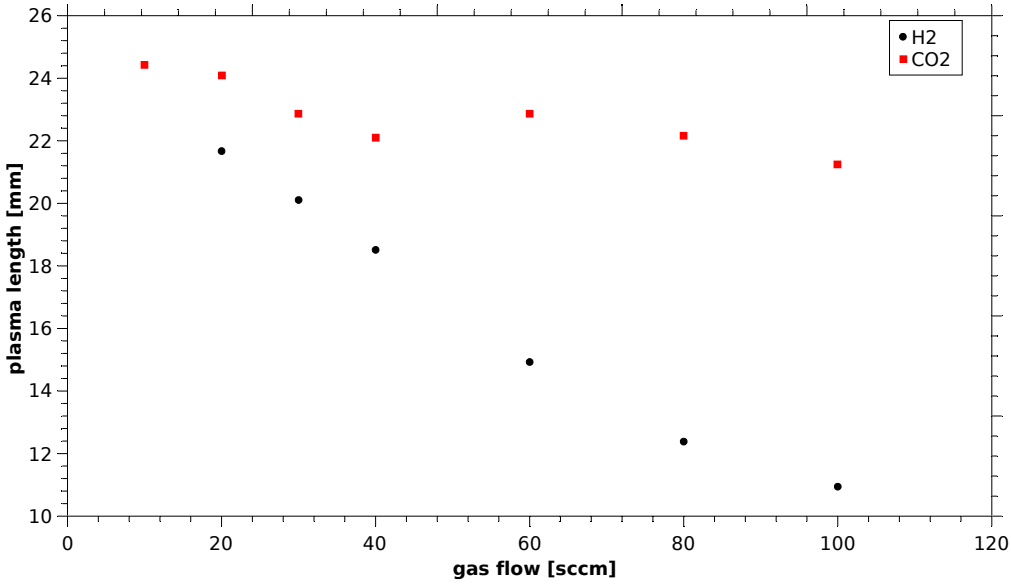

Fig. 3: Dependence of plasma length for P = 50 W in pure H_2 and pure CO_2 on the gas flowrate.

Mass spectrometry analysis of products of reactions under different CO_2:H_2 gas mixture ratios has shown a production of CO, H_2O and H_2 but only minor concentration of CH_x fragments was detected using 20:80 gas mixture ratio. PFTIR confirmed the presence of CO and H_2O molecules originating from reassociating reactions but no CH_4 was detected under studied conditions.

In conclusion, the catalyst-free plasma production of methane under Mars surface conditions was attempted using microwave plasma in various CO_2 + H_2 gas mixtures. Analysis of stable products by MS and FTIR showed presence of associating reactions products, but no definitive proof of hydrocarbon products could be obtained.

This work was supported by project LM2023039 funded by the Ministry of Education, Youth and Sports of the Czech Republic.

[1] R. Snoeckx and A. Bogaerts, *Chem. Soc. Rev.* **46** (2017) 5805.
[2] T. Ihara, T. Ouro, T. Ochiai, M. Kiboku, and Y. Iriyama, *Bull. Chem. Soc. Jpn.* **69** (1996) 241.
[3] C. Verheyen, T. Silva, V. Guerra, and A. Bogaerts, *Plasma Sources Sci. Technol.* **29** (2020) 095009.

Studying the interaction of scanner materials with EUV-generated plasma

A.S. Stodolna(*)[1], T.W. Mechielsen[1], K. Papamichou[1], S. Oostrom[1], M. van de Kerkhof [2], V. Navarro Parders[2]

[1] *TNO, P. O. Box 155, 2600AD Delft, The Netherlands*

[2] *ASML Netherlands B.V., De Run 6501, 5504 DR Veldhoven, The Netherlands*

(*) aneta.stodolna@tno.nl

Inside EUV lithography machines the propagating light ionizes a background gas resulting in a so-called EUV-generated hydrogen plasma. In the past at TNO we focused on investigating the properties of this plasma in order to mimic it in laboratory setups. In controlled experiments we studied the interaction between hydrogen plasma and EUV components, including construction materials. With increasing EUV source powers and repetition rates the density of the EUV-generated plasma and the amount of scattered light will also increase.

Taking a proactive approach together with ASML TNO is investigating interaction of selected construction materials with the EUV-generated plasma for higher source powers. As an example of this work, we studied behavior of an aluminum alloy in different types of hydrogen plasmas. Using the most common type of a plasma source, based on the electron cyclotron resonance (ECR) principle, we observed a process of Mg release from the alloy, which scales with total ion dose and depends on the background H_2O and N_2 pressures. In experiments employing a novel plasma setup at TNO called EBR (Electron Beam Research) the aluminum alloy was exposed both to hydrogen plasma generated by means of electron impact ionization and to a beam of electrons. The latter could be used to mimic EUV photons in processes like oxidation or carbon growth [1]. Post X-ray Photoemission Spectroscopy (XPS) measurements showed that at the locations illuminated with electrons the oxidation of the alloy extended to deeper layers in contrast to the locations exposed solely to hydrogen plasma. Moreover, a buildup of Mg underneath surface also depended on the electron beam location. Finally, to link the observations driven by electrons with EUV photons exposure have been scheduled at the EUV Beam Line 2 (EBL 2) facility at TNO early 2024. In this experiment the Al alloy will be exposed to EUV-generated plasma for ~1 day after which the sample will be analyzed with XPS (surface & depth profiles).

[1] Luo, C., et al., Review of recent advances in inorganic photoresists. RSC Advances, **10**, 8385 (2020)

Processing of diatomaceous earth after beer filtration process with non-equilibrium plasma

J. Pawłat(*)[1], K. Wolny-Koładka[2], P. Terebun[2], M. Kwiatkowski[2], D. Zarzeczny[2], M. Zdaniewicz[3], S. Bodziacki[2]

[1] *Department of Electrotechnic and Smart Technology, Faculty of Electrical Engineering and Computer Science, Lublin University of Technology, ul. Nadbystrzycka 38A, 20-618 Lublin, Poland*

[2] *Department of Microbiology and Biomonitoring, University of Agriculture in Krakow, al. Mickiewicza 24/28, 30-059 Krakow, Poland*

[3] *Department of Fermentation Technology and Microbiology, Faculty of Food Technology, University of Agriculture in Krakow, ul. Balicka 122, 30-149 Krakow, Poland*

(*) *j.pawlat@pollub.pl, askmik@hotmail.com*

Utilizing diatomaceous earth for beer filtration is regarded as one of significant technological advancements in brewing in recent years. This recognition stems from diatomaceous earth's distinctive porosity, substantial adsorption capacity, and low density. After filtration process the mass of spent diatomaceous earth significantly exceeds its original weight as it retains some water and other organic components (such as yeast, proteins, and polyphenols). Thus, such a spent diatomaceous earth is considered the primary brewing waste. The present study evaluates the antibacterial potential of non-equilibrium plasma against microorganisms isolated from diatomaceous earth. The treated samples were waste product from the beer filtration process.

Time min	0	10	30
X200	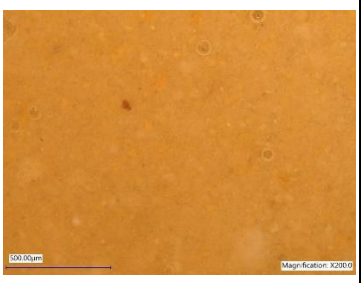	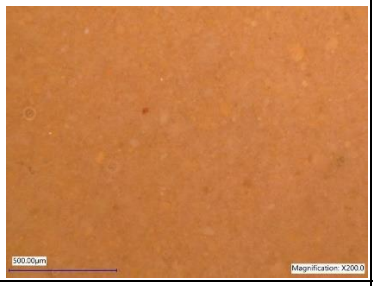	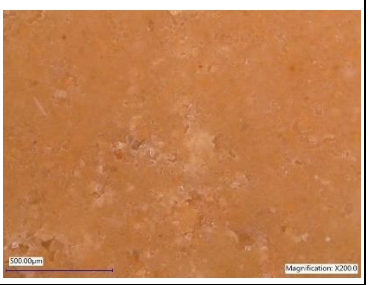
X800	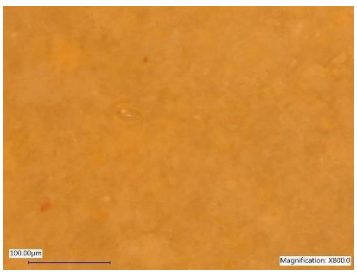	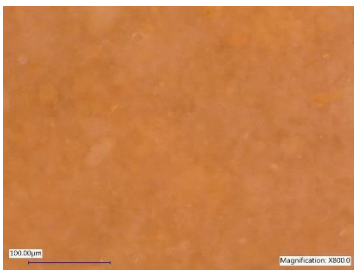	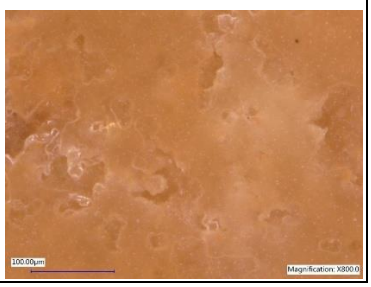

Fig.1: Microscopic imaging of diatomaceous earth before and after non-equilibrium plasma treatment

Non-equilibrium plasma was generated using a Glidearc reactor operating with air [1]. The temperature of the samples after treatment was monitored and it did not exceed 30ºC after 30 min, the plasma treatment.

The effect of plasma on the morphology of the treated material was observed with KEYENCE VHX-5000 optical microscope. Examination of the material's porous surface revealed that material damage resulting from plasma treatment was quite subtle. Visual effects were mostly from drying due to the flow of working gas. Furthermore, the FTIR spectra indicated no alteration in the chemical composition of the material across all treatment durations (5, 10, 20, 25, and 30 min.).

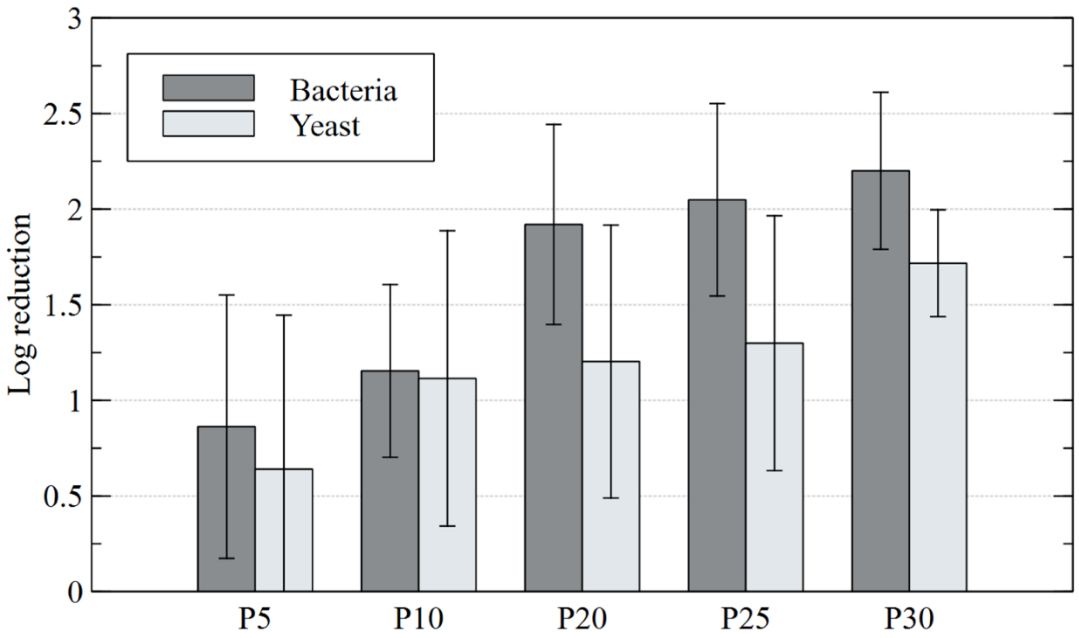

Fig.2: Logarithmic CFU reduction of microorganisms colonizing diatomaceous earth for different plasma treatment times.

Microbiological assessments identified three bacterial strains: *Hafnia alvei, Citrobacter freundii, Citrobacter braakii*. Additionally, three yeast strains: *Saccharomyces cerevisiae, Rhodotorula glutinis, Candida spherica*, were also present in the samples. The disinfection efficacy of plasma treatment was evident even at the shortest duration (5 min.), with its effectiveness increasing over time. Compared to control samples, reductions of 2.2 $\log_{10}$ CFU/g in total bacterial count and 1.72 $\log_{10}$ CFU/g in yeast were observed at a 30-minute exposition time.

References

[1] J. Pawłat, P. Terebun, M. Kwiatkowski, B. Tarabová, Z. Kovalová, K. Kučerová, Z. Machala, M. Janda, K. Hensel, *Plasma Chem Plasma Process* **39**, (2019) 627–642.

Distribution of radicals in plasma catalysis for CO_2 methanation using an atmospheric pressure plasma jet

A Saito(*)[1], T Nozaki[2], T Miyazaki[3], Y Inagaki[3], K Sasaki[3]

[1] *Innovative Technology Laboratories, AGC Inc., Japan*

[2] *Department of Mechanical Engineering, Tokyo Institute of Technology, Japan*

[3] *Division of Applied Quantum Science and Engineering, Hokkaido University, Sapporo, Japan*
* atsushi.saito@agc.com

Methanation is a process in which CO_2 is reduced with hydrogen to produce CH_4, aiming to contribute to carbon dioxide capture, utilization, and storage (CCUS). However, methanation is an exothermic reaction, and has challenges, including the intricate temperature control required during the process and catalyst degradation resulting from elevated temperatures.

Plasma catalysis is being considered as a solution to address this issue. It offers the advantage of lower activation energy compared to thermal catalysis by enabling non-thermal equilibrium plasma to act on the catalyst, and it exhibits a unique reaction [1]. Typically conducted in a packed-bed reactor, plasma catalysis involves packing the catalyst inside a dielectric tube, such as quartz glass. A mixture of CO_2 and H_2 gas is introduced into the tube, and plasma is applied to the catalyst. However, in the case of exothermic reactions, the catalyst temperature rises even in non-thermal equilibrium plasma, making it challenging to determine whether it is the effect of active species from the plasma or heat [2]. To investigate the interaction between radicals and catalyst surfaces, we generated H_2 and CO_2 plasma jets in dielectric barrier discharges (DBD) and irradiated Ru/TiO_2 to produce CH_4. The gases produced by plasma catalysis were analyzed by quadrupole mass spectrometer (QMS), and the catalyst surface conditions were analyzed by X-ray photoelectron spectroscopy (XPS). The distributions of H, OH, CO, and O radicals produced in this plasma experiment were measured by laser-induced fluorescence (LIF).

Figure 1 shows the QMS measurement results of gas compositions in both plasma catalysis and thermal catalysis. It reveals that CH_4 is produced in plasma catalysis when irradiated with Ar/H_2 plasma and Ar/CO_2 plasma, similar to the results observed in thermal catalysis. Upon comparing the specific energy input (SEI) for the same CH_4 yield, it is found that the reaction in plasma catalysis occurs at approximately a quarter of the energy in the thermal catalysis.

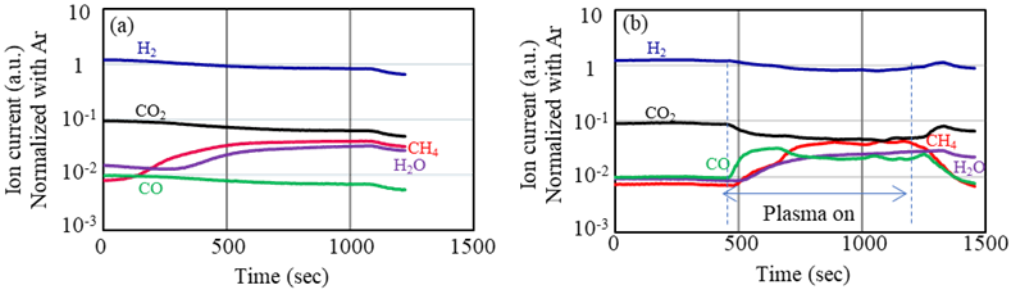

Fig.1 Gas analysis by QMS in catalytic reduction of CO_2 with H_2. (a) Thermal catalysis, (b) Plasma catalysis.

The XPS evaluation of the surface condition of Ru/TiO_2 is presented in Fig. 2. For reference, Fig. 2(a) shows the results without plasma, showing only the introduced gases, while Fig. 2(b) shows the outcomes of thermal catalysis. In both the cases, the gas introduction comprised 200 cm^3/min of Ar, 20 cm^3/min of CO_2, and 80 cm^3/min of H_2, resulting in more RuO_x than Ru metal. No significant difference is observed between the results presented in Figs. 2(a) and (b). Figure 2(c) shows the effects of treatment with Ar/H_2 plasma, while Fig. 2(d) shows the results of the simultaneous irradiation of Ar/H_2 and

Ar/CO_2 plasmas. In both instances, RuO_x is reduced to Ru metal, but the simultaneous irradiation of Ar/H_2 and Ar/CO_2 plasmas leads to a more substantial reduction. The simultaneous generation and irradiation of Ar/H_2 and Ar/CO_2 plasmas suggest a possible oxidation of Ru metal by O radicals, derived from CO_2 decomposition. However, contrary to this expectation, the result indicates an accelerated reduction of RuO_x to Ru metal. To clarify this observation, we conducted a measurement of radicals in the plasma using LIF.

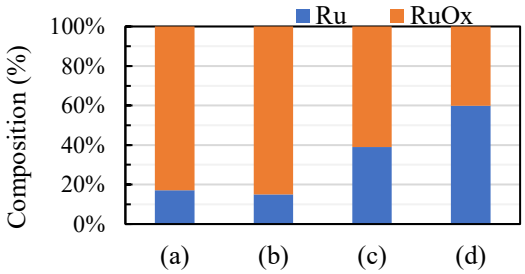

Fig. 2 XPS evaluation of Ru state on catalyst surface. (a) Only gas without power, (b) thermal catalysis, (c) Ar/H_2 plasma irradiation onto the catalyst, (d) simultaneous irradiatons of Ar/H_2 and Ar/CO_2 plasmas onto the catalyst.

Figure 3 shows the results of two-photon absorption laser-induced fluorescence (TALIF) measurements of H radical density. The laser wavelength used for exciting H radicals in the plasma is 205 nm. The state of H radicals generated solely by Ar/H_2 plasma is depicted in Fig. 3(a), while those produced by Ar/H_2 and Ar/CO_2 plasma are presented in Fig. 3(b). Notably, the H radical density is higher when the catalist was irradiated by the Ar/H_2 and Ar/CO_2 plasmas simultaneously, in comparison with the irradiation of the Ar/H_2 plasma alone. Additionally, in Fig. 3(b), the H radical density is higher in the Ar/CO_2 plasma side than the Ar/H_2 plasma side.

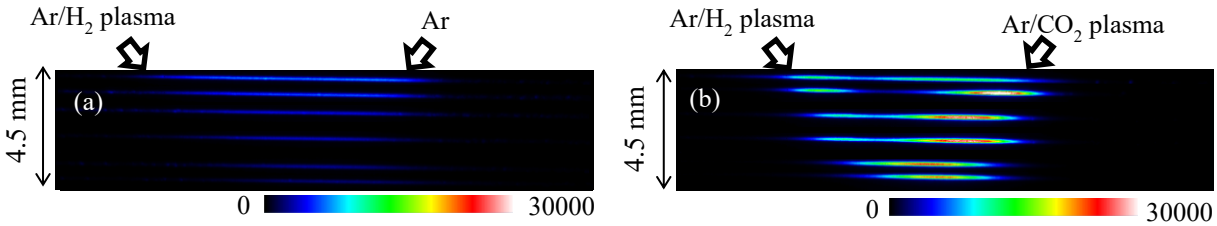

Fig. 3. H radical evaluation using TALIF. (a) Ar/H_2 plasma, (b) Ar/H_2 plasma and Ar/CO_2 plasma.

OH radical density in simultaneously generated Ar/H_2 and Ar/CO_2 plasmas were also measured using LIF, and the results are presented in Fig. 4. The laser wavelength for exciting OH radicals in the plasma is 262 nm. The OH radical density is higher in the Ar/CO_2 plasma side, aligning with the stronger intensity observed at the same position as the H radical in Fig. 3(b). These findings suggest that the O radical generated in the Ar/CO_2 plasma reacts with H_2 molecules to produce H radicals [3].

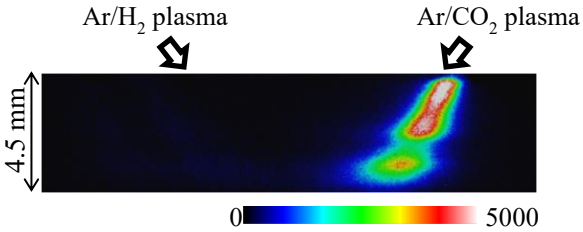

Fig. 4. OH radical evaluation using LIF with simultaneously generated Ar/H_2 plasma and Ar/CO_2 plasma.

In the plasmas examined in this study, H radicals were generated in the Ar/H_2 plasma, while O radicals were produced in the Ar/CO_2 plasma. Subsequently, the O radicals reacted with H_2 molecules, yielding H and OH radicals. These reactions, unique to plasma catalysis, are absent in thermal catalysis. The H radicals with a higher density, which is attributed to these reactions, reduce RuO_x to Ru metal on the catalyst surface, enhancing its activity. Consequently, methanation through plasma catalysis operates at lower energy levels than thermal catalysis.

References

[1] Z. Sheng, Y. Watanabe, H. Kim, S. Yao, T. Nozaki. Chem. Eng. J. 2020, 399, 125751.
[2] C. Zhan, D. Kim, S. Xu, H. Kim, T. Nozaki, Int. J. Plasma Environ. Sci. Technol. 2022, 16, e03006.
[3] T Peng, D Zhang, J Zhang, R Schinke, Chemical Physics Letters. 1996, 248, 37-42

Ionization layer with collision-free atoms at the edge of partially to fully ionized plasmas

Mikhail Benilov

Departamento de Física, FCEE, Universidade da Madeira, Largo do Município, 9000 Funchal, Portugal

Instituto de Plasmas e Fusão Nuclear, Instituto Superior Técnico, Universidade de Lisboa, 1041 Lisbon, Portugal

benilov@staff.uma.pt

Ionization (Saha) equilibrium, which holds in strongly ionized high-pressure plasmas, e.g., those generated in high-current arc discharges, is violated in thin layers near solid surfaces contacting the plasma. Of particular importance is the non-equilibrium layer near the cathode, since it is in this layer that the ion current to the cathode surface is formed, which heats the surface to the high temperatures necessary for electron emission. More precisely, the ion current is formed in the outer - quasi-neutral - section of the near-cathode non-equilibrium layer; the so-called ionization layer. An understanding and adequate theoretical description of the ionization layer are needed for evaluation of the ion current to the cathode.

The physics of the ionization layer may be briefly described as follows. Ions generated in the ionization layer move to the cathode surface where they recombine. (On their way to the cathode, the ions cross the space-charge sheath, where they are accelerated by the sheath electric field, but this is not directly relevant to this context.) Neutral atoms thus formed are desorbed from the surface and move into the plasma, with some or all of them being ionized while crossing the ionization layer. A theoretical description of the relative motion of the ions and the atoms in the ionization layer depends on the relationship between the scale of thickness of the ionization layer, l, and the mean free path for collisions between the atoms and the ions, λ_{ia}.

An example is shown in Fig. 1. Here l_{cf} and l_{dif} are scales of thickness of the ionization layer, evaluated in the limiting cases where a neutral atom, while moving across the ionization layer, suffers virtually no or many collisions, respectively. Also shown are characteristic mean free paths for collisions between the ions, λ_{ii}, and between the neutral atoms, λ_{aa}, the Debye length λ_D, the ionization degree ω, and the parameter α, which characterizes the ratio l/λ_{ia}. All these quantities refer to conditions at the "edge" of the ionization layer, where the plasma is in ionization equilibrium, and the partial composition of the plasma was evaluated by means of the Saha equation in terms of the electron temperature in the ionization layer, T_e, the heavy-particle temperature, T_h, which is set equal to 3000 K, and the plasma pressure.

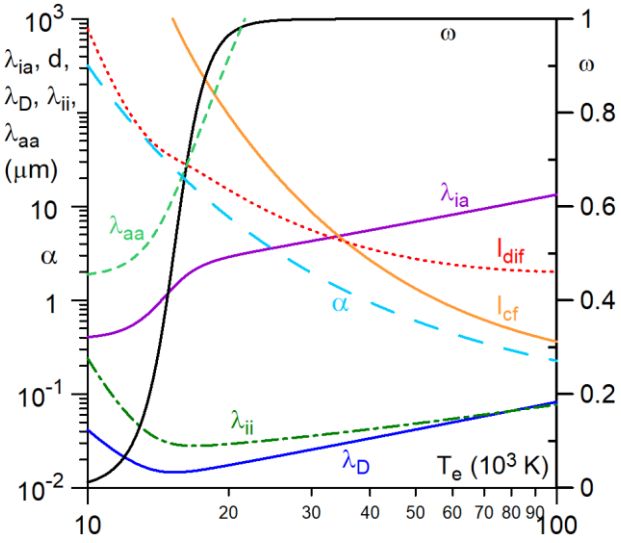

Fig. 1: Characteristic length scales in the ionization layer in atmospheric-pressure argon arc.

In the fully developed arc-cathode regime, the current-collecting part of the cathode surface is hot and the near-cathode voltage drop is low. As a consequence, T_e is relatively low as well and $l > \lambda_{ia}$. The ionization layer may be described in the diffusion approximation in this regime. The contrary situation occurs during glow-to-arc transitions: when a hot arc spot has just

formed on the cathode surface, a significant part of current still flows to the cold surface outside the spot in the glow-discharge regime, and therefore the near-cathode voltage continues to be high at all points of the cathode surface including in the spot. T_e is high in this case and $l < \lambda_{ia}$. The coupling between the ion and atom species in the ionization layer is not strong and the diffusion description of the ion-atom relative motion in the layer is not valid. Since $\lambda_{ii} < l$ and $\lambda_{aa} > l$, a fluid description of the ion motion should be combined with a kinetic description of the motion of the atoms. The resulting problem admits a simple analytical solution, which is used to derive formulas for evaluation of the ion current to the cathode surface for a wide range of conditions, including for arbitrary values of the ratio l/λ_{ia} and the ionization degree.

An example is shown in Fig. 2. Here f_w is the normalized ion current, coming to the cathode from the ionization layer across the space-charge sheath, and $\beta = T_e/T_h$. Also shown are the ion current evaluated in the diffusion approximation, in the approximation of collision-free atoms, and by means of the multifluid theory [1]. Also shown are experimental data taken from figure 5 of [2], which were transformed as described in [3] and refer to conditions with $\beta \approx 6$.

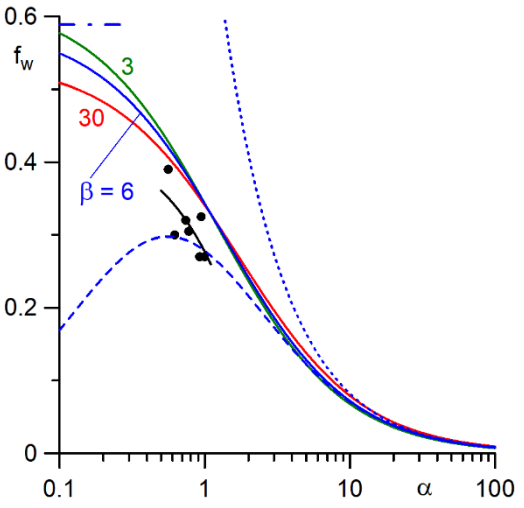

Normalized ion current to the cathode. Solid: this work, β = 3, 6, 30. Dotted: diffusion approximation, β = 6. Dash-dotted: approximation of collision-free atoms, β = 6. Dashed: multifluid theory [1], β = 6. Circles and short solid line: experimental data from [2] and their linear fit.

As expected, values of the normalized ion current given by the theory of this work, by the multifluid theory, and the diffusion theory are all close to each other for large α. For α of order unity and smaller, the diffusion values substantially exceed values given by the theory of this work. The multifluid theory gives lower values than the theory of this work and the difference increases as α decreases; a consequence of the difference in asymptotic behaviour of the function $f_w(\alpha)$ for small α.

Given that the theory of this work is better justified theoretically than both the diffusion and multifluid theories, one would expect that the theory of this work conforms to experiment better than both the diffusion and multifluid theories. This is clearly the case as far as the diffusion theory is concerned. This appears to be the case also for the multifluid theory, although the scatter of experimental data is too great to make an unambiguous conclusion.

The possibilities of using the obtained results to improve existing methods for modeling high-pressure arc discharges and their interaction with electrodes (e.g., review [4] and references therein) in order to increase their accuracy in relation to glow-to-arc transitions on cold cathodes will be discussed at the conference.

The work was supported by FCT - Fundação para a Ciência e Tecnologia, I.P. by projects UIDB/50010/2020, UIDP/50010/2020 and LA/P/0061/2020 and by European Regional Development Fund through the Operational Program of the Autonomous Region of Madeira 2014-2020 under project PlasMaM1420-01-0145-FEDER-000016.

[1] M. S. Benilov and G. V. Naidis, *Phys. Rev. E* **57** (1998) 2230.
[2] F. G. Baksht, G. A. Dyuzhev, N. K. Mitrofanov, S. M. Shkol'nik, and V. G. Yur'ev, *Sov. Phys. Tech. Phys*. **18** (1973) 1617.
[3] N. A. Almeida, M. S. Benilov, R. N. Franklin, and G. V. Naidis, *J. Phys. D: Appl. Phys*. **37** (2004) 3107.
[4] M. S. Benilov, *J. Phys. D: Appl. Phys*. **53** (2020) 013002.

Phenomenological description of vacuum breakdown and detailed modelling of cathode spots

Camila Cró[1,2], Helena Kaufmann[3], Nelson Almeida[1,2], Pedro Almeida[1,2] , Mikhail Benilov[(*)1,2]

[1] *Departamento de Física, FCEE, Universidade da Madeira, Largo do Município, 9000 Funchal, Portugal*

[2] *Instituto de Plasmas e Fusão Nuclear, Instituto Superior Técnico, Univ. de Lisboa, 1041 Lisboa, Portugal*

[3] *SE GT PRM D AIS VI, Siemens Energy Global GmbH & Co. KG, Berlin, Germany*

[(*)] benilov@staff.uma.pt

1. Introduction

Field electron emission is a necessary mechanism for the development of vacuum breakdown and is generally accepted that the field on the surface of the cathode is locally enhanced to values that lead to breakdown. In [1], the field enhancement is attributed to imperfections microprotrusions on the cathode surface, though these have not yet been observed experimentally. Alternatively, it has been suggested (e.g. [2], [3]) that breakdown could be attributed to the motion of dislocations on the metal surface as the electrodes are subjected to an electric field. A phenomenological approach was taken when considering the local enhancement of the field - a field enhancement factor, β, based on high-field measurements in high-voltage cryosystems [4] was introduced as a means of describing the enhancement of the field.

Simulations of vacuum breakdown initiated by field emission due to the enhanced electric field have been performed for axially symmetric planar copper cathodes and prove that that field emission is sufficient to cause a thermal instability underneath the surface that leads to a fast increase of the temperature and current density at the cathode's surface. The onset of a hot spot below the surface of the cathode that rapidly reaches the critical temperature of the cathode material was observed. This means that, in principle, no other mechanism in addition to field emission is necessary to cause vacuum breakdown. Preliminary work regarding other relevant physical mechanisms, such as the motion and deformation of the melt and contributions to current and energy transfers from the plasma has also been conducted.

2. The model

Simulations of the temperature and current distributions were made for an axially symmetric cylindrical copper cathode with a radius and height of $10\,\mu$m. The model consists of the heat conduction equation (supplemented with Joule heating) and the current continuity equation,

$$\begin{aligned} \rho c_p \frac{\partial T}{\partial t} &= \nabla\cdot(\kappa\nabla T) + \sigma\left(\nabla\varphi\right)^2, \\ \nabla\cdot\mathbf{j} = 0, &\quad \mathbf{j} = -\sigma\nabla\varphi, \end{aligned} \tag{1}$$

respectively, where T is the temperature, $\mathbf{j}$ is the current density, ρ is the mass density of the metal, c_p is the effective specific heat of the metal (which takes into account the change of phase from solid to liquid), κ and σ are the thermal and electric conductivities of the metal, respectively, and φ is the electric potential. The boundary conditions at the bottom and front-facing surface of the cathode were

$$\begin{aligned} z=0: &\quad \kappa\frac{\partial T}{\partial z} = q_{\text{rad}_0}, \quad \varphi = 0, \\ z=h: &\quad \kappa\frac{\partial T}{\partial z} + q_{\text{rad}_h} = -q_{\text{em}}, \quad \sigma\frac{\partial\varphi}{\partial z} = -j_{\text{em}}, \end{aligned} \tag{2}$$

where $q_{em} = (j_{em}/e)(2k_BT + A_{\text{eff}})$ is the energy flux due to field emission, j_{em} is the field emission current density, and A_{eff} is an effective work function. q_{rad} is the energy flux due to the radiation emitted by the cathode in terms of its temperature. The field emission current density was calculated in terms of

the effective electric field $E_{\text{eff}} = \beta E_w$, where $\beta(T)$ is the temperature-dependent enhancement factor. Finally, thermally and electrically insulating boundary conditions were considered for the lateral surface of the cathode.

3. Results and discussion

For a cathode initially at a temperature of 300 K to which a perturbation of 40 K on a 1 μm scale is introduced, the results are as follows: for an applied electric field of $E_w = 1.9 \times 10^7$ V/m, we initially have gradual heating of the surface. A region of subsurface heating appears at $t = 14.8$ ns; from here, a very rapid increase in temperature underneath the surface is observed - at $t = 15$ ns, a thermal instability region is well-developed, and the cathode reaches a maximum temperature exceeding the critical temperature of copper, located at a depth of about 60 nm from the surface, as shown in Figure 1. The region of melted metal has a maximum depth of 0.5 μm. It can be concluded that field electron emission on its own is sufficient to induce vacuum breakdown, and that the enhancement of the surface electric field need not be due to surface microprotrusions, but can be described by a temperature-dependent enhancement factor, $\beta(T)$, which may relate to dislocations.

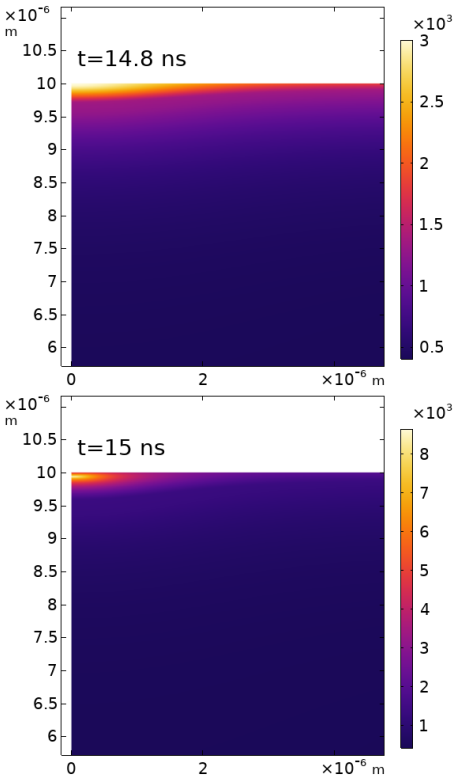

Fig. 1: Temperature (K) of the cathode for $E_w = 1.9 \times 10^7$ V/m, as a function of time.

From here, it is logical to consider what happens next. The results reported above concern the initial stage of breakdown. However, as the temperature increases, plasma contributions will have to be taken into account, similarly to the work presented in [5]. The goal is therefore to produce a thorough description of vacuum breakdown that takes into consideration all relevant physical mechanisms. At this stage, preliminary work has been completed regarding the implementation of the continuity and Navier-Stokes equations (which include the Lorentz force due to the self-induced magnetic field) to account for the motion of the melt, the current and energy contributions from the plasma to the cathode surface, and the deformation of the cathode surface. The final results are to be presented at the conference.

IPFN activities were supported by FCT - Fundação para a Ciência e Tecnologia, I.P. by project references UIDB/50010/2020, UIDP/50010/2020 and LA/P/0061/2020 and by European Regional Development Fund through the Operational Program of the Autonomous Region of Madeira 2014-2020 under project PlasMaM1420-01-0145-FEDER-000016.

[1] H. T. C. Kaufmann *et al.*, "Investigation of vacuum breakdown in pulsed dc systems," in *9th International Workshop on Mechanisms of Vacuum Arcs (online, March 8-12, 2021)*, 2021.

[2] E. Z. Engelberg *et al.*, "Stochastic model of breakdown nucleation under intense electric fields," *Phys. Rev. Lett.*, vol. 120, p. 124801, 2018.

[3] Y. Ashkenazy *et al.*, "Identifying critical plastic activity in electrodes under intense electric fields and the link to breakdown nucleation," in *29th Int. Symp. on Discharges and Electrical Insulation in Vacuum (ISDEIV; online, Sept. 2021, Padova, Italy)*, 2021.

[4] M. Jacewicz *et al.*, "Temperature-dependent field emission and breakdown measurements using a pulsed high-voltage cryosystem," *Phys Rev Appl*, vol. 14, p. 061002, 2020.

[5] H. T. C. Kaufmann *et al.*, "Detailed numerical simulation of cathode spots in vacuum arcs: Interplay of different mechanisms and ejection of droplets," *J. Appl. Phys.*, vol. 122, no. 16, p. 163303, 2017.

The impact of plasma treatment using the GlidArc generator on apple juice in a stationary and flow system

Dawid Zarzeczny(*)[1], Joanna Pawłat[1], Piotr Terebun[1], Michał Kwiatkowski[1], Agnieszka Starek-Wójcicka[2], Marta Krajewska[2], Elżbieta Grządka[3], Barbara Chudzik[4]

[1] *Lublin University of Technology, Faculty of Electrical Engineering and Computer Science, Department of Electrical Engineering and Smart Technology, Plasma technologies department, Nadbystrzycka 38a St., 20-618 Lublin, Poland*

[2] *University of Life Sciences in Lublin, Department of Biological Bases of Food and Feed Technologies, Głęboka 28 St., 20-612 Lublin, Poland*

[3] *Maria Curie-Skłodowska University, Faculty of Chemistry, Institute of Chemical Sciences, M. Skłodowskiej Curie 3 Sq., 20-031 Lublin, Poland*

[4] *Maria Curie-Skłodowska University, Department of Biological and Environmental Education with Zoological Museum, Akademicka 19 St., 20-033 Lublin, Poland*

(*) d.zarzeczny@pollub.pl

The consumption of fruit juices worldwide shows a constant upward trend, especially for juices without preservatives and other additives. This is due to increased consumer awareness, who pay attention to flavor qualities (lack of unpleasant aroma and artificial colors) and the positive impact on health. As a result, they are willing to pay more for fresh and more natural juices than for thermally processed juices with chemical preservatives. Numerous scientific studies confirm that fruit juices are a great source of important nutrients for the human body thanks to bioactive compounds such as carotenoids, polyphenols, phenols, anthocyanins, and phytochemicals. Moreover, consuming such juices prevents chronic diseases such as cancer and cardiovascular diseases. Therefore, it is extremely important to preserve as many valuable compounds and nutrients as possible during juice processing and treatment [1-8].

Currently, pasteurization based on thermal processing technologies is used to ensure the appropriate level of microbiological safety and enzyme inactivation. Unfortunately, these procedures can cause changes in the quality of juices, which is not acceptable to potential consumers. Various attempts are made to minimize the negative effects and preserve the sensory, nutritional, and functional properties of juices. Countless efforts are being made to replace current pasteurization methods with innovative non-thermal processing technologies [1], [9].

As it is widely known, during plasma treatment of various juices, certain general tendencies can be observed. However, the action of CAP (Cold Atmospheric Plasma) may vary depending on the plasma source used or the treatment parameters. Also, juice properties, including the type of fruits used to make the juice, may affect the obtained research results. A thorough understanding of CAP application for treating different juices is important for optimizing processing parameters to achieve microbiologically safe juices of high quality [1].

The aim of the study was to develop a cold plasma treatment system to improve the microbiological safety of juices while preserving their basic physicochemical values. The research material was freshly squeezed apple juice, which was subjected to plasma treatment using a Glid Arc reactor with air as the working gas, in both stationary and flow systems.

Studies have shown that regardless of the type of plasma treatment system used (stationary, flow and flow with attachment), the number of microorganisms considered decreased with the extension of treatment duration. The overall number of microorganisms in the control juice (not subjected to plasma treatment) was 4.60 log10 cfu/ml, whereas according to the current requirements set forth in the 2005 Codex Standards, it should not exceed 4 log10 cfu/ml. Treating samples in the stationary system helped

reduce the number of aerobic bacteria and obtain a product suitable for consumption that met the applicable criteria. The number of colonies ranged from 3.00 log10 cfu/ml (after 30 minutes of treatment) to 3.44 log10 cfu/ml (after 5 minutes of treatment). Meanwhile, the amount of yeast and mold in the same samples ranged from 2.59 log10 cfu/ml to 3.32 log10 cfu/ml, whereas in the control sample, the number of these microorganisms was at a moderate level of 3.34 log10 cfu/ml.

Flow-through plasma treatment with an attachment demonstrated the highest effectiveness in eliminating microorganisms present in apple juice. It was observed that in the control sample, the total number of microorganisms exceeded (by 1.79 log10 cfu/ml) the amount indicating the suitability of the juice for consumption. A 5-minute treatment was still insufficient in lowering this value, whereas extending the treatment duration to 15 and 30 minutes resulted in obtaining juice that met the required criteria. The overall number of microorganisms in these juice samples was 3.49 log10 cfu/ml and 3.22 log10 cfu/ml, respectively. Analyzing the results of yeast and mold counts also revealed the decontaminating effect of the applied treatment on the number of colonies grown. In the juice not subjected to plasma treatment, the number of colony-forming units was 3.47 log10 cfu/ml, while after 5, 15, and 30 minutes of this treatment, it decreased to 3.34 log10 cfu/ml, 3.17 log10 cfu/ml, and 2.55 log10 cfu/ml, respectively.

It was observed that plasma-treated juices (in most cases) showed slightly lower brightness (a decrease in parameter L*) compared to control products. Furthermore, fruit products included in the research program were more red (an increase in parameter a*) when subjected to plasma treatment in flow systems than their respective control samples. Conversely, the stationary treatment system (S) lasting 15 and 30 minutes resulted in a decrease in the examined chromaticity coefficient compared to products not treated with cold plasma. The parameter b*, indicating the yellowing of juices depending on the duration of all applied treatment systems, was at similar or lower levels compared to control beverage samples.

[1] E. Ozen and R. K. Singh, “Atmospheric cold plasma treatment of fruit juices: A review,” Trends Food Sci Technol, vol. 103, (2020) 144–151

[2] A. M. Jordão, “Phenolic Compounds in Fruit Beverages,” Beverages, vol. 4, (2018) p. 35

[3] Y. Hou et al., “Effect of cold plasma on blueberry juice quality” Food Chem, vol. 290, (2019), 79–86

[4] Ó. Rodríguez, W. F. Gomes, S. Rodrigues, and F. A. N. Fernandes, “Effect of indirect cold plasma treatment on cashew apple juice (Anacardium occidentale L.),” LWT, vol. 84, (2017) 457–463

[5] B. G. Dasan and I. H. Boyaci, “Effect of Cold Atmospheric Plasma on Inactivation of Escherichia coli and Physicochemical Properties of Apple, Orange, Tomato Juices, and Sour Cherry Nectar,” Food Bioproc Tech, vol. 11, (2018) 334–343

[6] S. K. Pankaj, Z. Wan, W. Colonna, and K. M. Keener, “Effect of high voltage atmospheric cold plasma on white grape juice quality,” J Sci Food Agric, vol. 97, (2017) 4016–4021

[7] R. Kongkachuichai, R. Charoensiri, K. Yakoh, A. Kringkasemsee, and P. Insung, “Nutrients value and antioxidant content of indigenous vegetables from Southern Thailand,” Food Chem, vol. 173, (2015) 838–846

[8] R. H. Liu, “Health benefits of fruit and vegetables are from additive and synergistic combinations of phytochemicals,” Am J Clin Nutr, vol. 78, (2003) 517S-520S

[9] A. I. Muhammad et al., “Effects of Nonthermal Plasma Technology on Functional Food Components,” Compr Rev Food Sci Food Saf, vol. 17, (2018) 1379–1394

Modelling non-equilibrium near-cathode plasma layers at ignition of high-pressure arcs on refractory cathodes

D. F. N. Santos[1,2], N. A. Almeida[1,2], L. G. Benilova[1], and M. S. Benilov[(*),1,2]

[1]*Departamento de Física, Universidade da Madeira, 9000 Funchal, Portugal*
[2]*Instituto de Plasmas e Fusão Nuclear, Instituto Superior Técnico, 1041 Lisboa, Portugal*
[(*)]benilov@staff.uma.pt

One of the important unsolved problems in the theory of high-pressure arc discharges is the lack of self-consistent methods for numerical modelling of the ignition of high-current arcs on refractory electrodes. The most difficult is the self-consistent description of the current transfer to the cathodes at the initial stage of arc ignition when the cathode surface is not yet hot enough for thermionic emission.

Various hypotheses on the dominating mechanism of current transfer to the surfaces of cold arc cathodes have been proposed in the arc discharge literature, and the theoretical conclusion that the ion current and secondary electron emission from the cathode are the most important mechanisms of current transfer to cold cathodes of arc discharges was confirmed by specially designed experiments [1]. Thus, this conclusion has by now been substantiated both theoretically and experimentally and there appears to be no reason to doubt it.

The development of an approximate model of non-equilibrium near-cathode plasma layers (NCPL) in high-pressure arc discharges, applicable over a wide range of cathode surface temperatures and near-cathode voltages, is the objective of this work. The model takes into consideration thermionic electron emission from the cathode and secondary electron emission resulting from ion impact. The applicability of the model will be limited to cathode surface temperatures below the boiling point of the cathode material, when the vaporization of the cathode material is not a dominating effect, and the arc may be considered as burning in the ambient gas.

The model is based on the previous work [2], which was supplemented with the secondary electron emission current. The density of electric current from the plasma to the cathode surface in the modified model is evaluated as

$$j_c = j_T + (1 + \gamma) j_i - j_{CD},$$

where j_T is the density of emission current caused by high values of the cathode surface temperature and/or electric field directed to the cathode surface, γ is the so-called effective secondary emission coefficient, j_i is the density of electric current transported to the cathode surface by the ions coming from the plasma, and j_{CD} is the density of current of fast plasma electrons counter-diffusing to the cathode surface against the sheath electric field.

The quantities involved in this expression are shown in Fig. 1 as functions of the cathode surface temperature T_c for two values of the near-cathode voltage drop U. Also shown is the electron temperature in the near-cathode layer, T_e. The conditions of the model are: the cathode is made of tungsten, the plasma-producing gas is atmospheric-pressure argon. j_T is determined by means of the Richardson-Schottky formula, values of the work function and the Richardson constant are 4.55 eV and 6×10^5 Am^{-2}K^{-2}, respectively. The secondary electron emission is 0.1. Also shown in Fig. 1 is parameter α characterizing the ratio of the scale of thickness of the ionization layer to the mean free path for collisions between the neutral atoms and the ions [3].

Let us first consider the case where U is small. For low and moderate values of T_c, the ion current density is roughly proportional to the thermionic emission current density. In this regime, the ion current to the cathode is limited not by a finite rate of diffusion of the ions from the ionization layer to the cathode surface, but rather by a finite rate of supply of the ionization energy to the ionization layer. This regime occurs on thermionic arc cathodes when they are not hot enough for the plasma in the near-

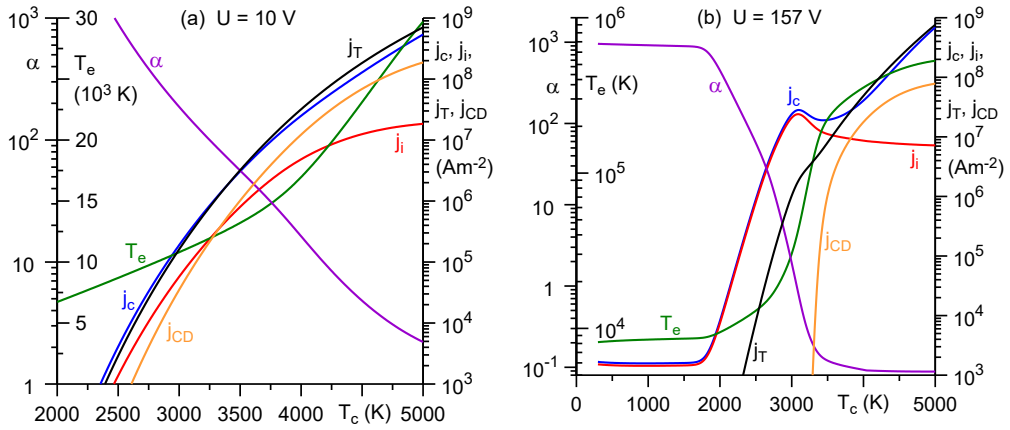

Fig. 1 Characteristics of the non-equilibrium NCPL on a tungsten cathode in atmospheric-pressure argon arc.

cathode layer to attain full ionization. In the case where U is high enough the ion current can be significant even for low cathode surface temperatures, when j_T is negligible. In other words, the secondary electron emission is strong enough to supply the necessary ionization energy to the near-cathode plasma; the glow discharge regime. The dependence of j_i on T_c is weak in this regime.

As T_c increases, the electron temperature in the ionization layer, T_e, increases as well and the ionization degree of the plasma also increases. As the plasma at the edge of the ionization layer approaches full ionization, the ion current j_i becomes saturated and is no longer proportional to j_T. For high values of U a maximum in the dependence $j_i(T_c)$ appears. After the maximum, the dependence $j_i(T_c)$ monotonically decreases and saturates. This causes a decrease in j_c. This decrease of the density of ion current is unrelated to the account of the secondary electron emission, introduced in this work. The detailed description of the reason for this decrease is provided in [3].

A comparison of results given by the approximate and unified models is shown in Fig. 2. The solid lines depict characteristics of the cathodic part of a steady-state arc on a 1 cm-high tungsten cathode in atmospheric-pressure argon. The dashed lines in in Fig. 2 represent results obtained with the use of the unified model [4]. The computation domain in this case included 1 cm-high tungsten cathode, 1 cm-high tungsten anode, and a 1 mm-long arc. T_e shown by the dashed line was evaluated in the unified model at an "edge" of the space-charge sheath, defined as a point where the charge separation is 10%. There is a good agreement between the two models.

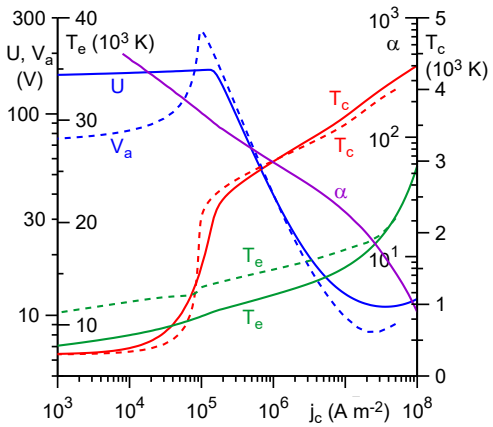

Fig. 2 Characteristics of the cathodic part of a steady-state arc on a 1 cm-high tungsten cathode in atmospheric-pressure argon.

The introduction of secondary electron emission into the approximate model of non-equilibrium NCPL of high-pressure arc discharges [2] allows one to self-consistently describe, in the framework of a single model, glow-like discharges on cold cathodes and thermionic arc discharges on hot cathodes. This is an essential step in the development of practicable self-consistent multidimensional modelling methods of ignition of high-current arcs on cold refractory cathodes.

Acknowledgments The work was supported by FCT - Fundação para a Ciência e Tecnologia, I.P. under projects UIDB/50010/2020, UIDP/50010/2020, LA/P/0061/2020 and by European Regional Development Fund through the Operational Program of the Autonomous Region of Madeira 2014-2020 under project PlasMa-M1420-01-0145-FEDER-000016.

[1] S Frohnert *et al, Plasma Physics* 1 (2022).
[2] M S Benilov *et al, Plasma Sources Sci. Technol.* **14** 517 (2005).
[3] M S Benilov *ESCAMPIG XXVI, Brno, Czech Republic, July 9–13* (2024).
[4] D F N Santos *et al, J Phys D Appl Phys* **54** 195202 (2021).

Surface recombination in Pyrex in CO_2 DC glow discharges

Pedro Viegas(*)[1], André Filipe[1], Jorge Silveira[1], Tiago Cunha Dias[1], Ana Sofía Morillo Candás[2], Olivier Guaitella[2], Vasco Guerra[1]

[1] *Instituto de Plasmas e Fusão Nuclear, Instituto Superior Técnico, Universidade de Lisboa, Portugal*

[2] *Laboratoire de Physique des Plasmas (UMR 7648), CNRS, Univ. Paris-Saclay, Sorbonne Université, École Polytechnique, France*

(*) pedro.a.viegas@tecnico.ulisboa.pt

CO_2 plasmas are an efficient way to convert green house gas CO_2 on Earth or to produce valuable products in space, for instance using the Martian CO_2 atmosphere. Indeed, through plasma, CO_2 can be converted into CO, which can be transformed into added value fuels, and breathable O_2. In CO_2 conversion plasmas, atomic oxygen is extremely important as reactant either for dissociation ($CO_2 + O \rightarrow CO + O_2$) or for recombination ($CO + O + M \rightarrow CO_2 + M$). O is essentially produced by electron-impact dissociation ($CO_2 + e \rightarrow CO + O + e$) and, particularly at low pressures (below 50 mbar), it can be lost by recombination on the wall through heterogeneous surface kinetics processes. As such, wall recombination plays a very important role in these plasmas. Yet, the recombination probability in CO_2 plasmas and the responsible processes still lack dedicated studies.

In the work by Morillo-Candás et al. (2019) [1], the wall loss frequencies of O atoms were measured in the positive column of a CO_2 DC glow discharge in a Pyrex tube (borosilicate glass) of 10 mm inner radius, at 50 ºC outer wall temperature, for several pressure values between 0.27 mbar (0.2 Torr) and 6.7 mbar (5 Torr) and several discharge currents between 10 mA and 50 mA. It was noticed that the O recombination probability is significantly lower than the one in an oxygen glow discharge in similar conditions (see fig. 1), measured by Booth et al. (2019) [2]. This implies that CO and CO_2 from the plasma interacting with the Pyrex surface not only avoid additional recombination of O but they may also be passivating sites for O recombination. Indeed, the same study [1] measured CO densities and fractions to be much higher than the ones of O. Since both species are expected to be produced mostly via electron-impact dissociation, it was concluded that most atomic oxygen is lost by recombining with O or O_2 (thus forming O_2 or O_3) and not with CO (in that case forming CO_2). However, the processes responsible for these features are still unknown.

In this work we employ numerical simulations to assess the dominant surface mechanisms in CO_2 glow discharges. The simulations are obtained from a mesoscopic model employing deterministic and Kinetic Monte Carlo methods [3-5]. The simulations assess the experimental conditions by Morillo-Candás et al. (2019) [1], but also a new set of experiments with currents of 20 mA and 40 mA, pressures between 1.3 mbar (1 Torr) and 10 mbar (7.5 Torr), wall temperatures of -20 ºC, 5 ºC, 25 ºC and 50 ºC and different CO_2-O_2 mixtures (25% CO_2, 50% CO_2, 75% CO_2 and 100% CO_2). Addressing the different sets of experimental data, with a large number of conditions, is important to verify the robustness of the model and thus of our knowledge of surface interactions. The surface reaction scheme employed in the mesoscopic model in previous works [3-5] is further developed to include the possible interactions of O_2 and CO with the surface and the possibility of O_3 and CO_2 formation as a result. It includes Eley-Rideal (E-R) recombination mechanisms involving gas-phase species O, O_2 and CO interacting with chemisorbed O_S and CO_S species, as well as physisorbed O_F, $O_{2,F}$ and CO_F species, and Langmuir-Hinshelwood (L-H) recombination between physisorbed species and other adsorbed species. The model involves a large number of parameters whose values have a high degree of uncertainty. This work assesses the influence of those parameters on numerical results and on their coherence with the knowledge obtained from experiments.

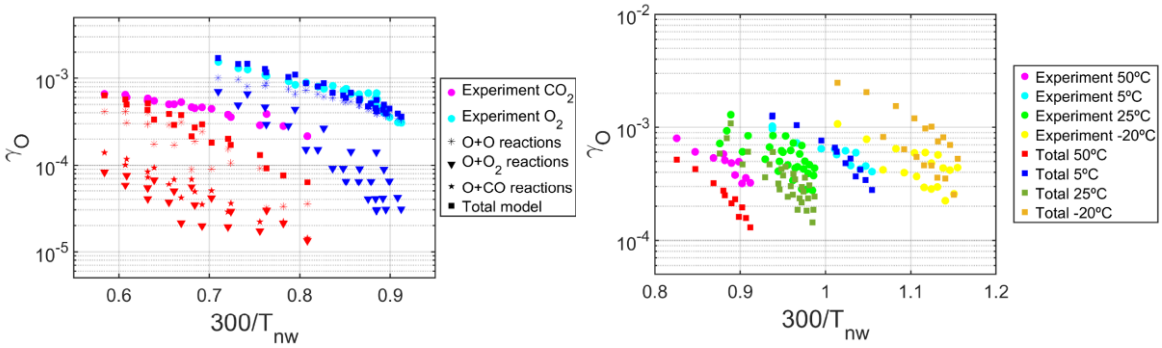

Fig. 1: Measured and simulated atomic oxygen recombination probability as function of the inverse of the near-wall temperature. On the left, for wall temperature of 50 ºC, in O_2 and CO_2 plasmas, with the contributions of the different processes. On the right, for different wall temperatures and O_2-CO_2 mixtures (25% CO_2, 50% CO_2, 75% CO_2 and 100% CO_2).

Fig. 1 shows examples of simulation results, compared to different measurements, for a given set of parameters. The example shows that the model can describe recombination in both O_2 and CO_2 plasmas (and mixtures of those), while holding consistency for different wall temperatures, current and pressure values. For the case of a CO_2 plasma, the simulation results show that recombination reactions between oxygen species are dominant over those between O and CO, in coherence with the analysis of experiments by Morillo-Candás et al. (2019) [1]. At 50 ºC wall temperature, the recombination is due to a mixture of different mechanisms: L-H recombination $O_F + O_F$, E-R recombination $O_2 + O_F$, E-R O + O_S and L-H $O_F + O_S$. These results show that this kind of mesoscopic model can have predictive capabilities when changing conditions, which makes it an excellent tool to contribute to predict different reactor performances.

Acknowledgements

This work was supported by the Portuguese FCT - Fundação para a Ciência e Tecnologia, I.P., by project references: UIDB/50010/2020 (https://doi.org/10.54499/UIDB/50010/2020), UIDP/50010/2020 (https://doi.org/10.54499/UIDP/50010/2020), LA/P/0061/2020 (https://doi.org/10.54499/LA/P/0061/2020), PD/BD/150414/2019 (PD-F APPLAuSE) and PTDC/FIS-PLA/1616/2021 (PARADiSE, https://doi.org/10.54499/PTDC/FISPLA/1616/2021). ASMC acknowledges LabEx Plas@par, receiving financial aid from the French National Research Agency (ANR) under project number ANR-11-IDEX-0004-0 and project SYCAMORE (ANR-16-CE06-0005-01).

References

[1] A. S. Morillo-Candás *et al., Plasma Sources Sci. Technol.* **28** (2019) 075010
[2] J. P. Booth *et al., Plasma Sources Sci. Technol.* **28** (2019) 055005
[3] V. Guerra, *IEEE Transactions on Plasma Science* **35** (2007) 1397
[4] V. Guerra and D. Marinov, *Plasma Sources Sci. Technol.* **25** (2016) 045001
[5] D. Marinov *et al., Plasma Process. Polym.* **14** (2017) 1600175

Concentration and rotational temperature of N_2^+ ions in RF plasma jet measured by LIF

Waseem Khan[1], Pavel Dvořák[1]

[1] *Department of Plasma Physics and Technology, Faculty of Science, Masaryk University, Brno, CZ*
491350@mail.muni.cz

Atmospheric pressure plasma jets (APPJs) ignited in Argon (Ar), Helium (He), and Nitrogen (N_2) are the source of many reactive species (H, O, N, NO, OH, N_2^+, O_2^+, O_2^-, O_3, N_2^*, O_2^*, H_2O_2, NO_2^-, and many others), which play an essential role in plasma chemistry and surface chemistry of many plasma processes [1, 2]. The plasma temperature and concentration of these reactive species in the plasma plume are critical factors that determine the effectiveness of a plasma source for specific uses [3], such as heat-sensitive surface treatment and biomedical applications [4, 5]. The key plasma parameters are controlled by feed gas composition, discharge configuration, and excitation frequency, influencing the plasma's ionization and excitation processes, producing various types of reactive species with different concentrations and temperatures of the plasma plume. This work focuses on the measurement of the concentration of N_2^+ ions and their rotational temperature in the plasma plume by laser-induced fluorescence.

A plasma pencil, a capacitively coupled atmospheric plasma jet driven by radio frequency (RF-13.56 MHz) sinusoidal voltage was ignited in helium, flowing through a silica tube. The APPJ (plasma pencil) is used as the source of N_2^+ ions. The outer and inner diameters of the silica tube are 4.3 mm and 2 mm, respectively. Plasma blows into the ambient atmosphere, where it mixes with the air [6].

The rotational spectrum of N_2^+ ions was obtained by scanning a dye laser across rotational transitions. The measured spectra were fitted to simulated spectra from LIFBASE [7], as shown in Figure 1, and the rotational temperature was calculated from the fitting.

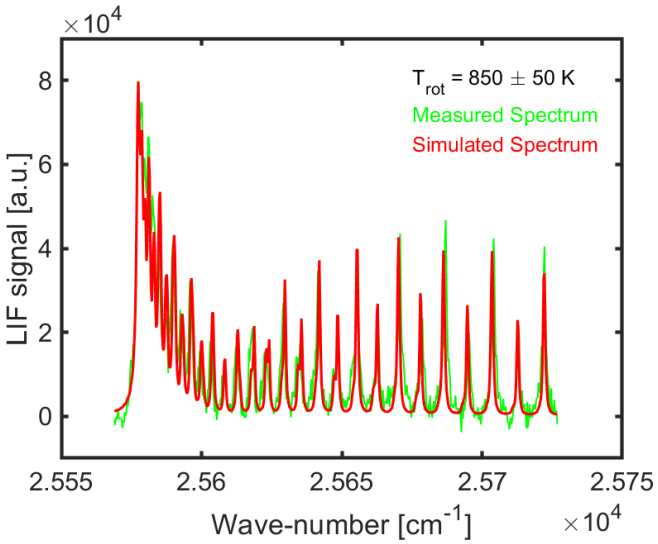

Fig. 1: Fitting of measured and simulated spectra to extract the rotational temperature is shown.

The total density of N_2^+ ions concentration was measured in the effluent of the plasma pencil. The N_2^+ ions concentration dependence on nitrogen gas admixture and RF power was measured as shown in Figure 2 by keeping the He flow rate constant.

The results show that the ions concentration increases up to $1.4 \cdot 10^{17}\,\mathrm{m}^{-3}$ firstly with N_2 flow rate and then decreases for further nitrogen admixture as shown in Figure 2 (left). As the N_2 flow rate increases, more nitrogen molecules are available in the effluent of the plasma pencil, and more collisions between the N_2 molecules with electrons and penning ionization lead to higher nitrogen ionization. So, the density of N_2^+ ions increases initially. However, if we continue increasing the N_2 flow rate, ionization saturation happens, which is caused by several reasons, including the electron energy loss through vibrational and rotational levels of N_2, increase in the collisional quenching rate of helium

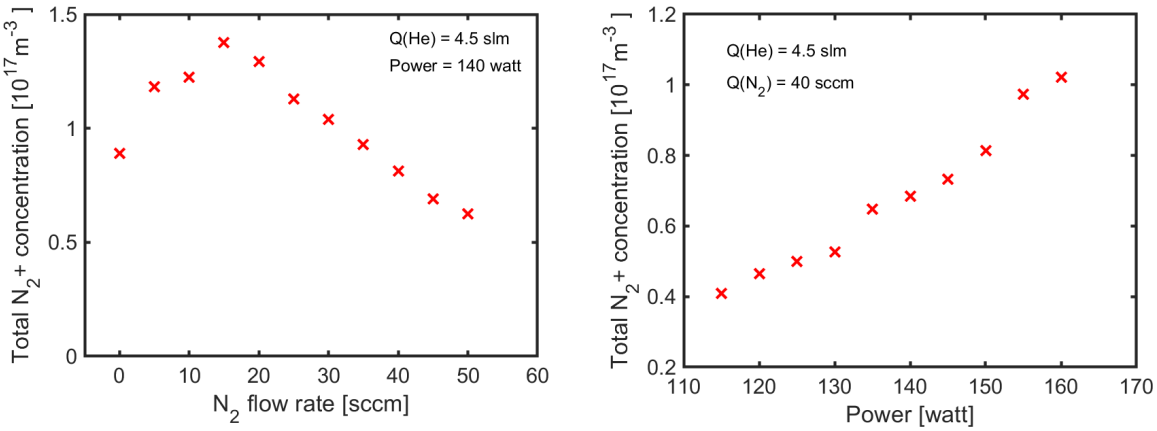

Fig. 2: Dependence of the N_2^+ on the flow rate of N_2 and RF power, keeping the He flow rate constant.

metastable atoms with N_2. Additionally, Jiang Y [8] reported that if N_2 impurity in helium plasma jet is higher than 0.1 % the destruction rates of N_2^+ by the following reactions,

$$N_2^+ + 2\,N_2 \longrightarrow N_4^+ + N_2$$
$$N_2^+ + N_2 + He \longrightarrow N_4^+ + He$$

exceed the production rates of N_2^+ ions occurred due to electron impact ionization and Penning ionization of nitrogen molecules by helium metastables.

The N_2^+ ions concentration increases with the RF power, as shown in Figure 2 (right). As the RF power increases, the overall electron concentration increases, increasing the concentration of high-energetic electrons, so more electrons impact the ionization are the source of N_2^+ ions production.

[1] Khlyustova A, Labay C, Machala Z, Ginebra M P, & Canal C *Front. Chem. Sci. Eng.* (2019) **13**, 238-252.
[2] Lu X, Naidis G V, Laroussi M, Reuter S, Graves D B, & Ostrikov K *Phys. Rep.* (2016) **630** 1-84.
[3] Dedrick J, Schröter S, Niemi K, Wijaikhum A, Wagenaars E, de Oliveira N, & Gans T *J. Phys. D: Appl. Phys.* (2017) **50** 455204.
[4] Fanelli F, & Fracassi F *Surf. Coat. Technol.* (2017) **322** 174-201.
[5] Wijaikhum A, Schröder D, Schröter S, Gibson A R, Niemi K, Friderich J, & Gans, T *Plasma Sources Sci. Technol.* (2017) **26** 115004.
[6] Voráč J, Dvořák P, Procházka, V, Ehlbeck J, & Reuter S *Plasma Sources Sci. Technol.* (2017) **22** 025016.
[7] Luque J, & Crosley D R *SRI international report MP* (1999) 99(009).
[8] Jiang Y, Wang Y, Cong S, Zhang J, & Wang D *Phys. Plasmas* (2020) **27**.

Reverse discharge in bipolar HiPIMS and its dependence on magnetic field geometry

A.D. Pajdarová*, T. Kozák, M. Farahani, J. Čapek

Department of Physics and NTIS – European Centre of Excellence, University of West Bohemia, Univerzitní 8, 301 00 Plzeň, Czech Republic

(*) adp@kfy.zcu.cz

Bipolar high-power impulse magnetron sputtering (BP-HiPIMS) represents a variant of high-power impulse magnetron sputtering (HiPIMS) discharge where the application of a positive voltage pulse (PP) follows a HiPIMS sputtering negative voltage pulse (NP). This PP plays an important role in propelling ions toward the substrate, increasing the deposition rate of films and enhancing their densification and hardness. However, during the PP, there is sometimes registered a reduction in both plasma and floating potentials, which indicates a reverse discharge (RD) occurrence (see Fig. 1). The RD arises mainly from two factors [1]: the generation of secondary electrons by Ar^+ ions impinging on the grounded metallic surfaces in the vacuum chamber and the presence of the mirror configuration of the magnetron's magnetic field in the direction to the target. Since RD is maintained mainly by the generation of Ar^+ ions that are accelerated to the substrate, the presence of RD may lead to a deterioration of deposited film quality. Here, we will focus on the effect of the magnetic field geometry on the presence of the RD during PP.

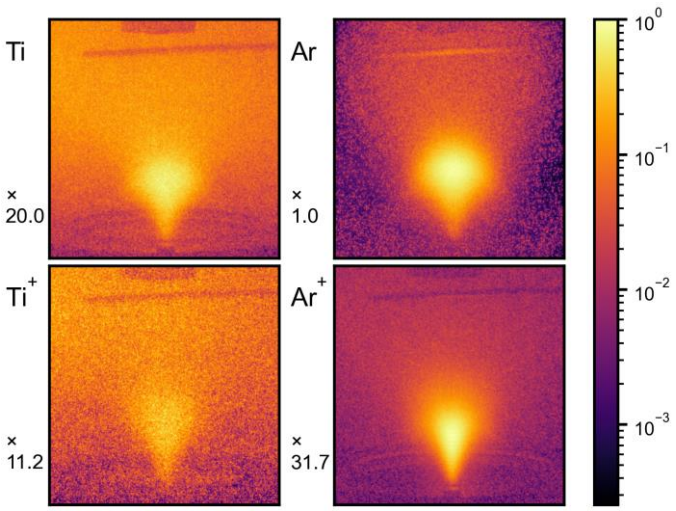

Fig. 1: Light emission from different plasma species proving the presence of RD during a long PP in BP-HiPIMS. Magnetron is positioned at the bottom and the substrate is at the top. Light is recorded by emICCD camera equipped with appropriate band-pass filters. Adapted from [1].

In the experimental setup, a BP-HiPIMS power supply was connected to a circular magnetron target made of titanium with a 100mm diameter. Adjustments to the magnetron's magnetic field, in terms of geometry and strength, were made by altering the positioning of its inner and outer permanent magnets. All experiments were carried out at a constant Ar pressure of 1Pa and an average power density in a period of 380Wcm^{-2}. The NP (a length of 100μs) was followed by the PP (a length of 500μs) after a delay of 10μs. The floating potential was monitored by wire probes located at the discharge centerline and distances of 35, 60, and 100mm from the target. An emICCD camera equipped with a band-pass filter (a central wavelength of 811nm and FWHM of 3nm) monitored light emission from Ar atoms with a time resolution of 5μs in the perpendicular direction to the discharge axis.

The findings indicate that the delay between the start of PP and the onset of RD, as evidenced by a drop in the floating potential, V_f, systematically decreases with a decrease in the outer magnetic field strength (transition from unbalanced to balanced magnetic field geometry). It is proved (see Fig. 2) that

the drop in V_f relates to the RD ignition as the anode light patterns appear (the target is anode during PP). When the inner magnetic field strength is decreased (the magnetic mirror effect at the discharge centerline is weakened), the ignition of RD is postponed. For the weak inner magnetic field, the transition into RD is not registered during the whole PP. The geometry of the magnetic field also influences the shape of the anode light patterns recorded immediately after the RD ignition (see Fig. 2(b) II and V). These patterns evolve during PP into a common shape that resembles a "light bulb" (see Fig. 2(b) III and VI).

We can conclude that the geometry and strength of the magnetron's magnetic field are crucial in influencing the RD ignition during PP. By selecting an optimal magnetic field configuration, it may be possible to either prevent the RD formation or expedite its occurrence during PP in BP-HIPIMS discharges.

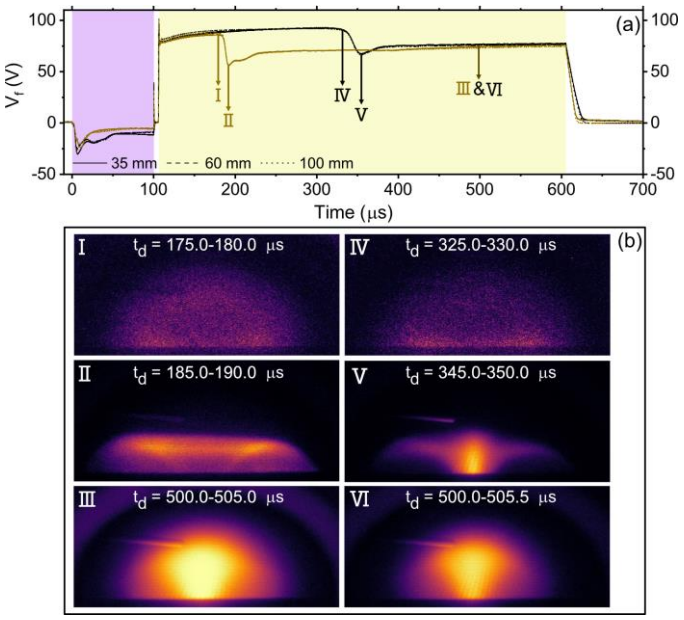

Fig. 2: (a) Time evolution of the floating potential (V_f) for unbalanced (black line) and balanced (brown line) magnetron's magnetic field configuration in BP-HiPIMS (purple and yellow sections of the graph mark NP and PP, respectively). (b) Light emission from Ar atoms recorded for both magnetic field configurations at times which corresponds to arrows in pane (a) marked by roman numerals. Adapted from [2].

[1] A.D. Pajdarová, T. Kozák, T. Tölg, J. Čapek: On double-layer and reverse discharge creation during long positive voltage pulses in a bipolar HiPIMS discharge, *Plasma Sources Sci. Technol.* 33 (2024) 055007.
[2] M. Farahani, A.D. Pajdarová, T. Kozák, J. Čapek: A reverse discharge in bipolar HiPIMS: The effect of the magnetic field configuration, *Plasma Sources Sci. Technol.*, prepared.

Machine learning prediction of the electron density and the electron energy distribution function from the optical emission spectra

Fatima Jenina Arellano[1], Minoru Kusaba[2], Stephen Wu[2,3], Ryo Yoshida[2,3], Satoshi Hamaguchi[1]

[1] *Graduate School of Engineering, Osaka University, Osaka, Japan;*

[2]*The Institute of Statistical Mathematics, Research Organization of Information and Systems, Tachikawa, Japan;*

[3]*Department of Statistical Science, The Graduate University for Advanced Studies, Tachikawa, Japan;*

E-mail: arellano@ppl.eng.osaka-u.ac.jp

Non-invasive diagnostics are invaluable to plasma applications such as semiconductor manufacturing, thrusters, or nuclear fusion, where the plasma should not be disturbed or cannot be easily measured with probes. Optical emission spectroscopy (OES) is a widely used non-invasive diagnostic that can be used to measure the plasma behavior in these applications. However, determining the plasma characteristics from the wealth of information contained in emission spectra is not an easy task. In this study, machine learning (ML) was used to determine the electron density (n_e) and the electron energy distribution function (EEDF) from the optical emission spectra. The ML models were trained on spectral line intensities calculated from a collisional-radiative model (CRM), with a varied combination of n_e and EEDF as the input parameters [1,2]. The n_e and EEDF used in the study include those calculated using a Particle-in-Cell/Monte-Carlo-Collisions (PIC/MCC) simulation [3]. The study was done on a capacitively coupled argon plasma with a pressure ranging from 2-100 Pa. Different ML models were used for the prediction, including Kernel Regression for Functional Data (KRFD) [4,5], an artificial neural network (ANN), and Random Forest.

In this presentation, details of the ML study and its resulting predictions will be discussed, along with the limitations encountered when using this method. Moreover, prediction results for experimentally-measured spectral intensity lines will also be presented.

[1] F. Arellano, M. Gyulai, Z. Donko, P. Hartmann, Ts. V. Tsankov, U. Czarnetzki, and S. Hamaguchi, Plasma Sources Sci. Technol., (2023) 32, 125007
[2] S. Siepa, S. Danko, T. Tsankov, T. Mussenbrock, and U. Czarnetzki, J. Phys. D: Appl. Phys., (2014) 47, 445201.
[3] Z. Donko, Plasma Sources Sci. Technol., (2011) 20, 024001.
[4] M. Iwayama, S. Wu, C. Liu, R. Yoshida, J. Chem. Inf. Model. (2022) 62, 4837-4851
[5] M. Kusaba et al. Kernel Regression for Functional Prediction in Materials Science, in preparation.

Investigation of Stark broadening in plasma conversion reactors by means of high resolution optical emission spectroscopy

Arne Meindl[(*)1], Christian K. Kiefer[1], Rodrigo Antunes[1], Ante Hecimovic[1], Ursel Fantz[1,2]

[1] *Max Planck Insitute for Plasma Physics, 85748 Garching, Germany*
[2] *University of Augsburg, 86159 Augsburg, Germany*
[(*)] arne.meindl@ipp.mpg.de

The emergent field of plasma conversion technology aims to convert certain molecules into other more valuable or useful products through volumetric plasma discharges or with the help of plasma-catalytic surface reactions. Some examples of such processes include CO_2 conversion [1,2], CH_4 pyrolysis [3], dry reforming of CH_4 [4], as well as NH_3 synthesis [5]. Microwave-driven plasma reactors allow for volumetric plasma conversion over a wide pressure range up to industrially relevant atmospheric pressures and beyond, where high gas temperatures T_{trans} enable thermal dissociation of the molecules [2]. Figure 1 displays a microwave-driven plasma torch reactor used for CH_4 pyrolysis.

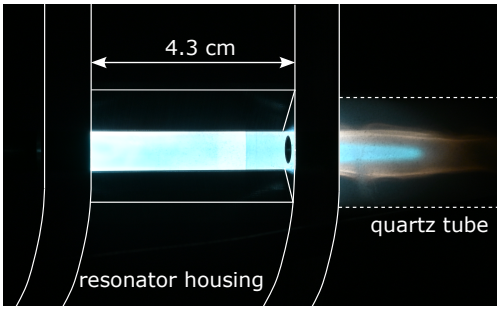

Fig. 1: Microwave-driven plasma torch reactor designed for CH_4 pyrolysis operated at near atmospheric pressure.

An important parameter for understanding the conversion processes is the electron density n_e, since the electrons are delivering the applied energy to the molecules through electron-neutral collisions. This study aims to determine both parameters, T_{trans} and n_e by means of high resolution optical emission spectroscopy of atomic hydrogen emission. T_{trans} is responsible for Doppler broadening of the emission lines, which is of Gaussian shape, while n_e can be determined from Stark broadening, which presents a Lorentzian contribution to the lineshape. A combination of both Gaussian and Lorentzian broadening mechanisms results in an overall lineshape in the form of a Voigt profile.

A high spectral resolution is crucial for precise quantification of the Gaussian and Lorentzian contributions to the lineshapes. For the optical emission spectroscopy (OES) of this investigation, an Echelle spectrometer is used. The spectrometer has a spectral resolution $R = \frac{\lambda}{\Delta\lambda} = 45000$, resulting in instrumental broadenings (FWHM) of $14.6\,\text{pm}$ at $656.3\,\text{nm}$ (H_α) and $10.8\,\text{pm}$ at $486.1\,\text{nm}$ (H_β). Moreover, it enables single-exposure detection of the spectral range from $240\,\text{nm}$ to $880\,\text{nm}$, thus covering the entire Balmer series of atomic hydrogen emission.

For the analysis of the detected spectral lines, lineshape models for H_α and H_β emission have been implemented. In order to approximate the overall lineshape of the atomic hydrogen emission, the hyperfine structure of the atomic hydrogen emission is considered. Figure 2 shows a breakdown of the different hyperfine structure components and the overall resulting profile of H_α emission. For approximation of each of the transitions, Voigt profiles are used, summing up to a resulting profile, which then corresponds to the profiles detected via OES.

The lineshape modeling is further complicated by additional broadening mechanisms that have to be considered. Besides Stark and Doppler broadening, the emission lines are subject to natural line broadening, instrumental broadening, Van-der-Waals broadening, and potentially resonance broadening [6]. Instrumental and Doppler broadening are Gaussian in shape, while the other mechanisms result in Lorentzian shaped broadening contributions. The lineshape model is applied to the measurement via a fitting algorithm. In the first instance, this results in a precise determination of the overall Gaussian and

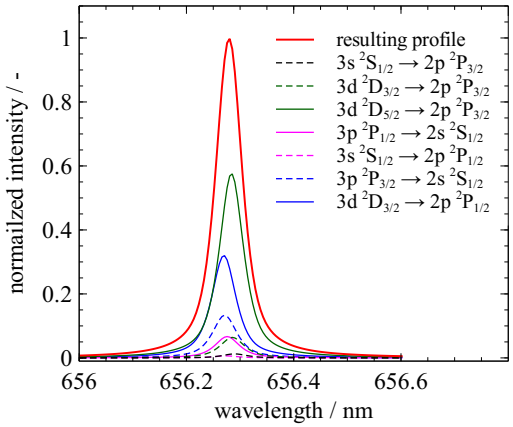

Fig. 2: Contributions of different hyperfine structure components to the overall lineshape of H_α for $T_{trans} = 2100\,\mathrm{K}$ and $n_e = 8 \times 10^{19}\mathrm{m}^{-3}$. Each transition is modeled using a Voigt profile.

Lorentzian components of the Voigt profiles. Knowing the instrumental broadening, the gas temperature T_{trans} can be determined directly from the Doppler contribution to the Gaussian width. Differentiating between the different Lorentzian contributions is more challenging and requires quantification of the other Lorentzian broadening mechanisms in order to determine the Stark contribution and ultimately n_{e} [7,8].

Figure 3 shows an example of an OES measurement taken in the resonator section of a CH_4 microwave discharge (see Fig. 1). The electron density n_{e} and gas temperature T_{trans} are determined using a lineshape model accounting for the hyperfine structure as well as natural, instrumental, Doppler, Van-der-Waals, and Stark broadening.

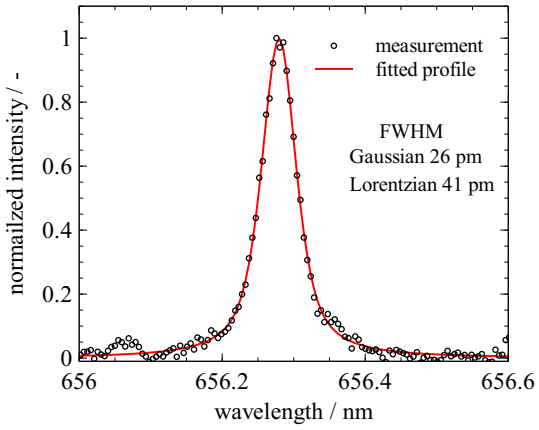

Fig. 3: High resolution measurement of H_α emission in a CH_4 microwave discharge at 100 mbar with lineshape fit resulting in $T_{\mathrm{trans}} = 2100\,\mathrm{K}$ and $n_{\mathrm{e}} = 8 \times 10^{19}\mathrm{m}^{-3}$.

[1] R. Snoeckx et al., *Chem. Soc. Rev.* **46** (2017) 5805–5863.
[2] A. Hecimovic et al., *Journal of CO_2 Utilization* **71** (2023) 102473.
[3] S. Kreuznacht et al., *Plasma Processes and Polymers* **20** (2023) 2200132
[4] S. Kelly et al., *Journal of CO_2 Utilization* **75** (2023) 102564.
[5] P. Navascués et al., *ACS Sustainable Chem. Eng.* **8** (2020) 14855-14866.
[6] A.Y. Nikiforov et al., *PSST* **24** (2015) 034001.
[7] D.E. Kelleher, *J. Quant. Spectrosc. Radiat. Transfer* **25** (1981) pp. 191-220.
[8] P.D.G. Maqueo et al., *J. Phys. D: Appl. Phys.* **51** (2018) 134005.

Spatial characterization of N(^{4}S) in a microwave plasma jet at atmospheric pressure by fs-TALIF

C. Pascual-Fort[1*], A. Brisset[1], N. De Oliveira[2], N. Minesi[1], C.O. Laux[1], G.D. Stancu[1]

[1] *Laboratoire EM2C, CNRS, CentraleSupélec, Université Paris-Saclay, 3 rue Joliot Curie, 91192, Gif-sur-Yvette Cedex, France*

[2] *Soleil, l'Orme des Merisiers, St. Aubin BP 48, 91192 GIF sur Yvette Cedex, France*

(*) carmen.pascual-fort@centralesupelec.fr

Non-thermal plasma jets at atmospheric pressure are effective sources of reactive species essential for applications in domains of energy, materials, environmental or biomedicine. Atomic radicals, such as atomic nitrogen, play a crucial role, for example, as precursors for species with a high economical value or for nitridation processes. Their characterization and understanding of generation mechanisms are key for development of many potential applications.

Two-Photon Absorption Laser-Induced Fluorescence (TALIF) enables *in situ* measurements of the atomic nitrogen ground state, N(^{4}S), with high spatial and temporal resolution. For ns-TALIF, the most commonly used technique, the signal analysis requires the consideration of quenching processes. Notice that quenching, acting as a competing decay path, can reduce fluorescence decay to a few hundreds of ps in atmospheric pressure plasmas, making the precise measurement of the ground state of atomic species challenging. Utilizing fs or ps lasers at very high intensity (> 100 GW/cm²) may provide a quench-free approach where stimulated emission and photoionization dominate over quenching processes [1].

Here, femtosecond laser pulses are produced by a Ti:sapphire laser system (Spectra Physics Solstice ACE) that generates pulses within the wavelength span of λ = 780–830 nm. The beam output of the Ti:sapphire laser is frequency-quadrupled to reach the TALIF wavelengths falling within the range of 204-207 nm. The fourth harmonic delivers around 20 μJ energy per pulse at a repetition rate of 1 kHz. To calibrate fs-TALIF, VUV absorption measurements of N(^{4}S) were performed in a low-pressure DC discharge, at the SOLEIL synchrotron facility, following the work of reference [2]. Because of the high accuracy of the VUV absorption cross sections, this method was preferred instead of the classical Kr calibration.

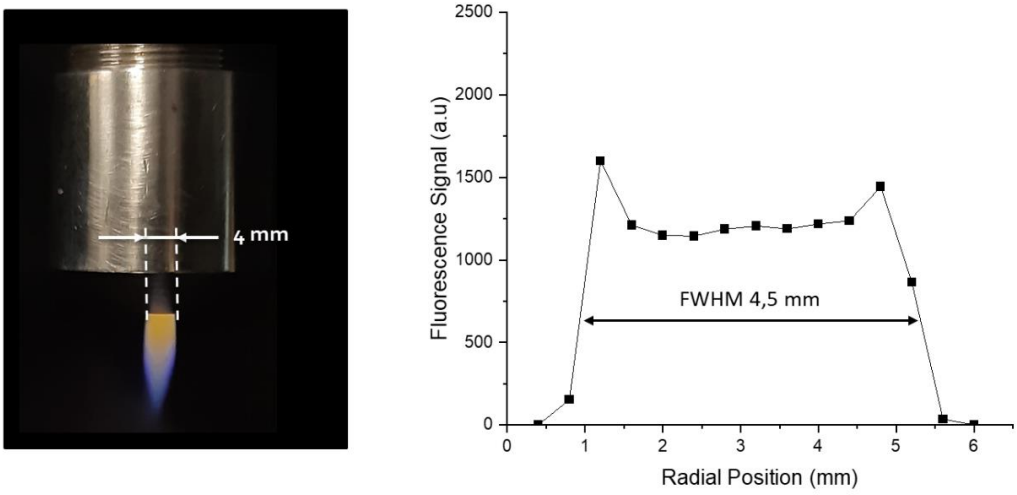

Fig. 1: Photograph of the microwave plasma jet (left). Radial nitrogen fluorescence profile measured using a laser intensity of a few TW cm^{-2} (right).

In this work, the density of $N(^4S)$ has been mapped in a microwave plasma jet operated at atmospheric pressure using the fs-TALIF technique. The MW jets were generated with powers in the range of few tens of watts, in gases containing pure nitrogen or mixture of air and argon and at flows of about a l/min. As shown in figure 1 (right), plasmas of about 4 mm diameter and 2 cm length were generated. In figure 1 (left) is presented a typical measurement of the fluorescence signal obtained radially across a pure nitrogen plasma jet at atmospheric pressure. This was performed using a laser intensity on the order of a few $TWcm^{-2}$.

In the present contribution the absolute spatially resolved $N(^4S)$ density measurements using calibrated fs-TALIF will be presented for different microwave plasma jet configurations.

[1] Stancu G.D. *Plasma Sources Sci. Technol*. **29** (2020) 054001
[2] Dumitrache C. et al. *Plasma Sources Sci. Technol.* **31** (2022) 015004

Breakdown with solid insulation flashover in naturally occurring gases, SF6, and its alternatives

Michal Krbal(*)[1], David Prokop[2], Lucia Kuthanová[2], Stanislav Kadlec[3], Tomáš Hoder[2]

[1]*Department of Electrical Power Engineering, Faculty of Electrical Engineering and Communication, Brno University of Technology, FEKT, Technická 12, Brno 616 00, Czech Republic*

[2] *Department of Plasma Physics and Technology, Masaryk University, Kotlářská 2, 611 37 Brno, Czech Republic*

[3] *Eaton European Innovation Center, Bořivojova 2380, 252 63 Roztoky, Czech Republic*

(*) krbal@vut.cz

Electrical engineering utilizes power components such as gas/solid insulated switchgear, switches, substations, or busbars for power distribution. The SF_6 gas with high global warming potential should be replaced with alternatives like C_4F_7N and its mixtures or with naturally occurring gases (air, N_2, CO_2) at higher pressures. Understanding the breakdown behavior in these gases with solid insulation flashover [1 - 4] is therefore important. Two different test cells were designed and built to study these phenomena[i]. The cells enable evacuation to high vacuum and gas filling up to 300 kPa, monitored by a pressure sensor. Both cells enable modification of the geometry (electrode distance, solid insulator position) without breaking the atmosphere. This work focuses on the measurement of the tested gas mixtures in both cells and statistical data evaluation of results.

The experiments were focused on the measurement of the process of streamer formation and propagation in time, the measurement of the electric strength/breakdown voltage of the gas dielectric with user-adjustable parameters: different distribution of the electric field and gas pressure, and on further analyzing the discharge activity near the surface of inserted solid dielectric materials. Areas of research on discharges in gases include experiments with streamers at the submillimeter levels and measurements of discharges at equivalent voltage levels with the power distribution industry, i.e., at dimensions in the order of millimeters and centimeters.

The first smaller test cell located at the workplace at Masaryk University is used for impulse measurement of streamer formation, barrier partial discharges, and advanced EFISH methods of non-invasive electric field distribution measurement. The maximum peak value of the input voltage is 15 kV - limited by input electrical bushing. The cell is equipped with a stainless-steel electrode system and the possibility of setting the flashover gap in the order of millimeters in the axial direction. The solid dielectric barrier can be placed and manipulated in two directions using an external manipulator in a perpendicular radial axis.

The larger test cell is located in the high voltage laboratory CVVOZEPowerLab at BUT. The test cell is designed for testing overvoltage conditions in equipment up to a nominal voltage level of 35 kV. This corresponds to tests with applied alternating effective voltage up to 70 kV and tests with applied impulse voltage (LI – lightning impulse 1.2/50 μs) up to the peak value of both polarities 170 kV. The flashover distance of the electrode system in the axial direction can be adjusted in the range of 0-50 mm. Using a bellows-sealed 3-axis manipulator, the inserted solid dielectric barrier can be manipulated in the direction perpendicular to the electrode`s axis in the range of 0-50 mm and the position of both other axes can be corrected in the range of ±10 mm.

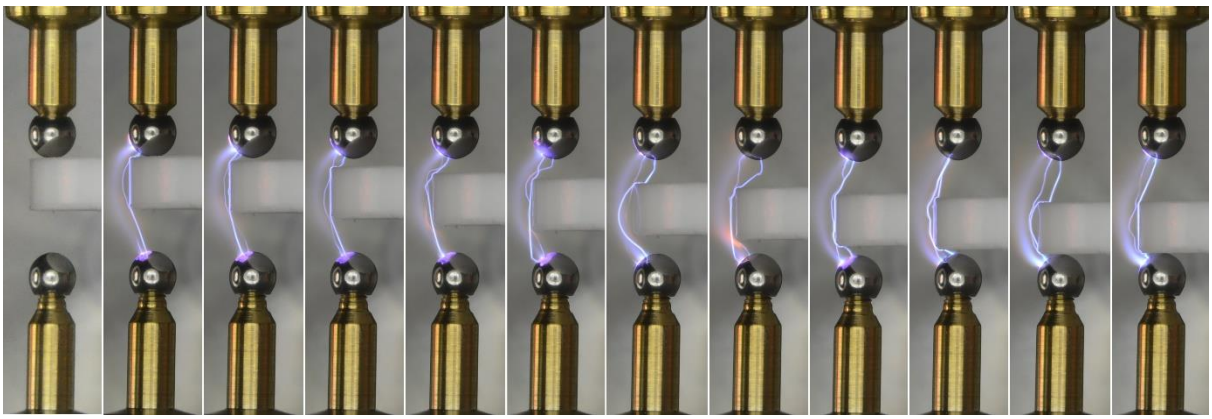

Figure 1: Sphere-sphere flashover in dry air with a PTFE solid dielectric barrier in different vertical positions.

Measurements of electric strength/breakdown voltage under different conditions of pressure, distribution/homogeneity of the electric field, and flashover distances are presented. The comparison of SF_6 results with other naturally occurring gases and C_4F_7N gas in various mixtures with CO_2, O_2, and N_2 is given. The analysis and measurement of the discharge activity are carried out not just by measurement of applied voltage and current time course, but also by recording a static photograph of the discharge track and by using advanced tools such as a high-speed camera and a high-speed spectrum analyzer. Examples of flashover in the air with a PTFE solid dielectric barrier in different positions are shown in Figure 1.

[1] M. Abdel-Salam et al., *J. Phys. D: Appl. Phys*., **34**, (2001) 1219.

[2] S. M. Lebedev et al., *IEEE Transactions on Dielectrics and Electrical Insulation*, **12**, (2005) 537.

[3] H. K. Meyer et al., *2016 IEEE Conference on Electrical Insulation and Dielectric Phenomena (CEIDP)*, Toronto, Canada, (2016) 1037.

[4] T. Ovad et al., J. *Chem. Phys*. **158**, (2023) 014303.

[i] This research has been supported by the Technology Agency of the Czech Republic within the project TK04020069: "*Streamers and surface flashover discharges on insulators in alternative gases to SF6*".

Optical Emission Spectroscopy of an Electron Beam Sustained Hybrid Discharge of Nitrogen at 1 mbar

D. J. Schreuder[1,2,3], G. Mattausch[2], B. Zimmermann[2], E. von Hauff[(*)2,3]

[1] *Boysen-TU Dresden-Research Training Group, TUD Dresden University of Technology, Dresden, Germany.*

[2] *Fraunhofer Institute for Organic Electronics, Electron Beam and Plasma Technology (FEP), Dresden, Germany.*

[3] *TUD University of Technology, Faculty of Electrical and Computer Engineering, Dresden, Germany.* [(*)] david.schreuder@tu-dresden.de

Power-to-X (PtX) processes can be exploited for conversion and storage of electrical energy from fluctuating renewable sources in chemical energy, and have great potential to contribute to a sustainable energy system and economy. Compared to other approaches, these processes can advantageously be realized in non-equilibrium gas discharges, serving as a reactive medium for the conversion of different gas molecules. In this context, the energy efficiency of CO_2 dissociation in cold discharges has been studied extensively over the past years [1]. Computational studies suggest that vibrational excitation provides an energy-efficient pathway for the dissociation of CO_2 (via ‚ladder climbing') [2]. In practice however, the conventional plasma sources such as microwave discharges (MW) and dielectric barrier discharges (DBD) suffer from a trade-off in conversion degree and energy efficiency [1]. This trade-off behavior originates from the facts that conventional discharges, first, operate at high electric field strength and feed energy in chemically less-effective dissociation, ionization and excitation processes (figure 1), and second, provide inhomogeneous power density across the educts' gas flow.

Electron Beam (EB) sustained hybrid discharges appear as promising tools for improving the current state of the art. The essential feature of such plasmas is that the ionization required for a voluminous atmospheric glow discharge is externally provided (‚non-self-sustained discharge') via EB irradiation at comparably low power. Because of that, the reduced electric field of the EB sustained hybrid discharge can be significantly lower than the minimum attainable field in self-sustained discharges. This allows flexibility in the choice of the electric field, which drives the high-power glow discharge, thus enabling mode-selective energy transfer to chemically most efficient molecular vibrations (figure 1).

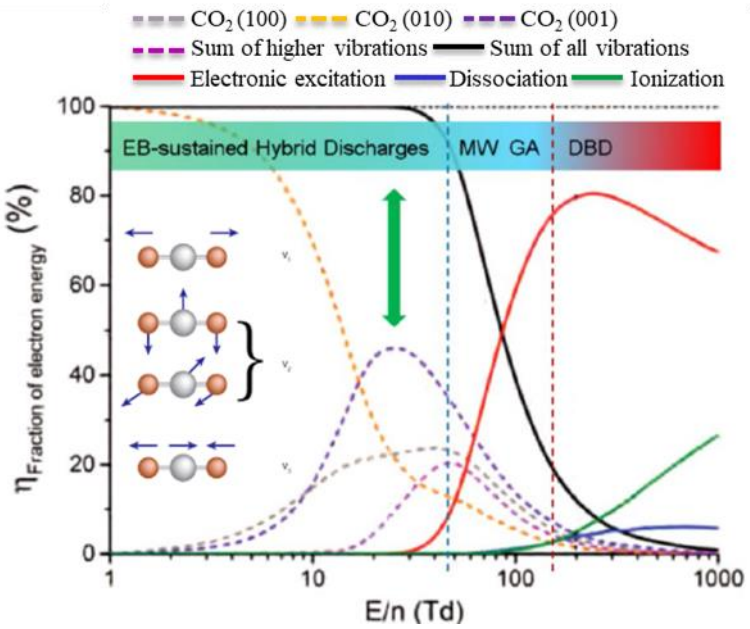

Figure 1: Fraction of electron energy transfer to different processes in CO_2 as a function of the reduced electric field E/n (adapted from [1]).

High-energy beam electrons transfer their energy to the gas via inelastic collisions resulting in ionization processes and secondary electrons [3]. The secondary electrons produced can be heated by electric and magnetic fields to couple supplementary power to the discharge.

In this work, we investigated in the potential for idependently controlling ionization and plasma excitation processes via the electron beam and the inductively coupled plasma (ICP), respectively, using nitrogen as a test gas. We performed quantitative analysis of emission from a 1 mbar N_2 ICP discharge sustained by an electron beam (U_b = 25 kV, I_b = 1-5 mA). The optical emission from the first negative system (FNS) and the second positive system (SPS) of nitrogen is quantified as a function of the EB and ICP currents. Within the beam current range investigated here (I_b = 1 – 5 mA), the FNS (0, 0) (391 nm) has the highest emission intensity (figure 2, solid line) and is linearly correlated to the electron beam current. Furthermore, the emission intensity agrees with the calculated and measured emission in low-pressure hollow cathode electron beam sources reported by Lock et al.[4]. Supplementary ICP power enhances the emission of the SPS bands, while the emission of the FNS (0, 0) signal at 391 nm remains constant. Under assumption of the Corona model, the vibrational energy distribution of the excited state N_2C_3 is calculated via the Boltzmann method and compared to results obtained from a glow discharge experiment at a similar pressure [5]. The influence of the pressure and other parameters on the measured optical emission signals will be discussed. The results show the potential of this experimental approach for chemical conversion processes in non-equilibrium plasmas.

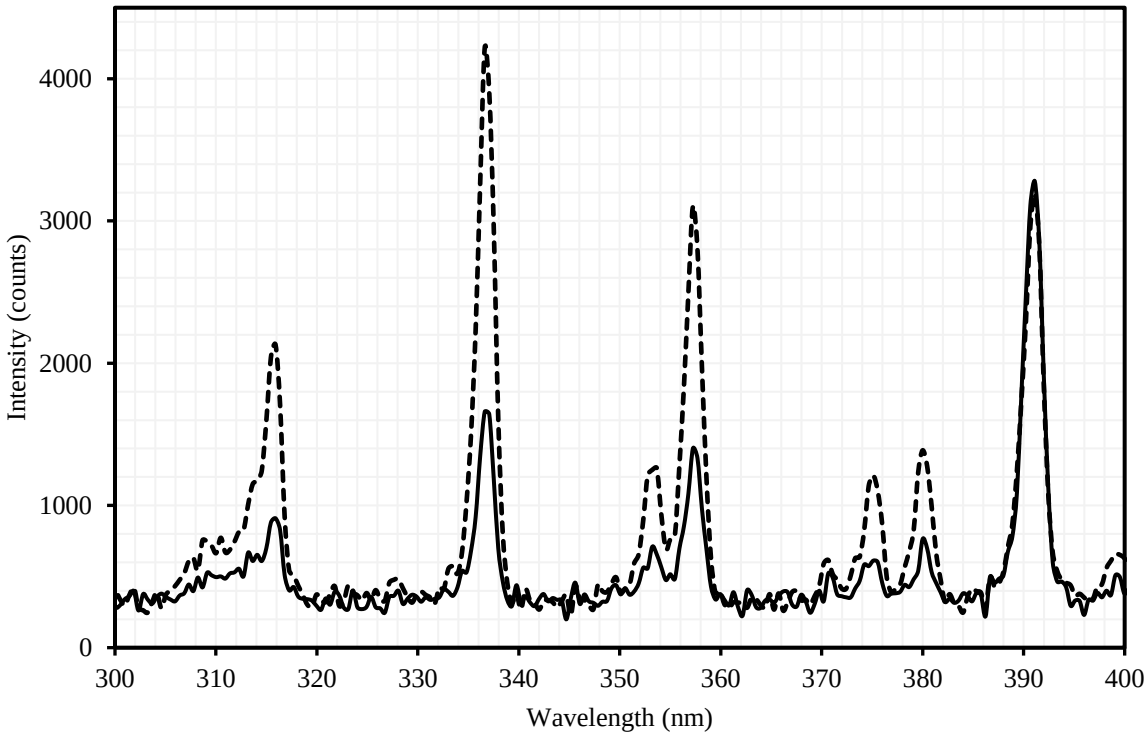

Figure 2: Optical emission spectrum of a 0.54 mbar nitrogen from an EB discharge (solid line) and an EB + ICP hybrid discharge (dashed line). For both spectra, conditions of the EB were U_b = 20 kV, I_b = 1 mA.

[1] R. Snoeckx, A. Bogaerts, *Chem. Soc. Rev.*, **46** (2017) 5805-5863.

[2] A. Bogaerts, T. Kozák, *Plasma Sources Sci. Technol*., **24** (2015) 015024.

[3] R.F. Fernsler, S.P. Slinker, S.G. Lambrakos, *J. Appl. Phys.* **104** (2008), 063312.

[4] E.H. Lock, R.F. Fernsler, S.P. Slinker, I.L. Singer, S.G. Walton, *J. Appl. Phys. D*, **47** (2014), 425206.

[5] J. Levaton, J. Amorim, V. Monna, J. Nagai, A. Richard, *Eur. Phys. J. Appl. Phys*., **26** (2004), 59-64.

Mass spectrometry measurements of the capillary single electrode helium plasma jet

D Maletić(*)[1], N Selaković[1], D Popović[2, 3], S Milošević[2], G Malović[1], Z Lj Petrović[4]

[1]*Institute of Physics, University of Belgrade, Pregrevica 118, 11080 Belgrade, Serbia*

[2]*Institute of Physics, Bijenička 46, 10000 Zagreb, Croatia*

[3]*N2 Applied, Dronning Eufemias gate 20, 0191 Oslo, Norway*

[4]*Serbian Academy of Sciences and Arts, Knez Mihajlova 35, 11000 Belgrade, Serbia*

(*)dejan_maletic@ipb.ac.rs

Plasma jets are simple in construction, but with unique and complex physical and chemical properties that have been in focus of extensive research in the last two decades. These nontermal plasma jets produce complex mixture of reactive species such as ions, radicals, electrons and RONS (reactive oxygen and nitrogen species) and have the potential to revolutionize material processing, biomedicine, agriculture and gas conversion. For example, plasma jets such as micro plasma jet, can be used to etch or deposit thin films on surfaces with high precision, making them useful in the manufacture of microelectronic devices. In biomedicine, plasma jets have been shown to have a range of therapeutic effects, including the ability to kill bacteria and promote wound healing [1]. Plasma jets are streams of highly ionized gas that are generated by an electric discharge. They typically consist of a plasma plume surrounded by a sheath of neutral gas. The electrons can reach high energies while ions and neutral molecules are close to room temperature. Low gas discharge temperatures are crucial in treatment of the thermo sensitive samples such as biological and polymer materials. Some of the recent applications are in production of plasma activated water (PAW) that has been used in sterilization of bacteria and in agriculture to promote plant growth [2]. Many different methods have been used for diagnostics of plasma jets such as optical emission spectroscopy, ICCD imaging, ultra fast imaging, electrical measuremts, mass spectrometry, laser diagnostics [3, 4, 5].

Here, we report mass spectrometry of atmospheric pressure plasma jet. The body of the jet is made of Teflon, the glass capillary (inner diameter of 1 mm and outer diameter 1.5 mm) and electrode copper wire (100 μm), see Fig. 1. The working gas was helium at a constant flow rate of 2 slm. The distance from the mass spectrometer HPR-60 was 15 mm in all measurements. We measure the current and voltage signals at the plasma jet electrode, while changing the output power of the high voltage power

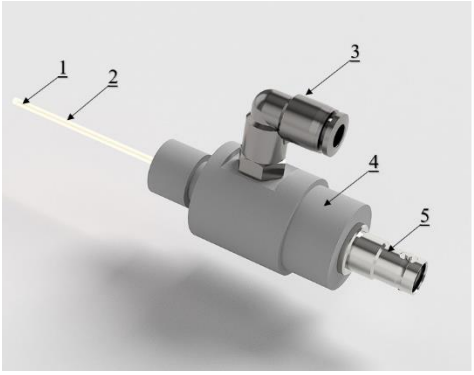

1. Electrode
2. Glass capillary
3. Gas connector
4. Plasma jet body
5. HV connector

Fig. 1: Plasma jet

supply. Mass spectrometer was used to measure the neutrals and ions present in the plasma jet plume. Before each measurement we record ion energy distribution for the most abundant ion present in plasma

N_2^+ to confirm that the discharge is not entering the mass spectrometer. The maximum of the ion energy distribution should be below 5 eV and there should be no additional maxima at higher energies (not shown here).

In figure 2 we presented the yields for the positive ion mass spectra (SIMS+ mode) for the 5.7 Vpp and feeding gas flow rate of 2 slm. From the graph we can see that the plasma jet plume is rich with ion species that are needed in treatment of surfaces for cleaning or sterilization.

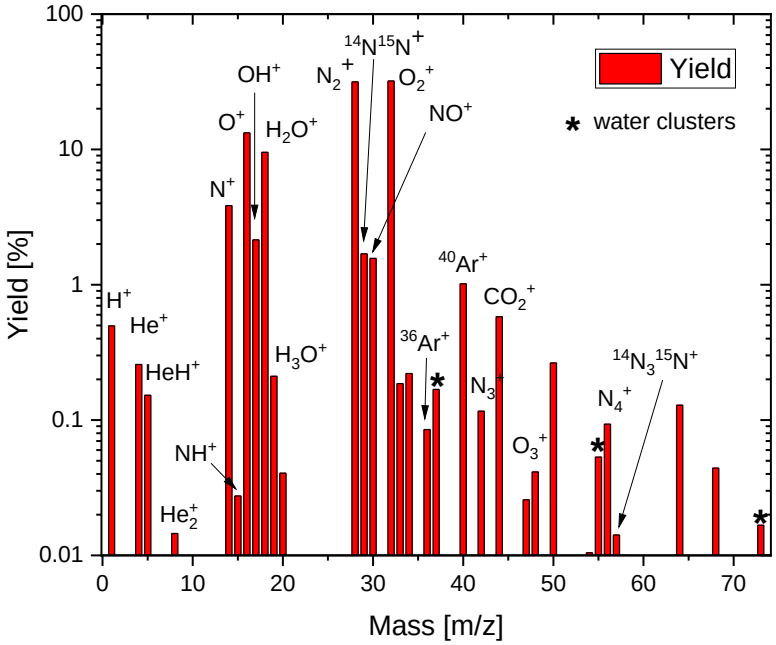

Fig. 2: Yields of the positive ions formed in plasma jet, 5.7 kVpp, 2 slm

In Figure 2 one can see mass spectrum of positive ions where the most abundant species are oxygen and nitrogen. The species formed by ionization of the working gas such as He^+, HeH^+ and He_2^+ are also significant.

Humidity in atmosphere influences production of OH^+, H_2O^+, H_3O^+ and appearance of water clusters $H^+(H_2O)_n$, which are shown in the image with an asterisk. The rich spectrum of positive ions obtained from the plasma jet indicates its potential application. The mass spectrometer technique itself is a powerful tool for monitoring and designing the spectrum itself.

Acknowledgment: This work was supported by MSTDI Republic of Serbia grant number 451-03-68/2023-14/200024. Z. Lj. P. is grateful to the SANU Project F155 for partial support. This work was supported by the project Adaptation of vegetables to new agrometeorological conditions in Slavonia (AVACS), KK.05.1.1.02.0004. The project was financed by the European Union from the European Regional Development Fund.

[1] E. H. Choi et al. *AAPPS Bulletin* **31** (2021) 10.
[2] N. Romanjek Fajdetić et al *Sustainability* **14** (2022) 16237.
[3] D. Maletić et al *Plasma Sources Sci. Technol.* **31** (2022) 025011.
[4] A. Stancampiano et al *J. Phys. D: Appl. Phys.* **51** (2018) 484004.
[5] J. Benedikt et al *Plasma Sources Sci. Technol.* **30** (2021) 033001.

Ro-vibrational temperatures of CO(X) deduced from emission of third positive and angstrom system of CO in CO_2 glow discharge.

D Sadi[1], E Barrate[1], T Silva[2] , O Guaitella[1]

[1] *Laboratoire de Physique des Plasmas, Ecole Polytechnique, Route de Saclay, 91128, Palaiseau, France*

[2] *Instituto de Plasmas e Fusão Nuclear – IPFN, IST Lisbon, Av. Rovisco Pais 1, 1049-001 Lisboa, Portugal*

Non-thermal plasmas (NTPs) offer a promising route for efficient CO_2 dissociation by inducing vibrational excitation in molecules. This process, driven primarily by electron temperature, selectively transfers energy to initiate chemical reactions like CO2 dissociation more efficiently than conventional methods. However, the non-equilibrium nature of NTPs complicates gas temperature determination, as electrons, ions, neutrals, and radicals are not in equilibrium. Additionally, different molecular degrees of freedom may be out of equilibrium, leading to varying characteristic temperatures. Various techniques, [6] such as Rayleigh and Raman scattering, Doppler broadening, thermocouples, absorption spectroscopy (FTIR or QCL), optical probes, IR cameras, and Optical Emission Spectroscopy (OES), are employed to measure gas temperature in non-equilibrium plasma. OES, offering a wide spectral range without disturbing the plasma, is particularly accessible and efficient. However, interpreting emission spectra requires caution, as emphasized in the literature.

We investigate on the possibility of using optical emission spectroscopy to quantify the degree of vibrational and rotational excitation of CO in CO_2 discharges. Experimental data is collected from glow discharges at pressures of 1-5 Torr and currents of 10-50 mA. We analyze CO vibrational and rotational excitation using optical emission spectroscopy of the 3rd positive and Angström systems, respectively spanning 250-360 nm and 400-570 nm. Those systems hold particular interest because they emit in an easily accessible spectral range, they do not overlap with other systems, and spectroscopic datas are available and multiples. Systematic comparison of those temperatures to those obtained from (i) infrared absorption spectroscopy in such discharges, (ii) the LisbOn KInetic (LOKI) simulation tool developed at IPFN [1] allow an estimation of the accuracy of the methods, as shown on figure 1.

Two methods are often used in plasma spectroscopy to deduce vibrational temperatures from molecular emission bands: 1) a "boltzmann plot", measuring the ratio of the peak intensity of vibrational transitions [8] 2) simulating the complete spectrum of the molecular band considered [9]. Both of these methods gives the vibrational temperature of the excited state that is responsible for the emission which is not representative of the vibrational temperature of the gas in the discharge [7]. A collisional-radiative model is needed to relate the obtained temperature of the emitting excited state to the vibrational distribution function of the ground state. In this study, we use a simplified method employing Frank-Condon factors without accounting for quenching.

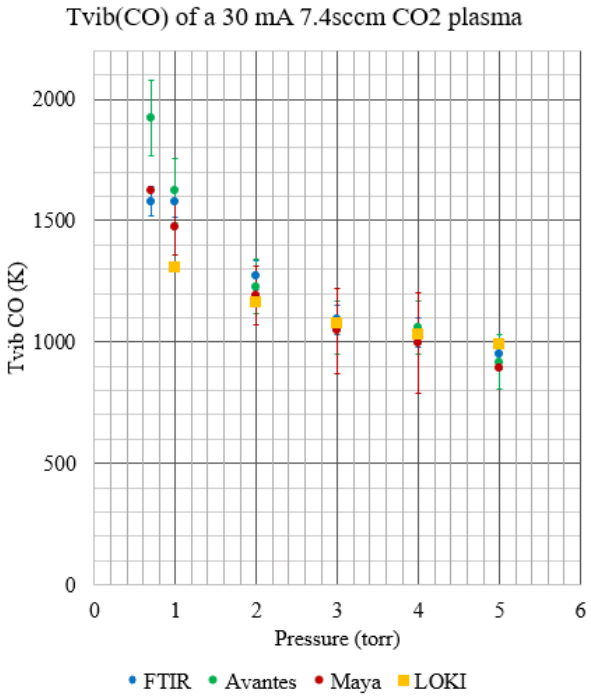

Figure 1 : Comparison of Tvib(CO) obtained through FTIR, OES and LOKI

The results of those methods depends strongly on the choice of the radiative parameters and spectroscopic constants. As a consequence this method can be use as a benchmark to validate important radiative parameters such as : Einstein coefficients of the b → a and B → A transitions which are given in the literature by [4] and [3]; Hönl London factors of the same transitions that are calculated using [10] and [5], Frank-Condon factors of b → a and B → a and X → b, either calculated using [2] or given by [4], and finally lifetimes of excited states given by [3].

This diagnostic is thus validated against FTIR measurements and can be used thanks to its spatial flexibility in order to measure vibrational and rotational temperature of CO in CO_2 containing plasmas with complex geometries.

[1] Antonio Tejero-del Caz, Vasco Guerra, D Gonçalves, M Lino Da Silva, L Marques, Nuno Pinhao, CD Pintassilgo, and LL Alves. The lisbon kinetics boltzmann solver. *Plasma Sources Science and Technology*, 28(4) :043001, 2019.
[2] JC López V, AL Rivera, Yu F Smirnov, and A Frank. Simple evaluation of franck–condon factors and non-condon effects in the morse potential. *International journal of quantum chemistry*, 88(2) :280–295, 2002.
[3] Z Qin, JM Zhao, and LH Liu. Radiative transition probabilities for the main diatomic electronic systems of n2, n2+, no, o2, co, co+, cn, c2 and h2 produced in plasma of atmospheric entry. *Journal of Quantitative Spectroscopy and Radiative Transfer*, 202 :286–301, 2017.
[4] M Lino Da Silva and M Dudeck. Arrays of radiative transition probabilities for co2–n2 plasmas. *Journal of Quantitative Spectroscopy and Radiative Transfer*, 102(3) :348–386, 2006.
[5] BS Beer. Rotationsanalyse der 0→ 4-, 0→ 5-, 1→ 4-und 1→ 5-banden des iii. pos. co-systems. *Zeitschrift für Physik*, 107 :73–85, 1937.
[6] Peter J Bruggeman, N Sadeghi, DC Schram, and V Linss. Gas temperature determination from rotational lines in non-equilibrium plasmas : a review. *Plasma Sources Science and Technology*, 23(2) :023001, 2014.
[7] G Dilecce, PF Ambrico, LM Martini, and P Tosi. On the determination of the vibrational temperature by optical emission spectroscopy. *Plasma Sources Science and Technology*, 31(7) :077001, 2022.
[8] N Britun, M Gaillard, A Ricard, YM Kim, KS Kim, and JG Han. Determination of the vibrational, rotational and electron temperatures in n2 and ar–n2 rf discharge. Journal of Physics D : Applied Physics, 40(4) :1022, 2007.
[9] Shota Yamada, Yuki Morita, Atsushi Nezu, and Hiroshi Akatsuka. Nonequilibrium characteristics in the rotational temperature of co excited states in microwave discharge co2 plasma. Japanese Journal of Applied Physics, 60(4) :046005, 2021.
[10] Vladimir N Ochkin. *Spectroscopy of low temperature plasma.* John Wiley & Sons, 2009.

Quantitative analysis of NO_2 generated in Atmospheric Pressure Plasma Jet using Ion Mobility Spectrometry

Emanuel Maťaš(*)[1], Michal Neogrády[1], Ladislav Moravský[1], Štefan Matejčík[1]

[1] *Department of Experimental Physics, Faculty of Mathematics, Physics and Informatics, Comenius University, Mlynská dolina F2, 84245 Bratislava, Slovakia*

(*) *emanuel.matas@fmph.uniba.sk*

Reactive oxygen and nitrogen species (RONS) play key roles in numerous biochemical, physiological, and pathological processes. Among them, species such as O_3, OH, NO_2, NO_3, N_2O_5, etc., can be efficiently generated utilizing atmospheric pressure plasma jets (APPJ) in Argon [1–4]. The controlled production of RONS by APPJ finds widespread applications in biomedicine for wound healing [5], cancer treatment [6], immune cell activation [7], surface treatment and sterilization [8, 9]. Various diagnostic techniques, including Fourier-transform infrared (FTIR) spectroscopy [10], chemical and semiconductive gas sensors [11, 12], have been employed for RONS detection.

The APPJ utilized in this study was developed at the Department of Experimental Physics, Comenius University Bratislava [1]. The Ar plasma jet was generated within a glass capillary with an internal diameter of 0.5 mm, employing a hollow needle to cylinder geometry configuration. A high voltage with an amplitude from 1 to 4 kV (0.09 to 1.2W) and a frequency of 9.45 kHz was applied to the needle. The flow rate of Ar (purity 4.6) was varied at 20, 50, 100, 150 and 200 mL/min.

The IMS employed for detection of NO_2 generated by APPJ and assessing electron transfer reactions between reactant ions (RI) $O_2^-.CO_2.(H_2O)_{0,1,2}$ and NO_2 was developed by MaSa Tech Company. The IMS is a rapid (milliseconds to seconds range) [13], highly sensitive (parts per billion to parts per quadrillion level) [14], good portable and powerful analytical technique useful in various fields [15]. Notably, NO_2 and other RONS can be detected in negative polarity mode.

The IMS spectra of the APPJ at discharge power ranging from 0.09 to 1.2 W and Ar gas flow of 100 mL/min are shown in the Fig. 1. The dominant peak with reduced mobility of 2.23 $cm^2.V^{-1}.s^{-1}$ represents RI. Peaks with reduced mobility of 2.50 and 2.38 $cm^2.V^{-1}.s^{-1}$ represent ions NO_2^- and $N_2O_2^-$, respectively. The ionization of neutral NO_x species was carried out using negative chemical ionization method, with RI. In the earlier study, was the IMS quantitative calibrated for NO_2 species [16]. The production of NO_2 generated in APPJ increased with increasing of discharge power (Fig. 1). The maximum NO_2 production of 5.3 ppm was observed at power of 1.2 W (4 kV) and Ar gas flow rate of 100 mL/min.

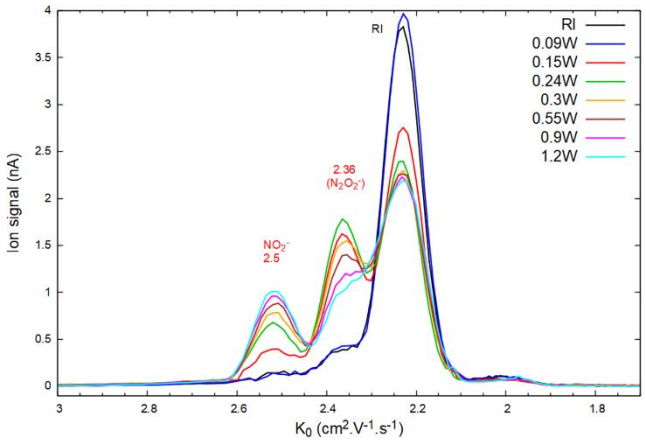

Fig. 1: The IMS spectra of the APPJ at discharge power ranting from 0.09 to 1.2 W and Ar gas flow of 100 mL/min.

The dependence of the concentration of NO_2 generated in the APPJ at different discharge powers, an Ar flow rate of 100 ml/min and different distances of the IMS from the APPJ is shown in the Fig. 2. The concentration of NO_2 slowly increased with increasing IMS-APPJ distance. The maximum NO_2 production (5.3 ppm) was observed at a distance 5 mm and decreased with further increasing IMS-APPJ distances.

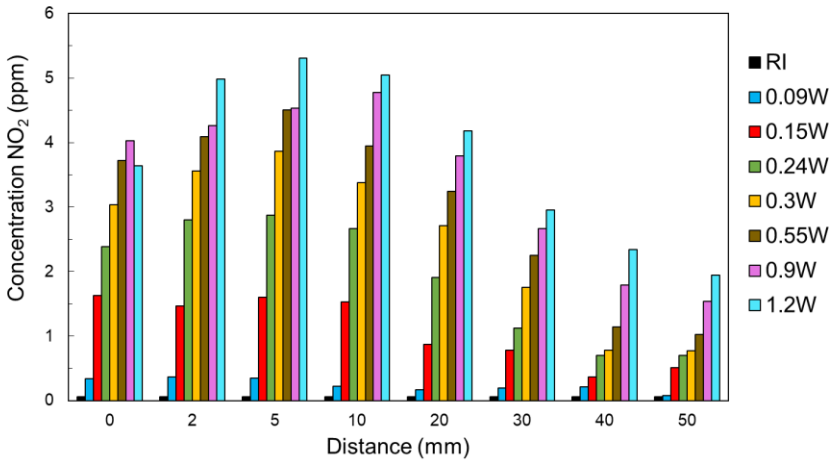

Fig. 2: Production of NO_2 generated in the APPJ at different discharge powers, Ar flow 100 mL/min and different distances of the IMS from the APPJ (0 – 50 mm).

Acknowledgments. The present studies were supported by the Slovak Grant Agency for Science VEGA Nr. 1/0489/21 and Nr. 1/0553/22, Slovak Research and Development Agency under project Nr. APVV-19-0386 and APVV-22-0133.

References:

[1] G. Horváth *et al., IEEE Trans. Plasma Sci.* **41(3)** (2013) 613–619
[2] I. Jõgi *et al., Contrib. Plasma Phys.* **60(3)** (2020) e201900127
[3] R. Brandenburg *et al., IEEE Trans. Plasma Sci.* **37(6)** (2009) 877–883
[4] B. C. Adhikari *et al., Results Phys* **30** (2021) 104863
[5] S. Bekeschus *et al., Clin Plasma Med* **4(1)** (2016) 19–28
[6] Y. Li *et al., Sci Rep* **7(1)** (2017) 45781
[7] A. Lin *et al., Int J Mol Sci* **18(5)** (2017) 966
[8] P. Lamichhane *et al., React Chem Eng* **5(11)** (2020) 2053–2057
[9] O. V. Penkov et al., *J Coat Technol Res* **12(2)** (2015) 225–235
[10] H. Yi *et al., Atmos Meas Tech*, **14(8)** (2021) 5701–5715
[11] S. Fischer *et al., Sens Actuators B Chem* **147(2)** (2010) 780–785
[12] M. T. Vijjapu *et al., ACS Sens* **5(4)** (2020) 984–993
[13] M. Sabo *et al., Talanta* **85(1)** (2011) 400–405
[14] V. A. Kostarev *et al., Talanta* **245** (2022) 123414
[15] G. A. Eiceman and Z. Karpas, *Ion Mobility Spectrometry* 2nd edition. CRC Press (2005) 350
[16] E. Mať aš *et al., Eur. Phys. J. D* **77(2)** (2023) 21

Coherent scattering from ponderomotive-driven density perturbations for plasma diagnostics

Gabriel Flores Alfaro[1,2*], Mikhail N.Shneider[3], Alexandros Gerakis[1,4]

[1] *Luxembourg Institute of Science & Technology, Belvaux L-4362, Luxembourg*
[2] *Université du Luxembourg, 2 avenue de l'université L-4365 Esch-sur-Alzette, Luxembourg*
[3] *Department of Mechanical and Aerospace Engineering, Princeton University, Princeton, New Jersey 08544, USA*
[4] *Department of Aerospace Engineering, Texas AM University, College Station, Texas 77845, USA*
(*) gabriel.floresalfaro@list.lu

Single-shot coherent Rayleigh Brillouin scattering (CRBS) [1] is a four-wave mixing diagnostic technique already established in atomic and molecular gases. It involves two laser beams with the same polarization interfering in a medium. This interference produces an optical dipole potential trapping and pushing atoms and molecules to high-electric field locations due to the dipole force, generating an optical lattice. A third laser beam, with polarization orthogonal to that of the pumps, called the probe, is Bragg diffracted off from the optical lattice, producing a fourth wave, called the signal. The resulting CRBS signal is the summation of a Rayleigh peak due to the individual motion of the atoms and molecules, and two Brillouin peaks due to the bulk movement of the particles centered at the speed of sound. The CRBS signal is proportional to the pump and probe intensities, the square of the induced density perturbation and the polarizability of the particles. By scanning the relative frequency difference between the two pumps, the velocity distribution function of the sampled species can be recovered and thus thermodynamic properties such as translational temperature, density, polarizability [2] can be determined [3].

The application of coherent scattering from optical lattices in plasmas is an unexplored area of research with potential applications in plasma diagnostics. Here, we report on the progress of this matter.

LTPs consist of electrons, ions, and neutrals, thus electromagnetic forces and collision phenomena play an important role. Charged species experience the ponderomotive force, driving them towards regions of low-intensity electric fields. Additionally, ions and neutrals are affected by the dipole force, directing them towards areas of high-intensity electric fields. Currently, our focus lies in developing a model to analyze the dynamics of optical lattices with charged particles and neutrals. Figure 1 illustrates preliminary findings regarding the density perturbation of electrons and ions. The density perturbation has been obtained by solving the two-fluid plasma equations numerically, where ponderomotive forces, collision with neutrals, and a self-consistent electric field have been considered.

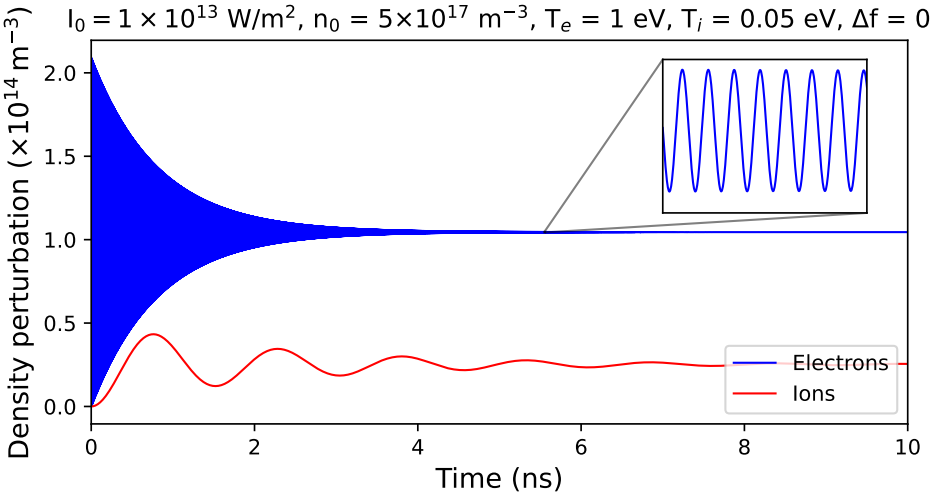

Fig. 1: Electron and ion density perturbation due to ponderomotive forces.

According to our initial findings, the enhanced density perturbations resulting from ponderomotive forces acting on electrons and ions suggest that scattering from these perturbations could provide a notable advantage for plasma diagnostics.

It is important to note that the hydrodynamic regime is used to study high-pressure gases in which Brillouin peaks are observable. At low pressures, in the kinetic regime, the neutral gas contributes mainly to Rayleigh scattering, but the Brillouin peaks do not always appear. In plasmas, scattering on charged particles is associated with Thomson scattering, and on collective periodic perturbations induced by ponderomotive forces - with coherent Thomson scattering.[4].

[1] A. Gerakis, M. N. Shneider, and P. F. Barker. Single-shot coherent rayleigh–brillouin scattering using a chirped optical lattice. *Opt. Lett.*, 38(21):4449–4452, Nov 2013.

[2] Xingguo Pan, Mikhail N. Shneider, and Richard B. Miles. Coherent rayleigh-brillouin scattering. *Phys. Rev. Lett.*, 89:183001, Oct 2002.

[3] A. Gerakis, M. N. Shneider, and B. C. Stratton. Remote-sensing gas measurements with coherent Rayleigh-Brillouin scattering. *Applied Physics Letters*, 109(3):031112, 07 2016.

[4] Mikhail Mokrov, Mikhail N. Shneider, and Alexandros Gerakis. Analysis of coherent Thomson scattering from a low temperature plasma. *Physics of Plasmas*, 29(3):033507, 03 2022.

Nitrogen atoms ps-TALIF in atmospheric pressure nanosecond volume DBD plasma

G Kreyder(*)[1], D Stefas[2], L Invernizzi[2], G Lombardi[2],
K Gazeli[2], S Prasanna[2], SM Starikovskaia[1]

[1] *Laboratoire de Physique des Plasmas, Sorbonne Université, Université Paris-Saclay, Ecole Polytechnique, Route de Saclay, Palaiseau, France*
[2] *Laboratoire des Sciences des Procédés et des Matériaux, CNRS, Université Sorbonne Paris Nord, 99 avenue J.B. Clément, Villetaneuse, France*
(*) geoffrey.kreyder@lpp.polytechnique.fr

Nanosecond (ns) discharges are studied for different applications, where dissociation of molecules often plays a key role. Because of their high electric fields, nanosecond discharges can be efficient for excitation of electronic levels of atoms as well as molecular excitation and dissociation. In the present work, picosecond Two-Photon Absorption Laser-Induced Fluorescence (ps-TALIF) was used to measure the absolute density of N-atoms produced in an atmospheric pressure ns Dielectric Barrier Discharge (DBD) in pin-to-plane configuration. The density measurements were calibrated by performing similar ps-TALIF experiments in Kr gas contained in a gas cell.

Applied voltage and discharge current waveforms were measured by a homemade back-current shunt (BCS) soldered in the shielding of a long coaxial high voltage (HV) cable so that the distance from the BCS to the HV generator and the distance from the BCS to the discharge setup are equal.
A volumetric DBD was ignited by applying 5.1 kV to room atmospheric air in the form of a ns pulse burst containing five pulses, with a 200 ns interpulse period (5 MHz), delivered by a HV generator (FPG-12-1NM FID; rise time 4 ns, pulse width 29 ns and 5 Hz burst repetition rate).

The electrode system (Fig. 1a) consists of a stainless steel needle (HV electrode), an aluminium plate (grounded electrode) covered with a 0.3 mm PVC layer, with 1.8 mm interelectrode gap.

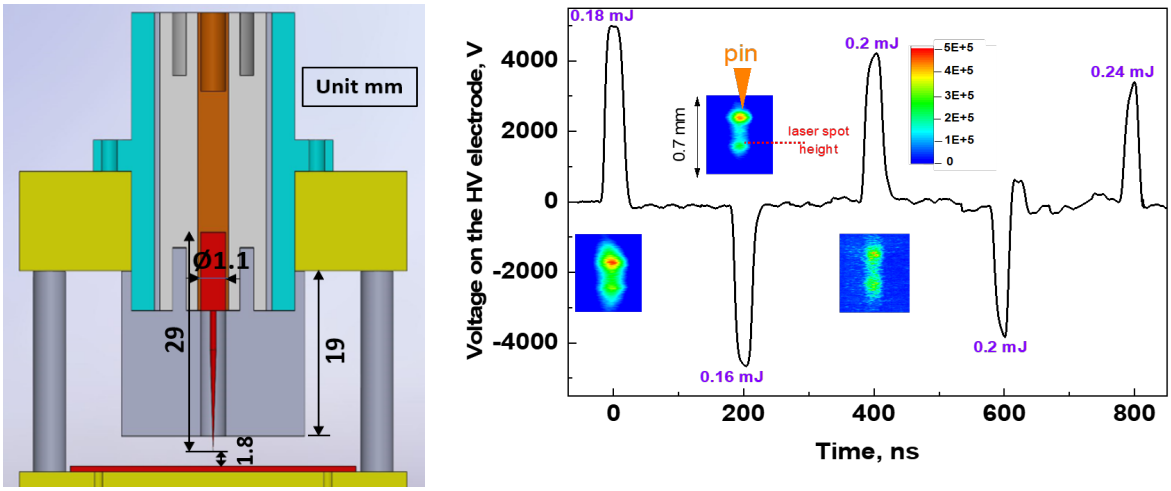

Fig. 1: a) schematic of ns DBD arrangement; b) applied voltage signal on the HV electrode, with delivered energy per pulse and streak camera images for the first three discharges, with a 450 ns time range. The intensity of the third image is multiplied by a factor of 40.

The total deposited energy was estimated to be 0.96 mJ, see Fig. 1b, quasi-equally provided by the five discharges (lowest at 0.16 mJ for the second discharge and highest at 0.24 mJ for the fifth discharge).

The emission of the second positive system of molecular nitrogen was measured with the help of the streak-camera (Hamamatsu C10910-05). The streak camera images corresponding to the first 3 discharge pulses are presented in Fig. 1b.

The ps laser system (Ekspla) [1] used consisted of a Nd:YLF pump laser (PL3140), a harmonic generator and amplifier (APL2100), and a solid-state optical parametric generator (PG411). This provided

10 ps laser pulses at 5 Hz frequency and 206.625, 206.63, 206.635 and 206.64 nm wavelengths, which were synchronized with the discharge using adequate delay generators. The laser energy per pulse has been chosen around 11 μJ to avoid laser-induced secondary processes (such as photoionization ansd amplified stimulated emission(citation) that lead to satured TALIF signals. The laser beam focal spot (200 μm) used for ps-TALIF was positioned near the maximum of emission, 0.4 mm below the HV electrode pin. The ps-TALIF fluorescence around 744 nm was collected by an optical system consisting of 2 lenses and focused at the entrance slit of the streak-camera.

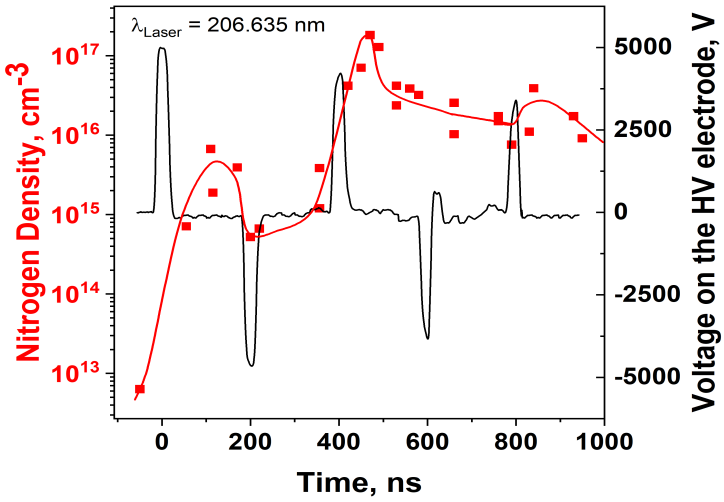

Fig. 2: Nitrogen absolute density evolution in time (red symbols) together with the applied voltage signal on the HV electrode (black curve).

The increase in N-atom density in the vicinity of the third discharge, see Fig. 2, is in correlation with a sharp drop of the fluorescence effective lifetime. Typical streak camera images of ps-TALIF signals are shown in Fig. 3. The decay time of emission was measured to be 150 ps at 200 ns (ie second voltage pulse), and 50 ps at 390 ns (ie third voltage pulse).

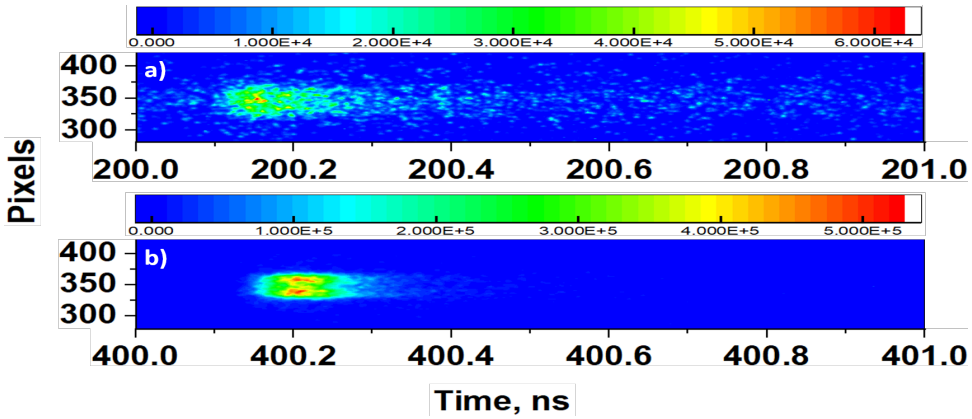

Fig. 3: Streak camera images of the ps-TALIF N-atom signals at a) 200 ns and b) 390 ns.

The maximum N atom absolute density is $2 \cdot 10^{17}$ cm^{-3} (measured after the end of the third pulse) corresponding to $\sim$ 1% of dissociation of N_2. As far as the energy deposited in the third discharge is practically identical to that in the other discharges, an in-depth analysis of kinetic processes involved in the TALIF scheme will be needed to explain a sharp maximum at 400 ns observed experimentally.

The work was partially supported by AID/CIEDS PPRINCE (3335), PEPS ENERGIE 2024 ZEPhiR, E4C (ANR-18-EUR-0006-02)/Engie Foundation, ULTRAMAP (ANR-22-CE51-0027) and Labex SEAM (ANR-10-LABX-0096 and ANR-18-IDEX-0001)

[1] L. Invernizzi, C. Y. Duluard, H. Hoeft, K. Hassouni and G. Lombardi, K. Gazeli, S. Prasanna, *Meas. Sci. Technol* (2023) 145–171.

Mapping the field around a Langmuir probe with charged dust particles

Peter Hartmann(*)[1,2], Jorge Carmona-Reyes[2], Lan-Yue Luo[3], Lorin Matthews[2], Truell Hyde[2]

[1] *HUN-REN Wigner Research Centre for Physics, Konkoly-Thege M. 29-33, Budapest 1121, Hungary*
[2] *CASPER, Baylor University, One Bear Place 97316, Waco, Texas 76798-7316, USA*
[3]*Department of Engineering Physics, Tsinghua University, Beijing 100084, China*
(*) hartmann.peter@wigner.hu

Langmuir and other probe diagnostics are routinely used to determine plasma properties such as electron density and electron energy distribution [1]. Although these experimental techniques are generally considered reliable, the main drawback is that, as an invasive method, the presence of the probe itself alters the properties of the discharge plasmas in its vicinity. Theoretical models, such as the orbital motion limited (OML) approximation of ion transport, can be used to estimate the magnitude and extent of the perturbation [2].

Here we use electrically charged solid dust particles dropped onto a DC biased tungsten probe tip inserted horizontally into the bulk region of an argon capacitively coupled RF discharge operated in a GEC reference cell to visualize and quantify the effect of the probe on the discharge. Fig. 1 shows stacks of 8000 individual sequential snapshots (each with 1/500 sec exposure time), representing two cases differing only in the DC voltage applied to the probe.

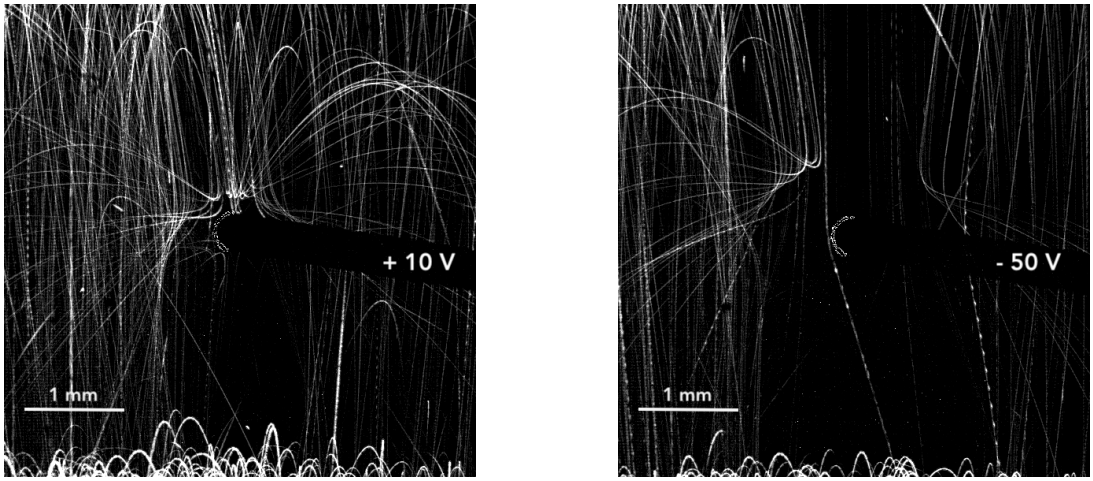

(a) Probe voltage = $+10$ V ($\approx$ floating potential). (b) Probe voltage = -50 V.

Fig. 1: Dust particles (8.89 μm diameter melamine-formaldehyde) raining down on the probe tip (in the center, 380 μm diameter) illuminated by a 1 mm thin vertical laser sheet. The 13.56 MHz RF discharge is driven in 10 Pa argon gas with ~ 10 W RF power.

When a large negative DC voltage (-50 V) is applied to the probe tip, the negatively charged dust particles are strongly repelled at about 1 ± 0.2 mm from the probe. When the probe bias is near the floating potential ($+10$ V), the particles can get as close as approximately 0.1 mm. This suggests that electrostatic repulsion between the probe and the particles dominates. However, at even larger negative probe voltages, the interaction becomes more complex, as shown in Figure 2.

Here we can see three different regions concentric around the probe tip. In the case of -150 V applied to the probe, at a large distance ($r > 1.9$ mm) the trajectories of the dust particles are not influenced by the presence of the probe: they fall from above, bounce in the repelling electric field of the RF sheath, reach an upper turning point, fall back into the RF sheath, undergo a second reflection and reach a lower turning point, and finally disappear completely from the field of view. This behavior indicates that the dust particles are charging fairly uniformly (reaching the same turning point heights), and the difference between the first and second turning point positions could be used to infer the friction coefficient between the dust particles and the background gas, which is not the subject of this work. At intermediate distances (1 mm $< r <$ 1.9 mm) the dust particles are repelled by the probe, but at small

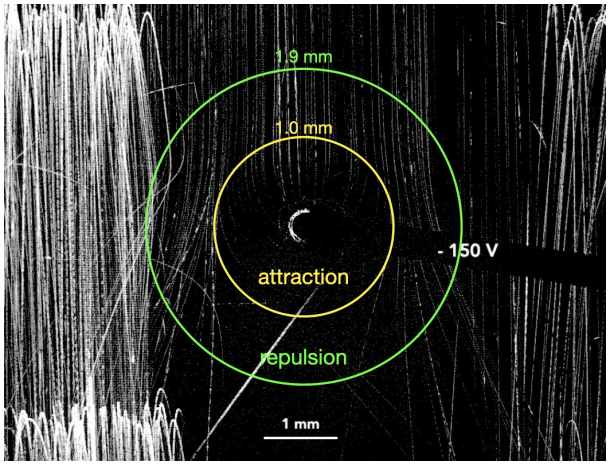

Fig. 2: Same as figure 1 with -150 V probe voltage. Circles indicate regions, centered around the probe tip, which show attractive and repulsive interaction between the probe and the dust particles.

distances ($r < 1$ mm) the dust trajectories are bent towards the probe tip, a clear indication of attractive interaction.

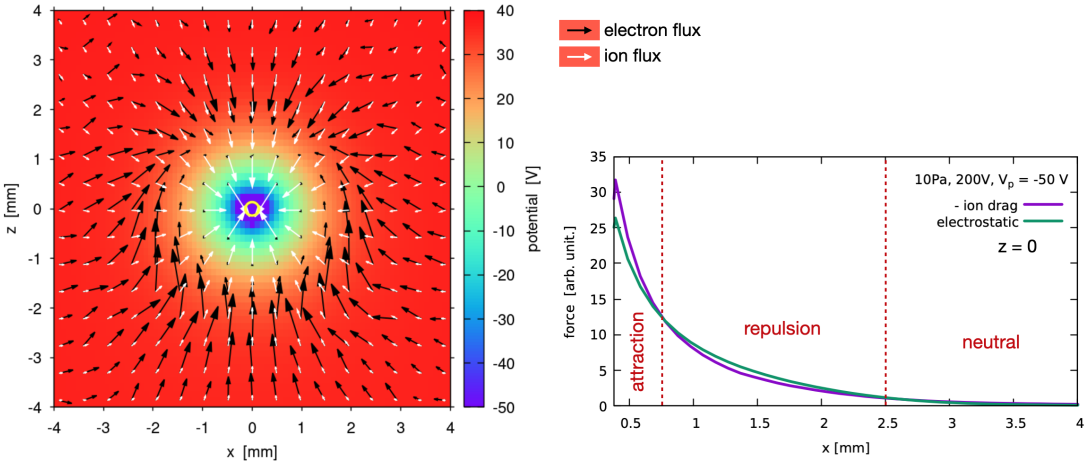

Fig. 3: PIC/MCC simulation results for 10 Pa, 200 V RF amplitude, -50 V probe voltage. Left: electron flux (black arrows) and Ar^+ ion flux (white arrows) distributions superimposed on the colormap of the electrostatic potential around the probe tip. Right: electrostatic and ion drag force distributions acting on 8.89 μm diameter dust particles with 10 000 electron charges.

Figure 3 shows PIC/MCC simulation results for the distribution of electron and Ar^+ ion fluxes around a negatively biased probe tip for discharge conditions 10 Pa pressure, 200 V RF amplitude, -50 V probe voltage. The formation of an electron-depleted sheath region, characterized by a significant ion flux towards the probe, is visible. Using the OML approximation to estimate the ion drag force experienced by the dust particles [3] we can compare the effects of electrostatic repulsion and attraction due to the drag force, which qualitatively reproduces the observed net force field structure with distinct attractive, repulsive, and neutral regions around the probe tip.

A detailed analysis of the experiments and PIC/MCC simulations will be presented, providing a deeper insight into the mutual interaction of the probe with the plasma and the dust particles. These findings suggest that using dust particles for the diagnosis of local plasma parameters can reveal information both on electrostatic and flow dynamic properties.

[1] V A Godyak, et al., *Plasma Sources Sci. Technol.* **11** (2002) 525.
[2] Francis F Chen, *Plasma Sources Sci. Technol.* **18** (2009) 035012.
[3] C M Ticos, et.al., *Phys. Rev. Lett.* **100** (2008) 155002.

Time and energy-resolved mass spectrometry study of the HiPIMS discharge operated in Ar and Ar-N_2 atmospheres

J. Hnilica[(*)1], K. Bernátová[1], P. Klein[1], Z. Hubička[2], M. Čada[2], P. Vašina[1]

[1] *Department of Plasma Physics and Technology, Masaryk University, Kotlářská 2, CZ-61137, Brno, Czech Republic*

[2] *Institute of Physics v. v. i., Academy of Science of the Czech Republic, Na Slovance 1999/2, CZ-182 21, Prague, Czech Republic*

[(*)] hnilica@mail.muni.cz

High Power Impulse Magnetron Sputtering (HiPIMS), a promising physical vapor deposition process, uses short voltage pulses with a low-duty cycle to produce a large number of ionized sputtered particles [1]. Adding a reactive gas to the HiPIMS method opens up new possibilities for synthesizing unique materials with various characteristics and compositions. Nonetheless, using HiPIMS in a reactive process is challenging due to the intricate time-dependent interaction between discharge characteristics and reactive gas supply [2]. Therefore, a more profound understanding of discharge behavior in reactive HiPIMS is needed to achieve control over the deposition process.

In this experimental study, an investigation of the reactive sputtering process using mass spectroscopy was performed. A titanium cathode was the sputtering source, and total pressure and supplied power were maintained constant. Two cases were studied: one with a low current (60 A) and another with a high current (150 A). A Speedflo Mini fast feedback control system was utilized to measure throughout the hysteresis curve. Four distinct points representing the metal, transition, and poisoned regimes were selected for the study. In these points, the ion flux of the species impinging the mass spectrometer was determined. Time-resolved and time-averaged ion energy distribution functions (IEDF) were captured for Ar^+, Ar^{2+}, Ti^+, Ti^{2+}, N^+, and N^{2+} under all investigated conditions. This study builds upon previous optical measurements [3], providing further insights into the reactive sputtering process.

Acknowledgments

This research was supported by project L M2023039 funded by the Ministry of Education, Youth and Sports of the Czech Republic.

[1] U. Helmersson, M. Lattemann, J. Bohlmark, A. P. Ehiasarian, J. T. Gudmundsson, *Thin Solid Films*, **513** (2006).
[2] M. Fekete, K. Bernátová, P. Klein, J. Hnilica, P. Vašina, *Plasma Sources Sci. Technol.* **28** (2019) 025011.
[3] K. Bernátová, P. Klein, J. Hnilica, P. Vašina, *Plasma Sources Sci. Technol.* **30** (2021) 125002.

Self consistent simulation of dust formation and dynamic in non-equilibrium RF Ar-acetylene plasma

G. Tetard[1], A. Michau[1], S. Prasanna[1], P. Brault[2] , K. Hassouni[1(*)]

[1] *LSPM, CNRS-UPR3407, Université Sorbonne-Paris-Nord, 99 Avenue J. B. Clément 93430 Villetaneuse, France.*

[2] *GREMI, CNRS-UMR XXX, Université d'Orléans*
(*) khaled.hassouni@lspm.cnrs.fr

Dust particle formation and dusty plasmas dynamics in electrical discharges are of great interest in many research or technological fields ranging from astrophysics to fusion sciences and including microelectronics processes and material processing [1]. In this paper, we present a computational investigation of dust formation and dusty plasma effects in capacitively coupled Ar/C_2H_2 RF discharges. More specifically, we developed a fully coupled dusty plasma model that describes the coupled effects of (i) discharge dynamics, (ii) complex chemical kinetics that results in molecular growth and dust-particle nucleation, and (iii) aerosol dynamics that govern the space-time evolution of dust-particle size distribution and plasma characteristics. The discharge dynamics is described using a drift-diffusion model taking into account flow effect that may be of a critical importance in the investigated plasmas [1]. Molecular growth routes through neutral radicals, negative ions or positive ions were considered in the chemistry and reactive flow models [2]. The impact of molecular growth kinetics on the discharge dynamics was fully taken into account by a proper consideration of the major heavy ions involved in the discharge equilibrium. The molecular growth kinetics is considered up to a largest molecular edifice (LME) with a prescribed maximum number of carbon atoms. The growth rate of this LME determines the nucleation rate in the model. The aerosol dynamics were described assuming a bimodal size-distribution with a nucleation mode and a core mode. This assumption proved to give accurate description as far as the evolution of the core distribution is concerned [3]. The aerosol dynamics model takes into account nucleation as determined by the molecular growth model, particle growth due to the deposition of radicals or ions inferred either form the plasma model or from the molecular growth model, and coagulation effects within the nucleation mode or between the nucleation and the growth modes. The enhancement of coagulation kinetics due charge fluctuation is also taken into account for the nucleation mode that may exhibits significant population of neutral or positively charged particles.

Simulations were carried out for several feed gas composition, i.e., C_2H_2% in Ar/C_2H_2 mixture. Results showed that, depending on the discharge conditions, the molecular growth is governed by either neutral or positively charged polyynes chemistries initiated by acetylene and C_2H radical. They also show that dust-nucleation competes with surface deposition on the electrodes, and strongly depends flow velocity [3]. In particular, dust particle formation kinetics significantly depends on the nature of the interaction between radicalar species or ions and electrodes. As for dust-particle formation, results showed that nucleation takes place continuously in the discharge gap. It is more enhanced in the bulk of the discharge when the positive ion molecular growth route is dominant, while it takes place in the whole discharge gap when the radical route is predominant. Eventualy, results showed that when increasing the amount of acetylene in the feed gas, the discharge transitions from (i) a low dust-particle density plasma with a small Havnes number, a fairly large particle diameter and almost no dusty plasma effect to (ii) a high density dust-particle density plasma with a large Havnes number, i.e., larger than 10, a fairly small particle diameter, i.e., <10 nm, and a strong dusty-plasma effect. They also show a counter-intuitive effect where larger dust-particle density significantly enhance positive ion density and therefore particle nucleation kinetics. This shows a self-promoting effect under large acetylene concentration in the feed gas, i.e., 50%, where larger dust particles density favours particle nucleation

Acknowledgement: This work was supported by the French 'Agence Nationale de la Recherche' and EUROFUSION. One of the author (KH) acknowledges the support of the Institut Universitaire de France.

[1] R. L. Merlino and J. A. Goree., Physics Today 57, 7, 32 (2004), doi: 10.1063/1.1784300.

[2] A. Michau et al., Plasma Sources Sciences and Technol. 25, 1 (2016) 015019.

[3] G. Tetard et al. Plasma Processes and Polymers, 19, 5 (2022), 2100204

[4] G. Tetard et al J. Phys D (2024)

Analysis of a radiofrequency-driven resonant plasma source

K. Jurik(*)[1], M. Stastny[1], P. Drexler[1], K. Mrozek[2], A. Obrusnik[3]

[1] *Brno University of Technology, FEEC, Department of Theoretical and Experimental Electrical Engineering, Brno, Czech Republic*

[2] *SpaceLab EU, SE, Brno, 602 00 Czech Republic*

[3] *PlasmaSolve s.r.o., Brno, 602 00 Czech Republic*

(*) karel.jurik@vut.cz

This work presents a design of our low-pressure plasma source, based on a high-frequency resonant network, and its characterisation using Optical Emission Spectroscopy and measurement of its electrical parameters (particularly extracted electron and/or ion current and the ratio of the reflected power). The characterisation is done for a wide range of input parameters (e.g., external magnetic field, operating pressure of working gas (Argon) and radiofrequency input power). The ion current brings an overview of the source behaviour at different conditions, while the OES shows the distribution of selected excited species (with special regard to the Argon metastables). These two methods are compared and linked together leading to the matrix of results for each set of the input parameters. Selected one or two-dimensional (charts, resp. maps) cuts of the results are presented and discussed against model and theory, to understand the behaviour of the plasma source.

Acknowledgement: This work was supported by the SILAS project awarded by the Technology Agency of the Czech Republic (grant no. FW06010622). The preparation of this paper was assisted by the general student development project in progress at Brno University of Technology.

Measurement of negative ion density in streamer discharge in air by transient cavity ringdown spectroscopy

Koichi Sasaki, Kimika Fushimi, and Naoki Shirai

Division of Applied Quantum Science and Engineering, Hokkaido University, Sapporo 060-8628, Japan
(*) sasaki@qe.eng.hokudai.ac.jp

Atmospheric-pressure discharges generated in air are expected to be electronegative, since oxygen and water vapor are electronegative gases. However, experiments that examine negative ion densities in atmospheric-pressure discharges are limited to date. In this work, we measured the temporal variation of the negative ion density in a streamer discharge generated in air [1]. We adopted cavity ringdown spectroscopy (CRDS). An issue of CRDS for the detection of negative ions (the detection of the photon loss due to photodetachment of negative ions) in streamer discharge is the fact that the lifetime of negative ion is shorter than the ringdown time. We solved this issue by applying the transient analysis of the ringdown curve.

A streamer discharge was generated between needle (the anode) and planar (the cathode) electrodes placed inside an optical cavity in air. The optical cavity was composed of two mirrors with high reflectivities at 770-785 nm. The cavity length was 20 cm. The distance between the needle and planar electrodes was 7.5 mm, and the distance between the optical axis of the cavity and the needle electrode was 2.5 mm. The needle electrode was connected to a high-voltage pulsed power supply, and the planar electrode was electrically grounded. We employed an optical parametric oscillator (OPO) as the light source in the CRDS measurement. The wavelength and the duration of the OPO laser pulse were 777 nm (the idler output) and 10 ns, respectively. The OPO laser oscillated at 5 μs before the the trigger of the high-voltage pulse, and the repetition frequencies of the laser oscillation and the discharge were 10 Hz. The laser pulse transmitted through the cavity was detected using a photomultiplier tube (PMT).

Figure 1 shows typical ringdown curves. The ringdown curves were obtained by averaging 300 laser shots using a digital oscilloscope. The origin of the horizontal axis corresponded to the trigger to the high-voltage pulsed power supply. As shown in the figure, the ringdown curve in the absence of the discharge was approximated by an exponential function. In the presence of the discharge, we detected the superposition of the discharge noise at $0 \leq t \leq 0.3$ μs. After the noise disappeared ($0.4 \leq t \leq 1.5$ μs), we observed a steeper decrease in the transmitted laser intensity than that in the absence of the discharge. The time constant of the ringdown curve was almost the same as that in the absence of the discharge at $t \geq 1.5$ μs.

Conventional CRDS supposes a steady-state absorber, and the absorber density is deduced from the time constant of the ringdown curve. However, in the present experiment, the negative ion density had a faster time constant than the ringdown curve. In this case, we can deduce the temporal variation of the negative ion density by the transient analysis of the ringdown curve. The negative ion density is obtained by

$$n(t) = -\frac{L}{c\sigma l}\left(\frac{1}{I(t)}\frac{\mathrm{d}I(t)}{\mathrm{d}t} + \frac{1}{\tau_0}\right), \qquad (1)$$

where $I(t)$ represents the ringdown curve in the presence of the discharge, τ_0 is the ringdown time constant in the absence of the discharge, L is the cavity length, l is the length of the discharge zone along the axis of the cavity, c is the speed of light, and σ is the cross section of optical absorption or photodetachment at 777 nm. $1/\tau_0 = 1.31 \times 10^5$ s^{-1} was deduced from the ringdown curve shown in Fig. 1. We needed the moving average of the ringdown curve in the numerical calculation of $\mathrm{d}I(t)/\mathrm{d}t$ since the differential of the experimental

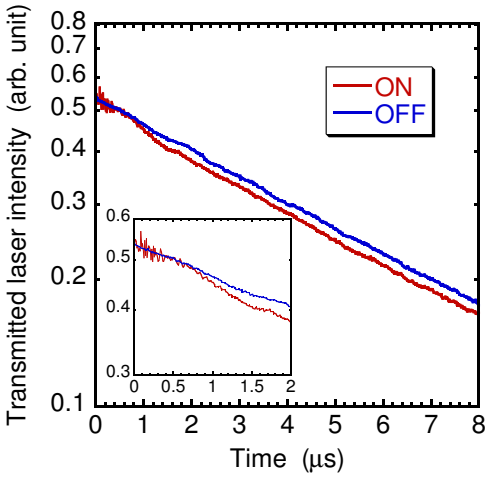

Fig. 1: Typical ringdown curves observed in the presence and absence of streamer discharge.

ringdown curve was a noisy procedure.

The temporal variation of the negative ion density was obtained as shown in Fig. 2(a) by calculating Eq. (1). We adopted the moving average with a duration of $\Delta t = 0.4$ μs. $l = 3$ mm was assumed based on the optical emission image of the streamer discharge, and we assumed $\sigma = 1 \times 10^{-22}$ m^2, which is the photodetachment cross section of O_2^- at 777 nm [2]. We cannot say anything about the phenomena at $t \leq 0.4$ μs, since we adopted moving average with $\Delta t = 0.4$ μs. The negative ion density started the increase at $t = 0.4$ μs, and the maximum negative ion density was observed at $t = 1$ μs. The maximum negative ion density was 2×10^{20} m^{-3}. Figures 2(b) and 2(c) show the waveforms of the pulsed voltage and the discharge current, respectively. It is understood from Fig. 2 that the increase in the negative ion density started after the disappearances of the discharge voltage and current. The decrease in the negative ion density was steep, and it was around the noise level at $t = 1.5$ μs.

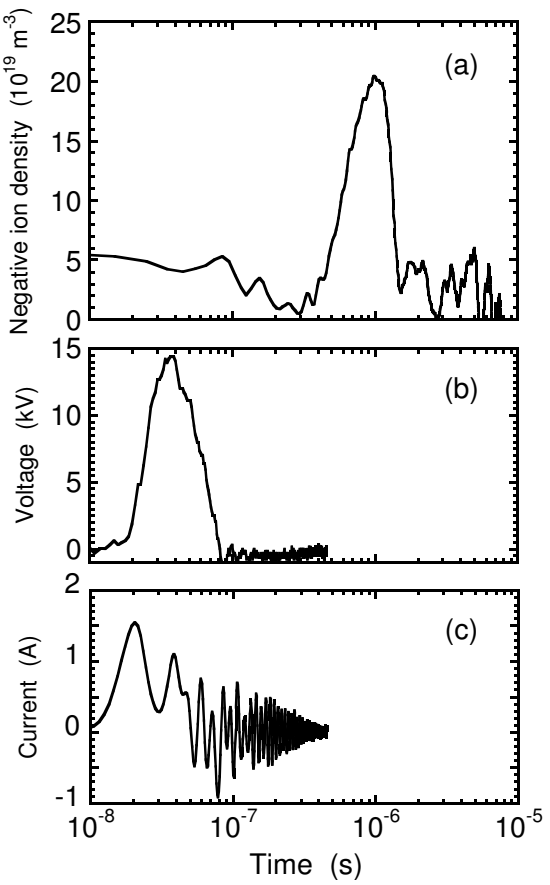

Fig. 2: Temporal variations of (a) negative ion density, (b) discharge voltage, and (c) discharge current.

It is well known that streamer discharge is composed of primary and secondary streamers [3]. The primary streamer has a high reduced electric field and a low negative ion density. It is estimated that the primary streamer arrives at the cathode at $t < 50$ ns in the present experimental condition [4]. Hence, it is considered that Fig. 2(a) represents the evolution of the negative ion density in the secondary streamer. The secondary streamer with a much lower reduced electric field enhances the electron attachment frequency to electronegative molecules, resulting in the evolution of the negative ion density at $t \geq 0.4$ μs. On the other hand, the decrease in the negative ion density at $1 \leq t \leq 1.5$ μs is consistent with the destruction of negative ions via mutual neutralization with positive ions. This is because the rate coefficient of mutual neutralization such as $O_2^- + O_2^+ \rightarrow O_2 + O_2$ is on the order of 10^{-13} m^3/s [5, 6].

In summary, we have measured the absolute negative ion density in a streamer discharge in air by transient CRDS. The present work shows the applicability of transient CRDS to the measurement of negative ion densities in atmospheric-pressure discharges.

[1] K. Fushimi, N. Shirai, and K. Sasaki, *Plasma Sources Sci. Technol.* **33** (2024) 02LT01.
[2] L. C. Lee and G. P. Smith, *J. Chem. Phys.* **70** (1979) 1727.
[3] F. Tochikubo and A. Komuro, *Jpn. J. Appl. Phys.* **60** (2021) 040501.
[4] A. Komuro. T. Ryu, A. Yoshino, T. Namihira, D. Wang, and R. Ono, *J. Phys. D: Appl. Phys.* **54** (2021) 364004.
[5] J. R. Peterson, W. H. Aberth, J. T. Moseley, and J. R. Sheridan, *Phys. Rev. A* **3** (1971) 1651.
[6] J. T. Moseley, W. Aberth, and J. R. Peterson, *J. Geophys. Res.* **77** (1972) 255.

Particle in Cell Simulations and Correlation Heating

M. D. Acciarri(*)[1], C. Moore[2], S. D. Baalrud[1]

[1] *Department of Nuclear Engineering and Radiological Sciences, University of Michigan, Ann Arbor, MI 48109, USA*

[2] *Sandia National Laboratories, Albuquerque, NM 87185, USA*

(*) acciarri@umich.edu

The Particle-in-Cell (PIC) method, a cornerstone of plasma modeling, is widely employed for its ability to simulate kinetic phenomena within device-scale domains. This capability stems from the representation of numerous physical particles by computational macroparticles. Our work investigates correlation heating in PIC simulations, focusing initially on the feasibility of employing the PIC method to observe physical phenomena pertinent to atmospheric pressure discharges, such as disorder-induced heating (DIH). Subsequently, we explore artificial correlation heating (ACH) and its implications as a constraint on the applicability of PIC simulations.

In the first part of this work, molecular dynamics simulations are used to test when the PIC method applies to atmospheric pressure plasmas. It is found that PIC applies only when the plasma density and macroparticle weight are sufficiently small because of two effects associated with correlation heating. The first is the physical effect of DIH. This occurs if the plasma density is large enough that a species (typically ions) is strongly correlated in the sense that the Coulomb coupling parameter exceeds one $\Gamma_{ii} > 1$. In this situation, DIH causes ions to rapidly heat following ionization [1]. PIC is not well suited to capture DIH because doing so requires using a macroparticle weight of one and a grid that well resolves the physical interparticle spacing. These criteria render PIC intractable for macroscale domains. Furthermore, it is shown that simulations in reduced dimensions exacerbate these issues.

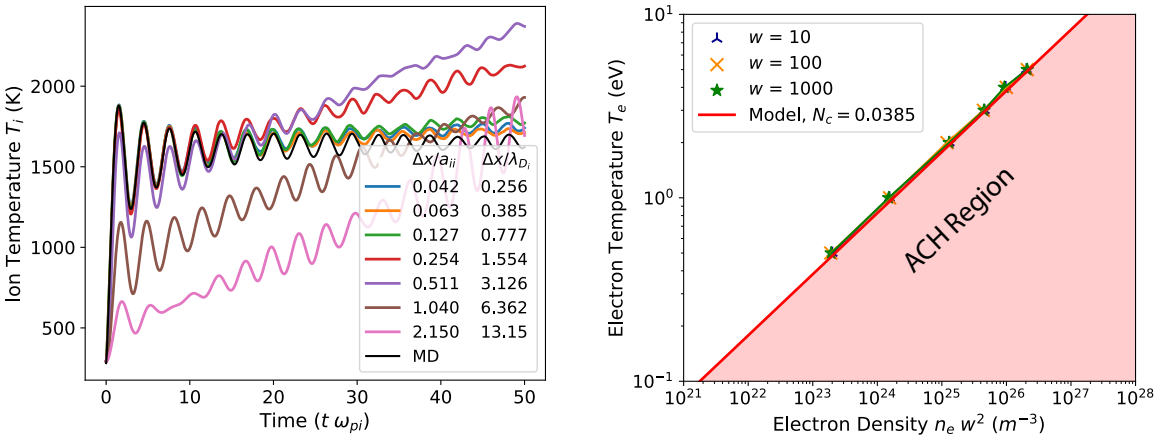

Fig. 1: (a) Evolution of the ion temperature for an ion density of $n_i = 2.5\times10^{24}$ m^{-3} and initial room temperature obtained from MD and using the PIC method for different grid spacing and unity macroparticle weight. (b) Limiting curve for ACH region from the the developed and numerical results from 3D-PIC simulations with different macroparticle weights.

The second part of this work is focused on a numerical error due to artificial correlation heating. ACH is like DIH in that it is caused by the Coulomb repulsion between particles, but differs in that it is a numerical effect caused by a macroparticle weight larger than one. Like DIH, it is associated with strong correlations. However, the macroparticle coupling strength is found to scale as $\Gamma^w = \Gamma w^{2/3}$, where Γ is the physical coupling strength and w is the macroparticle weight. So even if the physical coupling strength of a species is small, a sufficiently large macroparticle weight can cause the macroparticles to be strongly coupled and therefore heat due to ACH. We introduce a new constraint to PIC simulations necessary to avoid ACH. This requires that the macroparticle coupling strength be smaller than one $\Gamma^w < 1$. If this condition is violated, the finite macroparticle weight artificially enhances the coupling strength and causes the plasma to heat until the macroparticle coupling strength is near unity, depending

on the grid resolution. A comprehensive model of ACH is developed that incorporates density, temperature, macroparticle weight, and grid resolution. It is then tested using PIC simulations, delineating the boundaries of the method's applicability and offering a predictive framework for ACH. Moreover, the research explores a runaway heating process induced by ACH in the presence of ionization, which can lead to numerical instability. A critical conclusion of this study is that the onset of ACH imposes more stringent constraints on the macroparticle weight and average number of macroparticles per cell than those typically employed in standard PIC simulations, thereby establishing a new limitation to the method's applicability.

This work was supported in part by the US Department of Energy under award No. DE-SC0022201, and in part by Sandia National Laboratories. Sandia National Laboratories is a multi mission laboratory managed and operated by National Technology and Engineering Solutions of Sandia, LLC., a wholly owned subsidiary of Honeywell International, Inc., for the U.S. Department of Energy's National Nuclear Security Administration under Contract No. DE-NA0003525. This article describes objective technical results and analysis. Any subjective views or opinions that might be expressed in the paper do not necessarily represent the views of the U.S. Department of Energy or the United States Government.

[1] M D Acciarri et al 2022 Plasma Sources Sci. Technol. 31 125005
[2] M D Acciarri et al 2024 Plasma Sources Sci. Technol. 33 02LT02

Optimization of Null Collision Method in Monte Carlo Model

H Akashi(*), K Mizuno, T Yoshinaga

Departmetn of Applied Physics, National Defense Academy, Yokosuka 239-8686 Japan

(*) akashi@nda.ac.jp

Monte Carlo techniques have been developed by many researchers and acknowledged as one of the most useful and exact techniques in simulation methods. A major modification has been done by Skullerud in 1968[1], and introduced so call Null Collison method. Null Collision method decreases computational time significantly, but there is a problem of stochastic choice of free time. To determine the free time τ (=-$\nu^{-1}\ln\xi$, ξ: random number), large enough collision frequency(ν) should be chosen (guess work). Otheriwse a new ν should be chosen again until the condition is satisfied. In 1977, Lin and Bardsley[2] proposed the way to avoid the stochastic choice of free time. They introduced the concept of Null Collision Cross Section, which is no momentum transfer. In present time, many researchers calculating electron properties or other electron-neutral gas collisions using $\nu_{max}=N\{Q_{Real}(\varepsilon_{max})+ Q_{Null}(\varepsilon_{max})\}v=Const.(\gg NQ_{Real}(\varepsilon_{max})\, v)$ to determine the free time. If the ε_{max} is set to several hundreds of eV, almost over all electric field values are covered. This idea simplied the algorithm of Null Collision method. Brennan[3] proposed optimized Null Collision method, but only at low E/N region, and still has a slightly stochastic choice occurence. Recently, Nanbu[4], Horie et al[5] have made minor modification for Null Collision method, but these modifications have been applied on collision determinations or after this procedrues. Since Skullerud had proposed Null Collision method, rarely researchers have mentioned about CPU time. In the present paper, propose a new determination way of free time τ in Null Collision method, and have compared the CPU time to calculate the swarm parameters of severl gases, such as He, Ar, and so on. Fig.1 shows total collision frequency of He, and red line shows proposed method of $\nu_{max}(\varepsilon)$ and green line shows ν_{max} for Lin and Bardley's method. Electron enrgy assumes to vary 10^{-3}~10^{3} [eV], which means wide range electric field could be applied. In He gas, inelastic collision start from 19.5 [eV]. So assuming an electron accelerates from 10^{-3}eV till threshold of metastable state, change of collision frequnecy is less than 10^{2}. And in computer language FORTRAN, single precision real number range is 10^{-38}~10^{38}. Smallest random number ξ would be

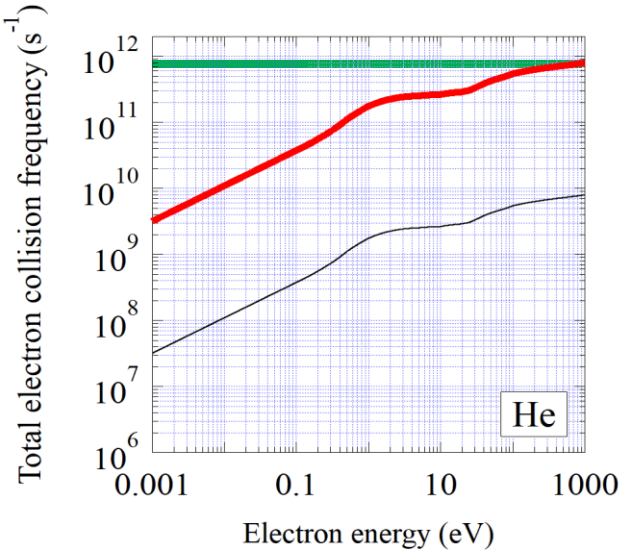

Fig. 1: Proposed total collision frequency used in the present paper for He. Black line: total real collision frequency, Red line: Proposed ν_{max}, Green line: Lin and Bardsley method's ν_{max}

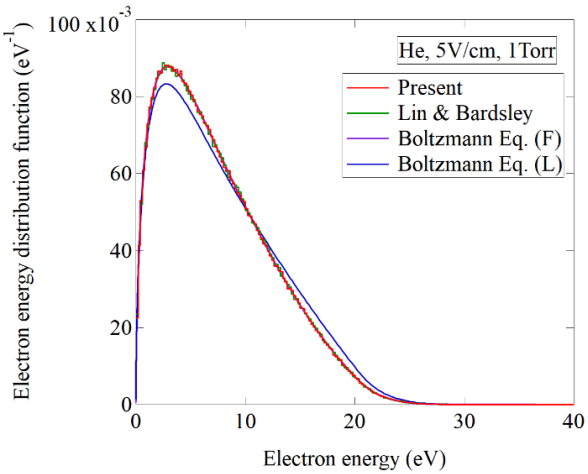

Fig. 2: Electron Energy Distribution Functions in He at E/p_0=5 [V/cm/Torr]

Table 1: Ratio of reduced Computation time (Proposed) / (Lin & Birdsely)

E/p_0 [V/cm/Torr]	He	Ar	N_2	O_2
5	35.7% (2.8)	29.4% (3.4)	21.7% (4.6)	5.4% (18.4)
30	38.5% (2.6)	45.5% (2.2)	35.7% (2.8)	8.2% (12.2)
100	43.5% (2.3)	55.6% (1.8)	50.0% (2.0)	13.5% (7.4)

calculated in 10^{-38} ($\tau=-\nu^{-1}\ln\xi$, $\ln\xi<90$), so $\nu_{max}(\varepsilon)=\nu_{Real}(\varepsilon)$x100 would be large enough to set as a total Null Collision frequency and this conditions are taken into the present calculations. For comparison, Monte Carlo model with Lin and Bardsley's Null Collision method are also calculated with constant ν_{max} ($=\nu_{real}(\varepsilon_{max})$x100) value at $\varepsilon_{max}=10^3$ [eV]. In the case of Ar, O_2, which Q_m values varies significantly in lower energy region, to avoid the stochastic choice of free time, minimum collision frequency $\nu_{min}=10^{10}$ [1/s] is needed to be set. Fig.2 shows the calculated results of Electron Energy Distribution Functions (EEDFs) with results from Boltzmann Equation Analysis. All EEDFs are in good agreement, but the results from 2term expansion Boltzmann Equation Analysis is slightly off. The results of EEDF at other conditions show also in good agreement. Table1 gives Ratio of reduced computational time in Helium and other tested gases. The calculations of swarm parameters have been done in the same conditions in each calculation (initial electron number, E/p_0, simulation time, and so on). The maximum speed up ratio is 18.4 times faster at lower E/p_0 condition in Oxygen. The minimum speed up ratio is 1.8 times faster at higher E/p_0 conditions in Ar. It depends on what kind of collision cross sections using, but proposed method could speed up calculations at least more than 2 times. From the table, it is found that the ratio of reduced computation time is getting higher at low E/p_0 in every gases. As shown in Fig.1, proposed $\nu_{max}(\varepsilon)$ is lower than that of Lin and Bardsley's method in lower energy region, this makes decrease the calculation step of free time until collision. At any E/p_0 computation times become faster than Lin and Bardsley's method, because there are certain number of lower energy electrons, and they consume a lot of computation time. To confirm these speed up in computation time, estimation method have been developed. From the value of product of $\nu_{max}(\varepsilon)$ and EEDF, derive the difference of collision number.The ratio of collision number would relate to ratio of speed up in computation. Fig.3 shows ratio of speed up in computation time. The results show similar tencencies in each gases. So the results of estimation would support the assumption of the proposed method. This method would be helpful to calculate in condition of numerous collisions occurrence, such as atmospheric discharges.

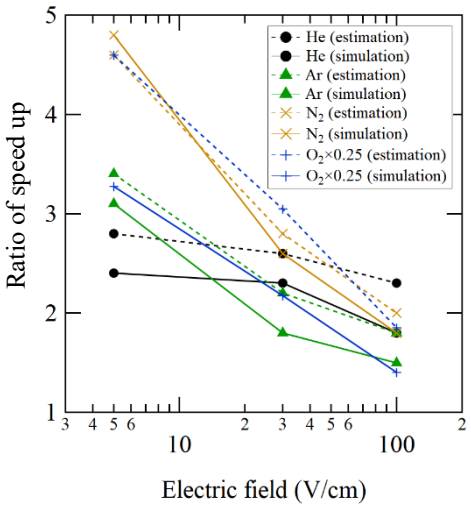

Fig. 3: Ratio of speed up in computation time

[1] H. R. Skullerud, "The stochastic computer simulation of ion motion in a gas subject to a constant electric field", Brit. J. Appl. Phys. (J. Phys. D), Ser.2, Vol.1, pp.1567-1568 (1968)
[2] S. L. Lin and J. N. Bardsley, "Monte Carlo simulation of ion motion in drift tubes", J. Chem. Phys., Vol.66, No.2, pp.435-445 (1977)
[3] Michael J. Brennan, "Optimization of Monte Carlo Codes Using Null Collision Techniques For Experimental Simulation at Low E/N", IEEE Trans. Plasma Sci., Vol. 19, No. 2, pp.256-261 (1991)
[4] Kenichi Nanbu, "Probability Theory of Electron-Molecule, Ion-Molecule, Molecule-Molecule, and Coulomb Collisions for Particle Modeling of Materials Processing Plasmas and Gases", IEEE Trans. Plasma Sci., Vol.28, No.3, pp.971-990 (2000)
[5] I. Horie, T. Suzuki, Y. Ohmori, K. Kitamori, K. Maruyama, "Monte Carlo Simulation of an Ar Parallel Plate Discharge Plasma Employing LPWS", IEEJ Trans. FM, Vol.123, No,9, pp.869-877 (2003)

Particle-in-Cell modeling of SPIDER negative ion source

F. Taccogna[1,2], A. Panarese[(*)1], P. Minelli[1,2], F. Cichocki[3]

[1] *Institute for Plasma Science and Technology ISTP, CNR, Bari, Italy*
[2] *National Institute of Nuclear Physics INFN, Bari, Italy*
[3] *Dipartimento "Nucleare", ENEA C.R. Frascati, Frascati, Italy*
[(*)] antonio.panarese@istp.cnr.it

SPIDER (Source for the Production of Ions of Deuterium Extracted from a Radio frequency plasma) is the ITER prototype negative ion source used for neutral beam injection (NBI). It is composed of 8 drivers, which are inductively coupled plasma discharges, where the plasma is produced [1]. Each driver is connected to a common expansion chamber and is coupled to an antenna connected to 1MHz RF generators (Fig.1) with the aim of maximizing the power transmitted to the ionized gas in order to generate and sustain the plasma.

The basic physical processes of a low temperature plasma occurring inside the SPIDER negative ion source were investigated by means of the numerical code PICCOLO (PIC COde for LOw temperature plasma) that uses the Particle-in-Cell method with Monte Carlo collisions (PIC/MCC) to model the kinetics of electrons and ions inside a negative ion source in a self-consistent electrostatic field. In detail, the Poisson equation is solved at each time step δt. Charged particles are moved between t and δt according to the Lorentz force $q\left(\mathbf{E}+\mathbf{v}\times\mathbf{B}\right)$, where $\mathbf{E}$ is the self-consistent electric field [2] and $\mathbf{B}$ is the imposed magnetic filter field. The two-dimensional simulation domain is shown in Fig.1(b). The field lines of the magnetic filter are perpendicular to the simulation plane. The configuration of the magnetic filter corresponds to a Gaussian profile, given by $B_x(z) = B_0\ exp\left[-(z-z_0)^2/(2L_z^2)\right]$, where $B_0 = 7\ mT$, $z_0 = 36\ cm$, and $L_z = 3.9\ cm$. An initial density of $5\cdot 10^{18}$ $particles/m^3$ is imposed for the electrons and ions inside the drivers. In order to reproduce the large size of the source, a scaling technique is used consisting of artificially increasing the value of the vacuum permittivity in the Poisson equation by a factor $f_s = \epsilon_0^{'}/\epsilon_0$, where ϵ_0 is vacuum permittivity and $\epsilon_0^{'}$ its scaled value used in the simulation. With the aim of decreasing the computational cost, a hybrid OpenMP/MPI parallelization approach was also used. Some of the electrons are randomly heated in the driver region by subjecting them to a prescribed power of 100 kW at a frequency of 4 MHz. A new velocity is assigned to the heated electrons [3] by sampling it from a Maxwellian distribution with a temperature equal to the heating temperature $T_h = \frac{2}{3}\left[< E_k >_h + P_{abs}/\left(eN_{eh}\nu_h\right)\right]$, where $< E_k >_h$ is the computed electron average energy in eV, P_{abs} is the absorbed power, ν_h is the heating frequency, and N_{eh} is the number of electrons to be heated. The heated electrons distribute the absorbed energy to heavier ions and neutrals by means of elastic and inelastic collisions. Various test simulations were carried out with different parameters such as density and scaling factors. In these tests only atomic hydrogen gas at a pressure of 0.3 Pa was considered, while negative ions and molecular positive ions were neglected. Fig.2 shows some quantities relating to the electrons, such as density, temperature and flux, in the case of $f_s = 2.25\cdot 10^4$. Furthermore, the time step is equal to $4\cdot 10^{-11}$ s and

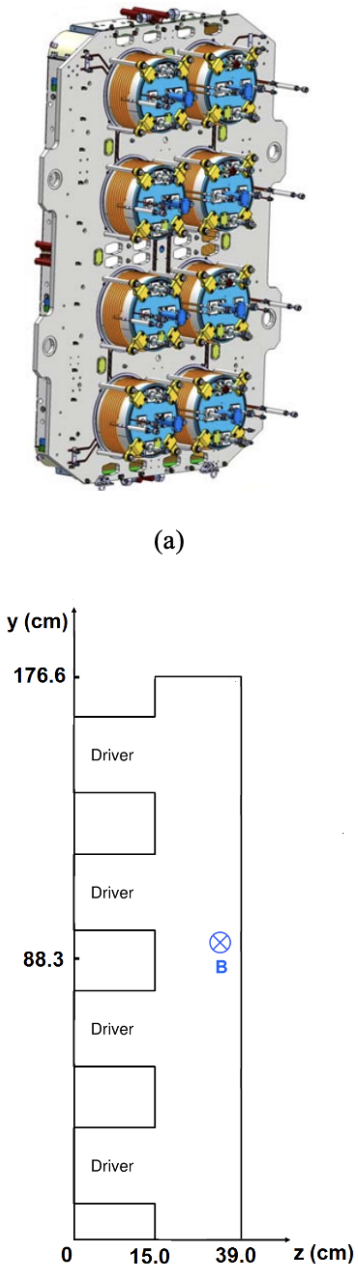

Fig. 1: SPIDER negative ion source prototype (a), simulation box (b).

the number of simulated time steps is $5 \cdot 10^6$. The numbers of grid nodes chosen for the PIC mesh along the three directions were 3 (along the fake periodic x direction), 1765 (along the y direction) and 389 (along the z direction perpendicular to the Plasma Grid plate). The map in Fig.2 (a) shows the behaviour of electron density while Fig.2 (b) shows that electron temperature. The electron flux map shows a complex structure due to the magnetic filter field. Electron transport is governed by the diamagnetic and $\mathbf{E} \times \mathbf{B}$ drifts leading to a Hall current. It causes important top-bottom dishomogeneities in the plasma characteristics along the extraction region on the left.
The *scaled* PIC-MCC code is able to provide a very useful insight of the physical phenomena that occur within SPIDER. In the next phase of the study, molecular collisions will be implemented that will allow obtaining 2D maps of the physical quantities of interest and highlighting the physics of the SPIDER negative ion source [4].

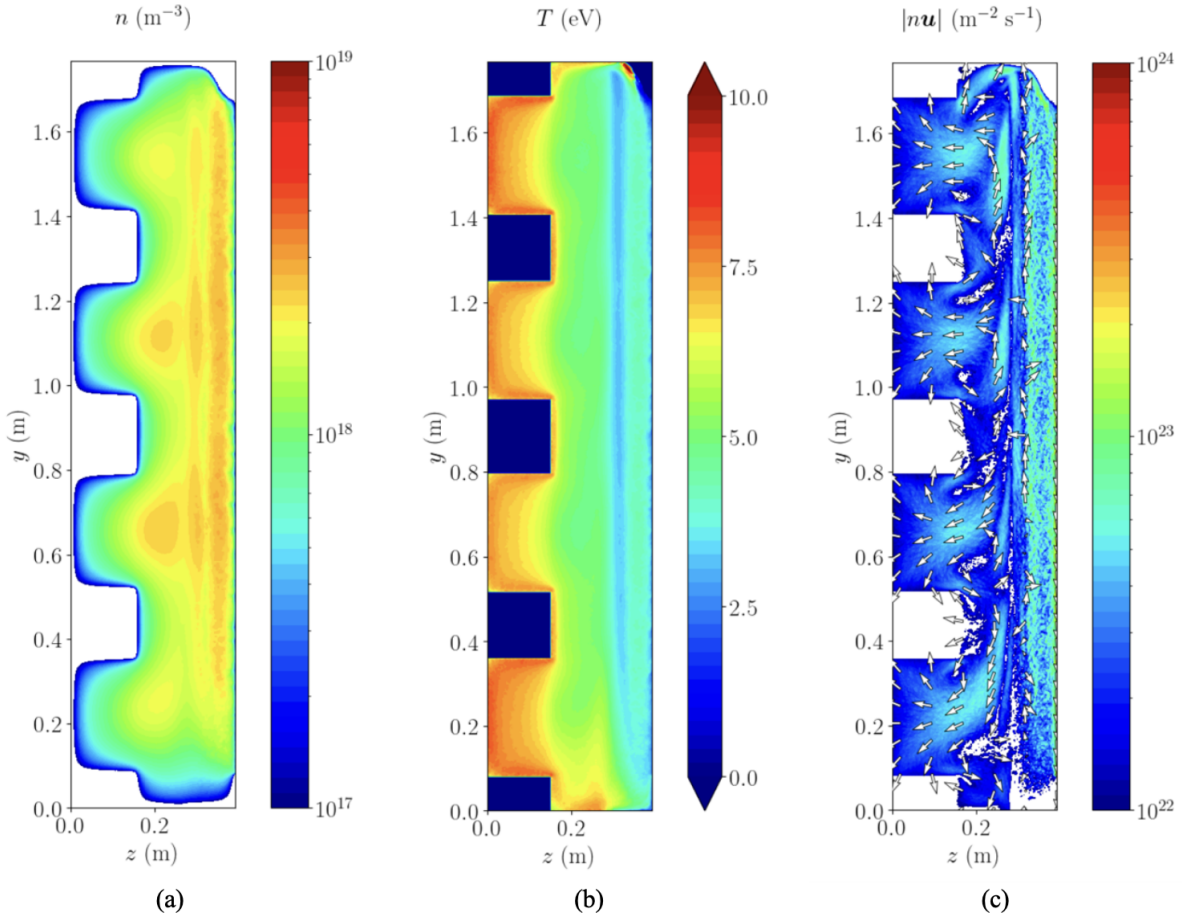

Fig. 2: Density (a) and temperature (b) maps of electrons, arrow map of electron flux (c).

Acknowledgments - Work carried out in the frame of project NEFERTARI - CUP B53C22003070006, funded by the European Union under the National Recovery and Resilience Plan (NRRP) - NextGenerationEU. Views and opinions expressed are however those of the authors only and do not necessarily reflect those of the European Union or the European Commission. Neither the European Union nor the European Commission can be held responsible for them.

[1] F. Taccogna, G. Fubiani and P. Minelli, *In: Bacal, M. (eds) Physics and Applications of Hydrogen Negative Ion Sources. Springer Series on Atomic, Optical, and Plasma Physics* **124** Springer.
[2] F. Taccogna and P. Minelli, *New J. Phys.* **19** (2017) 015012.
[3] G. Fubiani, L. Garrigues, G. Hagelaar, N. Kohen and J.P. Boeuf, *New J. Phys.* **19** (2017) 015002.
[4] F. Taccogna, F. Cichocki and P. Minelli, *Front. Phys.* **10** (2022) 10:1006994.

Development of an efficient plasma global model in MATLAB

A. Popoli[(*)1], G. Pierotti[1], F. Ragazzi[1], A. Cristofolini[1]

[1] *Department of Electrical, Electronic and Information Engineering "Guglielmo Marconi", University of Bologna, Viale Risorgimento 2, 40136 Bologna, Italy*

[(*)] arturo.popoli@unibo.it

As well known, performing multi-dimensional simulations of non-thermal plasmas is a very demanding task from the perspective of computational resources. This is especially true for kinetic models, which can resolve self-consistently the velocity distribution function of the species, but 2D and 3D fluid models are also affected by the same issue. Regardless of the employed methodology, the problem of performing simulations in reasonable times becomes a major challenge when extensive sets of chemical/kinetic processes are employed, or when the simulated phenomena takes place over long time-scales. Plasma sources for cold plasma biomedical treatments in molecular gases represent a typical example where both these challenges are present.

For the above reasons, volume-averaged (global) models represent a valuable tool for the study of plasma devices. We introduce MERLINO, an efficient 0D plasma code written in MATLAB. The goal of MERLINO, developed by members of the Plasma Technology Laboratory (PTL) of the University of Bologna, is to have a flexible structure while retaining performances comparable to the ones of existing codes written in compiled languages, such as the well-established ZDPlaskin code.

Expressions for rate constants can be written in arbitrary format, and may contain calls to user-defined functions. Their expressions can also be updated during runtime with a limited overhead. The rate constants of reactions involving electrons can also be computed using the Loki B electron Boltzmann solver [2, 3] under the local field approximation. By default, the user must specify a constant or time-dependent applied reduced field $E(t)/N$. However, MERLINO also allows to specify electrical parameters of an external electrical circuit that can be used to compute $E(t)/N$ at each time-iterations. One unique feature of the code is that it implements two different approaches for the evaluation of species production terms. The first, similar to the one used in ZDPlaskin and KPP [4], is to use a meta-programming approach where the code writes one or more m-function files that are then (just-in-time) compiled. In MERLINO this is performed using the MATLAB symbolic toolbox. Alternatively, a matrix

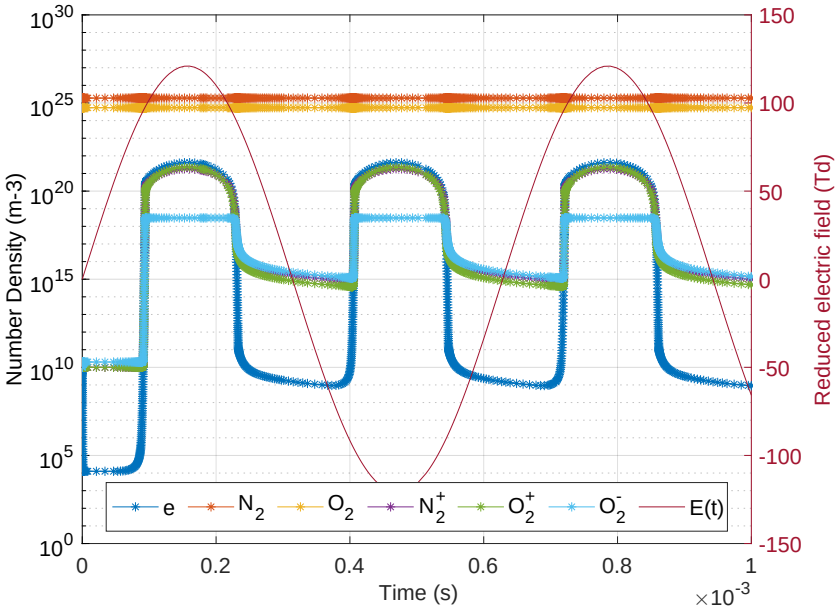

Fig. 1: Computed number densities and applied reduced electric field using the reaction scheme in [1]

.

technique is also implemented, based on automatically building a stoichiometry matrix ν used to compute the species production rates array $\{\Omega\}$ with $\{\Omega\} = [\nu^T]\{r\}$, where $\{r\}$ is an array of reaction rates. In this work we discuss the pros and cons of both approaches, and we perform a detailed performance benchmark for different reactions sets, ranging from simple ones with few tens of reactions such as the one in Figure to detailed kinetic models with hundreds of species and thousands of reactions.

[1] B. Parent, S. O. Macheret, and M. N. Shneider, "Electron and ion transport equations in computational weakly-ionized plasmadynamics," *Journal of Computational Physics*, vol. 259, pp. 51–69, Feb. 2014.

[2] A. T. del Caz, V. Guerra, D. Gonçalves, M. L. da Silva, L. Marques, N. Pinhão, C. D. Pintassilgo, and L. L. Alves, "The LisbOn KInetics Boltzmann solver," *Plasma Sources Science and Technology*, vol. 28, p. 043001, apr 2019.

[3] A. T. del Caz, V. Guerra, N. Pinhão, C. D. Pintassilgo, and L. L. Alves, "On the quasi-stationary approach to solve the electron Boltzmann equation in pulsed plasmas," *Plasma Sources Science and Technology*, vol. 30, p. 065008, jun 2021.

[4] V. Damian, A. Sandu, M. Damian, F. Potra, and G. R. Carmichael, "The kinetic preprocessor kpp-a software environment for solving chemical kinetics," *Computers & Chemical Engineering*, vol. 26, no. 11, pp. 1567–1579, 2002.

Electron kinetics in AC electric fields: testing the limitations of the HF approximation in the two-term Boltzmann equation

Tiago C Dias [1], Vasco Guerra[1], Carlos D Pintassilgo[1,2(*)]

[1] *Instituto de Plasmas e Fusão Nuclear, Instituto Superior Técnico, Universidade de Lisboa, Portugal*

[2] *Departamento de Engenharia Física, Faculdade de Engenharia Física, Universidade do Porto, Porto, Portugal*

[(*)] *cdp@fe.up.pt*

This work deals with the description of the electron kinetics in plasma discharges excited by AC electric fields. For this purpose, we have carried out a systematic study based on the comparison between two open–source codes recently developed by the N-PRiME team: (i) LoKI-B [1], an electron Boltzmann solver using the classical two-term expansion, and (ii) LoKI - MC [2], a numerical tool that solves the electron kinetics using Monte Carlo techniques. Two-term solvers have been used regularly in plasmas produced by AC electric fields under the *high-frequency (HF) field approximation,* also known as the effective-field approximation, expected to be more reliable when the frequency of the electric field is much larger than the typical frequency for the electron energy relaxation. Having in mind the high accuracy of Monte Carlo models in the description of the electron kinetics in low-temperature plasmas, we have compared the results obtained by LoKI - MC to the ones from LoKI-B for a wide range of discharge parameters, including both the microwave range (1-1000 GHz) and atmospheric pressure, and a radio-frequency of 13.56 MHz and several pressures (0.01 up to 10 Torr). This set of values corresponds to reduced angular frequencies ω/N ranging from $\sim 2.6.10^{-16}$ to $\sim 2.6.10^{-13}$ rad m^3/s.

Figure 1 shows the results obtained by LoKI-MC and LoKI-B for the mean electron energy and the ionization coefficient in the microwave range (10 and 1000 GHz) in a dry-air discharge. These figures show that for a high-frequency of 1000 GHz the results obtained by LoKI-MC and LoKI-B are quite similar, whereas larger differences between them occur for a lower frequency. This behaviour is easily understood from the inspection of Figure 2, where we compare the field frequency for 10 and 1000 GHz with the characteristic frequency for energy transfer in air at atmospheric pressure. On physical grounds, the isotropic component of the electron energy distribution at 1000 GHz (corresponding to $\omega/N \sim 2.6.10^{-14}$ rad m^3/s) remains practically unchanged during a cycle of the field oscillation and the HF-field approximation can be considered, where only a modulation in the anisotropic component is accounted for. For 10 GHz, this approximation is no longer valid.

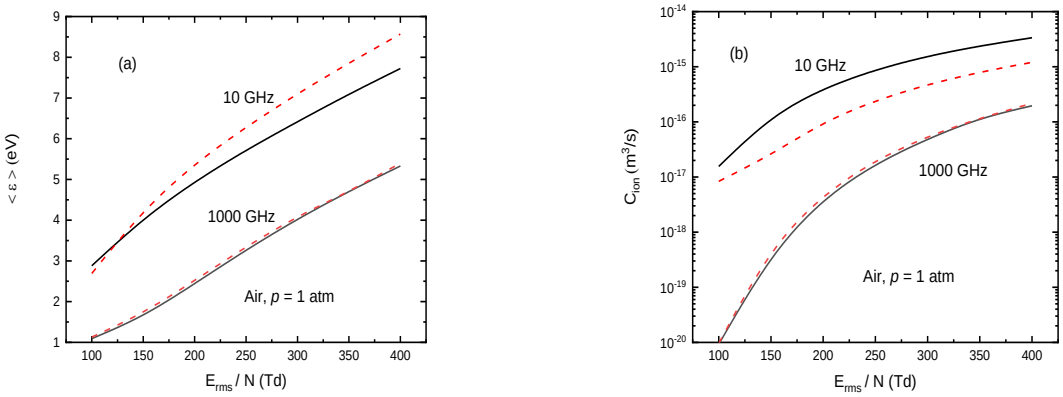

Fig. 1 (a) Mean electron energy and (b) ionization coefficient obtained by LoKI-MC (black curves) and by LoKI-B (dashed red curves) as a function of the root-mean-squared electric field (frequencies of 10 and 1000 GHz) in a dry-air discharge at atmospheric pressure.

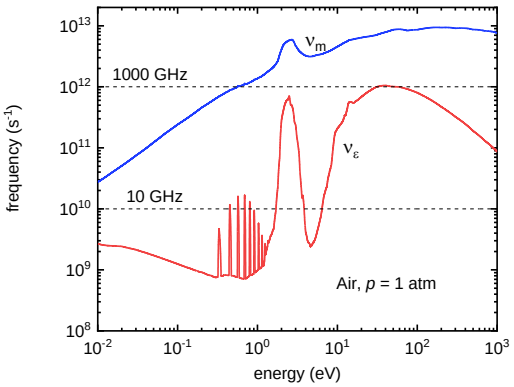

Fig. 2: Energy-dependent frequencies of momentum transfer (blue curves) and energy relaxation (red curves) in air at atmospheric pressure. Horizontal dashed lines indicate frequency values of 10 and 1000 GHz.

Figure 3 reports a similar analysis for Argon, considering lower pressures (0.01 and 1 Torr) and a radio frequency of 13.56 MHz. These results reveal that even for the situation of 0.01 Torr, corresponding to a lower collision frequency, the HF approximation on the two-term Boltzmann equation does not provide accurate results.

The examples shown here clearly exhibit the strong influence of the HF approximation on the results, failing in some cases around an order of magnitude in the ionization coefficient. In the conference, we will discuss in depth the physical reasons for such deviations, and provide advice on the check procedure that modellers should follow before using the HF approximation.

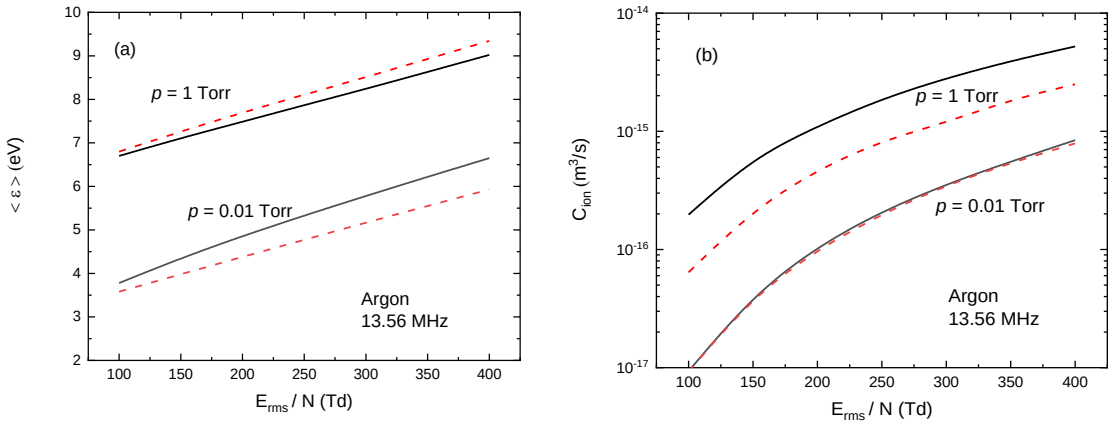

Fig. 3 (a) Mean electron energy and (b) ionization coefficient obtained by LoKI-MC (black curves) and by LoKI-B (dashed red curves) as a function of the root-mean-squared electric field (frequency of 13.56 MHz) in Argon for a pressure of 0.01 and 1 Torr.

IPFN activities were supported by the Portuguese FCT, under projects UIDB/50010/2020 (https://doi.org/10.54499/UIDB/50010/2020),UIDP/50010/2020)(https://doi.org/10.54499/UIDP/50010/2020) and LA/P/0061/2020 (https://doi.org/10.54499/LA/P/0061/2020).

[1] A. Tejero et al *Plasma Sources Sci. Technol.* **28** (2019) 043001
[2] T. C. Dias et al *Comput. Phys. Commun.* **282** (2023) 108554

Are Local-Field and Local-Energy approximations appropriate for nanosecond discharges?

Tiago C Dias and Vasco Guerra

Instituto de Plasmas e Fusão Nuclear, Instituto Superior Técnico, Universidade de Lisboa, Portugal

(*) vguerra@tecnico.ulisboa.pt

Interest in nanosecond-pulsed discharges (NPDs) is rapidly growing due to their remarkable non-equilibrium properties. However, their potential comes with considerable complexity, and a detailed study of the fundamental processes in the discharge is necessary to determine the most efficient configuration for a specific application. NPDs are characterized by very high reduced electric fields, E/N, that can be as high as ~ 1000 Td, with rising times on the nanosecond timescale. These characteristics represent significant modeling challenges, particularly concerning electron kinetics and their coupling with heavy species.

Obtaining a comprehensive solution of electron kinetics in gas discharges that accounts for dependencies in space, velocity and time is often unfeasible. Therefore, the electron behavior is frequently studied under one of two assumptions [1,2]: the local-field approximation (LFA), which equates the solution of electron kinetics to the steady-state calculation with the local and instantaneous value of the reduced electric field (E/N); the local-energy approximation (LEA), which includes an equation for the local mean energy, with the rate coefficients and the electron power distribution among different collisional channels depending on the local value of mean energy.

In this work, we focus on time-locality to assess the impact of the LFA and LEA assumptions on the calculation of the temporal evolution of electron kinetics in nanosecond discharges. To do so, we consider an accurate Monte Carlo (MC) time-dependent formulation as a golden standard, implemented in LoKI-MC [3,4]. The study involves a nanosecond pulse mirroring typical conditions found in experiments, with a maximum *E/N* of 300 Td at 2.5 ns and vanishing after ~30 ns. Moreover, we assess electron relaxation in two background gases (air and argon) and two pressures (10 and 100 Torr).

Figure 1 illustrates the mean electron energy $\langle\varepsilon\rangle$ as a function of time in air at both pressures, comparing the rigorous time-dependent MC approach with the LFA and the LEA. At 10 Torr, the evolution of $\langle\varepsilon\rangle$ calculated by the LFA differs significantly from the rigorous approach. This discrepancy arises because at lower pressures electrons do not collide rapidly enough to adapt to fast *E/N* variations. After ~2 ns, the solutions begin to converge. However, around 20 ns, when the *E/N* has decayed to 25 Td, the LFA again deviates from the time-dependent solution. Notably, the LEA captures much better both the rise and decay of the energy. At 100 Torr, where electron collisions are significantly more frequent than at 10 Torr, the LFA is valid over a broader interval, yet the LEA still offers a better description than the LFA.

Figure 2 shows $\langle\varepsilon\rangle$ as a function of time in argon at both pressures. While the conclusions are similar, the failure of the LFA and the higher quality of the LEA are even more evident than in air, since energy relaxation is generally much weaker in argon.

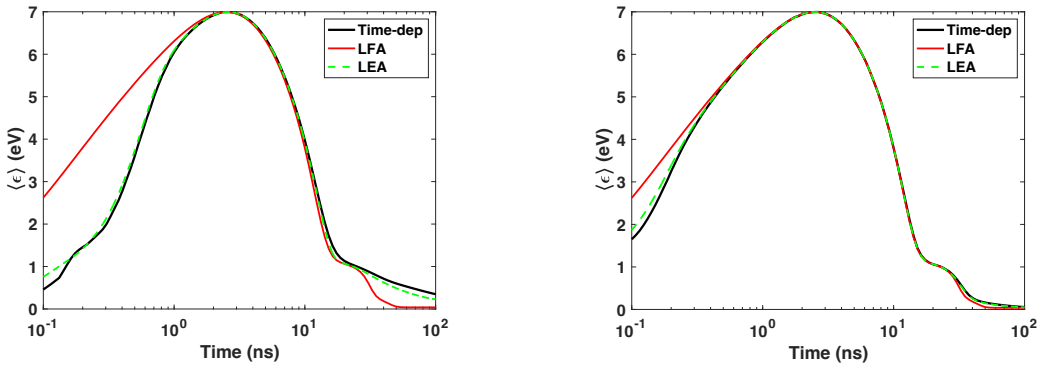

Figure 1: Temporal evolution of the mean electron energy in air at (a) 10 Torr and (b) 100 Torr.

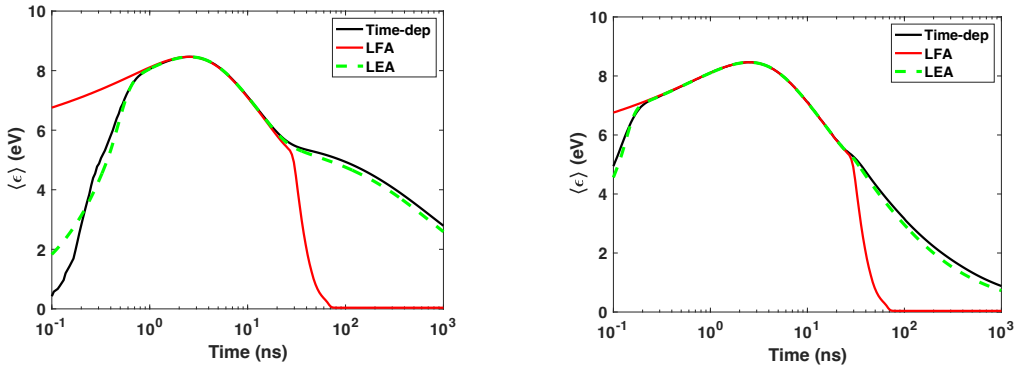

Figure 2: Temporal evolution of the mean electron energy in argon at (a) 10 Torr and (b) 100 Torr.

To evidence that these approximations can have an impact in the plasma chemistry, figure 3 illustrates the temporal evolution of the chemical kinetics in air at 10 Torr, using as input the different approaches for the electron kinetics. For the charged species depicted in figure 3a, the LFA significantly overestimates the decay of the ions. Additionally, figure 3b demonstrates that the neutral kinetics might also be affected, as the LFA cannot correctly capture the early rise of the excited states of N_2. Naturally, if we consider mixtures with rare gases, the differences would be greatly amplified.

In the conference, we will discuss in detail the physical reasons for the (in)success of the approximations, focusing on the comparison between the characteristic frequencies of relaxation and the time derivative of *E/N*. This discussion will also serve as a guideline on how modelers should check the validity of the time-locality approximations, even when a rigorous time-dependent solution is not available for benchmark.

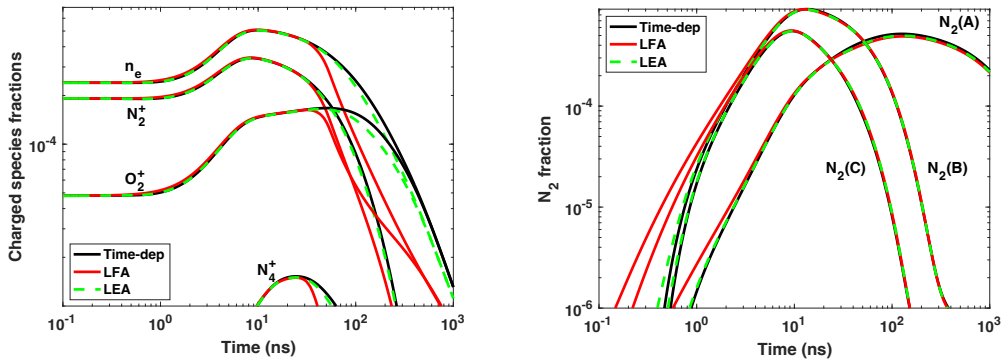

Figure 3: Temporal evolution of (a) charged species and (b) N_2 excited states, in air at 10 Torr.

IPFN activities were supported by the Portuguese FCT, under projects UIDB/50010/2020 (https://doi.org/10.54499/UIDB/50010/2020),UIDP/50010/2020(https://doi.org/10.54499/UIDP/50010/2020), LA/P/0061/2020 (https://doi.org/10.54499/LA/P/0061/2020) and PTDC/FISPLA/1616/2021 (https://doi.org/10.54499/PTDC/FIS-PLA/1616/2021).

[1] S. Dujko *et al.*, *J. Phys. D: Appl. Phys.* **46** (2013) 475202.

[2] G. K. Grubert *et al.*, *Phys. Rev. E* **80** (2009) 036405.

[3] T. C. Dias *et al.*, *Plasma Sources Sci. Technol.* **32** (2023) 095003.

[4] T. C. Dias *et al.*, *Comput. Phys. Commun.* **282** (2023) 108554.

Comparison of 2D and 3D PIC-DSMC Simulations of Pin-to-Plane Breakdown Through a Thin-Film Dielectric Coated Electrode

C.H. Moore(*)[1], A.K. Jindal[1], R. Martinez[1], A. Padgett[1]

[1] *Sandia National Laboratories, Albuquerque, NM 87185, USA*

(*) chmoore@sandia.gov

In devices where high voltages are present, thin (<1mm) dielectric coatings are often used to increase the standoff voltage in the presence of an air-filled gap (~mm–cm). When a device's surface is fully coated, breakdown can occur if an air-gap streamer produces fields inside the solid dielectric that exceed the dielectric's breakdown strength. If this happens, the resulting discharge is often catastrophic; damaging the device and/or preventing proper operation.

In prior work [1] we compared 2D electrostatic PIC-DSMC simulations using the Sandia code EMPIRE with experimentally measured breakdown voltages for a 1mm gap with various dielectric coating thicknesses, shown in Figure 1. Experimentally it was observed that the breakdown occurred through the dielectric for dielectric thicknesses less than ~100μm. However, based on the bulk dielectric holdoff strength EMPIRE simulations predict breakdown through the dielectric for much thicker dielectric films. Additionally, breakdown occurred at much lower voltages in the 2D EMPIRE simulations as compared to experiment.

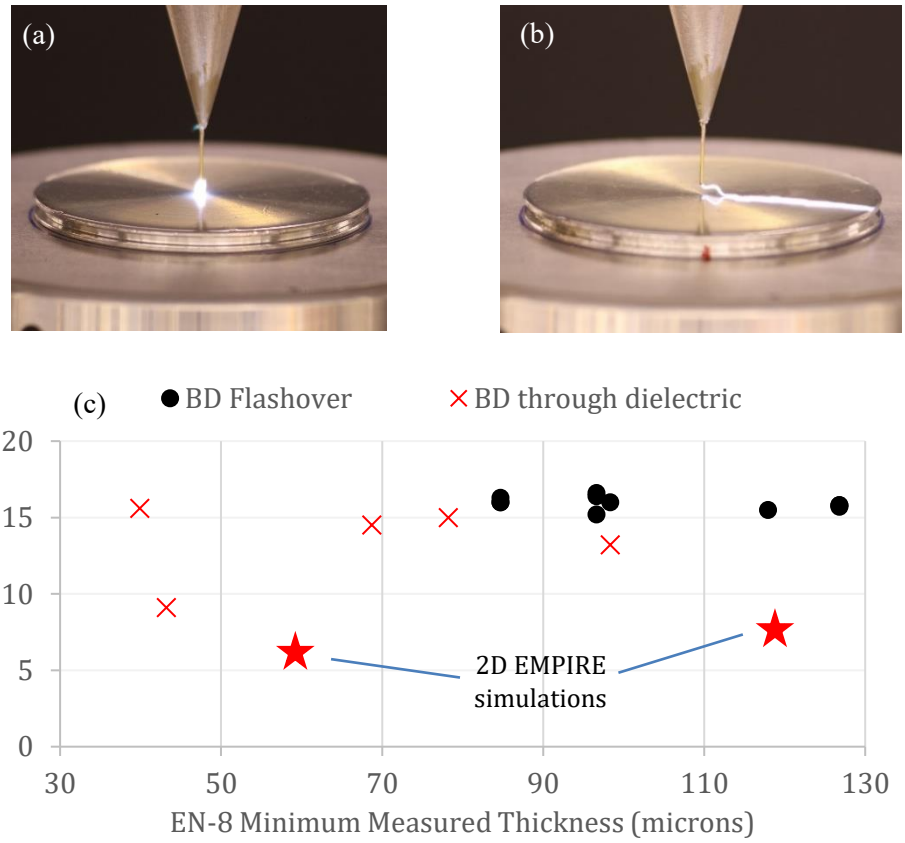

Fig. 1: (a) Breakdown through the EN-8 epoxy layer, (b) Surface flashover breakdown as the arc travel to the uncoated sample side, (c) Experimental breakdown voltage at various EN-8 thicknesses compared to simulated 2D EMPIRE breakdown voltage (through the dielectric film).

Figure 2 shows the electron density and E-field contours for a 2D EMPIRE simulation where the streamer, as it travels along the dielectric surface, results in an electric field inside the EN-8 dielectric that exceeds its bulk dielectric strength (~35MV/m). In order to predict surface flashover instead of breakdown through the dielectric, the EMPIRE simualtions needed significantly thicker dielectric coatings than experimentally observed. The present work will examine the effects of simulating the domain in a 3D wedge versus the prior 2D simulations and how much this changes the predicted breakdown votage and streamer dynamics.

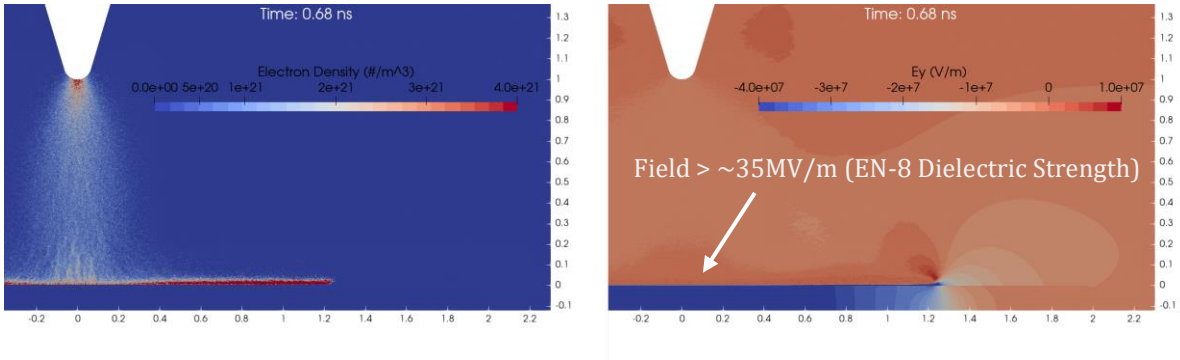

Fig. 2: 2D PIC-DSMC simulation of streamer formation from the pin to the dielectric covered planar electrode.

Acknowledgment: This work was supported in part by the U.S. Department of Energy under award No. DE-SC0022201, and in part by Sandia National Laboratories. Sandia National Laboratories is a multi-mission laboratory managed and operated by National Technology and Engineering Solutions of Sandia, LLC., a wholly owned subsidiary of Honeywell International, Inc., for the U.S. Department of Energy's National Nuclear Security Administration under Contract No. DE-NA0003525.

[1] C.H. Moore, et. al., APS Gaseous Electronic Conference (2023)

Simulations of centimeter-scale, atmospheric pressure, positive streamer discharges using EMPIRE-PIC

Dejan Nikic(*)[1], Andrew Fierro,[1], Christopher Moore[2], Jane Lehr[1]

[1] *University of New Mexico*
[2] *Sandia National Laboratories*
(*) dejan@unm.edu

Development of a new particle-in-cell (PIC) code EMPIRE-PIC has enabled simulations of high pressure discharges over wide electrode gaps. This is primarily due to implementation of scalable solvers allowing for 100's of millions of elements, sub-Debye length mesh sizes, and 10's of billions of macro-particles. EMPIRE-PIC allows an unlimited number of species and interaction possibilities, making it suitable for complex plasmas and plasma chemistry. Furthermore, stochastic behavior is intrinsic to the code by allowing random interaction rates. This is particularly important for positive streamer discharges where photo-ionization is a primary streamer propagation mechanism. In this instance it is the photons that photo-ionize secondary species in the gas which in turn generates additional charged particles to be created at random location within the electrode gap. Each of these locations is a source of a new electron avalanche formation and growth of a streamer branch that may or may not connect with the primary branch.

In previous work [3] we established the importance of the mean-free-path (MFP) of photo-ionizing photons. We have shown that the concentration of photo-ionizing gas and thus change in MFP changes the behavior of positive streamer discharge. Namely, that the short MFP photons create a more uniform discharge, while long MFP photons create a filamentary type of streamer discharge. In this work we are going further in establishing the importance of various other simulation parameters such as mesh sizing and particle counts. Comparisons between simulations are performed to determine key drivers in fidelity and accuracy of positive streamer discharges. Examples of two different types of discharge are shown in Figure 1a and 1b.

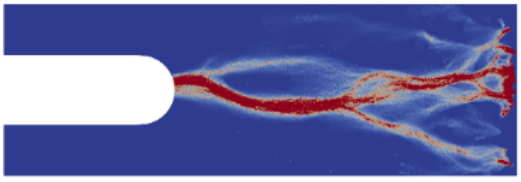

(a) Example of filamentary discharge. Electron density shown with red representing 10^{20} m^{-3}.

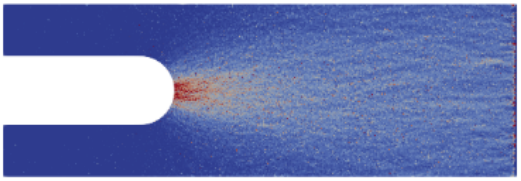

(b) Example of uniform discharge. Electron density shown with red representing 10^{20} m^{-3}.

Simulations presented in this work are of positive discharges between a pin and plate electrode set. In this configuration a pin is the anode and plate a cathode. Tip of the anode is exactly 1 centimeter away from the cathode plate. We apply a constant source of electric field between the two electrodes. For all simulations a voltage of 15 kV is used based on earlier breakdown studies [1]. Surrounding the electrodes is a uniform gas fill at atmospheric pressure. For our simulation we are using a synthetic, argon-like, gas A for which electron collision cross-sections are calculated using established theory [2]. Furthermore, gas A is capable of being in an excited state. When gas A de-excites a photon is released. We also introduce a separate gas B that can interact with these photons and generate an ionized species of gas B which serves as a source of charged species generated randomly through the volume. Gas B concentrations are kept low, nominally 0.01% to 1% of the total volume depending on the simulation and types of effects we choose to investigate. A full list of interactions used in our simulations is shown in (1).

$$
\begin{aligned}
e^- + A &\rightarrow e^- + A^+ + e^- \\
e^- + A &\rightarrow e^- + A \\
A^+ + A &\rightarrow A^+ + A \\
A^+ + A &\rightarrow A + A^+ \\
e^- + A &\rightarrow e^- + A^* \\
A^* &\rightarrow A + \gamma \\
\gamma + B &\rightarrow B^+ + e^-
\end{aligned}
\tag{1}
$$

Due to the large computing resources available at Sandia we are able to utilize computations requiring hundreds and even thousands of compute units. Utilizing these resources we were able to demonstrate the effects due to changes in computational parameters. Results of these simulations are used to determine the thresholds on number of macro-particles and the mesh sizes for which streamer discharges are behaving consistently. These thresholds will be used to simulate more complex configurations and larger spatial domain problems.

Acknowledgment: This work was supported in part by the U.S. Department of Energy under award No. DE-SC0022201, and in part by Sandia National Laboratories. Sandia National Laboratories is a multi mission laboratory managed and operated by National Technology and Engineering Solutions of Sandia, LLC., a wholly owned subsidiary of Honeywell International, Inc., for the U.S. Department of Energy's National Nuclear Security Administration under Contract No. DE-NA0003525.

[1] D. Nikic, et.al. *IEEE ICOPS* (2023)
[2] Y. Kim, *J. Res. Natl. inst. Stand. Technol.* **97** (1992) 689–692.
[3] D. Nikic, et.al. *APS GEC* (2023)

Nonadiabatic energization of electrons in spokes observed in magnetrons with a nonuniform magnetic field

D. Eremin(*)[1], L. Vogelhuber[1], J. Kallähn[1], K. Köhn[1], D. Krüger[1], L. Xu[2], R.P. Brinkmann[1]

[1] *Institute of Theoretical Electrical Engineering, Ruhr University Bochum, 44801, Bochum, Germany*
[2] *Department of Physical Science and Technology, Soochow University, 215006, Suzhou, China*
(*) Denis.Eremin@rub.de

Self-organized spoke structures are observed in many partially magnetized (with magnetized electrons, but unmagnetized ions) $\mathbf{E} \times \mathbf{B}$ plasmas such as planar and cylindrical magnetrons, Hall thrusters, Penning discharges, and others. They represent rotating zones of increased ionization and excitation leading to enhanced light emission. One of the fundamental questions is therefore where do energetic electrons causing these phenomena come from and what is the underlying energization mechanism. Since the magnetic field does no work, electrons gain energy only from the electric field. To the leading order of the drift-kinetic theory, electron guiding centers move along the equipotential surfaces with the $\mathbf{E} \times \mathbf{B}$ drift. In this case, electron kinetic energy oscillates with an amplitude determined by a potential difference over a Larmor radius [1]. However, this mechanism is too weak to create a strong localized population of electrons associated with a spoke structure. It was recently proposed that an additional electron heating occurs in a nonuniform magnetic field, where ∇B drift motion of the electron guiding center carries an electron into an area of increased potential at the spoke front [2]. It can be shown that the corresponding heating mechanism is adiabatic and therefore limits the electron energy boost by the need to conserve the magnetic moment (increase in the perpendicular kinetic energy is related to the increase of the magnetic field along the electron trajectory, rather than being determined by the potential jump). Indeed, the rate of energy change due to the guiding center motion is $-e\mathbf{E} \cdot \mathbf{v}_{\nabla B} = \frac{mv_\perp^2}{2B} \frac{\mathbf{E} \cdot [\mathbf{B} \times \nabla B]}{B^2}$, but on the other hand it can be written as $\frac{d}{dt}\frac{mv_\perp^2}{2} = \frac{d}{dt}(\mu B) = \mu(\mathbf{v}_{\mathbf{E}\times\mathbf{B}} \cdot \nabla)B$, which is derived under the ansatz of the magnetic moment conservation. At the same time, potential jumps at the spoke front, seen in both experimental studies and simulations of DC magnetrons, can be as large 100 eV and the simulations indicate existence of electrons with the corresponding energy. A question arises whether such a big increase in energy can be obtained while electron magnetic moment is held constant.

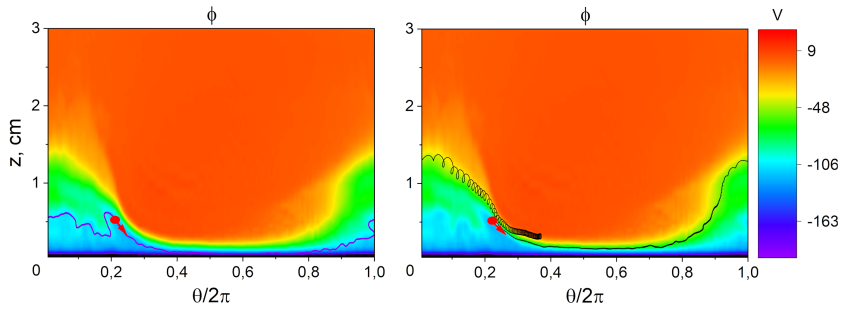

Fig. 1: Typical electron trajectories: quasiperiodic trajectory (left) of an electron far from the potential jump and trajectory of an energized electron crossing the potential jump (right). The cathode is at the bottom, the anode is at the top, the magnetic field is orthogonal to the page, and the magnetic field flux density decreases from the cathode.

To answer this question, the authors performed a 2D (θ, z) electrostatic PIC simulations with an implicit energy-conserving ECCOPIC2S-M code [3, 4] exhibiting formation of spokes. The simulation setup was similar to the one used in [2]. After the spokes were fully formed, the electrostatic potential was taken at a chosen time and thereupon was held fixed, whereas motion of test electrons was investigated in such a prescribed potential. This was done to eliminate possible electron heating mechanisms resulting from time-dependent electric fields (e.g., due to microinstabilities). It was explicitely checked that the total energy consisting of a sum of the kinetic and potential energies was constant for all electrons to a good accuracy (not shown). Fig. 1 shows orbits of a typical electron traversing a quasiperiodic orbit away from the spoke-related sharp potential jump and close to the cathode and of an electron

which crosses the potential jump and thus gains a lot of energy, which is evidenced by the Larmor radius growth (note, however, that the Larmor radius is decreased as the electron further enters an area of a larger magnetic field).

Fig. 2 reveals the electron heating explicitly by comparing properties of the first particle (top row) and the second particle (bottom row). Using the dependence of electron coordinates on time (leftmost column), one can see that the first electron exhibits an adiabatic evolution of energy, showing smooth evolution of the average energy as the ∇B drift pushes the electron into an area of elevated potential as well as the amplitude of its oscillations as the electron moves into an area of increased electric field underneath the potential hump, in full agreement with [2] and [1]. As expected, the magnetic moment extracted from the simulation remains approximately constant and equal to its initial value. It is worth noting that for a proper evaluation of the magnetic moment various guiding center drifts must be subtracted [5]. These were evaluated in the simulation results by identifying the rotation period as the time interval between the velocity vector passing the same angle and averaging the electron velocity.

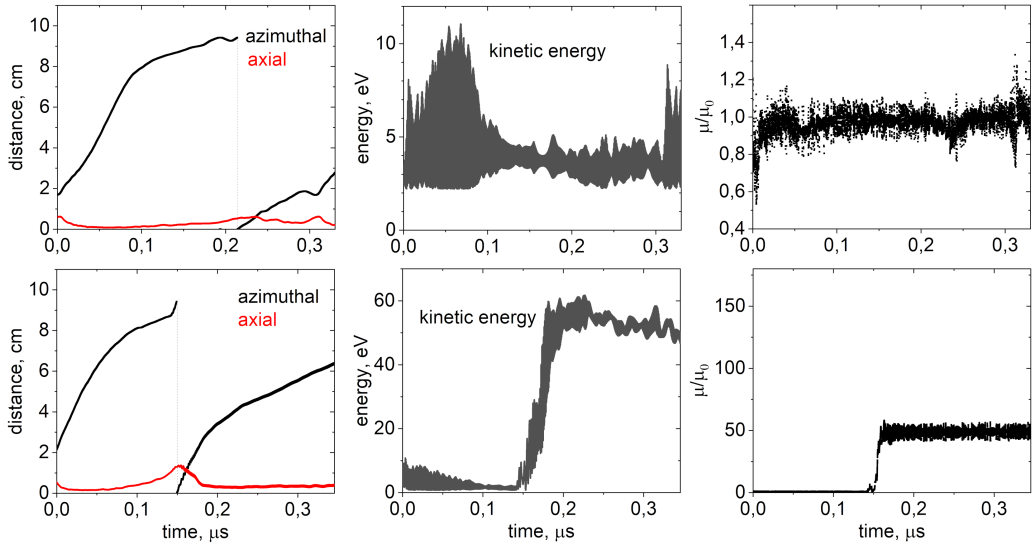

Fig. 2: Properties of the quasiperiodic (top row) and energized (bottom row) electron orbits shown in Fig. 1: coordinate evolution (left), kinetic energy (middle), and ratio of the magnetic moment to its initial value (right).

By inspecting the energized electron data (Fig. 2, bottom row) one can see that it acquires a large energy of 60 eV related to the potential jump at the spoke front. One can also see that in this case the electron's magnetic moment experiences a violent jump and becomes 50 times larger than its initial value. It clearly indicates that the corresponding energization mechanism is nonadiabatic and thus cannot be ascribed to the ∇B energization mechanism suggested in [2]. It can be seen that the electron energization consists of two phases, nonadiabatic heating, when electron perpendicular energy grows much faster than the magnetic moment conservation allows, followed by an adiabatic energization, which is related to the growth of the perpendicular velocity as the electron goes into a region of increased magnetic field flux density closer to the cathode. The existence of the nonadiabatic phase in the energization mechanism enables much stronger energy gains stored in the Larmor rotation compared to [2], which are governed by the large potential jumps in DC magnetrons and not the magnetic field nonuniformity. From Fig. 1 it can also be seen that the corresponding energized electron ends up on the other side of the potential jump, exactly where the maximum ionization is observed in simulations (not shown). One can therefore expect this mechanism to be important for the spoke physics.

[1] D. Eremin et al., *Plasma Sources Sci. Technol.* **32** (2023) 045007
[2] J.-P. Boeuf, M. Takahashi, *Phys. Rev. Lett.* **124** (2020) 185005
[3] D. Eremin, *J. Comp. Phys.* **452** (2022) 110934
[4] D. Eremin et al., *Plasma Sources Sci. Technol.* **32** (2023) 045008
[5] C.D. Stephens, R.W. Brzozowski, III, F. Jenko, *Phys. Plasmas* **24** (2017) 102517

Towards Sustainable Space Exploration: Assessing Hall Thrusters for CubeSat Missions

Tiago M. Santos[1], Eduardo Calvo[2], João P.L. Monteiro [3], Paulo Sá[2], Mario J. Pinheiro[(*)4,5]

[1] *Instituto Superior Técnico, Universidade de Lisboa, Avenida Rovisco Pais, 1049-001, Lisboa, Portugal*

[2] *Centro de Estudos de Fenómenos de Transporte e Departamento de Engenharia Física, Faculdade de Engenharia da Universidade do Porto, Rua Doutor Roberto Frias s/n, 4200-465 Porto, Portugal*

[3] *IDMEC, Instituto Superior Técnico, Universidade de Lisboa, Avenida Rovisco Pais, 1049-001, Lisboa, Portugal*

[4] *Departament of Physics, Instituto Superior Técnico-IST, Universidade de Lisboa, Avenida Rovisco Pais, 1049-001, Lisboa, Portugal*

[5] *Instituto de Plasmas e Fusão Nuclear, Instituto Superior Técnico, Universidade de Lisboa, Avenida Rovisco Pais, 1049-001, Lisboa, Portugal*

[(*)] mpinheiro@tecnico.ulisboa.pt

This study investigates Hall thrusters' applicability in CubeSats, assessing their maneuverability and efficiency under low-power constraints. CubeSats, known for cost-effectiveness, may benefit from propulsion systems, and this work studies the possible usefulness of Hall thrusters, known for their efficiency and high thrust-to-power ratio. Our analysis includes cataloguing CubeSat thrusters, developing an energy-based simulation for station-keeping and collision avoidance, and benchmarking different propulsion technologies. To date, only three Hall thrusters have flown in CubeSat missions and this research attempts to identify the potential strengths of these thrusters. Our findings underscore Hall thrusters' effectiveness in low Earth orbit collision avoidance, aligning with space debris regulatory standards.

Hall thrusters offer a distinct advantage over ion thrusters in terms of their thrust capabilities. Despite having similar levels of efficiency, Hall thrusters typically exhibit a thrust-to-power ratio that exceeds that of gridded ion thrusters by more than threefold. This trait positions Hall thrusters as particularly beneficial for missions requiring drag compensation and precise maneuverability [1]. For assessing orbital capabilities, an energy based simulator was coded and uses orbital energy, the drag equation and forces work to assess athmospheric decay and orbital corrections introduced by a thruster. [2]. The atmospheric model used is based on a scale height depending on Solar and Geomagnetic conditions and were set as the predicted for a cubesat launched after 2030. A validation exercise regarding the orbital decay was performed using DRAMA software, indicating satisfactory results [3]. In this study, we focus on two critical orbital maneuvers for CubeSats: station-keeping and collision avoidance. Station-keeping involves maintaining a specified orbital altitude to counteract decay due to atmospheric drag. Collision avoidance refers to the capability of maneuvering quickly in space, and requirement of rising 100 meters is set. Four different altitudes: 200, 250, 300, and 400 km. These altitudes were chosen because of the higher values of atmospheric density in those regions. To perform a thruster comparison, each maneuver is assigned two performance metrics related to time and energy consumed. In station-keeping, the time added to the orbit and the ratio of energy consumed to the time added to the orbit are utilized. In collision avoidance, the time of the maneuver and energy consumption are defined. After calculating the performance metrics for the thrusters, they are normalized to a scale between 0 and 1. The thrusters selected for the analysis are retrieved from [4] and have flown in Cubesats. Thrusters until 70 W and 1U volume were considered, from a range of solutions both chemical and electrical. The Hall thruster inputted in the database (ExoMG nano S [60W, including system losses]) have some features that distinguish them from other electric propulsion types. The thrust (2.5 mN) and thrust-to-power ratios are the highest. System efficiency levels are also high. On the other hand, it presents low specific impulse (I_{sp} of 800 s) and fuel mass (0.11 kg). The platform considered is a 12U cubesat, with a baseline

mass of 15 kg, surface area of 0.08 m^2 and CD (drag coefficient) of 2.2. Results for the two maneuvers are present in the following table.

Table 1 Hall thruster retrieved performance.

	Station-keeping			Collision Avoidance		
Alt. [km]	Time added [months]	Time Score	Energy Score	Time [minutes]	Time Score	Energy Score
200	0.2	1	0	19.7	0	0
250	0.7	0.11	0.74	8.1	0.95	0.94
300	2.5	0.05	0.83	6.9	0.99	0.94
400	24	0.05	0.83	6.5	0.94	0.83

Within the realm of electric propulsion, the Hall thruster displays the best scores, due to their high Thrust-to-Power ratio (T/P). Additionally, within a 12U system, Hall thrusters operate effectively at lower altitudes due to the higher trust, which allows them to combat atmospheric effects. Regarding the energy scores, for both station-keeping and collision avoidance, the Hall thruster presents the best energy scores among electric propulsion. This can be explained due to their high T/P and thrust that allow to perform maneuvers quickly and thus spend less overall energy on the maneuver. The top scores in this category are attributed to chemical propulsion. However, comparing them directly may not be entirely fair, as the energy output of chemical propulsion systems is derived from the chemical energy stored in fuels, oxidizers, and pressure chambers. Therefore, the chosen Hall thruster seems to be designed for evasive maneuvers without much consideration for longevity at the altitudes considered, due to its limited low I_{sp} and fuel capacity. It's unclear whether this latter issue stems from the technology being constrained by volume, having more weight than other options, or if it's simply an issue of challenging resizing for fitting into a 1U form factor. Results indicate minimal mission time extension below 300 km, yet the thruster maintains collision avoidance capabilities, unlike other electric propulsion options. The comparative analysis also highlights promising alternatives like the FEEP technology, which offers significantly extended orbital lifetimes. However, despite scoring lower in station-keeping due to factors such as low I_{sp} and fuel mass, the thruster allowed for a threefold increase in orbital lifetime beyond 400 km (without propulsion, at 400 km, a 12U would decay in one year) indicating satisfactory overall performance. New regulations restricting the orbital lifetime of spacecraft in low Earth orbit (LEO) to five years are being discussed, making collision avoidance requirements more important than longevity ones, so, the capabilities of Hall thrusters indicate a good solution to be employed in a CubeSat in LEO.

In summary, our study validates Hall thrusters choice for CubeSat propulsion, offering significant advantages in thrust-to-power ratio, maneuverability, and compliance with space debris mitigation requirements. These attributes not only enhance CubeSat mission effectiveness but also pave the way for safer, more sustainable low Earth orbit operations. Our research contributes valuable insights into propulsion technology selection, underscoring the potential of Hall thrusters to revolutionize small satellite missions in the emerging era of space traffic management and debris regulation.

[1] J. Dannenmayer. Scaling laws and electron properties in Hall effect thruster. PhD thesis, Oct. 2012

[2] T. Bozhanov. Analysis of Electric Propulsion Systems for Drag Compensation of Small Satellites in Low Earth Orbits. PhD thesis, May 2017.

[3] Space Debris User Portal. (n.d.). Retrieved January 2024, from https://sdup.esoc.esa.int/.

[4] C. Gentgen. Hybrid Chemical-Electric Propulsion Systems for Cubesats. Master thesis, Jun 2022.

Design and Validation of a Low-Power Hall Thruster for CubeSats: A Scaling Laws Approach

Tiago M. Santos[1], Eduardo Calvo[2], João P.L. Monteiro [3], Paulo Sá[2], Mario J. Pinheiro[(*)4,5]

[1] *Instituto Superior Técnico, Universidade de Lisboa, Avenida Rovisco Pais, 1049-001, Lisboa, Portugal*

[2] *Centro de Estudos de Fenómenos de Transporte e Departamento de Engenharia Física, Faculdade de Engenharia da Universidade do Porto, Rua Doutor Roberto Frias s/n, 4200-465 Porto, Portugal*

[3] *IDMEC, Instituto Superior Técnico, Universidade de Lisboa, Avenida Rovisco Pais, 1049-001, Lisboa, Portugal*

[4] *Departament of Physics, Instituto Superior Técnico-IST, Universidade de Lisboa, Avenida Rovisco Pais, 1049-001, Lisboa, Portugal*

[5] *Instituto de Plasmas e Fusão Nuclear, Instituto Superior Técnico, Universidade de Lisboa, Avenida Rovisco Pais, 1049-001, Lisboa, Portugal*

[(*)] mpinheiro@tecnico.ulisboa.pt

With the advent of small spacecraft, such as cubesats, existing propulsion technologies need to scale down for the low powers involved. This study delves into the application of Hall thrusters scaling laws to low power thrusters. These laws are applied to rapidly estimate specifications for a low-power Hall thruster and validated using Hallis software [1]. Despite scaling law discrepancies, the study provides a preliminary specification for a 20W thruster, with concerns for efficiency estimation.

For the preliminary specification of a 20W thruster, the laws utilized in this work are retrieved from [2]. The performance, size, and electrical parameters of thrusters are derived from established databases, not publicly available. The databases also contain low-power thrusters [2]. In [2], two methodologies based on high and low assumptions based on plasma physics are presented. Low assumptions differ from high assumptions in that they assume phenomena as the plume divergence, multiply charged ions, and voltage losses. However, in [3], it is demonstrated that the difference between high and low assumptions yielded minimal improvement in accuracy, indicating that the high assumptions are adequate for obtaining a preliminary estimate of the geometry and operating conditions of a Hall Thruster [2] [3]. The equations and model considered, provide a thruster geometry and performance with input power and voltage (V_d). From these inputs, one could retrieve mean channel diameter (D), channel thickness (H), channel length (L), discharge current, thrust and I_{sp}. Figure 1 illustrates the detailed geometry of the Hall Thruster, highlighting all pertinent parameters.

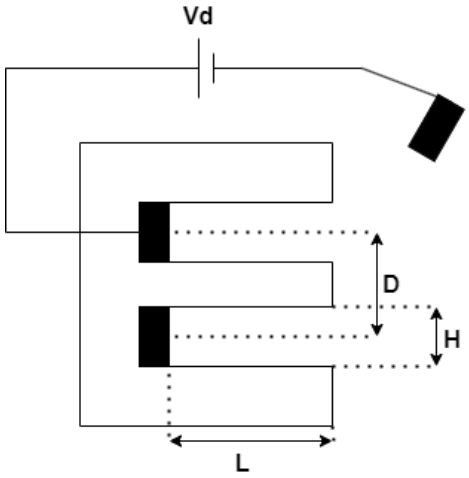

Figure 1 Detailed geometry of a Hall Thruster, showcasing its critical design parameters.

In this study, we begin by evaluating the accuracy of scaling laws against the SPT100 Hall thruster as a benchmark. By applying the SPT100's specifications—1350W power rating and 300V operation—through the scaling laws, we aim to assess the precision of these laws. This process yields estimated performance metrics and geometrical dimensions, which are then compared with the actual specifications of the SPT100 for validation. To ascertain the relevance of scaling laws for low-power Hall thrusters, we utilized the one-dimensional model provided by Hallis software [3]. To validate the applicability of scaling laws within low-power Hall thrusters, the 1D model of Hallis software is employed. [3] Throughout all simulations, consistency was maintained in terms of voltage, channel length, and magnetic field profile. Despite Hallis overestimating the power consumption, the overall performance aligns with the real performance of SPT100. The study reveals that scaling laws tend to overestimate the real performance of SPT100 by approximately 11%. When the geometry of the SPT100 is determined using scaling laws and then analysed using Hallis software, the scaling laws tend to overestimate the performance by approximately 14% in comparison to Hallis. For the designated 20W thruster, the scaling laws predict performance metrics that are 14.9% higher than expected, and also leading to an overestimation of efficiencies. The specifications derived from these scaling laws are summarized in the following table.

Thruster	Data	P [W]	V_d [V]	I_{sp} [s]	T [mN]	L [mm]	D [mm]	H [mm]	efficiency (%)
20W	Scaling Laws	20	300	1900	1.5	25	12	2	0.69
	Hallis	22.7	-	1637	1.29	-	-	-	0.45

Figure 2 Preliminary Specifications of a 20W Hall Thruster Derived from Scaling Laws.

Based on the observed errors between the scaling laws and Hallis software, one can conclude that the scaling laws method provides a reasonable approximation for initial performance estimation and does not seem to differentiate significantly between high and low power levels. However, the efficiency calculated in the simulation with the low-power thruster deviates from the literature. As mentioned in Reference [4], a 50W low-power thruster is reported to have an efficiency of 30%, whereas Hallis outputs an efficiency of approximately 45% for the 20W thruster. A potential explanation for this variance could be attributed to the fact that the Hallis software usually treats ion collisions with the walls as reflections after recombination or not included, as stated in the Hallis guide [1]. A potential explanation for this variance is that Hallis software typically models ion collisions with the walls as either reflections post-recombination or does not include them at all, as detailed in the Hallis guide [1]. In reality, sputtering affects a significant portion of the thruster wall, and the reduced area-to-volume ratio inherent to small thrusters leads to increased wall losses and efficiency decline. This in turn will influence performance. Employing practical measures like increasing channel thickness could help mitigate these losses, as recommended in [3].

In summary, this study examines the adaptation of scaling laws for low-power Hall thrusters. Through validation against empirical data and simulations via the Hallis software, we have formulated a preliminary design for a 20W thruster. This process underlines the critical role of scaling laws, alongside recognizing the constraints inherent in efficiency calculations.

[1] Hallis software page, Jan 2024. URL https://www.hallis-model.com/.

[2] K. Dannenmayer and S. Mazouffre. Elementary scaling relations for hall effect thrusters. 27(1), Jan 2011.doi:10.2514/1.48382.

[3] J. Dannenmayer. Scaling laws and electron properties in Hall effect thruster. PhD thesis, Oct. 2012

[4] I. Levchenko, et al. Space micropropulsion systems for cubesats and small satellites: from proximate targets to furthermost frontiers. 5(1), Feb 2018. doi:10.1063/1.5007734.23

Pulsed Low Bias Frequencies for High Aspect Ratio Plasma Etching

Evan Litch[1], Hyunjae Lee[3], Sang Ki Nam[3] and Mark J. Kushner[2]

[1]*Nuclear Engr. & Radiological Sci., University of Michigan, Ann Arbor, Michigan, USA*
[2]*Electrical Engr. & Computer Sci., University of Michigan, Ann Arbor, Michigan, USA*
[3]*Mechatronics Research, Samsung Electronics Co., Ltd., Republic of Korea*
elitch@umich.edu, hj0928.lee@samsung.com,sangki.j.nam@samsung.com, mjkush@umich.edu

Current roadmaps for microelectronics fabrication are focused on fabrication of 3-dimensional devices for higher functionality. Plasma etching steps during fabrication of these 3D devices are becoming increasingly more challenging due to the high aspect ratios (HARs) of the features [1]. For example, 3D-NAND memory structures contain hundreds of alternating layers of SiO_2 and Si_3N_4 requiring etching of vias having aspect ratios (AR) exceeding 100. Deep trench isolation (DTI) for electrical isolation of the 3D logic structures have similar HAR challenges. DTI etching of conductive substrates such as Si using halogen gas mixtures (e.g. HBr/Cl_2) is typically performed in inductively coupled plasmas (ICPs) with a substrate bias to facilitate highly anisotropic etching.

Plasma etching of HAR features requires ion energy and angular distributions (IEADs) that are narrow in angle while extending to energies exceeding several kV. These requirements motivate the use of very low frequency biases (VLF) – a few hundred kHz. Trends in the industry are also moving towards pulsed biases to optimize the ratio of radical to ion fluxes. Several challenges arise with the use of pulsed, low frequency, high voltage biases. The thickening of the sheath and charging of focus rings (structures surrounding the wafer) lead to edge exclusion – a region at the edge of the wafer where IEADs are perturbed from their desired, ideal anisotropic properties. These undesirable properties generally result from sheath curvature. The transient nature of pulsed biases exacerbate these challenges by introducing addition sheath curvature.

In this presentation, results will be discussed from a computational investigation of IEADs incident onto wafers and remediation of edge exclusion when using pulsed VLF biases in ICPs for etching of trenches for DTI. Simulations were conducted using the Hybrid Plasma Equipment Model (HPEM) [2]. Operating conditions are tens of mTorr mixtures of $Ar/Cl_2/O_2$ with bias frequencies from 250 kHz to 5 MHz. Bias voltages are up to a few kV with pulse repetition frequencies of up to several kHz. The consequences of these operating conditions on etching DTI features were evaluated using the Monte

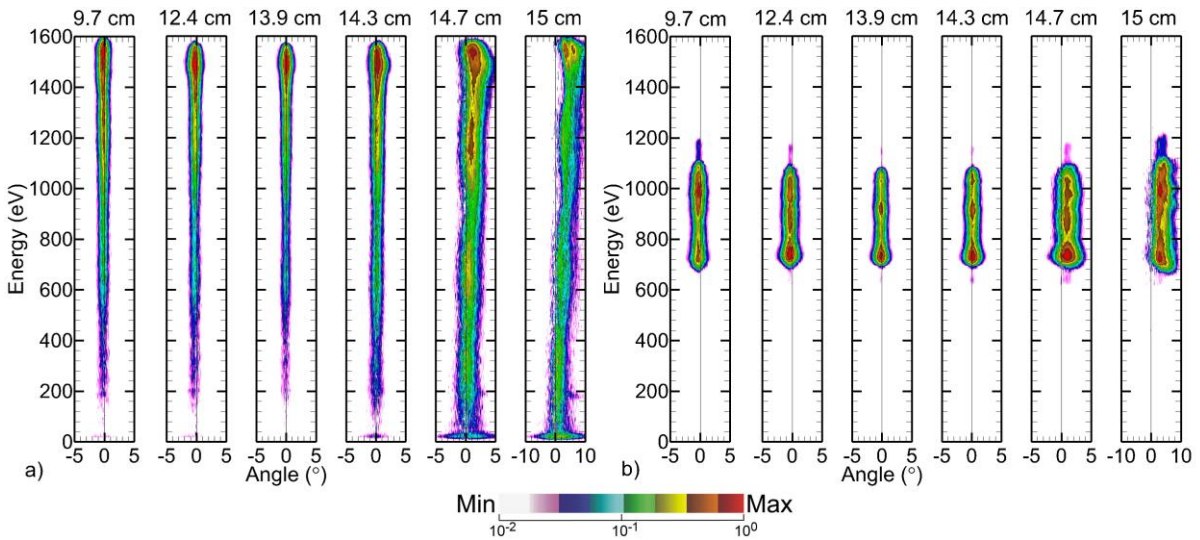

Fig. 1. Ion energy and angular distributions (IEADs) at radial positions approaching the wafer edge for (left) 250 kHz and (right) 5 MHz.

Carlo Feature Profile Model (MCFPM) [2]. When using continuous wave biases, the charging of the focus ring is sensitive to frequency, and this charging produces sheath curvature at the edge of the wafer, which perturbs IEADs. For example, IEADs are shown in Fig. 1 approaching the edge of a 30 cm diameter wafer for bias frequencies of 250 kHz and 5 MHz for an ICP sustained in $Ar/Cl_2/O_2$ with bias voltage amplitude of 1 kV. With pulsed biasing, the focus ring is transiently charged both during the VLF cycle and during the pulsed cycle, adding additional challenges to minimizing edge exclusion.

This work was supported by Samsung Electronics Co. and the US National Science Foundation (2009219).

[1] J. Kim,G. Choi,and K.-H. Kwon, Plasma Processes Polym. **20**, e2200167 (2023).
[2] S. Huang, et al., J. Vac. Sci. Technol. A **37**, 031304 (2019).

Particle-in-Cell modeling of needle-to-plate ns-pulse spark discharge

F. Taccogna(*)[1,2], P. Minelli[1,2], F. Cichocki[3]

[1] *Institute for Plasma Science and Technology ISTP, CNR, Bari, Italy*
[2] *National Institute of Nuclear Physics INFN, Bari, Italy*
[3] *Dipartimento "Nucleare", ENEA C.R. Frascati, Frascati, Italy*
(*) francesco.taccogna@istp.cnr.it

Nanosecond pulsed spark discharges are widely used in different low temperature plasma applications such as CO_2 reduction [1] and plasma-assisted ignition and combustion [2]. Pulses with nanosecond rise times can generate large transient electric fields with an efficient electron energy transfer. This leads to a large production of active species, neutrals in vibrational and electronic excited states by fast electron-induced collisions, while the gas stays cold and immobile during the ns-pulse. In such fields the energy distribution of free electrons is often far from equilibrium. A multiscale approach is necessary to represent the evolution of this discharge, whose first step is a self-consistent kinetic approach, necessary to give realistic initial conditions (vibrational distribution function, production rate of excited electronic states and radicals) for the following steps, i.e. state-to-state vibrational and chemical kinetic models [3].

In this work we present simulation results of high voltage nanosecond (HV-ns) pulse discharge in a two-dimensional axysimmetric needle-to-plane electrode geometry, using P=100 Torr atomic hydrogen gas. The model is based on the Particle-in-Cell / Monte Carlo Collision (PIC-MCC) methodology [4] by using the code PICCOLO (PIC COde for LOw temperature plasmas) developed at CNR-ISTP-Bari. Fig.1 shows the computational domain in green with the size and the boundary conditions used for Poisson's equation. We consider a positive discharge, i.e. the needle electrode (truncated cone shape on the bottom left in red) has a positive voltage whose temporal evolution is reported in Fig.2, while the plate (right boundary in black) is grounded.

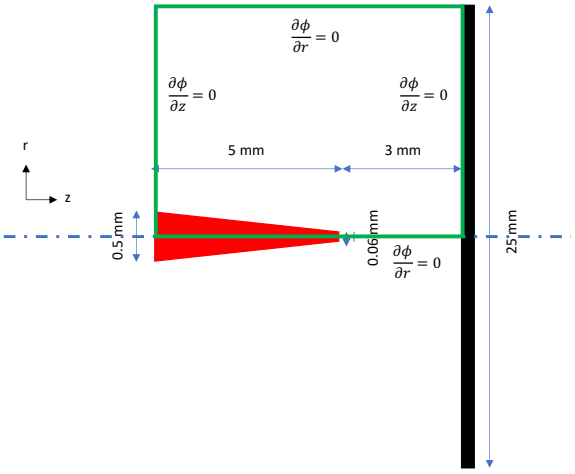

Fig. 1: Simulation domain with electrodes size (not in scale) and boundary conditions.

The most relevant collisions included are electron-atom collisions; elastic, electronic excitations and ionization are taken into account considering the atom always in its electronic ground state. The atomic background density is uniform. After all collisions, electrons are scattered isotropically, while in the ionization event, the parent and progeny electrons randomly share the total post-collisional available energy. With the aim of decreasing the computational cost, a hybrid OpenMP/MPI parallelization approach was used.

For the case studied, a uniform PIC mesh is used with a number of nodes equal to $N_r \times N_z = 6251 \times 4001$, corresponding to a cell size of $\Delta r = \Delta z = 2 \times 10^{-6}$ m (the minimum Debye length detected during the simulation). The time step is set to be $\Delta t = 5 \times 10^{-14}$ s, in order to guarantee the CFL condition and

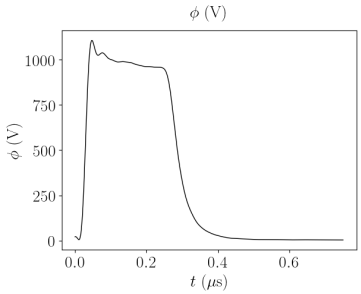

Fig. 2: HV ns pulse imposed on the anodic needle.

the MCC constraint. A run comprises $N_t = 1 \times 10^7$ time steps for an overall duration of T = 500 ns. The simulations start by seeding 50000 electrons/ions with a given weight w=80000, with uniform spatial distribution within the entire domain. These quantities define the initial plasma density $n_0 = 10^{15} m^{-3}$, mimicking the residual charges that are present in the system after the previous pulse in the experiment. Repetitive pulses are not described in the simulation due to the very long time between the pulses (few μs) in the experiment. The simulation presented here was performed on 32 nodes with 48 cores. It took up to 5 weeks, using at most $\sim 10^7$ simulation particles, to cover the entire 500 ns pulse.

Fig.3 shows the temporal evolution of the ns-pulse spark through the electric potential (top) and of the H^+ ion density (bottom) at five different times after the pulse starts: t=30, 40, 50, 100 and 400 ns.

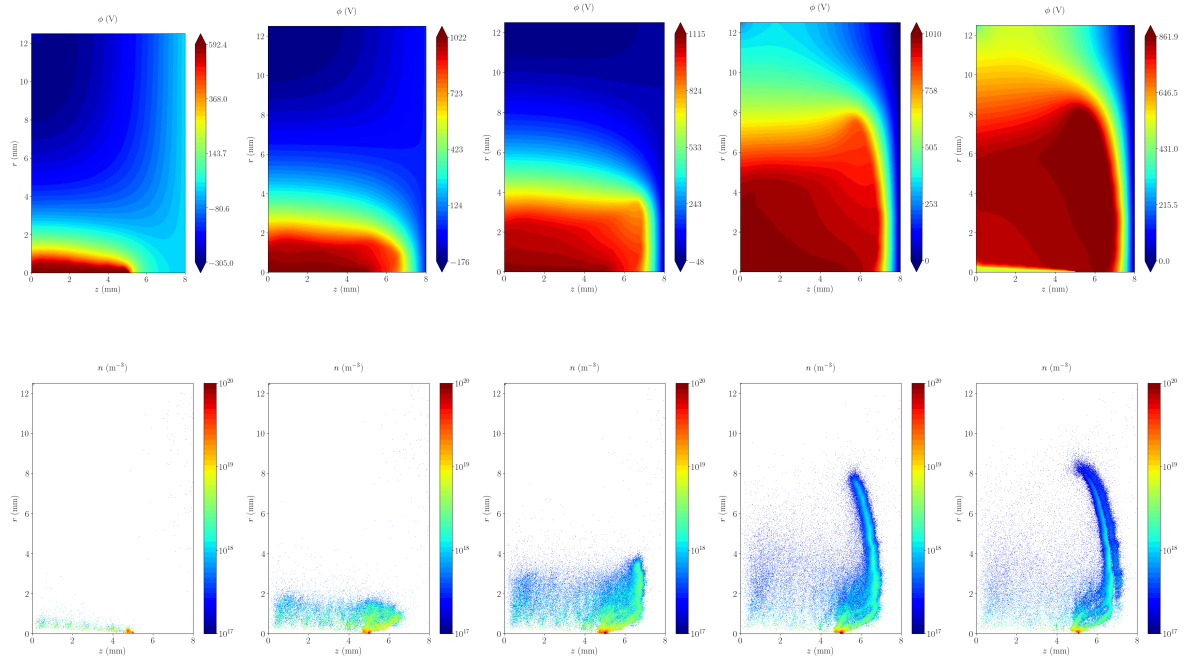

Fig. 3: Evolution of the electric potential (top) and H^+ ion density (bottom) at three different times during the ns-pulse: t=30 ns (first column), t=40 ns (second column), t=50 ns (third column), t=100 ns (fourth column), and t=400 ns (fifth column).

Acknowledgments - The work was funded by the European Union under NextGenerationEU. PRIN 2022 Prot. n. 2022J5NBBN project PLASMODD.

[1] C. Montesano, T.P.W. Salden, L.M. Martini, G. Dilecce, and P. Tosi, *J. Phys. Chem. C* **127** (2023) 10045-10050.

[2] I.V. Adamovich, and W.R. Lempert, *Plasma Phys. Control. Fusion* **57** (2015) 014001.

[3] M. Capitelli1, I. Armenise, D. Bruno, M. Cacciatore, R. Celiberto, G. Colonna, O. De Pascale, P. Diomede, F. Esposito, C. Gorse, K. Hassouni, A. Laricchiuta, S. Longo, D. Pagano, L.D. Pietanza, and M. Rutigliano, *Plasma Sources Sci. Technol.* **16** (2007) S30.

[4] D. Tskhakaya, K. Matyash, R. Schneider, and F. Taccogna, *Contrib. Plasma Phys.* **47** (2007) 563-594.

The effect of gas pressure on plasma dynamics in surface dielectric barrier discharges driven by nanosecond voltage pulses

G. Hübner[1], N. Schoeneweihs[1], D. Filla[1], S. Wilczek[1], T. Mussenbrock[1], I. Korolov[1]

[1] *Chair of Applied Electrodynamics and Plasma Technology, Faculty of Electrical Engineering and Information Sciences, Ruhr University Bochum, Bochum, Germany*

(*) huebner@aept.rub.de

The conversion of volatile organic compounds (VOCs) has long garnered interest in the plasma community [1, 2]. Non-thermal plasma sources such as surface dielectric barrier discharges (SDBD) have already shown their efficiency and advantages for VOC removal [3]. The formation of different metastable/reactive species [4] and gas flow fields induced by these discharges are responsible for the high observed conversion. As shown in [2], the induced flow fields are directly coupled to the discharge dynamics. Previous studies have demonstrated that depending on the applied microsecond or nanosecond voltage waveform pulse, the discharge can exhibit filamentary or homogeneous modes, respectively [5]. Despite the high interest, the formation and propagation of the surface discharge, particularly on a nanosecond time scale, is not yet fully understood.

In this work, we systematically investigate surface dielectric barrier discharges (SDBDs) driven by nanosecond voltage pulsed waveforms with peak voltages between 20 and 25 kV, with a full width half maximum (FWHM) of around 9 ns, and a repetition frequency of 1 kHz. The electrode is composed of an alpha aluminum oxide plate (L 190×W 88×H 0.635 mm^3) and metal square meshes printed on the top and bottom sides of the plate. The mesh consists of two layers: a 2-6 μm thick MoMn core and a 2–6 μm Ni coating. The mesh size is 10 mm with a lattice width of 0.450 mm [4]. One side of the plate is grounded, and on the other side, a positive voltage pulse is applied. The electrode is placed inside the vacuum chamber equipped with synthetic quartz windows to monitor emission from the plasma [5]. The vessel is filled with a mixture of helium and nitrogen gases, and the flow rates of the gases and pressure can be controlled within a wide range. Figure 1 shows an exemplary photograph of the ns-discharge ignited on the mesh electrode.

To investigate the ns-discharge, phase-resolved optical emission spectroscopy (PROES) measurements are performed under various conditions. By monitoring the He I 706.5 nm line, the diagnostic provides temporal and spatial distributions of the excitation dynamics of the He I $^3S_1$ (22.7 eV) state. Figure 2 illustrates the space and time-resolved electron impact excitation rate from the ground state into He I $^3S_1$, obtained experimentally for different pressures at the powered electrode. The data are spatially resolved in the x direction, with y fixed at the middle position of the mesh cell. The grid line is located at $x = 0$ mm.

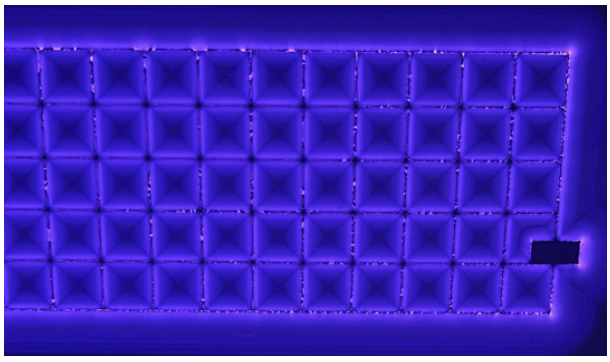

Fig. 1: Exemplary photograph of the ns-discharge (powered side) in He with 1% of Nitrogen at 1000 mbar

The behavior of the propagation speed of the excitation wave is calculated for different discharge conditions for both the grounded and the powered sides of the electrode. As can be seen from the figure, the speed of the surface excitation wave increases with decreasing pressure under otherwise fixed conditions. At the same time, the patterns of the excitation rate gradually widen with decreasing pressure, becoming less localized. The discharges are initiated from both sides of the mesh cell (at $x = 0$ mm and $x = 10$ mm) and converge towards each other. The effect of their interaction is visible on the propagation speed. At the meeting point, the excitation vanishes since the excitation/ionization wave heads from both sides carry the same polarity high net charge, causing them to repel each other and resulting in the local electric field at the meeting point dropping to zero.

We find that on the powered side of the electrode, the discharge can propagate only in the presence of photoionization, similar to positive streamers. At the same time, on the grounded side, the discharge splits into two: the first one propagates towards the center of the mesh cell against the applied field, exhibiting ionization dynamics of negative streamers, while the second one moves towards the center of the mesh wire.

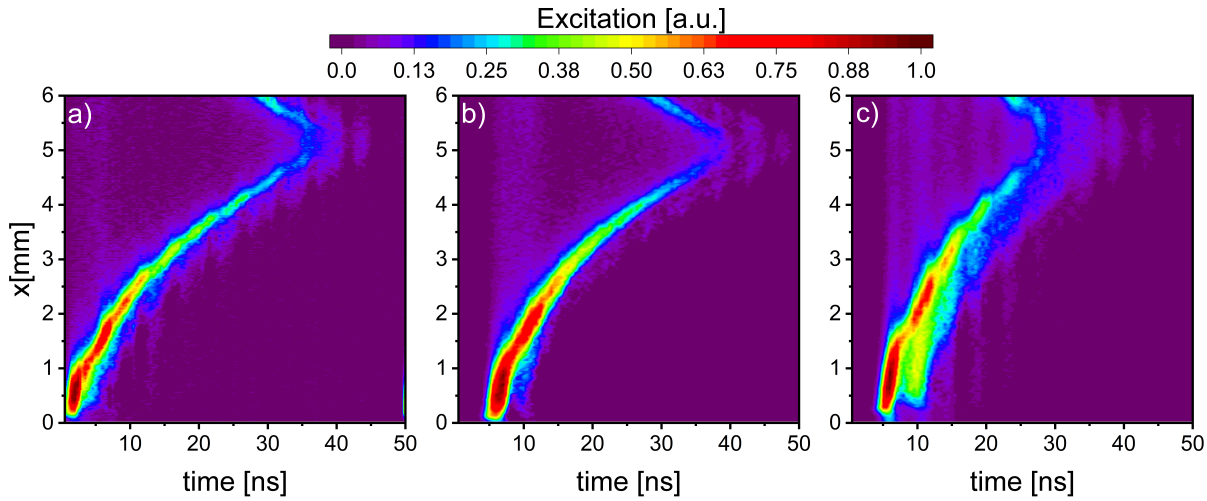

Fig. 2: Normalised spatio-temporal plots of the electron impact excitation rate from the ground state into He I $^3S_1$ obtained experimentally of the powered side of the SDBD electrode for different pressures (a: 1000 mbar, b: 800 mbar and c: 600 mbar). The examples given here are done for 99% helium and 1% nitrogen gas mixture. The Graphs are normalized individually.

Experimental findings are compared with fluid (nonPDPSIM) simulations, and a very good qualitative agreement is found, providing a deeper understanding of the discharge behavior on the ns time scale. Such understanding is essential for optimizing plasma-based technologies and applications for VOC conversion using SDBDs.

**This work is supported by the DFG via SFB1316 (A5)

[1] Li, Yizhuo, et al. "Removal of volatile organic compounds (VOCs) at room temperature using dielectric barrier discharge and plasma-catalysis." Plasma Chemistry and Plasma Processing 34 (2014): 801-810.

[2] Böddecker, Alexander, et al. "A scalable twin surface dielectric barrier discharge system for pollution remediation at high gas flow rates." Reaction Chemistry and Engineering 7.11 (2022): 2348-2358

[3] Schücke, Lars, et al. "Conversion of volatile organic compounds in a twin surface dielectric barrier discharge." Plasma Sources Science and Technology 29.11 (2020): 114003

[4] Offerhaus, Björn, et al. "Spatially resolved measurements of the physical plasma parameters and the chemical modifications in a twin surface dielectric barrier discharge for gas flow purification." Plasma Processes and Polymers 14.10 (2017): 1600255

[5] Nguyen-Smith, Ryan Thomas, et al. "s and ns twin surface dielectric barrier discharges operated in air: from electrode erosion to plasma characteristics." Plasma Sources Science and Technology 31.3 (2022): 035008.

PIC/MCC modeling of the dynamics of rotating spokes in a Penning discharge

G. Fubiani(*)[1], F. Gaboriau[1], L. Garrigues[1]

[1] *LAPLACE, Université de Toulouse, CNRS, 31062 Toulouse Cedex 9, France*

(*) gwenael.fubiani@cnrs.fr

Penning discharges are plasma sources generated inside a cylinder with a large geometrical aspect ratio (length over radius) and with a magnetic field aligned with the longitudinal axis [1]. The magnetic field strength is sufficiently large to magnetize the electrons but not necessarily the ions. In such plasma configurations, the boundary conditions can greatly modify the plasma properties. Electrons, being strongly magnetized, are attached to a field line which is short-circuited at both ends of the cylinder by either a biased metal plate or a dielectric surface. Biasing negatively the end-plates for instance will increase the residence time of the electrons inside the plasma discharge to a point where their mobility might be lower than the one of their ion counterpart. The plasma potential will then eventually become a well to confine electrostatically the ions and hence keep the whole plasma quasi-neutral. In such a situation, the plasma will become unstable and lead to the formation of large-scale rotating structures in the non-linear saturated regime. These structures, so-called spokes, rotate typically at a frequency of the order of 10's of kHz depending on the mass of the ions [2,3].

In this paper, we will simulate a Penning discharge powered by an electron beam using an explicit Particle-In-Cell (PIC) model with Monte-Carlo-Collisions (MCC) [4]. The algorithm is parallelized with both OpenMP and MPI libraries and can run on supercomputers. An arbitrary physical chemistry can be modeled. We will describe in detail the dynamics of the rotating spoke in 2D (i.e., assuming a Penning discharge of infinite length) for Helium as a background gas and discuss the effect of the boundary conditions on the plasma behavior in 2.5D and 3D. A 2.5D configuration corresponds to a model where particle losses in the third virtual dimension, parallel to the magnetic field lines (i.e., along the discharge axis), are calculated in a simplified manner: ion losses are evaluated by deducing a loss frequency from the local Bohm velocity while the electrons are followed in 3D and assumed absorbed at the boundary surface if their axial kinetic energies exceed the potential difference between the plasma and wall potentials. The numerical mesh for the plasma potential is 2D and the electric field along the magnetic field is null by assumption. Only the potential drop is considered to calculate electron losses and the fastest electrons, as in a normal ion sheath, are removed locally from the plasma. The plasma density is hence an average over the axial discharge length. We will compare the predictions from 2.5D and 3D models. We will use the latter to describe the plasma dynamics along the magnetic field lines and assess whether the assumption of a flute mode along that direction for the spoke is indeed valid.

[1] E. Rodriguez et al., Phys. Plasmas **26**, 053503 (2019).
[2] T. Powis et al., Phys. Plasmas **25**, 072110 (2018).
[3] M. Tyushev et al., Phys. Plasmas **30**, 033506 (2023).
[4] Fubiani et al., New J. Phys. **19**, 015002 (2017).

Simulation of a pulsed CO_2 plasma based on a six-temperature energy approach

I Tsonev[1(*)], O Biondo[1], A Bogaerts[1]

[1] *Research group PLASMANT, University of Antwerp, Department of Chemistry, Universiteitsplein 1, BE-2610 Wilrijk-Antwerp, Belgium.*

(*) Ivan.Tsonev@uantwerpen.be

Plasma-based CO_2 conversion has been extensively investigated as a promising pathway towards a carbon-neutral future [1]. The potential of the technology lies in the possibility to selectively excite the asymmetric stretch mode of the CO_2 molecule, which is believed to lower the activation energy for CO_2 dissociation and therefore increase the energy efficiency of the process [2]. Despite the significant research done in the field, there still are uncertanties regarding the utilization of the asymmetric stretch mode as an efficient dissociation mechanism. The main reason for this is the lack of detailed experimental data of the temporal dynamics of its excitation, along with that of the dissociation products of CO_2 (CO and O_2). Indeed, time-resolved vibrational temperature profiles are crucial to validate the existing kinetic models. Only recently, Klarenaar *et al*. and Damien *et al*. provided a detailed experimental analysis on the vibrational kinetics in a low-pressure, pulsed glow discharge [3,4]. These results spurred a substantial modelling effort led by the group of IST Lisbon to explain the observed trends [5-8]. However, a very large number of reactions had to be employed (reaching ca. 14 000 in Biondo *et al*. [8]) in order to secure agreement with the experiments. This means that such an extensive kinetic model would not be compatible with a self-consistent computational fluid dynamic (CFD) model, needed to develop new plasma reactors operating at high pressures or with complex flow patterns and capture the relevant dynamics. An alternative to this approach can be found in the field of laser modelling, specifically in the book of Smith and Thomson [9]. Therein, an energy approach was used to model the vibrational modes instead of a state-to-state kinetic approach. By virtue of its reduced computational cost and the possibility to implement it in CFD codes, the energy approach has been slowly substituting the state-to-state approach during the last decade. Recently, Kustova *et al*. put significant effort to extend and validate the theory underlying the energy approach [11]. Comparison between the energy model and experimentally measured relaxation rates revealed that one can model the vibrational modes of CO_2 and significantly improve the computational cost without any loss of accuracy, thus allowing an efficient implementation into CFD codes [11].

In this work, we implement the energy approach in a self-consistent plasma model and validate it with the single-pulse measurement of Klarenaar *et al*. The model solves separate vibrational energy balance equations for the asymmetric (T_3) and symmetric ($T_{1,2}$) modes of CO_2, as well as for the vibrational modes of CO and O_2, the gas temperature (T_g) balance equation, and the electron energy balance equation, making it a 6-temperature (6T) plasma model. The two-term Boltzmann equation is used to determine the electron energy distribution function and the electron density is calculated assuming quasi-neutrality. The comparison between the single-pulse experiment by Klarenaar and our model is presented in figure 1. Excellent agreement is found for the temporal evolution of T_3, T_{12}, and T_g between our model and the experiment. This confirms that the energy approach is suitable for modelling systems under significant non-equilibrium conditions, opening the path to the coupling of a detailed CO_2/CO/O_2/O kinetics with CFD codes.

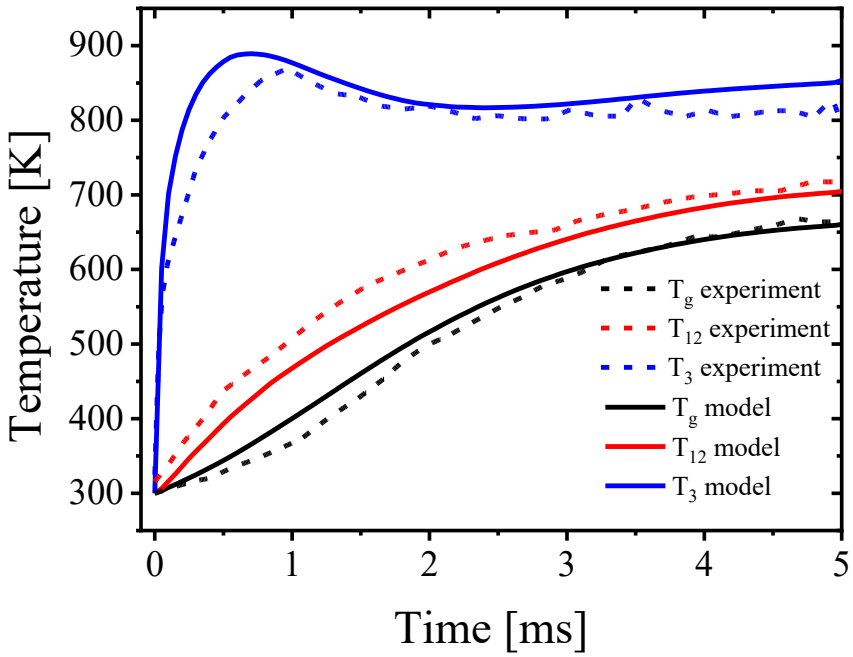

Figure 1. Comparison between the single-pulse experiment in [3] (dashed lines) and our model (solid lines) for T_3, T_{12} and T_g.

[1] A. Bogaerts and G. Centi G Front. Energy Res. **8** (2020) 111.

[2] Fridman A 2008 Plasma Chemistry (Cambridge: Cambridge University Press).

[3] B L M Klarenaar, R Engeln , D C M van den Bekerom, M C M van de Sanden, A S Morillo-Candas and O Guaitella Plasma Sources Sci. Technol. **26** (2017) 115008

[4] M A Damen, L M Martini and R Engeln Plasma Sources Sci. Technol **29** (2020) 065016

[5] Silva T, Grofulović M, Terraz L, Pintassilgo C D and Guerra V Plasma Chem. Plasma Process. 2020 **40** 713–25

[6] M Grofulović, T Silva, B L M Klarenaar, A S Morillo-Candas, O Guaitella, R Engeln, C D Pintassilgo and V Guerra Plasma Sources Sci. Technol. **27** 2018 115009

[7] C Fromentin, T Silva, T C Dias, E Baratte , O Guaitella and V Guerra Plasma Sources Sci. Technol. **32** (2023) 054004

[8] O Biondo, C Fromentin, T Silva, V Guerra, G van Rooij and A Bogaerts Plasma Sources Sci. Technol. 2022 **31** 074003.

[9] K Smith, R.M. Thomson, (1978). Stability Analysis of Laser Plasmas. In: Computer Modeling of Gas Lasers. Springer, Boston, MA.

[10] E.V. Kustova, E.A. Nagnibeda, Chemical Physics **398** (2012) 111-117

[11] E. Kustova, M. Mekhonoshina, Chemical Physics Letters (2021) 138288

Simulation of Space Platform Charging in Very Low Earth Orbit with Particle Methods

Jan Skácel[(*)1,2], Pietro Parodi[1], Giuseppe Gangemi[1], Federico Bariselli[1], Thierry Magin[1], Zdeněk Bonaventura[2]

[1] *Aeronautics and Aerospace Department, von Karman Institute for Fluid Dynamics, Sint-Genesius-Rode, Belgium*
[2] *Department of Plasma Physics and Technology, Masaryk University, Brno, Czech Republic*
[(*)] jan.skacel@vki.ac.be

This contribution aims to explore the physics of the interaction between spacecraft and charged particles in the ionosphere, specifically within Very Low Earth Orbit (VLEO). Employing particle methods, the primary objective is to simulate and comprehend the charging processes on spacecraft surfaces, concurrently revealing the resulting electric potential structure around the spacecraft. In addressing the VLEO conditions, particle methods are prominent for their accuracy, but also computationally most demanding.

VLEOs are essentially placed within the ionosphere, a region comprised of charged particles from atmospheric species such as oxygen ions O^+ and nitric oxide ions NO^+ [1]. The presence of these particles is a result of atmosphere gas ionization from solar radiation, with charge particle density distribution dependent on current solar activity [2, 3, 4]. It is essential to note that in VLEO and LEO conditions, drag caused by neutral particles becomes also highly significant.

To simulate spacecraft-plasma interaction physics, we employ PANTERA [5], a specialized numerical software developed in-house at the von Karman Institute. PANTERA utilizes Particle-In-Cell (PIC) plasma modeling [6] coupled with Monte Carlo collisions [7]. Spacecraft geometry, whether in 2D or 3D, is reconstructed on finite grids, particularly unstructured grids, representing the physical domain for numerical simulation. GMSH [8], a powerful open-source mesh generator, is instrumental in generating such geometries. This software allows for the creation of high-quality unstructured meshes, offering flexibility and accuracy in representing complex geometrical structures.

A common numerical simulation consists of a sphere interacting with plasma in the ionosphere at given altitude. An example result of such simulation is shown in Figure 1. The physical domain is represented in 2D axisymmetry to simulate a flow of oxygen ions O^+ and electrons e^- being injected from left boundary with velocity given by the orbit speed of the sphere. The important distributions are found, such as the electric potential shown in a) which shows the resulting floating potential on the sphere orignating from the plasma-spacecraft interaction.

Despite the establishment of theoretical backgrounds and experiments, the interaction between the charged particles and the spacecraft remains not completely understood. Numerical simulations utilizing particle methods, where individual charged particles of the ionosphere are simulated independently, are crucial for understanding the fundamental process of space platform charging [9]. However, in current scientific simulations, electrons in the ionosphere are often treated as a fluid using *the Boltzmann electron fluid model* for the sake of the improvement of computational efficiency.

This contribution aims to investigate accuracy and limitations of the Boltzmann electron fluid model through a direct comparison between full particle and particle (ions)-fluid (electrons) representations. Particular focus will be aimed on simulations of a specific phenomenon known as ionospheric drag: enhanced drag on the charged spacecraft caused by the direct interaction with ionospheric plasma.

[1] J. A. Bittencourt, *Fundamentals of Plasma Physics*, (2004), DOI: 10.1007/978-1-4757-4030-1
[2] C. T. Russell, J. G. Luhmann, and R. J. Strangeway, *Space Physics: An introduction*, (2016), University of California, ISBN: 9781107098824
[3] D. Bilitza, M. Pezzopane, V. Truhlik, D. Altadill, B. W. Reinisch, and A. Pignalberi, *The International Reference Ionosphere Model: A Review and Description of an Ionospheric Benchmark*, Reviews of Geophysics **60 4**, (2022), DOI: 10.1029/2022RG000792

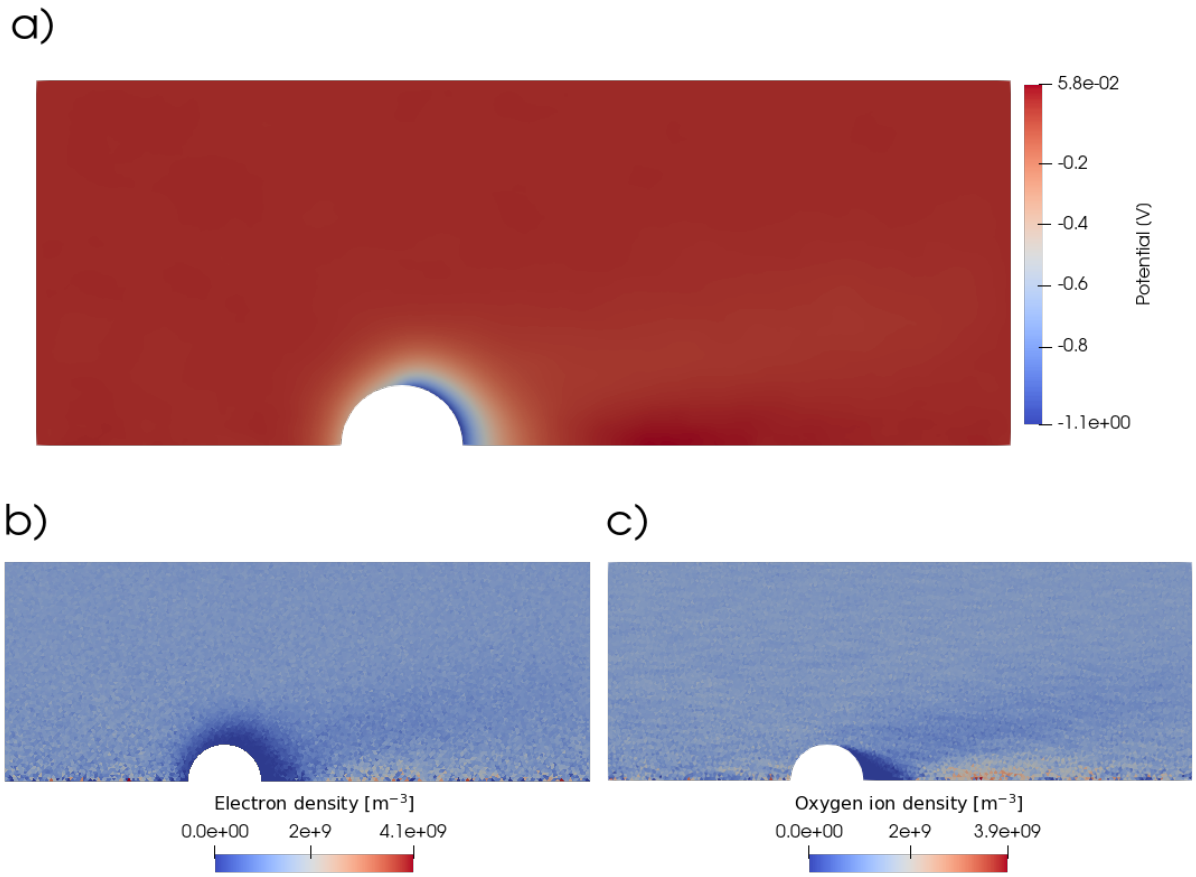

Fig. 1: Simulation of a sphere in 2D axisymmetry in orbit at altitude $h = 200$ km (flight direction is to the left). Here a) is the electric potential, b) is the electron density and c) the oxygen ion density.

[4] J. M. Picone, A. E. Hedin, D. P. Drob, and A. C. Aikin, *NRLMSISE-00 empirical model of the atmosphere: Statistical comparisons and scientific issues*, Journal of Geophysical Research: Space Physics **107 A12**, (2002), DOI: 10.1029/2002JA009430

[5] P. Parodi, D. Le Quang, G. Lapenta and T. Magin, *Particle-in-Cell simulation of the VKI DRAG-ON facility*, AIAA 2024-2710, (2024), DOI: 10.2514/6.2024-2710

[6] G. Lapenta, *Particle In Cell Method: A brief description of the PIC method*, Katholieke Universiteit Leuven

[7] C. K. Birdsall and A. B. Langdon, *Plasma physics via computer simulation*, (1991)

[8] C. Geuzaine and J.-F. Remacle, *Gmsh: a three-dimensional finite element mesh generator with built-in pre- and post-processing facilities*, International Journal for Numerical Methods in Engineering **79(11)**, (2009)

[9] R. Marchand and P. A. Resendiz Lira, *Kinetic Simulation of Spacecraft–Environment Interaction*, IEEE Transactions on Plasma Science **45 4**, (2017), DOI: 10.1109/TPS.2017.2682229

Plasma-surface coupled modelling of ammonia production in DC discharges

D. Simões[1], J. Martins[1], S. Baghel[1], J.P. Booth[1,2], D.R. Ferreira[1], O. Guaitella[1,2], L. Marques[3], N. Pinhão[1], C.D. Pintassilgo[1,4], L.L. Alves[(*)1]

[1] *Instituto de Plasmas e Fusão Nuclear, Instituto Superior Técnico, Universidade de Lisboa, Portugal*

[2] *LPP, Ecole Polytechnique, Sorbonne Université, Institut Polytechnique de Paris, CNRS, France*

[3] *Centro de Física das Universidades do Minho e do Porto, Universidade do Minho, Braga, Portugal*

[4] *Departamento de Engenharia Física, Faculdade de Engenharia, Universidade do Porto, Portugal*

[(*)] *llalves@tecnico.ulisboa.pt*

The search for a cleaner and more energy-efficient process for the synthesis of ammonia (NH_3) is a global concern, to which low-temperature plasma technology has emerged as a potential solution [1]. In this context, understanding the main kinetic paths leading to the plasma-assisted synthesis of NH_3 has topical interest, not only for the large-scale production of fertilizers at low cost, but also for the mitigation of ammonia generation in fusion machines. It is currently believed that plasma-surface interactions could be the dominant mechanisms for this process [2]. In this work we will propose, improve and validate kinetic models for N_2-H_2 plasmas, including the interplay between the volume and surface reactions.

We present the first steps of our research program on nitrogen-hydrogen plasmas under different surface conditions, leveraging complementary modelling and diagnostics analyses. We model cylindrical DC glow discharges (23 cm long and 2 cm inner diameter) with borosilicate glass walls [3], produced in N_2-H_2 gas mixtures with low H_2 concentrations (< 5%), at 5 sccm continuous flow, p = 50-500 Pa pressures and I_{dc} = 10-40 mA discharge currents.

The experimental measurements include: the reduced electric field E/N (where E is the electric field and N is the gas density), using the potential difference between two tungsten Langmuir probes immersed in the plasma; the electron density n_e, using microwave reflectometry with a hairpin resonator; the partial pressure of ammonia (FTIR absorption) and the relative concentrations of the main ion species, using mass spectrometry.

Simulations use the coupled solution of the electron Boltzmann equation (written under the two-term approximation [4]), and the chemical rate-balance equations of a kinetic scheme for nitrogen-hydrogen plasmas [5], which considers the main heavy species N_2(X, v=0-44), H_2(X, v=0-14), NH_3, N(^{4}S), H(^{1}S), in addition to: 13 electronic excited states (6 for N_2, 2 for N and 5 for H); positive ions N^+, N_2^+, N_3^+, N_4^+, H^+, H_2^+, H_3^+, N_2H^+, NH^+, NH_2^+, NH_3^+ and NH_4^+; negative ions H^- and NH_2^-; surface species H(S,F), N(S,F), NH(S), NH_2(S), (physically (F) or chemically (S) adsorbed on the wall); and other molecules and radicals. The surface kinetics is inspired by the mesoscopic model of Gordiets *et al.* [6], considering physical adsorption/desorption, chemical adsorption, surface transport, and Eley-Rideal and Langmuir–Hinshelwood recombination processes.

The model is solved numerically using the LisbOn KInetics (LoKI) simulation tool [4], comprising an electron Boltzmann equation solver (LoKI-B) and a Chemical solver (LoKI-C), which are coupled via a series of convergence cycles, ensuring a self-consistent solution for the electron energy distribution function, the species densities, and the reduced electric field, for given pressure, mixture composition and discharge current.

Figure 1 shows initial results for E/N vs I_{dc}, at p = 100 Pa and 5% H_2, and for the NH_3 partial pressure as a function of the H_2 concentration, at p = 130 Pa and I_{dc} = 20 mA. When comparing simulations with

measurements, one observes a fair agreement for the reduced electric field and a good qualitative agreement for the evolution of the NH_3 pressure with the $\%H_2$. However, the model still predicts absolute NH_3 densities that are 1 order of magnitude below the experimental measurements.

The model results confirm that the main production mechanisms of NH_3 occur at the surfaces (Langmuir-Hinshelwood, Eley-Rideal and NH_4^+ recombination), while the main destruction mechanisms are due to collisions with the atomic metastable $N(^2D)$ and with N_2H^+, the most abundant ion.

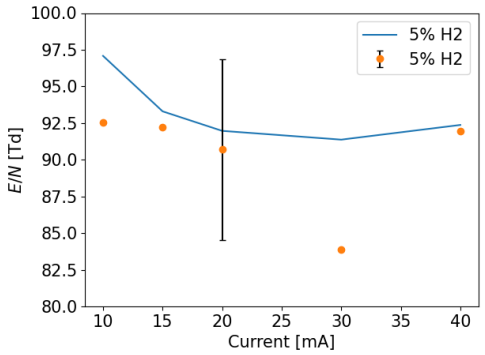

Fig. 1(a): Reduced electric field as a function of the discharge current, from numerical simulations (line) and experimental measurements (points) for 130 Pa pressure and 5% hydrogen concentration.

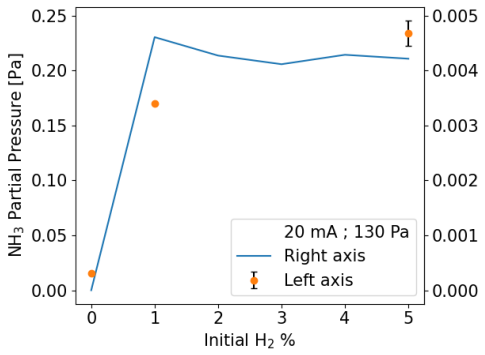

Fig. 1(b): Partial pressure of NH_3 as a function of hydrogen concentration, numerical simulations (line, right scale) and experimental measurements (points, left scale) for 130 Pa pressure and 20 mA discharge current.

We will also show simulations and measurements of the ammonia concentration and the relative densities of the most important ions, as a function of pressure and discharge current. In the future we aim to improve the model predictions of the NH_3 density, and to clarify the mechanisms of its creation and destruction. This will involve a critical review of the rate coefficients adopted in the kinetic scheme, with a special focus on the wall reactions, the reactions leading to the production/destruction of mixed H/N species, and the electron-impact reactions that will mostly affect the trends as a function of current.

Finally, the coupling of the volume and surface models has proved challenging. The evolution of the two kinetic schemes is mostly independent, with only a small number of species (such as $H(^1S)$ and $N(^4S)$) bridging the gap. In this regard, the convergence of simulations has proven to be highly dependent on the initial conditions adopted, and further work must be done to clarify this and optimize the calculation workflow.

Acknowledgements

This work was funded by FCT - Fundação para a Ciência e a Tecnologia under projects UIDB/50010/2020 (https://doi.org/10.54499/UIDB/50010/2020), UIDP/50010/2020 (https://doi.org/10.54499/UIDP/50010/2020), LA/P/0061/202 (https://doi.org/10.54499/LA/P/0061/2020) and 2022.04128.PTDC (https://doi.org/10.54499/2022.04128.PTDC).

References

[1] M. L. Carreon, *J. Phys. D: Appl. Phys.* **52** 0483001, 2019.
[2] A. Bogaerts *et al.*, *J. Phys. D: Appl. Phys.* **53** 443001, 2020.
[3] A. Chatain *et al.*, *Plasma Sources Sci. Technol.* **32** 035002, 2023.
[4] A. Tejero-del-Caz *et al.*, *Plasma Sources Sci. Technol.* **28** 043001, 2019.
[5] M. Jiménez-Redondo *et al.*, *Plasma Sources Sci. Technol.* **29** 085023, 2020.
[6] B. Gordiets *et al.*, *Plasma Sources Sci. Technol.* **7** 379–88, 1998.

Towards efficient data-driven numerical models for streamer discharges

A. Malagón-Romero(*)[1], J. Teunissen[1]
(Times 12, normal, centered)

[1] *Centrum Wiskunde & Informatica, Amsterdam, The Netherlands*

(*) malagon@cwi.nl

Streamer discharges are multiscale and strongly non-linear phenomena. While a typical streamer in air at atmospheric pressure spans several centimeters in length, the strong electric field driving its propagation is due to a steep density gradient in thin layers of a few micrometers. On the other hand, the non-linearity comes from the coupling between the electric field, transport terms, and source terms. Hence, the challenges for computer streamer simulations reside in the need of very high-resolution space meshes and small time steps to properly account for the various space and time scales. For that reason, most of the simulations are performed in 2D cylindrically symmetric domains as 3D simulations turn out to be extremely computationally demanding and out of reach for many research groups.

The recent advances in the field of machine learning are propelling its use in a wide range of applications. Some of this advances leverage the power of neural networks able to learn from data without explicit mathematical models when data is abundant. Nevertheless, Physics can be embedded in data-driven models through various techniques such as minimization of physics-informed cost functions, easing the lack of data due to costly numerical simulations.

In this work we report on our efforts to develop and incorporate machine learning methods that improve the efficiency of numerical simulations of streamer discharges.

Dynamics of Breakdown along a Dielectric Surface in Air at 1 atm

Rui Almeida[1,2], Nuno Ferreira[1,2], Pedro Almeida[1,2], George Naidis[3], Mikhail Benilov[(*)1,2]

[1] *Departamento de Física, FCEE, Universidade da Madeira, Largo do Município, 9000 Funchal, Portugal*

[2] *Instituto de Plasmas e Fusão Nuclear, Instituto Superior Técnico, Univ. de Lisboa, 1041 Lisboa, Portugal*

[3] *Joint Institute for High Temperatures, Russian Academy of Sciences, Moscow 125412, Russia*

[(*)] benilov@staff.uma.pt

1 Introduction

The dynamics of streamers over dielectric surfaces has been studied numerically by many authors, e.g. in [1] with a rectangular geometry using DC voltages, and in [2] with an axi-symmetric geometry using pulsed voltages. Various influencing factors on streamer dynamics are studied, like the applied voltage, the dielectric permittivity, secondary electron emission, the mobility of positive ions, distance of seeded streamer from dielectric surface, space charge on dielectric. Although their geometries are similar with qualitatively similar conclusions regarding the attraction of streamers to the dielectric surface, some conclusions differ regarding the role of secondary electron emission in increasing the surface streamer velocity, also the presented streamer dynamics show striking differences.

In this work streamers are generated in a weakly non-uniform electric field configuration in conditions of ~1% and more than 30% overvoltages as compared to the minimum breakdown voltage. The calculation of this minimum breakdown voltage is the topic of another contribution to this conference entitled 'Fast Calculation Tool for Breakdown Voltage in a setup with a Dielectric Surface'. The dynamics of streamer breakdown is studied under these conditions.

2 The Model

The studied setup has a 2D axi-symmetric geometry, in dry air at 1 atm, as shown in the figure. Numerical modeling was performed by solving transport equations for charged species, the Poisson equation and equations for photoionization source terms. The model is described in detail in previous work [3] and is, for these non-stationary calculations, supplemented on the dielectric surface by the boundary condition for charge accumulation,

$$\frac{\partial}{\partial t}(\varepsilon_D \boldsymbol{E}_D - \varepsilon_G \boldsymbol{E}_G)\cdot \boldsymbol{n} = \frac{\partial \sigma_s}{\partial t}$$

where subscripts *D/G* refer to Dielectric/Gas, ε is the dielectric permittivity, $\boldsymbol{E}$ the electric field, $\boldsymbol{n}$ the normal vector into the dielectric and $\sigma_s = \boldsymbol{j}_G \cdot \boldsymbol{n}$ is the normal current density. Initial conditions for the simulations at a certain DC voltage U were the 'no discharge' conditions, i.e. Laplace solution for the electric potential, homogeneous densities $n_{A^+} = 10^{10}\text{m}^{-3}$ for positive ions and $n_\alpha = \frac{1}{4}n_{A^+}$ for electrons and three sorts of negative ions. For the initial surface charge over the dielectric, two initial distributions were studied, namely either zero surface charge (un-stressed setup), or the initial surface charge was that of the self-sustained

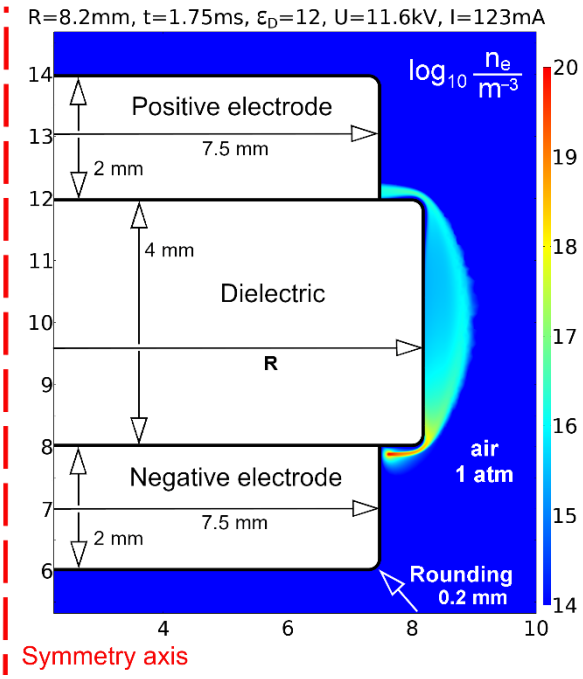

Figure 1: Schematic of setup. Logarithm of electron density just prior to breakdown for an overvoltage of 1%. Initial condition for surface charge was its distribution taken from the self-sustained discharge. Details in header of figure.

discharge, as calculated by the resonance method [3] with the boundary condition of zero current density across the dielectric surface (pre-stressed setup).

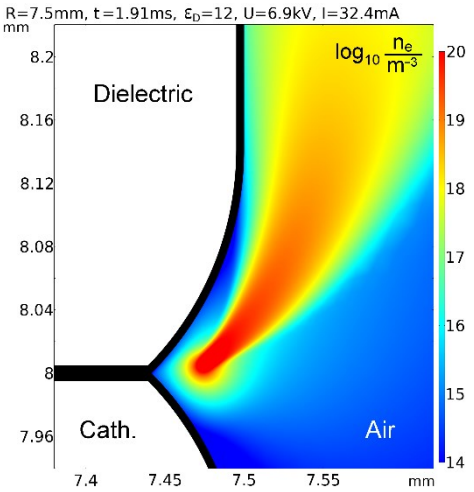

Figure 2: Logarithm of electron density just prior to breakdown for an overvoltage of 1%. Zoom of the cathode triple junction region. Details in header of figure.

3 Results and Discussion

Three positions of the dielectric surface relative to the electrodes are studied: retracted (R=3mm); aligned (R=7.5mm) and protruding (R=8.2mm). The case of an 1% overvoltage, starting from a 'fresh' un-stressed setup, or from a pre-stressed setup (Figs. 1&2), resulted in a qualitatively similar breakdown dynamics. A streamer developed in the volume at a certain distance from the cathode as a result of a gradual space-charge increase. Breakdown would ensue in a few miliseconds. A noticeable exception was the un-stressed higher permittivity protruding dielectric, where breakdown through the streamer mechanism developed along fieldlines connecting cathode to dielectric in the very close vicinity of the cathode triple junction. For the initial condition of an un-stressed setup with a 1% overvoltage, only minor qualitative differences were observed in comparison with the pre-stressed case. For pre-stressed setups subject to higher overvoltages, Figs. 3&4 show an instant just before a streamer bridges the gap. In these cases positive streamers develop much faster, i.e. of the order of microseconds, and originate at the anode surface. As can be seen in Fig. 3 for the R=3mm case with a 30% overvoltage, after a positive streamer having traversed about half of the gap, another positive streamer originates in the volume in front of the cathode and closes the gap. In Fig. 4, for the case R=8.2mm, a positive streamer originated at the anode is seen 'hugging' the dielectric surface. This dynamics is more in accordance with the results reported in [1].

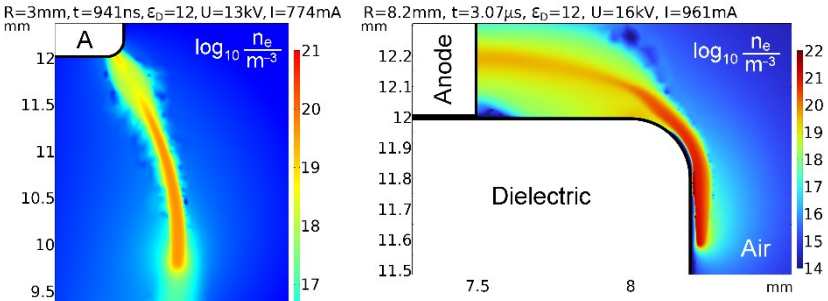

Figure 3&4: Logarithm of electron density just prior to breakdown for higher over-voltages. The case for R=3mm shows two streamers, one has developed in the volume close to the cathode. Above the case of R=8.2mm for an overvoltage of 38%. Details in headers of the figures.

This is an ongoing research, further simulations are planned for the higher overvoltages starting from an un-stressed setup. Future research will also clarify the effect, if any, of the effective secondary electron emission coefficient on streamer dynamics which in the present calculations was taken to be 3%.

IPFN activities were supported by FCT - Fundação para a Ciência e Tecnologia, I.P. by project references UIDB/50010/2020, UIDP/50010/2020 and LA/P/0061/2020 and by European Regional Development Fund through the Operational Program of the Autonomous Region of Madeira 2014-2020 under project PlasMaM1420-01-0145-FEDER-000016.

[1] Li, X. et al., *Plasma Sources Sci. Technol.* **29**, (2020) 065004– 065016.
[2] Meng, Y. et al., *J. Appl. Phys. D* **55**, (2022) 385203–385217.
[3] Benilov, M. S. et al., *J. Appl. Phys.* **130**, (2021) 121101–121123.

Oxygen atom kinetics in pulsed Radiofrequency Capacitively-coupled plasmas at intermediate pressures

JP. Booth[1], S. Zhang[1], and G. A. Curley[1]

[1]*Laboratoire de Physique des Plasmas (LPP), CNRS, Sorbonne Université, Ecole Polytechnique, Institut Polytechnique de Paris, Palaiseau, 91120, France*

(*) *jean-paul.booth@lpp.polytechnique.fr*

Radiofrequency capacitively-coupled plasmas (RF-CCP) operating at intermediate gas pressures (1-10 Torr) are significant for many applications, notably thin film deposition (PECVD), but have been much less studied than lower pressure RF-CCPs because common diagnostic techniques (such as Langmuir probes) cannot be used. Modelling of RF plasmas in this pressure range is also difficult, because Particle-in-cell simulations become prohibitively slow, whereas fluid models are unable to correctly describe the electron kinetics due to non-local and time dependent effects. We are studying a highly-symmetric CCP reactor (aluminium, 50 cm diameter with a 2.5 cm gap), excited at 13.56 MHz in pure O_2 at pressures from 1 to 8 Torr. The oxygen atom density and gas temperature are determined by mono-mode laser cavity ringdown spectroscopy (CRDS) at 630nm [1]. These results are complimented with measurements of the plasma impedance (giving the true voltage, current and power absorbed by the plasma) and the ion flux to the grounded electrode.

Figure 1 shows the steady-state oxygen atom density as a function of the gas pressure and the absorbed RF power. At gas pressures above 2 Torr the oxygen atom density increases with pressure and with injected RF power, as expected. However, the dissociation fraction decreases with pressure, reaching a maximum of about 14% at 2 Torr 200W. However, at 2 Torr the oxygen atom density passes through a maximum with power, and at 1 Torr the oxygen atom density decreases with RF power. Since the electron density (and therefore O_2 dissociation rate) increases monotonically with power at all pressures, this is a rather surprising result, indicating that the oxygen atom loss rate (principally due to recombination at the electrode surfaces) increases with power at these lower pressures. This corresponds to conditions where the energy and flux of ion bombardment of the surfaces is increasing, suggesting that this surface recombination is activated by the ion bombardment.

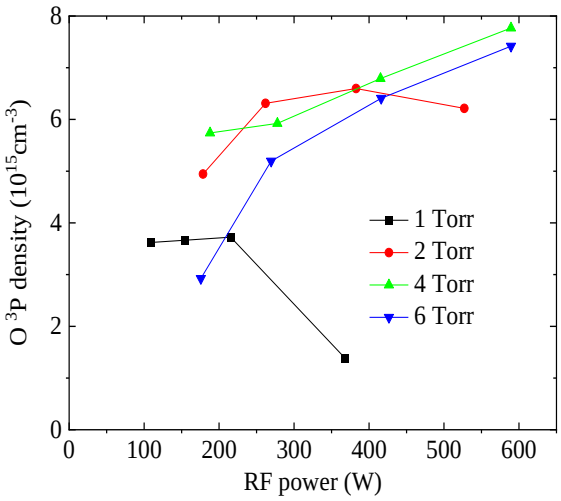

Figure 1. Oxygen atom density as a fuciton of O_2 pressure and injected RF power

In order to investigate this further, we performed time-resolved measurements of the oxygen atom density in pulse-modulated plasmas. Figure 2 shows the results at 2 Torr, clearly showing that the O atom density decay becomes faster as the RF power is increased. Nevertheless, the decays are

surprisingly slow - with decay time constants varying from 207 to 149 ms, corresponding to surface reaction coefficients of the order $3x10^{-4}$. These small values are rather surprising on bare metallic (aluminium) surfaces, and very comparable to the values observed on borosilicate glass[2], showing the importance of surface oxidation. This increase of surface reactivity with ion bombardment energy is also very similar to what is observed in a DC discharge in a borosilicate glass tube at pressures below 1 Torr[2]. The ion energies under these conditions are not sufficient to remove native oxide from an aluminium metal surface. Rather, the ions appear to activate surface reactions. At higher O_2 pressures the oxygen atom decays become faster, suggestion the onset of gas-phase reactions, and with a rate that becomes insensitive to the RF power.

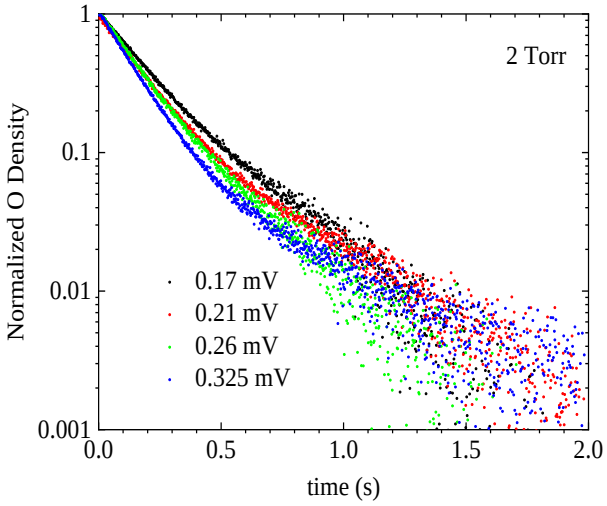

Figure 2. Decay of the oxygen atom density as a functon RF power at 2 Torr O_2 pressure

The time-resolved measurements also allow the O^- negative ion density to be measured, as well as indicating the creation of ozone in the afterglow, both in the gas phase and on the reactor surfaces, as previously observed in DC glow discharges[1]. Analysis and interpretation of this data is on-going.

These observations of oxygen surface recombination probabilities provide an intriguing bridge between surface recombination at higher pressures (where observed recombination coefficients are in the range 10^{-3}-10^{-4}) and lower-pressure plasma experiments where the coefficient can reach several 10s %.

Acknowledgements

SZ thanks China Scholarship Council for a PhD grant. We thank Applied Materials for financial support.

[1] Booth J P, Guaitella O, Zhang S, Lopaev D, Zyryanov S, Rakhimova T, Voloshin D, Chukalovsky A, Volynets A and Mankelevich Y *Plasma Sources Science and Technology* 2023 **32** 095016

[2] Booth J P, Guaitella O, Chatterjee A, Drag C, Guerra V, Lopaev D, Zyryanov S, Rakhimova T, Voloshin D and Mankelevich Y *Plasma Sources Science and Technology* 2019 **28** 055005

Modelling for RF-CCPs at Intermediate Pressure: Doubts on Drift-Diffusion Models

S. Zhang[1], A. Alvarez Laguna[1], N. Lequette, and J.P. Booth[1]

[1] *Laboratoire de Physique des Plasmas (LPP), CNRS, Sorbonne Université, École polytechnique, Institut Polytechnique de Paris, Palaiseau, 91120, France*

[(*)] *Jean-Paul.Booth@lpp.polytechnique.fr*

Radio-frequency capacitively coupled plasmas (RF-CCP) at gas pressures above ~1 Torr are often simulated by fluid models since Particle-in-Cell (PIC) models are too computationally intensive. The drift-diffusion approximation, is widely employed in fluid models [1]. Drift-Diffusion models require the electron transport coefficients (mobility, μ, diffusion, D, energy mobility μ_ε and energy diffusion D_ε), as well as the rate constants (for ionisation, energy loss, etc.), which are calculated from the electron energy distribution function (EEDF). Fluid models do not copntains information on the EEDF, which must be estimated in other ways. In this pressure range, the local energy approximation is commonly used (with an approximation on the energy transport coefficients and using the Einstein relation) [1], but a detailed comparison to PIC results is needed in order to quantify the impact of the abovementioned approximations. In this study we compare simulations of Argon plasmas using three different approches for the EEDF: the local energy assumption, Maxwellian assuming constant collision frequency, and Maxwellian with full calculation of the transport parameters. The fluid model results using these theree assupmtions are then compared to a benchmark PIC simulation.

In the local mean energy model, the EEDF is calculated, as a function of the electron mean energy <E>, using the Loki Boltzmann solver [2]. This assumption is well justified for homogeneous DC glow discharges, but its applicability to time-varying fields (e.g. RF-CCP) with strong spatial gradients is more debatable. When all four coefficients (μ, D, μ_ε and D_ε) are directly calculated from the local-field EEDF, the RF-CCP simulation gave unphysical negative values in the sheath for the electron density and energy, causing failure of the simulation. A widely-used solution for RF-CCP simulation [1] is to use the local energy mobility, and calculate the other coefficients from the mean electron energy using the Einstein relations (which are only strictly valid for a Maxwellian distribution) assuming a constant momentum-transfer collision frequency. This solution gives improved numerical stability and convergence speed.

For the Maxwellian assumption, the transport coefficients and rates can be calculated from the EEDF, most simply by assuming constant collision frequency assumption, or by a full calculation using the energy-dependent cross-section. The electron temperature is determined by the power balance in the simulation. However, at intermediate pressures (1-10 Torr) the EEDF is expected to deviate significantly from Maxwellian due to inelastic collisions.

The results of the different models (fluid and PIC) are compared in Fig. 1. Compaed to the PIC model, the local energy assumption overestimates the mean electron energy, (Fig. 1 (a)), while both Maxwellian assumptions (with and without a constant collision frequency assumption) underestimate

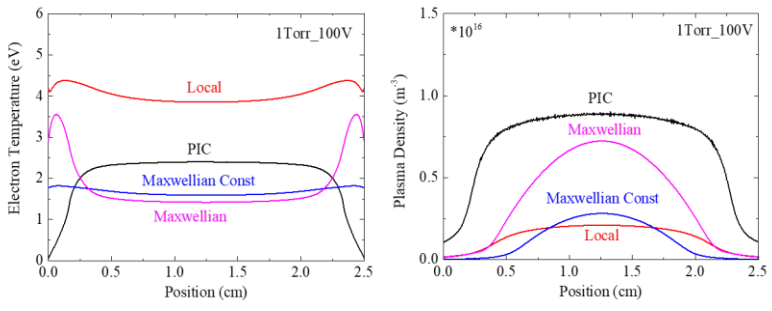

Fig. 1: (a) Mean electron energy, (b) Ion density profile at 1 Torr 100 V, with different models

it. This can be attributed to differences in the density of high-energy electrons: the EEDFs provided by the local energy assumption contain few high energy electrons, so that a high mean electron energy is necessary to provide enough ionization. Considering the central plasma density (Fig. 1 (b)), the full Maxwellian model is closest to the PIC, although there is poor agreement in the profile. While the density is very underestimated as compare to PIC.

The PIC model provides the true EEDF at different pressures and positions, shown in Fig. 2 (b). The problems in the fluid models can be explained by the spatial variation of EEDF. At low pressure (0.1 Torr), the EEDF at both the center and the ionization peak region is quite Maxwellian. At higher pressure, the high energy tail is depleted compared to a Maxwellian distribution due to the inelastic collisions, but this effect is more marked at the center compared to the regions of peak ionization (at the sheath edges).

At 1 Torr, the center EEDF, (Fig. 2 (f)) is already close to that predicted by the local energy assumption. As a result, the density profile is quite well predicted by this model. However, in the peak ionization regions neaer the sheath, the EEDF is much more Maxwellian, explaining why this model is betyter at predicting the peak density. Most of the electron heating and ionization happens in the peak ionization region, so the EEDF in this region decides the density.

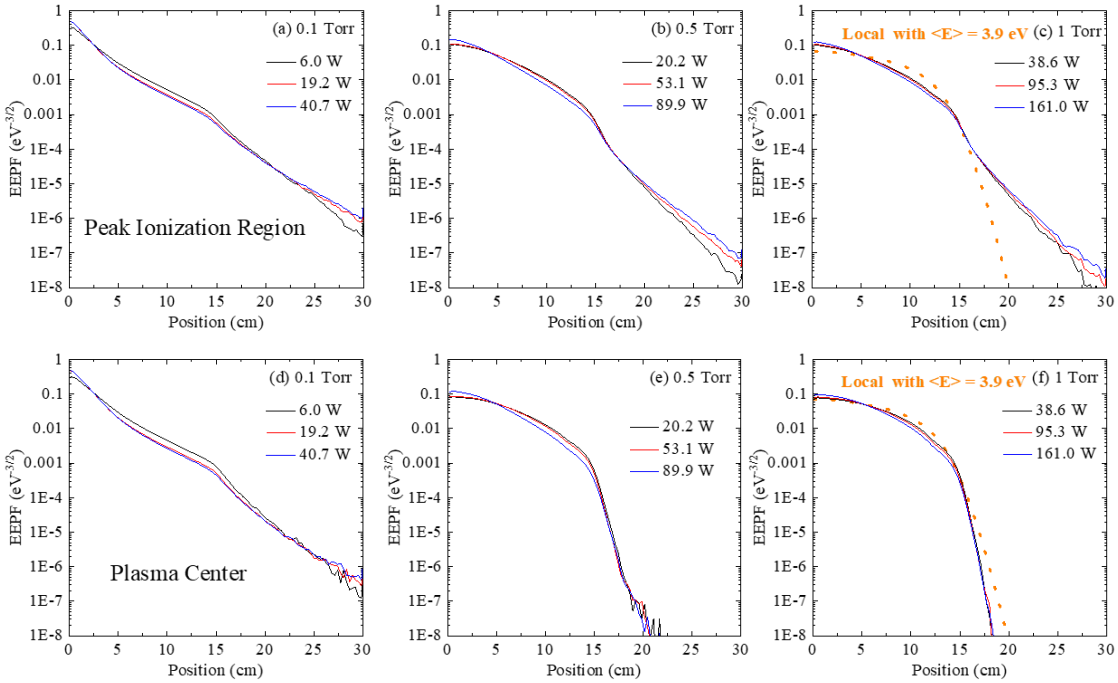

Fig. 2: (a) Ion density profile, (b) Mean electron energy at 1 Torr 100 V, with different models

In conclusion, we present a comparasion of Drift-Diffusion fluid simulations using different EEDF assumptions with a PIC benchmark. The source of the errors inthe Drift-Diffusion models are discussed. Drift-Diffusion fluid models should be used with caution in this pressure range due poor estimation of the EEDF.

Acknowledgements
SZ thanks China Scholarship Council for a PhD grant. We thank Applied Materials for financial support.

Reference

[1] Boeuf J P and Pitchford L C 1995 Two-dimensional model of a capacitively coupled rf discharge and comparisons with experiments in the Gaseous Electronics Conference reference reactor *Phys. Rev. E* **51** 1376–90

[2] Tejero-del-Caz A, Guerra V, Gonçalves D, Da Silva M L, Marques L, Pinhão N, Pintassilgo C D and Alves L L 2019 The LisbOn KInetics Boltzmann solver *Plasma Sources Sci. Technol.* **28** 043001

Characterization of nanomaterials obtained in DC glow discharge plasma of Ar/C_2H_2

A.U. Utegenov[1,2*], Ye. Yerlanuly[1], Zh. Onaybergenov[1,2], A. Abdrakhmanov[2], S.A. Orazbayev[2], T.S. Ramazanov[2]

[1] *Institute of Applied Physics and Information Technology, Almaty, Kazakhstan*

[2] *Al-Farabi Kazakh National University, NNLOT, Almaty, Kazakhstan*

[3] *Kazakh Physical Society, Almaty, Kazakhstan*

(*) almasbek@physics.kz

This paper presents experimental results on the characterisation of carbon nanomaterials synthesised in the plasma environment of Ar/C_2H_2 gas mixture of a DC glow discharge. An experimental setup consisting of a П-type glass tube with a vacuum system from a forevacuum and turbomolecular pump, and a gas inlet system from mass-flow controllers of 100 sccm and 1 sccm for Ar and C_2H_2, respectively, was used to obtain of plasma medium. The synthesis product materials were collected in the near-electrode areas, i.e. silicon wafers were located in the anode and cathode region. The main parameters of the DC glow gas discharge including voltage, current and chamber pressure were 1.5 kV, 1.45 mA and 1 torr, respectively. In order to obtain a large quantity of nanomaterials cyclic synthesis was performed, i.e. the plasma of inert and carbon containing gas mixture was switched on for 30 seconds and switched off for 60 seconds with a total cycle of 25. Thus, due to the cyclic synthesis, a constant growth of nanoparticles in the plasma volume with the same size was ensured. A 532 nm wavelength laser and LSR-PS-II output power control system was used to observe the nanoparticles synthesised in the plasma environment. It should be noted that in order to ensure that the percentage of Ar/C_2H_2 mixture gases was 98/2%, a constant gas supply of 25 and 0.5 sccm was carried out.

Experimental results revealed that in addition to the cyclic control of the ignition of the plasma itself, the growth of nanoparticles occurs by generations. The phenomenon of cyclic nanoparticle growth occurring during intervals of plasma cessation was observed, consistent with the characteristic nanoparticle synthesis within plasma environments discernible by direct observation [1]. Furthermore, it was determined that the presence of nanoparticles within the positive column of the glow discharge exerts a significant influence on the luminescence intensity of the discharge plasma, as illustrated in Figure 1 [2]. Additionally, in the course of the experiments, a correlation of the time interval between nanoparticle generations and the discharge voltage was observed. It was found that as the discharge voltage rises, the time between nanoparticle generations decreases.

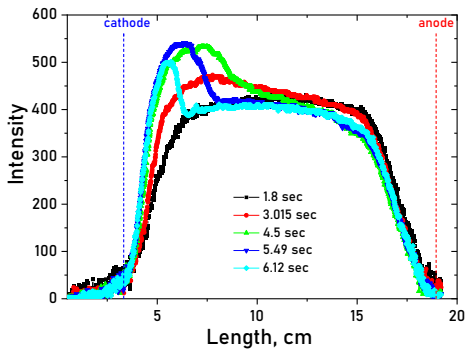

Fig. 1: Variation in plasma luminescence intensity due to the presence of nanoparticles.

The results of characterisation of nanomaterials synthesised in the plasma environment indicate a general trend wherein nanoparticle synthesis initiates predominantly in the anodic zone. This is supported by the observation of nanofilms with an approximate thickness of 66 nm. Conversely, within the cathodic zone, alongside nanofilms, nanoparticles with an average size of around 103 nm were also deposited, as depicted in Figure 2.

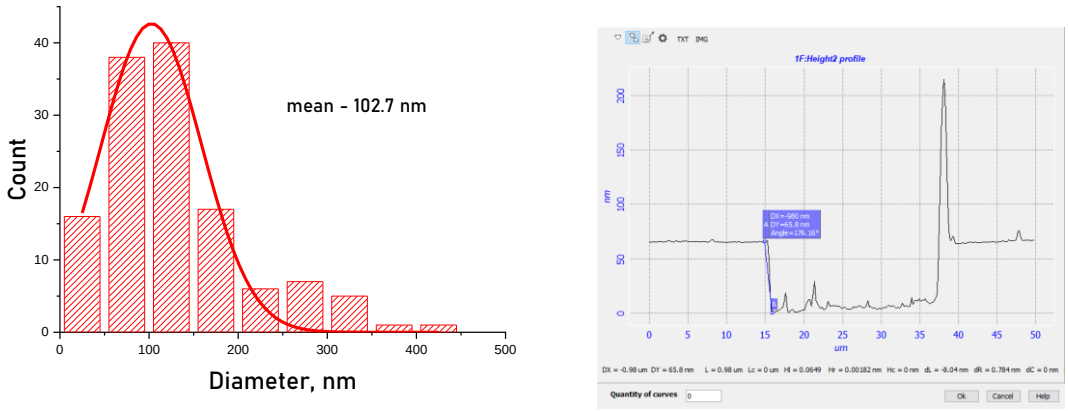

Fig. 2: Size distribution of synthesised nanoparticles and result of thickness analysis of nanofilms obtained in the anodic zone.

Additionally, EDAX microanalysis and X-Ray Photoelectron Spectroscopy (XPS) characterization were conducted to thoroughly understand and gather information about the resulting nanomaterials in the plasma environment.

[1] L. Worner et al. *New Journal of Physics* **14** (2012) 023024.
[2] S. Orazbayev et al. *Nanotechnology* **32** (2012) 455602.

Influence of gas temperature and neutral particle density on self-organized luminous patterns in atmospheric-pressure DC glow discharge

Toshiaki Miyazaki(*), Koichi Sasaki and Naoki Shirai

Division of Applied Quantum Science and Engineering, Hokkaido University, Sapporo 060-8628, Japan

(*) shun_me77@eis.hokudai.ac.jp

【Introduction】

When an atmospheric-pressure DC glow discharge is generated, self-organized luminous pattern formation is observed above anodes under some conditions [1]. In general, every self-organized pattern can be mathematically described by simultaneous partial differential equations with two variables, which is called "the reaction-diffusion system". It requires two formation factors whose densities increase or decrease as a result of the reaction and the diffusion [2]. The luminous patterns are observed both in the cases that metals and liquids work as the anode of the discharge. However, the pattern formation mechanism has not been understood yet in detail. To understand the mechanism, it is important to understand the plasma characteristics when the pattern is observed. We have considered that the presence of negative ions is a key in the pattern formation because the presence of oxygen gas is important for the pattern formation [1]. On the other hand, some papers, in which the authors carried out experiments and simulations of low-pressure discharges with lower densities of neutral species than those in atmospheric-pressure discharges, reported that self-organized luminous patterns were able to be observed even in noble gas discharges [3-6]. It is suggested by these papers that, when the patterns are formed in atmospheric-pressure plasmas, a decrease in the gas density may be caused by the temperature increase. In this study, the gas temperature in atmospheric-pressure DC glow discharge is estimated based on the rotational temperature of OH radicals, and influence of the gas density on the luminous pattern formation is discussed.

【Experimental method】

Figure 1 shows the experimental setup for generating the atmospheric-pressure DC glow discharge with a miniature helium flow. 1% NaCl aqueous solution was used for the liquid anode. The cathode was made of brass with a narrow hole of 500 μm diameter which was used for flowing helium toward the anode. A DC high voltage was applied between the liquid anode and the metal cathode to generate discharge plasma. The spatial distribution of the rotational temperature of OH radicals in the gas phase was measured by laser-induced fluorescence spectroscopy at various helium flow rates (200-300 sccm), the distances between the anode and the cathode (2-10 mm), and the discharge currents (20-80 mA). The laser beam was injected from the radial direction into the plasma, and the laser-induced fluorescence was detected using an ICCD camera from right angle to the incident laser beam. The rotational temperature of OH was deduced from the relative populations of three rotational states of OH at electronic and vibrational ground state. The luminous patterns above the liquid anode were observed at the same time.

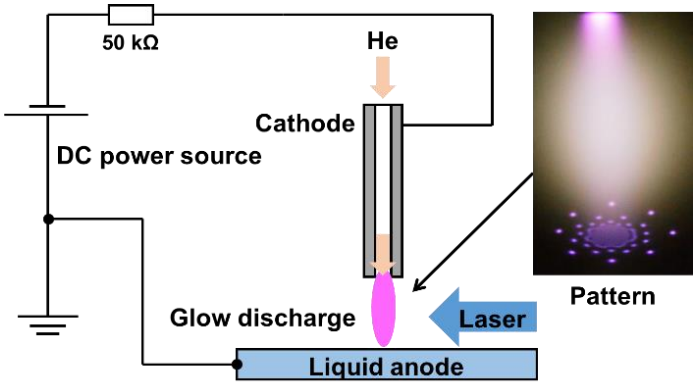

Fig.1 Experimental setup.

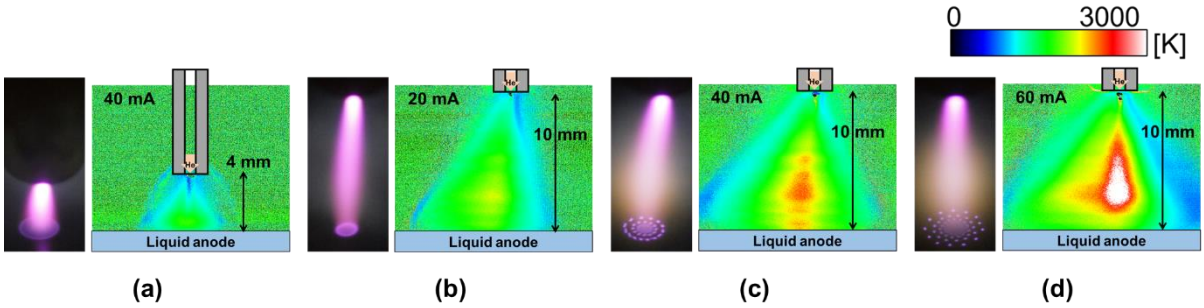

Fig.2 The rotational temperature distribution of OH radicals and the optical emission images of the discharge.

【Results and discussion】

Figure 2 shows the rotational temperature distribution of OH radicals and the optical emission image of the discharge. The helium flow rate was fixed at 300 sccm, and the discharge current and the electrode distance were varied. The luminous pattern on the anode did not form under the conditions of (a) 20 mA and 4 mm and (b) 40 mA and 10 mm, while the pattern formed under the conditions of (c) 40 mA and 10 mm and (d) 60 mA and 10 mm. Assuming that the rotational and translational temperatures are approximately equal under the atmospheric pressure, we may say that the luminous pattern is observed when the gas temperature is as high as 3000 K. In other words, the luminous pattern is formed when the gas density is as low as 10^4 Pa. References [3-6] report that the luminous patterns are observed at a certain range of the pressure. The experimental result shown in Fig. 2 also suggests that the gas density is an important parameter in the luminous pattern formation in the atmospheric-pressure DC glow discharge. As the gas density decreases, a reduced electric field (E/n) increases, which can change the mobility and diffusion coefficient of ions and electrons in the plasma. The changes in the mobilities and diffusion coefficients may alter the reaction and diffusion in the reaction-diffusion system, resulting in the pattern formation.

References

[1] N. Shirai, *et al.,* Plasma Sources Sci. Technol. 23, 054010 (2014).
[2] A. Turing, Phil. Trans. R. Soc. B237 37-72 (1952).
[3] K. Schoenbach, *et al.,* Plasma Sources Sci. Technol. 13, 177 (2004)
[4] S. Nasuno, Chaos 13, 1010-1013 (2003)
[5] W. Zho, *et al.,* Plasma Sources Sci. Technol. 23, 054012 (2014)
[6] S Stauss, *et al.,* Plasma Sources Sci. Technol. 22, 025021 (2013)

Lightning discharges in a Jovian atmosphere

A. Robledo-Martinez [(1)], L. A. Garcia-Villarreal, C. González-Armendáriz, J. M. Basurto

Departamento de Ciencias Básicas,Universidad Autónoma Metropolitana, Azcapotzalco, 02128 Mexico City, Mexico

[(1)] arm@azc.uam.mx

Since lightning in Jupiter's atmosphere was detected for the first time by a satellite in 1979 [1], numerous detections made afterward have produced a more detailed picture of the distribution and intensity of the strokes. Lightning was also detected by other probes such as Cassini [2], Galileo [3] and Juno [4]. Juno's team reported observations on shallow lightning flashes and identifies that out of six strokes, four of them were detected at altitudes corresponding to atmospheric pressures in the range 1.4-1.9 bar, which are within the scope of this work.

In the present work we set out to investigate some of the properties of lightning on a synthetic Jupiter atmosphere whose composition is: 90% hydrogen and 10% helium, both high-purity. For the experiments we used an encapsulated 300 kV Marx generator that has a rise-time of 0.7 μs and can deliver peak current of ~3 kA. A set of conical point-plane electrodes were set inside a large (6 m^3 capacity) vacuum chamber that contained the synthetic gas mix. The diagnostics used included: time-resolved spectroscopy, high-speed and conventional photography, as well as electric field and pulse current sensors.

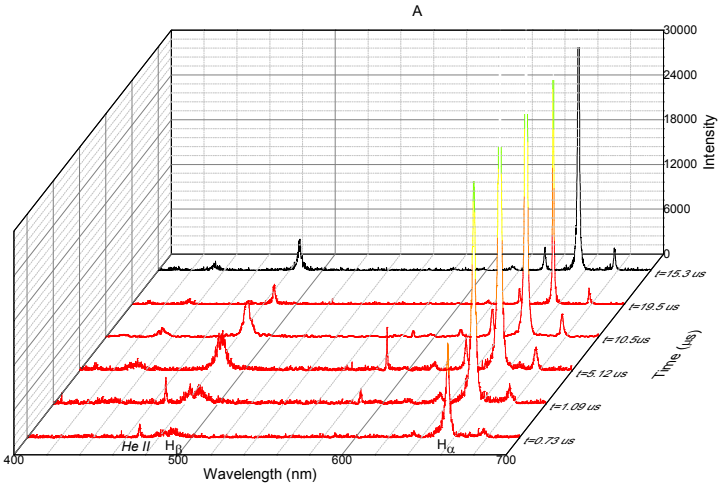

Fig. 1.Time resolved spectra. Pressure: 0.5 atmospheres. Peak current: 3.1 kA. Gap: 11.5 cm.

Figure 1 shows spectra of the discharge recorded with time resolution within the time interval 0.7-15 μs using an acquisition time that was roughly 10% of the delay time. The graphs shows that the spectrum has very little continuum, even at short times (t<1 μs) whereas this type of arc has strong continuum in other atmospheres. Similar experiments made in air showed strong continuum for delays up to 2 μs [5]. The H_α, H_β and the H_γ lines of the Balmer series are clearly visible in the spectra.

Figure 1 shows that most of the radiation emitted is contained in the H_α line. At short times (t<5 μs) the singly-ionized He II (468.5 nm) line is clearly visible but it disappears at later times.

The electronic excitation temperature was calculated using the line-to-continuum ratio method [6]. The H_β line was employed to obtain the temperatures shown in Fig. 2. The figure shows that the temperatures decrease sharply in the first 8 μs for the Jovian atmosphere. For the sake of comparison, this graph includes the results obtained in a discharge performed in an air atmosphere under identical circumstances [5].

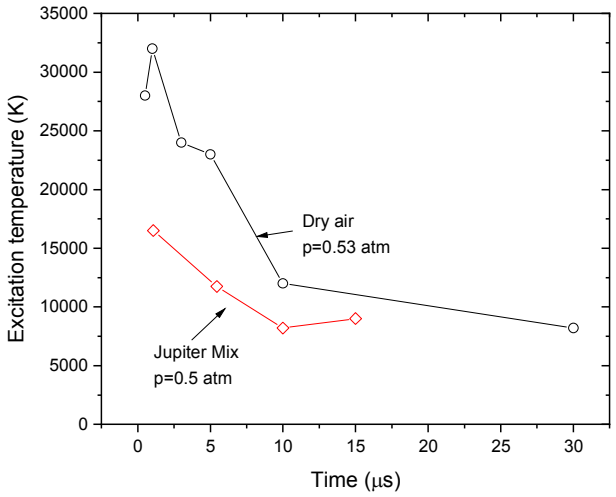

Fig. 2. Electronic excitation temperature. Comparison of the results obtained in the present work with discharges in dry air (see Ref. 5).

The experiments performed show that lightning in a jovian atmosphere emits surprisingly less continuum radiation than a similar discharge in atmospheric air. The fact that the He II line is clearly visible at short times is a clear indication that the plasma is quite hot initially and cools down at later times. This inkling is confirmed by the results of Fig. 2 that show that the temperature decreases rapidly from 17,000 K to 7,000 K in less than 8 μs. This figure also shows that an arc discharge performed under the same conditions in air (same gap separation, same peak current) results in electronic temperatures twice as large as those of the Jovian atmosphere.

[1] A. F. Cook II, T. C. Duxbury and G. E. Hunt, *Nature* **280** (1979) 794.

[2] D. A. Gurnett *et al.*, *Science* **253** (1991) 1522-1525.

[3] B. Little *et al.*, *Icarus* **142** (1999) 306.323.

[4] H. N. Becker *et al.*, Nature 584 (2020) 55-58.

[5] A. Robledo-Martinez, H. Sobral and A. Ruiz-Meza, *J. Phys. D: Appl. Phys.*, **41** (2008) 175207.

[6] H. R. Griem, *Principles of Plasma Spectroscopy*, Cambridge University Press, Cambridge, UK, 1997.

Determination of the effective secondary electron emission coefficient for low-pressure RF discharges based on pixel-based similarity of spatio-temporal excitation map images

A Derzsi[(*)1], R Masheyeva[1,2], F Beckfeld[3], J Schulze[3], Z Donkó[2]

[1] *HUN-REN Wigner Research Centre for Physics, Budapest, Hungary*

[2] *Department of General Physics, Satbayev University, 050013 Almaty, Kazakhstan*

[3] *Chair of Applied Electrodynamics and Plasma Technology, Faculty of Electrical Engineering and Information Sciences, Ruhr University Bochum, 44801 Bochum, Germany*

[(*)] derzsi.aranka@wigner.hun-ren.hu

The heavy-particle induced secondary electron emission coefficient (γ) is a crucial parameter in the modeling of low pressure RF plasmas. As shown by numerous Particle-in-Cell/Monte Carlo Collision (PIC/MCC) simulation studies for diverse discharge conditions, the value of γ can have very strong effects on the electron power absorption, excitation/ionization dynamics and the plasma parameters. Unfortunately, experimental data for γ under plasma exposure are very difficult to obtain.

To overcome the lack of data for γ, different approaches are used in the simulations, such as self-consistent determination of the effective γ (which is the ratio of the emitted secondary electron and the incident ion fluxes at the surface, implicitly including the contributions of the other species to the secondary electron emission) [1], theoretical models [2], or computationally assisted spectroscopic techniques [3]. This latter method (known as γ-CAST) is based on phase resolved optical emission spectroscopy (PROES) measurements of the electron impact excitation rate from the ground state into a specific level of neutral gas atoms. For electropositive gases at high pressures, these measurements typically exhibit two distinct maxima adjacent to each electrode at different times within the RF period, one caused by electrons accelerated by sheath expansion (α-peak) while the other is due to secondary electrons accelerated towards the bulk by the sheath electric field (γ-peak). Contrasting the intensity ratios of these two maxima with results of PIC/MCC simulations performed for a sequence of γ coefficients under conditions identical to the experiments, could yield an effective secondary electron emission coefficient, ensuring a reasonable agreement between the experimental and simulation results for several discharge characteristics [4].

Here, we introduce an alternative of the γ-CAST method that combines PROES measurements with PIC/MCC simulations for the determination of the γ coefficient. In contrast to γ-CAST, this approach does not necessitate the simultaneous presence of both the α-peak and γ-peak in the excitation rate, making it applicable across a wider range of discharge conditions. The method relies on the similarity of images, specifically the pixel-based similarity of the maps of the spatio-temporal distribution of the electron impact excitation rate from the ground state into a specific level, obtained from measurement and simulations. The method is illustrated below by using PROES data obtained from a geometrically symmetric capacitively coupled plasma reactor operated with Ar gas (with a 10% Ne admixture for the PROES) and Cu electrodes located at a distance of 4 cm, at 100 Pa pressure, 700 V peak-to-peak voltage and 13.56 MHz driving frequency. The simulations are performed using a 1d PIC/MCC code, with different γ coefficients set as input values.

For the comparison of the spatio-temporal maps of the electron impact excitation rate obtained from PROES and PIC/MCC simulations (see Fig. 1), the PROES data are initially processed to remove the background noise and the simulation data matrices are reshaped to match the size of the PROES data matrix. In the comparison, only the regions close to the powered electrode (highlighted by dashed rectangles in Fig. 1) are used. Within this specified region, a “scan area” is defined in the grayscale

PROES image (see Fig. 2), capturing the dominant excitation pattern at the powered electrode. This area (image) is then compared to rectangles (images) of the same size extracted from the simulation data for a given γ. The sum of squared differences (SSD), a measure of match based on pixel-by-pixel intensity differences, is calculated for all possible image pairs. This involves the summation of squares for the product of pixel subtraction between the two images. These steps are then performed iteratively for all simulations with different γ coefficients (see the minimum SSD values obtained for different γ in panels of Fig. 2). Overall, the best match between PROES and PIC/MCC results is indicated by the minimum of all SSD values. In order to eliminate slight shifts in time and space between the experimental and computed images a shift is allowed along both x and t during the fitting process.

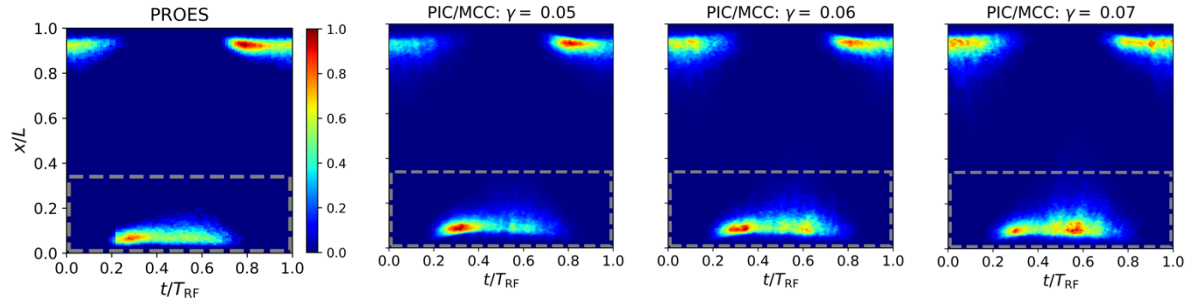

Fig. 1: Spatio-temporal plots of the electron impact excitation rate from the ground state into the Ar2p$_1$ level obtained by PROES and from PIC/MCC simulations for different values of the secondary electron emission coefficient, γ. The horizontal axes correspond to one RF period, the vertical axes show the distance from the powered electrode. The color scales of the plots are individually normalized to a maximum of 1. Discharge conditions: L = 2.5 cm, p = 100 Pa, f = 13.56 MHz, V_{pp} = 700 V. The grey dashed rectangles show the regions which are considered in the pixel-based comparison of the images.

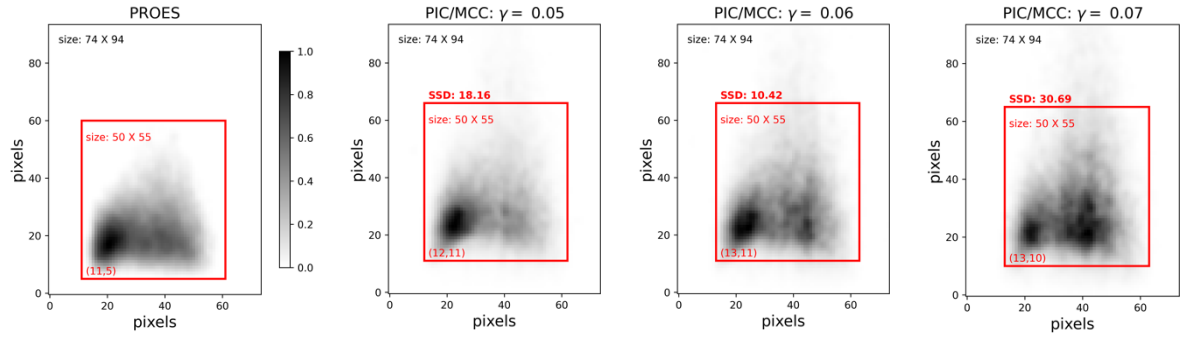

Fig. 2: Grayscale plots of the image regions marked by dashed gray rectangles in Fig. 1. The red rectangles indicate the “scan area” defined in the PROES image along with corresponding regions of the same size in the PIC/MCC images for which the best match (minimum SSD value) was obtained for the different γ coefficients. The SSD values for these cases are shown in the panels. Overall, γ = 0.06 results in the best agreement between PROES and PIC/MCC results.

This work has been supported by the National Office for Research, Development and Innovation (NKFIH, Hungary) via grant K134462 and by the J. Bolyai Research Fellowship of the Hungarian Academy of Sciences.

[1] A. Derzsi, B. Horváth, Z. Donkó, J. Schulze, *Plasma Sources Sci. Technol.* **29** (2020) 07400.
[2] M. Daksha, A. Derzsi, Z. Mujahid, D. Schulenberg, B. Berger, Z. Donkó, J. Schulze, *Plasma Sources Sci. Technol.* **28** (2019) 034002.
[3] M. Daksha, B. Berger, E. Schuengel, I. Korolov, A. Derzsi, M. Koepke, Z. Donkó, J. Schulze, J. *Phys. D: Appl. Phys.* **49** (2016) 234001.
[4] B Horváth, A Derzsi, J Schulze, I Korolov, P Hartmann, Z Donkó, *Plasma Sources Sci. Technol.* **29** (2020) 055002.

Electron density measurements and calculations in a helium capacitively-coupled radio-frequency plasma

Z. Donkó(*)[1], B. Z. Bentz[2], P. Hartmann[1], A. Derzsi[1]

[1] *HUN-REN Wigner Research Centre for Physics, Budapest, Hungary*

[2] *Sandia National Laboratories, Albuquerque, NM, USA*

(*)donko.zoltan@wigner.hun-ren.hu

The electron density is the most fundamental characteristic of various types of plasmas. Nonetheless, a precise measurement, as well as an accurate calculation of this quantity still represent challenges. In low-pressure radio-frequency (RF) discharges, in particular, various types of probes (Langmuir probes, hairpin probes, etc.) can be used for measurements of the electron density. These probes, however, inevitably cause some disturbance in the plasma due to their very presence. Microwave interferometry or laser diagnostics methods provide non-intrusive alternatives for these measurements. Computations of the electron density are also not straightforward, despite the availability of sophisticated numerical approaches and high-performance computational resources [1]. In this work, we report Laser-Collision Induced Fluorescence (LCIF) measurements and numerical modeling calculations of the electron density and the electron temperature in low-pressure capacitively-coupled radio-frequency discharges in helium gas. The experimental plasma source is a symmetric Capacitively Coupled Plasma (CCP) cell, with a pair of stainless-steel electrodes of 14.2 cm diameter, placed at a distance of L = 4 cm from each other. The gas pressure is between 50 mTorr and 200 mTorr and RF peak-to-peak voltages between V_{PP} = 150 V and 350 V are used at a frequency of f = 13.56 MHz.

The LCIF method is an extension of the Laser Induced Fluorescence (LIF) technique [2]. Both LIF and LCIF employ a laser to excite atoms in the plasma from a lower-lying level (L1) to a higher-lying level (L2). In LIF, the radiation emitted from the atoms as these decay spontaneously from the higher-lying level (L2) to a lower-lying level (L3, typically different than the original lower-lying level, L1) can be measured to quantify the density of the atoms in the level L1. In the case of LCIF, in addition to monitoring the LIF signal from the level L2, the emission is also monitored from additional levels, which are close to L2 but have somewhat higher energy. These excited levels are populated via collisions between the laser excited species (L2 level) and energetic electrons.

The numerical simulations are based on a Particle-in-Cell / Monte Carlo Collisions (PIC/MCC) simulation that includes He atoms in several excited levels in addition to the ground-state He atoms, as targets for electron-impact collisions. This way, besides the conventionally considered (direct) electron-impact excitation and ionization processes, stepwise excitation and ionization processes can also be included, as well as electron-impact de-excitation of the atoms in the excited levels, and ionization caused by collisions between excited (typically metastable) atoms. The density of the He atoms in the various excited levels is computed in a Diffusion-Reaction-Radiation (DRR) module that solves the diffusion equations of the He atoms in the excited levels, considering their sources and losses, which includes the rates of the electron-impact processes (obtained in the PIC/MCC module) as well as the rates of the radiative channels between the various levels, and quenching

processes [3]. We consider 18 excited levels of He atoms, with electron-impact cross sections taken from [4] and include 37 strong radiative transitions. The PIC/MCC and the DRR modules are executed repeatedly until convergence is reached. The importance of this computational approach lies in the fact that the accumulation of excited atoms in the plasma, even at relatively low pressures, can significantly change the plasma characteristics, like the electron energy distribution function and the electron density [3,5].

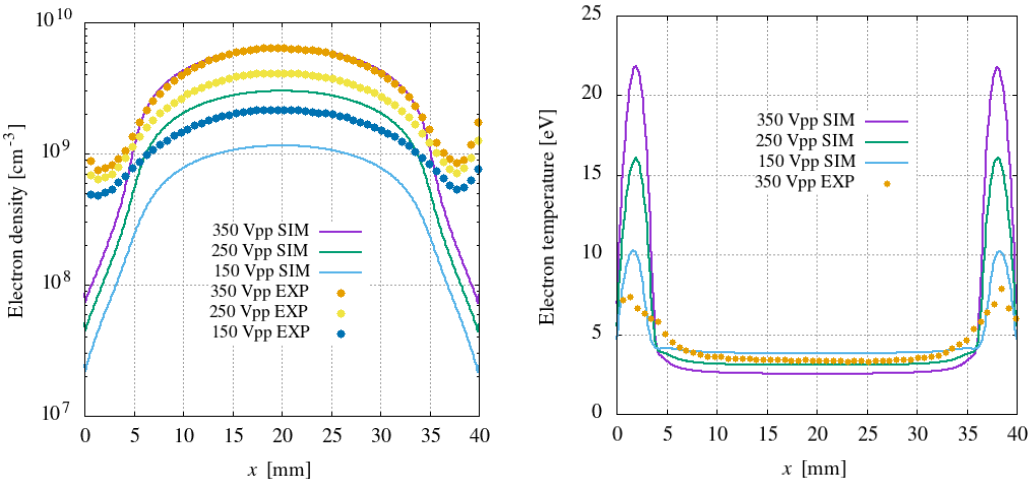

Fig. 1: The spatial distribution of the electron density (a) and electron temperature (b) in the He CCP at 200 mTorr gas pressure, as obtained from the experiments ("EXP") and the numerical calculations ("SIM") at the various excitation voltages.

The results of the measurements and the calculations are compared in Fig. 1. for the case of 200 mTorr He pressure. The best agreement between the data for the electron density (see panel (a)) is obtained at the highest driving voltage of V_{PP} = 350 V, the agreement gets worse with decreasing V_{PP}, but remains within a factor of two, which is acceptable considering the experimental errors as well as the accuracy of the input data of the discharge model. A general feature of the measured electron density distributions is the relatively high density in the sheath regions, which needs further clarification. The electron temperature values in the plasma bulk agree very well as it can be seen in Fig. 1(b). The measurement, however, appears to underestimate T_e in the sheath regions. Ongoing experimental studies target scanning the discharge characteristics over an extended domain of operating conditions (RF voltage and gas pressure).

This work has been supported by the National Office for Research, Development and Innovation (NKFIH, Hungary) via grant K134462 and by Sandia National Laboratories' Plasma Research Facility, funded by the U.S. Department of Energy Office of Fusion Energy Sciences. Sandia is managed and operated by NTESS under DOE NNSA contract DE-NA0003525.

[1] M. Vass, P. Palla, P. Hartmann, *Plasma Sources Sci. Technol.* **31** (2022) 064001
[2] E. V. Barnat and K. Frederickson, *Plasma Sources Sci. Technol.* **19** (2010) 055015
[3] Z. Donkó, P. Hartmann, I. Korolov, D. Schulenberg, S. Rohr, S. Rauf, J. Schulze, *Plasma Sources Sci. Technol.* **32** (2023) 065002
[4] Yu. Ralchenko, R. K. Janev, T. Kato, D. V. Fursa, I. Bray, F. J. de Heer, *Atomic Data and Nuclear Data Tables* **94** (2008) 603
[5] D.-Q. Wen, J. Krek, J. T. Gudmundsson, E. Kawamura, M. A. Lieberman, J. P. Verboncoeur, *Plasma Sources Sci. Technol.* **30** (2021) 105009

Plasma sheath tailoring by a magnetic field for three-dimensional plasma etching

Elia Jüngling(*)[1], Sebastian Wilczek[2], Thomas Mussenbrock[2], Marc Böke[1], Achim von Keudell[1]

[1] *Chair Experimental Physics II, Ruhr University Bochum, Germany*
[2] *Chair of Applied Electrodynamics and Plasma Technology, Ruhr University Bochum, Germany*
(*) elia.juengling@rub.de

Three-dimensional (3D) etching of materials by plasmas is an ultimate challenge in microstructuring applications. In the past, several attempts have been explored to reach 3D plasma processing capabilities including the charging of 3D structures in the plasma sheath to steer the ions [1], alternating chemistry during trench etching [2] and affecting trench charging by magnetic fields [3].

In our recent work [4] we proposed a method to reach controllable 3D structures by using masks in front of the surface in a plasma etch reactor in combination with local magnetic fields. This combination of electric and magnetic fields can modify the plasma sheath region and thereby modify the ion flux to reach 3D directionality during etching and deposition. This effect has the potential to be controlled by modifying the magnetic field and/or plasma properties to adjust the relationship between sheath thickness and mask feature size. However, because the guiding length scale is the plasma sheath thickness, which for typical plasma densities is at least tens of micrometers or larger, controlled directional etching and deposition target the field of microstructuring, e.g., of solids for sensors, optics, or microfluidics.

We investigated our approach both experimentally and by means of a 2d3v particle-in-cell/Monte Carlo collisions simulation (PIC/MCC). The etching experiments are performed in an inductively coupled plasma (ICP) at a pressure of 2 Pa with an additional RF-bias voltage applied to the substrate and metallic mask with a frequency of 13.56 MHz. The experiments as well as the simulation showed a modification of the etching profiles when using a magnetic field in combination with a metallic mask compared to the mask alone. Fig. 1 (a) and (b) show the etching profiles for both with and without a magnetic field for the etching of a-C:H layers and Silicon respectively. In both experiments the case with the magnetic field shows a modified etching trench with enhanced etching on the right-hand side of the trench (when the magnetic field is pointing out of the plane). The PIC/MCC simulation of a similar geometry showed an enhanced ion flux on the same side of the slit, which can be seen in Fig. 1 (c).

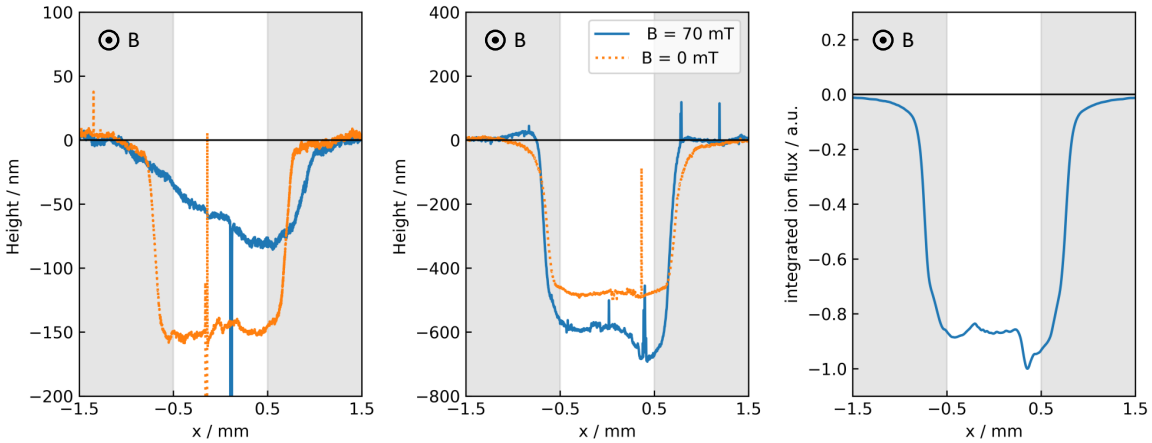

Fig. 1: 3D etching profiles of a-C:H in an argon-oxygen plasma with -100 V self-bias (a) and of silicon in a C:F plasma with -150 V self-bias (b) as well as the integrated ion flux from the simulation at 100 V applied voltage (c).

The simulation further revealed that the $\mathbf{E}\times\mathbf{B}$ drift of the electrons causes an asymmetric penetration of the plasma into the mask structure, as illustrated in Fig. 2 (a). This tailored local sheath expansion modifies the plasma density distribution and the transport when the plasma penetrates the mask during an RF cycle creating a 3D etch profile. Additionally, redeposition and ion scattering can further modify the etching profile, as illustrated in Fig. 2 (b).

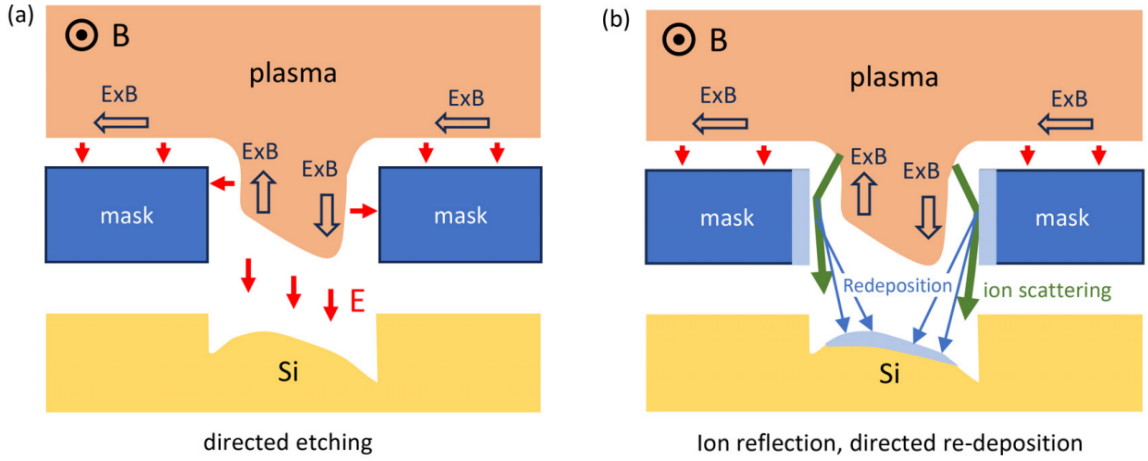

Fig. 2: Mechanisms to create a 3D deposition or etching profile: (a) varying penetration of the plasma into the mask structure depending on the $\mathbf{E}\times\mathbf{B}$ drifts, (b) ion focusing and re-deposition from the mask.

References

[1] Bingdong Chang. "Oblique Angled Plasma Etching for 3D Silicon Structures with Wiggling Geometries". In: *Nanotechnology* 31.8 (Feb. 2020), p. 085301.

[2] Shu Ni et al. "Wafer-Scale 3D Shaping of High Aspect Ratio Structures by Multistep Plasma Etching and Corner Lithography". In: *Microsystems & Nanoengineering* 6.1 (Mar. 2020), p. 25.

[3] Marc Schaepkens and Gottlieb S. Oehrlein. "Asymmetric Microtrenching during Inductively Coupled Plasma Oxide Etching in the Presence of a Weak Magnetic Field". In: *Applied Physics Letters* 72.11 (Mar. 1998), pp. 1293–1295.

[4] Elia Jüngling et al. "Plasma sheath tailoring by a magnetic field for three-dimensional plasma etching". In: *Applied Physics Letters* 124.7 (Feb. 2024), p. 074101.

Fluid simulation of a CCRF dusty plasma using COMSOL®: First stage under dust-free conditions

G. Saab[1(*)], C. Lahoud[2], S. Youssef[1], M. Mikikian[3]

[1] *Université Saint-Joseph, Ecole supérieure d'ingénieurs de Beyrouth, Campus des Sciences et Technologies, Mar Roukoz, B.P. 1514 - Riad El Solh Beyrouth, 1107 2050, Lebanon*

[2] *University of Balamand, Faculty of Engineering, Al Koura Campus, P.O. Box 100 Tripoli, Lebanon*

[3] *GREMI, UMR 7344, CNRS/Université d'Orléans, F-45067 Orléans, France*

(*) *ghinab.saab@gmail.com*

Low temperature plasmas are used in many industrial applications and processes due to their wide versatility. At low pressure, these plasmas can be easily generated by capacitively-coupled radio frequency (CCRF) discharges, but their numerical modeling represents a very challenging task. In this work, the simulation of a 2D axisymmetric RF argon discharge is performed for the experimental conditions of the PKE-Nefedov reactor [1] used to study dusty and complex plasmas [2,3].

The two-dimensional fluid simulation is conducted using COMSOL Multiphysics® software 6.1, in order to perform this model, a drift diffusion approximation using finite element method is combined with an electron energy distribution function resulting from the moments of Boltzmann equation. Figure 1 presents a schematic drawing showing the dimensions of the CCRF PKE-Nefedov reactor chamber. The electrodes are both driven by a radio-frequency power source with a frequency of 13.56 MHz, a power of 0.04 W, and a gas pressure of 40 Pa. In this model, key quantities such as electron temperature, fluxes, electron densities, and electric potentials are calculated. The present study focuses on the impact of the key parameters such as gas pressure, RF power, secondary electron emission coefficient (SEE), and the role of metastable, excited, and resonant states of argon atoms.

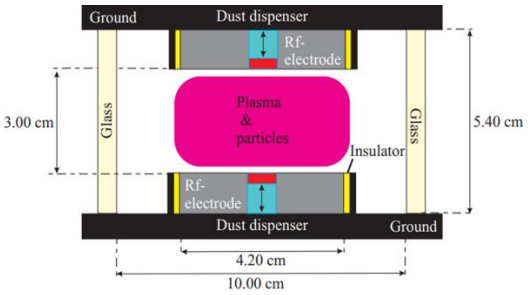

Figure 1: Schematic drawing of the CCRF PKE-Nefedov chamber

Typical results obtained from this simulation are presented in figure 2 showing the 2D electron density and electric potential. As shown in Figure 3, an increase in the gas pressure from 20 Pa to 160 Pa results in an increase of the maximum central electron density n_e, rising from 4.36×10^{14} m^{-3} to 9.09×10^{14} m^{-3} that leads to a reduction of the sheath width. The electron temperature also decreases due to the higher collision frequency with neutral particles.

One additional but essential objective of this work is also to check the ability of commercial codes to reproduce existing results. Remarkably, a high level of agreement exists between our results and the ones of Akdim et al. [4,5] who performed a similar simulation using homemade codes. A qualitative agreement is also obtained with other fluid models developed by other groups in slightly different geometries such as in Samir et al. [6] and Baldry et al. [7], this very last work being also developed with COMSOL.

In future works, dust particles will be added in the simulation in order to obtain their spatial distribution in the discharge under the actions of the various forces acting on them. The present results constitute a first step in order to first validate our simulation approach under dust-free conditions.

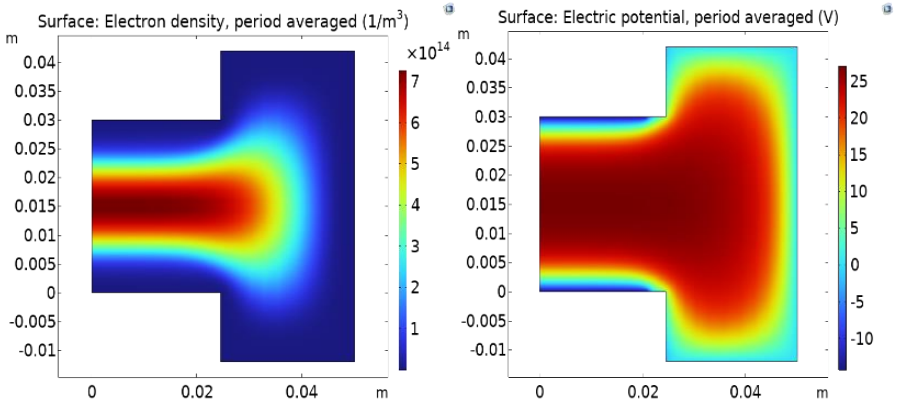

Fig. 2: 2D results at 40 Pa and 0.04 W for electron density (left) and electric potential (right)

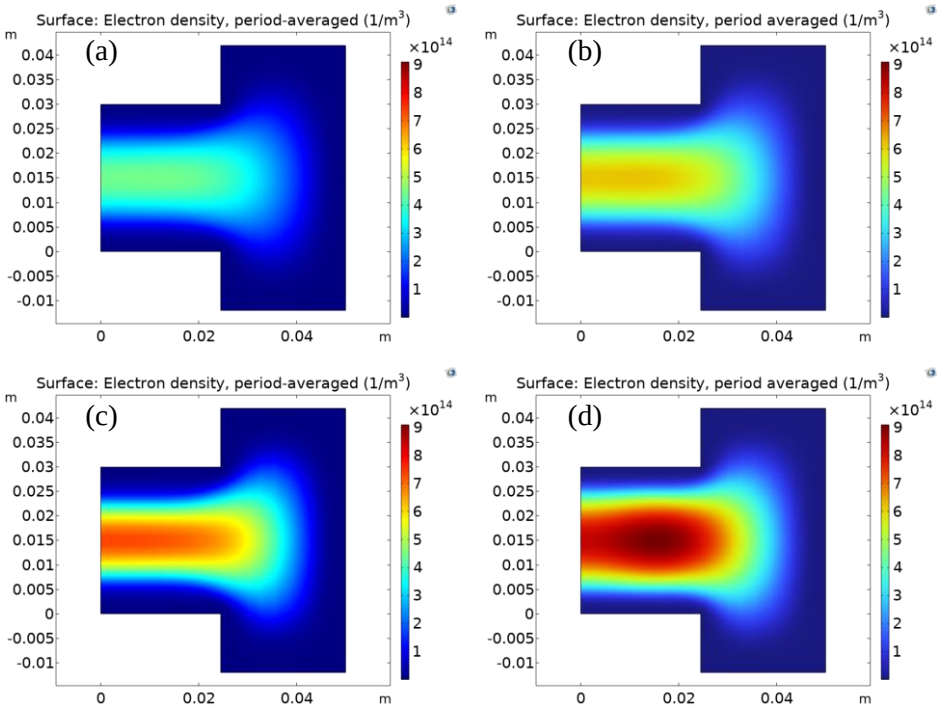

Fig. 3: Period-averaged electron density at (a) 20 Pa, (b) 40 Pa, (c) 80 Pa and (d) 160 Pa

This work was partly supported by the French National Research Agency (ANR) through the PERISTOCH project (ANR-19-CE40-0023)

[1] A.P. Nefedov et al., *New J. Phys.* **5** (2003) 33
[2] J. Beckers et al., *Phys. Plasmas* **30** (2023) 120601
[3] M. Mikikian et al., *New J. Phys.* **5** (2003) 19
[4] M.R. Akdim and W.J. Goedheer, *Phys. Rev. E.* **65** (2002) 015401(R)
[5] M.R. Akdim and W.J. Goedheer, *Phys. Rev. E* **67** (2003) 066407
[6] T. Samir, Y. Liu, L. Zhao, *IEEE Trans. Plasma Sci.* **46** (2018) 1738
[7] M. Baldry, L.L. Haidar, B. Akhavan, M.M.M. Bilek, *Plasma Process. Polym.* **18** (2021) e2000243

Multidimensional effects in low-pressure discharges

J. Thiel[(*)1,2], Ts. V. Tsankov[1,3], U. Czarnetzki[1]

[1] *Experimental Physics V - Plasma and Atomic Physics, Ruhr University Bochum, 44801 Bochum, Germany*
[2] *Experimental Physics II - Reactive Plasmas, Ruhr University Bochum, 44801 Bochum, Germany*
[3] *LPP, CNRS, Sorbonne Université, École Polytechnique, Institut Polytechnique de Paris, 91128 Palaiseau, France*
[(*)] jonas.thiel-n4w@rub.de

The transport in low-pressure discharges, such as those commonly used in many industrial applications, is governed by diffusion, generally in multiple dimensions. Most of the insights into the behavior of these plasmas, however, are obtained through the use of one-dimensional models. The side effect of such a treatment is that it forces equality of the ion and electron flux densities and leads to the well-known ambipolar diffusion. However, in realistic systems with metal walls, the balance of the flux densities has to be satisfied only globally and not locally. This can lead to a peculiar behavior, with regions where the ion current density to the walls locally exceeds the electron current density and vice versa. Some studies from the literature already noticed this behavior either in experiments [1] or in simulations [2, 3].

In this contribution, the effect is investigated experimentally for a large area rectangular discharge chamber, which provides a simple geometry. The plasma is generated by inductive coupling provided by the recently developed INCA configuration [4]. An array of 7×7 wall-mounted planar sensors made of stainless steel allows measuring the spatial profiles of the current-voltage (*I*-*V*) characteristics across the major wall opposite the antenna array. Using the regular evaluation procedure of Langmuir probe measurements, crucial plasma parameters can be obtained.

However, the antenna array consisting of 6×6 identical coils creates non-negligible capacitive coupling to the discharge. Thus, the DC plasma potential is superimposed by oscillations at the driving radio frequency (13.56 MHz) and, to a lesser extent, its harmonics. The capacitive coupling enhances the sputtering of the quartz plate in front of the antenna array and the redeposition of the sputtered material at the other discharge walls. This affects the conductivity of the individual sensors and shrinks the measurable direct current. To avoid this issue, an additional cleaning circuit has been established ensuring a constant bias of each sensor to -300 V. This guarantees continuous ion bombardment of their surface. During each measurement of a *I*-*V* characteristic, the biasing of the array has been deactivated for a duration of a few seconds avoiding any influence on the plasma sheath structure.

Despite the use of RF series resonance filters for the first and second harmonic, the measured *I*-*V* curves are distorted by the RF fluctuations of the plasma potential. This becomes particularly evident when computing the second derivative of the measured curves, as depicted in Fig. 1. There, two peaks are present with their distance in voltage corresponding to twice the amplitude of the first RF harmonic of the plasma potential. A similar effect has been observed also by others [5]. To compensate for this problem, a numerical deconvolution procedure has been developed in which the theoretical model of an ideal characteristic is disturbed by superimposing a potential oscillation. The perturbed curve is then fitted to the measured curve. For the unperturbed theoretical curve, the saturation currents of both electrons and ions have been modeled via the Orbital Motion Limited Theory to account for the sheath expansion with the probe voltage. Maxwellian electrons have been assumed for the electron retardation current. Fig. 2 shows a measured *I*-*V* curve (red) distorted by a high RF distortion (~ 10 V of amplitude) and the fitted curve (blue) from which a deconvoluted ideal

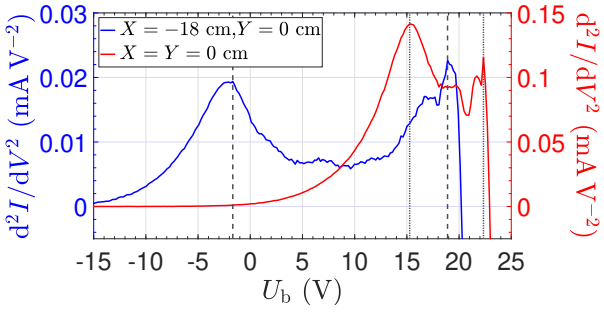

Fig. 1: Second derivative of two measured *I*-*V* curves for high and low RF distortion. The dashed and dotted lines represent the locations of the two maxima respectively. Argon plasma at 0.5 Pa and 450 W.

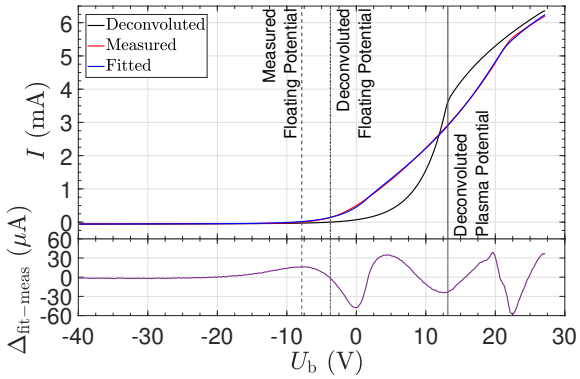

Fig. 2: Comparison of the measured *I-V* curve (red) with the modeled deconvoluted characteristic (black) and the fitted *I-V* curve (blue). Absolute deviation of the fitted curve from the measured one (purple). Argon plasma at $0.5\,\mathrm{Pa}$ and $450\,\mathrm{W}$.

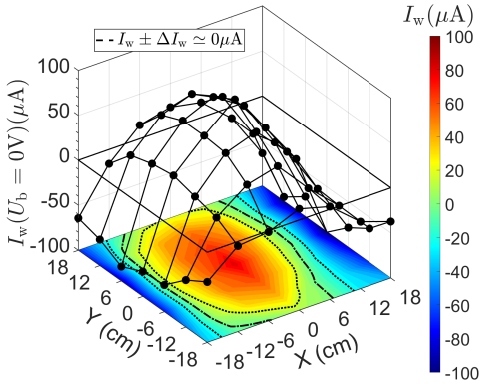

Fig. 3: Total current I_w, i.e. sum of electron and ion current, of the deconvoluted *I-V* curves at a bias voltage of $0\,\mathrm{V}$. The dashed-dotted line in the contour plot shows the level of zero total current. The dotted ones denote the interval of the uncertainty of about $19.6\,\mu\mathrm{A}$ for $I_\mathrm{w} \simeq 0\,\mu\mathrm{A}$. Positive current values correspond to a prevailing ion current to the wall. Argon plasma at 0.5 Pa and 450W.

characteristic is derived (black). The absolute deviation of the fitted curve from the measured one, also shown in the figure, demonstrates that this procedure well captures the features of the experimental *I-V* characteristic.

Applying this method to all sensors, the spatial distributions of the electron and ion current densities, the plasma potential, the particle densities both at the sheath edge and on the wall, as well as the electron temperature are obtained. Note that the measurement and the evaluation of the *I-V* curves of each sensor are done independently from each other. The smoothness of the profiles of the obtained quantities demonstrates the reliability of the developed procedure. The results reveal a homogeneous electron temperature as well as quasi-neutrality at the sheath edge. This further confirms the self-consistency of the measurements. The evaluation of some of the parameters depends on whether the charged particle flux densities balance locally (dielectric walls) or globally (metallic walls). However, quasi-neutrality at the sheath edge is only obtained when the condition for conducting, i.e. metal walls is used in the evaluation procedure. Fig. 3 presents the profile of the total current reaching each sensor for zero bias. Corresponding to the conditions at a conducting wall, the results show the expected deviation from local equality of the flux densities, while global equality is fulfilled within the uncertainty estimation. The asymmetry along the central Y-axis can be identified as an artifact of the electrical circuit of the antenna array that is intended to reduce the capacitive coupling by introducing a virtual zero point of the RF voltage on this axis [4].

In conclusion, the two-dimensional distribution of the plasma parameters in front of the wall in a low-pressure inductive discharge has been obtained experimentally. For that, an array of electrodes embedded in the wall has been used. A procedure has been developed to compensate for the RF oscillations in the potential that allows the *I-V* curves of the sensors to be evaluated using the theory of Langmuir probes. The results show a homogeneous electron temperature and a diffusion profile of the plasma density, consistent with the theoretical expectations for the low pressure in the experiments. Most importantly, a deviation from the local balance of the fluxes of electrons and positive ions has been observed. Such a deviation is permitted for conducting walls, such as the ones in the experiments. The results show that the common assumption for ambipolarity of the diffusion does not always hold.

[1] G. Mümken and U. Kortshagen, *J. Appl. Phys.* **80** (1996) 6639–6645.
[2] T. Lafleur and R. W. Boswell, *Phys. Plasmas* **19** (2012) 053505.
[3] R. Lucken *et al.*, *Plasma Sources Sci. Technol.* **27** (2018) 035004.
[4] P. Ahr *et al.*, *Plasma Sources Sci. Technol.* **27** (2018) 105010.
[5] M. Hannemann and F. Siegeneger, *Czech. J. Phys.* **56** (2006), B740–B748.

Statistical analysis of microgap vacuum breakdown mechanisms for palladium electrodes in pulsed electric fields

Mária Maťašová(*)[1], Matej Klas[1], Peter Čermák[1], Štefan Matejčík[1]

[1]*Department of Experimental Physics, Faculty of Mathematics, Physics and Informatics, Comenius University, Mlynská dolina, 842 48 Bratislava, Slovakia*

(*) maria.cibikova@fmph.uniba.sk

For uniform treatment of samples, it is essential to ensure the homogeneity of plasma. One of the ways how to achieve homogeneous plasma is by generation it within micrometric distances between electrodes. The first attempts to characterize phenomena of micrometric discharges were performed by Boyle, Germer, Kisliuk, and others [1,2,3]. They investigated the question of the origin of microgap discharge breakdown and field emission phenomena connected with it, mostly from a fundamental point of view. However, studying microdischarges at high pressures poses technical challenges due to the complex nature of field emission phenomena resulting from fast ionization processes within the discharge region. The solution to this can be found by working in a vacuum environment, where the influence of the carrier gas could be neglected.

In general, the field emission processes occurring in the pre-breakdown stage seem to be crucial for microgap vacuum breakdown initiation mechanisms accompanied by high electric fields. Despite numerous papers investigating these processes, they remain relatively unexplored and require deeper analysis [2,4,5]. In our previous work, we investigated field emission phenomena from stainless steel (SS) [6]. This study show a significant influence of high temperature due to the low thermal conductivity of SS. Following this research our focus has shifted to metals characterized by higher thermal conductivity, representing groups of noble metals. Despite the utilization of noble metals like palladium or iridium in spark plugs, there is a lack of available data describing breakdown processes. The objective of this work is to statistically characterize the breakdown and pre-breakdown stages for a better understanding of occurring mechanisms. Before conducting experiment, the conditioning of electrodes is needed. This process involves cleaning the electrodes from impurities by generating successive breakdowns between them, which is accompanied by an increase in breakdown voltage as shown in Fig. 1. The electric breakdowns were generated by a pulsed electric signal with a voltage ramp speed of 10^7 kV/s. The gap between electrodes was set at 10 µm. When the average breakdown voltage stabilized (saturated), the electrodes are considered to be conditioned, as represented in Fig 1.

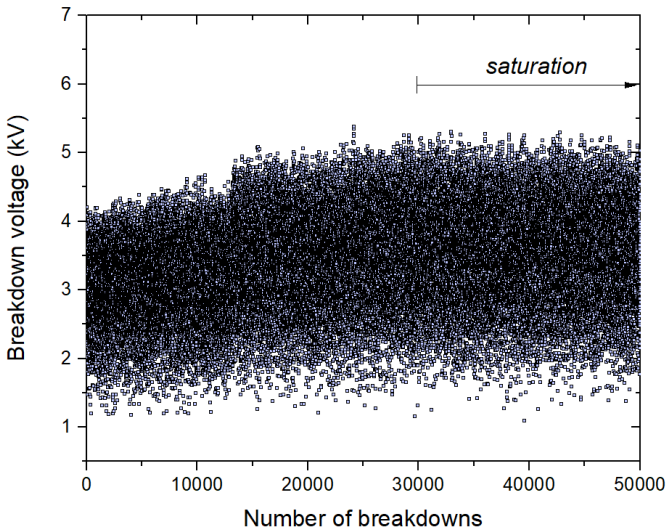

Fig. 1: The evolution of the breakdown voltage during conditioning process (10^7 kV/s, 10 µm).

One of the objectives of our statistical analysis was to investigate the relationship of the sequence of successful consecutive breakdowns, for samples over 10,000 sequences, measured in the saturated stage. To illustrate, the voltage-current waveform of one sequence (burst) is represented in Fig. 2. The length of the sequence (burst duration) was set at approximately 3 µs and contained several breakdowns.

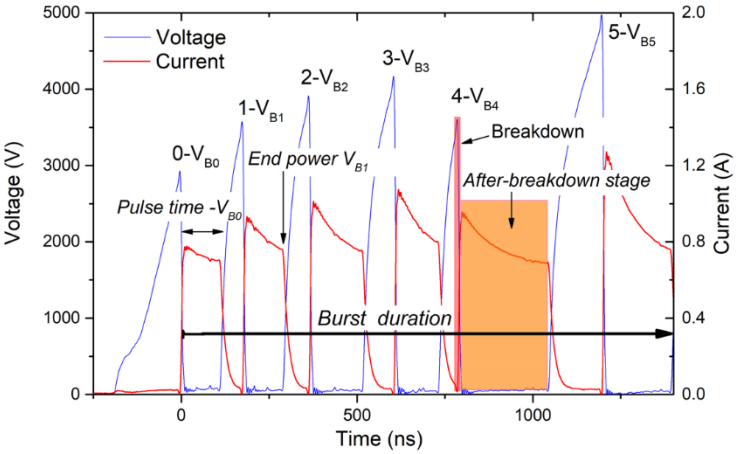

Fig. 2: The typical voltage-current waveform of the pulse sequence with several breakdowns.

For visual representation, we present a density scatter plot showing the dependence of breakdown voltage V_{Bi} on the difference between the subsequent breakdown voltage $V_{B(i+1)}$ and the previous breakdown voltage V_{Bi} for every sequence. The index i (i = 0,1,2,3...) represents the number of the breakdown in the sequence. The Fig. 3 illustrates the pattern 1-0 (for index i = 0, i. e. V_{B1}-V_{B0} versus V_{B0}) which represents the relation between the first and second breakdowns in the sequences. From Fig. 3, it can be observed that the initial breakdown in the pulse sequence (index i = 0) is most likely to occur within the range of 3 kV to 4.1 kV, with a subsequent probable increase to approximately 50-450 V. If the initial breakdown voltage was above 4.4 kV, the next breakdown voltage decreased to the range of 1kV to 3kV. Interestingly, a similar pattern was observed in all subsequent pairs of breakdowns in all pulse sequences (2-1, 3-2, 4-3). This leads to the conclusion that within the low voltage span (in this case, 3-4kV), there is a gradual step increase in V_{B0}.

The scatter density plot results clearly illustrate an observable relationship between successive breakdowns. If the initial breakdown begins in the low voltage region, the next breakdown increases in several voltage steps, ending with a large drop proportional to the maximum breakdown voltage This observation strongly suggests the presence of a memory effect between two consecutive breakdowns.

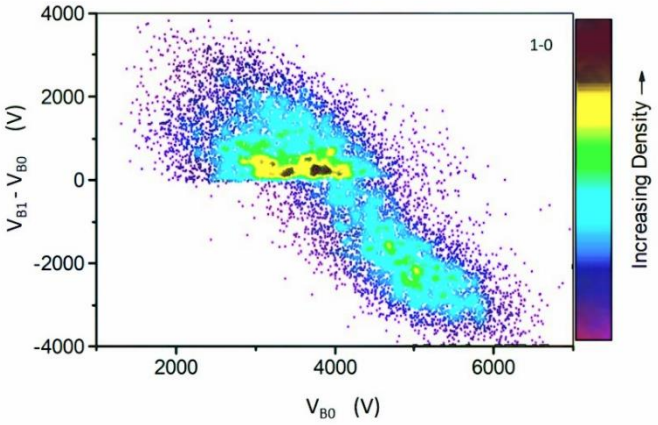

Fig. 3: The density scatter plot of $V_{B1} - V_{B0}$ versus V_{B0} representing the memory effect of two subsequent breakdowns (for 10 μm).

[1] Dyke, W. P., & Trolan, J. K. *Phys. Rev.* **89(4)** (1953) 799.
[2] Utsumi, T. *J. Appl. Phys.* **38(7)** (1967) 2989-2997.
[3] Boyle, W.S. Kisliuk, P. Germer, L.H. *J. Appl. Phys.* **26 (6)** (1955) 720–725.
[4] Tsuruta, K. *IEEE Trans. Electr. Insul.* **(3)** (1983) 204-208.
[5] Zouache, N., & Lefort, A. *IEEE Trans. Dielectr. Electr.* **4(4)** (1997) 358-364.
[6] Klas, M., Čermák, P., Borkhari, A. F., Satrapinskyy, L., Matejčík, Š., Radjenović, B., & Radmilović-Radjenović, M. *Vacuum* **191** (2021) 110327

Acknowledgements. This work was supported by the Slovak Research and Development Agency under project Nr. APVV −19−0386 and under the Contract no.SK-SRB 21-0004. The authors acknowledge also partial support from Slovak Grant Agency for Science VEGA Nr.1/0489/21.

A novel low-temperature hydrogen plasma source for EUV lithography applications

T.W. Mechielsen(*)[1], A.S. Stodólna[1], P. Van der Walle[1], C.J Meekens[1], H. Lensen[1]

[1] *TNO, Stietjesweg 1, Delft 2628CK, NL*

(*) *thomas.mechielsen@tno.nl*

Inside EUV lithography machines a hydrogen plasma is generated due to ionization of hydrogen molecules with EUV photons. Scanner components interact with this plasma, which is a topic of many life-time investigations. These studies can be rather costly when using experimental setups equipped with EUV sources. However, there are other ways to mimic certain aspects of the EUV-generated plasma using non-EUV plasma sources, but they all come with their own drawbacks. TNO presents a new novel experimental setup, where a low temperature hydrogen plasma is generated by electron impact ionization process (see Fig.1). The electron beam is generated using a high pressure/current e-beam (TES-63-ES, Polygon Physics). Using a retarding field energy analyzer the ion flux and ion energy distribution function were measured, which shown to be comparable to the scanner plasma. Moreover, experiments shows that carbon cleaning rates are similar to hydrogen radical generators but without the drawback of the high heat load. Finally, compared to setups equipped with microwave or RF sources, our setup shows a minimal molecular contaminations, which makes it suitable for life-time testing of various scanner components.

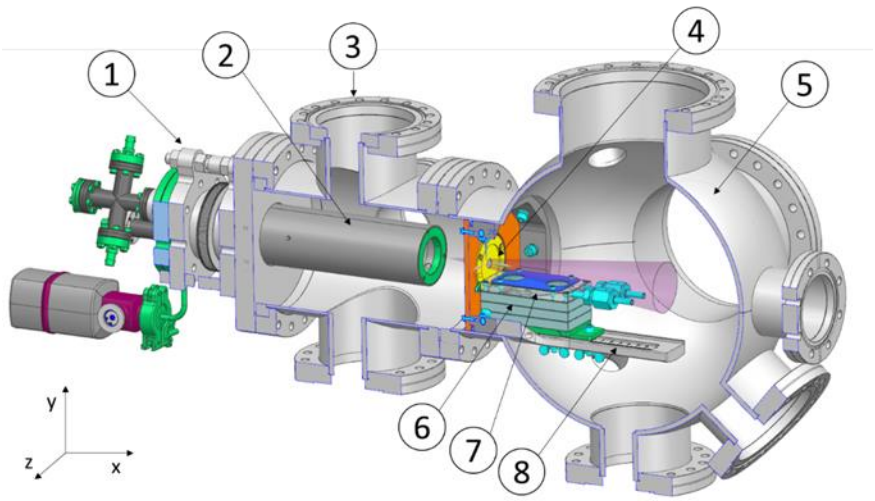

FIG. 1. Schematic cross-sectional view of the EBR setup containing a port aligner (1) used for mounting an e-gun (2) onto a smaller vacuum vessel (3), which is connected via a 10 mm orifice (4) with a main, exposure chamber (5). A sample stage (6) consist of 3 x 1 cm spacers and a top, water-cooled plate (7), which has openings for two 1” samples. The stage is positioned on a rail (8), which allows for its movement along the x-axis.

Investigation of a liquid droplet affected by an electrical charge injection

A. Takáčová(*)[1], T. Orrière[2], G. Gomit[2] and T. Hoder[1]

[1] *Department of Plasma Physics and Technology, Masaryk University, Kotlářská 2, 611 37 Brno, Czech Republic*
[2] *Institut PPRIME, UPR CNRS 3346, Université de Poitiers, ISAE-ENSMA, 86962 Futuroscope, France*
(*) alica.takac@mail.muni.cz

Plasma-liquid interaction became one of the important topics in the current low temperature plasma community [1]. It is thanks to an increased interest in biomedical plasma applications and due to a mere curiosity in the mechanisms of a more complicated, yet still simple, systems of a general interest. Several interesting problems were investigated, including plasma jet stabilization of a hydrodynamic instability [2], barrier discharge plasma driven destabilization of a liquid droplet surface [3, 4] or corona charging induced spreading of a dielectric liquid droplet [5].

In this contribution, we focus our interest onto the problem of the liquid droplet destabilization by charge injection from a positive corona discharge. We follow the whole process, by first understanding the mode of corona discharge operation using electrical current measurements and quantification of the transferred charge onto the droplet surface, then second by recording and reconstructing the topological changes of the droplet surface and finally by application of an appropriate model to describe the physical phenomena taking place.

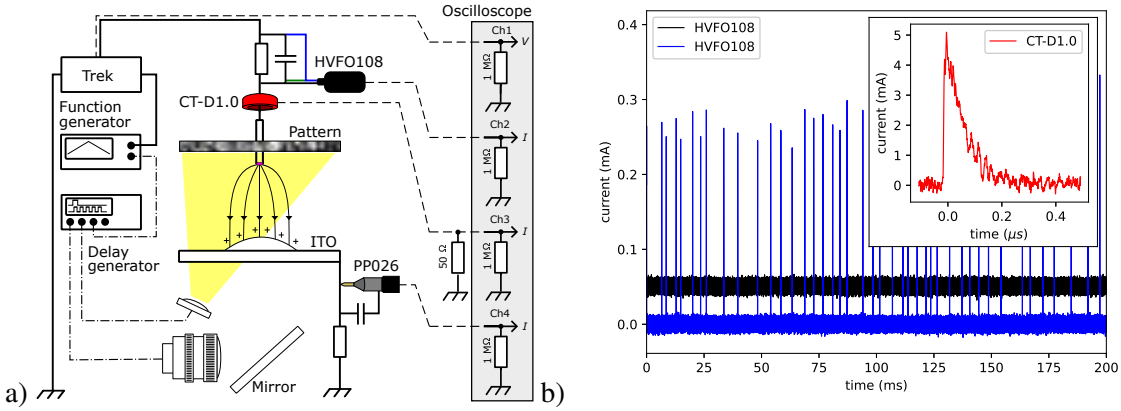

Fig. 1: a) Schematic representation of the experimental setup. b) Current measurements with $4\,\mathrm{cm}$ electrode gap distance representing the two modes of the corona discharge - the pre-onset pulses (blue and red) with applied voltage $7.9\,\mathrm{kV}$ and the stable corona mode (black) with applied voltage $30\,\mathrm{kV}$.

The source of the positive charge flow is a DC corona discharge in air at atmospheric pressure in a point-to-plane configuration as shown in figure 1a. The plane electrode is a $10 \times 10\,\mathrm{cm}$ transparent ITO plate and the point is the high voltage electrode made of a hypodermic needle with ending cut to a half-toroid shape. This results in a hollow circular cross section with a $0.45\,\mathrm{mm}$ internal diameter and a $0.73\,\mathrm{mm}$ external diameter. The gap distance is adjusted by a translation stage holding the tip. A dielectric silicon oil (Lukosiol M200) droplet is deposited onto the plate using a micro-syringe. The high voltage is produced using a TREK amplifier ($\pm 30\,\mathrm{kV}$) supplied by a DC power source. Ramp or triangular signal from function generator (Lecroy WaveStation 3082) is used to define the waveform. The current is measured on a $10\,\mathrm{k\Omega}$ shunt resistors by using a differential probe on the HV side (HVFO108) and a passive probe on the grounded side (PP026). All the signals are recorded by an oscilloscope (Lecroy WaveSurfer 4054), as well as the applied voltage from the TREK's internal voltage probe.

The morphological changes of the droplet are treated using a free-surface synthetic Schlieren (FS-SS) method [7]. The changes are observed from below by a camera equipped with a $50\,\mathrm{mm}$ objective (Hikrobot MV-CA050-20UM/UC). A randomized dot pattern is placed at a certain height from the ITO plate parallel to it. The pattern is enlightened from below using a LED (luminus CBT-120) with a self-assembled driving circuit. The signals for camera, light and oscilloscope triggering are controlled with a delay generator (DG645 Stanford research systems).

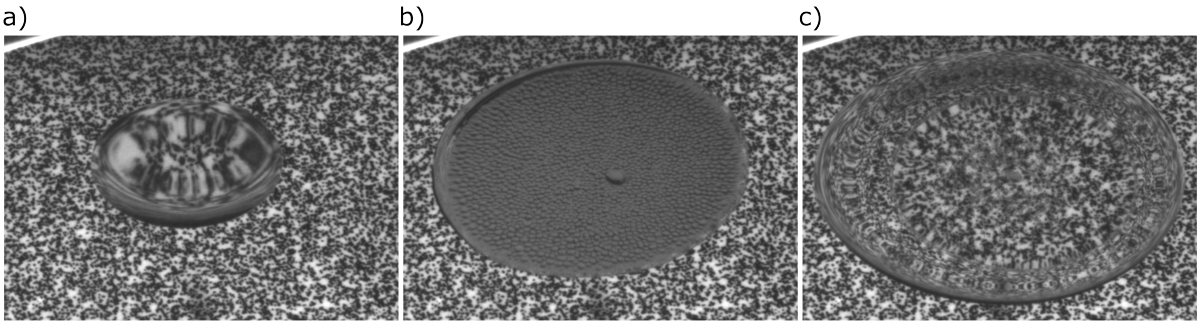

Fig. 2: Morphological changes of a $50\,\mu\mathrm{l}$ droplet under the influence of a charge injection. a) Droplet without corona discharge. b) Hydrodynamic instability after the ignition of the discharge. c) The shape of the droplet after the hydrodynamic instability disappearance.

The effects of two corona discharge modes on the dielectric droplet are studied. The steady corona glow mode and the intermittent regime right below the onset of steady corona, the pre-onset pulses [6]. These two modes are shown in figure 1b. Depending on the gap distance, the former manifests itself as a spreading of the droplet into a uniform thin film over the plate, or, at smaller gap distances, after the initial spreading, the droplet stays in a constant shape with a dimple in the middle, caused by a more concentrated electric pressure in the center of the droplet (figure 2c). A hydrodynamic instability appears on the droplet surface at the beginning of the spreading (figure 2b). The FS-SS method is used to obtain the three-dimensional topography of the droplet surface, which makes use of the distortion of the pattern when the surface of the droplet is modified. The surface topography can be reconstructed by comparing the undistorted and the distorted pattern. The procedure consist in using a digital image correlation algorithm (PIVlab) and an integration algorithm (Surfheight) available on Matlab.

[1] P. Vanraes, A. Bogaerts, *Appl. Phys. Rev.* **5** (2018) 031103.
[2] S. Park et al., *Nature* **592** (2021) 49–53.
[3] H. Y. Chu, H. K. Lee, *Phys. Rev. Lett.* **107** (2011) 225001.
[4] L. Kuthanová and T. Hoder, *Scientific Reports* **12** (2022) 16665.
[5] S. R. Mahmoudi, K. Adamiak, G. S. P. Castle, *Proc. R. Soc. A* **467** (2011) 3257–3271.
[6] L.B. Loeb (1965) Electrical Coronas (Berkeley: University of California Press)
[7] F. Moisy, M. Rabaud, K. Salsac, *Experiments in Fluids* **46** (2009) 1021–1036.

Memory effect of a diffuse dielectric barrier discharge obtained in air: surface and volume mechanisms

J Haton[1,2], A Belinger[1], S Dap[1], L Stafford[2] and N Naudé[(*)1]

[1] *LAPLACE, Université de Toulouse, CNRS, INPT, UPS, Toulouse, France*

[2] *Département de physique, Université de Montréal, Montréal, Québec, Canada*

[(*)] naude@laplace.univ-tlse.fr

There are generally two discharge regimes observed in Dielectric Barrier Discharge at atmospheric pressure: filamentary and diffuse regimes [1]. The discharge regime depends on factors such as the nature of the gas, the electrical parameters, and the electrode configuration. The filamentary regime is characterized by small and fast microdischarges randomly distributed on the electrode surface. As for the diffuse regime, it is characterized by only one discharge canal covering the whole electrode surface. In addition, it exhibits a more uniform distribution of the the energy provided to the electrode surface, making it more appropriate for various surface engineering applications, including thin-film deposition [2]. To obtain a diffuse discharge, a pre-ionization of the gas is needed. Recent studies have shown the potential to achieve a diffuse DBD in air [3–6]. The discharge is a Townsend one. As observed in other gases, the first discharge is always filamentary before a transition to a diffuse discharge (Fig. 1). Hence, the previous discharge influences the following one; this effect is called the memory effect. In N_2 discharges, this effect is related to $N_2(A)$ metastables, which are not present in air due to their efficient quenching by oxygen species. It is interesting to notice that a memory effect also exists in air. Currently, the mechanisms related to this memory effect and the production of seed electrons are not understood. It could be related to the features involved at the surface of the dielectrics and/or to processes occurring in the the gas volume. In this work, we examine these two potential mechanisms. Firstly, we assess any surface mechanisms by comparing two dielectric materials. Secondly, we investigate the volume effect by using a segmented electrode.

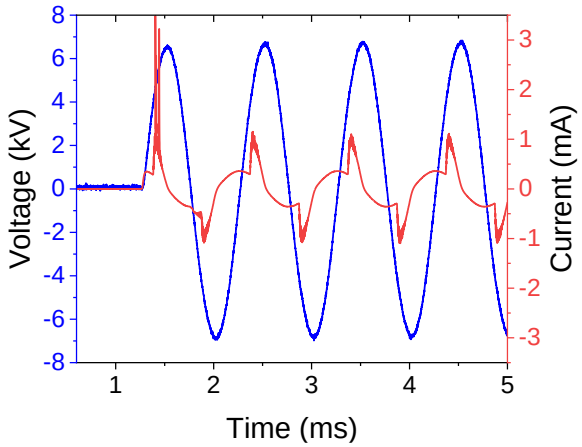

Fig. 1: Evolution of the applied voltage and the measured current during the first discharges for a DBD obtained in air (14 kV_{pp} and 1 kHz)

Fig. 2 (a) and (b) present the electrical measurements obtained with two different alumina. It is important to note that they have exactly the same dielectric properties (permittivity, thickness, percentage of purity); only the manufacturer and the surface morphology are different. Moreover, the same power supply conditions are applied in both cases. However, the discharge behavior is entirely different. With alumina 1, the discharge is diffuse, whereas with alumina 2, the discharge is filamentary. Hence, the surface has an enormous influence on the discharge regime. Hence, the alumina in contact

with the discharge affects the memory effect. More details concerning the impact of the surface on the production of seed electrons will be discussed.

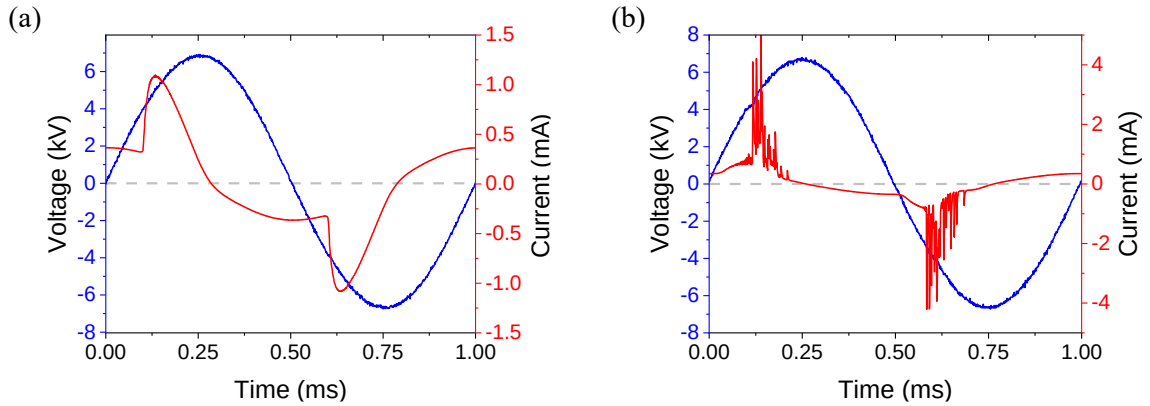

Fig. 2: Electrical measurements for a DBD obtained with alumina coming from two manufacturer with (a) alumina from manufacturer 1 and (b) alumina from manufacturer 2

To study the effect of the gas volume mechanism(s), we used a segmented ground electrode to obtain a spatial resolution of the current discharge and the gas voltage as a function of the gas residence time. The setup has been previously described [7]. As shown in Fig. 3, the breakdown voltage increases with the gas residence time until a saturation appears for a time longer than 200 ms. Consequently, the memory effect decreases with the gas residence time, which is counterintuitive and the opposite of what is generally observed in N_2 discharges. This evolution will be discussed to differentiate the influence of the different processes.

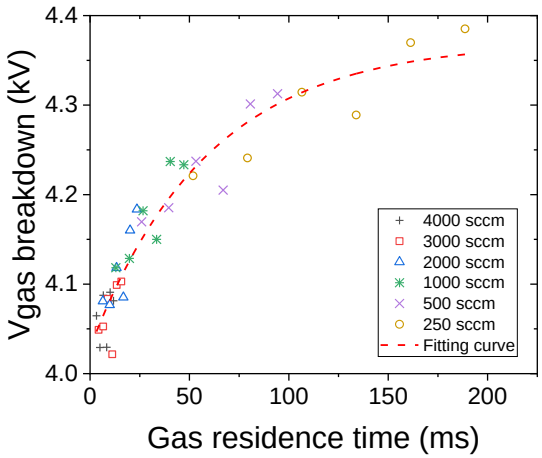

Fig. 3: Evolution of the breakdown voltage as a function of the gas residence time

[1] R. Brandenburg, *Plasma Sources Sci. Technol.* **26**, 053001 (2017).
[2] F. Massines et al., *Plasma Processes Polym.* **9**, 1041 (2012).
[3] N. Osawa and Y. Yoshioka, *IEEE Trans. Plasma Sci.* **40**, 2 (2012).
[4] N. Osawa et al., *Eur. Phys. J. Appl. Phys.* **61**, 24317 (2013).
[5] J. Ran et al., *Physics of Plasmas* **25**, 033511 (2018).
[6] A. Belinger, S. Dap, and N. Naudé, *J. Phys. D: Appl. Phys*. **55**, 465201 (2022).
[7] C. Tyl et al., *J. Phys. D: Appl. Phys.* **51**, 354001 (2018).

Radially and axially resolved optical emission observed during the initial phase of nanosecond discharge in liquid water

P. Bílek[1*], G. Arora[1], P. Hoffer[1], V. Prukner[1] and M. Šimek[1]

[1] *Institute of Plasma Physics of the Czech Academy of Sciences, Prague, Czech Republic*
[(*)] bilek@ipp.cas.cz

Electric discharges in contact with or directly in liquid water produce reactive species that are of interest for many biological and medical applications [1]. The simplest mechanism of the discharge initiation in liquids is associated with the local evaporation of liquid due to Joule heating in the discharge gap, followed by gas breakdown. However, in the case of (sub)nanosecond high-voltage pulses, the heating and vaporization of the liquid is not fast enough to enable the onset of the discharge. The mechanism that controls the initiation of discharge in such short timescales is still under investigation. Therefore, basic characteristics and signatures of the direct and bubble-assisted mechanism are still the subject of focused diagnostic studies. An experimental study [2] pointed out that a nanosecond discharge is composed of nonluminous and luminous phases, see Figure 1. The non-luminous dark phase, which created bush-like structures made of thin hair-like filaments, occurs with a delay of a few nanoseconds after the onset of the HV pulse, and the propagation of every single filament is accompanied by GPa shock waves [3]. In contrast, the luminous phase has a simple tree-like morphology and is characterised by broadband continua extending from ultraviolet to near-infrared (NIR) wavelengths [4]. The onset is delayed by about 600 ps with respect to the onset of the dark phase.

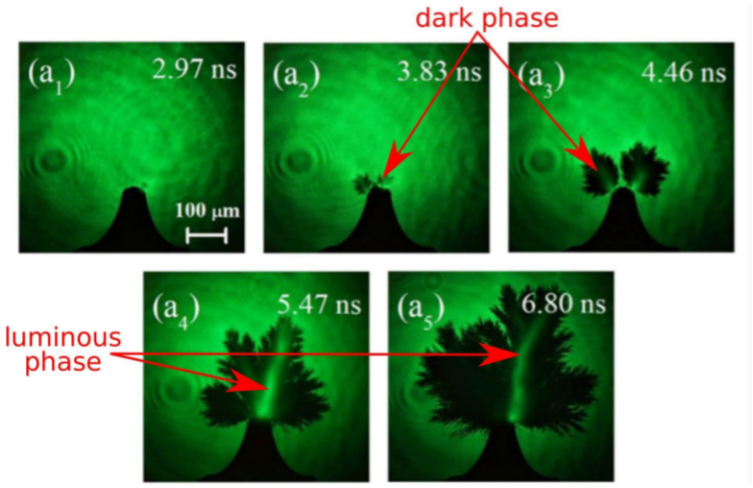

Fig. 1: Morphology of the nanosecond discharge in liquid water. Credits on [2].

Recently, we obtained temporally and spatially resolved emission spectra of the nanosecond discharge together with images registered using a four-channel ICCD imager [5]. This enabled us to connect the morphology of the luminous discharge phase with the specific characteristics of the plasma-induced emission in the vis-NIR region, as shown in Figure 2 [6]. We discovered that the initial diffuse morphology of the discharge is associated with broad-band emission spectra, whereas the subsequent filamentary morphology is linked to spectra featuring broadened hydrogen and oxygen atomic lines.

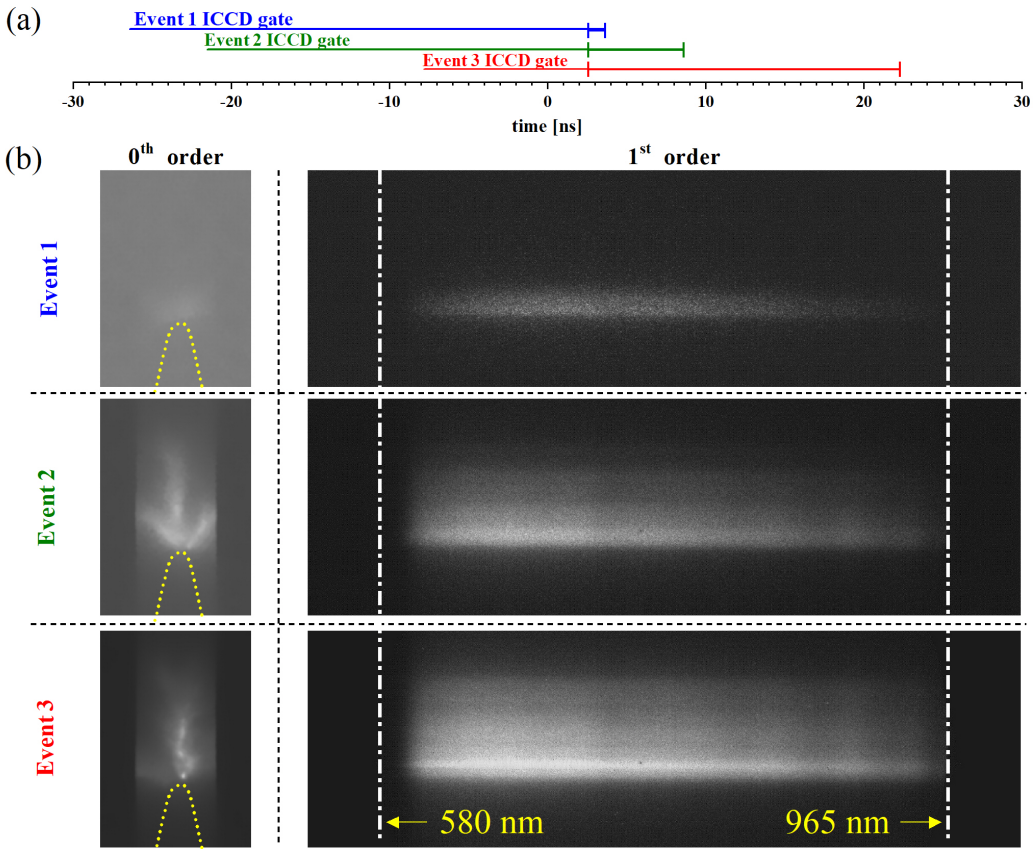

Fig. 2: Selected ICCD spectrometric images acquired in 0th and 1st diffraction orders using ICCD gate of 30 ns. Horizontal bars in (a) illustrate the timing of the MCP gates with respect to the onset (time t=0 ns) of the HV pulse. Images in panel (b) show the plasma-induced emission of selected events during the primary HV pulse.

In this work, we investigate the origin of the broad-band emission spectra captured in the first nanoseconds of the luminous phase by comparing them with model spectra obtained through three different methods:

(i) electron–neutral bremsstrahlung generated by a bell-like energy distribution of the electrons, which is coherent with the concept of electric field emission into electrostriction-induced nanovoids [7],

(ii) considering the electron–neutral bremsstrahlung due to electron energy distribution derived from state-of-the-art cross-section sets for H_2O [8],

(iii) considering high-pressure (GPa) broadening of hydrogen and oxygen atomic lines.

This study is supported by the Grant Agency of Czech Republic (GA 24-10903S).

[1] B. R. Locke et al., *Plasma Chemistry and Plasma Processing*, 32, 5, 875-917 (2021).
[2] M. Šimek et al., *Plasma Sources Science and Technology*, 29, 9, 095001 (2020).
[3] P. Hoffer et al., *Journal of Physics D: Applied Physics*, 54, 28, 285202 (2021).
[4] M. Šimek et al., *Plasma Sources Science and Technology*, 26, 7, 07LT01 (2017).
[5] V. Prukner et al., *Plasma*, 4, 1, 183-200 (2021).
[6] M. Šimek et al., *work under preparation*.
[7] P. Bílek et al., *Plasma Sources Science and Technology*, 30, 4, 04LT01 (2021).
[8] M. Budde et al., *Journal of Physics D: Applied Physics*, 55, 445205 (2022).

CO_2 and CO vibrational excitation in Townsend and filamentary DBD at atmospheric pressure: in situ FTIR measurements.

C Bajon[1], E Barrate[2], D Sadi[2], O Guaitella[2], A Belinger[1], S Dap[(*)1], T Hoder[3], N Naude[(*)1]

[1] *LAPLACE, Université de Toulouse, CNRS, INPT, UPS, Toulouse, France*

[2] *Laboratoire de Physique des Plasmas, Ecole Polytechnique, Route de Saclay, F-91128, Palaiseau Cedex, France*

[3]*Department of Plasma Physics and Technology, Masaryk University, Kotlářská 2, 61137 Brno, Czech Republic*

[(*)] simon.dap@laplace.univ-tlse.fr, nicolas.naude@laplace.univ-tlse.fr

In the last few years, study on CO_2 have gained interest. One of the current goals is to find a way to convert CO_2 into value-added products. Several technologies are already used for this purpose [1]. Plasma discharges allow to induce chemistry in gases at reduced energy cost, and thus constitute an interesting way to dissociate CO_2 molecules. Studies in microwave discharges reported a conversion factor of up to 90%. On the other hand, atmospheric pressure dielectric barrier discharges (DBDs) reach a lower percentage of conversion (a few per cent) and energy efficiency. However, these discharges are easy to set up and couple with catalytic materials, scalable and may consist of different driving mechanisms. As a result, DBDs are investigated to understand in detail the resulting plasma-chemical processes. At atmospheric pressure DBDs generally work in the classical filamentary regime. Under certain conditions, a Townsend breakdown could occur, allowing the discharge to work in a diffuse regime. This was observed for DBDs in a few gas compositions, such as N_2 [2], N_2 with oxygen admixture [3] or Air [4]. More recently, we also observed this regime in pure CO_2 for a DBD at atmospheric pressure [5]. This regime constitutes an interesting way to study the discharge mechanisms involved in CO_2 plasmas because of the easy determination of the reduced electric field. Indeed, for a Townsend discharge, the electric field in the gas gap is almost constant and can be easily determined thanks to electrical measurements.

Fourier transform infrared spectroscopy (FTIR) is used to measure concentrations of CO_2 and CO molecules and evaluated the vibrational temperatures. Recent works propose to use this method in atmospheric pressure RF jets [6][7]. Our contribution will present the first results obtained with *in situ* FTIR measurements in CO_2 DBDs at atmospheric pressure. We will compare the classical filamentary regime to a Townsend regime. For this purpose, conversion factor α is defined by equation 1. Where [CO] is the measured concentration of CO and $[CO_2]$ is the measured CO_2 concentration. It is known that dissociation by electron impact is the main dissociation mechanism in atmospheric pressure DBDs [8]. The large difference of the reduced electric E/N field between both filamentary and Townsend regimes leads to a difference in the conversion ratio α, as it is visible in Figure 1. It appears that CO concentration is higher in the case of filamentary discharge due to higher dissociation rate.

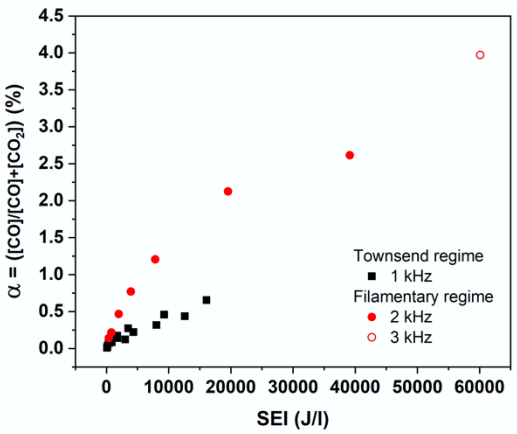

Fig. 1: Evolution of the conversion factor α as a function of the specific energy input (SEI).

$$\alpha = \frac{[CO]}{[CO] + [CO_2]} \quad (1)$$

The Figure 2 shows the rotational temperature (T_{rot}), the vibrational temperatures of CO_2 in the symmetric-bending mode (T_{12}), asymmetric mode (T_3), and the vibrational temperature of CO (T_{CO}). Despite problems in the determination of some points for certain conditions, the rotational and vibrational temperatures of CO_2 and CO were correctly evaluated. There is a non-equilibrium between T_{12} and T_3, while T_{12} remains close to T_{rot}. T_{CO} is still higher than the other temperatures and decline with the increase of the SEI. This evolution is consistent with results obtained in the literature for different discharge configurations. Our results will be discussed in detail during the presentation.

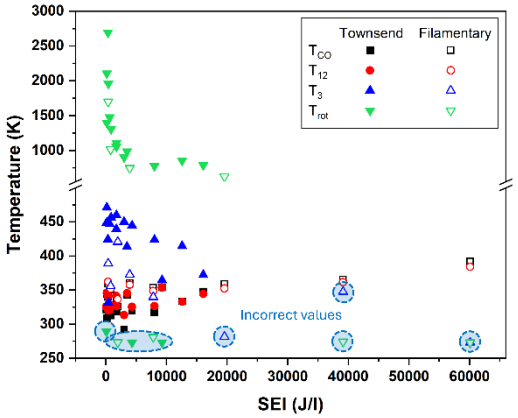

Fig. 2: Evolution of the vibrational temperatures of CO_2 and CO as a function of the specific energy input (SEI).

[1] R. Snoeckx, A. Bogaerts, *Chem. Soc. Rev.* **46** (2017) 5805.
[2] F. Massines et al., *Plasma Physics and Controlled Fusion* **47** (2005).
[3] C. Tyl et al., *Journal of Physics D: Applied Physics* **51** (2018).
[4] N. Osawa et al., *The European Physical Journal Applied Physics* **61** (2013) 24317.
[5] C. Bajon et al., *Plasma Sources Science and Technology* **32** (2023) 045012.
[6] T. Urbanietz et al., *Journal of Physics D: Applied Physics* **51** (2018) 345202.
[7] C. Stewig et al., *Journal of Physics D: Applied Physics* **53** (2020) 125205.
[8] L. D. Pietanza et al., *The European Physical Journal D,* **75** (2021) 237.

CaviPlasma: The properties of energy-efficient plasma source for the treatment of liquids on the scale of cubic metres per hour

J. Čech(*)[1], P. Sťahel[1], D. Trunec[1], R. Horňák[1], L. Prokeš[1], P. Rudolf[2], B. Maršálek[3], E. Maršálková[3], P. Lukeš[4], Z. Machala[5]

[1] *Dept. of Plasma Physics and Technology, Faculty of Science, Masaryk University, Kotlarska 2, 611 37 Brno, Czechia*
[2] *Brno University of Technology, Faculty of Mechanical Engineering, V. Kaplan Dept. of Fluid Engineering, Technicka 2896/2, 616 69 Brno, Czechia*
[3] *Institute of Botany, Czech Academy of Sciences, Lidicka 25/27, 602 00 Brno, Czechia*
[4] *Institute of Plasma Physics, Czech Academy of Sciences, U Slovanky 2525/1a, 182 00 Prague 8, Czechia*
[5] *Division of Environmental Physics, Faculty of Mathematics, Physics and Informatics, Comenius University, Mlynská Dolina, 842 48 Bratislava, Slovakia*
(*)cech@physics.muni.cz

In recent years, the study of plasma treatment of liquids, particularly water, gain high attention in the field of plasma physics [1-3]. The main liquid products of such treatment are reactive oxidizing species with, or without the nitrogen (ROS, RONS) [4-6]. Discharge-liquid technologies have found diverse applications, spanning cross-disciplinary fields such as pollution cleaning, bio-medical research, or food industry [7-9]. Despite two decades of dedicated research, a significant challenge persists: the development of an effective method for treating large volumes of liquid. In our contribution, we will present an innovative solution named CaviPlasma (depicted in Fig. 1). This approach leverages a synergistic combination of hydrodynamic cavitation and plasma generation within the cavitation vapor cloud. Our method holds promise for overcoming the technological barriers associated with large-scale liquid treatment [10-12].

The image of electric discharge generated in fast flowing liquid (water) using the latest generation of CaviPlasma technology is given in Fig. 1. The CaviPlasma technology consists of hydrodynamic circuit producing hydrodynamic cavitation cloud using Venturi nozzle. In this subatmospheric pressure environment (approx. 3 kPa at room temperature) the electric discharge is generated using a pair of metal electrodes placed in the throat of Venturi nozzle and a downstream electrode positioned at the collapsing end of hydrodynamic cavitation cloud. This configuration enables high-throughput at reduced hydrodynamic losses keeping a high plasma-chemical efficiency. The position and polarity of the nozzle electrode is indicated in green in Fig. 1.

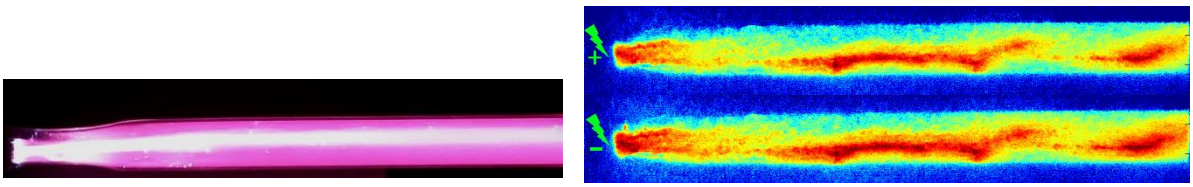

Fig. 1: CaviPlasma technology: image of discharge in reaction tube: P = 1.5 kW, f = 32 kHz, Q = 23 l/min (1.4 m^3/h), tube length 12 cm. (Left) Visual appearance, (right) phase-resolved imaging (half-periods).

In Fig. 2 the current-voltage waveforms for discharge generated in deionized (DI) water using titanium electrodes are given together with the avalanche photodiode signal following the spectrally unresolved emission of the discharge. The photodetector was positioned above the nozzle electrode. From the evolution of current and voltage we suppose that the discharge starts as a sub-µs transient spark discharge and then develops as a glow-like discharge for approx. 12 µs, repeating at the polarity reversal.

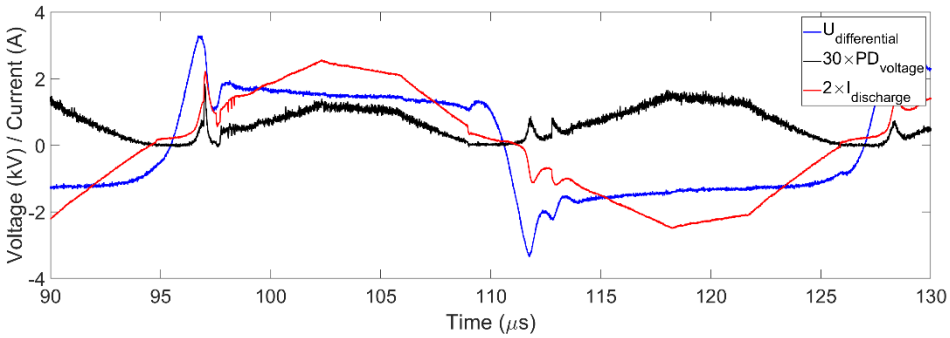

Fig. 2: CaviPlasma technology: (red) discharge current, (blue) imposed voltage, and (black) photodiode signal above nozzle electrode. Given for P = 1.5 kW, f = 32 kHz, Q = 23 l/min (1.4 m^3/h), tube length 12 cm.

In Fig. 3 the typical treatment efficiency and typical treatment conditions of lab-scale CaviPlasma unit are given for DI water, together with the experimental setup used for discharge diagnostics.

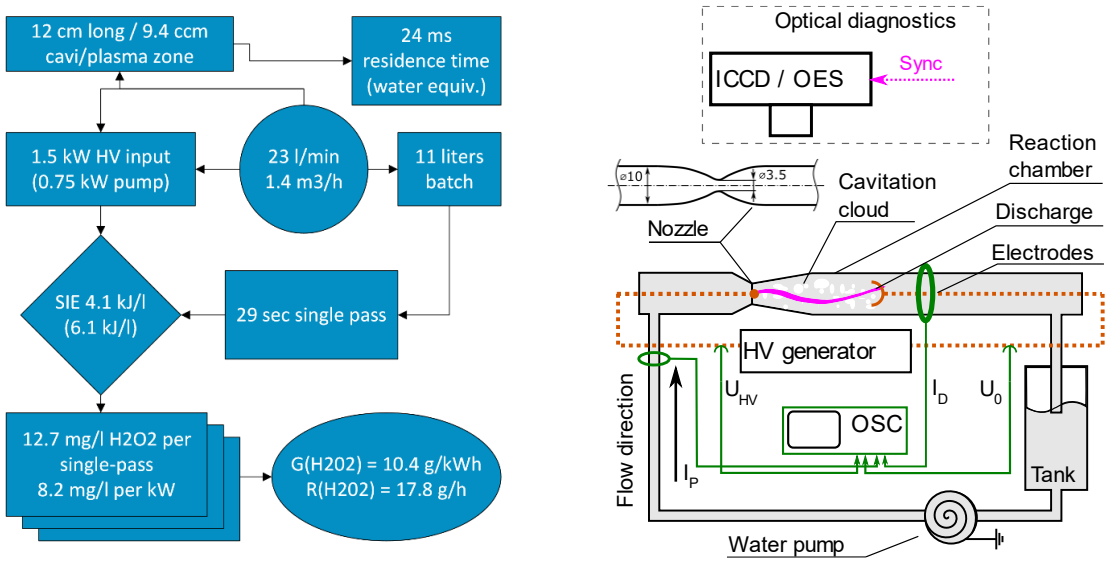

Fig. 3: CaviPlasma technology: (left) treatment efficiency graph, (right) diagnostics experimental setup.

The Czech Science Foundation is gratefully acknowledged for support of this research under project No. GA22-11456S "Exploring fundamental interactions of hydrodynamic cavitation and low-temperature plasma to enhance the disinfection effects". This work results within the collaboration of the COST Action CA19110. The cooperation among the institutions was supported by CEEPUS network AT-0063.

[1] I Adamovich *et al*., *J. Phys. D. Appl. Phys*. **50** (2017) 323001.
[2] P. J. Bruggeman *et al*., *Plasma Sources Sci. Technol*. 25 (2016) 0–125.
[3] K. Weltmann *et al*., *Plasma Process. Polym*. **16** (2019) 1800118.
[4] Z. Machala *et al*., *J. Phys. D. Appl. Phys*. **52**, (2019) 034002.
[5] K. Tachibana, T. Nakamura, *J. Phys. D. Appl. Phys*. **52** (2019) 385202.
[6] J. L. Brisset, J. Pawlat, *Plasma Chem. Plasma Process*. **36** (2016) 355–381.
[7] R. Thirumdas *et al*., *Trends Food Sci. Technol*. **77** (2018), 21–31.
[8] N. K. Kaushik *et al*., *Biol. Chem*. **400** (2018) 39–62.
[9] J. E. Foster, *Phys. Plasmas* **24** (2017) 055501.
[10] B. Maršálek *et al*., *Water* **12** (2020) 8.
[11] J. Čech *et al*., *Water* **12** (2020) 3167.
[12] P. Rudolf *et al*., PCT/WO2021115498 (2020).

CO_2 dissociation using a lab-scale microwave plasma torch: an investigation of industrially relevant parameters

Christian K. Kiefer(*)[1], Rodrigo Antunes[1], Ante Hecimovic[1], Arne Meindl[1], Ursel Fantz[1,2]

[1] *Max Planck Institute for Plasma Physics, 85748 Garching, Germany*
[2] *University of Augsburg, 86159 Augsburg, Germany*
(*) christian.kiefer@ipp.mpg.de

Under laboratory conditions, microwave plasma torches are known to be an energetically very efficient CO_2 conversion technology, for pressures ranging from 100 mbar up to atmospheric pressure. However, issues relevant for industrial application such as the wall-plug energy efficiency, including the electricity consumption of peripheral equipment, the performance for impure CO_2 streams (such as directly from carbon capture facilities), the stability at long-term operation and the suitability for intermittent operation are usually not addressed. This contribution aims to shed light on these industrially relevant parameters.

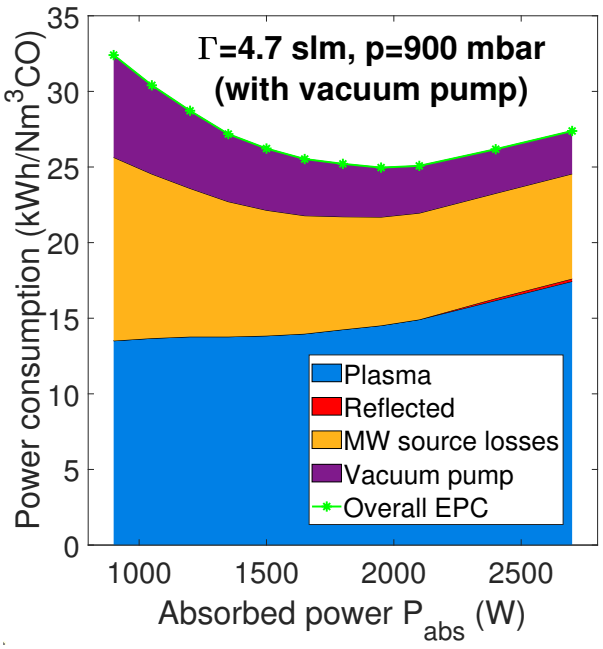

Fig. 1: Power distribution within the entire system [1].

Figure 1 illustrates the power requirements by the individual power consumption channels for the production of a certain amount of carbon monoxide. Energy efficiencies typically reported in literature consider only the plasma sub-system and are defined as follows:

$$\eta_\mathrm{p} := \chi \cdot \frac{\Delta H \cdot \tilde{\Gamma}_\mathrm{CO2,in}}{P_\mathrm{abs}}. \tag{1}$$

In this equation, χ denotes the conversion, $\tilde{\Gamma}_\mathrm{CO2,in}$ the particle inflow rate of CO_2 and P_abs the power that is absorbed by the plasma. As it is obvious from figure 1, this definition for the energy efficiency neglects several energy loss channels. However, to assess economic viability of CO_2 dissociation via microwave plasmas, it is crucial to consider the wall-plug energy efficiency η_tot taking into account all power requirements throughout the entire system:

$$\eta_\mathrm{tot} := \chi \cdot \frac{\Delta H \cdot \tilde{\Gamma}_\mathrm{CO2,in}}{P_\mathrm{active,tot}} = \eta_\mathrm{p} \cdot \eta_\mathrm{MW\ coupling} \cdot \eta_\mathrm{MW\ source} \cdot \eta_\mathrm{equipment}. \tag{2}$$

Besides the plasma energy efficiency η_p, this includes also the efficiency of the coupling of the microwaves to the plasma $\eta_\mathrm{MW\ coupling}$, the efficiency for the generation of microwaves $\eta_\mathrm{MW\ source}$ and an

energy efficiency representing the power consumption by peripheral equipment $\eta_{\text{equipment}}$.
Conversions and the different energy efficiencies of a representative power scan experiment are shown in figure 2. It is interesting to note the opposite trend behaviour of plasma energy efficiency and wall-plug energy efficiency: when the power is increased from 0.9 kW to 2.73 kW, plasma energy efficiency drops from $(27 \pm 4)\%$ down to $(25.1 \pm 1.2)\%$ while the wall-plug energy efficiency even increases from 11.1% to 15.9%. Throughout all experiments, the highest wall-plug energy efficiency that could be obtained was $\eta_{\text{tot}} = 17.9\%$, corresponding to an electrical power consumption of 19.6 kWh per produced Nm^3 of carbon monoxide.
In a durability test over 29 h, long-term stability and reproducibility of the performance of the microwave plasma torch was investigated. As it is the basic idea of Power-to-Gas technologies to utilize temporary surpluses of electrical energy from intermittent renewable sources to produce valuable gases, the plasma was not operated continuously, but switched off and on several times. Even after 29 h, no degradation in the performance was observed. In particular the short switch-on and switch-off times are a unique selling point of plasma conversion technology compared to other CO_2 conversion technologies.

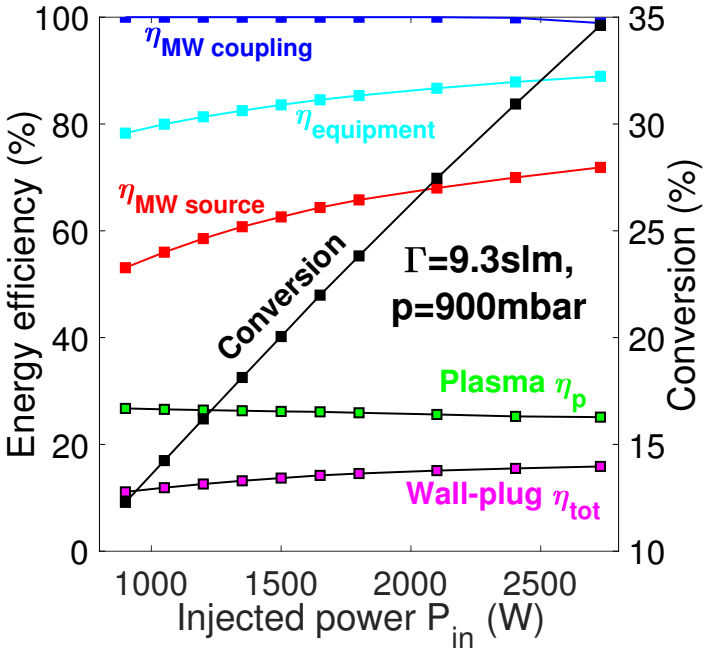

Fig. 2: Overview over conversion and the different energy efficiencies.

In order to assess the impact of impurities on the CO_2 conversion, experiments were performed in which controlled amounts of impurities (Ar, N_2, O_2, real air and synthetic air) were admixed to the CO_2 feed gas stream. Nitrogen, oxygen and argon concentrations of up to around 2% are tolerable for the plasma-based conversion. Humidity in the inflow, however, might have a very harmful effect on the conversion of CO_2. For industrial-scale application, this results in the requirement to use the microwave plasma torches only with dry CO_2 (water impurity $\leq$ 100 ppm).
Together with studies on the removal of oxygen [2], these investigations assess the industrial applicability of plasma-based CO_2 dissociation by considering the interfaces of the process. Wall-plug energy efficiencies allow direct determination of operational expenditure, a durability test demonstrated suitability to be used with intermittent electricity and experiments with gas admixture demonstrated high robustness against most relevant impurities, except for water.

[1] C. K. Kiefer et al.: Chemical Engineering Journal **481**, 148326, 2024.
[2] R. Antunes et al.: ACS Sustainable Chemistry & Engineering **11**, 15984-15993, 2023.

Atmospheric Pressure, Low Temperature Plasma applications for decontamination of agrifood products

D Aceto(*)[1], P R Rotondo[2], M Ambrico[1], G Dilecce[1], F Faretra[2], R M De Miccolis Angelini[2], P F Ambrico[1]

[1] *CNR Istituto per la Scienza e Tecnologia dei Plasmi – Sede di Bari – c/o Dipartimento Interateneo di Fisica - Università degli Studi di Bari "A. Moro", Via Giovanni Amendola 173 - 70126 Bari (BA)*

[2] *Dipartimento di Scienze del Suolo, della Pianta e degli Alimenti (Di.S.S.P.A.), Università degli Studi di Bari "A. Moro", Via Giovanni Amendola 165/A - 70126 Bari (BA)*

(*) domenico.aceto@istp.cnr.it

Over the past ten years, the demand for effective, novel, and non-chemical approaches to food production and plant protection has driven the development of new technologies. These tools aim to enhance microbial decontamination, trigger self-defense mechanisms against pathogens, and improve the biometric and nutraceutical properties of fruits and plants. Among these innovations, low-temperature plasma (LTP) has emerged as a groundbreaking tool in modern agriculture, offering diverse applications ranging from seed treatment to soil enhancement [1]. Such applications involve exposing agricultural systems to LTP, leading to the generation of reactive species such as reactive oxygen species (ROS) and reactive nitrogen species (RNS), which are widely regarded as responsible for the reported beneficial effects exhibiting significant potential in influencing plant growth, stress response, and overall crop performance. In this contribution, we report on various approches we have undertaken in an effort to exploit the potential application of LTP in the decontamination of agrifood product.

We used a volume dielectric barrier discharge (VDBD) reactor to directly treat fungal spores deposited on different agarized media to assess the decontamination potential of plasma technologies. VDBD is the richest plasma environment in terms of antimicrobial agents, exposing the samples to radiation (UV/VIS/NIR), direct impact of ions and electrons, radical and atomic species. Plasma was characterized in terms of Plasma Induced Emission (PIE) and electrical characteristic. From PIE a strong electric field was inferred together with a fast thermal heat shock (lasting hundreds of μs).

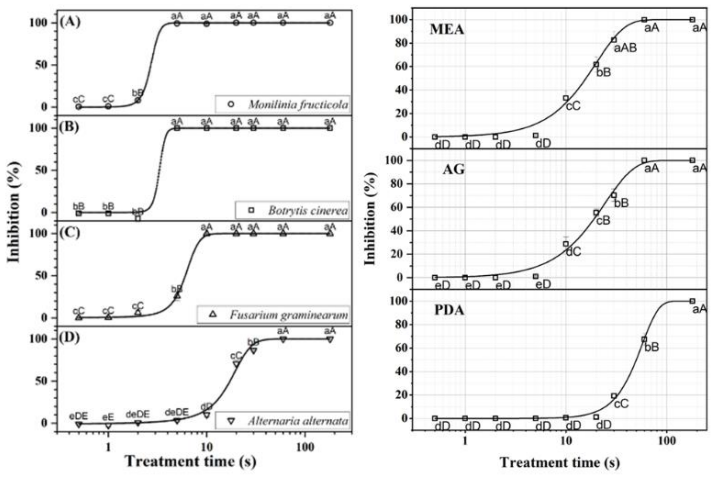

Figure 1 – A) Response of different fungal species to VDBD treatments in conidial germination tests on WA; B) Response of A. carbonarius to VDBD treatments in conidial germination tests on different agarized media.

The electrical characteristics of the discharge apparatus was shown to be dependent on the agarized medium used. In vitro studies on water agar (WA) showed that *B. cinerea* and *M. fructicola,* with unicellular conidia and similar melanin content, reacted similarly to the treatment (Figure 1A). *F. graminearum* and *A. alternata*, both having multicellular conidia, were more resistant, showing different

sensitivity likely due to a different content in melanin. In the case of *A. carbonarius* conidia the inhibition was influenced by the complexity and composition of the medium used, being PDA the artificial medium that more hindered the plasma treatment (Figure 1B). Low temperature plasma could thus be useful in the control of fungal species but different factors can influence antimicrobial activity, and treatment conditions must be carefully chosen to achieve a complete decontamination [2].

However, direct plasma treatment are confined to the surface of the samples, preventing interaction with the entire plant tissues, may expose them to harsh conditions and present a difficult to overcome technological challenge in their adaptation to the industrial pipeline. Consequently, alternative strategies are essential for specific applications, such as the production of plasma-activated media as means to vehiculate the reactive species produced in the plasma to the biological target of the treatment. Plasma Activated Water (PAW) has assumed a prominent interest, offering promising potential as a decontaminating agent. Using a custom-made surface dielectric barrier discharge (SDBD) reactor we produced PAW to elucidate its decontaminating potential against fungal (*B. cinerea*) and bacterial (*B. subtilis* and *X. campestris*) microorganisms. Almost complete decontamination was achieved by using PAWs produced in treatments of different duration (subjected to different plasma doses) highlighting the role of the concentration of RONS (in particular H_2O_2, NO_2^- and NO_3^-, shown in figure 2) in the inhibition process [3].

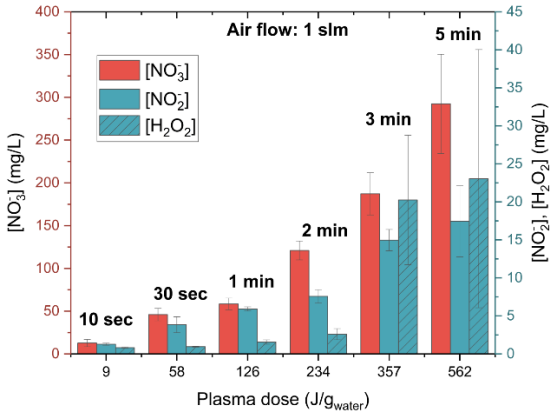

Figure 2 – Quantification of reactive species dissolved in PAW produced through a SDBD.

Finally, we present a novel and promising technological application of LTP to effectively eliminate harmful pathogens and chemical contaminants present on agricultural produce. In our approach, we utilized the effluent gas from a VDBD reactor (cylindrical geometry, coaxial electrodes) to nebulize water via the Venturi effect, resulting in the creation of Plasma Activated Fog (PAF). PAF can be conveyed in a treatment chamber, achieving an antimicrobial environment without apparently compromising the integrity or nutritional value of the food. RONS are vehiculated to the biological substrate by the microdroplets, thus increasing the possibility of their interaction with the sample. Moreover, the dimension of the droplets (< 5 μm) prevent the sample for becoming wet during the treatment, thus further limiting the rotting process and extending the shelf-life of the treated produce. Notably, our preliminary findings include successful decontamination against various fungal pathogens, the elimination of chemical pesticides and insecticides, as well as a potential insecticidal effects [4].

Acknowledgments

D.A. and P.F.A. Acknowledge the project ‘’Plasma Reactors for Agrifood industry (PlasmaReA)’’ b5667f07, in the framework of POC PUGLIA FESRT-FSE 2014/2020 Fondo Sociale Europeo (C(2015)5854 del 13/08/2015) Riparti (assegni di Ricerca per riPARTire con le imprese).

References

[1] E M Konchecov et al, *J. nt. J. Mol. Sci.* **2023**, *24*(20), 15093
[2] P R Rotondo et al, *Plasma Chem Plasma Process* **2023**, 43, 1819–1842
[3] P R Rotondo et al., „*Antimicrobial activity of plasma activated water against bacteria and fungi affecting the quality of plant products*“, under submission
[4] D Aceto et al, „*Plasma activated fog: a novel response to the agrifood industry demands*“, under submission

Optical emission spectroscopy characterization of a novel atmospheric pressure argon/ammonia gliding arc

S. Marín-Meana[1,2], M. Oliva-Ramírez [1,2], M.C. García [(*)3], J. Cotrino[2], A. R. González-Elipe[1], A. Gómez-Ramírez[1,2]

[1] *Laboratory of Nanotechnology on Surfaces and Plasma. Instituto de Ciencia de Materiales de Sevilla (CSIC-Universidad de Sevilla), Avda. Américo Vespucio 49, E-41092 Seville, Spain*

[2] *Departamento de Física Atómica, Molecular y Nuclear, Universidad de Sevilla, Avda. Reina Mercedes, E-41012 Seville, Spain*

[3] *Departmento de Física Aplicada, Radiología y Medicina Física, Campus Rabanales, Edificio C2, Universidad de Córdoba, 14071 Córdoba, Spain (*)*

fa1gamam@uco.es

Gliding arc plasma reactors find applications in a wide variety of fields, including environmental remediation, waste treatment, and energy conversion [1]. The energetic nature of the plasma discharge facilitates the decomposition of volatile organic compounds (VOCs), pollutants, and other hazardous substances present in gas streams, offering a sustainable approach to air and water purification. Moreover, the highly reactive species generated in gliding arc reactors with low power consumption make them suitable candidates for the synthesis of value-added chemicals and materials from renewable sources, contributing to the advancement of green chemistry and sustainable manufacturing practices.

In this work, we use a novel gliding arc reactor where the active electrode is an ovoid and the grounded electrode consists of a mesh that surrounds the former, both made of stainless steel (this configuration provides a large discharge region). A sinusoidal electrical signal (3kV and 300 Hz) was used to ignite the discharge and different mixtures of Ar and NH_3 were used as inlet gases. The emission of the plasma discharges was registered using a Horiba Ltd., Jobin-Yvon FHR640 spectrometer equipped with a 1201 grooves/mm diffraction grating centered at 330 nm. The emission was transversely collected from the most intense region of the plasma near the central electrode and recorded with a spectral resolution ranging from 0.05 to 0.1 nm.

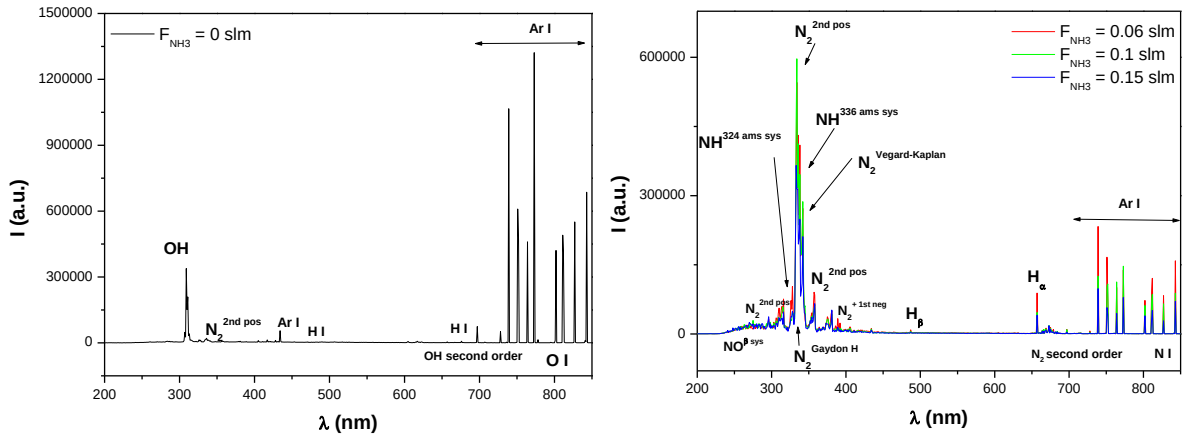

Fig. 1: OES spectrum detected for (left) the pure Ar and (right) Ar/NH_3 discharges.

For the pure argon discharge (Fig. 1(left)), the emission of atomic argon lines dominated. Excited species OH*, O*, and H* were also detected, which proved that some air entered the reactor. The addition of ammonia into the main gas resulted in a significant reduction in the emission of argon lines, while new molecular bands corresponding to species containing nitrogen (N_2, NH, N_2^+) appeared in the spectrum (Fig.1 (right)). Additionally, the emission of atomic hydrogen lines intensifies, and atomic nitrogen lines appear. The intensity evolution with the ammonia flow rate of the different excited species was tracked (Fig. 2).

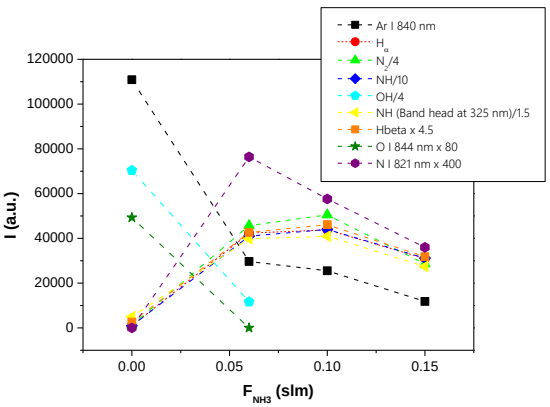

Fig. 2: Excited species in the plasma.

The plasma electron density (n_e) was measured from the Stark broadening of both H_α and H_β lines [2] (Fig. 3 (left)). A maximum was detected when moderate fractions of NH_3 were introduced in the discharge. The gas temperature (T_g) was measured from the collisional broadening of Ar I 840.82 nm emission line following the method proposed in reference [3] (Fig. 3 (right)). The gas temperature exhibited an increase upon NH_3 introduction. It's worth noting that the values of the rotational temperature $T_{rot,N2}$ derived from the simulation of the N_2 ($C^3\Pi \rightarrow B^3\Pi$) rotational band (band head at 353.67 nm) are notably higher than T_g, thus overestimating this plasma parameter.

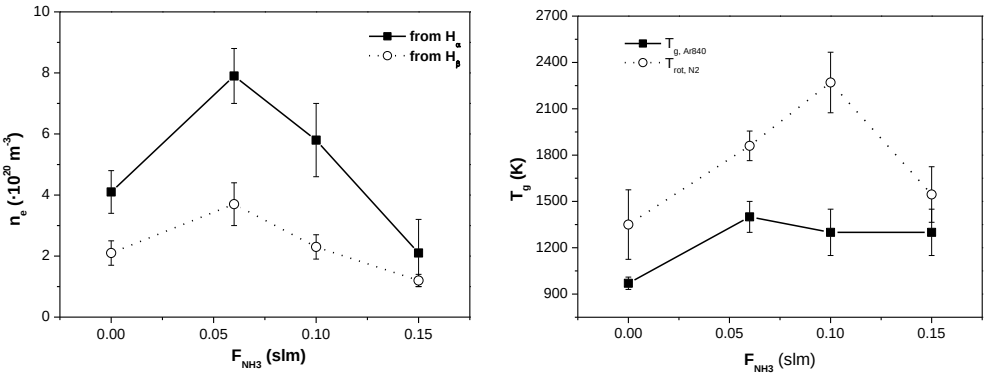

Fig. 3: n_e (left) and T_g (right) evolutions with NH_3 flow rate.

[1] A. Khan et al., *Journal of the Energy Institute* **109** (2023), 1743-9671
[2] C. Yubero, M.D. Calzada, M.C. Garcia, *J. Phys. Soc. Japan* **74** (2005) 2249–2254.
[3] A. Rodero, M.C. García, *J. Quant. Spectrosc. Radiat. Transf.* **198** (2017) 93–103.

Acknowledgements

The authors acknowledge projects PID2020-114270RA-I00, and PID2020-112620GB-I00 funded by MCIN/AEI/10.13039/501100011033, project TED2021-130124A-I00 funded by AEI/10.13039/501100011033/Unión Europea Next Generation EU/PRTR and projects P18-RT-3480, US-1381045, and US-1380977 funded by Conserjería de Economía, Conocimiento, Empresas y Universidad de la Junta de Andalucía (PAIDI-2020) and Programa Operativo Feder 2014-2020. M. Oliva-Ramírez acknowledges financial support from Grant IJC2020-045087-I funded by: MCIN/ AEI /10.13039/501100011033 and the European Union NextGeneration EU /PRTR and S. Marín Meana acknowledges financial support from Grant PRE2021-100465 funded by MCIN/AEI/10.13039/501100011033 and FSE+.

Toxicity reduction of landfill leachate by direct plasma treatment

E. Benova[(*)1], P. Marinova[1,2], T. Bogdanov[1,3], Y. Todorova[1,4], M. Kirilova[1,4], I. Yotinov[1,4], I. Schneider[1,4], Y. Topalova[1,4]

[1] *Clean & Circle Centre of Competence, Sofia University, 1164 Sofia, Bulgaria*

[2] *University of Forestry, Faculty of Forest Industry, 1756 Sofia, Bulgaria*

[2] *Medical University of Sofia, Faculty of Medicine, 1431 Sofia, Bulgaria*

[3] *Sofia University "St. Kliment Ohridski", Faculty of Biology, 1164 Sofia, Bulgaria*

[(*)] geni_benova@abv.bg

Leachate from solid waste landfills is highly toxic because it contains various organic and inorganic recalcitrant compounds including PFAS (per- and polyfluoroalkyl substances). The treatment of this complex mixture of environmental concern contaminants is a challenge for waste/wastewater management and conventional technologies usually have low efficiency. For this reason, the development of advanced approaches and innovative technologies for the removal of pollutants in leachate and sludges is an area of growing research interest in the last few years. Plasma methods have the potential to successfully contribute to solving existing treatment problems and to be the basis of effective hybrid technologies for the removal of hazardous pollutants [1].

Two types of plasma sources for landfill leachate treatment are used in this work – Surface-wave-sustained Argon plasma torch and DBD discharge with a liquid electrode. Both discharges operate at atmospheric pressure.

The Argon plasma torch is produced and sustained by 2.45 GHz electromagnetic wave excited by a Surfatron type wave exciter and travelling along the plasma–dielectric interface (Fig. 1a). Various types of such plasma sources knowing as surface-wave-sustained discharges (SWD) exist and can operate in wide range of discharge conditions producing non-equilibrium plasma with electron temperature T_e ~ 1–2 eV and much lower temperature of heavy particles (gas temperature T_g). Because of the charged particles (electrons and ions), UV radiation, reactive particles (excited atoms, molecules and radicals), electromagnetic field and the temperature such plasmas are highly reactive and useful for various applications [2]. In this work for the purpose of landfill leachate treatment the discharge conditions chosen are: wave power 100 W, Ar gas flow 3 l/min and treatment time is varied (1 min, 2 min, 3 min).

a) b)

Fig. 1: Experimental set-up for treatment of landfill leachate by a) Argon plasma torch; b) DBD discharge with liquid electrode.

The DBD discharge operates at electrical power of 36 W and frequency . The upper electrode is powered and the lower grounded electrode is a specially designed Petri dish with graphite electrode on the bottom and the treated liquid inside – the liquid electrode (Fig. 1b). The discharge is produced in the open space so the working gas is air. The treatment time is the same as for the Argon plasma torch, 1 min, 2 min, 3 min.

The toxicity of treated and untreated samples was studied by fluorescence staining of test bacterial culture *Escherichia coli* (Migula) Castellani and Chalmers (ATCC 700728). The fluorescence images were taken with a Leica DM6 B (Leica Camera AG, Wetzlar, Germany) epifluorescent microscope (Fig.2). The method assesses the intensity of metabolic processes in bacterial cells and their inhibition in the presence of toxic agents. The obtained images were processed with a digital analysis program daime 2.2 (University of Vienna, Vienna, Austria). The changes in the complex toxicity of the samples due to plasma treatment were assessed by comparing the effect of treated and untreated samples on two indicators of the test bacterial culture: (1) the share of viable cells; (2) the intensity of the CTC fluorescence. The share of viable bacteria was calculated based on the number of CTC-stained cells (metabolic active cells) and DAPI (all cells, including dead ones). The intensity of the fluorescence emitted by the CTC-stained cells corresponded to their level of metabolic activity [3].

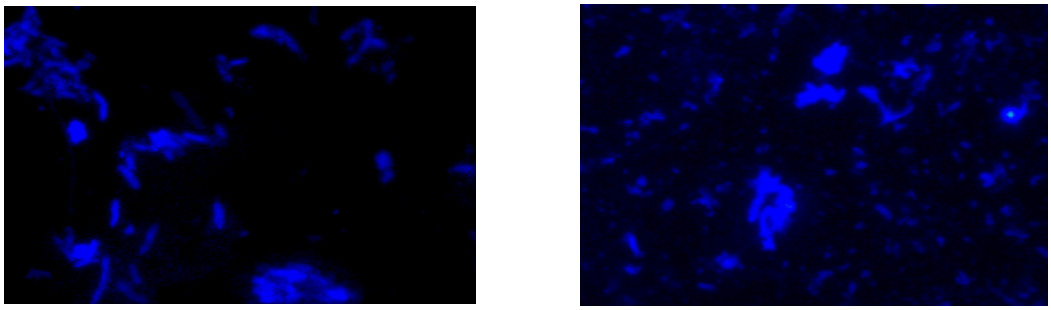

a) b)

Fig. 2 Fluorescence images *E. coli* cells from epifluorescent microscope: a) untreated leachate; b) plasma treated leachate.

The results obtained show that the cells in the presence of highly toxic leachate after 1 hour of exposure are totally inhibited – their metabolic activity and the share of viable cells are really low. After plasma treatment the metabolic active and the share of viable cells increase. The reduction of toxicity is obtained for both Argon plasma torch and DBD leachate treatment.

Acknowledgement:

This work is supported by the PROMISCES (Preventing Recalcitrant Organic Mobile Industrial chemicalS for Circular Economy in the soil-sediment-water System) project which has received funding from the European Union's Horizon 2020 research and innovation program under Grant Agreement No 101036449.

[1] R. K. Singh *et al*., *J. Hazardous Materials* **408** (2021) 124452.

[2] F. Krčma *et al*., *J. Phys. D: Appl. Phys*. **51** (2018) 414001.

[3] Y. Topalova *et al*., *Biomedicines* **10** (2022) 672.

Impact of convective flow on filaments in narrow gap DBD

A Ashirbek [(*)1,2], Y Ussenov[3], M Dosbolayev[4], M Gabdullin[5] and T Ramazanov[4]

[1] *Institute of Applied Sciences and IT, Almaty, Kazakhstan*

[2] *NNLOT, Al-Farabi KazNU, Almaty, Kazakhstan*

[3] *MAE Department, Princeton University, Princeton, United States of America*

[4] *IETP, Al-Farabi KazNU, Almaty, Kazakhstan*

[5] *Kazakh British Technical University, Almaty, Kazakhstan*

[(*)] azamat@physics.kz

Dielectric Barrier Discharges (DBDs) find extensive applications across diverse technological domains such as plasma medicine, agriculture, plasma material deposition, surface modification, additive manufacturing, plasma catalysis, and active flow control [1, 2]. In the case of volume DBD with symmetric-plane discharge electrodes driven by a sinusoidal high voltage (HV) signal, MD channels are randomly distributed. These channels exhibit complex collective phenomena and give rise to diverse self-organized patterns. Understanding the collective interaction and dynamics of MD channels is crucial not only for stationary volumetric DBDs in the air but also for DBDs influenced by external factors. The most popular factor of them is gas flow [3], there is also an unusual approach using convective flow or gas flow convection.

The gas flow convection in the discharge gap plays a role in determining the spatial distribution of charged particles, which in turn contributes to the pre-ionization process in the MD channels in DBD. This pre-ionization in the discharge gap is a crucial element influencing the subsequent development of individual microdischarges and the formation of collective phenomena, such as self-organized patterns. Even in the absence of external gas flow, particle transport occurs due to intense heat transfer and natural convection, since microdischarges in the dielectric gap are a local source of heat. Despite DBD being a transient thermal nonequilibrium discharge, Joule heating coupled with chemical energy dissipation within the discharge volume and the dissipation of a portion of the applied power as heat on dielectrics actively heat the walls of the discharge cell. We concluded in our previous work [4] that the continuous self-heating of the walls of barrier electrodes during the discharge operation generates natural convective flow due to the thermal gradient of the discharge cell electrodes and surrounding air. The velocity of the MD channels rises, following the convective flow velocity due to the elevated thermal gradient. During the self-heating of the barrier electrodes, the number of the MD channels increases, and the distance between the MD channels decreases which leads to more surface density of filaments on the dielectrics. The gas heating in the gap enhances the reduced electric field of the discharge due to a reduction in the density of gas molecules after heat expansion, which in turn results in the growth of the number of currents, amplitude, and reduction in the discharge sustaining voltage.

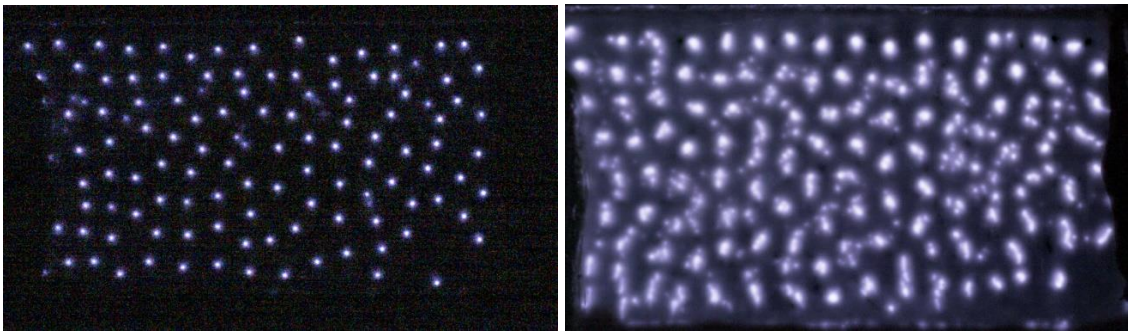

Fig. 1: Photos of the top view of the dynamics of MD behavior at an interelectrode distance of 1 mm at frame rates of 1000 and 24 fps

In this work, we are interested in investigating the effect of the balance between the forces driving the convective flow and the viscous forces at the wall in the boundary region when the discharge gap is significantly narrowed. The dynamics of filaments in the narrowed discharge gap are compared with our previous results on convective air flow [4]. Discharge parameters such as microdischarge and gas flow average velocities, and discharge and dielectric layer temperatures were also measured and compared with previous results. From high-speed imaging of the discharge (fig. 1) and Particle Image Velocimetry (PIV) analysis, the movement of the filaments is obtained, and the average velocity is measured at a certain temperature of the dielectric layer. The convective flow in the interelectrode volume has been modeled using COMSOL Multiphysics.

[1] R. Brandenburg, *Plasma Sources Science and Technology* **26** (2017) 5 053001.
[2] U. Kogelschatz, *Plasma Physics and Controlled Fusion* **46** (2004) 12B B63–B75.
[3] Ye. Ussenov *Plasma Phys. Reports* **46** (2020) 459–64
[4] Ye. Ussenov *Phys. Scr.* **99** (2024) 035608

Investigation of the liquid velocity gradient induced by a plasma dielectric barrier discharge and its impact on reactive species generation

L. Alomari(*)[1], T. Orriere[1], R. Bellanger[1], B. Teychene[2], E. Moreau[1]

[1] *Institut PPRIME, UPR CNRS 3346, Université de Poitiers, ISAE-ENSMA, 86962 Futuroscope, France*

[2] *Institut de Chimie des Milieux et des Matériaux de Poitiers, UMR CNRS 7285, Université de Poitiers, ENSIP, 86022 Poitiers Cedex, France*

(*) lara.alomari01@univ-poitiers.fr

In the applications of atmospheric pressure plasma interacting with a liquid phase, ensuring optimal plasma efficiency relies significantly on the effective transport of reactive species from the gas to the liquid and within the liquid itself. In the absence of external forces, and considering the relatively slow diffusion of these species inside the liquid, their movement is predominantly governed by the plasma-induced liquid flow. Depending on input parameters that affect the net force exerted on the liquid phase, two distinct plasma-induced liquid flows can be observed: 1) a linear downward flow occurring along the plasma discharge axis [1], and 2) an upward flow accompanied by the formation of vortices on both sides of the plasma discharge axis [2].

Several potential driving forces contribute to the generation of liquid flow, such as thermal instabilities arising from localized heating at the plasma-liquid interface, electrohydrodynamic (EHD) forces, mechanical coupling with the gas flow, pressure waves as well as the influence of the electric field and electrical surface stresses. Dickenson *et al.* [3] used a 2D-axisymmetric model and validated it through Particle Image Velocimetry (PIV) measurements to characterize the mechanical interaction between plasma and liquid in a pin-water electrode system. Their findings indicate that the driving mechanism for liquid flow is correlated with the charge relaxation time of the liquid. Interestingly, in their argon atmospheric pressure plasma jet (APPJ), Kawasaki *et al.* [1] demonstrate the possibility to switch the direction of the plasma-induced liquid flow simply by changing the frequency. Stancampiano *et al.* [2] investigated the origin of the vortex formation with a helium APPJ, and they conclude that the main causes are EHD forces and gas flow tangential components induced by the plasma jet.

The present study aims to extend our understanding of this phenomenon. In our experimental setup, the plasma discharge is ignited at the tip of a tungsten needle with a curvature radius of 100 µm. The needle is placed above an optical glass tank, filled with 20 mL of the liquid to be treated. The distance between the tip and the liquid surface (the electrode gap) is varied between 2 and 8 mm using a micrometer screw. The tank is placed symmetrically on a piece of copper tape (90 × 50 mm^2), which serves as the grounded electrode. The needle is connected to a high voltage amplifier (Trek 20 kV, 20 mA), which amplifies a low sinusoidal voltage produced by a function generator. The voltage between the needle and ground (discharge voltage) is measured with a high voltage probe (LeCroy PPE, 20 kV, 100 MHz). Note that this voltage is the sum of the voltages across the electrode gap, the liquid phase and the dielectric (the reactor bottom). The current is obtained by measuring the voltage across a shunt resistor. All signals are recorded with a digital oscilloscope (HDO6054, 500 MHz, 5 GS/s).

PIV measurements were conducted during the discharge process to obtain the velocity vector fields in the liquid. For this purpose, 5-µm polyamide particles doped with rhodamine B were used as tracers. A 32-mJ pulsed Nd:YAG laser, operating at 532 nm with a pulse duration of 7 ns, was employed to create two successive laser sheets with an adjustable time delay. Concurrently, a high-resolution camera (Imager pro X 4M, 2048 × 2048 pixels) was utilized to record a single laser pulse in each frame. The

2D velocity vector field for each pair of camera frames was then computed through a cross-correlation procedure.

The initial phase of the study aimed to confirm the key role of liquid flow in the transport of reactive species. To observe the motion of reactive species, we employed a potassium iodide solution. In fact, iodide ions can react with various oxidant species, resulting in the production of iodine that has a color spectrum ranging from yellow to brown, depending on its concentration. Consequently, in situ local iodine concentrations were obtained through grey levels acquired using a black and white camera (Point Grey, FL3-U3-32S2M-CS, 1600 × 1200 pixels). Prior calibration ensured a correlation between grey levels and known iodine concentrations in prepared solutions. In parallel (in a separate experiment conducted under the same conditions), PIV measurements provided information on the flow associated with the discharge over the potassium iodide solution.

As an illustration of the obtained results, Figure 1a displays the mean velocity vector field corresponding to a 5-minute plasma treatment of the potassium iodide solution, while Figure 1b presents the mean grey level image under identical experimental conditions. The formation of two vortices is observed on either side of the discharge axis, extending to a depth of approximately 10 mm below the interface (Fig.1a). Moreover, there is a significant velocity gradient between the plasma/liquid interface and the bulk liquid. The velocity is maximum at the plasma/liquid contact point, reaching 2 cm/s. A notable similarity exists between the higher velocity zones (Fig. 1a) and the regions with elevated iodine concentration (Fig. 1b), highlighting the potential to optimize the generation of reactive species and, consequently, the efficiency of plasma discharge, simply by controlling transport phenomena. To achieve this control, in the second phase of our study, we examined several parameters independently, including frequency, voltage, gap distance (with pure water as the liquid for these three variables), surface tension (using mixtures of ethanol and pure water with varying ethanol percentages), conductivity (using potassium chloride solutions at different concentrations) and discharge duration. The influence of all these input parameters will be discussed during the oral presentation.

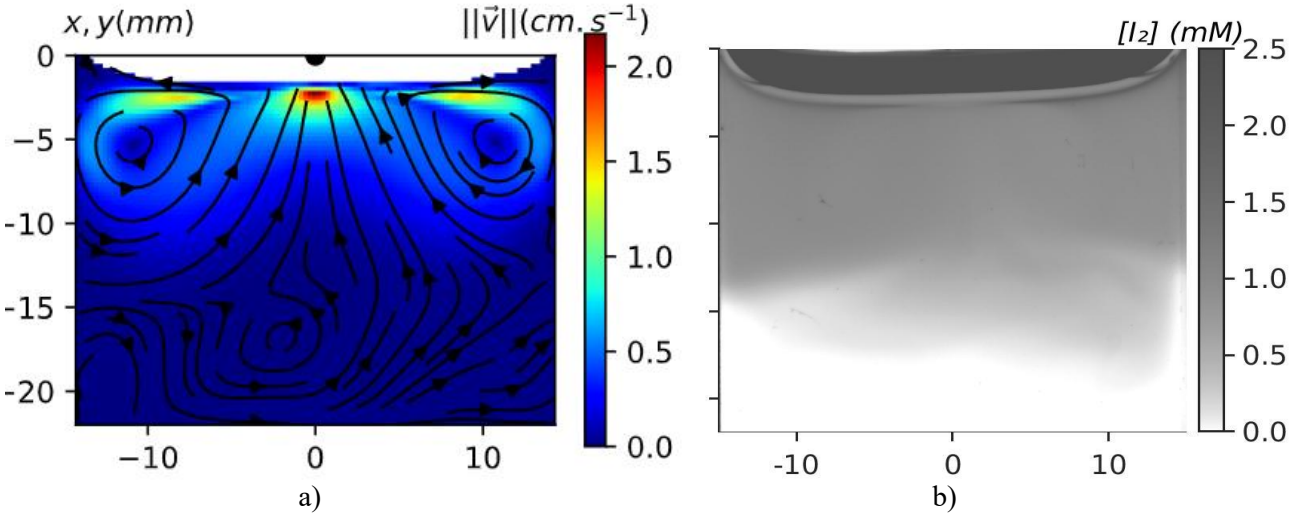

Fig 1: a) Mean velocity vector field and b) iodine production during 5 minutes of plasma treatment. Gap = 2 mm, frequency = 2 kHz and voltage = 9 kV.

[1] T. Kawasaki et al. , Jpn. J. Appl. Phys. ***62*** *(2023) 060904.*

[2] A. Stancampiano et al., Plasma Sources Sci. Technol. ***30*** *(2021) 015002.*

[3] A. Dickenson et al., J. Appl. Phys. ***129*** *(2021) 213301.*

Thermal modelling of an atmospheric pressure cylindrical DBD reactor for NOx removal

Nicolas Bente[1], Hubert Piquet[1], Nofel Merbahi[1], Eric Bru[1]

[1] *LAPLACE, Université de Toulouse, CNRS, INPT, UPS, Toulouse, France*

(*) nicolas.bente@laplace.univ-tlse.fr

Nitrogen oxides (NOx) emissions pose significant environmental and health issues, motivating the exploration of innovative technologies for their abatement. Cold plasma systems, particularly dielectric barrier discharge (DBD), have emerged as promising solutions for NOx reduction. Our investigations focus on understanding the impact of all physical parameters – electrical, thermal, fluidic, and geometric – on deNOx efficiency. To conduct these studies, we developed a complete deNOx test bench comprising an open-flow cylindrical DBD reactor [Fig. 1] operating at atmospheric pressure with a synthetic N2/NO gas mixture. The power supply, an AC square-wave current source designed at LAPLACE [1], allows adjustable frequency, amplitude, and duration of the current pulses.

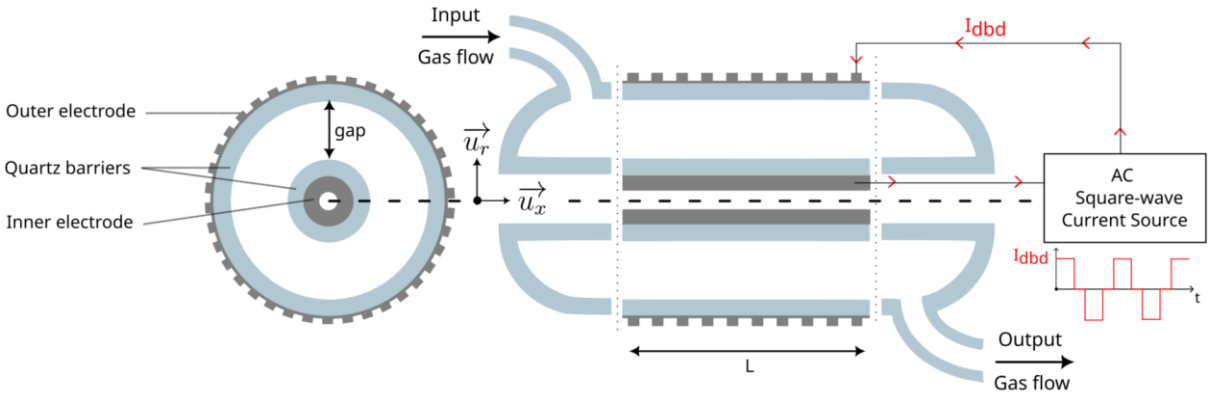

Figure 1: Reactor schematic

Initial simulations of the process using ZDPlasKin [2] and BOLSIG+ [3], two plasma chemistry simulation programs developed at LAPLACE lab., point out the crucial influence of gas temperature on treatment efficiency. However, to our knowledge, thermal studies of this reactor type are lacking. To address this gap, and to understand better the relation between the experimental setup and the performances, we propose a comprehensive analytical thermal model of our reactor. Under assumptions of steady-state thermal and laminar flow regime, the reactor can be discretized in infinitesimal dx length slices along the x-axis direction and modelled by three different temperature layers [Fig. 2]: one for the gas and two others for outer and inner quartz & electrodes. A thermal balance on each layer leads to the following coupled analytical differential equations:

$$\begin{cases} \lambda_1 S_1 r \dfrac{d^2T_1}{dx^2} - T_g - T_1\left(1+\dfrac{r}{R}\right) = \dfrac{r}{R}.T_0 & (1) \\ q_m c_g r \dfrac{dT_g}{dx} + 2T_g - T_1 - T_2 = r.p_j(x) & (2) \\ \lambda_2 S_2 r \dfrac{d^2T_2}{dx^2} - T_g + T_2 = 0 & (3) \end{cases}$$

Equation (2) describes the axial gas temperature distribution $T_g(x)$. Two modes of heat transfer are considered for the gas: convection at interfaces with outer and inner layers, and transport.

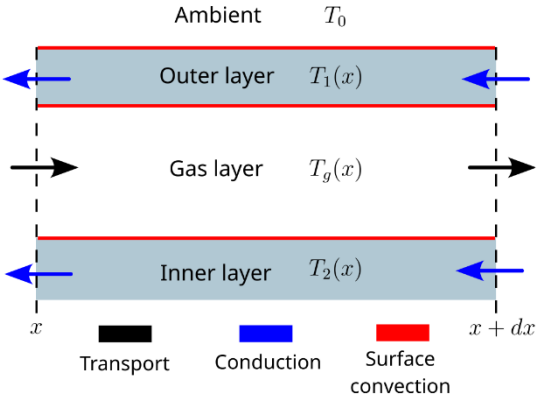

Figure 2: Heat transfer modes on a dx length slice

The heat transport is modelled by the first order x-derivative term, with q_m the gas mass flow rate and c_g the gas isobaric specific heat capacity. The plasma contribution is modelled via the source term $p_j(x)$ which represents the Joule losses density: we consider that all electrical power injected into the reactor is converted into heat. $p_j(x)$ has no variation along the radial direction, meaning that plasma sheath phenomenon is neglected. Equations (1) and (3) describe outer $T_1(x)$ and inner $T_3(x)$ wall temperatures. Two modes of heat transfer are considered: conduction along the x-axis and convection at interfaces with both gas and ambient air. The x-axis heat conduction is modelled by the second order x-derivative term with λ the thermal conductivity of the layer and S its axial cross-section surface. The two convective thermal resistances r and R model heat exchange at gas/walls interfaces and outer layer/ambient air interface. All these values can be easily determined for our test bench, except *R*, mainly influenced by parameters such as ambient air velocity, flow regime and hydraulic diameter that we don't know precisely. We chose *R* within a coherent range that matches similar flow found in literature [4]. We present [Fig. 3] two numerical solutions of the gas temperature distribution with uniform p_j. We also simulated a more complex equivalent 3D finite elements model on COMSOL for comparison. The experimental gas temperature distribution, which is measured in steady state via spectroscopic techniques [5] on a uniform plasma, shows good agreement with models.

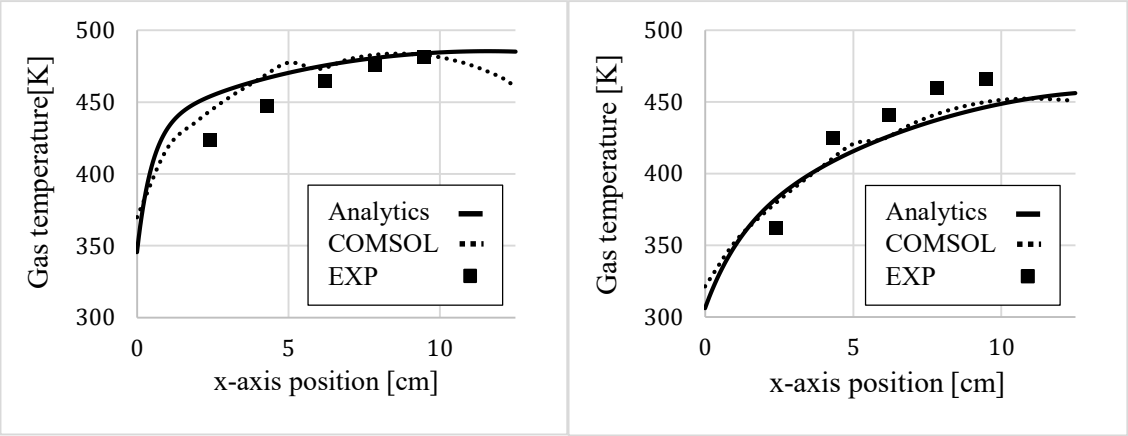

Figure 3: Gas temperature distribution comparison for $p_j = 360\ W/m$ at two gas flow rates : [Left : 2 LPM – Right : 6 LPM]

Conclusion: a concise and analytically thermal model is presented that characterizes the axial gas temperature distribution within a cylindrical open-flow DBD. Coupled with plasma chemistry simulator programm, this approach helps identifying the key physical parameters affecting deNOx treatment, thereby facilitating its enhancement. The same approach is also applicable for sealed systems, such as lamps.

[1] Rueda, V., Wiesner, A., Diez, R., & Piquet, H. (2019). *Power Estimation of a Current Supplied DBD Considering the Transformer Parasitic Elements.* IEEE Trans. on Industry Appls. DOI:10.1109/TIA.2019.2933519

[2] Pancheshnyi S., Eismann B., Hagelaar G.J.M., Pitchford L.C., Computer code ZDPlasKin, http://www.zdplaskin.laplace.univ-tlse.fr, University of Toulouse, LAPLACE, CNRS-UPS-INP, Toulouse, France, 2008.

[3] Hagelaar G. J. M., Pitchford L. C., (2005). *Solving the Boltzmann equation to obtain electron transport coefficients and rate coefficients for fluid models*, Plasma Sources Sci. Technol. **14**, 722-733. DOI:10.1088/0963-0252/14/4/011

[4] Rohsenow W. M., Hartnett J. H., Cho Y. I., *Handbook of heat transfert*. Third Edition.

[5] Britun, N., Gaillard, M., Ricard, A., Kim, Y. M., Kim, K. S., & Han, J. G. (2007). *Determination of the vibrational, rotational and electron temperatures in N2 and Ar–N2 rf discharge*. Journal of Physics D: Applied Physics, 40(4), 1022–1029. DOI:10.1088/0022-3727/40/4/016

Studies of the self-absorption of boron doublet at 249nm for an accurate CF-LIBS analysis of diboride thin layers.

Sanath J Shetty(*)[1], Sahithya Atikukke[2], Matej Veis[1], Tomáš Roch[1], Pavel Veis(*)[1]

[1] *Department of Experimental Physics, FMPI, Comenius Univ., Mlynská dol. F2, Bratislava 84248, Slovakia.*

[2] *Department of Astronomy, Physics of the Earth, and Meteorology, FMPI, Comenius Univ., Mlynská dol. F2, Bratislava 84248, Slovakia.*

(*)sanath.shetty@fmph.uniba.sk, pavel.veis@fmph.uniba.sk

With the increasing demand for lightweight refractory materials in the aerospace and machinery industries, transition metal borides (TMBs) have emerged as a promising solution. Coatings of TMBs, particularly those with an AlB2-type crystal structure, have been shown to enhance material strength significantly [1]. This study aims to accurately quantify the elemental composition of various TMBs using Calibration-Free Laser Induced Breakdown Spectroscopy (CF-LIBS).

LIBS is a well-established technique for characterizing materials through atomic emission spectroscopy, offering rapid and versatile analysis. The sample analyzed is a thin film of zirconium diboride (ZrB2) deposited on a silicon substrate. Plasma generation was achieved through laser ablation with an Nd:YAG laser operating at 1064 nm. Spectra were recorded at various gate delays and widths using an echelle spectrometer (ME5000 Andor tech.) with a bandwidth of 230-975 nm and a resolution of 4000. The experiments were performed in atmospheric conditions within a chamber designed for raster scanning of the sample. Upon thorough examination of the data hence obtained, the prominent spectral doublet of Boron I at 249.67 nm and 249.77 nm seems to exhibit self-absorption. To address this, an alternative approach involving experimentation in a vacuum UV spectral range under oxygen free atmosphere [2], which would allow observation of additional self-absorption free lines in the vacuum UV range using dedicated optics and vacuum setup. A preliminary study was conducted to observe and address the self-absorption of the aforementioned Boron doublet. An introductory analysis using a mixed TMB ($ZrTaB_2$) demonstrated accurate transition metal ratios (Ta: Zr), however, the estimation of boron quantity appears to be understated [6]. Accurate elemental quantification thus necessitates correction for the self-absorption of the doublet peak. Various analytical methods for self-absorption correction in LIBS have been utilized in the literature, including the Curve of Growth (COG) [3], Internal Reference Self-Absorption Correction (IRSAC) [4], and one-point calibration [5]. In this work, we are presenting the reconstruction of the self-absorbed peak that remediates the inaccuracy caused by self-absorption and leads to an accurate quantitative analysis of the sample.

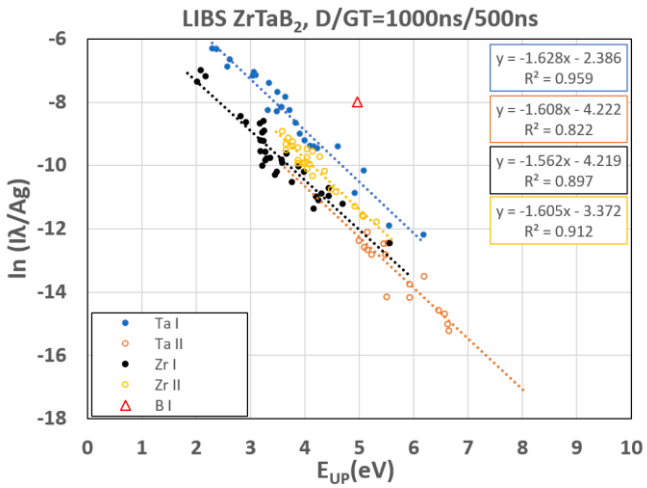

Fig. 1: Boltzmann Plot for $ZrTaB_2$ with only one peak for Boron from one of our recent works [6].

Acknowledgement. The authors would like to thank the financial support provided by the Scientific Grant Agency of the Slovak Republic (VEGA-1/0803/21, VEGA-2/0144/21) and by the Slovak Research and Development Agency (APVV16-0612, APVV-22-0548). This work has been carried out within the framework of the EUROfusion Consortium, funded by the European Union via the Euratom Research and Training Programme (Grant Agreement No 101052200 - EUROfusion). Views and opinions expressed here are however those of the author(s) only and do not necessarily reflect those of the European Union or European Commission. Neither the European Union nor the European Commission can be held responsible for them.

[1] M. Magnuson et al, *Vacuum* vol. **196** (2022) 110567.
[2] P. Veis, A. et al, *Plasma Sources Science and Technology* **27** (2018) 95001.
[3] D. Bulajic et al, *Spectrochimica Acta Part B: Atomic Spectroscopy* **57** (2002) 339–353.
[4] L. Sun et al, *Talanta*, **79** (2009) 388–395.
[5] Z. Hu et al, **48** (2023) *Opt Lett* 1.
[6] M. Veis et al. *Nordic LIBS conference*, Tampere, Finland (2024).

Effect of power density in cathode plasma of a vacuum arc

Isak I. Beilis

Department of Physical Electronics, School of Electrical Engineering, Faculty of Engineering, Tel Aviv University, Tel Aviv 69978, Israel; ***beilis@tauex.tau.ac.il****)*

Vacuum arc is an electrical discharge, in which the current supported by localized plasma generation in regions at the cathode surface called cathode spots [1]. The vacuum arcs is an excellent source of metal plasma in the form of highly ionized and high-energy jets [1,2]. The metallic plasma is widely used for thin film deposition, tool coatings, ion implantation, spacecraft thrusters, in microelectronics for production of metal connections in integrated circuit [1,3]. The mentioned arc utilization for wide applications require a deep knowledge of the mechanism of metallic plasma generation in order to control the plasma density, expansion and distribution. In the vacuum arc a relatively large power density concentrating in the cathode spots and the plasma are produced due to cathode thermal action. Attempts to understand the spot problems was provided during many years. The main difference of the theoretical approaches relate to models of heat-evolution and mechanism of plasma generation. One of the research groups takes into account specifics of the cathode high current electron emission, Joule heating (volume heat source) resulting in local exploding and new plasma plume formation. Another research group takes into account the cathode heat regime including the ion energy flux from the primary plasma (surface heat source) and the cathode vapor ionization for cathode plasma reproduction.

The first group [4] in the early stage, the phenomenon of Explosive Electron Emission (EEE) as an explosions of points on the non-ideally flat cathode surface was assumed explain the periodically spot appearing. This phenomenon was observed at a high voltage (>30 kV) and Joule heating of small spikes in presence of the critical explosive electric field of $E_{cr}=10^8$V/cm. In vacuum arc, the cathode spot occur under about 20-30 V and the critical electric field cannot be reached because the thickness of space charge region (~0.01μm) is significantly small relatively the protrusion sizes (~1μm) [1]. At later stage, a modified version of protrusion Joule heating was developed considering presence of an initial plasma that was arbitrary formed. As result of plasma action at the surface form some conditions for appearance of Joule heating, high current electron emission and formation of an *Emission Center* (EC). It was given the initial radius of emission area as very small of r_0=0.1 μm. The time dependent increase of Joule heating intensity of the cathode was supported by increase of the current of thermionic electron emission enhanced by the electric field (by given cathode potential drop of 15V) because increase the cathode temperature (up to 30000K). With time, the emission zone increases and also increase the energy dissipated due to cathode heat conduction, evaporation and electron emission, resulting in reduction of the current density and, therefore, reduction of the intensity of Joule heat source. Therefore, the current ceases, but up to this time a short-living portion of electrons is generated. This ***short ejection of electron portion is defined as an EC*** **(*later was named as ECton*)**. Note, fallibility of above approach, i.e. substantional large Joule cathode heating, sharply increased initial temperature, and therefore enormous thermionic electron emission occur from given initial very high current density due to given initial high plasma density, small protrusion size and currents of 10-100 A. Also it is questionable the indicated large current density remained as 3×10^9A/cm^2 (at r_0=0.3 μm) until the end of EC lifetime (~1ns).

The authors of both groups, in most cases, used the cathode potential drop as given input parameter because it was measured with good accuracy. However, an information about this parameter (and power) at spot initiation is absent. The cathode evaporation rate was determined by approach describing the vapor flow from heated surface by sound speed. However, the evaporation flux is subsonic because much heavy particles are returned due to ion current toward the cathode [1]. Previously developed the models (with volume and surface heat sources), did not considered the cathode plasma generation as a self-consistent processes of cathode and plasma electron heating. Some decades ago, an attempt for comprehensive description of the cathode spot including the cathode potential drop and rate of cathode erosion G in non-stationary formulation was develped in frame of kinetic model [1]. According to this

model, the ionized vapor structure near the cathode surface consists of several partially overlapping physical regions separated by characteristic boundaries with corresponding gasdynamic parameters, temperature T, density n and velocity v (Fig.1). The cathode region includes a space charge sheath, located between the cathode surface (boundary 1) and it external boundary 2, a non-equilibrium Knudsen plasma layer located between boundaries 2 and it external boundary 3.

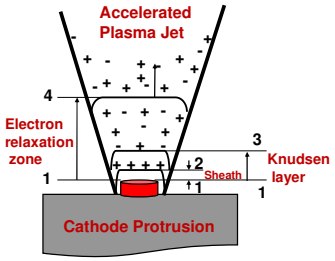

Fig.1

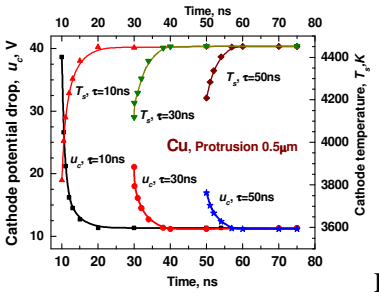

Fig.2

Fig.1. Schematic presentation of spot on protrusion cathode and numbers indicated the regions.
Fig.2. Cathode potential drop and cathode spot temperature as dependence on spot time with τ as parameter.

Two heavy particle fluxes (evaporated and returned) are formed in the Knudsen region and determines the plasma velocity v_3 & n_3 (i.e G) at 3. In the electron beam relaxation zone, the atoms are ionized by by emitted electrons as well as by plasma electrons, heated by electron beam. At the boundary 2, the plasma electrons are returned to the cathode, while the ions and emitted electrons are accelerated to energy determined by the cathode potential drop eu_c. The charge particle motion and their generation due to high power dissipation are coupled self-consistently with the potential barrier. Therefore, the corresponding height of the barrier, i.e. u_c is obtained self-consistently. ***Initial conditions*** for arc initiation are determined by presence of an initial plasma, which arise due to triggering by breakdown pulse, contact method or post plasma. Depending on trigger type, an initial plasma plume has different but minimal lifetime τ. As initiating plasma parameters should be self-consistent, such parameters were calculated assuming that the heat flux and other parameters are constant during an initial short time τ.

In order to demonstrate the result of closed approach, the calculation was conducted for a Cu cathode protrusion of R_0=0.5μm, current 10 A and for different τ. Fig. 4 shows that the cathode potential drop u_c is significantly large at spot initiation time and the u_c decreases significantly with time up to some value and then quickly approaches to an asymptotic value that is independent of τ. In contrary, the cathode temperature T_s increase from some initial value and, similarly to T_s, the other spot parameters also approaches to asymptotic values that are independent of τ. Thus, the model discovers an important not seen previously result. Unlike the traditional approach with *given constant cathode potential drop* u_c resulting in non-limited rise current density (at given small r_0) with time, the closed model show **weak change of the current density** j (spot radius) while significant variation of the u_c with time. This study indicated that the spot development is determined not only by j, but very importantly by ***electrical power density*** released in the near cathode region beginning from the triggering the arc. The non-stationarity of cathode heating requires significant electrical power at the beginning to reach the cathode temperature enough for electron emission, vapor density and reproduce the plasma density for development the process. As the initial plasma density and, therefore j cannot be supported by heating due to Joule energy or ion energy flux, the cathode thermal regime can be supported by significant rise of potential drop u_c.

[1]. Beilis, I.I. *Plasma and Spot Phenomena in Electrical Arcs*; Springer Nature Switzerland AG: Basel, Switzerland, 2020; Volumes 1 and 2.
[2]. Anders, A. *Cathodic Arcs: From Fractal Spots to Energetic Condensation*; Springer: Berlin/Heidelberg, Germany, 2008.
[3]. *Handbook of Vacuum Arc Science and Technology*; Boxman, R.L.; Martin, P.J.; Sander, D.M. (Eds.) Noyes Publisher: Park Ridge, NJ, USA, 1995.
[4]. Mesyats G.A. *Cathode Phenomena in a Vacuum Discharge: The Breakdown, the Spark, and the Arc* (Nauka, Moscow, 2000).

Detailed conference program Thursday 11th, 2024

	Morning Session Chairman: Eugen Stamate		
8:30	General Invited	G. D. Stancu	Conventional and ultrashort laser diagnostics for fundamental studies of atmospheric pressure plasmas
9:15	Topical invited	C. Vitelaru	Process control loops using optical emission spectroscopy in reactive sputtering
9:45	Hot Topic	Y. Guo	Electric field measurement of positive single channel streamers in air by E-FISH
10:05	Oral	C.L. da Silva	Atomic oxygen photometric plasma diagnostic of lightning
10:30	Coffee Break		
	Midday Session Chairman: Erik Wagenaars		
11:00	General Invited	K. Kutasi	Low-power atmospheric-pressure surface-wave microwave discharge in contact with liquids
11:45	Topical Invited	M. Jimenez Redondo	Cold plasmas and ion traps for laboratory astrochemistry
12:15	Oral	M. Rutigliano	The role of long-range interactions in the energy exchanges at surfaces: the case of nitrogen molecules on tungsten.
12:35	IUPAP Prize	J. Teunissen	A future perspective on modeling streamer discharges: longer time scales and other gases
13:10	Lunch		
14:30	Poster Session 2		
16:30	Coffee Break		
17:00	Woskshop 2	A. Dogariu	Non-equilibrium thermometry in gases and plasmas using hybrid CARS
17:30		A. Gerakis	Non-resonant four-wave mixing diagnostics for the determination of non-equilibrium in plasmas
18:00		P. Dvořák	LIF studies of hydride dissociation in electric discharges
18:30		J.-P. van Helden	Atomic oxygen measurements with THz absorption spectroscopy, ps-TALIF, and CRDS: A comparison
19:00			
20:00	Conference Dinner		
1:00			

Conventional and ultrashort laser diagnostics for fundamental studies of atmospheric pressure plasmas

G.D. Stancu

Laboratoire EM2C, CNRS, CentraleSupélec, Université Paris-Saclay, 3, rue Joliot Curie, 91192 Gif-sur-Yvette cedex, France

gabi-daniel.stancu@centralesupelec.fr

Based on the principle of stimulated emission introduced by Albert Einstein in 1917, laser sources have been incessantly developed since their discovery in the 1960s. Generated in continuous or pulsed mode, laser diagnostic techniques are today essential tools for the fundamental understanding of energy distribution, kinetic and dynamic processes in reactive and non-reactive plasma environments, as well as for plasma engineering. With photons of wavelength ranging primarily from UV to Mid-IR, they enable probing with high sensitivity, selectivity, spatial and temporal resolutions key plasma parameters such as species densities, pressures, temperatures, velocities, flux distributions and E&M fields.

Due to their strong potential of applications in the domains of materials, energy, environment, transport, health or agriculture, atmospheric pressure plasmas have attracted great scientific interest in recent years. In particular, non-equilibrium reactive plasmas generated under ambient conditions are complex environments governed by multi-physics interactions, are usually confined and present transient behaviors. Owing to much larger collision rates than at low pressures, they exhibit fast kinetic and dynamic processes with characteristic times often less than one ns and with reduced plasma volumes (e.g. sub-mm) dominated by large species, temperature and field gradients.

These peculiarities of atmospheric plasmas call into question the implementation of conventional laser diagnostic methods. For example, the sensitivity of classical absorption spectroscopy (AS) is lower because of the small absorption length, whereas the selectivity is poorer due to the large collisional broadening that enhances the spectral overlap. Furthermore, evaluating the density or temperature of plasma species becomes intricate because the line-of-sight AS signals represent integrated values over a highly non-uniform plasma for which even the absorption length is an unknow [1,2]. Significant challenges are also present in the case of the laser induced fluorescence (LIF) diagnostics. Although the sensitivity, selectivity, spatial and temporal resolution are exceptional, the uncertainties using LIF with single-photon or multi-photon absorption methods will increase, due to the quenching phenomena that are orders of magnitude larger than for low pressure plasmas. Additionally, photolytic processes in reactive plasmas will perturb measurements by intrusively increasing the densities of probed species [3,4,5]. Laser scattering techniques, which include elastic, inelastic, resonant or non-resonant, coherent or non-coherent scattering processes, are confronted either with a lack of sensitivity and selectivity, or with the sharp temperature and species gradients over reduced and transient plasma volumes [6,7].

The employment of ultrashort lasers such as mode-locked ps and fs for plasma and combustion diagnostics has increased over the past two decades. Large improvements in diagnostics have been reported particularly for multi-photon techniques, where the very high instantaneous intensity and photon statics favor the probability of laser-plasma interactions. For example, fluorescence techniques for species detection demonstrate higher sensitivities and photolytic-free capabilities [8,9,10], second harmonic generation methods for electric field measurements exhibit higher sensitivities [11], whereas coherent anti-stokes Raman spectroscopy methods allow for single-shot species and temperature measurements [12].

It should be noted that these developments pose new challenges for accurate description of the laser-plasma interactions. For instance, experiments employing ps and fs lasers for two-photon absorption laser induced fluorescence (TALIF) are reported for photon intensities on the order of $TWcm^{-2}$ or even higher, while conventional ns lasers have intensities usually below $GWcm^{-2}$ [10]. Their photon statistics

are determined by the mode-locked characteristic which is very different from that of ns lasers (e.g. multimode with stochastic phase fluctuations). As the second-order correlation factor increases by several orders of magnitude, the two-photon transition probability increases and hence, the sensitivity of the method. New phenomena, such as Stark detuning and coherent excitation are expected. At the Heisenberg limit, a 100-fs laser will have a spectral width of ~146 cm^{-1}, which is a few orders of magnitude larger than for a conventional ns laser (e.g. ~ 0.1 cm^{-1}). Therefore, excitation of multiple transitions and species is more likely. Furthermore, employing fs lasers, coherent processes are expected for two-photon excitations. Indeed, the decoherence time scale for laboratory plasmas are orders of magnitude greater than the excitation time. For example, the characteristic Doppler decoherence time at room temperature for hydrogen, nitrogen and oxygen atoms, for two-photon transitions at 97492 cm^{-1}, 96750 cm^{-1} and 88631 cm^{-1}, respectively, is on the order of ps and tens of ps, while the collisional decoherence time at atmospheric pressure plasmas is hundreds of ps or longer. This implies that appropriate models must consider coherence terms as described by the density matrix equations [3].

In Fig. 1 and 2, examples of two-photon excitation probability for the O atom with laser intensities of 1 $GWcm^{-2}$ and 100 $GWcm^{-2}$, and pulse widths of 6 ns and 200 ps, respectively, are computed using a density matrix model for negligible quenching (Fig. 1) and for typical quenching of atmospheric pressure plasmas (Fig. 2). We notice that probability amplitudes for 1 $GWcm^{-2}$ are significantly different, whereas at 100 $GWcm^{-2}$ they exhibit Rabi oscillations, and they are almost identical. Consequently, in high intensity regime the fluorescence probability, which is proportional to excitation probability, can become independent on quenching phenomena. This is a great advantage for accurate measurements of species using LIF techniques, particularly for non-uniform transient plasmas at atmospheric or high pressures, where quenching can vary considerably in time and space due to changes of the temperature and nature of colliders. Note that a classical ns LIF technique would require a tremendous number of experiments for quenching characterization.

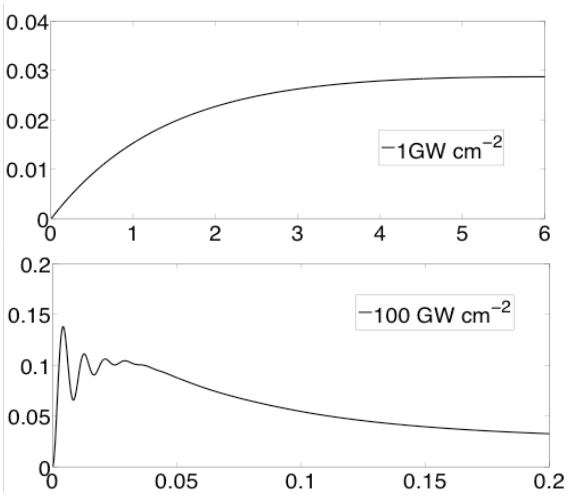

Fig. 1: Excitation probability for O atoms for laser intensities of 1 $GWcm^{-2}$ & 100 $GWcm^{-2}$, and pulse width of 6 ns & 200 ps, respectively, for negligible quenching.

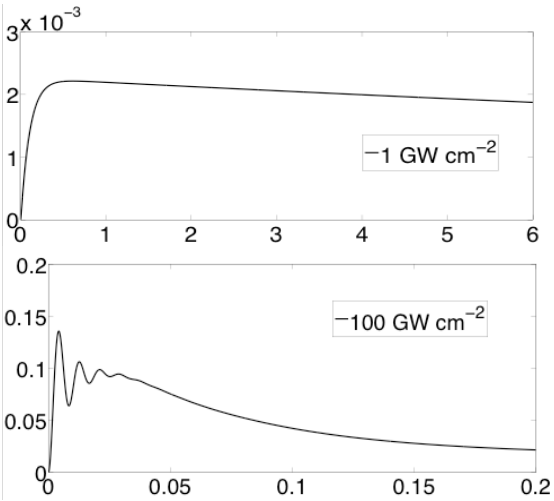

Fig. 2: Excitation probability for O atoms for laser intensities of 1 $GWcm^{-2}$ & 100 $GWcm^{-2}$, and pulse widths of 6 ns & 200 ps, respectively, for quencing rate of $9x10^9$ Hz.

In this contribution, insights and perspectives will be presented for conventional and ultrafast laser plasma diagnostics, such as time-resolved absorption enhanced by cavities or calibration techniques employed for femtosecond laser induced fluorescence. Examples of fundamental investigations of atmospheric pressure plasmas generated by nanosecond and microwave discharges using laser techniques will be shown along with plasma energy branching, kinetic and dynamic studies.

[1] Stancu G.D. et al. *J. Phys. Chem. A*, **114** (1) (2010) 201
[2] Reuter S. et al. *Plasma Sources Sci. Technol.* **29** (2020) 054001
[3] Stancu G.D. *Plasma Sources Sci. Technol.* **29** (2020) 054001
[4] Niemi K. et al. J. Phys D. Appl. Phys. **34** (2021) 2330-5
[5] Stancu G.D. *von Karman Institute Lecture Series* (2014) ISBN-13 978-2-87516-076-8
[6] Gerakis A. et al. *Phys Rev. Appl.* **9** (2018) 014031
[7] Kuhfeld J. et al. *J. Phys.D: Appl. Phys*. **54** (2021) 305204
[8] Kulatilaka W.D. et al. *Opt. Lett* **37** (2012) 3051
[9] Starikovski A. et al. *AIAA SciTech Forum*, (2024) 10.2514/6.2024-2786
[10] Dumitrache C. et al. *Plasma Sources Sci. Technol.* **31** (2022) 015004
[11] Dogariu A. et al. *Phys. Rev. Appl.* **7** (2017) 024024
[12] Pestov D. et al. *Science* **316** (2007) 265

Acknowledgements: This research was supported by the French National Research Agency, ULTRAMAP project (ANR-22-CE51-0027) and IdF-SESAME project DIAGPLAS.

Process control loops using optical emission spectroscopy in reactive sputtering

C.Vitelaru(*), I. Pana, A.C Parau, M. Dinu, L.R. Constantin, A. Vladescu

National Institute of Research and Development for Optoelectronics - INOE 2000, Department for Advanced Surface Processing and Analysis by Vacuum Technologies, 409 Atomistilor St., Magurele, RO77125, Romania

(*)catalin.vitelaru@inoe.ro

Optical emission spectroscopy (OES) is a valuable tool for plasma diagnostics, giving direct access to the excited species in the plasma volume. The main advantage of OES is its non-invasive nature, being well adapted for the investigation and control of technological plasmas that are used for thin film deposition. The use of this technique is illustrated in this contribution for characterizing and controlling the reactive sputtering process in a variety of cases. The use of two reactive gas configurations with variable gas mixing is presented as a first example, for the deposition of TaOxNy compounds. The use of control loops to actively control the reactive gas flow is presented both for single reactive gas (O_2 and N_2 respectively) and mixture of two reactive gases. Moreover, a special design that uses the emission of an additional plasma is presented, for the control of a reactive process involving two reactive gases.

The plasma-based technologies used for surface processing and thin film deposition are of great interest, being labeled as ecological due to their lack of harmful byproducts, when compared to chemical deposition methods. Physical vapor deposition in general and magnetron sputtering in particular are valuable technologies, intensively used both in research and industry [1,2]. Reactive magnetron sputtering is of particular interest, enabling the creation of a large variety of compounds, including oxides, nitrides, carbides, oxynitrides, carbonitrides, by using a metal target and a gas mixture that contains reactive species, such as oxygen, nitrogen and hydrocarbon gases. The reactive gas present in the plasma volume leads to complex and interdependent phenomena that occur on all surfaces and in the volume, involving compound formation and destruction. One typical characteristic of the reactive sputtering process is the presence of Hysteresis phenomena [3,4]. This can be made visible as a different variation path of a process parameter, such as partial or total pressure, voltage, power, emission lines intensity, etc., corresponding to the variation of a control parameter, such as reactive gas flow, target current or power. The process window where hysteresis occurs can lead to process instability, the process parameters being dependent on the history of the system. The same interval also offers a potential advantage, being precisely the one that can be used to tune the properties of the thin films.

Optical emission spectroscopy is a powerful tool that can be successfully used for analyzing the reactive process [5,6,7], providing knowledge of process intervals and giving insight on the elementary processes. Using such process intervals, it becomes possible to choose the best suited process parameters, so that tunability of thin films properties can be achieved. In this contribution an illustration is given for different configurations, including one gas and two gas processes, with and without process control loops, presented in the form of 4 case studies.

TaO_xN_y, tuning in a 2 reactive gases process

The first case study refers to the processes involving two reactive gases, namely oxygen and nitrogen, for the deposition of oxynitride thin films. The contribution of each reactive gas is different, resulting in a more complex reactive environment. The process that will be described implies the sputtering of Ta target in an $Ar/N_2/O_2$ gas mixture, for the deposition of TaO_xN_y thin films with tunable composition and properties. The specific constant parameters for this process were: DC power applied to the target P_{DC} = 150 W, 5 mTorr of Ar pressure, Ar gas flow of 5 sccm.

The chosen emission lines to be followed for describing the process are: λ=337.13 nm N_2 line, λ=534.1 nm Ta line, λ=706 nm Ar line and λ=777.19 O line. The analysis of the hysteresis behavior, investigated individually for each of the reactive gas, reveals a hysteresis interval from 1.8 to 3 sccm of O_2, while for the Nitrogen process there is no visible hysteresis effect. The most reactive process conditions were identified for an oxygen flow of 2.5 sccm. In order to identify the most reactive conditions for nitrogen process, the derivative of the intensity variation vs gas flow was used, as described in [5], resulting that 1 sccm of N_2 corresponds to the most reactive conditions. In order to simplify the experimental procedure, we propose the use of only one control parameter. This parameter is the sum of the reactive gas flows, coupled with a fixed ratio of 2.5 between the two reactive gases flows, in order to account for their different reactivities. Using this approach, the hysteresis behavior for a two reactive gas process cand be derived, leading to the identification of the process interval best suited for obtaining tunable composition and properties. By choosing three experimental conditions situated in the interval that defines the hysteresis loop, the tunability of the film properties is proven in terms of composition and optical properties. Refractive index variation from 2.1 to 3.3 is achieved, while the optical bandgap variation lays in the interval from 1.6 to 3.2 eV.

CuO_x and CuN_y tunning by active control loop with one reactive gas

The second case study refers to the implementation of active control loops, for the sputtering of Cu target in a reactive environment containing Ar and one reactive gas, either O_2 or N_2. Plasma emission monitoring and control of the plasma is employed, by using a spectrometer that collects the emitted light from the vicinity of the magnetron plasma via an optical fiber. The ratio of selected line intensities, $I(\lambda O_{777\ nm})/I(\lambda Cu_{327\ nm})$ and $I(\lambda N_{337\ nm})/I(\lambda_{Cu327nm})$respectively, is transformed by a digital-analog convertor, becoming the „control signal" for a programable PID controller unit. This unit controls the reactive gas flow, such as the desired ratio between emission lines is kept.

The reactivity of the processes with one reactive gas, O_2 or N_2 is evaluated by using the reactive gas flow as a control parameter and following the evolution of voltage, pressure, or emission line intensities. The Hysteresis effect is more pronounced for the process involving oxygen, a clear interval being visible between 3.5 and 4.5 sccm of O_2. The correct setting of the PID parameters enables a precise control of the desired line intensity ratio, enabling both stable operation at exact setpoint and also quick transition to the desired setpoint in the event of a simulated perturbation of the system. Moreover, the gradual increase of the setpoint value enables stable operation of the system inside the hysteresis loop, represented either as voltage or line intensities ratio as a function of oxygen gas flow. Typical variation of the process parameters as a function of Oxygen flow is represented in Figure 1.

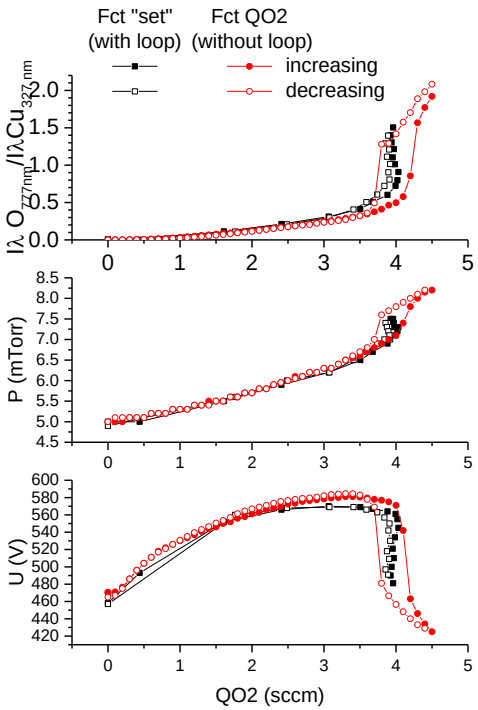

Fig. 1: Hysteresis behavior with and without control loop

The direct link between process conditions and thin film properties is revealed by evaluating the deposition rate, the Cu to O ratio, measured by EDS or the optical band gap variation. Moreover, the XRD spectra of the samples shows that by controlling the ratio of emission line intensities $I(\lambda O_{777\ nm})/I(\lambda Cu_{327\ nm})$it is possible to obtain different crystalline phases, including Cu_2O, Cu_4O_3 and CuO, depending on the composition and the O/Cu ratio.

TiOxNy tunning by active control loop with 2 reactive gases

For the third case study, a process with two reactive gasses is used, namely O_2 and N_2, for the sputtering of a Ti target. For this study the chosen ratio of selected line intensities is $I(\lambda N_{391\ nm})I(\lambda Ti_{504\ nm})$ and $I(\lambda O_{777\ nm})/I(\lambda Ti_{504\ nm})$ respectively, The „control signals" being transmitted to two controllers that use a PID algorithm. The simultaneous use of two reactive gases and two reactive control loops poses additional difficulties, the process being prone to instabilities and oscillations induced by the independent control of each reactive gas. Therefore, the careful choice of PID control parameters is of crucial importance for the stability of the process. Both independent control, with each individual gas, and simultaneous control with both reactive gases is achieved.

The direct relation between the set parameters and the thin film properties is revealed by the composition variation, expressed as N/Ti, Ti/(O+N) or N/O ratios. The optical properties can be also tuned in wide range, in terms of reflected color, transmittance and absorbance, refractive index etc.

Process stability in 2 reactive gas process by using additional plasma emission

The fourth case study proposes an indirect way to probe the gas composition, without need to use the emission from the sputtering plasma. For this purpose, a Penning gauge connected to the vacuum chamber is used as excitation source for plasma emission, the collected spectra being used for the process control. The emission line intensity, for Ar or reactive gases such as N_2 and O_2, is pressure dependent, giving an opportunity to analyze the gas composition without need to collect light from the sputtering plasma. This gives an important advantage, since the collecting optics is protected from deposition during the process and the collection of emitted light from the pressure gauge is much easier. The control signals in this case have to be linked to the Ar emission as a reference, since there is no emission from the sputtered metal. The chosen emission line intensities ratios are in this case $I(\lambda N_{391\ nm})I(\lambda Ar_{750\ nm})$ and $I(\lambda O_{777\ nm})/I(\lambda Ar_{706\ nm})$. By using these signals, it becomes possible to sweep the entire hysteresis loop going from metallic mode to compound mode, for each individual reactive process. The nitrogen process shows no visible hysteresis effect, whereas the Oxygen process shows a pronounced hysteresis loop. By actively controlling the set parameter $I(\lambda O_{777\ nm})/I(\lambda Ar_{706\ nm})$ it become possible to establish stable functioning that correspond to the interior of the Hysteresis loop, giving access to a completely new process window that can be exploited.

Acknowledgment: This research was funded by a grant of the Romanian National Authority for Scientific Research and Innovation, CCCDI – UEFISCDI, project number COFUND-M-ERANET-3-HardCoat-1, no. 311/2022 (INOE), within PNCDI III, and by the Romanian Ministry of Research, Innovation and Digitalization through the National Plan of Research, Development and Innovation 2022-2027, Core Program, Project no: PN 23 05, Contract no: PN11N-03-01-2023, and through Program 1- Development of the National Research-Development system, Subprogram 1.2 - Institutional Performance - Projects to Finance the Excellent RDI, Contract no. 18PFE/30.12.2021

[1] Baptista, A.; Silva, F.; Porteiro, J.; Míguez, J.; Pinto, G. *Coatings*, ***8*** (2018) 402.

[2] Bräuer, B. Szyszka, M. Vergöhl, R. Bandorf, *Vacuum* **84** (2010) 1354–1359.

[3] S. Berg, H.-O. Blom, M. Moradi, and C. Nender, *Journal of Vacuum Science & Technology A* **7**, (1989) 1225.

[4] K. Strijckmans, R. Schelfhout, and D. Depla, *Journal of Applied Physics* **124**, (2018) 241101.

[5] I. Pana, C. Vitelaru, N.C. Zoita, M. Braic, *Plasma Processes and Polymers*, **13** (2016) 208-216.

[6] C. Vitelaru, I. Pana, A.E. Kiss, N.C. Zoita, A. Vladescu, M. Braic, Journal of Optoelectronics and Advanced Materials, **21** (2019) 717-725.

[7] G.Zambrano, H.Riascos, P.Prieto, E.Restrepo, A.Devia, C.Rincón, Surface and Coatings Technology, **172**, (2003) 2–3.

Electric field measurement of positive single channel streamers in air by E-FISH

Y. Guo[1], J.H. Laarman[1], A.A.A. Limburg[1], A. van Gils[1], S. Nijdam[(*)1]

[1] *Department of Applied Physics and Science Education, Eindhoven University of Technology, Eindhoven, 5600 MB The Netherlands*

[(*)] s.nijdam@tue.nl

Streamers are fast developing ionized channels that occur when a high voltage is quickly applied to a gas gap [1]. The space charge layer formed at the head of a streamer channel can enhance the electric field ahead of it and help its development. The electric field also determines the energy transfer, gas temperature, and chemical activity, *etc.*, in the discharges. Therefore, determining the electric field of streamer discharges is of great significance. Dijcks *et al.* [2] determined the electric field of streamers in pure nitrogen and synthetic air at pressures from 33 to 266 mbar by using optical emission spectroscopy (OES). However, this method has the disadvantages that it depends on optical emission and has a rather low spatial and temporal resolution.

Recently, a new technique called electric field induced second harmonic generation (E-FISH) has been introduced to the plasma community to measure the electric field of various kinds of plasmas [3, 4]. Initially, this method was considered as easy to implement and the measured signals straightforward to interpret. However, it has been shown that the measured signals are strongly related to the laser beam profile and to the electric field profile [5]. Recent advances on the interpretation of E-FISH signals provide us the possibility to restore the electric field distribution if cylindrical symmetry is assumed.

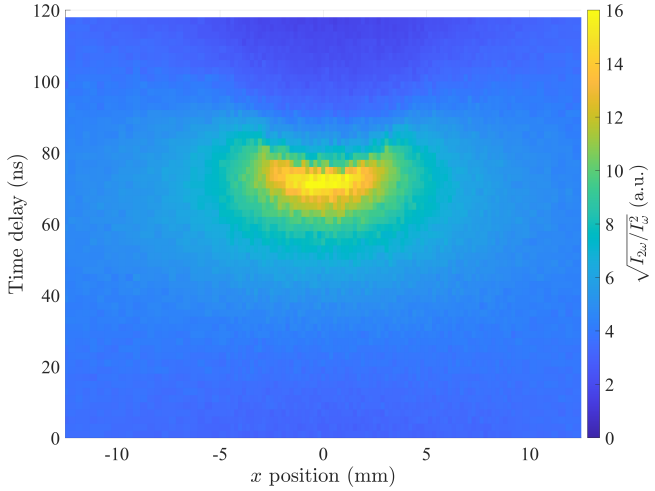

Fig. 1: A 2D map of E_y signals of a streamer in 70 mbar air with an applied voltage of 8 kV. The streamer propagates in the y-direction.

In this work, we built an E-FISH setup that mainly consists of a laser, optics, and streamer generation vessel. A Nd:YAG laser (EKSPLA SL234) with a pulse width of 120 ps is used for a high temporal resolution and a high signal intensity. The laser has a Gaussian beam profile and is focused to the discharge region inside the vessel by a lens with focal length of 500 mm. The second harmonic that is generated from the interaction between the laser and the electric field of the streamer is separated from the fundamental by a prism and a series of dichroic mirrors and is then directed to a photomultiplier tube (PMT). The orientation of the electric field vector is determined by implementing a polarizer in front of the PMT. The streamers are generated by repetitive high voltage pulses that are applied to a protrusion-to-plate gap (12 mm pin protrusion, 100 mm plates separation). Simultaneously to the E-FISH measurements, discharge images are captured by an ICCD camera (Andor iStar DH334T) to show the stability and cylindrical symmetry of the streamers. Figure 1 shows the E-FISH signals of E_y of a streamer in 70 mbar air with an applied voltage of 8 kV at different position and time delays. The space charge layer with a crescent shape, where the electric field is the most intense, is clearly visible

in the figure. Furthermore, a dimmer screened channel that follows the space charge layer can also be seen.

In this work, we measure the E-FISH signals of single channel positive streamers in air and air-like mixtures at pressures around 100 mbar. The line-of-sight integrated signals are then restored into electric field distributions by a deconvolution method. The absolute electric field is determined by measuring a known field from calibration electrodes. These results are also compared with existing simulation results and previous OES measurement under the same conditions. More details and the fully processed experimental results will be presented at the conference.

[1] Sander Nijdam, Jannis Teunissen, and Ute Ebert. The physics of streamer discharge phenomena. *Plasma Sources Science and Technology*, 29(10):103001, nov 2020.

[2] Siebe Dijcks, Lukáš Kusýn, Jesper Janssen, Petr Bílek, Sander Nijdam, and Tomáš Hoder. High-resolution electric field and temperature distributions in positive streamers. *Frontiers in Physics*, 11, 2023.

[3] Arthur Dogariu, Benjamin M. Goldberg, Sean O'Byrne, and Richard B. Miles. Species-independent femtosecond localized electric field measurement. *Physical Review Applied*, 7(2):024024, February 2017.

[4] Tat Loon Chng, Maya Naphade, Benjamin M. Goldberg, Igor V. Adamovich, and Svetlana M. Starikovskaia. Electric field vector measurements via nanosecond electric-field-induced second-harmonic generation. *Optics Letters*, 45(7):1942, mar 2020.

[5] Tat Loon Chng, Svetlana M Starikovskaia, and Marie-Claire Schanne-Klein. Electric field measurements in plasmas: how focusing strongly distorts the e-FISH signal. *Plasma Sources Science and Technology*, 29(12):125002, dec 2020.

Atomic oxygen photometric plasma diagnostic of lightning

Caitano L. da Silva(*)[1], J. Wemhoner[1], A. F. R. Leal[1], J. G. Pantuso[1]
(Times 12, normal, centred)

[1] *Department of Physics & Langmuir Lab, New Mexico Tech, Socorro, NM, USA*
(*) caitano.dasilva@nmt.edu

For thousands of years lightning has been one of the most astonishing natural phenomena, being both frightening and fascinating. Lightning is an important process in the atmospheric energy budget, contributing to the global electric circuit and to the production of nitrogen oxide in the troposphere. Concurrently, lightning discharges are known to be a major source of damages for a wide range of systems, amounting up to $5 billion/year economic losses in the United States (alone), mostly in the air flight and electric power distribution industries. In the United States dry southwest, lightning is a major cause of forest fires every year. For many years, the primary, if not the only, kind of widespread lightning diagnostics has been radio-frequency remote sensing of lightning peak currents. Lightning peak currents serve as proxy for the potential damage a strike may cause, including producing the effects listed in the previous paragraph. However, a simple argument can be made that the plasma temperature is substantially more informative about the potential deleterious effects of lightning flashes. Lightning return strokes establish a near-equilibrium plasma at peak temperatures of ∼30–40 kK. This value is 5–7 times the surface temperature of the Sun, several times higher than the melting temperatures of metals used in practical applications, and tens of times higher than the value required for ignition of a forest fire.

In this work, we present a new methodology to probe lightning temperatures from its optical signals. More specifically, we perform narrowband (1 nm) photometric measurements of lightning around key atomic oxygen lines in the near-infrared: 777, 844, and 926 nm. In thermal equilibrium, the light intensity emitted by an electronic transition is proportional to the overall plasma temperature. Thus, the ratio of two line emissions (e.g., 844/777) uniquely defines the temperature [14, 2]. If the plasma is not in equilibrium, the inferred temperature effectively is the temperature of the species probed (oxygen atoms in this case). Nonetheless, in practice, this value should be a good predictor of the overall temperature of neutral species in the hot plasma. Narrowband photometry is a relatively-inexpensive approach to probe the spectral properties of lightning optical emissions [10, 15]. Additionally, the setup introduced here has great potential to provide fully-automated, routine measurements of the lightning plasma temperature.

In the Summer of 2023, we performed measurements of lightning, using multi-band optical and radio sensors, at New Mexico Tech's Langmuir Laboratory for Atmospheric Research — a mountain-top facility in the southwest of the United States dedicated to lightning and thunderstorm research. Instrumentation used included: the atomic oxygen photometer array, fast and slow electric field change antennas, and a 3D VHF lightning mapping array [11]. Supporting data sets included lightning location provided: by the Earth Networks Total Lightning Detection Network (ENTLN), and by the Geostationary Lightning Mapper (GLM) on board of NOAA's Geostationary Operational Environmental Satellites (GOES) [7]. In this presentation, we report the inferred temperature of lightning and how it relates to its spatial and electromagnetic properties. We ascertain what factors determine temperature, such as peak current, occurrence context, height above ground of sources, discharge polarity, etc. We also compare the photometric measurements to simulation [5, 13] and determine that the field-of-view-integrated photometric measurements predict a temperature which corresponds precisely to the optical power-weighted-average temperature. This means that the measured peak temperature is not exactly identical to the actual peak temperature in the plasma. It approaches that value, but because of the average across the field of view, it falls a couple thousands of degrees Kelvin shorter. If time permits, we shall also take this opportunity to provide a brief overview of the atmospheric electricity research taking place at Langmuir Lab, including: rocket-triggered lightning [6], high-resolution lightning mapping [8], lightning initiation [1, 12], sprite observations [3], and runaway electron acceleration [9, 4].

References

[1] A. Attanasio, C. L. da Silva, and P. R. Krehbiel. Electrostatic conditions that produce fast breakdown in thunderstorms. *J. Geophys. Res. Atmos.*, 126(19):e2021JD034829, September 2021. doi: 10.1029/2021JD034829.

[2] L. Boggs, N. Y. Liu, A. Nag, T. D. Walker, H. Christian, C. L. da Silva, H. Rassoul, M. Austin, and F. Aguirre. Vertical temperature profile of natural lightning return strokes derived from optical spectra. *J. Geophys. Res. Atmos.*, 126(8):e2020JD034438, April 2021. doi: 10.1029/2020JD034438.

[3] L. Contreras-Vidal, R. G. Sonnenfeld, C. L. da Silva, M. McHarg, D. Jensen, J. Harley, L. Taylor, R. Haaland, and H. Stenbaek-Nielsen. Relationship between sprite current and morphology. *J. Geophys. Res. Space Phys.*, 126(3):e2020JA028930, 2021. doi: 10.1029/2020JA028930.

[4] L. Contreras-Vidal, C. L. da Silva, and R. G. Sonnenfeld. Production of runaway electrons and x-rays during streamer inception phase. *J. Phys. D Appl. Phys.*, 56(5):055201, 2023. doi: 10.1088/1361-6463/acaab9.

[5] C. L. da Silva, R. G. Sonnenfeld, H. E. Edens, P. R. Krehbiel, M. G. Quick, and W. J. Koshak. The plasma nature of lightning channels and the resulting nonlinear resistance. *J. Geophys. Res.*, 124 (16):9442–9463, August 2019. doi: 10.1029/2019JD030693.

[6] C. L. da Silva, W. P. Winn, M. C. Taylor, G. D. Aulich, S. J. Hunyady, K. B. Eack, H. E. Edens, R. G. Sonnenfeld, P. R. Krehbiel, E. M. Eastvedt, and J. J. Trueblood. Polarity asymmetries in rocket-triggered lightning. *Geophys. Res. Lett.*, 50(17):e2023GL105041, 2023. doi: 10.1029/2023GL105041.

[7] S. J. Goodman, R. J. Blakeslee, W. J. Koshak, D. Mach, J. Bailey, D. Buechler, L. Carey, C. Schultz, M. Bateman, E. McCaul, and G. Stano. The GOES-R Geostationary Lightning Mapper (GLM). *Atmos. Res.*, 125-126:34–49, 2013. doi: 10.1016/j.atmosres.2013.01.006.

[8] D. Jensen, R. G. Sonnenfeld, M. Stanley, H. Edens, C. L. da Silva, and P. Krehbiel. Dart-leader and K-leader velocity from initiation site to termination time-resolved with 3D interferometry. *J. Geophys. Res. Atmos.*, 126(9):e2020JD034309, April 2021. doi: 10.1029/2020JD034309.

[9] J. G. Pantuso, C. L. da Silva, J. T. Sanchez, and G. S. Bowers. Geant4 simulations of x-ray photon pileup produced by runaway electrons in streamer discharges. *Physics of Plasmas*, 29(5):053506, 2022. doi: 10.1063/5.0086579.

[10] M. G. Quick and P. E. Krider. Optical power and energy radiated by return strokes in rocket-triggered lightning. *J. Geophys. Res.*, 122(16):8816–8832, August 2017. doi: 10.1002/2017JD027363.

[11] W. Rison, R. J. Thomas, P. R. Krehbiel, T. Hamlin, and J. Harlin. A GPS-based three-dimensional lightning mapping system: Initial observations in central New Mexico. *Geophys. Res. Lett.*, 26 (23):3573–3576, December 1999. doi: 10.1029/1999GL010856.

[12] S. Senay, P. R. Krehbiel, C. L. da Silva, H. E. Edens, D. Bennecke, and M. A. Stanley. Analysis of narrow bipolar events using mode decomposition methods. *J. Geophys. Res. Atmos.*, 128(21): e2022JD038444, 2023. doi: 10.1029/2022JD038444.

[13] M. C. Taylor, C. L. da Silva, T. D. Walker, and H. J. Christian. Data-constrained simulations of the lightning return stroke channel properties. *IEEE Trans. Electromag. Compat.*, 64(5):1461–1469, 2022. doi: 10.1109/TEMC.2022.3189590.

[14] T. D. Walker and H. J. Christian. Triggered lightning spectroscopy: 2. A quantitative analysis. *J. Geophys. Res.*, 124(7):3930–3942, 2019. doi: 10.1029/2018JD029901.

[15] J. Wemhoner, L. Wermer, C. L. da Silva, P. Barnett, C. Radosevich, S. Patel, and H. Edens. Lightning radiometry in visible and infrared bands. *Atmos. Res.*, 292:106855, 2023. doi: 10.1016/j.atmosres.2023.106855.

Low-power atmospheric-pressure surface-wave microwave discharge in contact with liquids

Kinga Kutasi[1], Peter Hartmann[1], Zsolt Tóth[2], Cédric Noel[3]

[1] *HUN-REN Wigner Research Centre for Physics, H-1121 Budapest, Hungary*
[2] *Department of Medical Physics and Informatics, University of Szeged, H-6720, Szeged, Hungary*
[3] *University of Lorraine, CNRS, IJL, 54000 Nancy, France*
(*) kutasi.kinga@wigner.hun-ren.hu

The surface-wave microwave discharge generated with the help of a surfatron wave launcher in a few mm diameter dielectric tube is a very flexible system, since discharge can be ignited in a wide pressure range from mbar up to atmospheric pressure [1]. Both at low and atmospheric pressures, the species concentrations in the discharge and afterglow region can be easily tuned with the system parameters, initial gas mixture compositions and flow rate [2]. The discharge is sustained by the surface-wave travelling on the dielectric and plasma column boundary. At low pressure the dielectric is well defined, while in the case of the atmospheric pressure, where the plasma plume exits into the free air, as illustrated in Fig. 1 (dischare ignited in a quartz tube of outer diameter 6 mm and I.D. 4 mm, using Ar gas at 2000 sccm flow rate and MW input power of 25 W), the boundary conditions become variable. The presentation will discuss how these variable boundary conditions influence the discharge characteristics, such as temperature and electron density.

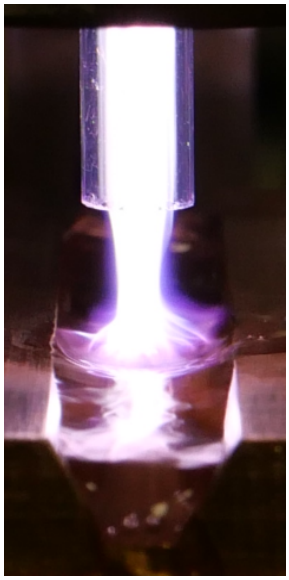

Fig.1. Surface-wave microwave discharge in contact with water flowing in a 9 mm trapezoid channel.

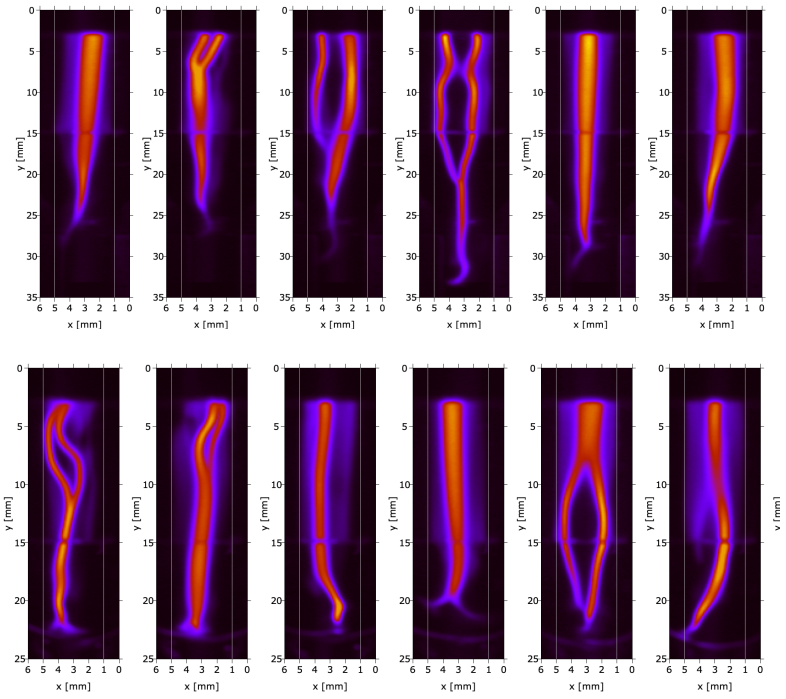

Fig. 2. The ICCD images of the plasma plume in free air (1st row) and in contact with water at 6 mm distance from the discharge tube (2nd row) recorded with 50 μs exposition time.

The surfatron is designed to launch the wave in the (0,0) mode, which results in a plasma column filling the central part of the discharge tube, as illustrated in Fig. 2. However, during operation the filamentation of the discharge can occur. The random appearance, the moving and collapsing of the

filaments can be observed at μs scale. The filamentation of the discharge in free air and in contact with the water flowing in a trapezoid channel is shown in Fig. 2. The presentation will discuss the effect of the operation conditions on the stability of the plasma column, the filamentation of the discharge.

One of the potential applications of the atmospheric-pressure surface-wave microwave discharge is the deposition of reactive species into the liquids [3-5]. It has been shown that both in batch and flowing liquids reactive species can be efficiently deposited. The presentation will discuss the interaction of the plasma plume with the liquid surface and the deposition of reactive species into the batch and flowing liquids.

The reactive species deposited into the liquids through plasma-liquid interaction have been shown to have great potentials in several application in the fields of plasma medicine and plasma agriculture. Here we show a new potential application of the plasma-deposited reactive species in the laser assisted "green" synthesis and stabilization of nanoparticles and nanostructures [6].

Acknowledgment The work has been supported by the Hungarian Science Foundation NKFIH, through project K-132158.

[1] Moisan M and Zakrzewski Z, *J. Phys. D: Appl. Phys* **24** (1991) 1025-1048.

[2] K. Kutasi *et al* ., *Plasma Sources Sci. Technol.* **25** (2016) 055014.

[3] K. Kutasi *et al., Plasma Sources Sci. Technol.* **28** (2019) 095010.

[4] K. Kutasi *et al., Plasma Sources Sci. Technol.* **30** (2021) 045015.

[5] K. Kutasi *et al., Plasma Process. Polym.* **20** (2023) 2200143.

[6] K. Kutasi *et al., J. Phys. D: Appl. Phys.* **57** (2024) 315201

Cold plasmas and ion traps for laboratory astrochemistry

M. Jiménez-Redondo[(*)1], R. J. Peláez[2], B. Maté[2], I. Tanarro[2], V. J. Herrero[2], P. Dohnal[3], P. Jusko[1], P. Caselli[1]

[1] *Max Planck Institute for Extraterrestrial Physics, Gießenbachstraße 1, 85748 Garching, Germany*
[2] *Instituto de Estructura de la Materia (IEM-CSIC), Serrano 123, 28006 Madrid, Spain*
[3] *Department of Surface and Plasma Science, Faculty of Mathematics and Physics, Charles University, V Holešovičkách 2, Prague 18000, Czech Republic*
[(*)] mjimenez@mpe.mpg.de

Astronomical observations reveal the rich and complex chemistry occurring in molecular clouds. The observations need to be complemented by laboratory studies in order to understand the physico-chemical processes involved. In this work, we present the use of $Ar+C_2H_2$ plasmas as a tool to study the formation of carbonaceous dust and the polymerization pathways for the charged species, and show the use of ion traps to precisely characterize specific ion-molecule reactions in astrochemically relevant conditions.

The insterstellar medium (ISM) contains dilute gas in varying conditions of density and temperature. Ice, dust and molecules have been detected in the colder and denser regions, known as interstellar clouds. In recent years, the number of molecules detected in the ISM has rapidly grown, and currently more than 300 molecules have been identified towards both galactic and extragalactic sources, including charged species and several complex organic molecules. In order to understand the physico-chemical processes leading to this rich chemistry, a combination of astronomical observations, astrochemical modeling, and theoretical and experimental efforts are required [1].

Most of these interstellar molecules are found in so-called dense clouds. In these regions, the low temperatures make ion-molecule reactions an efficient pathway to the formation of complex species, along with reactions on the surface of dust grains. However, many of these reaction pathways are not well characterized, specially when dealing with complex molecules and the formation of interstellar dust [1, 2]. In this work, we use cold plasmas and ion traps to tackle some of these problems through laboratory experiments.

Carbonaceous materials represent a significant fraction of cosmic dust and a relevant reservoir of carbon in space. Interstellar carbonaceous dust originates characteristic IR absorption bands, revealing the presence of aliphatic and aromatic functional groups in variable proportions. Among the various products investigated in the laboratory as possible carriers of these bands, hydrogenated amorphous carbon (a-C:H) leads to the best agreement with observations [3], although the formation pathways, composition and structure are still not clear. We have used capacitively-coupled RF plasmas of C_2H_2 / Ar mixtures to study the gas-phase formation of a-C:H particles as interstellar dust analogues. The diagnostics of the gas phase has been performed by mass spectrometry of neutrals and ions and Langmuir probes.

Carbonaceous dust analogues were generated in the capacitively coupled RF reactor using different sets of experimental parameters. The discharge was pulsed repetitively in periods of 20 s with varying duty cycles to allow the periodical growth of dust up to a given size and its subsequent fall on the lower electrode, which was grounded. The dust was collected on Si and Al substrates placed on this lower electrode. The samples were extracted later and characterized ex-situ by means of Fourier Transform Infrared (FTIR) spectroscopy and field emission Scanning Electron Microscopy (SEM), to analyze the final particle composition, size and structure.

Results from the characterization of the dust can be seen in Fig. 1. The SEM image of the left panel shows that the dust grains formed are homogeneous in shape and size. The average diameter of the particles was found to be mainly influenced by the duty cycle of the discharge. The variation of the FTIR spectra of the samples with one of the discharge parameters, the coupled power, is shown on the right panel. The assignment of the bands evinces the presence of both aliphatic, aromatic and acetylenic bands, with relative intensities that depend on the plasma conditions employed for the generation of the

analogues. The features observed in the IR spectra are comparable to the astronomical observations of carbonaceous dust towards IRAS 08572+3915 [4].

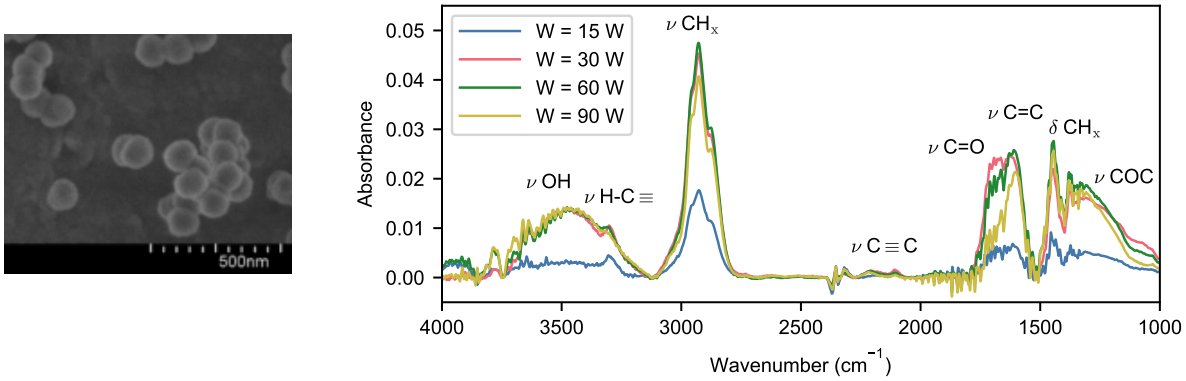

Fig. 1: Left: SEM image of a dust particle sample generated using a mixture of Ar (5 sccm) + C_2H_2 (2 sccm) with a coupled power of 15 W. The average diameter is ∼130 nm. Right: FTIR spectra of various dust analogues generated using different values for the coupled power in an Ar + C_2H_2 plasma.

For the study of charged species, the parameters of the discharge were adjusted to inhibit the formation of dust, since it was observed to induce the depletion of anions. The discharge was also pulsed with a frequency of 100 Hz to allow the extraction of the anions in the off part of the cycle. In these conditions, the measured ion distributions of both signs were clearly dominated by species with an even number of carbon atoms, reflecting the characteristic polyyne structures, typical of the polymerization of acetylene [5]. The ion distributions are shown in Fig. 2. For the cations, a monotonic decrease in intensity from ions with two carbon atoms till the highest number of atoms is observed. The distributions extend till 16 C atoms. The anion distributions extend further, and compounds with up to 24 C atoms are observed. In this case, the maximum signal was observed for the $C_6H_x^-$ group. Both for cations and anions, the C_nH_x peak profiles were found to be highly specific for each C_n group. From the measured mass spectra, it was not possible to decide on the possible presence of charged aromatic species with more than 6 carbon atoms.

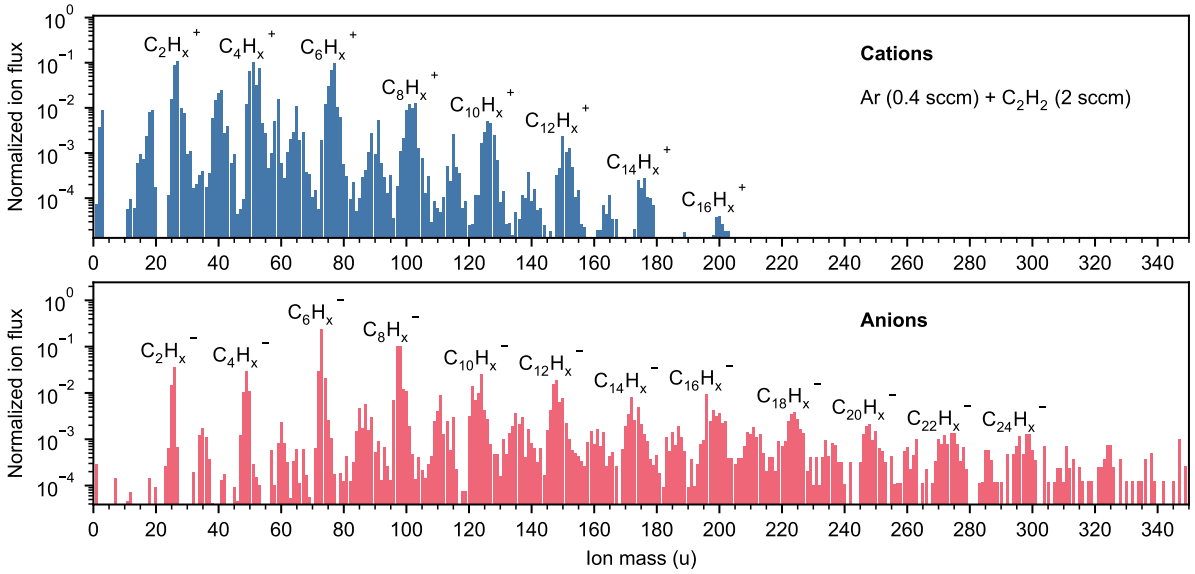

Fig. 2: Mass spectra for the charged species in the steady state of an Ar (0.4 sccm) + C_2H_2 (2 sccm) discharge with a coupled power of 50 W and a total pressure of 0.11 mbar.

A simple kinetic model that included aliphatic species up to 12 C atoms and assumed a homogeneous discharge was developed to rationalize the experimental data. The model includes the main types of ions

observed, and incorporated basically radicalic and ionic polymerization mechanisms leading to polyyne structures by addition of C_2 growth precursors, accounting for the spacing of the main peaks in the mass spectra.

While cold plasmas allow us to look at the full production network for the species of interest, experiments with an ion trap are better suited for the precise characterization of the individual reactions. Radio-frequency traps allow the storage of charged particles for long times, during which they can interact with photons, electrons or neutral species [6]. Ion traps can be used to study the ion-neutral processes prevalent in interstellar environments, and, with cryogenic cooling, temperatures close to those found in such regions can be achieved. Here we show measurements of the rate coefficient at cryogenic temperatures for the reactions of CN^+, HCN^+ and HNC^+ with H_2.

HCN and its higher energy isomer HNC are presumably the two simplest isomers in chemistry. Both have been detected in a variety of interstellar environments with comparable abundances. Some of the main production channels for these molecules include ionic chemistry, with mechanisms involving HNC^+ and its higher energy isomer HCN^+. The lack of experimental studies for many of these processes hinders current astrochemical models involving HCN / HNC [7].

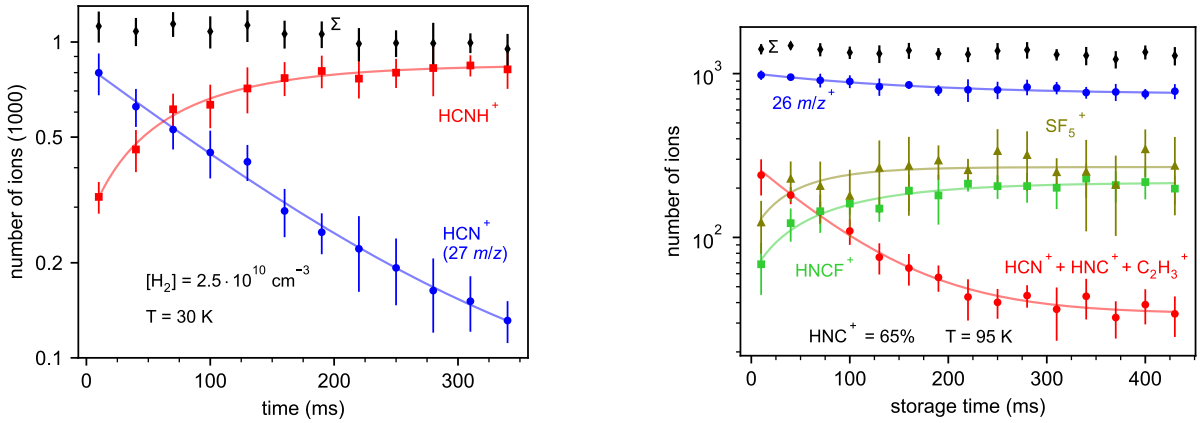

Fig. 3: Number of ions in the trap as a function of storage time for two of the processes studied. Left: time evolution of HCN^+ ions reacting with H_2. Right: determination of the branching ratio of the $CN^+ + H_2$ reaction using SF_6 as a chemical probe. SF_5^+ ions are formed from HCN^+, while $HNCF^+$ is produced from HNC^+. The sum of all the ions in the trap is denoted by Σ.

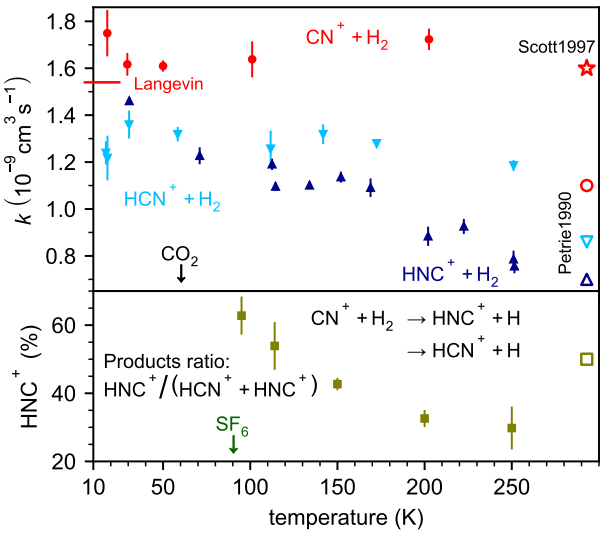

Fig. 4: Upper panel: rate coefficients of the reactions of CN^+ / HCN^+ / HNC^+ with H_2 as a function of temperature. Lower panel: branching ratio of the $CN^+ + H_2$ reaction as a function of temperature.

A 22 pole trap setup [8] was used to determine the reaction rate coefficients for production and destruction of HCN^+ and HNC^+ in collisions with H_2 in the range of 17 – 250 K, using chemical probing to differentiate the two ionic isomers [9]. The ions are produced in a storage ion source and mass selected by passing through a first quadrupole mass filter. After a set storage time in the 22 pole trap, the ions are mass selected in a second quadrupole and subsequently detected.

In order to determine the rate coefficient of the reactions of interest, the trap is filled with H_2 at various densities, and the rate at which the primary ions disappear is determined as shown in the left panel of Fig. 3. Regarding isomer production, the high energy isomer HCN^+ was the major ion produced in the ion source ($\sim 90\%$), and isomerization to HNC^+ could be achieved in the trap by adding a sufficient amount of CO_2. The ratio of both isomers in the trap could be determined by analyzing the different products obtained when reacting with O_2 or SF_6, as shown in the right panel of Fig. 3.

The measured rate coefficients are shown in Fig. 4. The rate coefficients for the CN^+ and HCN^+ reactions with H_2 are stable with temperature and close to the Langevin value, while the one for HNC^+ + H_2 presents a noticeable increase at lower temperatures. The product branching ratios for the CN^+ + H_2 reaction also show a marked temperature dependence, favoring the production of HNC^+, the lower energy isomer, at lower temperatures.

References

[1] E. F. van Dishoeck, *Faraday Discuss.* **168** (2014) 9–47.

[2] J. Cernicharo, *ApJ* **608** (2004) L41–L44.

[3] E. Kovačević, I. Stefanović, J. Berndt, Y. J. Pendleton, and J. Winter, *ApJ* **623** (2005) 242.

[4] E. Dartois, T. R. Geballe, T. Pino, A.-T. Cao, A. Jones, D. Deboffle, V. Guerrini, P. Bréchignac, and L. d'Hendecourt, *A&A* **463** (2007) 635–640.

[5] M. Jiménez-Redondo, I. Tanarro, and V. J. Herrero, *Plasma Sources Sci. Technol.* **31** (2022) 065003.

[6] D. Gerlich and M. Smith, *Phys. Scr.* **73** (2005) C25–C31.

[7] F. Fontani, L. Colzi, E. Redaelli, O. Sipilä, and P. Caselli, *A&A* **651** (2021) A94.

[8] P. Jusko, M. Jiménez-Redondo, and P. Caselli, *Mol. Phys.* (2023) e2217744.

[9] P. Dohnal, P. Jusko, M. Jiménez-Redondo, and P. Caselli, *J. Chem. Phys.* **158** (2023) 244303.

A theoretical-computational approach to highlight the role of long-range interactions in the energy exchanges at surfaces: the case of nitrogen molecules on tungsten.

Maria Rutigliano(*)[1] and Fernando Pirani[2,3]

[1] *CNR-ISTP (Istituto per la Scienza e Tecnologia dei Plasmi), Via Amendola 122/D, 70126 Bari, Italy*

[2] *Dipartimento di Chimica, Biologia e Biotecnologie, Università di Perugia, via Elce di Sotto 8, 06123 Perugia, Italy*

[3] *Dipartimento di Ingegneria Civile ed Ambientale, Università di Perugia, Via G. Duranti 93, 06125 Perugia, Italy*

(*) maria.rutigliano@cnr.it

The long-range anisotropic interactions affect the evolution of microscopic elementary processes occurring under a variety of conditions. In particular, they determine all basic features of the precursor state (the adduct formed by collisions of reagents) that further evolves towards the product final states of fundamental chemical/physical processes occurring in gaseous and condensed phases, as well as at the gaseous-solid/liquid inter-phases [1,2]. However, the role of such interactions is often not described at the required level of detail. The long-range forces play a primary role in the interaction of molecules with a surface, therefore, only an accurate description of the latter permits to properly account for all basic details of molecular scattering by surface, especially under thermal and sub-thermal conditions where the role of weak long range forces is exalted [3]. Recently, we have proven that the Improved Lennard Jones (ILJ) potential function, formulated in Ref. [4] for the interaction in the gas phase, is also suitable for an accurate and detailed description of the processes taking place at the gas-surface interface, providing better results in comparison with those from Density Functional Theory (DFT) functionals corrected for long-range interactions [3]. Over time we have developed a well-tested theoretical-computational approach to study the dynamics of elementary processes, promoted by gas-surface collision events. Such an approach exploits Molecular Dynamics (MD) calculations based on a chemical state-to-state semiclassical collisional method (see for instance Refs. [5,6] and references therein).

In this framework, we have undertaken the study of nitrogen molecules, taken in well-defined initial roto-vibrational states (j_i, v_i), interacting with a tungsten surface. The interest in this topic arises from the fact that nitrogen impinging on this surface is considered a prototype case useful to understand and explain the processes occurring on other metal surfaces of interest in nitrogen industrial processes, the ammonia synthesis *in primis*. Lately, MD calculations have been performed by us adopting a new Potential Energy Surface (PES), in which long-range interactions are suitably characterized through the ILJ function. Accordingly, for the sticking probability of nitrogen molecules on W(001), we were able to provide results further improving the already good comparison, recently obtained with calculations performed using interactions from DFT method corrected for long-range van der Waals contributions, with the experimental data [6].

In this contribution, the results obtained for the inelastic scattering of nitrogen molecules on two different tungsten surface planes (001) and (110) are presented and discussed with respect to process probability, roto-vibrational accommodation coefficients, final roto-vibrational distributions, reaction energetics and reaction mechanism. The final target is to highlight the role of long-range forces in the energy exchanges at the surface. In Figure 1 the scattering probability of $N_2(0;0)$ from W(001) is reported as a function of molecule collision energy (E_{coll}). It appears that the probability of molecular

inelastic scattering is an activated process that rises steeply to a nearly constant value of 0.7 independently of collision energy.

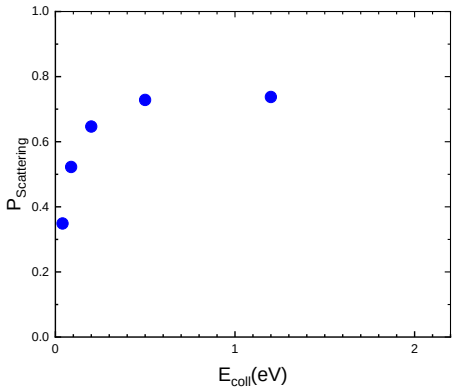

Fig. 1: Inelastic scattering probability for $N_2(0;0)$ from W(001). The surface temperature is 300K.

Molecules scattered from W(001) are rotationally excited and this excitation, from a preliminary investigation of the reaction mechanism, can be attributed to the energy exchange mechanisms that are activated when the molecule approaches the surface due to the formation of a precursor state stabilized by long-range forces. As an example, in Figure 2 the final rotational distribution of $N_2(0;0)$ colliding with E_{coll}=0.088eV on the surface is displayed.

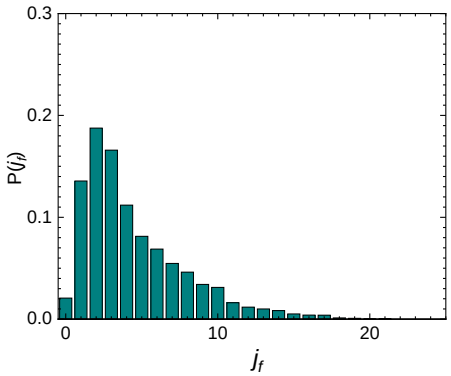

Fig. 2: Final rotational distribution for $N_2(0;0)$ colliding W(001) with E_{coll}=0.088eV. The surface temperature is 300K.

[1]L. Vattuone, L. Savio, F. Pirani, D. Cappelletti, M. Okada, M. Rocca, *Prog. Surf. Sci.* **85** (2010) 92-160.

[2] B.G. Perkins Jr., D.J. Nesbitt, *Proc. Natl. Acad. Sci.* **105** (2008) 12684-12689.

[3] Maria Rutigliano and Fernando Pirani, *Chem. Phys. Lett.* **770** (2021) 138444.

[4] F. Pirani, S. Brizi, L.F. Roncaratti, P. Casavecchia, D. Cappelletti, F. Vecchiocattivi, *Phys. Chem. Chem. Phys.* **10** (2008) 5489-5503.

[5] G. D. Billing GD (2000) *Dynamics of molecule surface interactions*. (2000) Wiley, New York.

[6] Maria Rutigliano and Fernando Pirani, *Molecules* **28** (2023) 7546.

A future perspective on modeling streamer discharges: longer time scales and other gases

J Teunissen[1]

[1] *Centrum Wiskunde & Informatica, Science Park 123, Amsterdam, the Netherlands*
(*) jannis.teunissen@cwi.nl

Streamer discharges are the precursors of lightning leaders and sparks, they occur above thunderstorms as sprites, and they are used in diverse technological applications [1]. Because streamers develop strongly non-linearly at velocities of 10^5 to 10^7 m/s, numerical simulations have become a valuable tool to understand and predict their behavior. In recent years, quite some progress has been made in the modeling and understanding of streamers in air. Two examples that I was involved in are the comparison of single-streamer evolution between simulations and experiments [2] and the comparison of streamer branching between simulations and experiments [3].

Streamer simulations are usually performed with a fluid model, although more expensive particle simulations are sometimes also used. The cost of such 'microscopic' simulations is typically quite high, due to the thin charge layers that have to be resolved and due to the small time steps that have to be used to describe the electron dynamics. In many applications we want to consider multiple voltage pulses, combined with a complex chemistry. It is currently not feasible to perform 3D simulations of such phenomena. Similarly challenging is the study of the streamer-to-leader transition, which involves time scales on the order of microseconds or more, and typically also a complex discharge structure with many streamer branches.

Yet another challenge is that we are now often interested in streamers in gases other than air. In such gases, there are typically two main challenges: first, there can be a lack of input data, for example regarding electron-neutral cross sections, chemistry or photoionization parameters. Second, discharges in gases other than air often develop in a much more stochastic way than discharges in air, since photoionization in air is exceptionally strong. Such stochastic growth is intrinsically three-dimensional, and computationally even more expensive to describe than the relatively smooth discharge growth in air.

In this talk, I will give a future perspective on the modeling of streamers with these challenges in mind. I will discuss advances in numerical and computational methods, for example the use of large scale computations, GPUs (graphics processing units), or the development of alternative models such as the "kinetic Monte Carlo" method of Marskar [4]. Somewhat related is the topic of developing reduced models, in which we do not resolve the smallest temporal and spatial scales relevant for electrons. I will briefly discuss the present state of such models, and the remaining challenges before they can be used in practical applications. Yet another category of models are those based on data and machine learning, which I will also briefly mention. Finally, I will discuss what kind of input and experimental data could contribute to more accurate streamer discharge modeling.

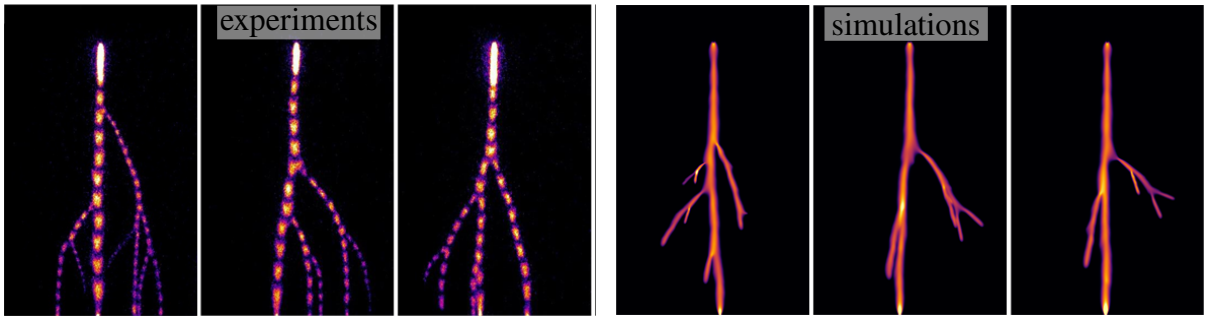

Fig. 1: Comparison of streamer branching between simulations and experiments, adapted from [3].

[1] Sander Nijdam, Jannis Teunissen, and Ute Ebert. The physics of streamer discharge phenomena. *Plasma Sources Science and Technology*, 29(10):103001, November 2020.

[2] Xiaoran Li, Siebe Dijcks, Sander Nijdam, Anbang Sun, Ute Ebert, and Jannis Teunissen. Comparing simulations and experiments of positive streamers in air: Steps toward model validation. *Plasma Sources Science and Technology*, 30(9):095002, September 2021.

[3] Zhen Wang, Siebe Dijcks, Yihao Guo, Martijn Van Der Leegte, Anbang Sun, Ute Ebert, Sander Nijdam, and Jannis Teunissen. Quantitative modeling of streamer discharge branching in air. *Plasma Sources Science and Technology*, 32(8):085007, August 2023.

[4] R Marskar and H K H Meyer. A kinetic Monte Carlo study of positive streamer interaction with complex dielectric surfaces. *Plasma Sources Science and Technology*, 32(8):085010, August 2023.

Non-equilibrium thermometry in gases and plasmas using hybrid CARS

Arthur Dogariu[1,2]

[1] *Department of Aerospace Engineering, Texas A&M University, College Station, TX 77843, USA*

[2] *Department of Mechanical and Aerospace Engineering, Princeton University, Princeton, NJ 08544, USA*

adogariu@tamu.edu

Coherent Anti-Stokes Raman Scattering (CARS) has been proven to be a very useful spectroscopic tool for measuring Raman rotational and vibrational spectra [1]. Our fs/ps hybrid CARS diagnostic allows for single shot in-situ coherent Raman spectroscopy [2]. The molecular excitation is achieved using a combination of broadband femtosecond laser pulses, which coherently stimulate the transitions in the fingerprint spectral region. A time delay between the excitation pulses and the probe pulse ensures a drastic reduction of the non-resonant background, otherwise a limiting factor in CARS. This allows for real-time identification of molecular species based on their chemical fingerprint, with applications in the standoff detection and identification of chemical [3], biological [4], and explosive traces [5], with high specificity and sensitivity. For a half of century, CARS has been successfully used to measure the temperature in gases in plasmas by identifying the Maxwell-Boltzmann distribution of the vibrational and rotational modes of the constituent molecules (Eq. (1)).

$$N(v,J) \propto exp\left(-\frac{E_{vib}(v)}{kT_{vib}}\right) exp\left(-\frac{E_{rot}(J)}{kT_{rot}}\right) \quad (1)$$

The hybrid fs/ps CARS allows for measuring the distributions expressed in Eq. (1), and, hence, determine the vibrational and rotational temperatures in a single laser shot. This capability offers not only the identification of the state of thermodynamic non-equilibrium of the system, but it also provides the temporal dynamics of the vibrational and rotational temperatures. The talk will present rotational and vibrational temperature results obtained in conditions of thermodynamic equilibrium such as in steady-state flows, combustion, and plasmas, and also in non-equilibrium conditions such as in hypersonic flows and nanosecond discharge plasmas. Fig. 1 shows the case of a methane:air flame where the rotational and vibrational modes are thermodynamically in equilibrium, hence the vibrational and rotational temperature are identical. In the case of nanosecond plasma discharges we obtain thermal non-equilibrium during and immediately after the discharge, and we monitor the evolution towards equilibrium by recording the time delayed CARS spectra. During highly non-equilibrium conditions such as hypersonic flows, over-population of the higher vibrational levels occurs, such that the non-equilibrium is not only between the rotational (and hence translational) and the vibrational modes, but also between the vibrational modes which no longer follow a Maxwell-Boltzmann distribution. In this case the definition of temperature given by Eq. (1) fails completely, and we

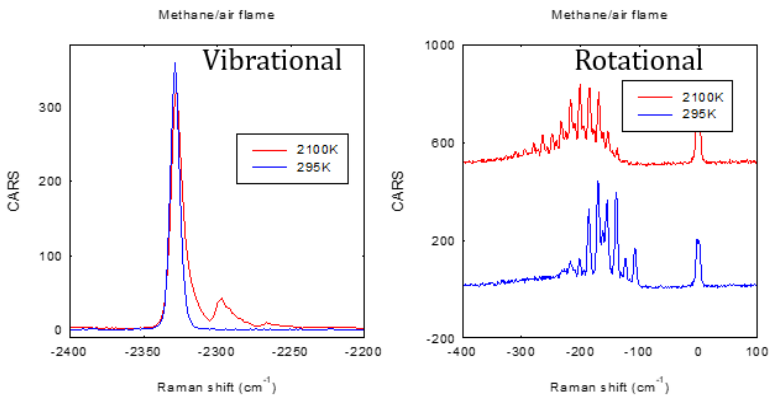

Fig. 1: Vibrational (left) and rotational (right) spectra indicating thermodynamical equilibrium in a methan:air flame.

can no longer measure a gas temperature. As an example, Fig. 2 shows the CARS spectra measured behind a normal shock in a Mach 6 hypersonic flow. During the high enthalpy flow (left in Fig. 2), the CARS spectra cannot be uniquely fitted using a Boltzmann distribution. The distribution of the first vibrational peaks indicate a temperature slightly higher than 3000K, while the higher vibrational levels are populated according to a distribution closer to 5000K. In this case the non-equilibrium is defined by the population distribution rather than a temperature. The right CARS spectrum in Fig. 2 shows that a vibrational temperature can be used to thermodynamically characterize the gas 1ms after the hypersonic interaction, while the gas there is still significant non-equilibrium between the vibrational and rotational energetic levels.

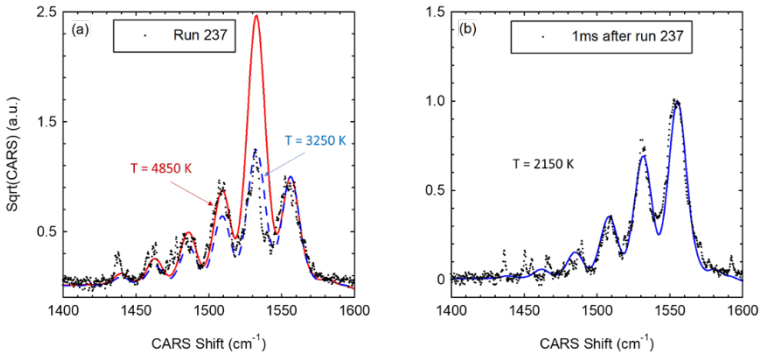

Fig. 2: CARS spectra during a highly vibrational non-equilibrium hypersonic flow (left), and in vibrational equilibrium 1ms after the Mach 6 flow (right).

[1] M. D. Levenson, *Introduction to Nonlinear Laser Spectroscopy*, Academic Press, Boston (1988).
[2] Pestov et al., *Science* 316, 265 (2007).
[3] Dogariu et al., *J. Appl. Phys.* 103, 036103 (2008).
[4] A. Dogariu, A. Goltsov, and M. O. Scully, "Real-time monitoring of blood using coherent anti-Stokes Raman spectroscopy," *J. Biomed. Opt.* 13, 54004 (2008).
[5] A. Dogariu and A. Pidwerbetsky, *Proc. SPIE* 8358-27, (2012).

Non-resonant four-wave mixing diagnostics for the determination of non-equilibrium in plasmas

Alexandros Gerakis(*)1,2

[1] *Luxembourg Institute of Science & Technology, Belvaux L-4362, Luxembourg*
[2]*Department of Aerospace Engineering, Texas A&M University, College Station, Texas 77845, USA*
(*) alexandros.gerakis@list.lu

Coherent Rayleigh-Brillouin scattering (CRBS), a non-linear and non-resonant four wave mixing process, is a powerful diagnostic technique for the measurement of thermodynamic properties of neutral species in weakly ionized plasmas, particularly the density, flow velocity and the translational temperature. Based on the interaction of intense, fast moving optical lattices with the particles in a medium (atoms or molecules, neutral or charged) CRBS can provide with a single shot ($\sim$ 200 ns) measurement of the velocity distribution function (VDF) of the medium and thus detect departures from Maxwellian VDFs. Here, the current state-of-the-art of CRBS will be presented, while directions towards the utilization of CRBS for the detection of the VDF of ions (Maxwellian or not) will be discussed.

Plasma diagnostics play a crucial role in quantifying the thermodynamic state of the plasma (e.g. density, temperature of plasma constituents), aiding in verifying theory and validating developed plasma models. Diagnostics based on mechanical probes, although relatively inexpensive and easy to fabricate, are by nature invasive, hence altering the state of the plasma they seek to measure; additionally, their operation is heavily relying on modelling and their application is limited to selected plasma conditions. Laser diagnostics in plasmas on the other hand, present the inherent difficulty of low scattering cross-sections coupled with intense optical background interfering with the measurement and thus significantly lowering the signal-to-noise-ratio (SNR).

To overcome this hurdle, four-wave mixing laser diagnostics, mainly in the forms of coherent Rayleigh-Brillouin scattering (CRBS) and coherent anti-Stokes Raman scattering (CARS) have been developed over the last few decades and have been consequently applied for the study of plasmas: CRBS can provide with translational temperature and density in the plasma while CARS can provide the ro-vibrational temperature as well as the density. The significant advantage of both techniques is that the resulting signal they produce is another laser beam, emanating out of the interaction region. Since the background noise scales as r^{-2} with distance r, this means that these techniques enable the placement of the measurement detector far away from the measurement region, thus both protecting the detector while additionally increasing the SNR, as opposed to their linear counterparts (spontaneous Rayleigh-Brillouin scattering and spontaneous Raman scattering). Here we present the state-of-the-art and the work currently pursued in utilizing single shot CRBS for performing *in-situ*, non-resonant and non-perturbative plasma diagnostics.

The single shot CRBS diagnostic technique, enables the acquisition of a Rayleigh-Brillouin spectrum in $150 - 200$ ns (in both atomic and molecular, ionized or neutral gas environments) [1, 2]. Fig. 1 illustrates a schematic of a typical counter-propagating laser beam geometry in CRBS. The main procedures leading to a single shot CRBS spectrum acquisition are as follows:

(1) Variation of the relative frequency difference Δf of the two intense laser beams, termed the *pumps*, generates an optical interference pattern, which moves at a phase velocity given by $v_g = (\Delta f \cdot \lambda_{pump})/(2 \cdot \sin(\phi/2))$, where λ_{pump} is the wavelength of the two pumps and ϕ is the pump half-crossing angle.

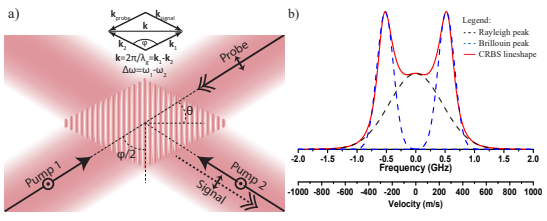

Fig 1: a) Schematic of a typical CRBS counter-propagating geometry. b) Simulation of a typical CRBS spectrum (red solid line) for CO_2 at 700 Torr, 300 K. The resulting CRBS spectrum is the result of the summation of the Rayleigh peak and the two Brillouin peaks.

(2) Particles whose translational velocity, v, is equal or close to v_g feel an attraction towards the high intensity regions of the interference pattern due to the optical dipole force, $F = -\nabla U = \frac{1}{2}\alpha_{\text{eff}}\nabla(E^2)$, where U is the potential between the induced dipole and the electric field that created it, α_{eff} is the effective polarizability of the particle, and E is the amplitude of the laser electric field [3]. Hence, in the interaction of the optical interference pattern with the medium, a periodic density modulation is generated, termed the *optical lattice*. Using a chirp for the pump beams [1], i.e., by varying Δf, different density modulations corresponding to different particle velocities, v, can be probed within the duration of the laser pulse. Thus, using CRBS, the VDF of the particles can be probed within a single laser shot. Since the technique is only interacting with the polarizability of the particles, it can interact with any species, atomic or molecular, neutral or ionized, as long as they manifest a non-zero polarizability. This is also a key advantage of single shot CRBS, since it enables non-resonant measurements and the measurement of a variety of gases and gases mixtures, with the same laser system.

(3) A third beam, called the probe, with wavelength λ_{probe} and polarization perpendicular to that of the two pumps, is incident upon the optical lattice at an angle θ that fulfills the first order Bragg condition $\lambda_{probe} = \lambda_g \cdot \sin(\theta)$ [4]. A fourth beam, termed the *signal*, is generated through the interaction of the probe beam with the optical lattice.

(4) A CRBS spectrum is obtained by measuring the intensity of the signal beam, I_S, versus the optical lattice velocity, v_g. Here, the CRBS signal intensity I_S is proportional to the square of the induced refractive index modulation [5, 2], from which density and polarizability can be measured. From an experimental stand-point, this also means that, for single shot CRBS, the spectroscopic measurement is performed in the time domain (and read on the oscilloscope) rather than the frequency domain (which would entail the use of a spectrometer), along with the experimental difficulties this entails.

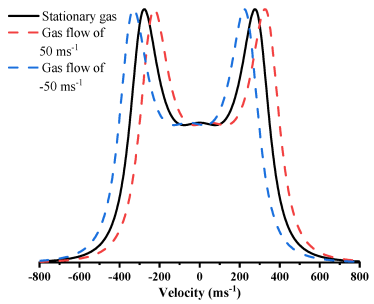

Fig 2: Blue and red Doppler shift on the CRBS lineshape due to gas flow in two opposite directions along the CRBS lattice's axis.

Importantly, single shot CRBS does not rely on any assumption regarding the thermodynamic state of the gas, since it directly measures the velocity distribution function (VDF) of the gas. This means that through single shot CRBS any departures from Maxwellian distributions can be detected and quantified directly. Additionally, if there exists a bulk flow in the gas, this can be trivially characterized through the Doppler shift induced in the CRBS spectrum, as shown in Fig. 2 [6]. Finally, dual-color CRBS enables both density and temperature measurement simultaneously at even sub-Torr pressures, by utilizing a probe at 532 nm instead of 1064 nm, as demonstrated in Ref. [7].

Since its initial demonstration, single shot CRBS has proven to be a powerful technique for the determination of the temperature, speed of sound, pressure, polarizability, shear, and bulk viscosity of a gas or gas mixture, with temporal and spatial acquisition times on the order of 150 ns and 100 μm, respectively [2, 8, 9, 10, 11].

One of the first demonstrations of single-shot CRBS in plasma was the measurement of carbon nanoparticles ($\sim$ 5 nm) in an arc discharge environment [12]. Figure 3 shows the first *in-situ* measurement of carbon nanoparticles ($\sim$ 5 nm) in an arc discharge environment using CRBS [12]. Nanoparticles were generated by an ablating graphite arc discharge for the demonstration of CRBS ability to measure *in-situ* nanoparticle masses. Additionally, this study confirmed the hypothesis that nanoparticle synthesis is dependent on the arc operating parameters (e.g. arc current and interelectrode gap) as well as on the distance from the arc core. Other optical diagnostic tools, including OES and LIF, were used as part of the same study, to evaluate nanoparticle production from graphite arc discharges with respect to the plasma properties [13].

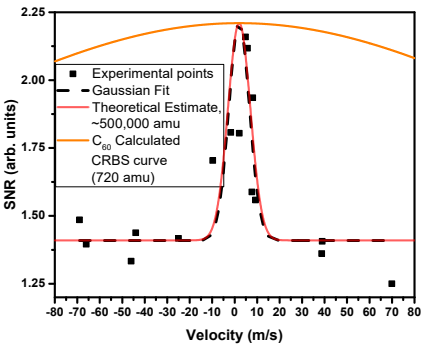

Fig 3: Measurement of the VDF of nanoparticles with dimensions of $\sim$ 5 nm, using the CRBS technique (Figure taken from Ref. [12]).

Utilizing the dual color CRBS approach [7], the temperature and density of neutral heavy species in a xenon glow discharge, operating at a pressure of 15 Torr was characterized radially [14]. Here, the main assumption is that since the ionization fraction in the glow discharge is very low (order of 10^{-4}-10^{-6}), the majority of the CRBS signal originates from the neutral species in the CRBS interaction region, thus providing with a direct measurement of their translational temperature and density. Indeed, by physically translating the interaction region around the crossing of the single shot CRBS beams, the temperature and density distribution of neutral species in the glow discharge was mapped out , starting from the plasma core and extending to its periphery (Fig. 4). As anticipated, the temperature is maximum in the center of the discharge and drops at the periphery, while the opposite trend is observed for the density profile.

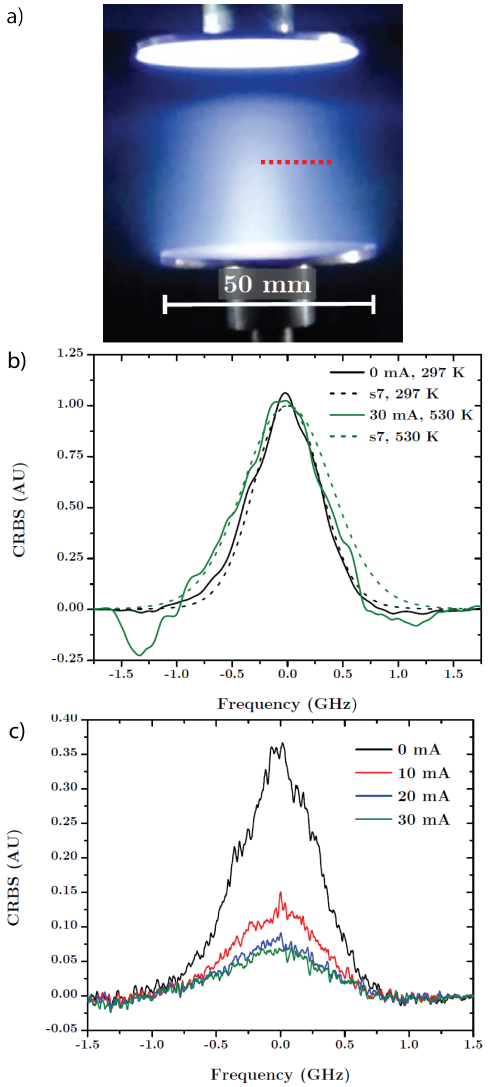

Fig 4: a) The xenon glow discharge and the radial points of measurement, b) Normalized VDFs, demonstrating temperature measurement at various currents, c) Non-normalized VDFs, demonstrating single shot density measurements at different currents. (Figures taken from Ref. [14]).

Apart from neutral species diagnostics in plasma discharges, we are currently working towards utilizing the optical lattice concept found in CRBS, for the measurement of ionic temperature. In the general case, similar to neutrals, ions are also high-field seekers and feel an attractive force towards regions of high electric field strength. Their polarizability is similar to their neutral state, only minimally affected by the magnitude of their positive charge (e.g. for N_2 it is 1.710 Å^3; for N_2^+ it is 2.091 Å^3). A CRBS lineshape from ions alone would effectively be the same as that from their neutral state at the same temperature, due to their almost equal mass. On the other hand, electrons in the plasma are repelled, due to the ponderomotive force, from regions of high electric field strength, and are thus low field-seekers. In the presence of an electric field potential landscape, such as the one created by e.g., the optical interference generated by the two high power laser beams, the two species (electrons and positive ions) will populate its antinodes, thus creating a charge separation electric field. The interaction among the dipole, ponderomotive and Coulomb forces with electrons, ions and neutrals, leads to an optical lattice with neutrals and charged particles. Different time scales must be considered due to the different time responses of light and heavy particles. We are currently developing a model to describe these dynamics, and are subsequently working towards performing CRBS measurements in a discharge with a high degree of ionization, to demonstrate this capability.

Finally, we have hypothesized that a similar four-wave mixing concept can be utilized for the measurement of electronic temperature, in the form of four-wave mixing Thomson scattering [15]. It is foreseen that, if successful, this method will largely improve the capabilities of Thomson scattering, enabling the characterization of electronic temperature at much lower densities than attainable today, while detecting departures from Maxwellian distributions, as is the case with single shot CRBS.

[1] A Gerakis, M N Shneider, and P F Barker. Single-shot coherent Rayleigh-Brillouin scattering using a chirped optical lattice. *Optics Letters*, 38(21):4449–4452, 2013.

[2] A Gerakis, M N Shneider, and B C Stratton. Remote-sensing gas measurements with coherent Rayleigh-Brillouin scattering. *Applied Physics Letters*, 109(3):31112, 2016.

[3] Robert W Boyd. Nonlinear optics. In *Handbook of Laser Technology and Applications (Three-Volume Set)*, pages 161–183. Taylor & Francis, 2003.

[4] W H Bragg and W L Bragg. The Reflection of X-rays by Crystals. *Proceedings of the Royal Society of London. Series A*, 88(605):428, 1913.

[5] Xingguo Pan, Mikhail N Shneider, and Richard B Miles. Coherent Rayleigh-Brillouin Scattering. *Physical Review Letters*, 89(18):183001, 2002.

[6] A. Gerakis and M. N. Shneider J. Bak, R. Randolph. Seedless, non-resonant gas flow velocimetry with single shot coherent Rayleigh-Brillouin scattering. *Physical Review Applied*. (in press).

[7] Junhwi Bak, Robert Randolph, and Alexandros Gerakis. Torr-level, seedless, non-resonant velocity distribution function measurement with a dual-color, single-shot coherent rayleigh–brillouin scattering scheme. *Journal of Physics D: Applied Physics*, 56(7):074001, jan 2023.

[8] Xingguo Pan, Mikhail N Shneider, and Richard B Miles. Coherent Rayleigh-Brillouin scattering in molecular gases. *Physical Review A*, 69(3):33814, 2004.

[9] Jacob Graul and Taylor Lilly. Coherent Rayleigh-Brillouin scattering measurement of atmospheric atomic and molecular gas temperature. *Optics Express*, 22(17):20117–20129, 2014.

[10] M O Vieitez, E J van Duijn, W Ubachs, B Witschas, A Meijer, A S de Wijn, N J Dam, and W van de Water. Coherent and spontaneous Rayleigh-Brillouin scattering in atomic and molecular gases and gas mixtures. *Physical Review A*, 82(4):43836, 2010.

[11] A S Meijer, A S de Wijn, M F E Peters, N J Dam, and W van de Water. Coherent RayleighBrillouin scattering measurements of bulk viscosity of polar and nonpolar gases, and kinetic theory. *The Journal of Chemical Physics*, 133(16):164315, 2010.

[12] Alexandros Gerakis, Yao-Wen Yeh, Mikhail N. Shneider, James M. Mitrani, Brentley C. Stratton, and Yevgeny Raitses. Four-Wave-Mixing Approach to In Situ Detection of Nanoparticles. *Phys. Rev. Applied*, 9:014031, Jan 2018.

[13] BC Stratton, A Gerakis, I Kaganovich, M Keidar, A Khrabry, J Mitrani, Y Raitses, MN Shneider, V Vekselman, and S Yatom. In situ diagnostics for nanomaterial synthesis in carbon arc plasma. *Plasma Sources Science and Technology*, 27(8):084001, 2018.

[14] Robert Randolph, Junhwi Bak, and Alexandros Gerakis. Measurement of translational temperature of neutral species in low temperature plasmas. In *AIAA SCITECH 2022 Forum*, page 0287, 2022.

[15] Mikhail Mokrov, Mikhail N. Shneider, and Alexandros Gerakis. Analysis of coherent Thomson scattering from a low temperature plasma. *Physics of Plasmas*, 29(3):033507, 03 2022.

LIF study of hydride dissociation in electric discharges

P. Dvořák(*)[1], M. Mrkvičková[1], W. Khan[1], N. Bolouki[1], T. Medek[1], A. Obrusník[1], J. Kratzer[2], M. Svoboda[2], J. Dědina[2]

[1] *Dep. of Plasma Physics and Technology, Faculty of Science, Masaryk University, Brno, Czech Republic*
[2] *The Czech Academy of Sciences, Institute of Analytical Chemistry, Brno, Czech Republic*
(*) pdvorak@physics.muni.cz

The fact that plasma is able to dissociate number of molecules is the basis for number of plasma applications including applications in analytical chemistry, where plasma is used for the dissociation of volatile compounds, frequently hydrides, which are used as carrier molecules for number of toxic, hazardous or biogenic elements [1]. Recently, dielectric barrier discharges (DBDs) have been systematically studied as atomizers, i.e. as a tool for the decomposition of hydrides or other volatile molecules [2]. The situation in DBDs is relatively complicated, because the volume dissociation of hydrides combines with surface reactions on walls, which can lead to unwanted losses of analyte atoms or be used for in-situ preconcentration of analytes and to improve the detection limit of the analytical methods.

Our work is a systematic (TA)LIF study of reactive species in various atomizers, including both the dominant radicals originating from the main plasma gases (i.e. atomic hydrogen [3, 4], atomic oxygen [5], OH radicals) and various free analyte atoms (Pb, Te, Bi, Se, Sn, Ge, Sb) [6, 7]. In order to increase the LIF signal-to-noise ratio, we developed a LIF method based on partially saturated fluorescence [8] and verified it by comparison with absorption measurements. The laser-based diagnostics on discharge-based atomizers were supplemented by E-FISH measurements of the electric field in the discharge. Experimental results were complemented by a numerical model of the plasma chemistry and gas flow in the atomizers.

Regarding the atomization mechanisms, we confirmed the theory that the decomposition of hydrides in both plasma and flame atomizers is based on reactions with atomic hydrogen, we revealed differences in spatial distribution of various analytes demonstrating the important role of the surface reactions, explained the difference of the performance of various atomizers, observed the preconcentration of analyte atoms on the wall and explained why a small (i.e. significantly substoichiometric) amount of oxygen manages to initiate the preconcentration on walls.

As an example of LIF measurements, the fig. 1 shows the distribution of free Sb atoms in a DBD atomizer, when stibine (SbH_3) from a 1 ng/l-solution was supplied to the plasma together with Ar and H_2. The results obtained with a continuous supply of SbH_3 (black curve) reveal a nearly homogeneous distribution of free Sb atoms through the whole active discharge (-25 to +25 mm). The homogeneous distribution of Sb atoms through the whole reactor and the relatively high Sb concentration demonstrate a good performance of the DBD for atomization of SbH_3.

The colour curves show the increase of Sb concentration (by more than an order of magnitude) which was reached by the Sb preconcentration on walls and which had a character of a wave travelling from the discharge center towards its edges. The strong increase of Sb concentration demonstrate the possibility to control the surface reactions and use them for analyte preconcentration and improvement of the detection limit of studied species in DBD-based atomizers.

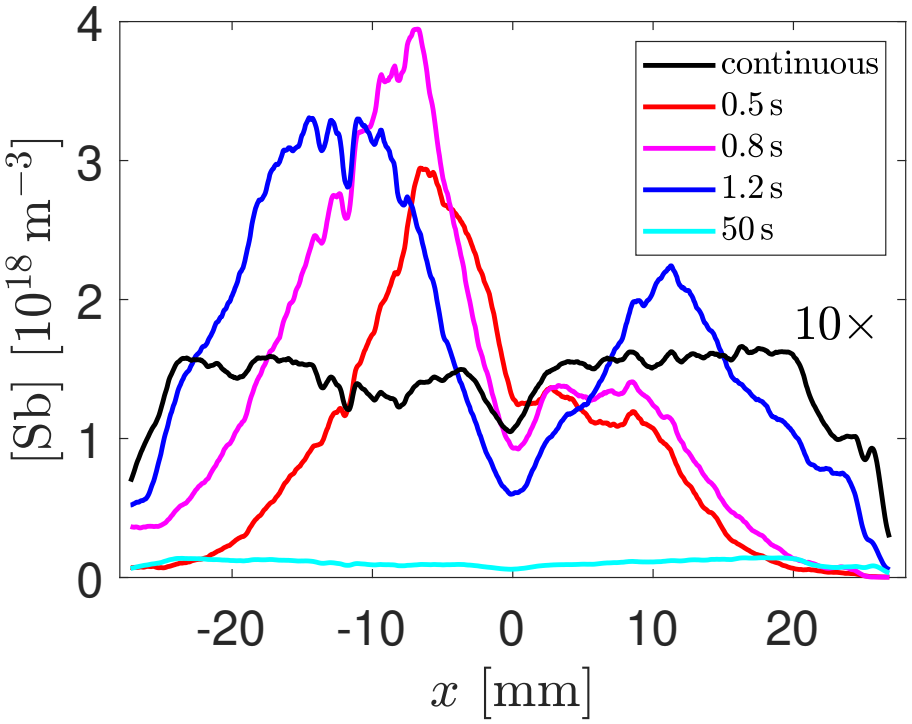

Spatial profile of the concentration of free Sb atoms in a DBD atomizer. The black curve (10-times increased) shows the situation when SbH_3 is continuously fed to the DBD. The colour curves show Sb distribution in various moments of the release process after the pre-concentration of Sb on the reactor walls.

[1] J. Dědina, D.L. Tsalev 1995 *Wiley and Sons Inc.* Hydride generation atomic absorption spectrometry
[2] S. Brandt et al. *Spectrochim Acta B* **126** (2016) 6.
[3] P. Dvořák et al. *Chemical Science* **10** (2019) 3643.
[4] P. Dvořák et al. *Plasma Sources Sci. Technol.* **26** (2017) 085002.
[5] P. Dvořák et al. *Plasma Sources Sci. Technol.* **26** (2017) 065020.
[6] K. Bufková et al. *Spectrochim Acta B* **171** (2020) 105947.
[7] M. Albrecht et al. *Spectrochim Acta B* **166** (2020) 105819.
[8] M. Mrkvičková et al. *Combustion and Flame* **241** (2022) 112100.

Acknowledgement: This research has been supported by the Czech Science Foundation under Contract 23-05974K, by the Project LM2023039 funded by the Ministry of Education, Youth and Sports of the Czech Republic and by the Czech Academy of Sciences (Institutional research plan RVO: 68081715).

Atomic oxygen measurements with THz absorption spectroscopy, ps-TALIF, and CRDS: A comparison

J. R. Wubs[1], U. Macherius[1], A. S. C. Nave[1], L. Invernizzi[2], K. Gazeli[2], G. Lombardi[2], X. Lü[3], L. Schrottke[3], K.-D. Weltmann[1], J. H. van Helden[(*)1]

[1] *Leibniz Institute for Plasma Science and Technology (INP), Greifswald, 17489, Germany*

[2] *Laboratoire des Sciences des Procédés et des Matériaux (LSPM), CNRS, Université Sorbonne Paris Nord, Villetaneuse, 93430, France*

[3] *Paul-Drude-Institut für Festkörperelektronik, Leibniz-Institut im Forschungsverbund Berlin e.V., Berlin, 10117, Germany*

[(*)] jean-pierre.vanhelden@inp-greifswald.de

Despite an ever-growing number of applications of low-temperature plasma technology, the common processes that occur in the plasma active zone and post-discharge region are still poorly understood. In particular, the non-equilibrium plasma chemical kinetics, and especially the atomic and molecular origins of many chemical and transport processes confined near surfaces remain mysterious. A detailed understanding of the complex chemical reaction networks would enable customised compositions of reactive species to be tailored for a specific plasma application. This requires highly sensitive and selective measurements of transient atoms, molecules and free radicals, their spatial and temporal distributions, and their transport behaviour. Of importance is also the evaluation of the gas temperature via the rotational and vibrational temperatures of the species and their respective temperature profiles, as these determine not only the density distribution of the species but also play a key role in the chemical kinetics. To detect atomic and molecular species, absorption spectroscopy has become a popular method as it has several advantages over other optical diagnostic techniques. Moreover, molecular spectroscopy in the infrared region is highly favourable because of the plethora of molecular bands that can be accessed, enabling selective and very sensitive spectroscopic measurements of a large number of compounds. However, the direct selective detection of atoms is only possible in the far-infrared spectral region, in addition to the well-known vacuum-ultraviolet spectral region. For a long time, the electromagnetic radiation in the terahertz (THz) spectral region from microwaves to the far-infrared (100 GHz – 30 THz) was known as the so-called THz gap due to the lack of suitable radiation sources and detectors in this spectral range. During the last three decades, however, this has changed as the related technology has advanced and the emerging technology has started to leave the laboratory environment. This region contains many transitions of atoms and molecules that are of interest to the plasma community, such as O, Si, Al, F, N^+, OH, NH_3. In this contribution, the recent progress in spectroscopy in the THz spectral region to detect ground-state atomic oxygen will be discussed.

Terahertz absorption spectroscopy with quantum cascade lasers (QCLs) has recently been developed and implemented as a novel diagnostic technique for determining atomic oxygen densities in plasmas [1,2]. It is based on the detection of the $^3P_1 \leftarrow {}^3P_2$ fine structure transition of ground-state atomic oxygen at approximately 4.75 THz (i.e., approximately 63 µm or 158 cm^{-1}). THz absorption spectroscopy allows for direct measurements (i.e., no calibration is required) of absolute ground-state atomic oxygen densities, and its accuracy depends almost exclusively on the accuracy to which the line strength of the transition is known. Furthermore, the narrow laser linewidth of QCLs of just a few MHz makes it possible to determine the temperature from the detected absorption profiles as well. In addition, the experimental setup for THz absorption spectroscopy is relatively compact, especially compared to two-photon absorption laser induced fluorescence (TALIF) setups that typically involve bulky laser systems, and the requirements for the optical alignment are not as strict as for cavity ring-down spectroscopy (CRDS). These features make THz absorption spectroscopy an attractive diagnostic technique for atomic oxygen density measurements in plasmas.

To confirm the accuracy of THz absorption spectroscopy, we performed ps-TALIF [3] and CRDS measurements of atomic oxygen densities on the same capacitively coupled radio frequency (CCRF) oxygen discharge, for a variation of the applied power (20W to 100 W) and the gas pressure (0.7 mbar and 1.3 mbar). TALIF is currently the most established method for determining atomic oxygen densities and especially known for its high spatial and temporal resolution [4], while CRDS is an absorption technique that yields line-of-sight integrated densities in a similar manner as THz absorption spectroscopy [5]. The obtained atomic oxygen densities are in excellent agreement with each other, as can be seen in Fig. 1. This demonstrates that the three different diagnostic methods can be used interchangeably, provided that no spatial resolution is required. In addition, the results seem to confirm the new value for the two-photon absorption cross-section of xenon [6]; this has been a topic of discussion for years and remains one of the main systematic sources of error when performing TALIF experiments.

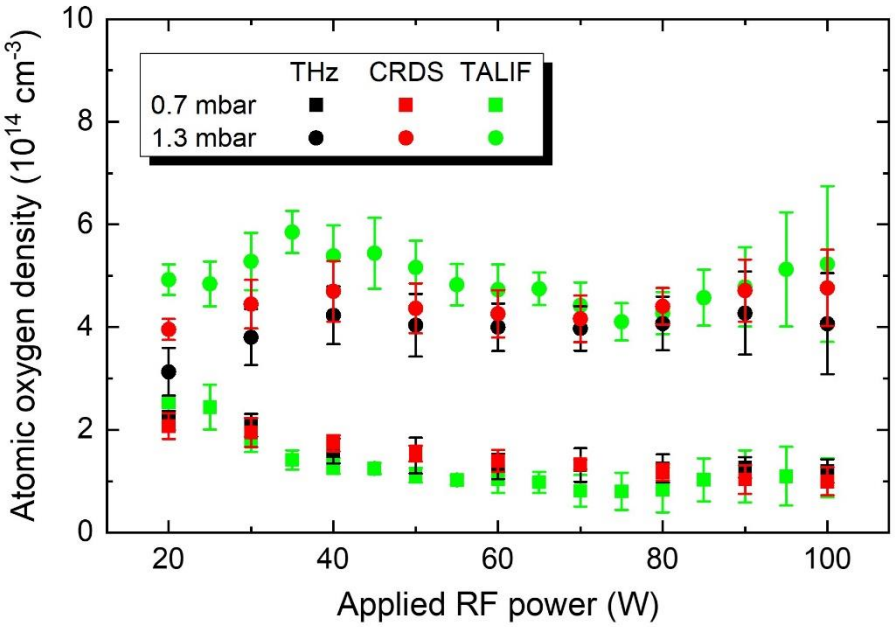

Fig. 1: Atomic oxygen densities measured with THz absorption spectroscopy, TALIF, and CRDS.

[1] J. R. Wubs, U. Macherius, K.-D. Weltmann, X. Lü, B. Röben, K. Biermann, L. Schrottke, H. T. Grahn, and J. H. van Helden, *Plasma Sources Sci. Technol.* **32** (2023) 025006.

[2] X. Lü, B. Röben, K. Biermann, J. R. Wubs, U. Macherius, K.-D. Weltmann, J. H. van Helden, L. Schrottke, and H. T. Grahn, *Semicond. Sci. Technol.* **38** (2023) 035003.

[3] J. R. Wubs, L. Invernizzi, K. Gazeli, U. Macherius, X. Lü, L. Schrottke, G. Lombardi, and J. H. van Helden, *Appl. Phys. Lett.* **123** (2023) 081107.

[4] G. D. Stancu, *Plasma Sources Sci. Technol.* **29** (2020) 054001.

[5] R. Peverall, S. D. A. Rogers and G. A. D. Ritchie, *Plasma Sources Sci. Technol.* **29** (2020) 045004.

[6] C. Drag, F. Marmuse, and C. Blondel, *Plasma Sources Sci. Technol.* **30** (2021) 075026.

POSTER SESSION 2, Thursday, July 11, 14:30-16:30

P2-T1-01 **S. Kawaguchi**; Y. Iwabe; K. Takahashi; K. Satoh; *Electron collision cross section set of O_2*

P2-T1-02 **V. J. Herrero**; R. J. Pelaez; M. Jimenez-Redondo; I. Tanarro; *Ion chemistry in C_2H_2:N_2:Ar cold plasmas: Anions of astrophysical interest*

P2-T1-03 **W. Graef**; E. Carbone; L. Vialetto; M. Hopkins; L. L. Alves; *The 2024 status report on the LXCat project*

P2-T3-04 **L. Kuijpers**; C.F.A.M van Deursen; E.J. Devid; W.A. Bongers; M.C.M. van de Sanden; *Experimental investigation of the complex chemistry in dry reforming microwave discharges*

P2-T3-05 **N. Babucic**; K.Kutasi; N.Skoro; N.Puac; *Characterization of Microwave Surface-Wave Launchers operating at Atmospheric pressure for Water Treatment*

P2-T3-06 V. Ilbeigi; **P. Kumari**; S. Matejcik; *Study plasma-chemical processes of alkanes in atmospheric pressure corona discharge by ion mobility spectrometry-mass spectrometry (IMS-MS)*

P2-T3-07 S. Lazarova; Ts. Paunska; V. Vasilev; **St. Kolev**; *CO_2 Conversion in a Gliding Arc Discharges with Different Electrode Materials and Magnetic Field Configurations*

P2-T4-08 **F. J. Morales-Calero**; A. Cobos-Luque; J. Munoz; R Rincon; A. M. Raya; J. A. Alcuson; N. Y. Mendoza-Gonzalez; M. D. Calzada; *Fundamental study of atmospheric pressure Ar-N_2 postdischarges and their application for metallic surfaces cleaning and activation*

P2-T4-09 **G. Cartry**; R. MaGee; J. Broude; T. Gans; J. Dedrick; M-A Pinault-Thaury; M. Sasao; Jocelyn Archard; J.M. Layet; *Surface production of negative-ions in hydrogen plasmas: comparative analysis of different surface materials*

P2-T4-10 **L. Zajickova**; M. Janusova; D. Necas; M. Elias; D. Hegemann; P. Navascues; L. Janu; *Insight into plasma polymerization with the significant contribution of ions towards deposition and etching balance*

P2-T4-11 **R. Masheyeva**; P. Hartmann; L.-Y. Luo; K. Dzhumagulova; Y.-X. Liu; J. Schulze; Z. Donko; *On the in-situ determination of the effective secondary electron emission coefficient in low pressure capacitively coupled radio frequency discharges based on the electrical asymmetry effect*

P2-T4-12 **T. Nonaka**; K. Takahashi; A. Uchida; O. Tsuji; *Deposition rates and chemical compositions of C_4F_8 plasma polymerization films on trench sidewalls*

P2-T4-13 **V. Mazankova**; D. Trunec; *Kinetics of ozone production by surface processes*

P2-T4-14 A. Siby; D. Stefas; Y. Agha; L. Invernizzi; C.Y. Duluard; K.. Gazeli; G Lombardi; K. Hassouni; **S. Prasanna**; *Usefulness of ps-TALIF to measure gas temperature and collisional cross-sections*

P2-T4-15 **P. Viegas**; J. Afonso; J. Silveira; T. C. Dias; L.Vialetto; A. S. Morillo-Candas; V. Guerra; *Surface recombination in Pyrex in oxygen DC glow discharges*

P2-T5-16 **N. Selakovic**; D. Maletic; N. Puac; G. Malovic; Z. Lj Petrovic; *Time-resolved images and detection of positive and negative ion species of atmospheric pressure plasma jet with spiral electrodes*

P2-T5-17 **G. LaCombe**; J. Wang; J. Rouxel; M. S. Simeni; *New Coherent Techniques for Ultrafast Diagnostics in Plasmas*

P2-T5-18 **M. Pazderka**; A.P. Jovanovic; M. Cernak; M.M. Becker; T. Hoder; *Sub-nanosecond development of electrical current in argon barrier discharge at atmospheric pressure*

P2-T5-19 L. Beving; **M. Hopkins**; G. Severn; *Sheath Expansion around Langmuir Probes in Flowing Plasmas*

P2-T5-20 **M. Mrkvickova**; P. Dvorak; B. Stadlerova; J. Kratzer; *Atomizers of tin hydride studied by laser-induced fluorescence*

P2-T5-21 **D. Prokop**; M. Mrkvickova; J. Tungli; P. Dvorak; S. Kadlec; T. Hoder; *Electrical charge relaxation on a dielectric surface*

P2-T5-22 **O. Jovanovic**; F. Krcma; L. Dostal; N. Puac; N. Skoro; *Time evolution of emission profiles and spatial structure of a plasma jet streamer discharge in contact with liquid*

P2-T5-23 **P. Skopal**; P. Dvorak; *The ignition of low-pressure capacitively coupled discharge*

P2-T5-24 **K. Polaskova**; P. Drexler; M. Klima; J. Machac; D. Necas; M. Svanda; L. Zajickova; *Antenna measurement of electric field and higher harmonics in atmospheric plasma jets interacting with different targets*

P2-T5-25 **R. Labenski**; D. Steuer; H. van Impel; M. Boeke; V. Schulz-von der Gathen; J. Golda; *Surface charge tailoring for plasma catalysis*

P2-T5-26 F. Enescu; A. Gobarev; G. Rotaru; C. Ionita; **R. Schrittwieser**; *Spectral investigation on two spherical cathode discharges*

P2-T5-27 **K. Sasaki**; K. Takada; S. Nishiyama; *Estimation of sheath electric field based on Dopper broadened absorption spectrum of hydrogen Balmer-alpha line*

P2-T5-28 P. Bilek; G. Arora; P. Hoffer; V. Prukner; T.C. Dias; V. Guerra and **M. Simek**; *Advanced analysis of overlapping emission spectra induced by highly transient discharges*

P2-T5-29 **Y. Yamashita**; K. Doi; T. Kiyota; S. Watanabe; K. Shimatani; W. Kikuchi; Y. Ye; A. Nezu; H. Akatsuka; *Electron temperature diagnosis of CF_4 O_2 plasma based on fluorine atomic corona model by tomographic optical emission spectroscopic measurement*

P2-T5-30 **Z. Navratil**; L. Kusyn; Z. Bonaventura; T. Hoder; *On the line intensity ratio for electric field measurement in dielectric barrier discharge in argon at atmospheric pressure*

P2-T5-31 **Z. Shu**; N.A. Popov; S.M. Starikovskaia; *Absolute calibration of Xe/O cross-section ratio for TALIF in nanosecond capillary discharge: optimization of the discharge parameters*

P2-T6-32 **D. F. N. Santos**; O. Ojeda Mena; M. Lisnyak; M. S. Benilov; *Exploring arcing phenomena in low-voltage contactors: a comprehensive study through numerical modelling and experiment*

P2-T6-33 **P. G. C. Almeida**; G. V. Naidis; and M. S. Benilov; *Theory of stability of self-sustaining DC discharges at inception with application to negative corona*

P2-T6-34 **J. Tungli**; Z. Bonaventura; D. Prokop; L. Kuthanova; T. Hoder; J. Fedor; M. Rankovic; M. Horky; S. Kadlec; *Determination of photoionization properties of C_4F_7N - N_2 mixture and their application in streamer simulation*

P2-T6-35 **J. Jansky**; R. Janalizadeh; V. P. Pasko; *Investigating of ignition of positive corona discharge in air using a time dependent fluid model*

P2-T6-36 **K. Tomankova**; K. Mrozek; A. Obrusnik; A. Fromm; F. Burmeister; *Sensitivity analysis of various physics processes in industrial HiPIMS: A global plasma modelling perspective*

P2-T6-37 **L.Y. Luo**; P. Hartmann; Z. Donko; H.P. Li; *Argon metastable atom quenching in low pressure Ar O_2 CCPs*

P2-T6-38 **Y. Liu**; T. Silva; T. C. Dias; P. Viegas; X. Zhao; Y. Du; J. He; V. Guerra; *Kinetic study of gas heating in low pressure CO_2 plasmas*

P2-T6-39 **S. Van Rompaey**; M. Gromov; E. Morais; A. Bogaerts; R. Morent; *Diagnostic characterisation and 0D modelling study of ns-pulsed plasma-assisted methane pyrolysis*

P2-T6-40 **U. Ebert**; D. Bouwman; J. Teunissen; *Macroscopic parameterization of positive streamers in air: velocity, radius, field etc.*

P2-T6-41 **M. M. Becker**; A.P. Jovanovic; L. Kusyn; T. Hoder; *Influence of voltage waveform and repetition frequency on atmospheric-pressure barrier discharges in argon*

P2-T6-42 **N. G. C. Ferreira**; P. G. C. Almeida; A. E. Taher; G. V. Naidis; M. S. Benilov; *Numerical investigation of stability of low-current point-to-plane negative corona in air*

P2-T6-43 **E. Calvo**; T. Santos; J. Henriques; M. J. Pinheiro; P. Sa; *Three-Dimensional Charged Particle Tracing of ExB Plasma Discharge in Hall Thrusters*

P2-T6-44 **P. Burda**; N. Corthouts; G. May; Z. Bonaventura; T. Magin; *Solving steady and unsteady multi-physics problems using a hybridized discontinuous Galerkin solver*

P2-T6-45 K. Koehn; D. Krueger; L. Vogelhuber; D. Eremin; L. Xu; **R.P. Brinkmann**; *The electric potential in high power magnetron discharges: A toy model*

P2-T6-46 **R. Almeida**; P. Almeida; H. Kaufmann; M. Benilov; *Fast Calculation Tool for Breakdown Voltage in a setup with a Dielectric Surface*

P2-T6-47 **R. Brunovsky**; A. Obrusnik; Z. Bonaventura; G. D. Stancu; *Multi-physics simulation of microwave capillary discharge in Argon: towards comprehensive power balance*

P2-T6-48 **S. J. Doyle**; R. W. Boswell; C. Charles; J. P. Dedrick; *Magnetic Enhancement of the Electrical Asymmetry Effect in Capacitively Coupled Plasmas*

P2-T6-49 **Q. Shen**; A. Pikalev; J. Gans; and R. van de Sanden; *Understanding NO formation and destruction by non-thermal effect in the quenching process of microwave air plasma*

P2-T6-50 **M. Stastny**; K. Mrozek; K. Jurik; L. Havlicek; M. Novotny; A. Obrusnik; *Numerical simulation of a low-pressure electrodeless ion source intended for air-breathing electric propulsion*

P2-T6-51 A.Tejero del Caz; D. Simoes; T. C. Dias; V. Guerra; M. Lino da Silva; L. Marques; N. Pinhao; C. D. Pintassilgo; **L. L. Alves**; *The LisbOn KInetics LoKi-B+C simulation tool*

P2-T6-52 **Z. Belkaid**; E. Morel; A. Revel; T. Minea; *Plasma model for high power impulse magnetron sputtering (HiPIMS) with helium*

P2-T6-53 **F. Zmeko**; E. Mullerova; Z. Bonaventura; *Macroscopic Model of Non-thermal Plasma Filament Based on Probabilistic Approach*

P2-T7-54 **S.S. Ussenkhan**; A.T. Zhunisbekov; Y. Yerlanuly; A.U. Utegenov; S.A. Orazbayev; T.S. Ramazanov; L. Boufendi; H.Vach; *Obtaining of silicon nanoclusters by the PECVD method*

P2-T8-55 **F. Krcma**; Z. Kozakova; F. Zbytek; M. Moravcik; *Influence of discharge kind on processes in Titan like atmosphere*

P2-T8-56 **M. Moravcik**; F. Krcma; *Influence of water vapor on electrical discharge-initiated processes in prebiotic atmospheres*

P2-T8-57 **F. J. Pérez-Invernón** ; J. F. Ripoll; F. J. Gordillo-Vázquez; P. Camino-Faillace; T. Neubert; O. Chanrion; N. Ostgaard; *A Comprehensive Analysis of Optical Emissions in Exposed Lightning Channels*

P2-T9-58 S. J. Doyle; **M. J. Kushner**; *Toroidal Plasma Sources for Remote and Isotropic Processing*

P2-T9-59 **J. Marjanovic**; D. Maric; Z. Lj Petrovic; *Emission properties of low-pressure low-current DC discharge in freons of new generation*

P2-T9-60 **V. Orlandi**; M. Dion; J. Brochie; A. Paillet; M. L. Kahn; L. Stafford; R. Clergereaux; *Effects of argon pulsed injection on a surface-wave plasma column at low pressures*

P2-T9-61 **V. Wolf**; R. Friedl; U. Fantz; *Ammonia production in a low- to mid-pressure microwave discharge*

P2-T10-62 **T. Bogdanov**; E. Benova; P. Marinova; *Novel microwave plasma source for wastewater treatment and prevention of chemical pollution in the environment*

P2-T10-63 **J. Thiel**; S. Kreuznacht; M. Boeke; A. von Keudell; *Iron oxide reduction in a high-performance argon-hydrogen plasma*

P2-T10-64 **L. Silberer**; S. Soldatov; G. Link; A. Navarrete; R. Dittmeyer; J. Jelonnek; *Investigation of emission spectra of atmospheric CO_2 plasmas sustained with microwave pulsation in a high Q resonator*

P2-T10-65 S. Soldatov; **L. Silberer**; G. Link; A. Navarrete; R. Dittmeyer; J. Jelonnek; *Optimization of gas quenching of atmospheric CO_2-plasma sustained in microwave reactor by application of water-cooled nozzles*

P2-T10-66 **M. Khasenov**; S. Samarkhanov; E. Batyrbekov; Yu. Gordienko; Yu. Ponkratov; V. Bochkov; E. Saparbek; A. Sluyanov; S. Tolmachev; *Reaction of lithium-6 with thermal neutrons as a source of nuclear-induced plasmas of gas mixtures*

P2-T10-67 E. Bizeray; A. Belinger; S. Dap; F. Fanelli; **N. Naude**; *Synthesis of metal polymer nanocomposite thin film through interaction of a gold salt solution aerosol with a Dielectric Barrier Discharge*

P2-T10-68 **N. Skoro**; O. Jovanovic; G. Malovic; N. Puac; *Characterization and optimization of 3-pin atmospheric pressure plasma jet system for water treatment*

P2-T10-69 **P. Marinova**; T. Bogdanov; E. Benova; M. Kirilova; Y. Todorova; I. Yotinov; I. Schneidern; Y. Topalova; *Non-thermal plasma treatment of landfill leachate for detoxification of hazardous pollutants*

P2-T10-70 G. Regodon; H. Acosta-Rivera; R. Alvarez; V. Rico; A. Palmero; **M. C. Garcia**; *Modifying atmospheric pressure surface-wave-sustained plasmas with silicon plates for discharge stability*

P2-T10-71 T. Ohara; S. Kinoshita; **K. Takahashi**; *Inactivating C.sphaerospermum and its mechanism in atmospheric pressure plasmas with water mist*

P2-T11-72 **O. Jašek**; J. Toman; P. Sťahel; J. Jurmanová; M. Stupavská; *Tunable stability of microwave plasma synthesized few-layer graphene dispersion in water*

P2-T11-73 F. J. Morales-Calero; A. Cobos-Luque; J. M. Blázquez-Moreno; A.M. Raya**; R. Rincón**; J. Muñoz; A. Benítez; N. Y. Mendoza-González; J.A. Alcusón; A. Caballero; M. D. Calzada; *Experimental Evidence of TIAGO Torch Plasma as a Surface Wave Discharge and Identification of the Radiation Zone: Improving Graphene Synthesis*

P2-T11-74 **A. Obrusnik**; M. Mrkvickova; W. Khan; N. Boulouki; T. Medek; M. Svoboda; J. Kratzer; J. Dedina; P. Dvorak; *Simulation of plasma; chemistry; and flow dynamics in flame-based and plasma-based hydride atomizers*

P2-T11-75 **R. Vertongen**; G. De Felice; H. van den Bogaard; F. Gallucci; A. Bogaerts; S. Li; *A different take on DRM in DBD: combining sorbents and plasma for single-stage CCU*

P2-T11-76 V. Lafaurie; Z. Shu; M. Sadauskaite; P. Vidal; **S. M. Starikovkaia**; *Nanosecond plasmas generation of a chemical gradient for detonation initiation: O-TALIF and OES characterisation*

Electron collision cross section set of O_2

S Kawaguchi(*)[1], Y Iwabe[1], K Takahashi[1], and K Satoh[1]

[1] *Division of Information and Electronic Engineering, Graduate School of Engineering, Muroran Institute of Technology, Muroran, Hokkaido, 050-8585, Japan*

(*) *skawaguchi@muroran-it.ac.jp*

A reliable and detailed electron collision cross section set of O_2 is required for precisely modelling and simulating O_2 containing plasmas. There are numerous studies on electron collision cross sections of O_2 for various processes. In the LXCat [1], seven kinds of self-consistent cross section sets for O_2, which include momentum transfer, excitation, electron attachment, and ionization cross sections, are available. However, the number and the shape of electron collision cross sections in the cross section sets differ from each other. This would yield different values of electron transport coefficients and rate coefficients; therefore, an assessment of the cross section sets is needed by comparing calculated and measured coefficients. The aim of this work is to construct reliable and detailed electron collision cross section set of O_2. The priority for constructing cross section set is to respect measured and theoretically calculated cross sections. The neutral dissociation cross sections and ionization cross sections for excited O_2^+ are carefully considered. The validity of the constructed cross section set is demonstrated by comparing measured and calculated electron transport coefficients in O_2 in a wide range of reduced electric fields.

The present electron collision cross section set consists of one vibrationally elastic momentum transfer, 15 rotational excitation, 15 rotational de-excitation, four vibrational excitation, 10 electronic excitation, 1 ion-pair formation, 3 neutral dissociation, 2 electron attachment, and 4 ionization cross sections. The rotational excitation and de-excitation cross sections were taken from Ridenti *et al.* [2] The vibrationally elastic momentum transfer cross section, q_{vm}, is defined as the sum of elastic momentum transfer cross section, rotational excitation, and rotational de-excitation cross sections. The shape of q_{vm} was determined to follow the q_{vm} measured by Shyn and Sharp [3], Iga *et al*. [4], Sullivan *et al.* [5], and Linert *et al*. [6]. Below 1 eV, the shape of q_{vm} was determined to reproduce the measured electron drift velocity and longitudinal diffusion coefficient at low reduced electric fields. The vibrational excitation cross sections are based on Laporta *et al*. [7]; however, their cross sections were multiplied by 0.31 to reproduce measured electron transport coefficients and modified to follow the measured vibrational excitation cross sections [8-10]. The electronic excitation cross section, q_{ex}, for $a^1\Delta_g$ and $b\ ^1\Sigma_g$ was determined to follow q_{ex} measured by Linder and Schmidt [11], Shyn and Sweeney [12], and Wakiya *et al*. [13]. The q_{ex} for $c\ ^1\Sigma_u^-$, $A'\ ^3\Delta_u$, and $A^3\Sigma_u^+$ was based on Shyn and Sweeney [14]. The q_{ex} for the Schumann-Runge continuum consists of q_{ex} for $1^3\Pi_g$, $B^3\Sigma_u^-$, and 8.87 eV state. The q_{ex} for $1^3\Pi_g$ and 8.87 eV state are based on Shyn *et al.* [15]. The q_{ex} for $B^3\Sigma_u^-$ is based on the BEf scaling result [16], but the shape near its threshold energy is modified to reproduce the measured ionization coefficient. The q_{ex} for $E^3\Sigma_u^-(v'=0)$ and $E^3\Sigma_u^-(v'=1)$ are based on Campbell *et al*. [17] and Suzuki *et al.* [16] A neutral dissociation cross section calculated by Laporta *et al.* [18] was included. Furthermore, we added two kinds of neutral dissociation cross sections the threshold energies of which are 10.5 eV and 12.1 eV. The former is determined to reproduce the sum of q_{ex} for the exsited states ranging from 9.7 to 12.1 eV. The latter is determined to reproduce measured ionization coefficieint and represents the neutral dissociation of superecited O_2 molecules[19]. The dissociative electron attachment cross section and cross section for ion-pair formation ($O^- + O^+$) were determined from total cross section for negative ion formation measured by Rapp and Briglia [20], which was multiplied by 0.74 in this work. Three-body attachment collisions were considered in accordance with Taniguchi *et al*. [21]. The ionization cross sections consists of cross sections for yielding $O_2^+(X^2\Pi_g)$, $O_2^+(A^2\Pi_u)$, $O_2^+(a^4\Pi_u)$, $O_2^+(b^4\Sigma_g^-)$, O^+, and O^{2+}. The ionization cross sections for $O_2^+(b^4\Sigma_g^-)$ and $O_2^+(A^2\Pi_u)$ were obtained from the total emission cross sections for the first negative system of O_2^+ ($b^4\Sigma_g^- \rightarrow a^4\Pi_u$) and the second negative

system of O_2^+ ($A^2\Pi_u \rightarrow X^2\Pi_g$) measured by Terrell *et al*. [22], respectively. The ionization cross section for $O_2^+(X^2\Pi_g)$ and $O_2^+(a^4\Pi_u)$ was determined as follows: The sum of cross sections for $O_2^+(b^4\Sigma_g^-)$ and $O_2^+(A^2\Pi_u)$ is subtracted from the total ionization cross section for O_2^+ recommended by Itikawa [23], and the residual cross section is splitted into cross sections for $O_2^+(X^2\Pi_g)$ and $O_2^+(a^4\Pi_u)$ using the branching ratio of cross sections for $O_2^+(X^2\Pi_g)$ and $O_2^+(a^4\Pi_u)$ reported by Doering and Yang [24]. The ionization cross sections for O^+ and O^{2+} recommended by Itikawa [23] were used.

We calculated the electron drift velocity, ionization coefficient, electron attachment coefficient, effective ionization coefficient, and longitudinal diffusion coefficient in O_2 by Monte Carlo simulation. It is found that the electron transport coefficients calculated from the cross section sets obtained from LXCat do not necessarily reproduce the measured electron transport coefficients [25-30]. The cross section set reported by IST-Lisbon well reproduces the measured transport coefficients compared to the other cross section sets; however, the calculated ionization coefficient is higher than measured data above 400 Td. The electron transport coefficients calculated from the present cross section set were found to agree with measured data in a wide range of reduced electric fields. This indicates the validity of the present cross section set of O_2.

[1] LXCat [https://nl.lxcat.net/].
[2] M. A. Ridenti, L. L. Alves, V. Guerra, and J. Amorim, *Plasma Sources Sci. Technol.* **24** (2015) 035002.
[3] T. W. Shyn and W. E. Sharp, *Phys. Rev. A* **26** (1982) 1369.
[4] I. Iga, L. Mu-Tao, J. C. Nogueira, and R. S. Barbieri, *J. Phys. B: At. Mol. Phys.* **20** (1987) 1095.
[5] J. P. Sullivan, J. C. Gibson, R. J. Gulley, and S. J. Buckman, *J. Phys. B: At. Mol. Opt. Phys.* **28** (1995) 4319.
[6] I. Linert, G. C. King, and M. Zubek, *J. Phys. B: At. Mol. Opt. Phys.* **27** (2004) 4681.
[7] V. Laporta, R. Caliberto, and J. Tennyson, *Plasma Sources Sci. Technol.* **22** (2013) 025001.
[8] C. J. Noble, K. Higgins, G. Wöste, P. Duddy, P. G. Burke, P. J. O. Teubner, A. G. Middleton, and M. J. Brunger, *Phys. Rev. Lett.* **76** (1996) 3534.
[9] I. Linert and M. Zubek, *J. Phys. B: At. Mol. Opt. Phys.* **39** (2006) 4087.
[10] T. W. Shyn and C. J. Sweeney, *Phys. Rev. A* **48** (1993) 1214.
[11] F. Linder and H. Schmidt, *Z. Naturforsch. A* **26** (1971) 1617.
[12] T. W. Shyn and C. J. Sweeney, *Phys. Rev. A* **47** (1993) 1006.
[13] K. Wakiya, *J. Phys. B: At. Mol. Phys.* **11** (1978) 3931.
[14] T. W. Shyn and C. J. Sweeney, *Phys. Rev. A* 62 (2000) 022711.
[15] T. W. Shyn, C. J. Sweeney, A. Grafe, and W. E. Sharp, *Phys. Rev. A* 50 (1994) 4794.
[16] D. Suzuki, H. Kato, M. Ohkawa, K. Anzai, H. Tanaka, P. Limão-Vieira, L. Campbell, and M. J. Brunger, *J. Chem. Phys*. **134** (2011) 064311.
[17] L. Campbell, H. Tanaka, H. Kato, S. Jayaraman, and M. J. Brunger, *Eur. Phys. J. D* **66** (2012) 26.
[18] V. Laporta, R. Caliberto, and J. Tennyson, *Phys. Rev. A* **91** (2015) 012701.
[19] Y. Hatano, *Phys. Rep.* **313** (1999) 109.
[20] D. Rapp and D. D. Briglia, *J. Chem. Phys.* **43** (1965) 1480.
[21] T. Taniguchi, K. Kawamura, S. Sakamoto, and H. Tagashira, *J. Phys. D: Appl. Phys.* **15** (1982) 1187.
[22] C. A. Terrell, D. L. Hansen, and J. M. Ajello, *J. Phys. B: At. Mol. Opt. Phys.* **37** (2004) 1931.
[23] Y. Itikawa, *J. Phys. Chem. Ref. Data*, **38** (2009) 1.
[24] J. P. Doering and J. Yang, *J. Geophys. Res.* **102** (1997) 9691.
[25] B.-H. Jeon and Y. Nakamura, *J. Phys. D: Appl. Phys.* **31** (1998) 2145.
[26] B.-H. Jeon and Y. Nakamura, *IEEJ Trans. Fundam. Mater*. **118** (1998) 874.
[27] K. Yoshida, H. Tagashira, T. Ohshima, H. Ohuchi, and Y. Kishimoto, *J. Phys. D: Appl. Phys*. **29** (1996) 2124.
[28] S. A. J. Al-Amin, H. N. Kucukarpachi, and J. Lucas, *J. Phys. D: Appl. Phys.* **18** (1985) 1781.
[29] D. R. Nelson and F. J. Davis, *J. Chem. Phys*. **57** (1972) 4079.
[30] T. Rasmus, E. Kalev, P. Peeter, R. Jüri, P. Toomas, and J. Indrek, *Phys. Scr*. **98** (2023) 045613.

Ion chemistry in $C_2H_2/N_2/Ar$ cold plasmas: Anions of astrophysical interest

V. J. Herrero(*)[1], R. J. Peláez[1], M. Jiménez-Redondo[2], I. Tanarro[1]

[1] *Instituto de Estructura de la Materia, (IEM-CSIC) Serrano 123, 28006 Madrid, Spain*

[2] *Max Planck Institut Für Extraterristrische Physik, Gießenbachstraße 1, 85748 Garching, Germany*

(*) v.herrero@csic.es

Hydrocarbon anions with the general formula $C_{2n}H^-$ (n=2-5) have been detected in circumstellar envelopes (CSEs) and cold molecular clouds in the interstellar medium [1]. These anions are coincident with the dominant negative ions observed in polymerizing acetylene cold plasmas [2, 3], where the stepwise addition of acetylenic monomers favors the formation of species with an even number of C atoms [4]. C_2H_2 plasmas have long been of interest in the astrophysical context, where they are often used for the production of laboratory analogs of carbonaceous interstellar dust [5], but the implications of similarities and differences between the gas-phase chemistry of laboratory plasmas and astronomical environments have not been explored. Nitrile ions with a general formula $C_{2n+1}N^-$ (n=0-4) have also been observed in CSEs and cold clouds, but as far as we know no laboratory anion distributions have been reported for N-containing acetylene plasmas. In this work we present the first results of a systematic investigation of ion distributions in $C_2H_2/N_2/Ar$ mixed plasmas and a comparison of these results with astronomical observations.

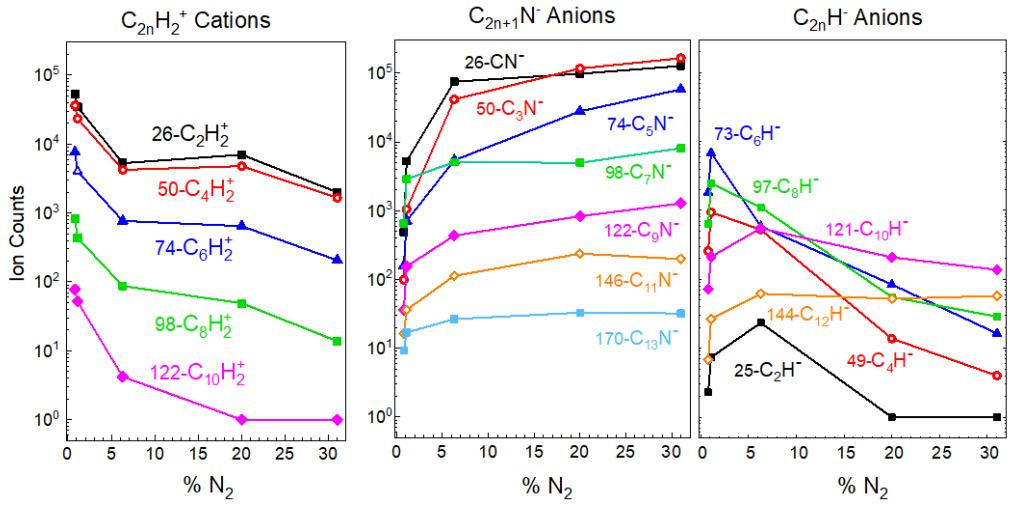

Fig 1: Evolution of characteristic ion-family distributions in RF discharges of $C_2H_2/N_2/Ar$ with increasing N_2 proportion

The experimental conditions were selected to observe incipient polymerization without particle formation. The experiments were performed in the capacitively coupled RF (13.56 MHz) reactor described in [3]. It has two electrodes, made of 20 cm diameter parallel plates, separated by 3 cm. The flows of the different gases to the reactor chamber were set with flow controllers, and the total chamber pressure was regulated with a valve connecting the chamber to the pumping system. Flows of 2 sccm C_2H_2, 0.2-0.4 sccm Ar, and 0.0-0.8 sccm N_2 were used. The total pressure before discharge ignition was 0.1 mbar, and the RF effective power was 50 W. The discharge was pulsed at 100 Hz with a 50% duty cycle, so that anions could fly out of the plasma volume in the off part of the cycle. Two differentially pumped quadrupole mass spectrometers (QMS) were used for the detection of species in the plasma. A residual gas analyzer (RGA, 0-100 u) for neutrals, and a plasma process monitor, (PPM, 0-340 u) for ions.

Distributions of neutrals, cations and anions were recorded for N_2 mixing ratios ranging from 0.8 to 31%. It was not possible to reach lower N_2 concentrations due to a residual N_2 impurity in acetylene. Among the neutral species formed in the discharge, HCN is worth mentioning. Its concentration increased appreciably with growing N_2 proportion. Changing the N_2 concentration in the discharges from 1.1 % to 6.3 % produced a drastic decrease in the total amount of detected cations and a corresponding growth in the global anion concentration (see Fig.1). Further increase in the N_2 mixing ratio up to 31% had a less drastic effect. Carbonaceous cations in the discharges are dominated by families of the $C_{2n}H_x^+$ type and their distributions are not much altered with growing N_2 proportion. In the case of anions, N_2 addition leads to significant changes in the more complex $C_nN_mH_x^-$ distributions. We focus here on the two anion families detected in space. For the lowest N_2 concentrations investigated (0.8% and 1.1 %) the $C_{2n}H^-$ (n=2-5) intensities are larger or comparable to those of the adjacent $C_{2n+1}N^-$ (n=1-4). For N_2 mixing ratios larger than 6.3 % nitrile anions dominate all distributions.

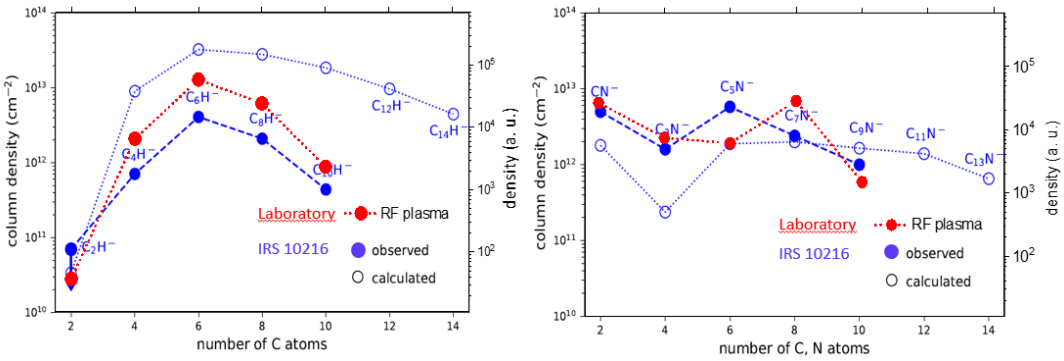

Fig 2: Comparison of laboratory $C_{2n}H^-$ and $C_{2n-1}N^-$ anion distributions (red, right y-axis) with astronomical observations and astrochemical calculations from [1] (blue, left y-axis) of the IRS+10216 circumstellar envelope. The laboratory data are for C_2H_2 (83.6%), N_2 (1.1%), Ar (15.3%)

Figure 2 shows a comparison between astronomical observations and laboratory measurements for a plasma containing a small N_2 proportion (1.1%). The astronomical results shown correspond to a CSE, but the anion distributions found in cold clouds are alike. The similitude between the measurements and observations is worth noting, especially for the $C_{2n}H^-$ family. This result is particularly puzzling if one considers the contrasting chemical mechanisms usually assumed for the two very different environments considered. Astrochemical models take a neutral polymerization route, initiated by UV photons, for the formation of $C_{2n}H$ and then, radiative electron attachment to produce $C_{2n}H^-$. In contrast, models of cold plasmas assume anionic polymerization usually driven by C_2H^- formed in turn by dissociative electron attachment to C_2H_2. Both astrochemical and plasma models have some controversial issues and we are presently working on the chemistry of these systems in an attempt to clarify the reasons for the observed similarities in the anion distributions.

Acknowledgements.V. J. H., I.T. and R.J. P acknowledge financial support by MCIN of Spain under Grant PID2020-113084GB-100.

[1] J. Pardo et al. *Astron. Astrophys.* **677** (2023) A55

[2] C. Descheneaux et al. *J. Phys. D.* **32** (1999) 1876

[3] M. Jiménez-Redondo, I. Tanarro, V. J. Herrero, *Plasma Sources Sci. Technol.* **651** (2022) 065003

[4] J. Benedikt, *J. Phys. D. Appl. Phys.* **43** (2020) 043001

[5] V. J. Herrero et al. *Front. Astron. Space Sci.* **9** (2022) 1083288

The 2024 status report on the LXCat project

W Graef[1], E Carbone[2], L Vialetto[3], M Hopkins[4], L L Alves[5] on behalf of the LXCat Team[(*)]

[1] *Plasma Matters B.V., De Zaale 20, DIFFER Building, 5612AJ Eindhoven, The Netherlands*
[2] *Institut National de la Recherche Scientifique, Centre Énergie Matériaux Télécommunications, 1650 blvd Lionel Boulet, Varennes, Quebec J3X 1P7, Canada*
[3] *Aeronautics and Astronautics, Stanford University, 496 Lomita Mall, Stanford, CA 94305, USA*
[4] *Applied Optical and Plasma Science, Sandia National Laboratories, P.O. Box 5800, Albuquerque, NM 87185-1423, USA*
[5] *Instituto de Plasmas e Fusão Nuclear, Instituto Superior Técnico, Universidade de Lisboa, Av. Rovisco Pais, 1049-001 Lisboa, Portugal*
[(*)] info@lxcat.net

The LXCat project [1] aims to provide an on-line platform for the curation of data required for modeling the electron and ion components of Low Temperature Plasmas (LTPs). This platform is the open-access LXCat website (`https://lxcat.net`). The data is provided by individual contributors, each maintaining their own database. The LXCat project is a truly global project as over 60 people from around the world participate by contributing data or by voluntarily working on other aspects, such as development, administration, or community outreach activities. The available types of data are electron-neutral and ion-neutral scattering cross sections (both integrated and differential), interaction potentials, oscillator strengths, rate coefficients, and transport parameters, such as mobility and diffusion coefficients. The goal of the LXCat project is dissemination of LTP data, and it does not recommend data. Therefore, data for the same process can occur multiple times as it can be part of different databases.

The platform provides tools for searching and downloading specific data, and results can be plotted and compared between different databases. In addition, complete sets of electron-neutral cross sections are available for a range of pure gases and mixtures, which can directly be used in an on-line version of the BOLSIG+ Boltzmann solver [2]. The calculated transport parameters and rate coefficients can subsequently be compared to data from other databases.

The services provided by LXCat have not changed significantly since its inception over a decade ago. To keep up with evolving needs of the LTP community, the LXCat team has been working on a complete redesign and reimplementation of the platform [3]. The new LXCat uses a new data format, new database, and new frontend, and provides many new functionalities. In order to gather valuable feedback from the community, a demonstration of the new platform is made available, which exhibits most capabilities. This demonstration platform offers a small set of representative data from the IST-Lisbon [4] and Phelps [5] databases converted from LXCat.

Latest updates of the current platform are presented as well as the status and goals of the redesign. The LXCat team is interested in contacting members of the LTP community about data needs and about how people can volunteer to participate in this project.

L.L. Alves was supported by Portuguese FCT under project 2022.04128.PTDC [6].

[1] E. Carbone *et al.*, Data needs for modeling low-temperature non-equilibrium plasmas: The LXCat project, history, perspectives and a tutorial, *Atoms* **9** (2021). `https://www.mdpi.com/2218-2004/9/1/16`

[2] G.J.M. Hagelaar, L.C. Pitchford, Solving the boltzmann equation to obtain electron transport coefficients and rate coefficients for fluid models, *Plasma Sources Science and Technology* **14** (2005) 722. `https://dx.doi.org/10.1088/0963-0252/14/4/011`

[3] D. Boer, S. Verhoeven, S. Ali, W. Graef, J. van Dijk, LXCat3. `https://github.com/LXCat-project/LXCat`

[4] L.L. Alves, The IST-Lisbon database on LXCat, *J. Phys. Conf. Series* (2014), 565, 1.

[5] Archived copy of Arthur V. Phelps website `https://web.archive.org/web/20180820113924/http://jilawww.colorado.edu/~avp/`

[6] Interação-Plasma-Superfície (Dados e ferramenTas) Modelização aCOplada `https://doi.org/10.54499/2022.04128.PTDC`

Experimental investigation of the complex chemistry in dry reforming microwave discharges

L. Kuijpers(*)[1], C.F.A.M van Deursen[1], E.J. Devid[1], W.A. Bongers[1], M.C.M. van de Sanden[1,2]

[1] *Dutch Institute For Fundamental Energy Research (DIFFER), De Zaale 20, 5612 AJ Eindhoven*

[2] *Eindhoven Institute of Renewable Energy Systems (EIRES), Eindhoven University of Technology, The Netherlands*

(*) l.kuijpers@differ.nl

In the endeavour to electrify the chemical industry, plasma based Dry Reforming of Methane (DRM) has been identified as a carbon neutral technology for syngas production. Traditionally syngas production is carbon intensive, as it is generated using steam methane reforming combined with the water gas shift reaction. In DRM it is attempted to couple carbon dioxide and methane directly into syngas, without the need for a subsequent gas separation step:

$$CO_2 + CH_4 \rightarrow 2\,CO + 2\,H_2 \quad \Delta H_r^{\ominus} = +247 \text{ kJ/mol} \tag{1}$$

Precisely the high endothermicity of this reaction makes plasma technology an ideal candidate to drive the process. While DRM in plasma is less well studied when compared to methane pyrolysis or carbon dioxide dissociation, especially warm plasma (i.e. microwave or arc discharges) have given promising results.

In this work we present an experimental investigation of DRM plasma in a vortex stabilised 2.45 GHz microwave discharge operating at 150 mbar and 1 kW power. Several diagnostics are set up, firstly effluent gas composition is measured using gas chromatography. Secondly, the plasma is characterised using optical emission spectroscopy that is both spatially and spectrally resolved. This is combined with axisymmetric tomography (the Abel inversion) to resolve local emissions. Lastly the core gas temperature is probed using a high resolution spectrometer to resolve the Doppler broadening of the atomic oxygen triplet at 777 nm.

The methane fraction is varied and the change in gas composition is seen to greatly influence the discharge. Upon increasing the methane fraction the emission profile is found to change: The discharge increases in size, atomic and chemiluminescent emissions shift in relative intensity, and Planckian radiation from solid carbon particles in the gas is seen for higher methane fraction.

The Spectral Soot Emission (SSE) technique [1] is applied on the 700-900 nm range to probe the carbon particle temperature and volume fraction based on the Planckian radiation and the assumption of Rayleigh-Debye-Gans scattering for fractal aggregates. The density of solid carbon particles in the discharge as determined from SSE is seen to increase with increasing methane fraction, eventually leading to carbon deposition on reactor walls and discharge instability.

The coupling of temperature profiles with local optical emission profiles greatly enhances our understanding of chemical and plasma processes in the discharge. It allows for a qualitative analysis of the highly complex chemistry found in DRM discharges.

[1] R. R. Snelling, *AIAA Journal* Vol. 40 No. 9 (2002) 1789–1795.

Characterization of Microwave Surface-Wave Launchers operating at Atmospheric pressure for Water Treatment

N.Babucić[1(*)], K. Kutasi[2], N.Škoro[1], N.Puač[1]

[1] *Institute of Physics, University of Belgrade, Pregrevica 118, 11080 Belgrade, Serbia*

[2] *Wigner Research Centre for Physics, Konkoly-Thege Miklós út 29-33, Budapest, Hungary*

(*) nedab@ipb.ac.rs

In recent years, spanning over large ranges of electron densities and temperatures, atmospheric pressure non-equilibrium plasmas have gained renewed interest for their ability to treat liquids and heat-sensitive materials, opening new applications in medicine, disinfection, water treatment, nanoparticle synthesis, food processing, and agriculture [1]. In this work we present results obtained by microwave (MW) discharge, chosen due to its electrodeless nature that prevents liquid contamination with nanoparticles during treatments resulting from electrode sputtering, as observed in some instances [2]. MW discharge was used for production of plasma-activated water (PAW). Interest in PAW has surged for its wide applications in biological sciences, agriculture, and the food industry. PAW's effects result from reactive oxygen and nitrogen species (RONS) generated in the liquid due to the plasma exposure and their concentration depends on the discharge parameters. RONS involvement correlates with diverse plant signaling pathways, governing metabolic processes, plant development, and stress responses [3]. This interaction can enhance germination rates, accelerate processes, and improve plant growth. Additionally, microwave-generated plasma serves as an efficient source, delivering higher RONS concentrations while treating bigger water volumes compared to other plasma sources, potentially amplifying its efficacy.

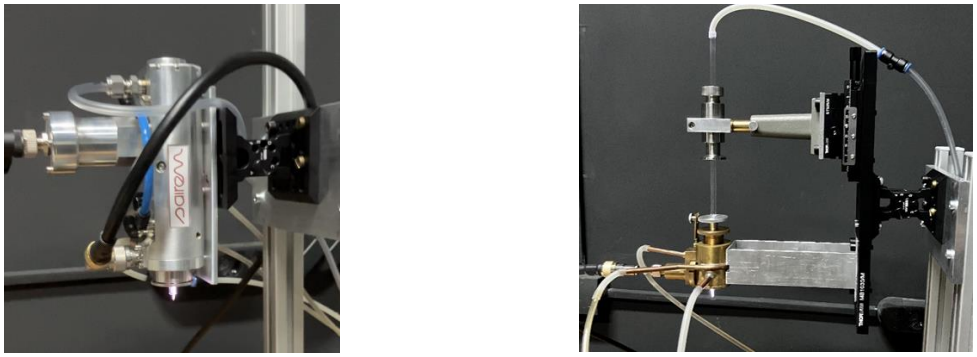

(a) (b)

Fig. 1: (a) Sairem S-Wave Launcher; (b) Home-made S-Wave Launcher

In the work presented here we have compared two different MW plasma sources, inductive Sairem S-Wave Launcher and capacitive home-made S-Wave Launcher, both powered by a Sairem GMS200W generator (see Fig. 1). One of the aims of research was the study of differences between devices in relation to the type of coupling. Tested powers were in range from 25 W to 60 W with argon as working gas (from 1 slm to 7 slm). We have used an O.D.=6/I.D.=4 mm quartz tube placed inside the launchers. By using Optical Emission Spectroscopy, the plasma emission inside and outside the tube was recorded. Due to their importance in the formation of reactive species, the lines of OH, N_2 and O were additionally analyzed. Fig. 2 shows examples of spectra for both investigated MW devices. The emission of the OH band is higher in the case of the inductive Sairem S-Wave Launcher (see Fig. 2(a)), indicating higher dissociation of water molecules from water vapor present as humidity. In the case of capacitive home-made S-Wave Launcher (see Fig. 2(b)) , the N_2 lines are more evident. With increasing power and gas flow, it is observed that plasma emission from the inductive Sairem S-Wave is higher with significantly increased temperature of plasma and

surrounding gas. In case of capacitively coupled S-Wave by changing the parameters, especially the gas flow, it was possible to obtain plasma at room temperatures.

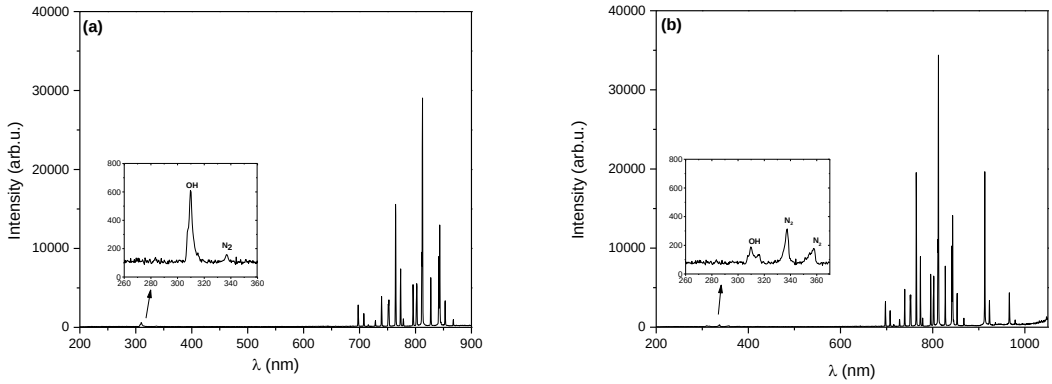

Fig. 2: Emission spectra of (a) inductive Sairem S-Wave Launcher; (b) capacitive home-made S-Wave Launcher, outside the quartz tube. Parameters: Ar flow of 2 slm, power of 28 W. Distance from the quartz tube was 3 mm.

By analyzing the spectra obtained using different lengths of quartz tubes through which the plasma is extended, and different distances from the end of the tubes, we came to the conclusion what combinations of parameters would give the highest concentrations of OH and N_2 lines, responsible for chemical reactions in the process of bacterial decontamination. Since the device creates colder plasma, the treatment of water was performed by using home-made S-Wave Launcher for 10 min, with a generator power of 50 W and an argon flow of 1 slm (scan the QR code). The value of the water temperature measured immediately after the treatment was 42,2°C. The water sample contained 32 ml of deionized water with 50 mg of zinc oxide powder added to water for the purpose of preventing the decomposition of RONS and preserving the pH value (pH=5), according to work [2]. The graph in Fig 3. shows the concentrations of nitrates, nitrites and hydrogen peroxide measured via calorimetric methods, immediately after treatment, as well as days after.

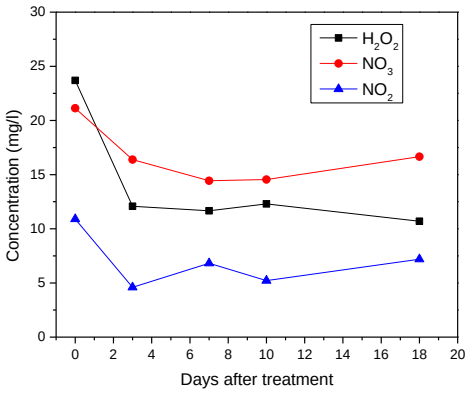

Fig. 3: Concentrations of NO_2, NO_3 and H_2O_2 measured in different days after the treatment.

Acknowledgments: This research was supported by the Science Fund of the Republic of Serbia, 7739780, APPerTAin-BIOM project and MSTDI- 451-03-66/2024-03/200024.

[1] P.J. Bruggeman et al., Plasma Sources Sci. Technol. 26, 123002 (2017).
[2] K. Kutasi et al., Plasma Sources Sci. Technol. 28, 095010 (2019).
[3] C. Bradu et al., J. Phys. D: Appl. Phys. 53, 223001 (2020).

Study plasma-chemical processes of alkanes in atmospheric pressure corona discharge by ion mobility spectrometry-mass spectrometry (IMS-MS)

Vahideh ILbeigi, Priyanka Kumari, Stefan Matejcik *
Faculty of Mathematics, Physics and Informatics, Mlynska dolina F2, 84248 Bratislava, Slovak Republic
* matejcik@fmph.uniba.sk

In this work, we aim to study the plasma-chemical processes of alkanes (pentane, hexane, heptane, octane) in atmospheric pressure corona discharge. Detection of the neutral products will be carried out by ion mobility spectrometry (IMS) and mass spectrometry (MS) using the Atmospheric Pressure Chemical Ionization (APCI) method. In IMS, ions are separated based on both mass and size, allowing for the identification of various ions that may share the same mass (isomers). This capability enhances our ability to discern and characterize different forms of ions, providing valuable insights into the complex ionization products generated during the corona discharge of alkanes.

The processes of fragmentation alkanes and synthesis of new hydrocarbons will be studied in the corona discharge reactor. The analysis of saturated hydrocarbons (alkanes) remains a challenge using mass spectrometry due to their low acidity/basicity and the lack of ion acceptor functional groups in their structures [1, 2].

Sekimoto et al. studied direct analysis of alkanes in real time (DART)-mass spectrometry associated with corona discharge using He gas (corona-DART) [3]. The alkanes are ionized by Corona-DART as positive ions via hydride abstraction and oxidation. The product ions are $[M+O-3H]^+$ (M+13) and/or the analogous monohydrates $[M+2O-H]^+$ (M + 31) which are primarily formed in the plasma jet with relatively high stability. Atmospheric pressure chemical ionization (APCI) of alkanes in air or in nitrogen with traces of oxygen is shown to yield regioselective oxidation, dehydrogenation, and fragmentation of alkanes [4]. Soft plasma ionization (SPI)-MS with a glow discharge ionization source was developed for ionization of alkanes [5]. They proposed a four-step reaction of alkane transformation with the resulting substance a protonated ketone ($[M+O-3H]^+$) [5].

A standalone IMS and an IMS-time-of-flight mass spectrometer (IMS-TOFMS) used in this study were homemade instruments constructed at the Department of Experimental Physics of Comenius University [6].

In this work, we used atmospheric pressure corona discharge for the ionization of saturated hydrocarbons. The experimental setup for ionization and transforming alkanes to IMS is shown in Fig.1. It consists of the external corona discharge, carrier gas, syringe pump for injecting sample, and IMS as a detector. Alkanes are ionized by using ext. CD system and the neutral products are transferred to IMS to be ionized and detected. The experiment is done at low and high current (3µA and 10 µA) of ext. CD in different type of gas: Air, nitrogen (N_2), and oxygen (O_2).

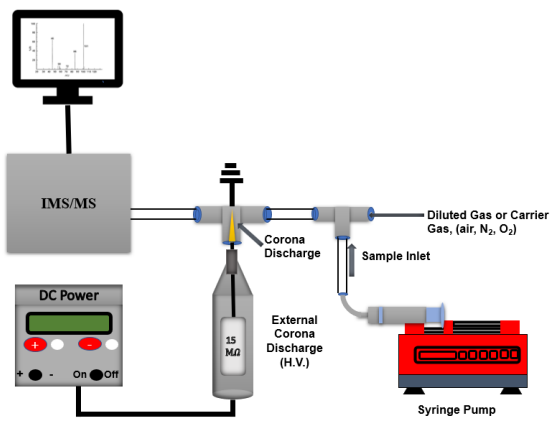

Figure 1: Schematic view of the external Ion Source (Corona Discharge) for ionization of alkanes.

Figures 2a and b show ion mobility and mass spectra of n-pentane (pent-72 g/mol) in positive polarity of ext. CD in air atmosphere. The main products ions are detected as $[pent+O-3H]^+$(m/z 85, $[C_5H_{10}O_2\text{-}OH]^+$, $[pent+O-H]^+$ (m/z 87, 2-pantanone and 3-pentanone) and $[pent+O-H]^+H_2O$ (m/z 105), originating from hydride abstraction and oxidation reactions.

The experiment was repeated in O_2 and N_2 atmosphere as carrier gas into ext.CD system. Oxygen is known to produce ozone in corona discharges [7] and is likely responsible for the oxidation of saturated Hydrocarbons [8]. Fig. 2 (c) shows the comparison of IMS spectra with different carrier gasses (Air, N_2 and O_2). The mass spectra in Fig.2 show that the ion mobility peak at drift times of 5.3 ms (m/z 145) and 5.8 ms (m/z 173) are probably related to a proton-bound dimer $[2Pentane]H^+$ and $[2Pentanone]H^+$ respectively in O_2 atmosphere.

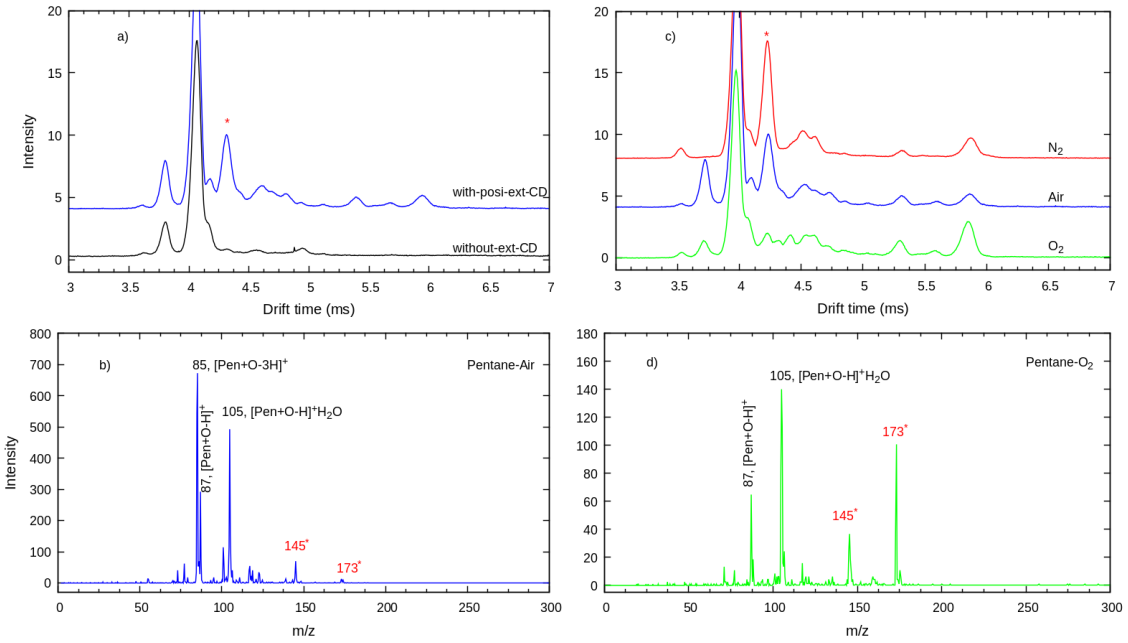

Figure 2: a) Ion mobility spectra of 30 ppm-pentane with and without ext.CD in positive polarity, b) Mass spectra of pentane in positive ext.CD, c) Comparison of ion mobility spectra of 30 ppm-pentane in O_2, N_2 and Air in positive polarity of ext.CD, d) Mass spectra of pentane in O_2.

Keywords: Saturated hydrocarbons, Mass spectrometry, Corona discharge, Oxidation reaction, ion formation

Acknowledgment

The present studies were supported by the Slovak Grant Agency for Science VEGA Nr. 1/0489/21, Slovak Research and Development Agency under project Nr. APVV-19-0386 and Nr. APVV-22-0133.

References

1. Wu, Chunping, Kuangnan Qian, Marcela Nefliu, and R. Graham Cooks. "Ambient analysis of saturated hydrocarbons using discharge-induced oxidation in desorption electrospray ionization." *Journal of the American Society for Mass Spectrometry* 21 (2010): 261-267.
2. Zhang, Ting, Zi-Yu Li, Mei-Qi Zhang, and Sheng-Gui He. "Gas-Phase Reactions of Atomic Gold Cations with Linear Alkanes (C2–C9)." *The Journal of Physical Chemistry A* 120, no. 25 (2016): 4285-4293.
3. Sekimoto, Kanako, Motoshi Sakakura, Takatomo Kawamukai, Hiroshi Hike, Teruhisa Shiota, Fumihiko Usui, Yasuhiko Bando, and Mitsuo Takayama. "Improvement in ionization efficiency of direct analysis in real time-mass spectrometry (DART-MS) by corona discharge." *Analyst* 141, no. 16 (2016): 4879-4892.
4. Ayrton, Stephen T., Rhys Jones, David S. Douce, Mike R. Morris, and R. Graham Cooks. "Uncatalyzed, regioselective oxidation of saturated hydrocarbons in an ambient corona discharge." *Angewandte Chemie* 130, no. 3 (2018): 777-781.
5. Nunome, Yoko, Kenji Kodama, Yasuaki Ueki, Ryo Yoshiie, Ichiro Naruse, and Kazuaki Wagatsuma. "Direct analysis of saturated hydrocarbons using glow discharge plasma ionization source for mass spectrometry." *Talanta* 204 (2019): 310-319.
6. Sabo, Martin, and Stefan Matejcik. "Corona discharge ion mobility spectrometry with orthogonal acceleration time of flight mass spectrometry for monitoring of volatile organic compounds." *Analytical chemistry* 84, no. 12 (2012): 5327-5334.
7. a) A. Yehia, A. Mizuno, Int. J. Plasma Environ. Sci. Tech. 2008, 2, 44 – 49; b) K. Yanallah, F. Pontiga, A. Fernµndez-Rueda, A. Castellanos, A. Belasri, J. Phys. D 2008, 41, 195—206.
8. a) R. Lee, M. L. Coote, Phys. Chem. Chem. Phys. 2016, 18,24663 – 24671; b) C. Clarence, S. J. Schubert, R. N. Pease, J. Am.Chem. Soc. 1956, 78, 2044 – 2048.

CO_2 Conversion in a Gliding Arc Discharges with Different Electrode Materials and Magnetic Field Configurations

S. Lazarova, Ts. Paunska, V. Vasilev, St. Kolev(*)

[1] *Faculty of Physics, Sofia University, 5 James Bourchier Boulevard, 1164 Sofia*

(*) skolev@phys.uni-sofia.bg

In this work, the dissociation of CO_2 gas in a gliding arc discharge (GAD) at atmospheric pressure is studied. The discharge device is built in three different configurations, all of them with the classic design with diverging electrodes (Figure 1). The first one employs the configuration of GAD discharge without an external magnetic field. In the other two, magnetic field is applied in a direction perpendicular to the arc current and the gas flow. The field is produced by permanent neodymium magnets. The magnetic field can be oriented in two ways. It can be in a direction, so that the arc is accelerated downstream due to the J×B drift, a case referred to in this paper as Magnetically Accelerated GAD (MAGAD). Alternatively, it can be oriented in a way that slows down the arc, a situation called Magnetically Retarded GAD (MRGAD). The gas flow and the arc are contained in a gas channel, formed between the electrodes and two quartz glasses with a distance between them equal to the electrode thickness, as shown in Figure 1.

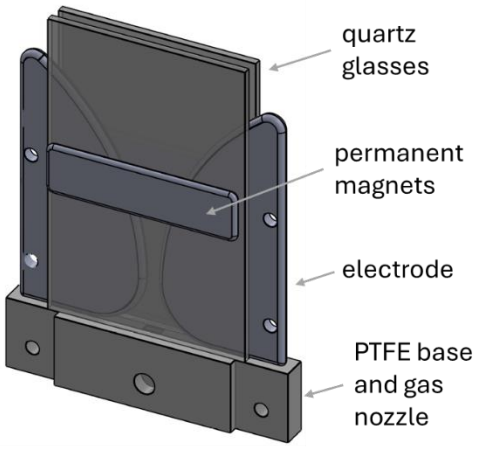

Fig. 1: Schematic 3D view of the discharge configuration including the electrode, the quartz glasses, and the permanent magnets. Note that there is an active cooling system over the quartz glasses which is not shown here.

This study is an extension of a previous work [1] and presents experimental results for the CO_2 dissociation and the energy efficiency for various modifications of the above-described discharge configurations. The applied diagnostic methods are electrical measurements of the arc currents and voltages, as well as Fourier Transform Infrared Spectroscopy (FTIR) for the determination of the outlet gas composition and thus the CO_2 conversion rate. The main differences from the previous study are: 1) the discharges use active cooling on the outer quartz glass walls, in order to improve gas quenching in the afterglow and the discharge stability in long time operation; 2) the distance between the quartz glasses d_{qw} is varied in the range 1 - 4 mm in order to evaluate the effect of this parameter for the CO_2 dissociation; 3) the effect of the electrode material on the CO_2 dissociation performance is also studied for three different electrode materials – stainless steel, copper and aluminium. Similarly to the previous work [1], the discharge is operated at three different current values – 50 mA, 100 mA, 210 mA.

The obtained results show a large variation in the CO_2 conversion rate and energy efficiency depending on the configurations and the current values. With respect to the distance between the quartz glasses, the optimal values are around 2 and 3 mm. At $d_{qw} = 1$ mm the results are the worst with low energy efficiency and conversion rate.

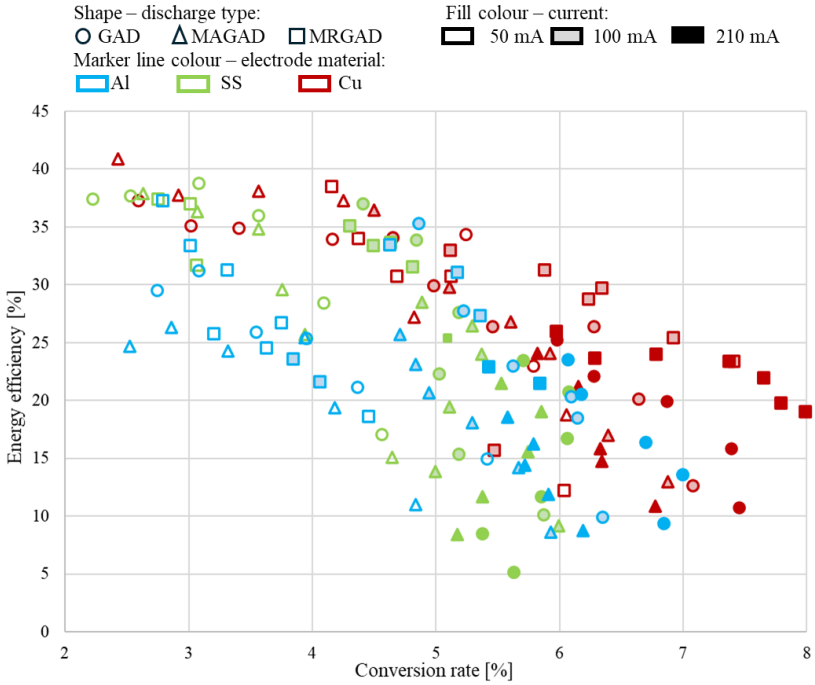

Fig. 2: Plot of the obtained energy efficiency vs the CO_2 conversion rate for $d_{qw} = 3$ mm for the three different configurations (GAD- circles, MAGAD – triangles, MRGAD - squares) with three different electrode materials (Cu – red symbols, SS – green symbols, Al – blue symbols). The discharge current is presented as the filling rate of the symbols (empty – 50 mA, semi filled – 100 mA, filled – 210 mA).

The effect of the electrode material on the results for $d_{qw} = 3$ mm is shown in Figure 2. All experimental points are obtained at different gas flow values in the interval 2 - 12 L/min. Overall, the Cu electrodes (the red symbols in Figure 2) show better performance compared to SS and Al with the MRGAD achieving the best combined performance of high conversion rates and energy efficiency. In the case of Al electrodes, the advantage of MRGAD is not so well pronounced and the overall performance is on a par with GAD. In the case of stainless steel electrodes, no configuration has a clear advantage over the other two.

Acknowledgements: This study is financed by the European Union-NextGenerationEU, through the National Recovery and Resilience Plan of the Republic of Bulgaria, project № BG-RRP-2.004-0008-C01.

[1] V. Ivanov, Ts. Paunska, S. Lazarova, A. Bogaerts and St. Kolev, *Journal of CO2 Utilization* **67** (2023) 102300

Fundamental study of atmospheric pressure Ar-N_2 postdischarges and their application for metallic surfaces cleaning and activation.

F.J. Morales-Calero[1], A. Cobos-Luque[1], J. Muñoz[(*)1], R. Rincón[1], A.M. Raya[1], J.A. Alcusón[1], N.Y. Mendoza-González[1], M.D. Calzada[1].

[1] *Laboratory of Innovation in Plasmas, Universidad de Córdoba (Spain).*

[(*)] jmespadero@uco.es

Surface wave discharges (SWDs) are at the forefront of technological advances, playing a key role in the development of new applications, particularly in surface modification of materials [1]. Surfatron is one of the better-known electromagnetic field applicators for SWDs generation. When nitrogen gas is introduced into an argon discharge generated with the surfatron device, the discharge shortens and changes its color from white to pink (Fig. 1), suggesting a modification of the excited species existing in the plasma. Moreover, the appearance of a fainter orangish region upstream, commonly known as remote plasma, afterglow or postdischarge, is observed. However, the absence of a visible post-discharge after an Ar discharge does not imply its nonexistence, but rather that it is not emitting radiation in the visible spectrum domain.

In the discharge region, charged species, excited species, and neutrals coexist. However, in the postdischarge there is no energy input, so mostly metastable states with longer lifetimes are present. Another feature of postdischarges is the significant decrease in the gas temperature along the afterglow, even reaching room temperatures. So, postdischarge are an exceptional tool for the treatment of materials avoiding thermal damage and ion bombardment. Moreover, the ability to work at atmospheric pressure makes this processes to be more manageable and affordable, eliminating the requirements of vacuum pumps. To optimize industrial applications, understanding behavior and internal kinetics is essential, but no deep fundamental studies concerning Ar-N_2 postdischarges exist up to date. First step is the identification of the species present in this region. Optical emission spectra of Ar and Ar-N_2 postdischarges appears in Fig. 2. When nitrogen is injected into the plasma, the emission spectra is modified, resulting in a significant drop of the emission of argon lines, together with the appearance of molecular bands: First Positive System (FPS) and Second Positive System (SPS) of the nitrogen molecule, as well as a few intense signal coming from the First Negative System (FNS) of the nitrogen molecular ion. In the postdischarge, reaction pathways are more limited compared to the discharge, where electrons play a fundamental role in internal kinetics, so the existence of excited species is caused by long-lived metastable states. In the case of Ar, the pooling of Ar metastables (4s levels) gives rise to the formation of Ar^+ and Ar_2^+ ions [2]. Recombination of these ionic species, either by three-body recombination or by dissociative recombination, leads to the production of excited species. Moreover, in Ar-N_2 postdischarges, Ar metastables can participate in excitation transfer reactions producing $N_2(C)$ excited molecules from the ground state [3], subsequently giving rise to FPS and SPS emissions via fast radiative decay. Regarding FNS emissions, N_2^+ ions can be generated via atomic nitrogen metastables pooling [2]. The presence of these active species in postdischarge region would enable the treatment of thermosensitive materials, as well as metallic materials in situations where high temperatures or charge effects should be avoided, such as in microelectronic devices.

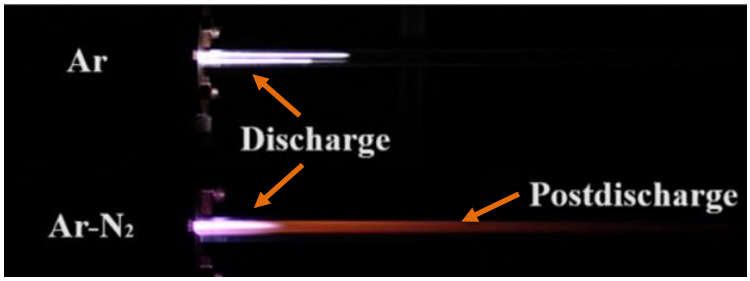

Fig. 1: Ar and Ar-N_2 plasmas generated with surfatron device.

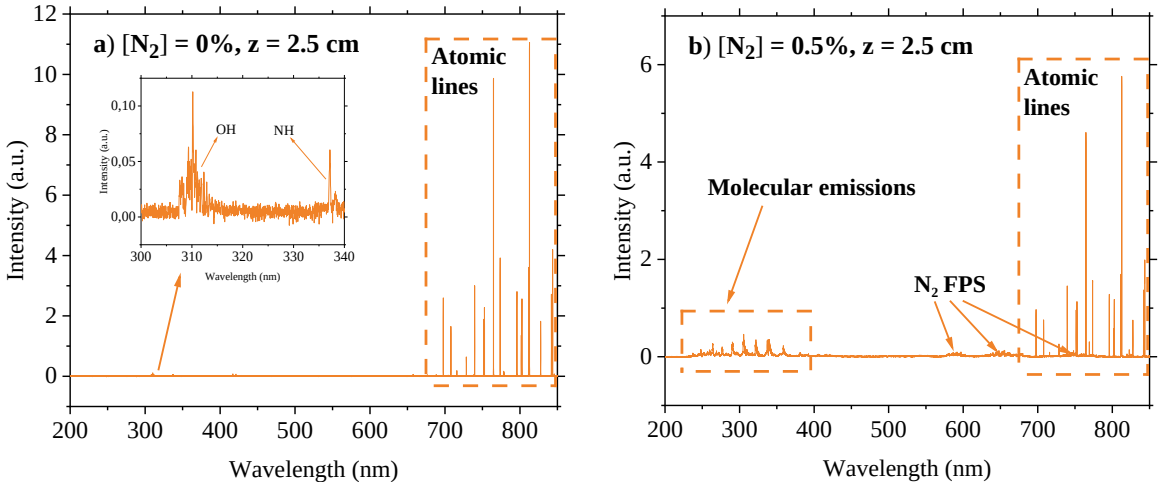

Fig. 2: Emission spectra of an Ar postdischarge (a) and Ar-N_2 ([N_2] = 0.5 %) postdischarge (b) sustained with a surfatron at atmospheric pressure. *z* is the distance between the end of the discharge and the optical fiber position at the postdischarge.

When an Ar or Ar-N_2 ([N_2] = 0.5 %) postdischarge is applied over a metallic surface, notable changes in the water contact angle (WCA) are observed (Fig. 3). The untreated surfaces of aluminum and steel display an averaged WCA of 61º and 54º, respectively. Following treatment with an Ar postdischarge, these values decrease to 32º and 21º, while treatment with an Ar-N_2 postdischarge results in averaged WCA values of 26º and 20º for aluminum and steel, respectively. These results may be attributed to modifications in surface roughness or to changes in the chemical composition of the surface. To investigate potential modifications in surface roughness and topography that may cause the observed changes, a Confocal and Interferometric Microscopy analysis of the surfaces has been conducted, revealing that there are no significant changes in surface roughness or in the mean values of the maximum peak height or the maximum valley depth, and other parameters derived from this analysis, such as root mean square roughness. X-Ray Photoelectron Spectroscopy (XPS) analysis has been then conducted to assess physicochemical changes in the plates, showing a reduction in surface carbon content, suggesting the removal of the outer hydrocarbon layer [1]. Additionally, there is an increase in oxygen proportion, possibly attributed to the incorporation of hydrophilic radicals such as OH or NO, explaining the decrease in the WCA of the metallic surfaces. This induced change in surface wettability facilitates the development and implementation of innovative applications, such as enhancing the adhesion of functional dyes or depositing graphene dispersions to improve surface corrosion resistance.

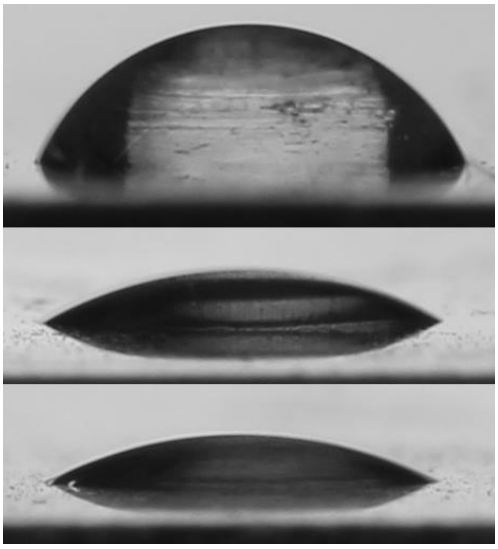

Fig. 3: Aluminum surfaces: (a) Untreated (b) after Ar postdischarge treatment and (c) after Ar-N_2 postdischarge treatment.

[1] J. Muñoz, *Applied Surface Science,* **407** (2017) 72-81.
[2] J. Henriques, *Journal of Applied Physics*, **109** (2011) 023301.
[3] J. Henriques, *Journal of Applied Physics*, **109** (2011) 023302.

Aknowledgments: This work was partially supported by Grant TED2021129261AI00 funded by MCIN/AEI/ 10.13039/501100011033 and by the European Union NextGenerationEU/PRTR. The predoctoral contract of F.J. Morales-Calero was granted by a MOD-2.2 from Plan Propio de la Universidad de Córdoba (2020).

Surface production of negative-ions in hydrogen plasmas: comparative analysis of different surface materials

G. Cartry(*)[1], R. Magee[2], J. Broude[1], T. Gans[2], J. Dedrick[2], M-A Pinault-Thaury[3], M. Sasao[4], Jocelyn Archard[5], J.M. Layet[1]

[1]*Aix-Marseille Université, CNRS, ISFIN, PIIM, UMR7345, F-13013 Marseille, France*

[2]*York Plasma Institute, Dep. of Physics, University of York, Heslington, York, YO10 5DD, UK*

[3]*GEMaC-CNRS/UVSQ, Université Paris-Saclay, Versailles , France.*

[4] *Organization for Research Initiatives and Development, Doshisha University, Kyoto 602-8580, Japan*

[5]*LSPM, CNRS-UPR 3407 Université Sorbonne Paris Nord, 99 Avenue J. B. Clément, F-93430 Villetaneuse, Fr*

(*) *gilles.cartry@univ-amu.fr*

Low pressure negative-ion sources find applications in several fields such as particle injection in linear accelerators or cyclotrons, surface analysis by SIMS, or neutral beam injection for magnetically confined fusion. These negative-ion sources rely on the process of negative-ion surface production, a process in which positive ions or atoms scattered from a plasma wall capture one or two electrons from the surface and lead to the production of a negative-ion. This process is occuring in any plasma source working with an electronegative gas but the negative-ion surface production yield is usually very low. In negative-ion ion sources a surface material having low-work function is employed to favour electron capture and negative-ion emission yield. The most common low work function metal used is Caesium (work function = WF = 2.1 eV versus 4-5 eV for common metals). Caesium vapour is injected in the plasma and deposit on the plasma chamber walls creating a low work function layer which favour negative-ion surface production. However, caesium drawbacks push to the use of other materials. In this contribution we are exploring several alternative materials for negative-ion surface production with the aim of detailing surface processes at play [1]. We are particularly interested in dielectric materials for which it is known that electron capture by an incident particle is made more difficult by the high energy required, but electron loss to the surface from the negative-ion created is greatly reduced due to the presence of a band gap. To that aim a conductive ceramic, the electride material C12A7 [2], having a low work function (WF = 2.4 eV) and a band gap, is compared with a low work function metal, Gadolinium (WF = 2.9 eV). Also, several diamond layers are compared together. In particular we have made the first study of negative-ion surface production on a phosphorous doped diamond layer (type n doping).

Measurements are performed in an ICP reactor at 2 Pa and 150W injected power. A negatively biased sample material is placed in the middle of the plasma chamber 40 mm away from a negative-ion detector, being whether a magnetized retarding field energy analyser or a mass spectrometer. Positive ions from the plasma bombard the sample and form negative-ions, which are then accelerated toward the detector and collected. The interaction of the plasma with the material lead to an evolution of the surface state. In order to collect in-situ information about changes of surface electronic properties due to plasma exposure a photoemission yield spectroscopy (PYS) diagnostic has been developed to measure material work-function.

In this contribution, negative-ion and WF measurements will be presented with a focus on in-situ photoemission yield spectroscopy. WF measurements will be compared with negative-ion yields and tentative correlations will be made with the aim of determining the parameters influencing at most on negative-ion surface production. A clear distinction is made between metal-like and dielectric like materials behavior with respect to negative-ion surface production meachnisms.

[1] Cartry, G. et al (2017). New Journal of Physics, 19(2), 025010A. N. Other, *J. Defined Ambiguity* **22** (2018) 37–47

[2] M Sasao et al, Applied Physics Express, 11(6), 2018

Insight into plasma polymerization with the significant contribution of ions towards deposition and etching balance

L. Zajíčková(*)[1,2], M. Janůšová[1], D. Nečas[1], M. Eliáš[1],
D. Hegemann[3], P. Navascués[3], L. Janů[1]

[1] *Central European Institute of Technology - CEITEC, Brno University of Technology (BUT), Purkyňova 123, Brno 61200, Czechia*
[2] *Deptartment of Condensed Matter Physics, Faculty of Science, Masaryk University, Kotlářská 2, Brno 61137, Czechia*
[3] *Empa, Swiss Federal Laboratories for Materials Science and Technology, Plasma & Coating Group, Lerchenfeldstrasse 5, St.Gallen 9014, Switzerland*
(*) lenkaz@physics.muni.cz

Low pressure radio-frequency (RF) discharges in CO_2/C_2H_4 can be used for the deposition of organic coatings with carboxyl and other oxygen functional groups that provide permanent hydrophilic surfaces [1] required in many applications. Moreover, carboxylated surfaces can be platforms for immobilizing biomolecules, *i. e.* creating biointerfaces for biosensors and artificial tissues [2, 3, 4]. The CO_2/C_2H_4 plasmas are processing environments in which etching and deposition are competing processes, especially in CO_2-rich mixtures. The etching effect is further enhanced in low pressure discharges that can provide significant ion energy flux toward the growing film. We studied neutral and ionic species in CO_2/C_2H_4 RF capacitively coupled plasma (13.56 MHz) with Hiden EQP 500 mass and energy analyzer placed between the powered and grounded electrodes. To obtain information about plasma chemistry for gas mixtures that were used previously for the deposition of carboxyl plasma polymers [5, 6], we carried out the measurements for different CO_2:C_2H_4 ratios (1:1, 2:1, and 6:1), with and without admixed Ar. The mass spectra of neutrals from plasma contained a small amount of oligomers. The compounds with four carbon atoms were still clearly detected. Larger ionic species were observed when extracting the positive ions directly from the discharge (Fig. 1). In the case of $Ar/CO_2/C_2H_4$ discharge, Ar ions were not at all the most abundant ionic species because ArH^+ (41 a.u.) and hydrocarbons combined with CO_2 and CO, *e. g.*, $C_2H_2^+$ (26 a.u.), $C_2H_3^+$ (27 a.u.), $C_2H_4^+/CO^+$ (28 a.u.), $C_2H_5^+/COH^+$ (29 a.u.), $C_3H_3^+$ (39 a.u.) and CO_2^+ (44 a.u.), had much stronger signals.

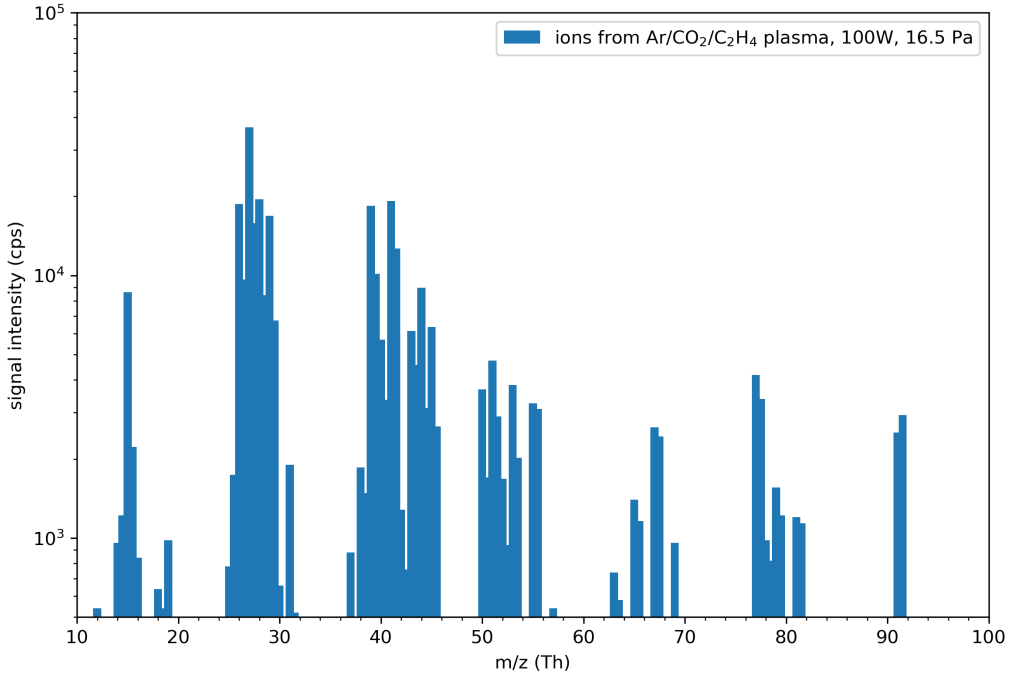

Fig. 1: ions from $Ar/CO_2/C_2H_4$ plasma, 100W, 16.5 Pa

In CCP discharges, the energy flux brought by ions towards the growing film can be substantial. In the asymmetric discharge, the substrate is often placed on the RF electrode, which acquires negative DC self-bias added to the plasma potential to create a high-voltage plasma sheath. In the symmetric discharge, the substrate is usually at the grounded electrode, but the plasma potential is high, i.e., resulting in a high-voltage sheath adjacent to the substrate. The effect of ions on the growing film depends on the deposited energy, the kinetic energy delivered at the surface per condensing atom (or molecule) [6]:

$$\varepsilon = \frac{E_{\mathrm{mean}}\Gamma_i}{R},$$

where R is the film deposition rate, Γ_i is the ion flux, and E_{mean} is the mean ion energy, which depends on the sheath voltage and collision processes governed by the pressure.

Understanding how the ions contribute to the overall deposition process requires complex plasma diagnostics combined with thin film characterization. A dedicated experiment involving the deposition into cavities partially shielding the incoming ions offers an easier way to gain insight into the process without detailed plasma diagnostics. Using the cavity with a slit opening [7], we studied the film deposition rate and chemistry in the CCP discharges of 2:1 and 6:1 CO_2/C_2H_4 mixtures at 10 Pa. In the 6:1 mixture characterized by the high contribution of etching, besides the deposition, the deposition rate inside the cavity below the slit opening (0.5, 1 and 2 mm) was about $2.5\times$ higher than on the flat surface exposed directly to the plasma. In the 2:1 mixture, the deposition rate inside the cavity was higher than on the flat surface only for the largest cavity, 2 mm.

We performed a simple Monte Carlo simulation of the film deposition to find what effects will be able to explain the film thickness profiles at two different gas mixtures and three types of slits, 0.5, 1 and 2 mm. The observed higher deposition rate in the cavity required a small probability of etching species being deactivated at the collision. However, this probability had to be low because the explanation of narrow thickness profiles inside the cavity required the presence of the directional etching species that etch sideways diffusion-caused deposition. Thus, to obtain the observed narrow profiles, the angular distribution of the sputtering yield with the maximum at around 35 ° angle of incidence was taken from the work of Hamaguchi *et al.* [8].

[1] D Hegemann, E Lorusso, MI Butron-Garcia, et al. *Langmuir* 32.3 (2016), pp. 651–654.
[2] AG Guex, D Hegemann, MN Giraud, et al. *Coll. Surf. B* 123 (2014), 724–733.
[3] M Jaganjac, A Vesel, L Milkovic, et al. *J. Biomed. Mater. Res. A* 102.7 (2014), 2305–2314.
[4] A Manakhov, E Kedroňová, J Medalová, et al. *Mater. Des.* 132 (2017), pp. 257–265.
[5] E Koerner, G Fortunato, and D Hegemann. *Plasma Process. Polym.* 6.2 (2009), 119–125.
[6] D Hegemann, E Koerner, K Albrecht, et al. *Plasma Process. Polym.* 7.11 (2010), 889–898.
[7] P Navascués, M Buchtelová, L Zajíčková, et al. *Applied Surface Science* 645 (2024), p. 158824.
[8] S Hamaguchi, AA Mayo, SM Rossnagel, et al. *Japanese Journal of Applied Physics* 36.7S (1997), p. 4762.

On the in-situ determination of the effective secondary electron emission coefficient in low pressure capacitively coupled radio frequency discharges based on the electrical asymmetry effect

R. Masheyeva[(*)1,2], P. Hartmann[1], L.-Y. Luo[1,3], K. Dzhumagulova[2,4], Y.-X. Liu[5], J. Schulze[6], Z. Donkó[1]

[1] *HUN-REN Wigner Research Centre for Physics, 1121 Budapest, Hungary*
[2] *Department of General Physics, Satbayev University, 050013 Almaty, Kazakhstan*
[3] *Department of Engineering Physics, Tsinghua University, 100084 Beijing, China*
[4] *Research Institute of Experimental and Theoretical Physics, Al-Farabi Kazakh National University, 050040 Almaty, Kazakhstan*
[5] *Key Laboratory of Materials Modification by Laser, Ion, and Electron Beams (Ministry of Education), School of Physics, Dalian University of Technology, 116024 Dalian, People's Republic of China*
[6] *Chair of Applied Electrodynamics and Plasma Technology, Department of Electrical Engineering and Information Sciences, Ruhr University Bochum, D-44780 Bochum, Germany*
[(*)] masheyeva.ranna@gmail.com

Radio frequency (RF) driven Capacitively Coupled Plasma (CCP) sources are extensively used in surface modification, layer deposition, and etching applications, particularly in the field of microelectronics. To reveal the fundamentals of such sources and to achieve the most effective processing, the knowledge-based optimization of these plasma sources is necessary, which requires well-defined laboratory experiments and high-fidelity simulations. The latter need a set of reliable input data for both the gas-phase and surface processes taking place in the plasma source. Among these data, the ones that describe the interaction of the plasma species with the surrounding surfaces are often not known with the desired accuracy. Therefore, in modeling studies, the interaction of ions and electrons with the surfaces is often approximated by a simplified approach: the models use (i) an effective ion-induced secondary electron yield, γ, which also includes contributions of species other than ions [1] and (ii) an effective elastic electron reflection coefficient, R, which is a reasonable approximation as long as the energy of the electrons at the surfaces remains low. Even these coefficients are not available to modelers for various gas/electrode material combinations due to the effects of the gas/plasma on the surface [2] and a lack of the in-situ surface diagnostics. The situation is further complicated by the fact that these values may depend on the particle energy distribution functions and electrode surface conditions and that the surface coefficient values available in the literature often originate from surface physics experiments conducted under ultrahigh vacuum conditions with heavily sputtered samples, which scenario differs strongly from those found in practical discharge physics experiments and applications. Therefore, during the past years a number of studies applying various approaches have been carried out to determine the values of γ and R, in situ [3, 4, 5]. In these studies, experimental recordings of some plasma characteristics and computational description have been combined to derive the surface coefficients in CCPs, by fitting the measured and computed data via the unknown surface coefficients.

In our previous work [6] we have explored the possibility to determine the surface coefficients discussed above via measurements of the DC self-bias voltage that develops in a geometrically symmetrical CCP due to the Electrical Asymmetry Effect [7] when the discharge is driven by a base RF harmonic and its second harmonic with a controllable phase angle. In [6] it was found that η is sensitive to γ, but can be taken independent of R, this way offering a way to determine γ based on the measurement of η.

Here we report our combined experimental and simulation studies that utilise this behavior. The operating conditions in the experiment are chosen in a way that (i) a precise measurement of the RF discharge voltage waveform is possible and (ii) the secondary electron emission from the electrodes has a strong effect on the measured DC self-bias voltage. For our investigations, a geometrically symmetric experimental cell is used, which consists of a glass cylinder with an inner diameter of 92 mm and two stainless steel electrode plates facing each other at a distance of L = 27.5 mm. The top electrode of the cell is driven by the RF voltage

$$\phi(t) = \phi_1 \cos(2\pi f_1 t) + \phi_2 \cos(4\pi f_1 t + \theta), \quad (1)$$

while the other electrode is grounded. Base frequency values of f_1 = 2 MHz and 4 MHz and Ar operating pressures of p = 40 Pa and 80 Pa are used, as well as voltage amplitudes ϕ_1 = 150 V and ϕ_2 = 75 V. By applying a voltage waveform given by eq. (1), the DC bias is controlled by the phase angle θ. By scanning θ over the $[0°, 360°]$ interval the $\eta(\theta)$ function exhibits a nearly triangular shape with relatively flat parts near the maximum and minimum (see figure 1). The match between the measured and computed bias voltage values is searched for phase angles at/near $\theta = 0°/180°$.

In the simulations, we use a computational framework that consists of two code modules: (i) a PIC/MCC code that traces electrons and Ar^+ ions (more precisely electron and ion 'superparticles') in the neutral background gas that comprises ground-state Ar atoms and Ar atoms in an number of excited levels, and (ii) a Diffusion-Reaction-Radiation (DRR) module, which computes the spatial density distributions of the Ar atoms in these excited levels, based on the rates of the collision processes computed in the PIC/MCC module and on the rates of the radiative channels (spontaneous emission and re-absorption) within the system of the excited levels and between some of these excited levels and the Ar atom ground-state [8]. The calculations also take into account pooling ionization between the excited atoms, as well as electron-impact stepwise ionization from the excited levels and quenching of the excited levels by neutrals, as well as diffusion losses. The elastic reflection coefficient of electrons is taken to be $R = 0.7$, based on [4, 5] and the simulations are conducted with various γ values to find the best match with the experimental value of the DC self-bias voltage, η.

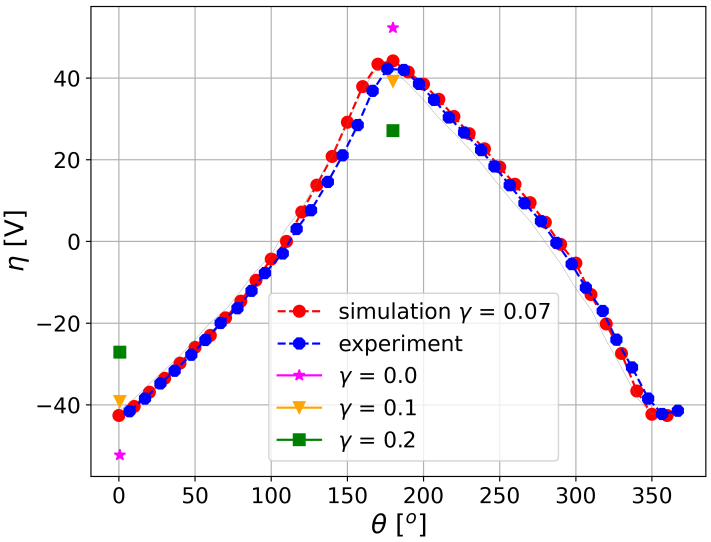

Fig. 1: Experimental and computed $\eta(\theta)$ curves for $\gamma = 0.07$ and DC self-bias values at $\theta = 0°/180°$ for various values of γ (individual points). Discharge conditions: Ar, p = 80 Pa, L = 2.75 cm, f_1 = 4 MHz, ϕ_1 = 150 V, ϕ_2 = 75 V, R = 0.7.

Figure 1 illustrates the dependence of the DC self-bias voltage on γ near the extrema of the $\eta(\gamma)$ curve, based on which a γ value of 0.07 was determined for the actual discharge conditions (Ar, p = 80 Pa, L = 2.75 cm, f_1 = 4 MHz, ϕ_1 = 150 V, ϕ_2 = 75 V), as well as the full $\eta(\gamma)$ curve obtained from the calculations using $\gamma = 0.07$ and the same curve measured in the experiment. These latter two curves show a very good agreement, confirming the in-situ effective secondary electron yield of ≈ 0.07.

[1] A. V. Phelps and Z.L. Petrović, *Plasma Sources Sci. Technol.* **8** (1999) R21.
[2] P. A. Bokhan, P. P. Gugin, M. A. Lavrukhin, V. A. Kim, G. V. Shevchenko, D. E. Zakrevsky, *Plasma Sources Sci. Technol.* **31** (2022) 125009.
[3] M. Daksha, B. Berger, E. Schuengel, I. Korolov, A. Derzsi, M. Koepke, Z. Donkó and J. Schulze, *J. Phys. D: Appl. Phys.* **49** (2016) 234001.
[4] D. A. Schulenberg D A, I. Korolov, Z. Donkó Z, A. Derzsi A and J. Schulze, *Plasma Sources Sci. Technol.* **30** (2021) 105003.
[5] J. Schulze, Z. Donkó Z, J. Benedikt, *Plasma Sources Sci. Technol.* **31** (2022) 105017.
[6] R. U. Masheyeva, K. N. Dzhumagulova, M. Myrzaly, J. Schulze and Z. Donkó Z, *AIP Advances* **11** (2021) 075024.
[7] Z. Donkó, J. Schulze and B.G. Heil, and U. Czarnetzki, *J. Phys. D: Appl. Phys.* **42** (2008) 025205.
[8] Z. Donkó, P. Hartmann, I. Korolov, D. Schulenberg, S. Rohr, S. Rauf, J. Schulze, *Plasma Sources Sci. Technol.* **32** (2023) 065002.

Deposition rates and chemical compositions of C_4F_8 plasma polymerization films on trench sidewalls

T. Nonaka [(*)1,2], K. Takahashi[3], A. Uchida[1] and O. Tsuji[1]

[1] *Research and Development Department, Samco Inc., Kyoto, Japan*
[2] *Department of Electronics, Kyoto Institute of Technology, Kyoto, Japan*
[3] *Faculty of Electrical Engineering and Electronics, Kyoto Institute of Technology, Kyoto, Japan*

[(*)] *nonaka-tomoyuki@samco.co.jp*

In the Bosch process, passivation films are deposited using C_4F_8 plasmas to protect the silicon sidewalls. In this study, deposition rate at each depth of the trench sidewall was measured and the chemical composition was analyzed to classify the precursor types produced in the C_4F_8 plasmas. The deposition rate at each depth is closely related to the sticking probability of the precursor. The results showed that polymerization reactions in the gas phase contributed significantly to the formation of precursor in the Bosch process.

1 Introduction

The Bosch process [1], suitable for processing high-aspect-ratio features, is used to fabricate trenches with high aspect ratios. This process involves three steps: passivation using C_4F_8 plasmas, film etching using ions in SF_6 plasmas, and Si etching using F-radicals in SF_6 plasmas. The sidewalls of silicon features are protected by passivation films during the process. In the C_4F_8 plasmas, a wide variety of precursors exist, and their sticking probabilities differ. In the shallow part of the trench, precursors with high sticking probability preferentially stick to the sidewalls, and a polymerized film with a large contribution of precursors with high sticking probability is deposited [2]. Since the precursors with high sticking probability are lost from the gas phase in the shallow part of the trench, the ratio of precursors with low sticking probability increases in a deep part of the trench, and the polymerized film with a large contribution of precursors with low sticking probability is deposited in the deep part of the trench. In this study, we measured the film thickness at different depths of the trench sidewalls under different discharge conditions to investigate the characteristics of the precursor produced in the C_4F_8 plasmas. The contribution of the polymerization reaction in the gas phase to the precursor formation was then discussed.

2 Experiment

An inductively Coupled Plasma (ICP) etcher RIE-800iPBC (Samco) for the Bosch process was used as a plasma generator. The distance from the ICP coil to the stage was 400 mm, which was longer than that of a typical ICP etching system. Passivation films were deposited on wafers and the sidewalls of trench illustrated in Fig. 1 using C_4F_8 plasmas. The passivation film thicknesses were measured by a reflectance spectrometer (FE-3000, Otsuka Electronics). The chemical compositions were analyzed by x-ray photoelectron spectroscopy (XPS: JPS-9010MX, JEOL).

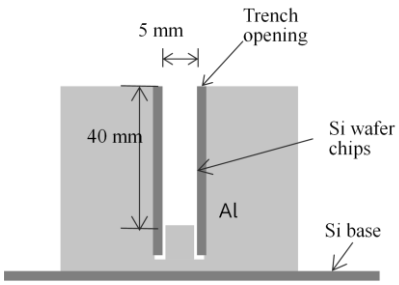

Fig. 1: Schematic of trench with a 5-mm gap and holder. Two diced silicon coupons were placed 5 mm apart, facing each other, in an aluminium holder.

3 Results and discussion

Analyses of the chemical composition of the C_4F_8 plasma polymerized film deposited on the wafer at flow rates of 50, 200, 800 sccm are shown in Fig. 2. At C_4F_8 flow rates of 50 and 200 sccm, the chemical composition is almost the same and the CF_2 bond content is high. At a flow rate of 800 sccm, the CF_2 bond content is lower and the C-CF_x bond content is higher than those at the other flow rates [3]. This difference is attributed to the different dissociation products of C_4F_8 molecules in the ICP region.

The Deposition rate of the polymerized film on the sidewalls of the trench (Fig. 1) is shown in Fig. 3. The deposition rate at the trench opening (0 mm) was highest at 50 sccm and lowest at 200 sccm. Among the three C_4F_8 flow rates, the film thickness thinned most rapidly with increasing depth at 800 sccm. This indicates that at this flow rate, precursor of films with high sticking probability and high C-CF_x bond content are produced. Comparing the film thickness deposited at flow rates of 50 and 200 sccm, which produce films with the same high CF_2 bond content in chemical composition, a relatively thick polymerized film was deposited at a deeper position with the flow rate of 50 sccm. The difference in the precursors produced at these two flow rates was caused by the difference in residence time in the downstream region of the plasma. When the residence time was longer, the polymerization reactions proceeded and largely less reactive precursors were produced.

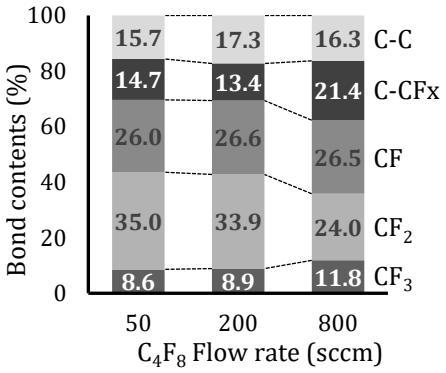

Fig. 2: Chemical composition of deposited films on wafer surface using C_4F_8 plasmas analyzed by XPS.

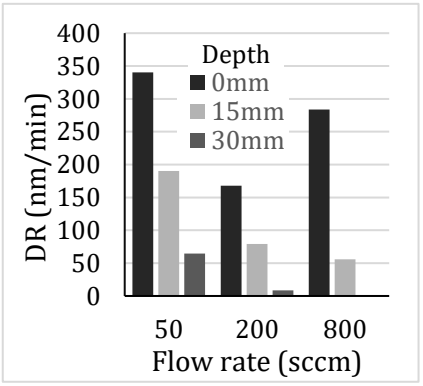

Fig. 3: Deposition rate (DR) of passivation films at sidewall depth of 0, 15, and 30 mm, and flow rate of 50, 200, and 800 sccm.

References

[1] F. Laermer, A. Schilp, Patents DE4241045, US 5501893 and EP 625285

[2] M. Izawa, N. Negishi, K. Yokogawa, and Y. Momonoi, Jpn. J. Appl. Phys. **46** (2007) 7870.

[3] T. Nonaka, K. Takahashi, A. Uchida, S. Lundgaard, and O. Tsuji, J. Vac. Sci. Technol. A **41** (2023) 063004.

Kinetics of ozone production by surface processes

Vera Mazankova(*)[1], David Trunec[2]

[1]*Department of Mathematics and Physics, Faculty of Military Technology, University of Defence in Brno, Kounicova 65, 662 10 Brno, Czech Republic*
[2]*Department of Plasma Physics and Technology, Masaryk University, Kotlarska 2, 611 37 Brno, Czech Republic*

(*) *vera.mazankova@unob.cz*

Plasma surface interactions are of considerable importance for a wealth of discharge phenomena. They are especially important in the formation and destruction of ozone in the afterglow of a DC low-pressure discharge in pure O_2 [1] and also in a dielectric barrier discharge at atmospheric pressure [2]. Nevertheless, the rates or probabilities associated with these surface reactions remain unknow. This contribution focuses on elucidating the determination of ozone production rates on silica surfaces.

When the solid surface is into contact with oxygen discharge or ozone, the surface is quickly covered by adsorbed atomic oxygen species and also by molecular oxygen species. Then the ozone is created by surface reactions via Langmuir-Hinshelwood (LH) mechanism or via Eley-Rideal (ER) mechanism. The LH mechanism is described by reaction

$$O_{2S} + O_S \rightarrow O_3 + 2S, \quad (1)$$

where O_S and O_{2S} are adsorbed oxygen atoms and molecules, respectively, S is the vacant site. The ER mechanism is described by reaction

$$O_2 + O_S \rightarrow O_3 + S, \quad (2)$$

where O_2 is molecule arriving at the surface from gas phase. These reactions were studied in the experimental set-up shown in Fig.1.

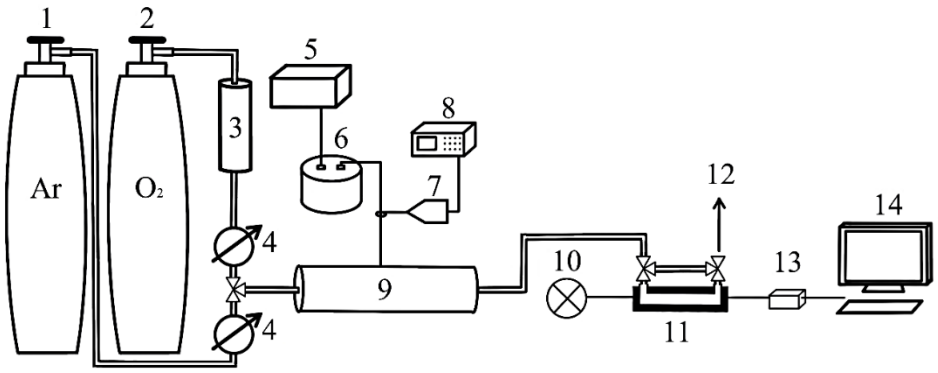

Fig.1: 1 – argon bottle, 2 – oxygen bottle, 3 – zeolites, 4 – mass flow controllers, 5 – high voltage generator, 6 – transformer, 7 – high voltage probe, 8 – oscilloscope, 9 – ozonizer, 10 – light source, 11 – measuring cuvette, 12 – gas outlet, 13 – spectrometer, 14 – PC.

The inner surface of the cuvette was treated by ozone for 5 min. After that the ozone was removed from the cuvette and the cuvette was filled by the mixture of oxygen and argon with different ratio. The time dependence of originated by surface reaction was measured using absorption spectroscopy. The results are shown in Fig.2. For short reaction time the ozone concentration increases linearly, when the ozone concentration increases above $2 \cdot 10^{14}$ cm^{-3} also the destruction processes of ozone occur. When the cuvette is filled by argon only, the ozone originated by LH processes only. If the oxygen is added to the argon, the ozone is created also by ER mechanism and the increase of ozone concentration is faster and

the final ozone concentration is also higher, see Fig.2. The ozone concentration produced by LH mechanism is described by equation

$$n(O_3) = \frac{2}{R} \cdot \frac{n_0^2(O_S) \cdot k \cdot t}{1 + n_0(O_S) \cdot k \cdot t} \quad , \tag{3}$$

where R is the cuvette radius, $n_0(O_S)$ is the initial surface concentration of adsorbed O atoms, k is the rate coefficient and t is the time. For short times this equation (3) reduces to

$$n(O_3) = \frac{2}{R} \cdot n_0^2(O_S) \cdot k \cdot t \, . \tag{4}$$

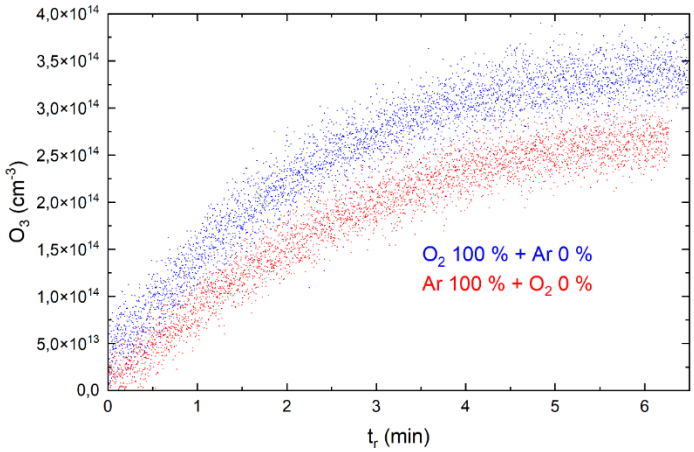

Fig.2: The dependence of ozone concentration on reaction time.

So, the initial slope of time dependence of ozone concentration is $a = \frac{2}{R} \cdot n_0^2(O_S) \cdot k$. The slopes are shown in Fig. 3.

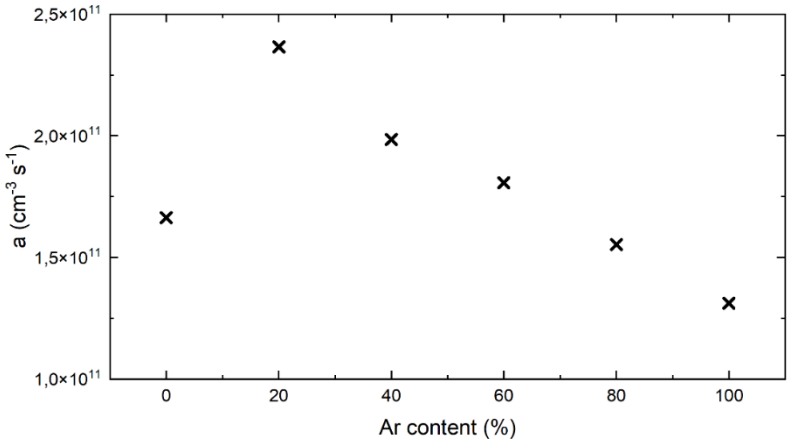

Fig.3: The dependence of the initial slope on argon content in the mixture.

We assumed that the surface concentration of active sites is 10^{16} cm^{-2} and one half of these sites is occupied by atomic oxygen and second half is occupied by molecule oxygen. Under this assumption the rate coefficient derived from these slopes is $1.56 \cdot 10^{-20}$ cm^{-2}s^{-1} for LH mechanism and for ER mechanism is $1.0 \cdot 10^{-28}$ cm^{-2}s^{-1}.

[1] J. P. Booth et al, *Plasma Sources Sci. Technol.* **32** (2023) 095016.
[2] M. Meyer, J. Foster and M. J. Kushner. *Plasma Sources Sci. Technol.* **32** (2023) 085001.

Acknowledgement

This research work was supported by the Project for the Development of the Organization "DZRO Military autonomous and robotic systems" under Ministry of Defence and Armed Forces of Czech Republic.

Usefulness of ps-TALIF to measure gas temperature and collisional cross-sections

A Siby[1], D Stefas[1], Y Agha[1], L Invernizzi[1], CY Duluard[1], K Gazeli[1], G Lombardi[1], K Hassouni[1], S Prasanna[(*)1]

[1] *Laboratoire des Sciences des Procédés et des Matériaux (LSPM)*
CNRS, UPR 3407, Université Sorbonne Paris Nord,
99 avenue J.B. Clément, 93430 Villetaneuse, France
[(*)] swaminathan.prasanna@lspm.cnrs.fr

In this work, we will discuss about the application of ps-TALIF to H_2 plasmas at low to moderate pressures to obtain more for meaurement of gas temperatures as well as collisional cross-sections, in addition to the H-atom densities. TALIF has become the standard approach to measure atom densities in reactive environments [1]. The principle of TALIF is to excite ground-state atoms to a fluorescing state by absorption of two photons of a pulsed laser and subsequently recording the resulting fluorescence signal. Combinination of ps-laser with a streak camera having ps-time resolution allows for application of TALIF for diagnosing reactive moderate to high pressure plasmas where the effective lifetimes τ_X of the fluorescence are of sub-nanosecond or ps-time scales[1].

In addition to the measurement of atomic densities, measurement of τ_H serves as a probe of local plasma conditions as it encapsulates all the radiative and collisional quenching processes

$$\frac{1}{\tau_i} = A_H + Q_H = A_H + \frac{P}{k_B T_g} \sum_{j}^{quenchants} k_{Q_{i/j}} x_j \tag{1}$$

Where Q_H and A_H are the quenching rate and the total Einstein coefficient of radiative decay of the excited state. P is the local pressure, T_g is the gas temperature, k_B is the Boltzmann constant, and x_j is the molar fraction of the quenchant j. One can identify, 3 distinct regimes based on the radiative and collisional cross-sections

- Radiation dominated regime at extremely low pressures i.e. $A_H >> Q_H$
- Collision dominated regime at high pressures where $A_H << Q_H$
- Competition between radiative and collisional processes at intermediate pressures i.e. $A_H \sim Q_H$

Therefore, the measurement of τ_H and exploitation of equation 1 allows one to gain more insight about the reactive environment.

At low pressure conditions, the depopulation mechanism of the laser excited state H(n=3) is dominated through radiative processes. In fact, the normally optically thick Lyman$_\beta$ becomes optically thin in these limits and its contribution to the overall radiative lifetimes A_H can no more be ignored. With respect to collisional quenching of the laser excited state, molecular H_2 is the most dominant. Previous experimental studies have reported a wide range of collisional quenching cross-section $\sigma_{Q_{H/H_2}}$ between 65 to 156 A^2. Measurement of τ_H over a range of low pressure, where the radiative processes are dominant, allows for the measurement of the radiative decay rate $1/A_H$ and collisional quenching cross-section $\sigma_{Q_{H/H_2}}$ using the Stern-Volmer plot. ps-TALIF measurements was performed on a Sairem Hi-wave source at pressures between 0.01 to 3 mbar. Lyman$_\beta$ line is only partially trapped in these conditions and $1/A_H$ is no more constant. This implies that Stern-Volmer method cannot be used to determine the quenching cross-sections. In such a scenario, it is necessary to use a collisional-radiative model in order to obtain the collisional cross-sections. Using such an approach we deduced a value of 98 ± 10 A^2 for $\sigma_{Q_{H/H_2}}$ [2].

Experiments were also performed on a moderate pressure microwave plasma torch to investigate the validity of $\sigma_{Q_{H/H_2}}$ estimated from low pressure conditions. In fact at moderate to high pressure conditions dominated by the highly collisional regime, one can estimate the gas temperature directly from the measured fluorescence lifetimes τ_H following Similarly, with the knowledge of radiative and

collisional decay constants, it would be possible to deduce the gas temperature T_g by rewriting equation 1 as

$$T_g = \frac{8}{\pi k_B}\left(\frac{P\tau_i}{1-\tau_i A_i}\sum_j \frac{x_j \sigma_{Q_{i/j}}}{\sqrt{\mu_{i/j}}}\right)^2 \quad (2)$$

The peak of the gas temperatures obtained from τ_H that represent the emissive region of the plasma has been compared with rotational temperature determined from the emission spectra of H_2 rotational bands of R branch of the transition $G^1\sum_g^+, \nu' = 0 \rightarrow B^1\sum_u^+, \nu'' = 0$, and lower and upper limits of the Q-Branch $d^3\prod_u, \nu' = 0 \rightarrow a^3\sum_g^+, \nu''= 0$ of the Fulcher-α band. With regard to the σ_{H/H_2} of H_2 molecule, values ranging between 65 [3] to 156 [4] A^2 have been reported in the literature and the gas temperatures estimated using the respective σ_{H/H_2} are either too low when compared to the rotational temperature of Fulcher or far too high to be realistic (c.f. Figure 1(a)). This validates the value of σ_{H/H_2} (98 A^2) measured for the experiments at lower pressure.

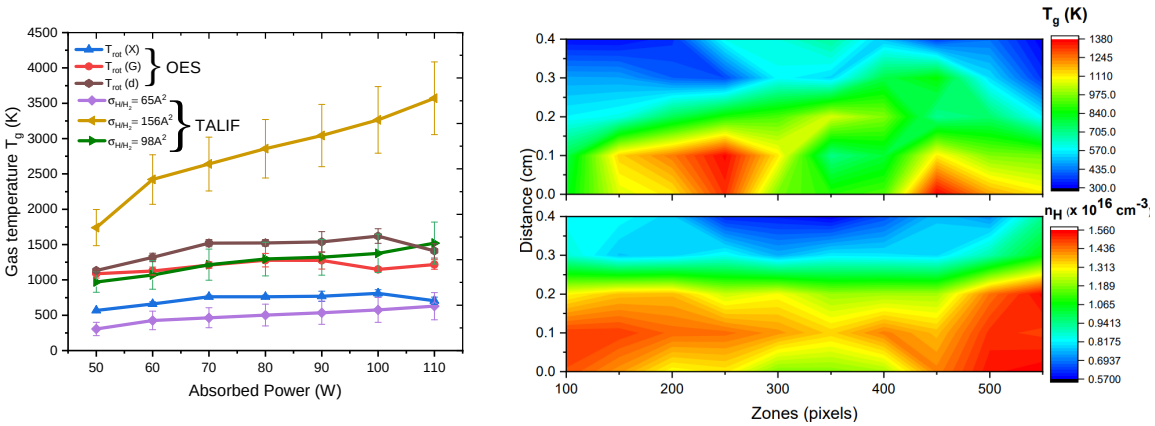

Fig. 1: (a) Comparison of gas temperatures measured using OES and ps-TALIF and (b) Constructed 2D contour plots of H-atom density and T_g at 100 mbar.

Furtheremore, the present methodology of gas temperature measurement allows us to make simultaneous measurement of H-atom density as well as gas temperature. Figure 1 (b) shows the contour plot of the H-atom density and gas temperatures measured from the ps-TALIF procedure.

Acknowledgements

This work was funded by the French Agence Nationale de la Recherche (ANR), under grants ANR-22-CE51-0013 (project NANODIAPLAS) and ANR-22-CE51-0027-02 (project ULTRAMAP), Labex SEAM (ANR-10-LABX-0096; ANR-18-IDEX0001) and IDF regional project SESAME DIAGPLAS. One of the authors (Khaled Hassouni) acknowledges the support of the Institut Universitaire de France.

[1] Gazeli, K et al., *plasma* **1(4)** (2018) 145–171.
[2] Duluard, CY et al., *PSST* **33(1)** (2024) 015003.
[3] Bitttner, J et al., *Chemical Physics Letters* **143(6)** (1988) 571–576.
[4] Catherinot, A et al., *Chemical Physics Letters* **18(3)** (1978) 1097.

Surface recombination in Pyrex in oxygen DC glow discharges

Pedro Viegas(*)[1], José Afonso[1], Jorge Silveira[1], Tiago Cunha Dias[1], Luca Vialetto[2], Ana Sofía Morillo Candás[3], Vasco Guerra[1]

[1] *Instituto de Plasmas e Fusão Nuclear, Instituto Superior Técnico, Universidade de Lisboa, Portugal*

[2] *Plasma Dynamics Modeling Laboratory, Stanford University, California, United States of America*

[3] *Laboratoire de Physique des Plasmas (UMR 7648), CNRS, Univ. Paris-Saclay, Sorbonne Université, École Polytechnique, France*

(*) pedro.a.viegas@tecnico.ulisboa.pt

In most plasma processes, surfaces interact with either the active discharge or its afterglow. Heterogeneous surface kinetics plays a role there, affecting both the plasma and surface properties. In particular, in oxygen-containing discharges the adsorption and recombination of atomic oxygen on reactor surfaces determine the gas composition, the availability of O for important volume reactions (e.g.: $CO_2 + O \rightarrow CO + O_2$; $CO + O + M \rightarrow CO_2 + M$) and eventually the flux of reactive oxygen species (ROS) towards target surfaces.

In the work by Booth et al. (2019) [1], the wall loss frequencies of O atoms were measured in the positive column of an oxygen DC glow discharge in a Pyrex tube (borosilicate glass) of 10 mm inner radius, for several pressures and discharge currents. However, the surface mechanisms determining recombination are not fully known yet. In particular, the increasing atomic oxygen recombination frequency and probability with decreasing pressure (see fig. 1) for a plasma operating in the pressure range between 0.27 mbar (0.2 Torr) and 1 mbar (0.75 Torr) is not fully understood. It is complemented by an increase of the recombination probability with current observed in the same pressure range, which is not the case at higher pressures. In our previous publication [2] we showed, via numerical simulations and comparisons with experiments (see fig. 1), that this change in regime results from a modification of the Pyrex surface, which may impact intermediate pressure plasma reactors where plasma-surface interactions are present. The simulations were obtained from a mesoscopic model employing deterministic and Kinetic Monte Carlo methods [3-5].

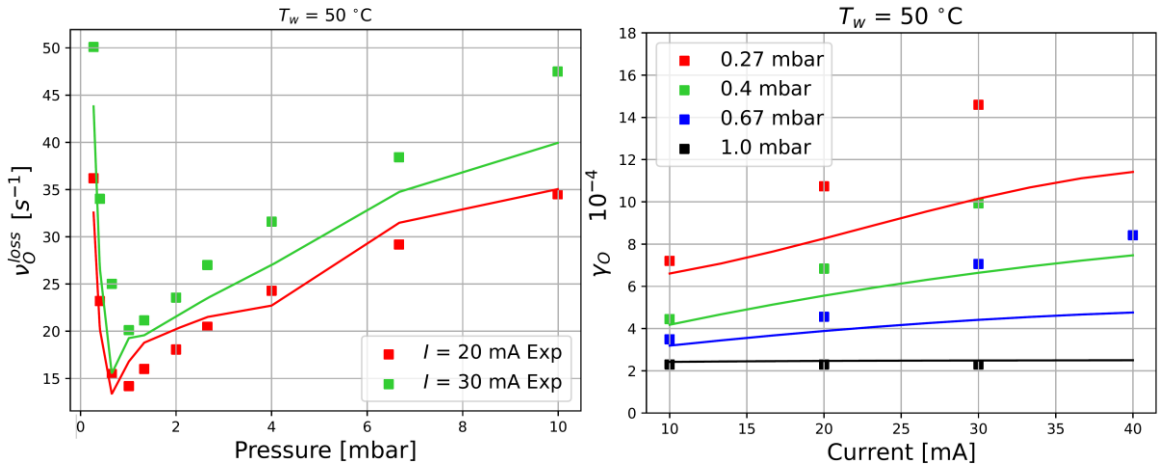

Fig. 1: Atomic oxygen loss frequency as function of pressure for 20 mA and 30 mA discharge current values (on the left), and atomic oxygen recombination probability as function of current for several pressure values (on the right), for a wall temperature of 50 ºC. Results from experiments [1] (square symbols) and simulations employing the deterministic method [2] (full lines).

In this work we employ the LisbOn Kinetics (LoKI) simulation tool [6-8], including the description of surface kinetics of oxygen species, to highlight the most relevant mechanisms and simulate self-consistently the evolution of those species in both gaseous and adsorbed phases in the experimental conditions of [1] and further experimental conditions at wall temperatures between -20 ºC and 50 ºC. The description of surface kinetics proceeds via the kind of mesoscopic modelling employed in the past [3-5], with a new reaction scheme including O+O and O+O_2 surface recombination reactions and a wall temperature dependent desorption frequency. The employment of this description in a coupled model that does not require fluxes and temperatures as input parameters allows to verify the appropriateness of the new reaction scheme and rates in the context of a self-consistent model that simulates the plasma-wall system as a whole in experimental conditions.

Through the self-consistent approach, the fluxes of species from the plasma directly affect the surface, and the surface processes directly affect the available densities in the gas phase, as well as the gas temperature. In particular, the flux of ions from the plasma induces the production of metastable chemisorption sites at the surface. As such, the Langmuir-Hinshelwood (L-H) and Eley-Rideal (E-R) recombination mechanisms take place involving not only physisorption and stable chemisorption sites, but also metastable chemisorption sites, produced by the impact of fast O_2 ions and neutrals, and where recombination can take place with lower energy barrier [9]. The production of metastable chemisorption sites decreases with pressure due to the incident energy of these particles and increases with current due to the flux of incident particles. The presence of metastable sites can be reversed by increasing the plasma pressure, since the destruction of these sites takes place through the collision of incident neutrals from the plasma, which increases with pressure.

The coupled model is validated for a total of 106 experimental conditions, accurately describing the experimental dependence of the atomic oxygen recombination probability on pressure, current, gas temperature and wall temperature. This shows not only the robustness of the model when facing different conditions, but also its versatility bridging different timescales from electron kinetics (below ns) to surface kinetics (up to seconds). The analysis of the simulation results highlights that for wall temperatures of -20 ºC and 5 º C the dominant recombination mechanisms involve physisorbed oxygen atoms (O_F) in L-H recombination $O_F + O_F$ and in E-R recombination $O_2 + O_F$, while for wall temperatures of 25 ºC and 50 ºC processes involving chemisorbed oxygen atoms (O_S) in E-R $O + O_S$ and L-H $O_F + O_S$ also play a relevant role. Moreover, this work demonstrates that the plasma has important effects on the surface at low pressures and that surface recombination processes lead to high ozone wall production rates at high pressures.

This work was supported by the Portuguese FCT - Fundação para a Ciência e Tecnologia, I.P., by project references: UIDB/50010/2020 (https://doi.org/10.54499/UIDB/50010/2020), UIDP/50010/2020 (https://doi.org/10.54499/UIDP/50010/2020), LA/P/0061/2020 (https://doi.org/10.54499/LA/P/0061/2020), PD/BD/150414/2019 (PD-F APPLAuSE) and PTDC/FIS-PLA/1616/2021 (PARADiSE, https://doi.org/10.54499/PTDC/FISPLA/1616/2021).

References

[1] J. P. Booth *et al., Plasma Sources Sci. Technol.* **28** (2019) 055005
[2] J. Afonso *et al., J. Phys. D: Appl. Phys.* **57** (2024) 04LT01
[3] V. Guerra, *IEEE Transactions on Plasma Science* **35** (2007) 1397
[4] V. Guerra and D. Marinov, *Plasma Sources Sci. Technol.* **25** (2016) 045001
[5] D. Marinov *et al., Plasma Process. Polym.* **14** (2017) 1600175
[6] http://nprime.tecnico.ulisboa.pt/loki/index.html
[7] A. Tejero-del-Caz *et al., Plasma Sources Sci. Technol.* **28** (2019) 043001
[8] V. Guerra *et al., Plasma Sources Sci. Technol.* **28** (2019) 073001
[9] Schwartzentruber *et al., AIAA International Space Planes and Hypersonic Systems and Technologies Conference* (2015) 3567

Time-resolved images and detection of positive and negative ion species of atmospheric pressure plasma jet with spiral electrodes

N Selaković(*)[1], D Maletić[1], N Puač[1], G Malović[1] and Z Lj Petrović[2,3]

[1] *Institute of physics, University of Belgrade, Pregrevica 118, 11080 Belgrade, Serbia*

[2] *Serbian Academy of Sciences and Arts, Knez Mihailova 35, 11000 Belgrade, Serbia*

[3]*School of Engineering, Ulster University, Jordanstown, Co. Antrim, BT37 0QB UK*

(*)nele@ipb.ac.rs

The potential use of cold atmospheric pressure plasma sources has emerged in recent decades in number of fields, including metalurgy, agriculture, biology, medicine, and more. The use of atmospheric pressure plasma jet (APPJ) with spiral electrodes introduces an interesting approach to plasma generation, offering increased source length and extention of potential applications in medicine [1]. In this study, we explore the experimental setup and diagnostic techniques employed to characterize the APPJ and its chemical composition. Our focus lies on the potential application of non-thermal plasma in sterilization, particularly in sterilizing catheters and infusion hoses [2]. By utilizing spiral electrodes wrapped around a glass tube, we aim to harness the benefits of APPJ for practical applications, while also gaining insights into discharge dynamics and chemical composition through diagnostic techniques such as time resolved ICCD imaging and mass spectrometry [3].

The experimental setup (shown in Fig. 1) consisted of a 30 cm long glass tube wrapped with two isolated copper wires arranged in a spiral configuration (10 mm interelectrode gap), ensuring no contact between them. One wire was powered by a sine wave at 70 kHz excitation frequency and the second wire served as grounded electrode. A signal generator was used to provide a sine voltage of few volts, which was then amplified to the range of kV and applied to the powered electrode. A high voltage probe and oscilloscope were employed to measure voltage and current signals, enabling the calculation of power delivered to the discharge. Helium gas was used as the feeding gas at a rate of 4 slm The discharge appeared inside the glass tube as the ionization front that followed closely the shape of electrodes and then propagated as a plume a few centimeters outside the glass tube.

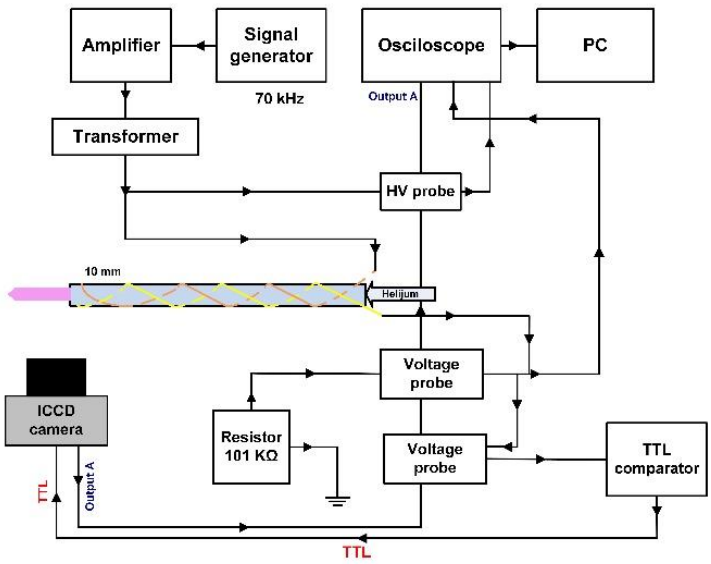

Fig. 1: Experimental setup of APPJ with spiral electrodes

We have performed time resolved ICCD imaging for various applied voltages and used these images to determine the velocity of PAPS (Pulsed Atmospheric Plasma Streamer). A frame of the temporal evolution captured by the ICCD camera is shown in Fig. 2, where the occurrence of PAPS (Pulsed Atmospheric Plasma Streamer) is displayed for the highest voltage value. This demonstrates that the discharge is not continuous but rather it consisted of plasma packages traveling at a velocity far faster than the working gas flow.

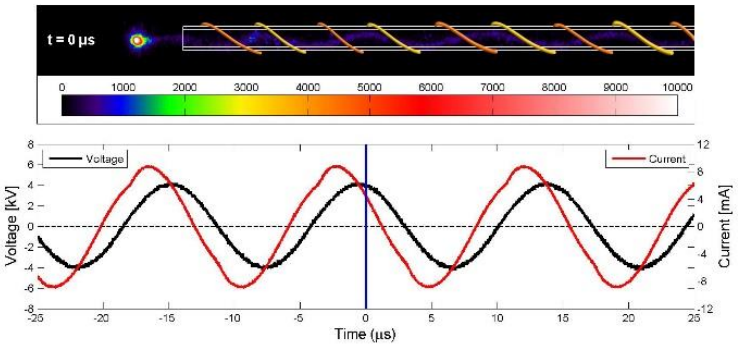

Fig 2.: Time-resolved ICCD frame synced with V-I signals

The positive ion mass spectrum acquired by the Hiden HPR60 MBMS mass spectrometer is shown in Figure 3. The predominant ions of N^+, O^+, N^+, O^+, H_2O^+, H_3O^+, $He^+$and HeH^+ were produced by ionization in a combination of the working gas with atomic and molecular species from the surrounding air, humidity and atmospheric impurities.

Additionally, oxygen species like O^-, OH^-, O_2^-, and O_3^- dominate the mass spectra of negative ions that we have obtained (spectra not shown here). Observations of the $O^- \cdot (H_2O)_n$ and $OH^- \cdot (H_2O)_n$ indicated a potential for water cluster chemistry in the APPJ plume.

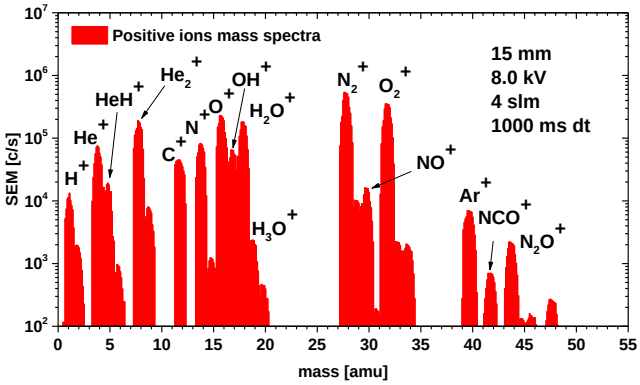

Fig 3.: Positive ions mass spectra

The rich spectrum of positive and negative ions produced in APPJ with spiral electrodes makes this source of non-thermal plasma interesting for potential application in sterilization of long tubes. The appearance of the discharge outside of the glass tube expands the potential application to the other area of interest such as medicine, biotechnologies, agriculture, and more.

Acknowledgment: This work was supported by MSTDI Republic of Serbia grant number 451-03-68/2023-14/200024. Z. Lj. P. is grateful to the SANU Project F155 for partial support. This work was by the Science Fund of the Republic of Serbia, 7739780, Atmospheric pressure plasmas operating in wide frequency range – a new tool for production of biologically relevant reactive species for applications in biomedicine - APPerTAin-BIOM.

[1] M. Polak et al., *Plasma processes and polymers* **9**(1) (2012) 67-76.
[2] T. Sato *et al.*, *Plasma Processes and Polymers*, **5**(6) (2008) 606-614.
[3] A. Stancampiano *et al.*, *Journal of Physics D: Applied Physics*, **51**(48) (2018) 484004.

New Coherent Techniques for Ultrafast Diagnostics in Plasmas

Grayson LaCombe[1], Jianan Wang[1], Jérémy Rouxel[2], Marien Simeni Simeni[(*)1]

[1] *Department of Mechanical Engineering, University of Minnesota, Minneapolis, MN, USA*

[2] *Chemical Sciences and Engineering 354 Division, Argonne National Laboratory, Lemont, IL, USA*

[(*)]msimenis@umn.edu

Research groups at Ohio State [1] and Sandia National Laboratories [2] have recently demonstrated the feasibility of highly spatially-resolved electric field measurements in electrical discharges using electric field-induced second harmonic (E-FISH) generation with two probe beams in a noncollinear phase matching geometry. However, they both reported orders of magnitude decrease of the measured signal with the increase of the angle between the probe beams, therefore limiting any further gain in spatial resolution following the crossing of the probe beams.

We have developed an ultrasensitive E-FISH experimental setup showcasing a detection limit about 3 orders of magnitude lower than that of E-FISH setups from the literature. Figure 1-a highlights sample E-FISH waveforms measured with a photomultiplier tube. The waveforms were averaged over a thousand laser pulses for different sub-breakdown DC voltages applied across a pair of parallel plate copper electrodes in atmospheric pressure air as depicted in Figure 1-b.

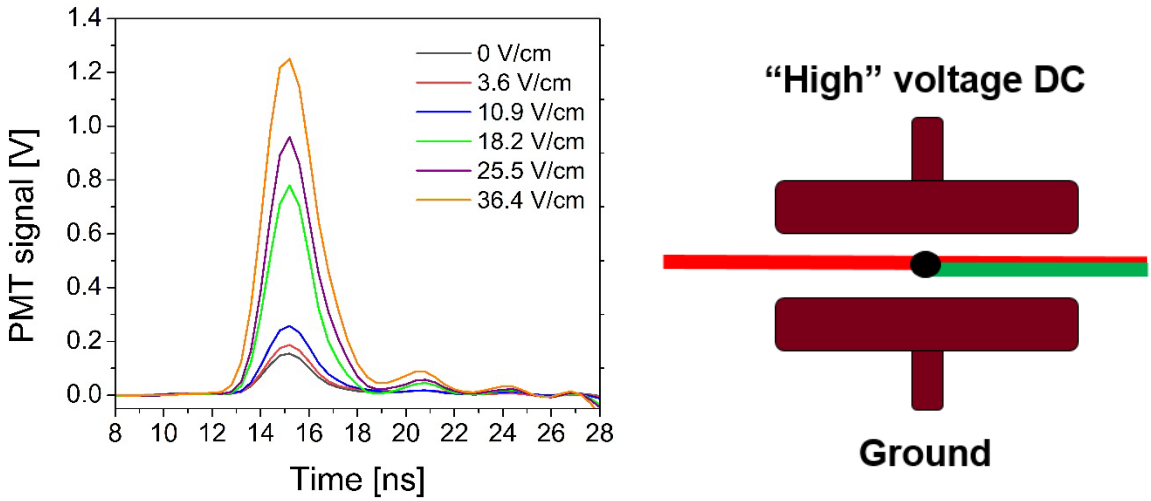

Fig. 1: (a) Sample E-FISH waveforms for different sub-breakdown DC electric field values. (b) Electrode contraption

From Figure 1-a it is readily apparent that electric field magnitudes as low as 4 V/cm can be detected using our novel approach. Furthermore, the measured PMT signal increases with the increase of the externally applied electric field between 4 and 36 V/cm. We expect to be able to further push the capabilities of our system to reach measurement thresholds as low as 0.1 V/cm at atmospheric pressure. Such improved sensitivity at atmospheric pressure holds great promise for deploying E-FISH under low gas-pressure environments.

Now turning our attention to density measurements in plasmas, we have recently reported the observation of three-wave mixing (TWM) in the gas phase [3], a process normally forbidden in centrosymmetric media under the electric dipole paradigm. The experimental setup for this diagnostic is shown in Figure 2-a. Briefly, light generation at 355 nm is observed when mixing the fundamental (at 1064 nm) and the second harmonic (at 532 nm) beams of a picosecond Nd:YAG laser in collinear phase-matching geometry. Figure 2-b displays the relative TWM signals from 5 different gases: He, N_2,

O_2, Ar, and Kr as a function of the gas pressure. Remarkably, the measured signals appear to grow monotonically with the test cell gas pressure. Besides that, PMT signals for species with higher nonlinear susceptibilities [4,5] appear to be stronger.

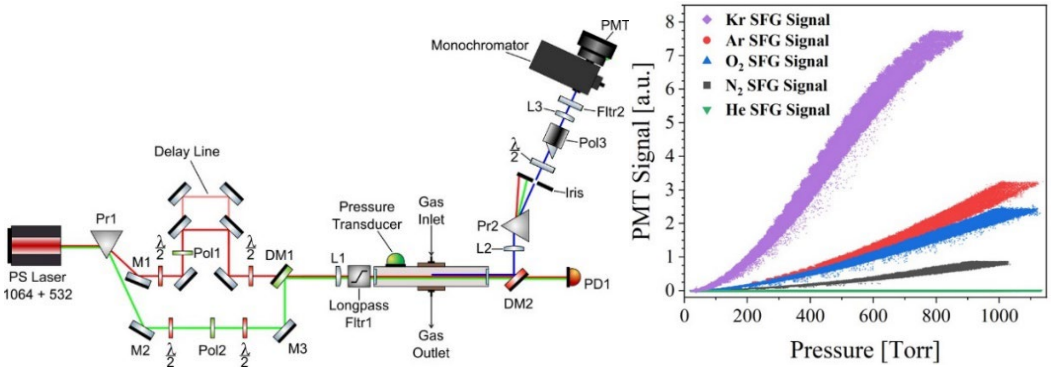

Fig. 2: (a) Schematic of the three-wave mixing experimental setup. (b) Three-Wave Mixing signal at 355 nm for 5 different gases VS Gas pressure

Such observations make the case for leveraging three-wave mixing as a novel technique for density measurements. This would greatly complement CARS (Coherent Anti-Stokes Raman Scattering), which is limited to Raman-active molecules while TWM applies in principle to both atomic and molecular species.

[1] S Raskar et al 2022 Plasma Sources Sci. Technol. 31 085002

[2] M VorenKamp et al 2023 Opt. Lett. 48(7) 1930-1933

[3] G. laCombe et al 2024 AIAA SciTech Forum (p. 2789)

[4] R.S. Finn, and J.F. Ward 1971 Phys. Rev. Lett. 26 285

[5] D.P. Shelton, and J.E. Rice 1994 Chem. Rev. 94 3-29

Sub-nanosecond development of electrical current in argon barrier discharge at atmospheric pressure

M Pazderka(*)[1], AP Jovanović[2], M Černák[1], MM Becker[2], T Hoder[1]

[1] *Department of Plasma Physics and Technology, Masaryk University, Kotlářská 267/2, 61137 Brno, Czech Republic*
[2] *Leibniz Institute for Plasma Science and Technology (INP), Felix-Hausdorff-Str.2, 17489 Greifswald, Germany*
(*) michpa@mail.muni.cz

Barrier discharges are plasma sources widely used in fundamental as well as application-oriented research [1]. The most common basic diagnostics of such discharges is by electrical measurements. Using appropriate approaches on various types of barrier discharges one can obtain a large amount of information by analysing just the electrical signals, i.e. the applied voltage and the electrical current. Determination of implicit parameters of the plasma in the gas gap, like effective electric field or transferred charge etc., can be made based on different equivalent electrical circuit models. Nevertheless, at the beginning, there is the necessity to have the right input data, e.g. the current and the voltage have to be measured with high sensitivity and high temporal resolution to enable further complex analysis [2].

In this contribution, we perform precise measurements of the electrical current using a transverse electromagnetic (TEM) cell. We measure the electrical current of a barrier discharge in argon at atmospheric pressure. Using these measurements we intend to validate the results of a time-dependent and spatially two-dimensional fluid-Poisson model made for a similar setup [3].

Typically under given conditions, the experimental validation of numerical results requires current measurements at sub-ns time scale. This is highly challenging mainly because the wavelength corresponding to the rapidly changing signals on (sub)-nanosecond time scale becomes comparable with the apparatus dimensions and the attenuation and phase shift on various parts of the apparatus significantly affects the measured current profile. This can cause two main issues: reflections of the transient signals on impedance jumps and deformation of the signal profile.

To avoid reflections from unmatched power supply, a long coaxial cable between power supply and the discharge chamber was introduced (see e.g. [5, 6]). This gives us several tens (depending on the coaxial length as well as the used dielectric) of ns of manifestly reflection-free signal. Similarly, long coaxial cables can be used between measuring probe and oscilloscope. The discharge itself was placed into a TEM cell [4] that is properly matched to coaxial cables (checked by time domain reflectometry). The measurement of S-parameters by a vector network analyser can be used to properly measure the attenuation and phase shift of individual components [6]. Another potential possibility for transient events could be direct measurement of peak response function in time domain and (de)convoluting the measured signal to reveal the correct current profile.

Here, we present the first results of testing measurements. Fig. 1 (left panel) shows the current peak profile of a volume dielectric barrier discharge (VDBD) in half-sphere to plane configuration, where both electrodes are covered with alumina. The right picture in Fig. 1 shows the TEM cell connected to HV coaxial cables. The alternating voltage (6.28 kHz, sinusoidal) is on the central conductor (septum). The current probe consists of electrode covered by alumina, 50 Ω resistor and SMA coaxial connector.

This research was funded by the Czech Science Foundation under contract no. 21-16391S and supported by the project LM2023039 funded by the Ministry of Education, Youth and Sports of the Czech Republic and partly funded by the Deutsche Forschungsgemeinschaft (DFG) – project number 466331904.

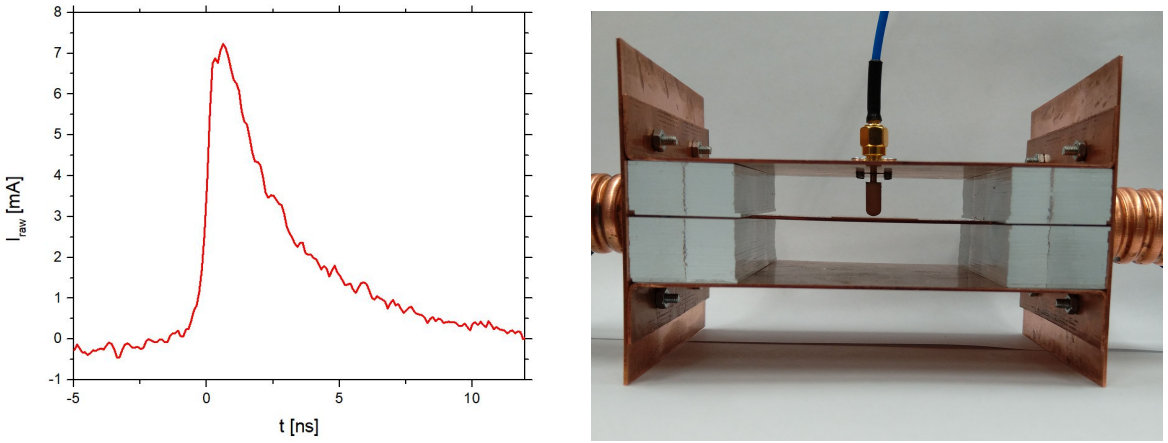

Fig. 1: An example of raw current peak profile of VDBD in ambient air captured with the 1 GHz oscilloscope LeCroy WAVERUNNER 6100 (left) and apparatus picture (right).

[1] U. Kogelschatz, *Plasma Chemistry and Plasma Processing* **31** (2003) 1–46.
[2] P. Synek, M. Zemánek, V. Kudrle and T. Hoder, *Plasma Sources Sci. Technol.* **27** (2018) 045008.
[3] A. P. Jovanović, D. Loffhagen and M. M. Becker, *Plasma Sources Sci. Technol.* **32** (2022) 04LT02.
[4] T. Zhou, X. Peng, S. Huang, J. Zhao and H. Sun, *Progress In Electromagnetics Research M* **106** (2021) 93–104.
[5] A. Khomenko, V. Podolsky and X. Wang, *Electrical Engineering* **103** (2021) 57-66.
[6] T. Huiskamp, F. J. C. M. Beckers, E. J. M. van Heesch and A. J. M. Pemen, *IEEE Sensors Journal* **16** (2016) 3792-3801.

Sheath Expansion around Langmuir Probes in Flowing Plasmas

L Beving[1], M Hopkins[1(*)], G Severn[3]

[1] *Applied Optical and Plasma Sciences, Sandia National Laboratories, Albuquerque, NM 87185, USA*

[3] *Department of Physics, University of San Diego, San Diego, CA 92110, USA*

(*) mmhopki@sandia.gov

Sheaths form on probes, walls, and dust immersed in a bulk plasma. Understanding sheath properties is critical to applications like etching, and diagnostics like Langmuir probes. However, sheaths are not always immersed in static bulk plasmas, and may instead be immersed in a flowing plasma. For example, the sheath on a Langmuir probe positioned near a wall would be immersed in the ambipolar flow of the presheath attached to the wall. Here we use particle-in-cell simulations to characterize the structure of a sheath immersed in a flowing plasma.

Modeling sheath expansion around a Langmuir probe is necessary to analyze the probe signal since the sheath width determines the effective collection area. However, the current model of sheath expansion does not account for the effects of a flowing plasma. Furthermore, recent experiments have indicated that the current model of sheath expansion fails in the presheath, where there is significant plasma flow [1]. The experimental measurements were made in a multi-dipole plasma device, where the plasma is produced by a population of hot, dilute electrons from a thermionic cathode. A Langmuir probe was used to calculate the electron and ion densities at different distances from a grounded electrode. Specifically, the electron and ion densities determined from the probe agree well in the bulk plasma when the current model for sheath expansion is used. However, when the probe is moved into the presheath (or the sheath) region of a flat grounded electrode the electron and ion densities disagree such that the electron density is higher than that of the ions. This is exactly the wrong prediction, as the electron density should be smaller than that of the ions throughout the presheath and sheath regions.

Motivated by these shortcomings, we leverage simulations of a Langmuir probe near a biased electrode to correct the current model. We find that the sheath area expands significantly as the ambient plasma flow increases. The expansion is nonuniform and is greater on the downstream side of the probe, where the density is different compared to the upstream side. Accounting for the increase in

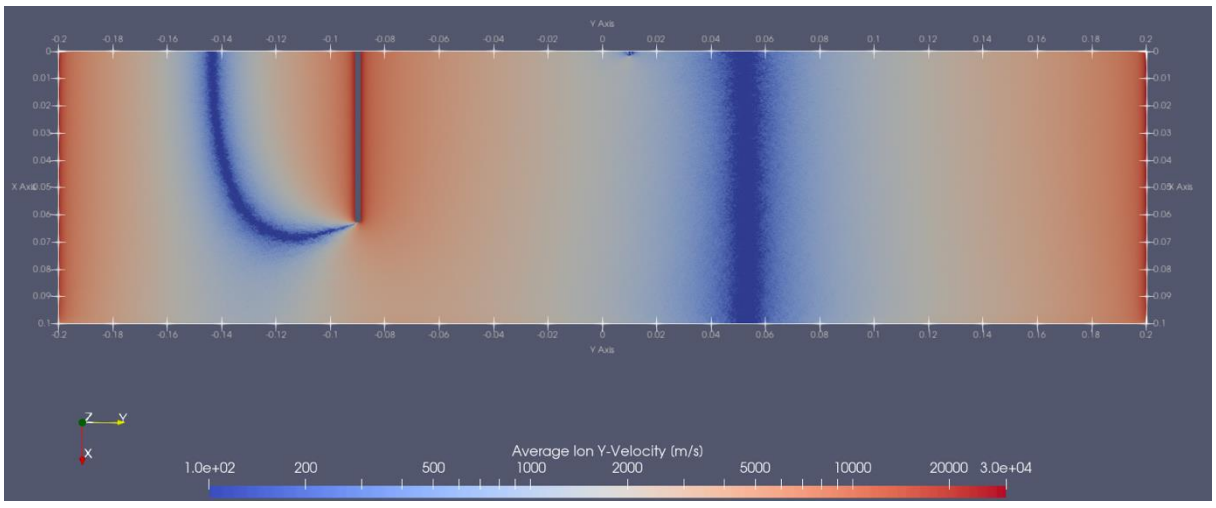

Fig. 1: Magnitude of the average y-velocity of ions in the simulation domain containing the grounded electrode. In this simulation the probe is located at $x = 0$ m and $y = 0.01$ m and represents a situation where the ion flow toward the probe is small.

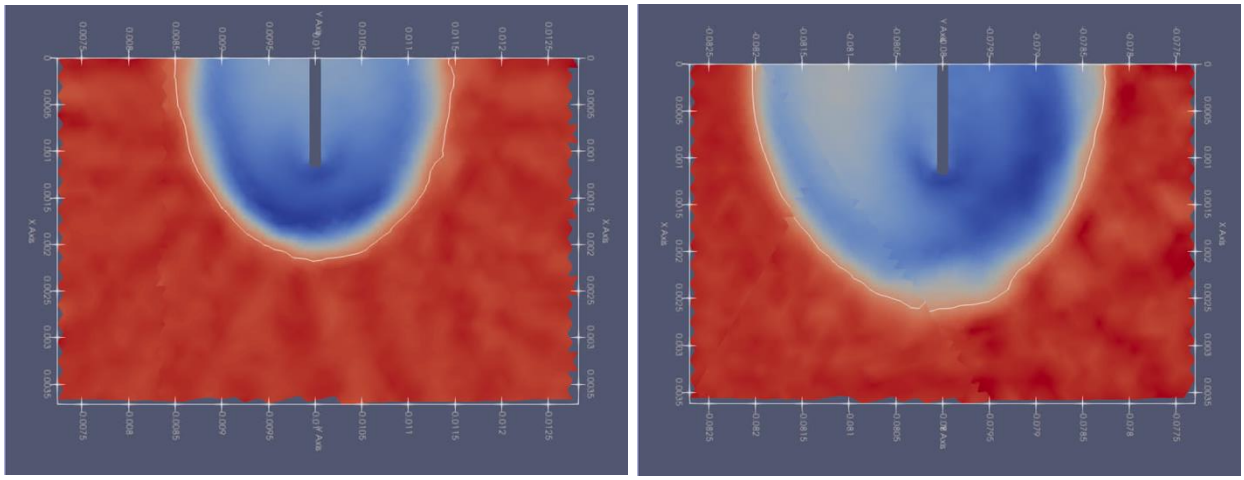

Fig. 2: Charge density around the probe for two cases: (left) where the probe is in a relatively stationary plasma and (right) where the probe is immersed in plasma flowing from right to left. The sheath edge is the white contour defined by $\rho = -5 \times 10^6\ C/m^3$.

the effective collecting area should act to correct the current sheath expansion model, allowing for accurate measurements of plasma density near other sheath regions using a Langmuir probe.

The simulations use a 2D domain, shown in Figure 1, where the boundary along x = 0 m is reflecting and represents a plane of symmetry, while all other boundaries are perfectly absorbing. The position of the probe is moved along the y = 0 m axis toward the electrode located at y = -0.09 m in a series of simulations designed to illustrate the effect a flowing plasma has on a probe. Figure 2 shows the charge density around a positively biased probe at two locations: (left) far from the grounded electrode and (right) near the grounded electrode. The structure of the charge density changes due to the relatively strong flow of plasma from right to left; namely, the sheath expands in all directions, but most notably on the downstream side of the probe. Similar behavior is observed for different probe biases and positive biases are shown here for convenience.

This work was supported by DOE grant No. DE-SC0022201. This work used the capabilities of the SNL Plasma Research Facility, supported by DOE SC FES. SNL is managed and operated by NTESS under DOE NNSA contract DE-NA0003525.

[1] P. Li et al, Plasma Sources Sci. Technol. **29** 025015 (2020).

Atomizers of tin hydride studied by laser-induced fluorescence

M. Mrkvičková[1(*)], P. Dvořák[1], B. Štádlerová[2], J. Kratzer[2]

[1] *Department of Plasma Physics and Technology, Faculty of Science, Masaryk University, Brno, Czechia*

[2] *Intitute of Analytical Chemistry of the Czech Academy of Sciences, Brno, Czechia*

(*) mrkm@mail.muni.cz

Hydride atomizers play a crucial role in analytical chemistry by allowing for ultra-trace level determinations of elements in solutions. In particular, they are essential components in the hydride generation atomic absorption or fluorescence spectrometry (HG-AAS or HG-AFS) method [1]. This method boasts impressive detection capabilities for elements like As, Se, Pb, Sn, Bi, Sb, or Te, reaching sensitivities of 100 ng l^{-1} for AAS and even 10 ng l^{-1} for AFS, respectively. The process involves the reduction of the analyte through a reaction with $NaBH_4$, producing the corresponding hydride. Under optimized conditions, the generation efficiency approaches nearly 100% for common hydride-forming elements. Subsequently, the hydride is atomized to liberate free analyte atoms. This is accomplished by the device known as the "atomizer". Finally, the free atoms are detected using atomic or fluorescence spectroscopy.

Various atomizer types have been developed, such as those based on flames (diffusion flame atomizer), high-temperature tubes (quartz-tube-atomizer) or electrical discharges (DBD atomizer). Each of these atomizers is suited for different analyte atoms. While the quartz-tube-atomizer and the DBD atomizer yielded comparable detections for tellurium atoms, the DBD setup performed significantly poorer in the case of tin hydride (stannane) decomposition [2] without a clear explanation for this discrepancy.

Our study aims to investigate the efficacy of stannane molecule decomposition into free atoms using two specific atomizer types: diffusion flame atomizer and DBD atomizer. The diffusion flame is ignited at the end of silica tube (inner diameter 6 mm) in the mixture of argon, hydrogen, and stannane flowing into the surrounding air. The DBD atomizer is based on a volume dielectric barrier discharge ignited inside a silica optical arm (inner dimensions 8 mm $\times$ 3 mm $\times$ 75 mm) with two planar electrodes on its outer surfaces. Two power-supply regimes are tested: sinusoidal voltage of frequency 33 kHz and peak-to-peak amplitude of 10 kV, and rectangular voltage with a frequency of 29 kHz and peak-to-peak amplitude of 7 kV (thus, the effective voltage was similar in both cases).

The laser-induced fluorescence method (LIF) was employed to analyze the spatial distribution of tin atom concentrations inside atomizers under varying conditions. Tin atoms were excited by laser pulses with a wavelength 224.6 nm, the consequent fluorescence radiation of wavelength 365.6 nm was observed by ICCD camera. In the case of the diffusion flame atomizer, the laser beam was extended by couple of lenses to a thin sheet, facilitating comprehensive observation of the entire flame height under all operational conditions. To enhance the signal-to-noise ratio, a partially saturated LIF technique [3] was implemented. Additionally, calibration of concentration values was achieved through the absorption of laser beam energy.

An illustrative example of the fluorescence signal obtained from the diffusion flame atomizer is provided in Figure 1. Two feeding conditions are compared: a) 180 sccm Ar + 120 sccm H_2 + tin hydride, and b) 700 sccm Ar + 300 sccm H_2 + tin hydride, mimicking thus typical atomization conditions employed in AAS and AFS, respectively. Lower flow rates resulted in a 5 mm high active flame with tin atom concentration centered in the flame core, while higher flow rates extended the active flame to 20 mm, redistributing tin atoms towards the flame tip and edges.

The spatial maps of atomic tin concentrations in both atomizer types under various conditions will be presented. As the atomisation is supposed to be controlled by reactions of stannane with atomic hydrogen [4], the LIF results will be accompanied by information on the spatial distribution of hydrogen atoms measured by the TALIF method. In the case of the DBD atomizer, the electric field evolution in the two power supply regimes will be determined by the electric field induced second harmonic generation (EFISH) method. Based on all the results, we will further discuss potential strategies for improving various atomizer efficiencies.

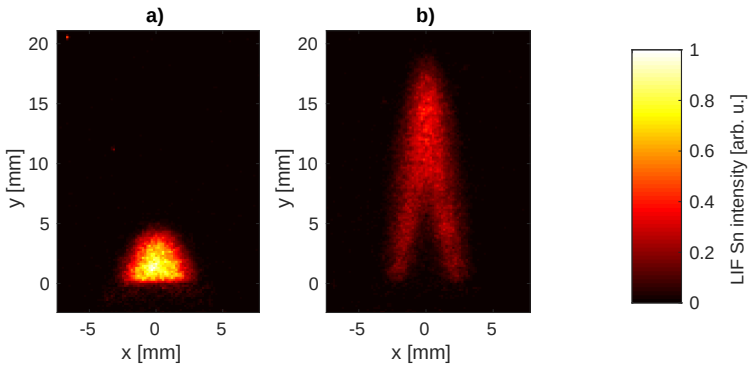

Fig. 1: Examples of LIF Sn signal captured in the diffusion flame atomizer feeded by a) 180 sccm Ar + 120 sccm H_2 + tin hydride, and b) 700 sccm Ar + 300 sccm H_2 + tin hydride. In both cases, the tin hydride was generated from a sample containing 100 ng ml^{-1} Sn.

Acknowledgement

This research has been supported by the Czech Science Foundation under Contract 23-05974K and by Project LM2018097 funded by the Ministry of Education, Youth and Sports of the Czech Republic.

References

[1] J. Dědina, D. L. Tsalev, Wiley and Sons Inc., Hydride generation atomic absorption spectrometry (1995)
[2] L. Juhászová, et al., *Spectrochimica Acta Part B* 158 (2019) 105630
[3] M. Mrkvičková et al., *Combustion and Flame* 241 (2022), 112100
[4] P. Dvořák, et al., *Plasma Sources Sci. Tech.* 26 (2017) 085002

Electrical charge relaxation on a dielectric surface

D. Prokop(*)[1], M. Mrkvičková[1], J. Tungli[2], P. Dvořák[1], S. Kadlec[2] and T. Hoder[1]

[1] *Department of Plasma Physics and Technology, Masaryk University, Kotlářská 2, 611 37 Brno, Czech Republic*
[2] *Eaton European Innovation Center, Bořivojova 2380, 252 63 Roztoky, Czech Republic*
(*) david.prokop@mail.muni.cz

Electrical charge deposited on a dielectric surface by gas discharges is a phenomenon occurring in many situations connected to fundamental as well as applied fields of low-temperature plasma physics. It is common to find charging effects both in the field of barrier discharges and their application in surface treatment or thin film deposition and in the field of electrical engineering utilizing the gas/solid insulation.

One of the motivations for this work is the development of an ultra-fast gas-filled sealed miniaturized relay carrying high currents of tens to hundreds of amps to be used in novel AC and DC hybrid circuit breakers. The relay can be filled with various gases - air, nitrogen, SF_6, or in mixtures of its alternative gases, such as C_4F_7N. The relay contacts are fully open to a gap of the order of 0.1 mm after a given semiconductor bypass time (of the order of 0.1 ms). The dielectric strength of the filling gas is of high importance, as well as the effects of the electrical charge deposited on nearby dielectric surfaces.

The studies of surface charges on dielectrics started already by Lichtenberg and his famous dust figures in 1778 [1]. Recently, the amount of the deposited charge was quantified under different conditions using complex methods [2, 3]. It was found that the surface charge can relax and slowly disappear [4] and an analytical model was reported as well [5].

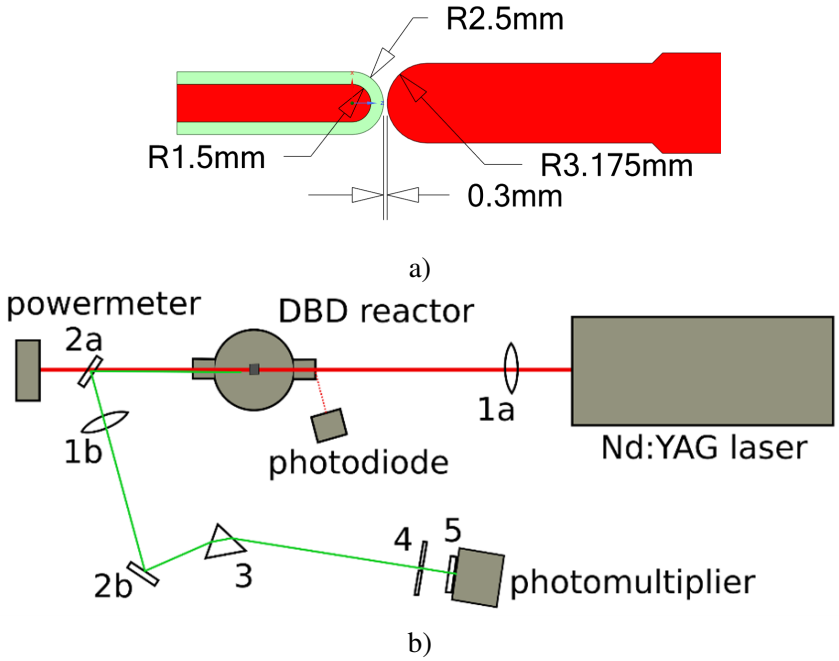

Fig. 1: Experimental setup for barrier discharge, part a), and of the EFISH method, part b).

In this contribution, we investigate a charge deposition and relaxation on a dielectric surface by measuring the residual electric field in the gap above the surface using the electric field induced second harmonic generation (EFISH) method, see [6, 7]. In this method we assume that the intensity of the EFISH signal depends quadratically on the applied electric field. This attribute can be then used to assess the dependence of the EFISH signal in time. The experimental setup is displayed in Fig.1. Single breakdown was initiated by powering a hemispherical electrode (radius 3.175 mm) against another

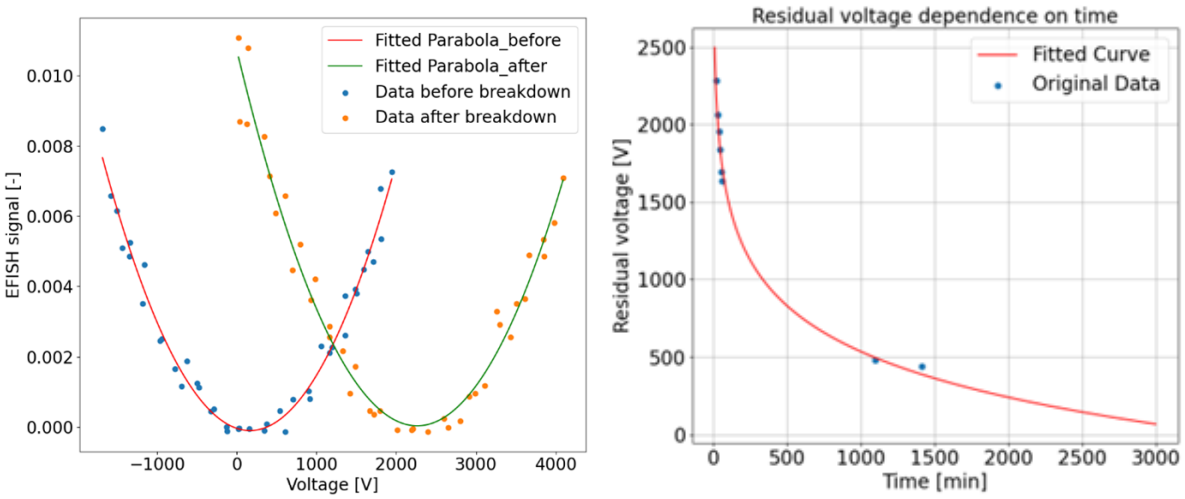

Fig. 2: Dependence of the EFISH signal on the applied voltage and change of the residual voltage in time.

electrode covered by Al_2O_3 ceramic (inner radius 1.5 mm, outer one 2.5 mm). The shortest gap was 0.3 mm. A DC power supply (FuG Elektronik GmbH, HCP 1400-20000 MOD) was utilized as a voltage source. The measurements were performed in a closed reactor filled with atmospheric pressure nitrogen and also in a nitrogen mixture with C_4F_7N. Measurements of the EFISH signal were obtained using high-definition oscilloscope Keysight Infiniium (20 GSa/s).

We conducted several experiments using the setup shown in Fig.1(b) to measure the EFISH signal at different time delays after charge deposition. As a result, we determined a voltage shift of the zero point of the EFISH signal (residual voltage) corresponding to the relaxation of the charge deposited on the dielectric surface. Preliminary results for pure nitrogen are displayed in Fig.2. The results obtained will serve as data for the validation of numerical models.

[1] G. C. Lichtenberg, *Novi commentarii Societatis Regiae Scientiarum Gottingensis* (1778) 168–180.
[2] L. Stollenwerk, J. G. Laven, H. G. Purwins *Phys. Rev. Lett.* **98** (2007) 255001.
[3] A. Kumada, S. Okabe, K. Hidaka *J. Phys. D: Appl. Phys.* **42** (2009) 095209.
[4] R. Brandenburg et al. *J. Phys. D: Appl. Phys.* **46** (2013) 464015.
[5] O. Emelyanov, M. Shemet *Journal of Electrostatics* **81** (2016) 71–75.
[6] A. Dogariu, B. M. Goldberg, S. O'Byrne, and R. B. Miles *Phys. Rev. Appl.* **7** (2017) 024024.
[7] M. Mrkvičková et al. *Plasma Sources Sci. Technol.* **32** (2023) 065009.

This research has been supported by the Technology Agency of the Czech Republic within the project TK04020069: *Streamers and surface flashover discharges on insulators in alternative gases to SF6*.

Time evolution of emission profiles and spatial structure of a plasma jet streamer discharge in contact with liquid

O Jovanović(*)[1], F Krčma[2], L Dostál[2], N Puač[1], N Škoro[1]

[1] *Institute of Physics, University of Belgrade, Pregrevica 118, 11080 Belgrade, Serbia*

[2] *Faculty of Chemistry, Brno University of Technology, 612 00 Brno, Czech Republic*

[3] *Faculty of Electrical Engineering and Communication, Brno University of Technology, 612 00 Brno, Czech Republic*

(*) olivera@ipb.ac.rs

Atmospheric pressure plasma jets have been intensively studied for the last two decades due to their wide field of application [1-2]. One of the most common targets exposed to cold plasma is liquid. Numerous investigations have demonstrated that the electrical properties of the plasma and its reactivity impact the water target by modifying physicochemical features such as pH, electrical conductivity, and the transfer of reactive species into the liquid [3]. In order to fully comprehend the complex interaction between discharge characteristics and treated liquid properties, an in-depth diagnostic of the plasma jet is required. Analysis of emission profiles from the discharge can provide various infomration. Ultrafast cameras can capture clear discharge images on a timescale ranging from ns to μs, which allows insight of development of discharge profiles and interactions with the water surface [4].

In this research we used two ultrafast framing cameras to record temporal evolution of the streamer emission generated by using a specially designed pin-type atmospheric pressure plasma jet operating in contact with a liquid sample. The experimental setup of the atmospheric pressure pin-electrode jet operating in contact with liquid sample is presented schematically in Figure 1. The powered electrode was connected to the high-voltage (HV) and the second electrode was the target – a water sample placed in a grounded quartz vessel.

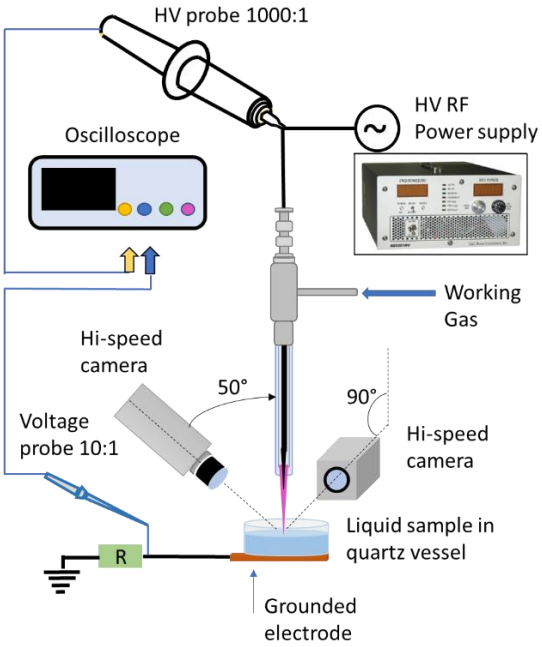

Fig. 1: Schematic representation of the experimental setup.

Distilled water, tap water, and saline solutions were used as targets in order to test targets with different conductivities. Pure He or Ar were used as working gases with gas flows of 1 slm and 2 slm,

respectively, adjusted by a mass flow controller.The plasma in the experiments was generated and controlled by using a commercial HV high-frequency power supply providing continuous sinusoidal signal with the frequency of 350 kHz. To monitor voltage and current waveforms we used an oscilloscope, and corresponding probes. The discharge current flowing through the ground line was obtained by measuring voltage drop across a 1 kΩ resistor.

Ultrafast frame imaging of the streamer discharge was performed by useing of two Hi-speed cameras (I-Speed 726, IX Cameras, and FASTCAM SA-X2, Photron). The development and propagation route of streamers formed between powered pin electrode of the jet and the liquid surface were observed from side-on positions. The first camera was positioned perpendicular to plasma jet axis in order to observe the development and expansion of the streamer between the powered electrode and the liquid. To capture formation and propagation of smaller filaments on the liquid's surface, the second camera was installed above the sample, at an angle of 50° from plasma jet axis. Fast-framing cameras allowed observation of the transient behaviour of the streamer by recording of the emission profiles in a time frame short enough to see the effect. The spatial distribution of the emission generated by the streamer discharge and branching of the filaments at the water surface were recorded for different jet operating parameters and the liquid target conductivity.

Figure 2 shows discharge profiles in argon (a) and helium (b) in the case when the target was 4 ml of distilled water (conductivity 2.1 μS/cm). The images were taken with a camera placed at an angle of 90° with respect to the vertical axis of the plasma jet. The results showed that the contact surface of the Ar streamer and water was much larger than in the case of helium. Branching at the interface level was more pronounced in Ar streamers. The streamer was more intense, less distorted and with more homogeneous emission along its axis in the case of He plasma.

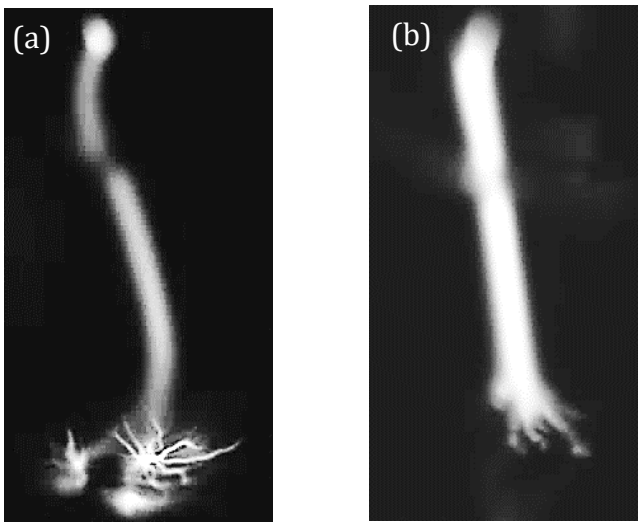

Fig. 2: Streamer spatial profiles in argon (a) and helium (b) in the case when the target was 4 ml of distilled water.

Acknowledgments: This work was supported by a STSM Grant from the COST Action CA19110 PlAgri, supported by the COST Association (European Cooperation in Science and Technology), Republic Serbia MSTDI- 451-03-66/2024-03/200024 and Science Fund of the Republic of Serbia, 7739780, APPerTAin-BIOM project.

[1] N. Puač, M. Gherardi, M. Shiratan, *Plasma processes and polymers* **15(2)** (2018) 1700174.
[2] Y. Morabit, M. I. Hasan, R. D. Whalley, E. Robert, M. Modic, J. L. Walsh, *EPJ D* **75** (2021) 1-26.
[3] P. J. Bruggeman, M. J. Kushner, B. R. Locke et al., *PSST* (2016) ***25*(5)** 053002.
[4] P. Marinova, E. Benova, Y. Topalova, Y. Todorova, T. Bogdanov, M. Zhekova, I.Yotinov, F. Krcma, *Processes* (2023) ***11*(12)**, 3313.

The ignition of low-pressure capacitively coupled discharge

Petr Skopal[1], Pavel Dvořák[1]

[1] *Department of Plasma Physics and Technology, Faculty of Science, Masaryk University, Kotlářská 2, Brno 611 37, Czech Republic*
petr.skopal@mail.muni.cz

Radiofrequency discharges, especially capacitively coupled discharges, are highly used in both science and industry. Main reasons for that are etching and deposition, in which ion bombardment (induced by high electric field in sheaths) plays an important role. Sheaths in stationary CCP control the discharge character by means of the stochastic heating [1], gamma processes [2] and field reversal [3]. However in the early stages of CCP, sheaths are not fully developed and a strong electric field affects the whole interelectrode space. This means that during ignnition the plasma heating mechanisms and its whole nature needs to develop from a bulk-field driven to a sheath-driven character. CCP ignition needs to be carefully described as it considerably differs from its well studied stationary state. But works describing RF breakdown are rare, even though ignition of DC and low-frequency discharges are well described by Townsend and streamer theory.

Still, works describing some parts of the CCP ignition were done. It was shown that CCP undergoes sequence of various heating modes [4, 5]. In the phase of rise of electron concentration, which lasts typically $\sim 10\,\mu$s [6, 7], the temperature of electrons reaches significantly higher value from what is known in the stationary value [5, 8, 9, 10]. Similarly, the plasma potential can reach an unusually high value during the CCP ignition [11]. It was also found that in asymmetric discharge that development of sheaths last approximately tens of μs [8]. However, most of the papers focused on CCP ignition were concentrated on geometrically symmetric discharges and, consequently, were not able to describe the evolution of DC bias. That is why we studied ignition of an asymmetric CCP by means of combination of two probe techniques: The standard RF compensated Langmuir probe used for the study of electron energy distribution and the probe with no RF compensation used for study of the frequency spectrum of floating potential [12, 13, 14].

A series of 15 measurements in various positions in the discharge (with a step 2 mm) were done with the uncompensated probe to obtain both the temporal and spatial dependence of floating potential during the plasma ignition. The behaviour of the amplitude of the fundamental RF (13.56 MHz) and DC components of the probe voltage are shown in the fig. 1. The measurements demonstrate the development of the bulk plasma in the center of the interelectrode gap (as the region with a weak electric field), the development of sheaths with strong field and the non-monotonic evolution of the floating (and plasma) potential.

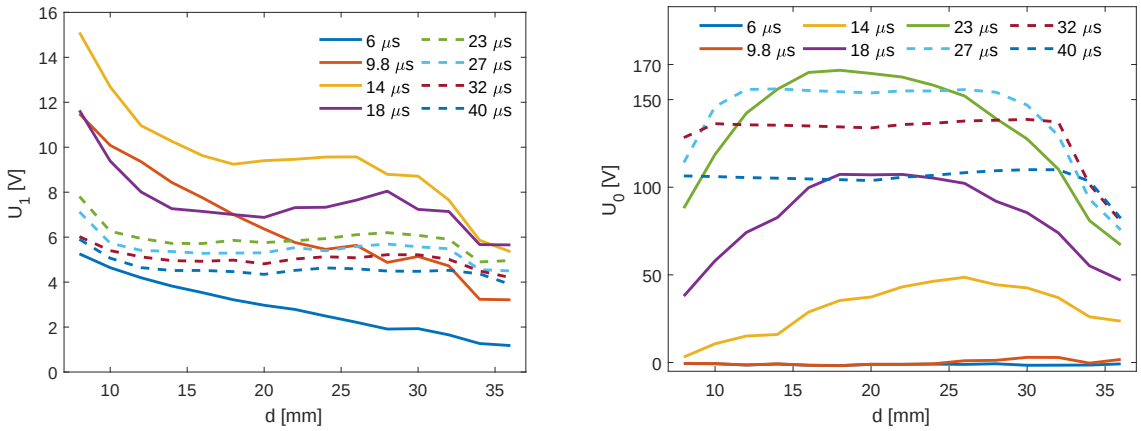

Fig. 1: Amplitude (left) and mean value (right) as functions of position in various moments of the discharge pulse.

RF compensated Langmuir probe was used to get probe VA characteristics in various times during ignition. Second derivation of the VA characteristics has to be done in order to obtain electron concen-

tration and electron energy distribution. The EEDF revealed existence of several groups of electrons: the relatively cold bulk electrons and at least two groups of electrons with unusually high energy. The fig. 2 presents the development of electron concentration and mean energy for these various electron groups.

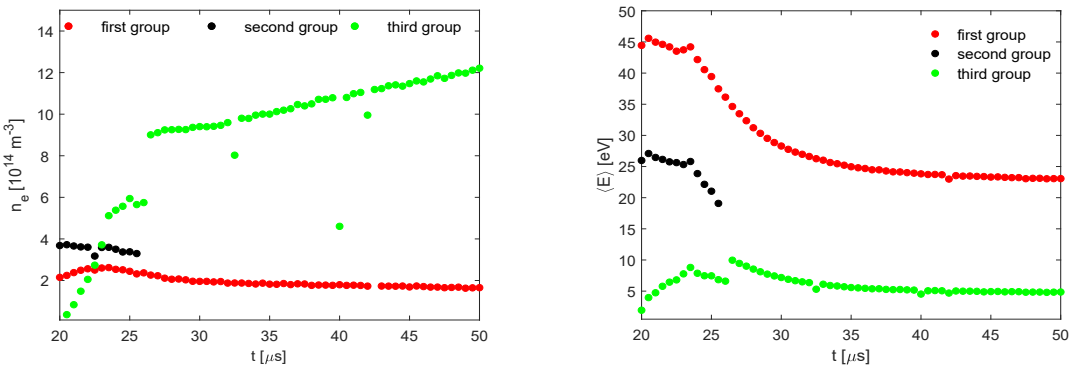

Fig. 2: Electron concentration (left) and energy (right) during discharge for various peaks from VA characteristic.

These measurements are supported by simple quantitative model, which describes the discharge asymmetry evolution. The sheaths with homogeneous ion concentration and negligible electron concentration, a negligible field in the bulk plasma and a monofrequency sinusoidal discharge current were assumed in the model. The model reproduced well the slow evolution of the DC bias.

Acknowledgment
This research has been supported by the Project LM2023039 funded by the Ministry of Education, Youth and Sports of the Czech Republic.

[1] Schulze, B G Heil, D Luggenhölscher, T Mussenbrock, R P Brinkmann, and U Czar- netzki, *J. Phys. D: Appl. Phys* (2008) 41:042003.
[2] Y P Raizer, *Gas Discharge Physics* (1997)
[3] J Schulze, Z Donkó, B G Heil, D Luggenhölscher, T Mussenbrock, R P Brinkmann, and U Czarnetzki, *J. Phys. D: Appl. Phys.* (2008) 41:105214.
[4] Y X Liu, X Y Wang, Q Z Zhang, Z Donkó, K Zhao, J Schulze, and Y N Wang, *Plasma Sources Sci. Technol.* (2020) 29:12LT03
[5] H Wu, Y Zhou, J Gao, Y Peng, Z Wang, and W Jiang, *Plasma Sources Sci. Technol.* (2021) 30:065029
[6] N Sirse, M H Jeon, G Y Yeom, and A R Ellingboe, *Plasma Sources Sci. Technol.* (2014) 23:065046
[7] V Šamara, M D Bowden, and N St J Braithwaite, *J. Phys. D: Appl. Phy.s* (2010) 3:124017
[8] J P Booth, G Cunge, N Sadeghi, and R W Boswell *J. Appl. Phys.* (1997) 82:552
[9] S-H Song and M J Kushner, *Plasma Sources Sci. Technol.* (2012) 21:055028
[10] W-Z Jia, X-F Wang, Y-H Song, and Wang Y-N, *J. Phys. D: Appl. Phy.s* (2017) 50:165206
[11] Mishra, M H Jeon, K N Kim, and G Y Yeom *Plasma Sources Sci. Technol.* (2012) 21:055006
[12] P Dvořák, M Tkáčik, and J Bém, *Plasma Sources Sci. Technol.* (2017) 26:055022
[13] M Sobolewski *IEEE T Plasma Sci* (1995) 23:1006
[14] P Dvořák, J Pálenik, M Tkáčik, and Z Pospíšil, *Plasma Sources Sci. Technol.* (2022) 1:ac- cepted

Antenna measurement of electric field and higher harmonics in atmospheric plasma jets interacting with different targets

Kateřina Polášková[(*)1,2], Petr Drexler[3], Miloš Klíma [3], Jan Macháč[4], David Nečas[1], Milan Švanda[4], Lenka Zajíčková[1,2]

[1] *Plasma Technologies, CEITEC, Brno University of Technology (BUT), Brno 61200 CZ*
[2] *Department of Condensed Matter Physics, Faculty of Science, Masaryk University, Brno 61137 CZ*
[3]*Department of Theoretical and Experimental Electrical Engineering, FEEC, BUT, Brno 61600 CZ*
[4]*Department of Electromagnetic Field, FEL, Czech Technical University in Prague, Prague 16000 CZ*
[(*)] polaskova@vutbr.cz

Cold atmospheric pressure plasma jets (APPJs) are used in many applications (*e. g.*, material treatment, gas conversion, plasma activation of water, and plasma medicine) with widely differing setups: ignited into an open space or against a target, which can be dielectric or metal, grounded or floating. Therefore, understanding how the target properties affect the fundamental plasma parameters is crucial for optimizing the jet application. The electric field is one of the most essential discharge parameters because its magnitude determines the production and energy of the charged particles, hence the plasma chemistry. However, the measurements of APPJ electric fields are scarce due to the hard requirements on either the equipment (high-power picosecond lasers are needed for the electric field-induced second harmonic generation [1] and coherent anti-Stokes Raman scattering measurements [2]) or on the plasma gas chemistry (methods based on optical emission spectroscopy [3, 4]). Measurements by electro-optic sensors based on the Pockels effect [5], although not species-specific or overly experimentally demanding, require discharge to be in contact with the sensor, thus affecting the plasma parameters.

We present an alternative approach to measuring the APPJ electric field using antennas. This relatively simple and non-expensive method provides a semi-quantitative value of a discharge macroscopic electric field. Measurements of spatial or temporal distribution are not possible. The antennas can also non-intrusively monitor discharge nonlinearity (generation of higher harmonics, subharmonics, and ultraharmonics), presenting an alternative to current probes for setups with inaccessible electrodes.

The RF ($f = 13.56\,\mathrm{MHz}$) plasma slit jet (PSJ) and plasma capillary jet (PCJ) were ignited against several different targets (Fig. 1a): floating dielectrics of different permittivities, dielectrics with a ground beneath, a water surface, and a grounded aluminum plate. Both the discharges use Ar as working gas. In the PSJ, Ar could be mixed with different additives (O_2, N_2, and H_2O aerosol). The plasma jets' nonlinearity and electric field were measured by commercial biconical antenna BicoLOG 20300 (350 mm diameter). All the measurements were carried out in the reactive near-field region. In this region, the radiated electric field can be modified by coupling of the antenna and discharge or distorted by adjacent conductive objects absorbing and re-emitting the radiation. The affected cases were identified by comparing the antenna frequency spectra against the frequency spectra of discharge current measured by a current probe at the grounded electrode. The antenna records effective voltage induced at the connector by a global mix of external electric fields. During the recalculation, we approximated the different sources by the electric field of the plasma sheath, which is expected to be the highest contributor.

All the measured frequency spectra shared one feature, a dominant fundamental frequency peak (Fig. 1b). The relative intensities of other peaks differed with the plasma jet. The PSJ frequency spectrum contained relatively intense odd harmonics and significantly weaker even harmonics. This alternation of relative intensities was more pronounced after the admixing of molecular gas (Ar/N_2 PSJ spectra in Fig. 1b). The intensity of even harmonics was presumably connected with the volume ionization. Molecular gas admixing led to its decrease, which was reflected in the higher nonlinearity of the discharge. The appearance of weaker even harmonics is linked to the opposing action of parallel sheaths that form inside the slit. The intensity of even harmonics increases as the symmetry of the opposing sheaths decreases. In the Ar/N_2, the abundant long-lived nitrogen metastables were more likely to diffuse onto the slit surface, knocking out an electron from it, thus distributing the sheaths symmetry. The PCJ nonlinearity was lower compared to the PSJ ignited against the same target (Fig. 1b). Moreover, as no opposing sheaths formed on the inner discharge capillary walls, the even and odd harmonics had

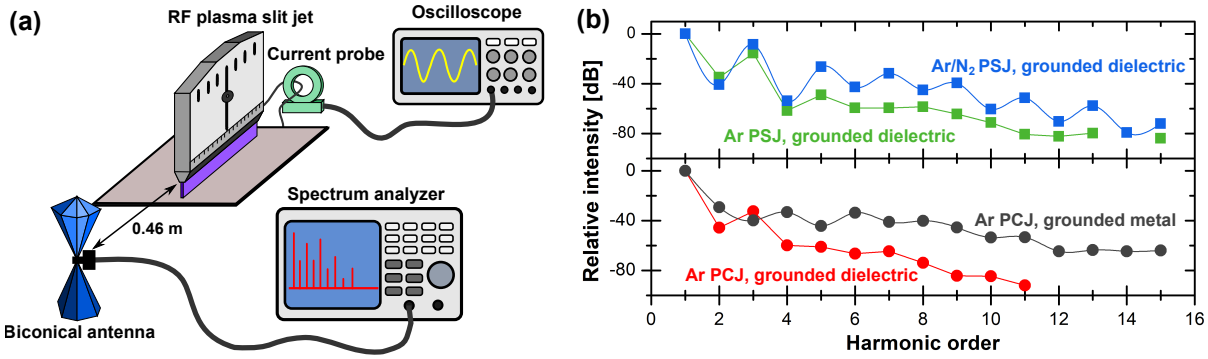

Fig. 1: (a) Schematic drawing of the experimental setups used for antenna measurements. The PSJ is used to demonstrate the position of a plasma jet. (b) Relative intensities of higher harmonics measured by the biconical antenna for PSJ and PCJ ignited against different targets. The PSJ settings were 67 slm of Ar, 1.5 slm of N_2, and 500 W applied power. The corresponding PCJ settings were 5 slm Ar and 50 W. In all the measurements, the distance between the jet outlets and the target surface was 10 mm.

similar relative intensities. The higher relative intensity of 3$^{\mathrm{rd}}$ harmonic (Fig. 1b) was unrelated to the processes occurring inside the discharge tube, as it was enhanced only in the presence of a grounded dielectric target.

The target influence on the PSJ nonlinearity differed with the gas chemistry. Using a grounded dielectric target as an example, the relative intensities of odd harmonics in the Ar PSJ spectrum decreased compared to the open space configuration when the plasma impinged on the target surface, presumably due to the enhanced volumetric ionization. On the other hand, the frequency spectra of the Ar/N_2 PSJ were identical for both the open space and the grounded target configurations, as the addition of molecular gas limited the probability of ionizing collisions. In the PCJ, the target influence was connected to how the plasma filament interacted with its surface. The PCJ nonlinearity was low when the filaments formed a broad base on the target surface (grounded dielectric targets of different permittivities). Conversely, when PCJ impinged on conductive targets, the filament attached itself to the surface in a small circular spot. This anode attachment caused a drastic increase in the relative intensities of higher harmonics, starting with the fourth. Furthermore, in contact with the metal, many peaks with random frequencies caused by random sparks appeared in the spectra.

Though the obtained values of the electric field were only semi-quantitative (10–200 kV/cm, depending on the jet and the configuration), the antennas exhibited high sensitivity to the changes. Out of the studied gas feeds, the strongest electric field was generated in pure Ar discharge. Admixing of oxygen or nitrogen gas halved the measured strength. As for the target influence, only the conductivity and grounding had any notable effect. The dielectric permittivity and the ground configuration (plate, mesh) had negligible impact on the final value. The electric field of the PSJ impinging on the grounded target was, on average, 2× higher than in the floating target configuration and 3–4× higher than in the open space configuration. The PCJ results demonstrated the effect of target conductivity. The highest electric field was induced when PCJ impinged on the grounded aluminum target, followed by the water surface, and the lowest strength was obtained for the grounded dielectric targets (about 3× lower than for the metal target).

[1] K. Orr et al. *Plasma Sources Sci. T.* **29** (2020) 035019.
[2] P. Böhm et al. *Plasma Sources Sci. T.* **25** (2016) 054002.
[3] A. Sobota et al. *Plasma Sources Sci. T.* **25** (2016) 065026.
[4] A. Obrusník et al. *Plasma Sources Sci. T.* **27** (2018) 085013.
[5] A. Sobota, O. Guaitella and E. Garcia-Caurel *J. Phys. D Appl. Phys.* **46** (2013) 372001.

Surface charge tailoring for plasma catalysis

Robin Labenski(*)[1], David Steuer[1], Henrik van Impel[1], Marc Böke[2], Volker Schulz-von der Gathen[2], Judith Golda[1]

[1] *Research Group Plasma Interface Physics, Ruhr University Bochum, Bochum, Germany*
[2] *Chair Experimental Physics II, Ruhr University Bochum, Bochum, Germany*
(*) robin.labenski@rub.de

In photo- and electrocatalysis it is already well-established that surface charges can alter the chemical adsorption and reaction paths of the catalyst [1]. However, the novel realm of plasma catalysis lacks experimental exploration regarding the impact of plasma-induced surface charges on catalysis. So far, only a handful of theoretical density functional theory (DFT) calculations focusing on CO_2 splitting were carried out by the group surrounding Annemie Bogaerts. They suggest that negative plasma-generated surface charges can indeed lead to improved CO_2 activation resulting in higher conversion efficiencies [2–4].

Finding experimental methods to take a closer look at the relation between plasma-deposited surface charges and catalysis is therefore worth the effort. Our recent studies pave that way by presenting a new, yet simple method for precisely charging the dielectric (and eventually potential catalyst) using the plasma's ability to deposit surface charges. The charged dielectric is part of a Micro Cavity Plasma Array (MCPA) - a dielectric barrier discharge microplasma reactor introduced by Dzikowski et al. [5]. The method involves a relais circuit, with which the externally applied voltage $V(t)$ can be precisely shut off immediately extinguishing the plasma. This brings the surface charge deposition on the dielectric to a distinct halt and is shown in the left figure of Fig. 1.

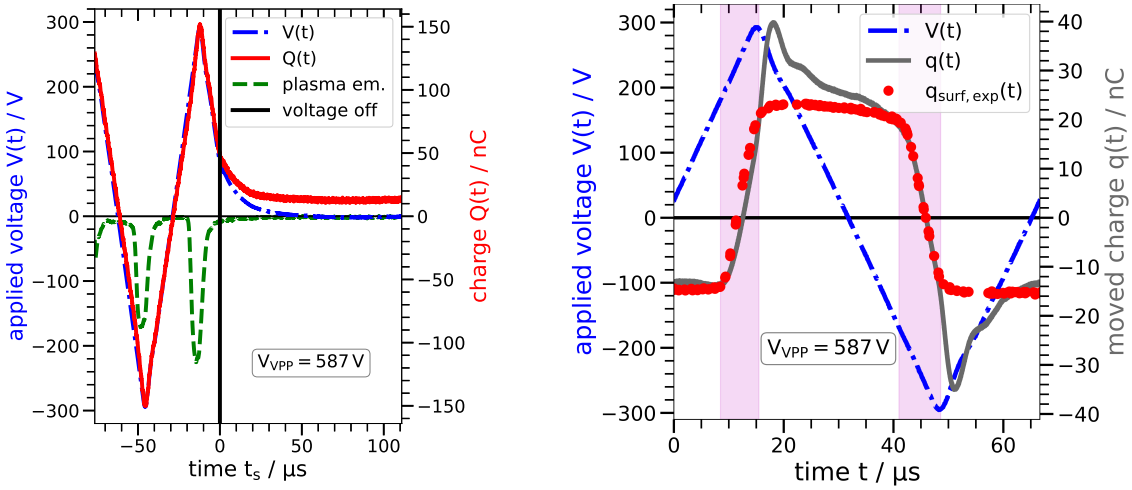

Fig. 1: Left figure: Switching of the relais circuit at $t_s = 0$ resulting in a shut off of the applied voltage $V(t)$ and revealing positive surface charges (positive offset in charge $Q(t)$). Right figure: Time-resolved comparison between the conventionally determined moved charge $q(t)$ and surface charge $q_{\mathrm{surf,\,exp}}(t)$ utilizing the relais circuit. The pink highlights represent the discharge time frames. In both figures an excitation peak-to-peak voltage of $V_{\mathrm{VPP}} = 587\,\mathrm{V}$ at 15 kHz is applied.

Switching the relais at $t_s = 0$ results in a rapid decay of $V(t)$ revealing a (in that case) positive offset in the charge $Q(t)$. The latter is measured utilizing a monitor capacitor and corresponds to positive surface charge on the dielectric. By varying the moment in time the relais is switched the amount and polarity of surface charge can be precisely tuned. The time resolved amount of surface charge $q_{\mathrm{surf,\,exp}}(t)$ on the dielectric is computable from charge $Q(t)$, when combined with a common equivalent circuit approach. Conventionally this only allows for the determination of moved charge $q(t)$ [6] containing surface charges, volume charges and potential artifacts. The addition of the relais circuit, however, enables

a retrospective artifact- and volume charge-free determation of the actual surface charge $q_{\mathrm{surf,\,exp}}(t)$ during the discharge cycle as depcited in the right figure of Fig. 1.

The relais circuit is perfectly suitable for the charging of the dielectric, while also decoupling surface charges from the plasma. A manipulation of surface charge during an ongoing discharge is not possible though, as the switching of the relais results in the unavoidable shut down of the reactor. However, the introduction of a nanosecond laser allows for this *operando* manipulation of surface charge. As already found by Tschiersch et al., laser-induced electronic surface charge ablation of the pre-charged dielectric is possible, but the amount of ablated charge per pulse is small (order of $10\,\mathrm{pCcm^{-2}}$ in their case) [7]. A significant amount of surface charge in a comparably short time frame (few microseconds) could therefore be ablated by employing high repetition lasers.
A complementary laser-based method to accomplish a quick not decrease, but increase in surface charge is investigeated in our latest research. We find that with just a single nanosecond pulse (having the same wavelength of 532 nm and similar pulse energy in the order of 50 mJ as used by Tschiersch et al. [7]) an additional gain of surface charge of up to 15 % within $3.5\,\mu\mathrm{s}$ after irradiation and potential for even higher yields is achievable. The origin of these additional surface charges and their implication on the consecutive plasma cycle is also assessed.

References

[1] Annemie Bogaerts et al. “The 2020 plasma catalysis roadmap”. In: *Journal of Physics D: Applied Physics* 53.44 (2020), p. 443001.

[2] Amin Jafarzadeh et al. “Activation of CO2 on copper surfaces: the synergy between electric field, surface morphology, and excess electrons”. In: *The Journal of Physical Chemistry C* 124.12 (2020), pp. 6747–6755.

[3] Amin Jafarzadeh et al. “CO2 activation on TiO2-supported Cu5 and Ni5 nanoclusters: effect of plasma-induced surface charging”. In: *The Journal of Physical Chemistry C* 123.11 (2019), pp. 6516–6525.

[4] Kristof M Bal et al. “Effect of plasma-induced surface charging on catalytic processes: application to CO2 activation”. In: *Plasma Sources Science and Technology* 27.2 (2018), p. 024001.

[5] Sebastian Dzikowski et al. “Modular constructed metal-grid arrays—an alternative to silicon-based microplasma devices for catalytic applications”. In: *Plasma Sources Science and Technology* 29.3 (2020), p. 035028.

[6] FJJ Peeters and MCM Van de Sanden. “The influence of partial surface discharging on the electrical characterization of DBDs”. In: *Plasma Sources Science and Technology* 24.1 (2014), p. 015016.

[7] Robert Tschiersch et al. “Influence of released surface electrons on the pre-ionization of helium barrier discharges: laser photodesorption experiment and 1D fluid simulation”. In: *Plasma Sources Science and Technology* 26.7 (2017), p. 075006.

Spectral investigation on two spherical cathode discharges

F. Enescu[1], A. Gobarev[2], G. Rotaru[2], C. Ionita[1], R. Schrittwieser[1(*)]

[1]*Institute for Ion Physics and Applied Physics, University of Innsbruck, Austria*

[2]*Faculty of Physics, Alexandru Ioan Cuza University of Iasi, Romania*

[(*)]*roman.schrittwieser@uibk.ac.at*

Introduction

Cathode discharges in Argon were investigated, using mainly emission spectroscopy. The cathodes were either concentric hollow spheres or cylinders of stainless-steel mesh [1-3], allowing better observation of the processes inside the electrodes. However, irregular chaotic discharges between cathodes and the vacuum chamber walls were detrimental of these cathode systems. Better resolution for the spectra is achieved in this study with two larger cathodes not made of grids but with smooth surfaces.

Experimental setup

Cathodic discharges were analysed in a system consisting of two hollow polished stainless-steel spheres with radii of 4,8 cm each (wall thickness 1 mm), placed at 5 cm distance from each other (surface to surface). The experiments were conducted in a grounded cylindrical stainless-steel chamber of 92 cm length and 53,5 cm diameter. Both spheres were simultaneously biased negatively in Argon at a pressure between p = 7 and $8 \cdot 10^{-2}$ mbar. The best conditions for the discharge were found for voltages around V = –400 V for both spheres. The experimental setup is shown in Fig. 1(a). The spatial structure of the plasma discharge appearing around the spheres is indicated schematically.

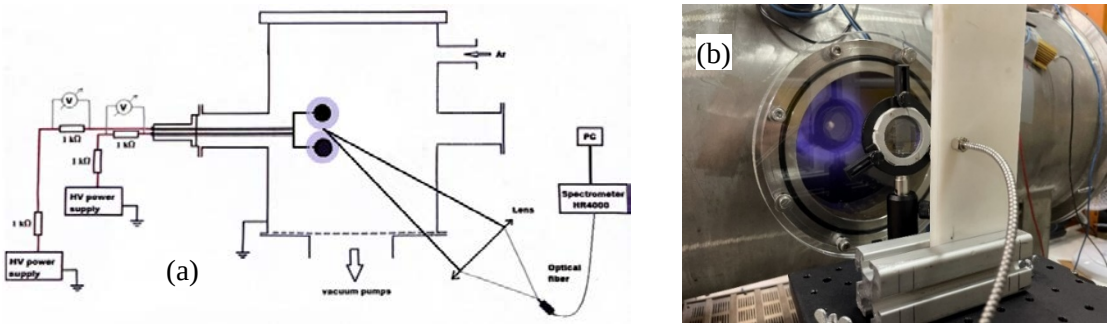

Fig. 1. (a) Schematic of the experimental setup. (b) Installation for emission spectroscopy.

Fig. 1(a) also shows the arrangement for recording emission spectra using an Ocean Optics HR4000 spectrometer. The emission was measured from a point located at mid distance between the spheres. Focusing through a lens onto an optical fiber, the emission of a cubic plasma volume of approx. 7,8 cm^3 could be registered, with the aim to derive the plasma's spectral diagram during discharges (Fig. 1(b)).

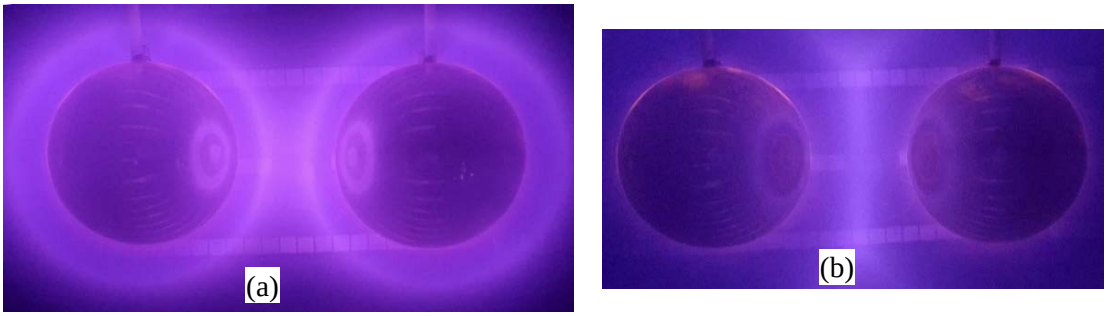

Fig. 2(a) The two discharges without visible interference between the spheres, (b) with visible intersection of space charge sheaths surrounding the spheres.

Experimental results

Various spatial structures were observed around the spheres (see Fig. 2). The best conditions for discharge were found at a voltage of V = –390 V for both spheres with a current of 13 mA in both circuits, at Ar pressure p = 7,8·10^{-2} mbar. Spectral measurements of the optical emission enabled the generation of the plasma's spectral diagram. The spectroscopic data were used to determine the electronic temperature of the plasma (~ 5479 K) at the midpoint between the spheres with eq.(1) and (2).

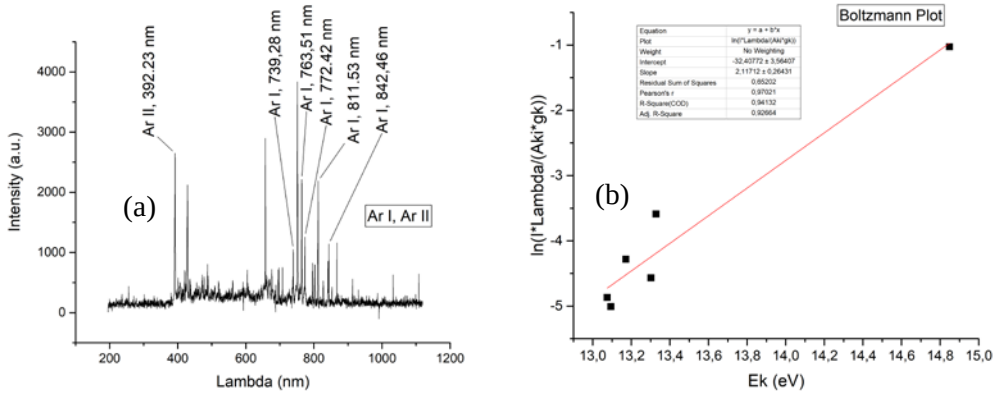

Fig. 3(a) Ar I, II lines spectrum of plasma, (b) Boltzmann plot for derivation of temperature.

Electron temperature from Boltzmann plot slope eq. (1):

$$I_{ki} = N_0 \frac{1}{4\pi} \frac{hc}{Z(T)} \frac{A_{ki}}{\lambda} g_k \exp\left(-\frac{E_k}{kT_e}\right)$$

Electron density from Saha Eggert equation eq. (2):

$$n_e = \frac{2g^+A^+\lambda^*I^*}{g^*A^*\lambda^+I^+} \frac{\left(2\pi m_e kT_e\right)^{3/2}}{h^3} \exp\left(-\frac{E^+ - E^* + E_i}{kT_e}\right)$$

I_{ki} – Intensity of line for an electronic transition between k and i
g_kA_{ki} (s^{-1}) – Transition probability
λ (nm) – Wave length
$Z(T)$ – Partition function
$E_{i,k}$ (cm^{-1}) – Energy of lower and upper level, respectively
k_BT_e (J)– Thermal energy
n_e (cm^{-3}) – Electronic density
+,* - refers to ion, neutral species
m_e (kg) – mass of electron
N_0 – Total concentration of atoms

Conclusion

These findings are useful for understanding the fundamental physical processes responsible for the ignition and behaviour of cathode systems. Future experiments will create spatial electronic temperature and density maps for experimental conditions as previously stated. Also experiments with modified spheres are planned by making opposing 1 cm diameter holes in the sphere along their horizontal axis and the formation of ion beams from the spheres and their interactions will be investigated.

References

[1] F. Enescu et al., *XXXVth Int. Conf. Phenomena Ionized Gases (ICPIG)* (Egmond aan Zee, The Netherlands, 9-14 July 2023), Poster P1-3, Program p. 113.

[2] C.T. Konrad-Soare, F. Enescu, et al., Plasma Sources Sci. Techn. **30** (2021), 085006.

[3] F. Enescu, et al., Joint Annual Meeting of the Austrian Phys. Soc.& the Swiss Phys. Soc. (Innsbruck, Austria, 30 Au. – 3 Sept. 2021) *Session on Appl. Phys. & Plasma Phys.*, poster 641.

Estimation of sheath electric field based on Dopper broadened absorption spectrum of hydrogen Balmer-α line

Koichi Sasaki[1], Kosuke Takada[1], and Shusuke Nishiyama[2]

[1]*Division of Applied Quantum Science and Engineering, Hokkaido University, Sapporo 060-8628, Japan*
[2]*Japan Healthcare University, Sapporo 062-0053, Japan*
(*) sasaki@qe.eng.hokudai.ac.jp

The measurement of sheath electric field is still an important issue in plasma physics. In this work, we examined the applicability of the Doppler-broadened absorption spectrum of the hydrogen Balmer-α line to the estimation of the sheath electric field [1]. Measuring the absorption spectrum of the hydrogen Balmer-α line using a tunable single-mode diode laser is not too difficult. In addition, since the cost for the experimental setup is also relatively small, laser absorption spectroscopy at the hydrogen Balmer-α line is useful for the measurement of the sheath electric field, even though the detection limit is intermediate in various methods developed to date.

The experiment was carried out in inductively coupled hydrogen plasmas at a pressure of 47 mTorr. A one-turn rf antenna was inserted into a vacuum chamber, and it was connected to an rf power supply at 13.56 MHz via a matching circuit. The rf antenna was electrically insulated from the plasma by covering its surface with glass fibers. The rf power was pulse modulated at a frequency of 20 kHz to amplify the absorption signal using a lock-in amplifier. The instantaneous rf power and the duty factor were 1 kW and 50%, respectively. A planar electrode which was connected to a dc power supply was inserted into the vacuum chamber from the opposite side to the rf antenna. A linearly-polarized, single-mode diode laser beam was injected into the plasma. The wavelength of the diode laser was scanned around the Balmer-α line of atomic hydrogen. The distance between the diode laser beam and the surface of the planar electrode was approximately 0.5 mm. The electric field of the laser beam was adjusted to be parallel (the π polarization) to the sheath electric field using a $\lambda/2$ plate. The laser beam transmitted through the plasma was detected using a photodiode.

A typical absorption spectrum is shown in Fig. 1, where a dc bias voltage of -160 V with respect to the ground potential was applied to the planar electrode. The origin of the horizontal axis corresponds to the center frequency of the $2p\,^2P^{\rm o}_{3/2} - 3d\,^2D_{3/2}$ transition line. The theoretical absorption spectrum was calculated by solving the time-independent Schrödinger equation with the perturbation of the electric field [2], and it was fitted with the experimental absorption spectrum. The parameters that were deduced by the fitting were the gas temperature and the electric field. The method of least squares was adopted to find the best fitting. The gas temperature and the electric field deduced by the fitting shown in Fig. 1 were 460 K and 650 V/cm, respectively. The electric field and the gas temperature, which were deduced by the spectral fitting, are summarized in Fig. 2 as a function of the electrode potential. The magnitudes of the error bars were evaluated on the basis of the ambiguity in the spectral fitting. We could not deduce the electric field at an electrode potential of 0 V, where the electrode potential was still lower than the plasma potential, since the ambiguity in the spectral fitting was too significant. As shown in the figure, we observed the monotonic increase in the electric field strength with the electrode potential. In contrast, we observed roughly constant gas temperature as a function of the electrode potential. This is a reasonable result since the heating of atomic hydrogen is not expected inside the nearly collisionless sheath at a pressure of 47 mTorr.

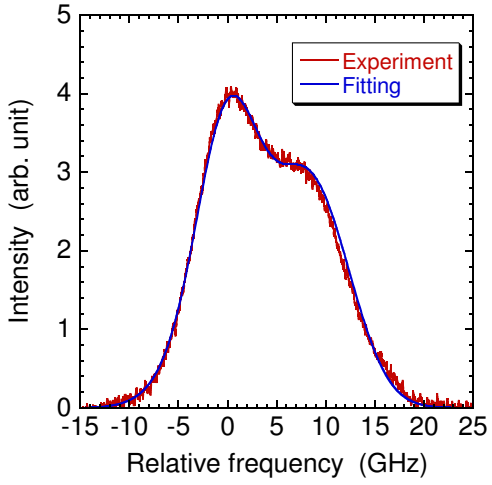

Fig. 1: Absorption spectrum of the hydrogen Balmer-α line observed at an electrode potential of -160 V.

The detection limit of the electric field was evaluated by comparing the theoretical field-free spectrum with the theoretical spectrum in an electric field. The difference between the two spectra was evaluated by the standard deviation. We have judged that the estimation of the electric field is possible if the difference between the field-free and in-field spectra exceeds the standard deviation between the theoretical and experimental spectra. As a result, it has been evaluated that the minimum electric field that can be determined by the present method is approximately 350 V/cm. This detection limit is comparable to the detection limits obtained by optogalvanic spectroscopy [3, 4] and laser-induced collisional fluorescence spectroscopy [5, 6], where pulsed dye lasers are used for exciting metastable states of helium and argon to Rydberg states with principal quantum numbers of $n = 7 - 14$.

[1] S. Nishiyama, K. Takada, and K. Sasaki, *Jpn. J. Appl. Phys.* **60** (2921) 076001.
[2] T. Fujimoto and A. Iwamae (Eds.), *Plasma Polarization Spectroscopy* (Springer, Berlin, 2008).
[3] D. K. Doughty and J. E. Lawler, *Appl. Phys. Lett.* **45** (1984) 611.
[4] V. P. Gavrilenko, H. J. Kim, T. Ikutake, J. B. Kim, Y. W. Choi, M. D. Bowden, and K. Muraoka, *Phys. Rev. E* **62** (2000) 7201.
[5] K. E. Greenberg and G. A. Hebner, *Appl. Phys. Lett.* **63** (1993) 3282.
[6] Y. W. Choi, M. D. Bowden, and K. Muraoka, *Appl. Phys. Lett.* **69** (1996) 1361.

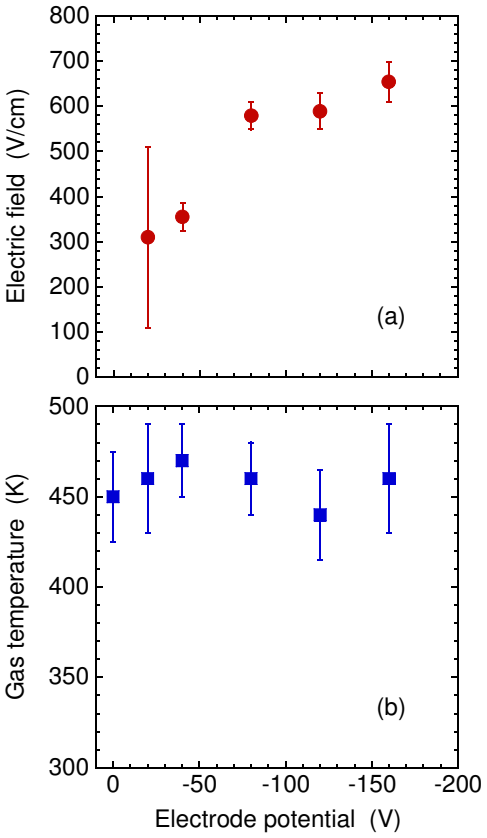

Fig. 2: (a) Electric field strength and (b) gas temperature, which are deduced by the fitting between experimental and theoretical spectra, as a function of the electrode potential.

Advanced analysis of overlapping emission spectra induced by highly transient discharges

P. Bílek[1*], G. Arora[1], P. Hoffer[1], V. Prukner[1], T.C. Dias[2], V. Guerra[2] and M. Šimek[1]

[1] *Institute of Plasma Physics of the Czech Academy of Sciences, Prague, Czech Republic*
[2] *Instituto de Plasmas e Fusão Nuclear, Instituto Superior Técnico, Universidade de Lisboa, Lisboa, Portugal*
(*) simek@ipp.cas.cz

Vibrational distributions of electronically excited states of N_2 obtained through dipole-allowed radiative transitions provide an important tool to study the kinetics of non-equilibrium plasmas under various discharge conditions and provide benchmark data for the validation of advanced kinetic schemes for numerical models. Our testing discharge is a streamer monofilament developed in a dielectric barrier discharge configuration, powered by a specific high-voltage waveform based on periodic (10 Hz) bursts composed of two consecutive HV AC waveforms (1 kHz) and a nanosecond HV pulse [1], see Fig. 1.

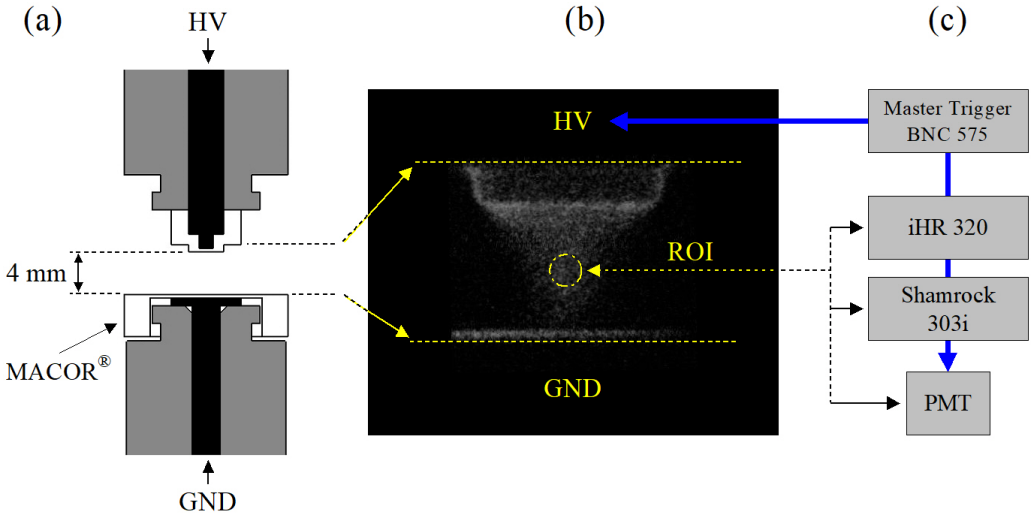

Fig. 1: Experimental setup. Credits on [2].

In this case, the active discharge phase (dominated by electron impact processes and characterized by the high reduced electric field (E/N)) persists for tens of nanoseconds. By varying the neutral gas pressure between 300 and 15 Torr, we can obtain reduced electric fields in a wide range (300-1500 Td). The experimental emission spectra considered in this work are first positive system (FPS, $B^3\Pi_g \longrightarrow A^3\Sigma_u^+$), second positive system (SPS, $C^3\Pi_u \rightarrow B^3\Pi_g$) of N_2 and first negative system (FNS, $B^2\Sigma_u^+ \rightarrow X^2\Sigma_g^+$) of N_2^+. These emissions can provide information about $v = 0-21$ vibrational levels of $N_2(B^3\Pi_g)$ state, $v = 0-4$ vibrational levels of $N_2(C^3\Pi_u)$ state and $v = 0-2$ vibrational levels of $N_2^+(B^2\Sigma_u^+)$ state.

In this contribution, we will present diagnostic procedures and analytical approaches to obtain the vibrational distributions of important electronically excited states using the acquisition and processing of optical emission spectra in a wide spectral range (200 - 1100 nm) with increased spatiotemporal resolution. We show that the vibrational distribution function of $N_2(B^3\Pi_g)$ state during the first nanoseconds after the discharge onset follows the Franck-Condon-like distribution, while during the streamer relaxation, it is influenced by the complex interaction between triplet excited states of N_2. Additionally, the observed $N_2(B^3\Pi_g$, v=13-21) vibrational levels are likely produced by the interaction of high vibrational levels of $N_2(W^3\Delta_u, B'^3\Sigma_u^-, B^3\Pi_g)$ with $N_2(C^3\Pi_u)$ state [2].

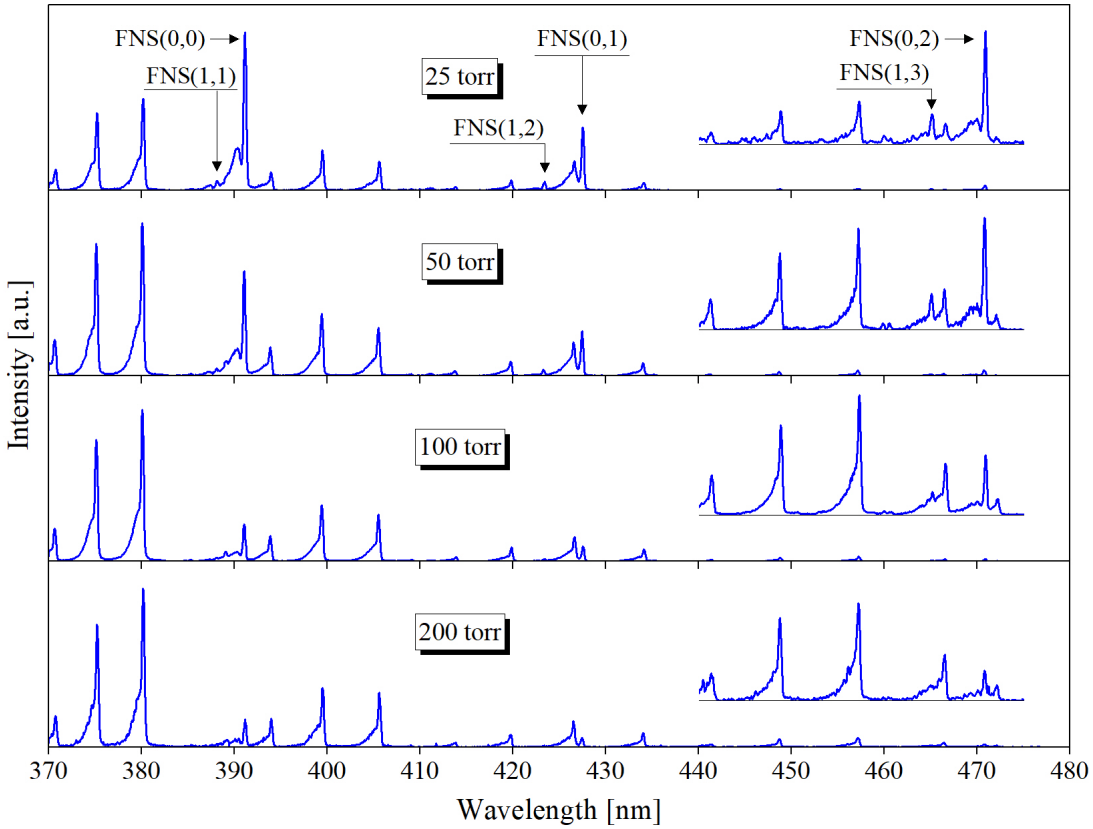

Fig. 2: Examples of time-resolved emission obtained in wavelength region 370-480 nm in pure nitrogen for pressures ranging from 25 to 200 Torr.

The VDFs of $N_2(C^3\Pi_u)$ and $N_2^+(B^2\Sigma_u^+)$ states are investigated at various pressures in air as well as pure nitrogen [3], see Fig. 2. The measurements of VDFs over such different ranges of conditions bring new insight into processes influencing the production of these states and set the limits of the use of FPS, SPS and FNS bands for diagnostic purposes. Moreover, the measured VDFs serve as reference data suitable for testing and validation of complex collisional-radiative models for N_2, N_2-O_2 and air streamer discharges.

Acknowledgement: This study is supported by the Grant Agency of Czech Republic (GA 24-10903S). IPFN activities were supported by FCT - Fundação para a Ciência e Tecnologia under projects UIDB/50010/2020 (https://doi.org/10.54499/UIDB/50010/2020), UIDP/50010/2020 (https://doi.org/10.54499/UIDP/50010/2020), LA/P/0061/202 (https://doi.org/10.54499/LA/P/0061/2020) and PTDC/FIS-PLA/1616/2021 (https://doi.org/10.54499/PTDC/FIS-PLA/1616/2021).

[1] P. Bílek, T. C. Dias, V. Prukner, P. Hoffer, V. Guerra and M. Šimek 2023 *Plasma Sources Sci. Technol.* **32** pp 105002.
[2] P. Bílek, T. C. Dias, V. Prukner, V. Guerra and M. Šimek 2024 *Plasma Sources Sci. Technol.* **33** pp 015011.
[3] Bílek, Arora, Šimek 2024 in prep.

Electron temperature diagnosis of CF_4/O_2 plasma based on fluorine atomic corona model by tomographic optical emission spectroscopic measurement

Yuya Yamashita(*)[1,2], Kenta Doi[3], Tetsuji Kiyota[4], Shuhei Watanabe[1], Kazuki Shimatani[1], Wataru Kikuchi[1], Yuchen Ye[1], Atsushi Nezu[5,6], and Hiroshi Akatsuka[6,1]

[1] *School of Engineering, Tokyo Institute of Technology, 2-12-1-N1-10 Ookayama, Meguro-ku, Tokyo, Japan*

[2] *Research Fellow DC, Japan Society for the Promotion of Science*

[3] *Institute of Advanced Technology, ULVAC, Inc., 1220-1 Suyama, Susono-shi, Shizuoka, Japan*

[4] *Strategic Planning Department, ULVAC, Inc., 2500 Hagisono, Chigasaki-shi, Kanagawa, Japan*

[5] *Open Facility Center, Tokyo Institute of Technology, 2-12-1-N1-10 Ookayama, Meguro-ku, Tokyo, Japan*

[6] *Institute of Innovative Research, Tokyo Institute of Technology, 2-12-1-N1-10 Ookayama, Meguro-ku, Tokyo, Japan*

(*) yamashita.y.an@m.titech.ac.jp

1. Introduction

In recent years, there has been an increasing number of reports on plasma position profile diagnostics by tomographic optical emission spectroscopic (OES) measurement [1-2]. Simultaneous measurement of all lines of sight is essential for *in-situ* measurement of position profiles. We have previously reported electron temperature and density diagnosis for Ar plasma based on tomographic OES measurement and collisional radiative model [2]. In this study, we report an attempt to diagnose the positional distribution of electron temperature T_e by tomographic emission spectroscopy in CF_4/O_2 inductively coupled plasma which is frequently used for etching.

2. Experiment

CF_4/O_2 plasma was generated by an inductively coupled plasma system (chamber inner dimensions Φ177.5 x H 211.8 mm (largest part), bias stage outer diameter 291 mm) as shown in Fig.1. The total pressure was set at 1.0 Pa (constant), the O_2 partial pressure p_{O2} = 0 - 25% of the total pressure, and the radio frequency (RF) power P_a = 50 - 400 W (antenna, 13.56MHz) and P_b = 0 - 100 W (stage bias, 12.5MHz). The cross section was observed 12 mm above the Si wafer by 34 lines of sights as shown in Fig.2. A multichannel spectrometer (UV-M135A, Horiba, Ltd.) was used to simultaneously measure the line-of-sight dependence of the spectral radiance $L_{air}(\lambda)$ at the atmospheric side of the window [3].

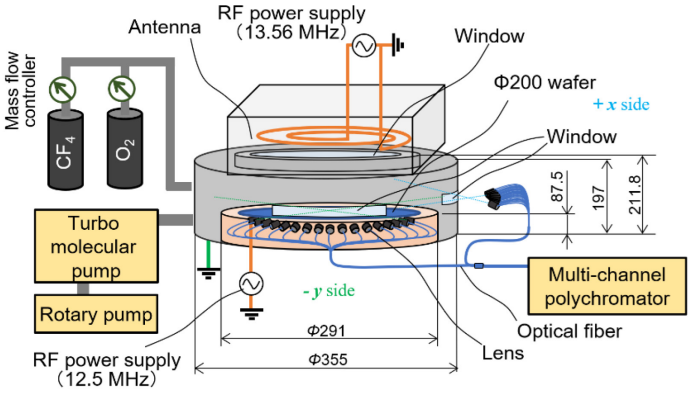

Fig. 1: The experimental setup.

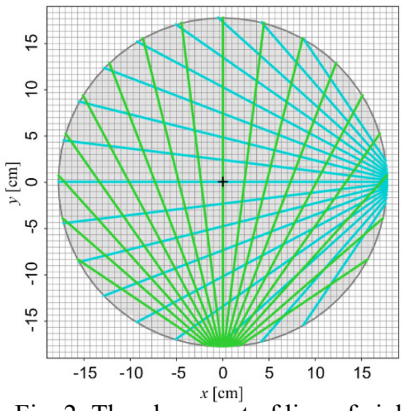

Fig. 2: The placement of line-of-sight.

3. Analysis

Taking $L_{air}(\lambda)$ as input, the line-of-sight dependence of the spectral radiance at the vacuum side window was calculated, taking into account the Fresnel reflection due to window surface refraction

and the line-of-sight shift [4]. Furthermore, the positional distribution of the spectral emission coefficients was reconstructed using a tomography spectral emission calculation program [2] based on the constrained regularization method [5]. From the emission coefficients of natural fluorine (F_I) lines, the excited level number densities of $3p^4\ 4D^\circ$ and $3p^2\ 2P^\circ$ of F_I : n_j and n_j' were calculated, respectively. The rate of electron collisional excitation from the ground level was calculated as a function of T_e and the cross section. Assuming coronal equilibrium, the elementary processes intervening in the relevant excited levels are the inflow by electron collisional excitation from the ground level to the relevant level and the outflow by spontaneous emission from the relevant level. Therefore, T_e was diagnosed by fitting the following equation:

$$f(T_e) = \sqrt{\left(\frac{\int_0^\infty \varepsilon\sigma(\varepsilon) \exp\left(-\frac{\varepsilon}{T_e}\right) \mathrm{d}\,\varepsilon}{\int_0^\infty \varepsilon\sigma'(\varepsilon) \exp\left(-\frac{\varepsilon}{T_e}\right) \mathrm{d}\,\varepsilon} - \frac{n_j \sum_i A_{ji}}{n_j' \sum_i A_{j'i}} \right)^2}, \qquad (1)$$

where ε is electron energy; $\sigma(\varepsilon)$ and $\sigma'(\varepsilon)$ are the electron collisional excitation cross section [6] of the transition from the ground level to $3p^4\ 4D^\circ$ and $3p^2\ 2P^\circ$, respectively; A_{ji} and $A_{j'i}$ are A coefficients from $3p^4\ 4D^\circ$ and $3p^2\ 2P^\circ$ to the ground level, respectively.

4. Results and Discussion

Figure 3 shows the dependence of T_e diagnostic results on P_b at p_{O2} = 20%. T_e at the center of the stage was lower than the outside. The asymmetry is considered due to the spiral shape of the edge of the antenna for inductive coupling or the placement of line-of-sights. Furthermore, an increase of T_e due to bias application was also observed. The dependence of the spectral emission coefficient and electron temperature on p_{O2}, P_a, and P_b, which are omitted for reasons of space limitation, will be discussed in my presentation.

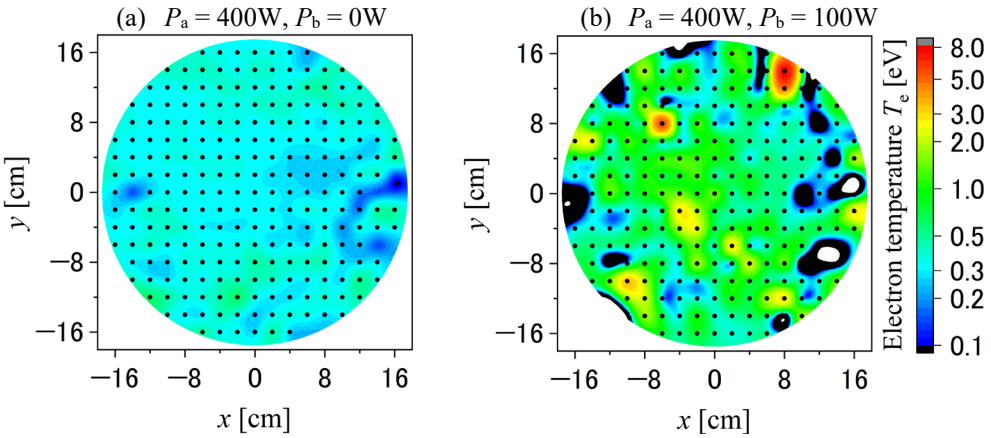

Fig. 3: The dependence of electron temperate on *x*-*y* position.

Acknowledgments

The authors thank Mr. Akira Kobayashi of the (then) Tokyo Institute of Technology for providing the initial version of the fluorine atom electron temperature analysis program based on the corona model. This work was supported by JSPS KAKENHI Grant Number JP23KJ0884.

[1] D. Lee, et al., *Plasma Sources Sci. Technol.*, **31** (2022) 125004.
[2] Y. Yamashita, et al., *J. Vac. Sci. Technol. A*, **42**, (2024) 023003.
[3] Y. Yamashita, et al., *Ext. Abstr. 71st JSAP Spring Meet. 2024*, (2024) 22a-12G-8 [in press].
[4] Y. Yamashita, et al., *Rev. Sci. Instrum.*, **94**, (2023) 083503.
[5] D.R. Ferreira, https://github.com/diogoff/isttok-tomography.
[6] LXCat https://nl.lxcat.net/home/.

On the line intensity ratio for electric field measurement in dielectric barrier discharge in argon at atmospheric pressure

Z Navrátil(*), L Kusýn, Z Bonaventura and T Hoder

Department of Plasma Physics and Technology, Faculty of Science, Masaryk University, Kotlářská 2, 611 37 Brno, Czech Republic
(*) zdenek@physics.muni.cz

Argon discharges belong to the most important plasma sources for non-thermal plasma applications at atmospheric pressure. Various cold plasma jets, relying on argon gas and AC, RF, MW or pulsed DC power have been developed [1]. However, no reliable optical emission spectroscopy method of local electric field measurement in the argon atmospheric pressure discharge has been yet developed. The intensity ratio of intensive lines from 4p ($2p_i$ levels in Paschen notation) levels can be better used for electron density measurement [2] than for the electron energy and the electric field diagnostics. Another complication for optical diagnostics is the filamentary nature of the argon plasma [3].

This contribution aims to measure the line intensity ratios of several argon lines originating from $3p^5$ 4p and $3p^5$ 5p levels using time-correlated single photon counting (TCSPC). The TCSPC method provides both the sensitivity required for the measurement of weak 5p lines as well as the capability to capture the evolution of streamer breakdown in random-in-time microdischarges with an exceptional time resolution (<0.2 ns).

A filamentary volume dielectric barrier discharge was generated by harmonic AC voltage (4.3 kV_{pp}) in 1 mm gap between hemispherical electrodes (4 mm in diameter, covered with a 0.5 mm thick 96% Al_2O_3 dielectric layer). The spatially resolved emission was monochromatized and measured by a time-correlated single photon counter (Becker & Hickl SPC-150). Four Ar I lines originating from $3p^5$ 4p levels (750.4, 751.5 nm) and $3p^5$ 5p levels (419.8, 420.1 nm) were measured.

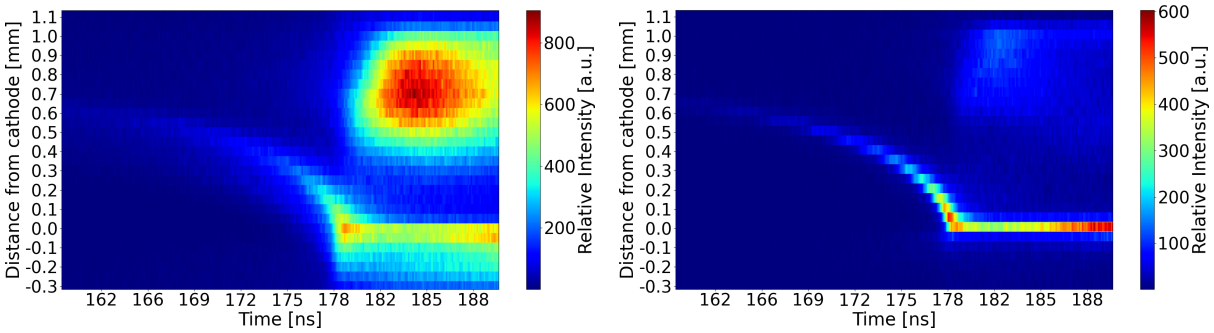

Fig. 1: Spatio-temporal distribution of the light emitted from the argon microdischarge on 751.5 nm transition (4p level $2p_5$, left) and 419.8 nm transition (5p level $3p_5$, right). The instantaneous cathode is located at zero position, the anode is at the position of 1 mm.

The spatio-temporal development of light emission from the argon microdischarge is for two wavelengths displayed in figure 1. Whilst the light emission from $2p_5$ level is broader and the light at the anode is more intensive than the light emitted by the cathode directed streamer, the emission from higher $3p_5$ level clearly maps the streamer development.

The example of the obtained temporal developments of the line intensity ratios is displayed in figure 2. The streamer passage at a position close to the cathode, starting the light emission of the discharge, is not captured at all when combining the lines both originating from 4p levels (750.4, 751.5 nm, top right). The intensity ratio constructed of 5p 419.8 and 420.1 nm lines (top left), developed to measure electron temperature at low pressures [4], seems to lose the sensitivity at high electric fields. This may be explained by the low importance of step-wise excitation through metastable states at atmospheric pressure. The intensity ratios combining the lines out of 4p and 5p levels seem to have the ability to track the streamer field depending on the line sensitivity to the electric field calculated from a simple collisional radiative model and the Boltzmann equation.

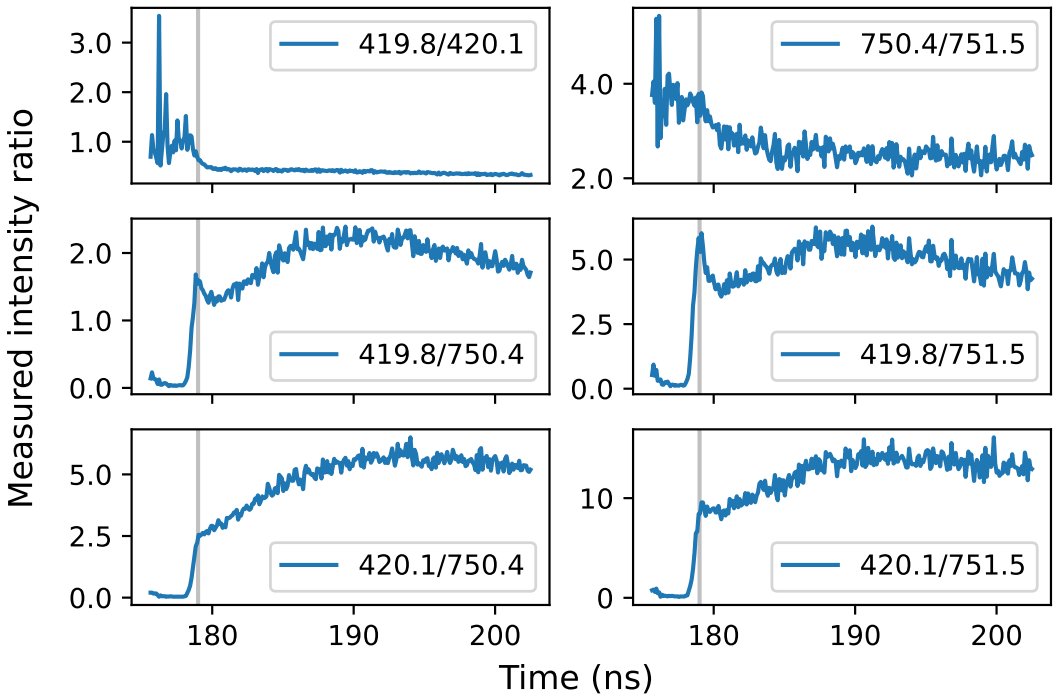

Fig. 2: Line intensity ratios during microdischarge ignition constructed from argon lines originating from $3p^5$ 4p and $3p^5$ 5p levels. The streamer passage is observed at the times around 179 ns (marked by a vertical line in the plots).

Acknowledgements This research was funded by project No. 21-16391S of the Czech Science Foundation and by projects LM2018097 and LM2023039 of the Ministry of Education, Youth and Sports of the Czech Republic.

[1] M. Laroussi and T. Akan *Plasma Process. Polym.* **4** (2007) 777–788.
[2] X. M. Zhu, Y. K. Pu, N. Balcon and R. Boswell *J. Phys. D: Appl. Phys.* **42** (2009) 142003.
[3] R. Brandenburg *Plasma Sources Sci. and Technol.* **26** (2017) 053001.
[4] J. B. Boffard, R. O. Jung, C. C. Lin, L. E. Aneskavich and A. E. Wendt *J. Phys. D: Appl. Phys.* **45** (2012) 045201.

Absolute calibration of Xe/O cross-section ratio for TALIF in nanosecond capillary discharge: optimization of the discharge parameters

Z Shu(*)[1], N A Popov[2], S M Starikovskaia[1]

[1] *Laboratory of Plasma Physics (CNRS, Ecole Polytechnique, Univ. Paris-Sud, Observatoire de Paris, Sorbonne Université, l'Institut Polytechnique de Paris), Ecole Polytechnique, route de Saclay, 91128 Palaiseau, France*
[2] *Skobeltsyn Institute of Nuclear Physics, Moscow State University, Moscow, 119991, Leninsky gory, Russia*
(*) zhan.shu@lpp.polytechnique.fr

Atomic species are readily produced in reactive media, such as discharge or combustion environments. Absolute measurements of the density of these reactive atoms are essential for the validation of models of plasma in molecular gases. Two-photon absorption laser-induced fluorescence (TALIF), offers a well-suited technique for detecting the densities of main atomic species, such as atomic O, H, and N, with sub-millimeter spatial resolution and high temporal resolution. However, high accuracy is difficult to achieve due to precise calibration of all the components of the diagnostic facility.

O-TALIF was initially developed in the 1980s as a gas discharge diagnostics tool. In 2005, Niemi *et al* suggested a calibration method for determining absolute atomic oxygen densities, based on a comparative measurement with a noble gas xenon that exhibits a two-photon resonance close to the transition of atomic oxygen [1]. In that paper, the atomic oxygen density was determined by titration and a "kit" for O-TALIF measurements was provided, including radiative lifetimes, room temperature quenching coefficients, and the ratio of the two-photon absorption cross-sections $\sigma^{(2)}_{\mathrm{Xe}}/\sigma^{(2)}_{\mathrm{O}} = 1.9 \pm 20\%$. Although it has been widely used, the cross-section ratio was only measured by Niemi's group. Recently, more and more papers have been dedicated to comparing different techniques to calibrate the Xe/O cross-section ratio. Drag *et al* [2] directly measured the two-photon absorption cross-section for the Xe transition, and found a value of about one-half of that implied by Niemi's measurement. By the use of this new ratio, Wubs *et al* [3] obtained an absolute O-atom density 25% smaller compared to the THz absorption spectroscopy results on the same capacitively coupled radio frequency oxygen discharge.

Our latest work [4] proposes a novel approach to calibrate the two-photon absorption cross-section ratio $\sigma^{(2)}_{\mathrm{Xe}}/\sigma^{(2)}_{\mathrm{O}}$ by using a nanosecond discharge with 100% dissociation of molecular oxygen, and so with a known 'reference' density of oxygen atoms ($[\mathrm{O}]_{ref} = 2 \times [\mathrm{O_2}]$). The discharge was initiated between two pin electrodes, with 53 mm of inter-electrode distance, and in the capillary tube with 2 mm of internal diameter. High-voltage pulses, with 9 kV of amplitude, 30 ns of FWHM and 10 Hz of repetitive frequency, were delivered to the electrodes via coaxial cables. A gas mixture of nitrogen plus a few percent of oxygen flowed through the capillary at 27 mbar with a total flow rate of 50 sccm so that each discharge was initiated in the new gas portion. Voltage at the electrodes, electrical current in the plasma, longitudinal electric field and energy delivered to the gas were measured by the technique of back current shunt and capacitive probe, giving the value of a few hundred Td of the reduced electric field and about 1 eV/molecule of the specific deposited energy. Additionally, the radial distribution of emission of excited nitrogen molecules and gas temperature in the discharge and afterglow were obtained experimentally. A detailed 1D numerical modeling was developed to analyze the main reactions and confirm the complete dissociation of $\mathrm{O_2}$ in the afterglow (5 μs to 25 μs after ignition). Therefore, by comparing the data from TALIF technique in the afterglow and Xe calibration with the 'reference' density of O-atoms, the two-photon absorption cross-section ratio was calculated as:

$$\sigma^{(2)}_{\mathrm{Xe}} / \sum_{J'} \sigma^{(2)}_{\mathrm{O}(J \to J')} = 1.8\ (\pm 0.2), \tag{1}$$

where J is the angular momentum quantum number of the ground-state oxygen atom level, and J' is the angular momentum quantum number of the upper fine structure level of atomic oxygen.

In this work, we are aiming to design a cell that is closed with known concentration of oxygen under tens of mbar. By using this portable device, similar nanosecond discharge could be applied to

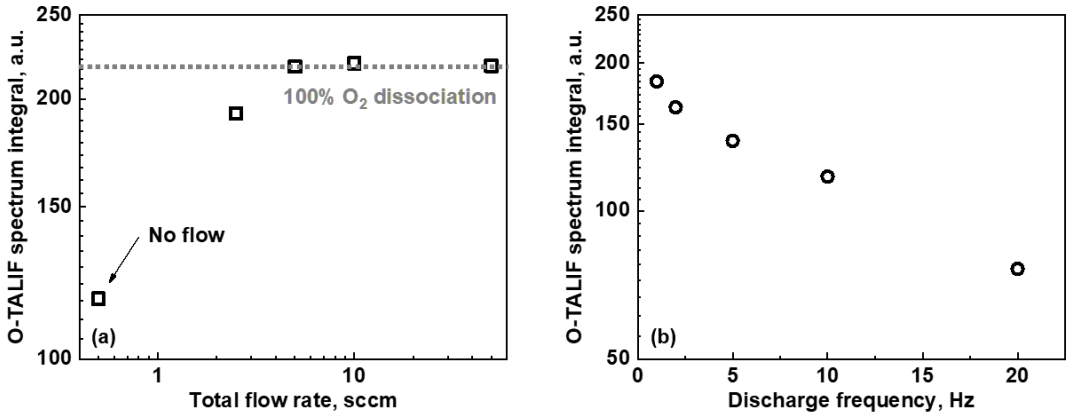

Fig. 1: (a) O-TALIF signal with different total flow rate of $N_2 + 5\%$ O_2 mixture at 5 μs, laser and discharge pulse repetition frequency of 10 Hz. (b) O-TALIF signal with discharge frequency in static $N_2 + 5\%$ O_2 mixture at 5 μs and laser pulse frequency of 10 Hz.

help calibrate the parameters in more diagnostic methods such as cross-section ratio in picosecond or femtosecond TALIF. An attempt was made for the nanosecond discharge in the same capillary tube to verify the feasibility of the new device by changing the flow rate of N_2: O_2 mixture and the repetition frequency of the discharge pulses. Fig.1(a) shows that O-TALIF signal maintains the level of 100% O_2 dissociation at 5 sccm minimum, which is coherent with the calculated flow rate to keep the gas renewal under 10 Hz discharge frequency in the existing capillary tube. However, the signal decreases when the flow rate reduces to 2.5 sccm or 0 sccm (static state). This may caused by the disturbance of long-lived species, like nitric oxide, accumulated after multiple discharges. In that case, it is reasonable to check the signal again with lower discharge and acquisition frequencies. Fig,1(b) gives the increasing trend of the O-TALIF signal with lower discharge frequency. When the frequency decreases to 1 Hz, the signal reaches almost 80% of the intensity where O_2 is fully dissociated.

Further work will be focused on two paths. One is to try to get the highest possible O-TALIF signal in N_2: O_2 mixtures and analyze the gas composition during and after each discharge. In other words, this is to keep the same dissociation fraction for different applications. The other way is to try different gas mixtures like Ar + O_2 to achieve full oxygen dissociation and avoid disturbance terms.

Acknowledgements

This work was partially supported by E4C IP Paris (ANR-18-EUR-0006-02), Engie Foundation and LIA/IRP KaPPA. The work of Dr. Nikolay Popov was partially supported by the RSF 23-17-00264. The support for Mr. Zhan Shu by the China Scholarship Council (CSC) program for PhD students is gratefully acknowledged.

[1] K. Niemi, V. Schulz-Von Der Gathen, H. F. Döbele *Plasma Sources Sci. Technol.* **14(2)** (2005) 375.
[2] C. Drag, F. Marmuse, C.Blondel *Plasma Sources Sci. Technol.* **30** (2021) 075026.
[3] J. Wubs, L. Invernizzi, K. Gazeli, U. Macherius, X. Lü, L. Schrottke, G. Lombardi, K. D. Weltmann, J. van Helden *Plasma Sources Sci. Technol.* **123** (2023) 081107.
[4] Z. Shu, N. A. Popov, S. M. Starikovskaia, *Plasma Sources Sci. Technol.* **33** (2024) 025019.

Exploring arcing phenomena in low-voltage contactors: a comprehensive study through numerical modelling and experiment

D. F. N. Santos(*)[1,2], O. Ojeda Mena[3], M. Lisnyak[3], and M. S. Benilov[1,2]

[1]*Departamento de Física, Universidade da Madeira, 9000 Funchal, Portugal*
[2]*Instituto de Plasmas e Fusão Nuclear, Instituto Superior Técnico, 1041 Lisboa, Portugal*
[3]*Schneider Electric Science and Technology, 38050 Grenoble Cedex 9, France*
(*)diego.santos@staff.uma.pt

Since the experiment cannot allow to describe in detail all the physical phenomena of arcing in low voltage contactors, it is best to implement a numerical model based on the first principles and not relying on a priori assumptions. In this work, numerical modelling of arcing in low-voltage contactors on cold electrodes in atmospheric-pressure argon is investigated by means of the unified 1D modelling. The explosion of the last bridge of the contactors is not described by the model. The modelling starts from an "after explosion" state. The effect of initial conditions, assumed at this state, is studied. Results are compared with results of experiments performed at Schneider Electric. A good agreement is observed between the numerical and experimental results.

The unified arc modelling approach, developed and used by workers from different countries, allows one to describe, in a natural way, the whole process of development of short non-stationary arcs, including the arc ignition and the switching of polarity, until the arc is extinguished. In [1] the first quarter-period after the ignition, from a cold state, of a short AC arc between parallel electrodes in atmospheric-pressure argon was studied. In this work the study is extended to longer times to investigate the changes of polarity with subsequent reignitions of the arc after each change of polarity. The equations and the boundary conditions are written in the spirit of previous work [2].

The explosion of the last bridge, occurring when the electrodes of a contactor begin to open, is not described by the model; the modelling starts from an "after explosion" state. The effect of initial conditions, assumed at this state, is studied. It is found that the computed ignition voltage exceeds experimental ones. Effects that can be responsible for this deviation are investigated: increased value of the secondary electron emission coefficient, increased surface temperature of the electrodes, and/or field electron emission from the cathode surface enhanced by the presence of microprotrusions on the surface.

The setup of an experiment with contractors, carried out at Schneider Electric in Grenoble, consists of the power supply, a resistor and two electrodes: one static and the other mobile. The experimental condition of arcing in low-voltage contactors is with cold electrodes and in atmospheric-pressure air. During the experiment, the arc current, arc voltage, and the displacement of the mobile electrode carrier are recorded. In this experiment, new electrodes were used. The contacts separate until the distance between them is 8 mm.

The numerical modelling of the AC current transfer in a contactor is compared with the experimental result. For that, it is necessary to evaluate the amplitude of the current density to be used in the modelling to perform a comparison. Assuming 5 mm for the attachment diameter and taking 800 A for the amplitude of the applied arc current, one obtains a value of the order of 4×10^7 Am^{-2} for the current density amplitude. The electrode material was assumed to be copper, and the plasma-producing gas was argon instead of air; approximations that are deemed reasonable for a quantitative comparison. The modelling results reported here refer to a fixed interelectrode gap of h=100 μm.

The initial temperatures of the gas and the electrodes must be specified as initial conditions. In principle, the initial conditions should describe the post-initial explosion state. Unfortunately, there appears to be no reliable information on this state. Therefore, suitable initial conditions must be

identified by trials and errors. Let us first consider results obtained assuming the typical cold initial conditions.

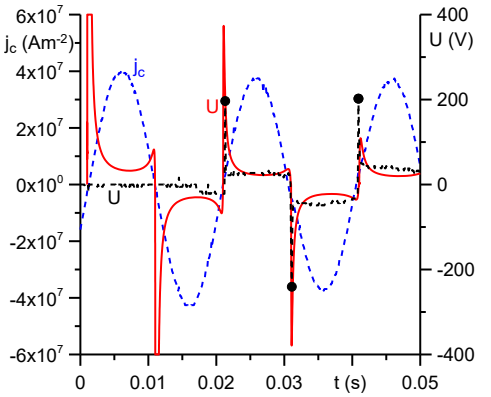

Fig. 1 Solid: computed arc voltage. Dashed: current density and arc voltage from the experimental data.

The computed arc voltage and the measured arc voltage are shown in Fig. 1, along with the current density, evaluated as described above in terms of the measured arc current for the experimental date. The arc voltages in the simulation begin at the first CZ and in the case of the experimental the opening of the electrodes occurs approximated at the 16 ms. These two points are not comparable, because the initial conditions of the simulations are not for the conditions of the "after explosion". Nevertheless, at the instant 16 ms the arc voltage of the experimental and the modelling are very close. This means that at the instant 16 ms of the modelling can be the initial conditions that describe the "after explosion" state of the electrodes. After this point one can see that there is a clear qualitative agreement between the modelling and the experiment: there are significant overvoltage peaks after each CZ according to both the modelling and the experiment, and the height of the peaks (the overvoltage value) decrease with time.

In Fig. 1, it is shown that, in the experiments, the electrodes open under high current conditions, resulting in an arc voltage of approximately 20 V. Additionally, based on the final state of the electrodes, it can be concluded that the typical temperature remains below the boiling point. That means that for reaching the same conditions in the modelling, it will be necessary to improve the modelling initial conditions. This can be done by increasing the value of the secondary electron emission coefficient, γ, by changing the initial surface temperature of the electrode, and/or by introduction of the field enhancement factor, β. The impact of these three mechanisms can be observed in Fig. 2. Here the current density linearly increases with time from 0 to 10^7 Am^{-2} within 1 ms and is maintained constant after 1 ms, the electrodes separation is 10 mm and the material is tungsten.

The three mechanisms studied in this work have an impact on the initial arc discharge voltage, but they do not bring it down to the values observed in the experiment. There are several parameters to be adjusted in the model: the current value, or current density at the instant of the opening of the electrodes, the effect of the opening of the electrodes, or maybe increased β until 300. This will be addressed in the next works.

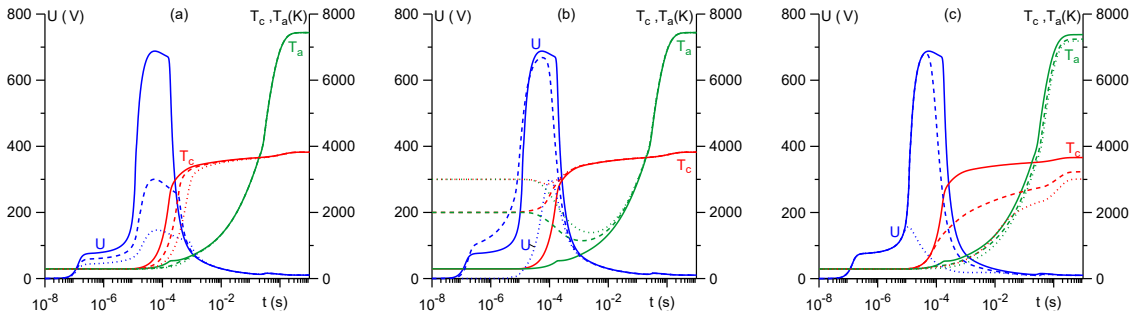

Fig. 2 Evolution of the arc voltage and electrode surface temperatures for different values of: (a) γ. Solid: γ=0.1. Dashed: 0.2. Dotted line: 0.4, (b) T_s. Solid: T_s=300 K. Dashed: 2000 K. Dotted: 3000 K and (c) β. Solid: β=1. Dashed: 50. Dotted: 100.

Acknowledgments The work was supported by FCT - Fundação para a Ciência e Tecnologia, I.P. under projects UIDB/50010/2020, UIDP/50010/2020, LA/P/0061/2020 and by European Regional Development Fund through the Operational Program of the Autonomous Region of Madeira 2014-2020 under project PlasMa-M1420-01-0145-FEDER-000016.

[1] D F N Santos *et al, J Phys D Appl Phys* **54** 195202 (2021).
[2] D F N Santos *et al, Phys Plasmas* **29** 043503 (2022).

Theory of stability of self-sustaining DC discharges at inception with application to negative corona

P. G. C. Almeida[1,2], G. V. Naidis[3], and M. S. Benilov[1,2] (*)

[1] *Departamento de Física, Faculdade de Ciências Exatas e da Engenharia, Universidade da Madeira, 9000 Funchal, Portugal*

[2] *Instituto de Plasmas e Fusão Nuclear, Instituto Superior Técnico, Universidade de Lisboa, 1041 Lisboa, Portugal*

[3] *Joint Institute for High Temperatures, Russian Academy of Sciences, Moscow 125412, Russia*

(*) benilov@staff.uma.pt

The inception of self-sustaining DC discharges is analyzed in terms of the bifurcation theory. The existence of a non-physical solution with negative ion and electron densities must be taken into account in order to identify the bifurcation type. The bifurcation is transcritical for positive and negative corona discharges and, in more general terms, it is expected to be transcritical for all discharge configurations except for the parallel-plate discharge, where the bifurcation is pitchfork. General trends of the bifurcation theory suggest that the corona discharges should be stable immediately after the inception. This conclusion is tested numerically for negative coronas in atmospheric-pressure air in coaxial-cylinder geometry. Two independent approaches have been used: (1) study of linear stability against infinitesimal perturbations with the use of an eigenvalue solver and (2) following the time development of finite perturbations with the use of a time-dependent solver.

The numerical model of non-thermal discharges in high-pressure dry air, described in [1], is employed in this work. In brief, the model comprises equations of conservation and transport of charged species, written in the drift-diffusion approximation, and the Poisson equation. Charge-particle species accounted for in the model are the electrons, one representative species of positive ions, which are mostly O^{+2}, and three species of negative ions, O^{-2}, O^{-}, O^{-3}. Transport and kinetic coefficients are assumed to depend on the local reduced electric field and the neutral-gas temperature. Photoionization is evaluated by means of the three-exponential model [2]; the gas temperature is set equal to 300K. Calculations reported in this work are performed for a one-dimensional negative corona discharge between concentric-cylinder electrodes in dry atmospheric-pressure air, which is an appropriate test case for the theory. The calculations refer to the inner electrode radius of 0.1mm, the outer electrode radius of 2mm, and the pressure of 1atm. Stationary, eigenvalue and time-dependent solvers of COMSOL Multiphysics® are used.

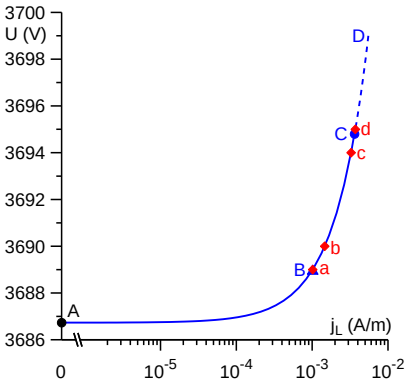

Fig. 1: Stability of negative corona discharge against small perturbations.

The stability of the negative corona discharge is illustrated by Fig. 1, and was calculated within the framework if the linear stability theory following a procedure similar to that employed in [3]. The black circle marked A in the figure designates the ignition of the self-sustaining discharge. Results from stability analysis, reveal that states in section AB are associated with increments which are real and negative. Therefore, this section is stable and perturbations decay monotonically with time. Section BC is associated with increments which have negative real part and nonzero imaginary part. This section is still stable, but perturbations decay with oscillations. Section CD is associated with positive real part and nonzero imaginary part. This section is unstable, and perturbations eventually lead to Trichel pulses.

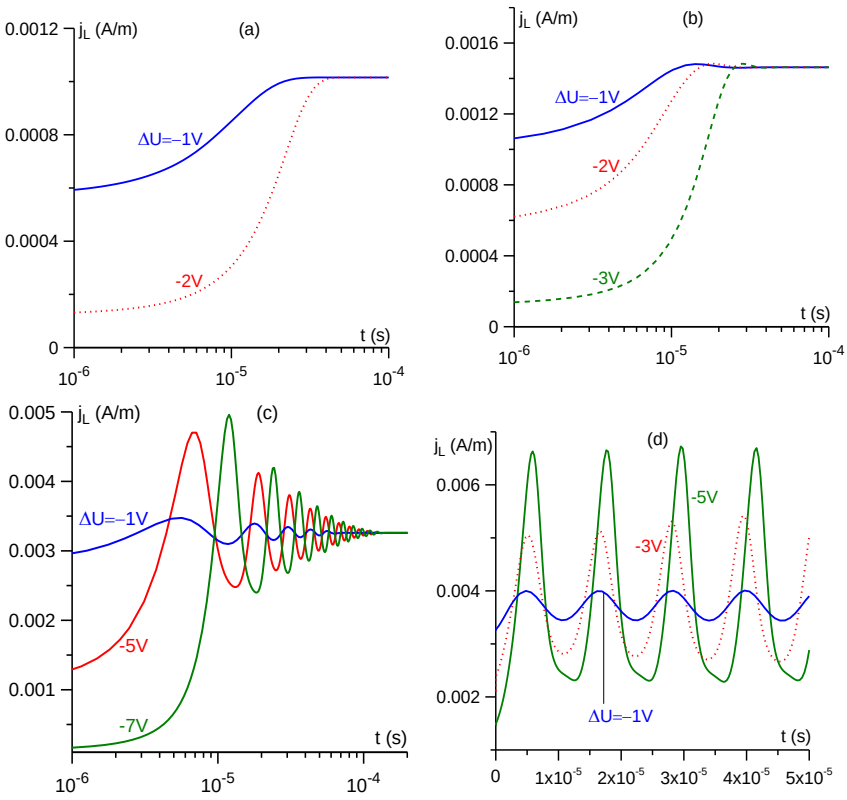

Fig. 2: Stability of negative corona discharge against finite perturbations.

The stability of the negative corona discharge against finite perturbations was also studied. As an example, results are shown in Fig. 2 for the states *a-d* shown by diamonds in Fig. 1. The procedure is the same as in [1, 4]: a small perturbation is introduced in applied voltage and the evolution of the discharge is followed by means of a time-dependent solver. If a stationary state is reached, the discharge is deemed stable. The procedure also allows one to determine whether the growth or decay of the perturbations is monotonic or oscillatory.

One can see from Fig. 2 that state *a* is stable and the perturbations decay monotonically. States *b* and *c* are also stable, but the decay of perturbations is oscillatory. State *d* is unstable, the perturbations grow accompanied by oscillations. For higher voltages, the perturbations lead to Trichel pulses. Detailed results will be given at the conference.

Numerical results are in perfect agreement with each other. In particular, the theory, the linear stability analysis, and the time-dependent modelling show that the negative corona is pulseless, immediately after the ignition. The stability is lost on harmonic perturbations, which evolve into Trichel pulses. Results are of theoretical interest and offer insights into physics of negative coronas. A number of interesting questions arise for future works, e.g., investigating the mechanism of the oscillations, exploring the potential effect of negative ions in this mechanism, and understanding the transition from harmonic oscillations to Trichel pulses and the potential effect of negative ions in this transition. A major challenge is to find the conditions under which a stable negative corona discharge occurs over a substantially wider range of voltages than 10V , in order to facilitate its unambiguous observation in experiment. This work has shown that results of linear stability analysis are in excellent agreement with results of time-dependent modelling of finite perturbations. Therefore, future numerical investigations of stability of negative corona discharges are likely to employ the latter approach, as was done in [4].

IPFN activities were supported by FCT - Fundação para a Ciência e Tecnologia, I.P. by project UIDB/50010/2020 and DOI 10.54499/UIDB/50010/2020, by project UIDP/50010/2020 and DOI 10.54499/UIDP/50010/2020 and by project LA/P/0061/202 and DOI 10.54499/LA/P/0061/2020.

[1] M. S. Benilov *et. al.*, *J. Appl. Phys.* **130** (2021), 121101.
[2] A. Bourdon *et. al.*, *Plasma Sources Sci. Technol.* **16** (2007), 656.
[3] P. G. C. Almeida, M. S. Benilov, and M. J. Faria, *J. Phys. D: Appl. Phys.* **44** (2011), 415203.
[4] N. G. C. Ferreira, P. G. C. Almeida, A. E. Taher, G. V. Naidis, M. S. Benilov, *Numerical investigation of stability of low-current point-to-plane negative corona in air*, submitted to ESCAMPIG XXVI (2024), Brno, Czech Republic.

Determination of photoionization properties of C_4F_7N – N_2 mixture and their application in streamer simulation

J. Tungli[(*)1], Z. Bonaventura[2], D. Prokop[2], L. Kuthanová[2], T. Hoder[2], J. Fedor[3], M. Ranković[3], M. Horký[1], S. Kadlec[1]

[1] *Eaton European Innovation Center, Bořivojova 2380, 252 63 Roztoky, Czech Republic*
[2] *Department of Plasma Physics and Technology, Masaryk University, Kotlářská 2, 611 37 Brno, Czech Republic*
[3] *J. Heyrovský Institute of Physical Chemistry, Czech Academy of Sciences, Dolejškova 3, Prague 8, Czech Republic*
[(*)] JanTungli@eaton.com

In the gas-filled electric power equipment, SF_6 gas has been extensively used for its insulating properties [1]. However, due to its high global warming potential, alternatives to SF_6 are being considered. A promising candidate is the C_4F_7N gas and its mixtures, e.g. with CO_2 or N_2, offering high electronegativity, and significantly inhibiting discharge inception and propagation. In a gas, where excited states produce ionizing radiation, the question of photoionization is of interest. The effect of photoionization is significant in some gases, e.g. in air [2]. In contrast, in other gases the ionizing radiation, even if produced, may be quickly absorbed without ionization, e.g in CO_2 [3]. In this work, we study the effect of the photoionizing radiation on the streamer propagation in a nitrogen - C_4F_7N mixture .

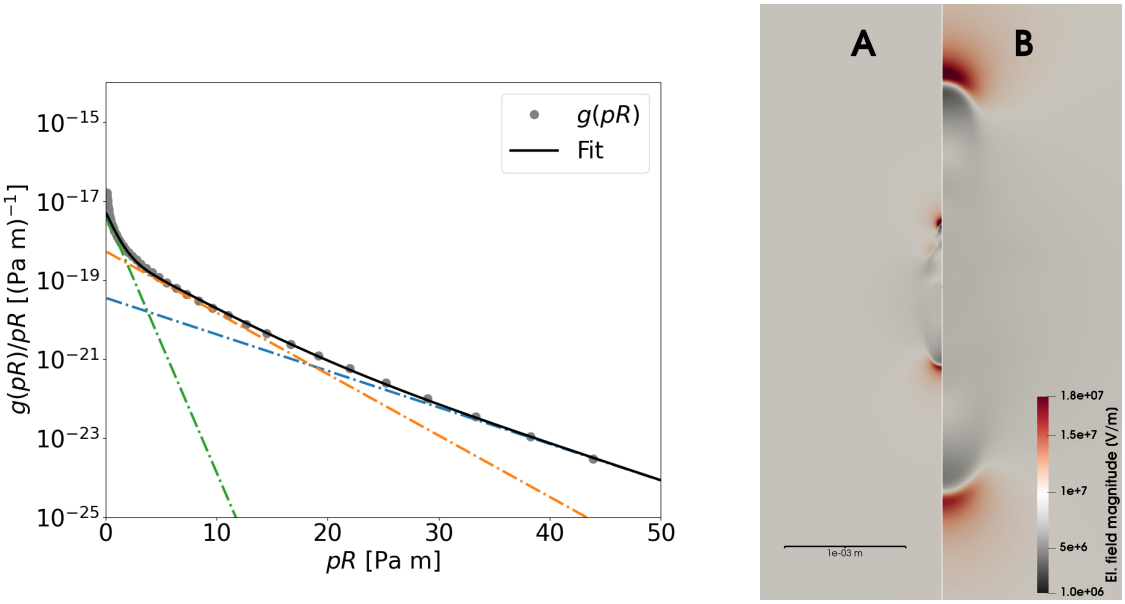

Fig. 1: *Left:* The fit of the photon propagator function for 10% C_4F_7N 90% N_2 mixture. *Right:* Electric field magnitude comparison in axisymmetric streamer simulation of double-headed streamers propagating from a seed charge cloud: (A) without and (B) with photoionization model.

We model the ionizing radiation by a system of screened Poisson's equations as proposed in [2, 4, 5]. The parameters are obtained by the procedure suggested in [6] where the coefficients l_j and A_j are obtained from fitting the function:

$$\frac{g(pR)}{pR} = \sum_j A_j \mathrm{e}^{-l_j pR} \tag{1}$$

where $g(pR)$ is the photon propagator. Based on the experimental data, C_4F_7N in mixture with N_2 may be ionized by the radiation emitted by excited nitrogen states, similarly as oxygen molecules are in nitrogen-oxygen mixtures (e.g., in air).

The input data used in this model were measured for this work. The photoabsorption cross-section of C_4F_7N [7] was measured on the AU-UV beamline of the ASTRID2 synchrotron in Aarhus, Denmark, and the photoionization cross-section [8] was measured on the VUV beamline of the SLS synchrotron in Villigen, Switzerland.

From these data, the photon propagator function is constructed and fitted (see Fig.1 (left)). Radiation from plasma is assumed to originate solely from the excited nitrogen states and is assumed to have the same emission rate as is assumed in the photoionization model for air.

The effect of the inclusion of the photoionization model is shown in fluid dynamics streamer simulation. We compare double-headed streamers modeled in C_4F_7N - N_2 mixture when this photoionization model is used and without it (Fig.1 (right)). The use of photoionization results in a wider streamer channel and faster streamer propagation. As expected, while the negative streamer initiates easily without photoionization, the propagation of the positive streamer is significantly enhanced with the addition of photoionizing radiation.

[1] L.G. Christophorou et al. In: *IEEE Electrical Insulation Magazine* 13.5 (Sept. 1997), pp. 20–24.

[2] A Bourdon et al. In: *Plasma Sources Science and Technology* 16.3 (Aug. 2007), pp. 656–678.

[3] Baohong Guo et al. In: *Plasma Sources Science and Technology* 32.11 (Nov. 2023), p. 115001.

[4] P Ségur et al. In: *Plasma Sources Science and Technology* 15.4 (July 2006), pp. 648–660.

[5] Alejandro Luque et al. In: *Applied Physics Letters* 90.8 (Feb. 2007), p. 081501.

[6] R Janalizadeh and V P Pasko. In: *Plasma Sources Science and Technology* 28.10 (Oct. 2019), p. 105006.

[7] T. Ovad et al. In: *J. Chem. Phys.* 158 (2023), p. 014303.

[8] Nag, P. et. al. “To be published”. In: (2024).

This research has been supported by the Technology Agency of the Czech Republic within the project TK04020069: *Streamers and surface flashover discharges on insulators in alternative gases to SF6.*

Investigating of ignition of positive corona discharge in air using a time dependent fluid model

Jaroslav Jánský [*1], Reza Janalizadeh[2], Victor P. Pasko[2]

[1] *Department of Mathematics and Physics, University of Defence, Brno, Czechia*

[2] *Department of Electrical Engineering, Penn State University, University Park, PA, USA*

[(*)] jaroslav.jansky@unob.cz

Sharp point electrodes generate significant electric field enhancements where electron impact ionization leads to formation of electron avalanches that are seeded by photoionization. Photoionization of molecular oxygen due to extreme ultraviolet emissions from molecular nitrogen is a fundamental process in the inception of positive corona in air [1]. In a positive corona system, the avalanche of electrons in bulk of discharge volume is initiated by specific distribution of photoionization far away from region of maximum electron density near the electrode where those photons are emitted [2,3,4]. Here we present an approach using a time dependent fluid model in one dimensional spherical geometry to obtain electric field threshold for postive corona inception. The results are compared to Pasko et al., 2023 [5], where a novel approach to finding inception conditions of positive corona was introduced. The results agree well with steady state solutions. The time dependent model additionally shows that the steady state solutions are reached on timescale of electron drift. The time dependent model demonstrates the time dynamics of the space charge regime due to the increase of particle densities when the applied field is above threshold. The results emphasize significance of correct photoionization boundary conditions for accurate modeling of corona.

[1] Zheleznyak M B, Mnatsakanyan A K and Sizykh S V, *High Temp.* **20** (1982) 357–62.
[2] Naidis G V, *J. Phys. D: Appl. Phys.* **38** (2005) 2211–4.
[3] Naidis G V, *Sov. J. Plasma Phys.* **13** (1987) 645–8.
[4] Liu N, Dwyer J R and Rassoul H K, *J. Atmos. Sol.-Terr. Phys.* **80** (2012) 179–86.
[5] Pasko V P, Janalizadeh R, Jansky J, *Plasma Sources Sci. Technol.,* **32(7)** (2023) 075014.

Sensitivity analysis of various physics processes in industrial HiPIMS: A global plasma modelling perspective

Kristína Tomanková(*)[1,2], Kryštof Mrózek[1,2], Adam Obrusník[2], Alexander Fromm[3], Frank Burmeister[3]

[1] *Department of Plasma Physics and Technology, Masaryk University, Brno 611 37, Czech Republic*

[2] *PlasmaSolve s.r.o., Brno 602 00, Czech Republic*

[3] *Fraunhofer Institute for Mechanics of Materials IWM, Freiburg 79108, Germany*

(*) kristinatomankova@mail.muni.cz

High Power Impulse Magnetron Sputtering (HiPIMS) presents a revolution in the coating industry, enabling the production of superior-quality thin films with high density. As opposed to conventional magnetron sputtering, power fed into a HiPIMS process takes the form of short highly energetic pulses followed by a longer off-time allowing for cooling of the target. The HiPIMS plasma is then characterized by a high degree of ionization. [1] However, introducing peak power of amplitudes up to two orders of magnitude higher than during regular magnetron sputtering unveils a whole new range of physics phenomena that govern the process. Understanding these processes on a deep level is crucial in order to enhance the efficiency of this technology, especially on a larger scale. In this context, physics-based numerical simulations stand out as a valuable tool to provide insight into such complex plasma processes. Considering that one experiment with an industrial HiPIMS coater requires 100-800 kWh of electricity to run, plus additional material and operational costs, a well-validated predictive simulation model would enable significant energy and material savings.

This contribution presents a time-dependent volume-averaged global plasma model of reactive HiPIMS that can predict the overall behavior and macroscopic response to variations in operational parameters. This model is designed to reflect the functionality of a commercial HiPIMS coater used for deposition of Al_2O_3 and SiO_2 thin films.

Even though literature features several advanced HiPIMS models [2], works aiming for a detailed model description of HiPIMS for practical and industrial applications are still rare. The developed models typically require many non-orthogonal tuning parameters or they lack experimental validation.

In contrast to previously published global models, our approach was to develop the model from the ground up, focusing on each key physics phenomenon intrinsic to HiPIMS. Utilizing the high computational efficiency of global models, it is possible to clearly demonstrate the importance of various physics processes in a very short amount of time. We perform a sensitivity analysis on multiple effects to quantitatively outline their influence on the process. The analysis covers phenomena like sputter wind, target heating, ion return probability or target poisoning. Additionally, an estimation of the model inaccuracy is presented with respect to the plasma kinetic system and different rate coefficient expressions. In this context, our research involves a “stepping back” from already published numerical models that include dozens of source terms, and it is not clear whether all these source terms hold equal importance.

The contribution will also describe concrete steps that we are undertaking towards the development of a spatial model of an industrial HiPIMS process and preliminary simulation results, if available. The ultimate goal is to reach a „digital twin“ of HiPIMS by employing a combination of different simulation methods.

This work was supported in the frame of the international IraSME project called FastPIMS – a collaboration among PlasmaSolve, Fraunhofer IWM and Aurion GmbH. On the Czech side, the project is organized by Ministry of Industry and Trade within the Applications I framework (grant agreement CZ.01.01.01/01/22_002/0000106).

[1] Ehiasarian, Arutiun P. "High-power impulse magnetron sputtering and its applications." *Pure and applied chemistry*82.6 (2010): 1247-1258.

[2] Gudmundsson, Jon Tomas, et al. "An ionization region model of the reactive Ar/O2 high power impulse magnetron sputtering discharge." *Plasma Sources Science and Technology* 25.6 (2016): 065004.

Argon metastable atom quenching in low pressure Ar/O_2 CCPs

Lan-Yue Luo[1,2], Peter Hartmann[(*)2], Zoltán Donkó[2], He-Ping Li[(*)1]

[1] *Department of Engineering Physics, Tsinghua University, Beijing 100084 China*

[2] *Institute for Solid State Physics and Optics, HUN-REN Wigner Research Centre for Physics, Budapest 1121 Hungary*

[(*)] hartmann.peter@wigner.hu; liheping@tsinghua.edu.cn

The kinetics of excited particles could exert a significant effect on low-temperature discharges. For CCPs operated in argon, stepwise ionization and pooling ionization involving argon metastable atoms provide alternative pathways beside direct ionization from the ground state by electron impact. Though the density of metastable levels ($1s_5$ and $1s_3$) is a few magnitudes lower than that of the ground state atoms, the lower energy thresholds of stepwise processes can lead to substantial reaction rates. It is indicated that the ionization from argon metastable atoms can surpass the direct one as the pressure approaches 1 Torr [1]. Nevertheless, the density of metastable atoms can decrease rapidly by a small amount of oxygen as shown by measurements [2] as well as numerical simulations [3]. The limited quantity of oxygen might come not only from intentional mixture but also as gas impurity in experiments. Hence one-dimensional kinetic simulations and experiments in argon/oxygen CCPs under low pressures are conducted to investigate the physical processes of argon metastable population and de-population.

Table 1: device parameters and discharge conditions.

Physical parameter	Value
Electrode gap	4 cm
Electrode diameter	14 cm
Driving frequency	13.56 MHz
Peak-to peak voltage	60-300 V
Gas pressure	2-10 Pa
Oxygen ratio	0-6%

The experimental setup consists of a geometrically symmetric cylindrical discharge chamber and tunable diode laser absorption spectroscopy (TDLAS) system for argon metastable atom density measurements. Some of the device parameters and discharge conditions are shown in Table 1. The transitions having wavelengths 772.376 nm and 772.421 nm are employed in TDLAS for $1s_5$ and $1s_3$, respectively.

The simulation model for argon/oxygen plasmas is based on a full model [4] for pure argon discharges. Simplification has been made to reduce computation time while preserving good agreement at low pressures, which is proved by code-to-code benchmarks in pure argon cases. The simplified model consists of basic 1d PIC/MCC code and extended diffusion-reaction-radiation (DRR) code. The former includes the charged particles and the oxygen metastable $O_2(a^1\Delta g)$ due to its important contribution to quenching of negative oxygen ions. The electron impact excitation rates from ground state (GS) argon atoms to 30 excited levels are recorded after the convergence of the PIC code and are used as inputs for the DRR code. Taken the excitation rates as sources, the diffusion equations of the two metastable levels are solved in the DRR code to get their density distributions,

$$-D\frac{\partial^2 n_m}{\partial x^2} = S_{\mathrm{GS}} + S_{\mathrm{rad}} + S_{\mathrm{cas}} - L_{\mathrm{rad}} - L_{\mathrm{step}} - L_{\mathrm{oxy}}, \quad (1)$$

where D is the diffusion coefficient, n_m refers to the metastable density. "S" represents the source of the Ar metastable levels from GS excitation, radiation from 2p levels and cascades from Rydberg levels with subscripts of "GS", "rad" and "cas", respectively. Similarly, "L" with different subscripts stands for the losses due to radial diffusion, stepwise excitation of Ar atoms, and quenching of Ar metastables by O_2 molecules with a rate coefficient taken from [5]. Eq. (1) is solved with a boundary condition taken from [6].

The computed and experimental densities at the centre of electrode gap are presented here. For pure argon, the metastable densities always increase initially with the rise of discharge voltages and tend to saturate as shown in Fig. 1. The ratios of the computed densities to the experimental values are approximately 2-3, which is reasonable considering the performance of the full model and experimental uncertainties.

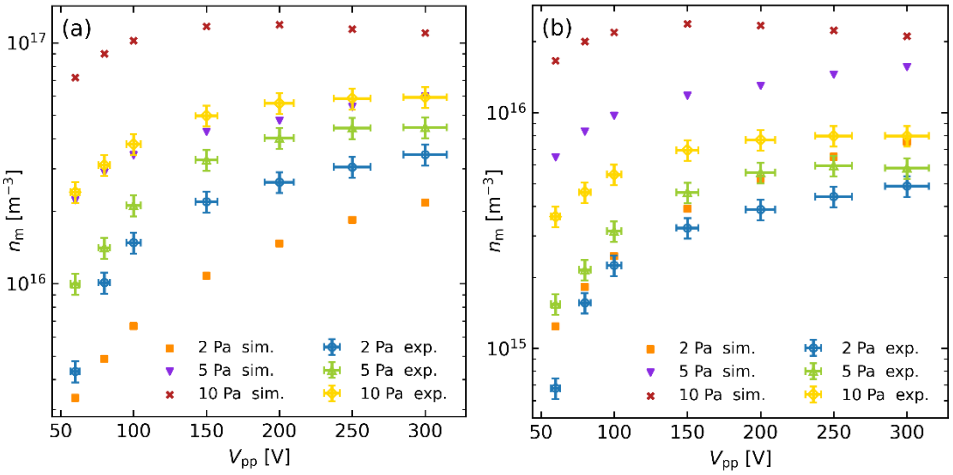

Fig. 1: Densities of Ar metastable atoms: (a) $1s_5$ and (b) $1s_3$, at the centre of electrode gap spacing at different pressures as a function of RF peak-to-peak voltage.

With the addition of oxygen, the metastable densities decrease rapidly, and then, the trend slows down when the gas pressure and discharge voltage are fixed. Good agreement between the simulations and the experiments is achieved for both metastable levels. The results prove that the simplified model is applicable for argon/oxygen CCPs at low pressures.

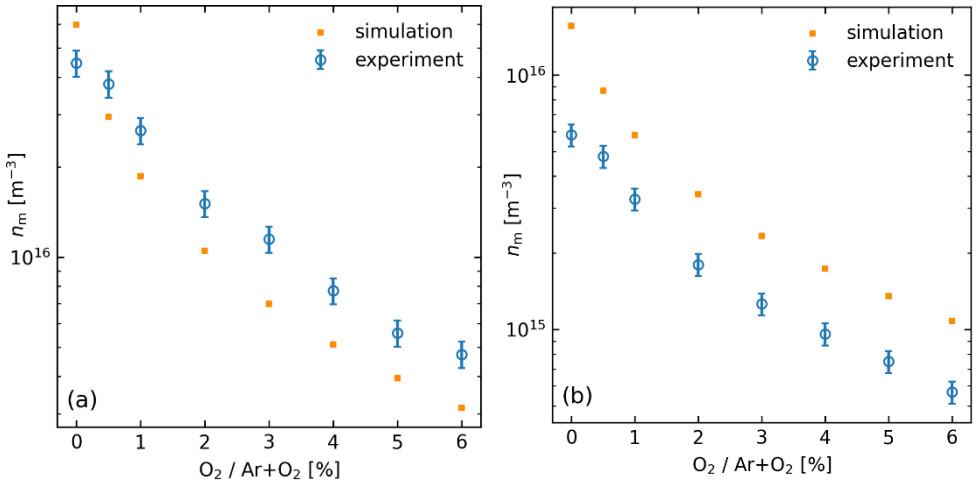

Fig. 2: Densities of Ar metastable atoms: (a) $1s_5$ and (b) $1s_3$ at the centre of electrode gap at 5 Pa and 300 V, as a function of oxygen content in the gas mixture.

[1] C M Ferreira, J Loureiro and A Richard. *Appl. Phys.* **57** (1985) 82-90.

[2] T Kitajima, T Nakano and T Makabe. *Appl. Phys. Lett.* **88** (2006) 091501.

[3] S Rauf and M Kushner. *J. Appl. Phys.* **82** (1997) 2805-2813.

[4] Z Donkó, P Hartmann, I Korolov, et al. *Plasma Sources Sci. Technol.* **32** (2023) 065002.

[5] J T Gudmunsson and E G thorsteinsson. *Plasma Sources Sci. Technol.* **16** (2007) 399-412.

[6] D Q Wen, J Krek, J T Gudmundsson, et al. *Plasma Sources Sci. Technol.* **30** (2021) 105009.

Kinetic study of gas heating in low pressure CO_2 plasmas

Yang Liu[1, 2], Tiago Silva[2], Tiago C Dias[2], Pedro Viegas[2], Xiangen Zhao[3], Yaping Du[3], Junjia He[1], Vasco Guerra[(*)2]

[1] *State Key Laboratory of Advanced Electromagnetic Technology, School of Electrical and Electronic Engineering, Huazhong University of Science and Technology, Wuhan, 430074 China*

[2] *Instituto de Plasmas e Fusão Nuclear, Instituto Superior Técnico, Universidade de Lisboa, Lisboa, 1049-001 Portugal*

[3] *Department of Building Environment and Energy Engineering, The Hong Kong Polytechnic University, HongKong, 999077 China*

[(*)] vguerra@tecnico.ulisboa.pt

Carbon dioxide (CO_2) is an important component of our atmosphere and a dominant constituent in the atmospheres of Venus and Mars. Atmospheric CO_2 emission need to be net-zero by 2050 to reduce global warming[1], while sustained exploration on Mars and Venus requires in-situ utilization of CO_2 resources[2]. One promising and environmentally friendly solution is to convert CO_2 into high value-added chemical products by plasma technology, due to its abundant reactive species and high chemical activity.

In recent years, numerous works have been published for CO_2 dissociation in plasma by means of experimental diagnostics, modelling, or a combination of the two. Species density, O atom loss frequency, reduced electric field, and vibrational and gas temperatures were measured in situ in a CO_2 glow discharge at low pressure[3]. These measurements provide an ideal set of constraints for validating CO_2 plasma kinetic models. A detailed self-consistent kinetic model for CO_2 plasma at low pressure was recently developed and validated[4]. However, the gas thermal balance equation was not included in the model and the gas temperature was given as an input parameter. In this work, the reaction mechanism previously established[4] is used to study the gas heating in continuous glow discharges. To this purpose, the gas thermal balance equation is added to the model to calculate the average gas temperature, assuming a gas discharge under isobaric conditions and that the heat conduction is the dominant convective cooling mechanism, and following the procedure proposed by Dias et al[5].

The calculations in this work are performed with the LisbOn KInetics (LoKI) 0D simulation tool[6], for CO_2 DC discharges at gas pressures of 1-5 Torr and currents of 10-50 mA. The electron collision cross sections and chemical reaction setup are taken from our previous work[7, 8]. In particular, two electronically excited states of CO_2 are considered, with the cross sections adopted from Phelps[9]. The contribution to gas heating adds the relaxation of CO_2 electronically excited states[8] to the traditional assumption for vibrational energy exchanges, exothermic chemical reactions, electron elastic collisions and deactivation/recombination at the wall.

Figure 1 shows the simulation results and measurements of the gas temperature as a function of the gas pressure, for various discharge currents. The gas temperature increases approximately linearly with gas pressure (1-5 Torr) and discharge current (10-50 mA). Taking the relaxation of the CO_2 electronically excited state into account for gas heating, the simulation results of the gas temperature are improved by 30 K to 50 K compared to the case where gas heating due to the quenching of electronically excited states is neglected. To further compare the simulation results and the measurements, the gas temperature is plotted against discharge power per unit length ($E*I$) in Fig. 1(b). It can be seen that the gas temperature is nearly proportional to $E*I$, and that the simulation results considering the CO_2 electronically excited state show a good agreement with the measurements.

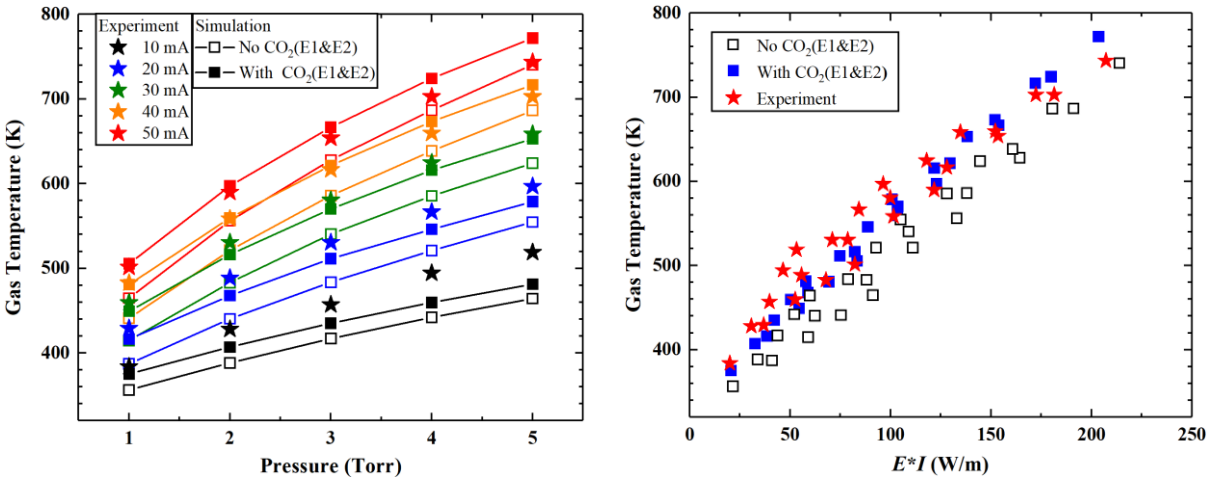

Fig. 1: Comparison between simulation and measurement results of the gas temperature against (a) the gas pressure, for discharge currents of 10-50 mA, and (b) the discharge power per unit length (*E*I*). Experimental data from [3].

It is worth noting that Naidis and Babaeva[10] have calculated the gas temperature for the conditions shown here, simply assuming that all the input energy, besides that transferred to the walls or emitted spontaneously by molecules at excited levels of asymmetric vibrational mode and that spent to dissociation through electronically excited states, goes to gas heating. Their calculations led to a very good agreement with experiment, but lack information on the detailed energy transfer pathways. The kinetic model established here provides such information. The results indicate a role of the CO_2 electronically excited states (in addition to vibrational relaxation) to the gas heating, in line with previous results obtained in pulsed discharges[8].

IPFN activities were funded by FCT (Fundação para a Ciência e a Tecnologia) under projects UIDB/50010/2020, UIDP/50010/2020, LA/P/0061/202 and PTDC/FIS-PLA/1616/2021 (https://doi.org/10.54499/UIDB/50010/2020) (https://doi.org/10.54499/UIDP/50010/2020) (https://doi.org/10.54499/LA/P/0061/2020) (https://doi.org/10.54499/PTDC/FIS-PLA/1616/2021). In addition, this work was funded by the China Scholarship Council (CSC) and Environment and Conservation Fund of Hong Kong Government (Environmental Research, Technology Demonstration and Conference Projects; Project No. 26/2022).

[1] Snoeckx R. and Bogaerts A., *Chemical Society Reviews* **46** (2017): 5805-5863.
[2] Guerra V. et al, *Plasma Sources Sci. Technol.* **26** (2017): 11LT01.
[3] Morillo-Candas A. S. et al, *Plasma Sources Sci. Technol.* **28**.7 (2019): 075010.
[4] Fromentin C. et al, *Plasma Sources Sci. Technol.* **32** (2023): 024001.
[5] Dias T. C. et al, *Plasma Sources Sci. Technol.* **32** (2023): 084003.
[6] Tejero-del-Caz A. et al, *Plasma Sources Sci. Technol.* **28** (2019) 043001.
[7] Silva T. et al, *Plasma Sources Sci. Technol.* **27** (2018): 015019.
[8] Biondo O. et al, *Plasma Sources Sci. Technol.* **31** (2022): 074003.
[9] Lowke J. J. et al, *J. Appl. Phys.* **44** (1973) 4664–71
[10] Naidis G. V. and Babaeva N. Yu., *Plasma Sources Sci. Technol.* **30** (2021) 105016

Diagnostic characterisation and 0D modelling study of ns-pulsed plasma-assisted methane pyrolysis

S. Van Rompaey[1,2 (*)], M. Gromov[2], E. Morais[1], A. Nikiforov[2], A. Bogaerts[1], R. Morent[2]

[1] *PLASMANT, Department of Chemistry, University of Antwerp, Wilrijk-Antwerp, 2610, Belgium*

[2] *RUPT, Department of Applied Physics, Ghent University, Gent, 9000, Belgium*

(*) stijn.vanrompaey@uantwerpen.be

Methane (CH_4) is the second largest contributor to global warming [1] and consequently, there is a growing focus on converting CH_4 into value-added products. CH_4 conveniently contains four hydrogen atoms which can be used to synthesise hydrogen gas (H_2), offering a viable alternative for storing energy in a chemical form. This strategy enables the retention of the energy surplus generated during peak production hours (in the form of H_2) and later employment for eventual energy deficits, thus addressing issues related to the intermittent nature of renewable energy sources.[2] Additionally, H_2 stands out as a valuable energy source because it can supply more energy per kilogram than fossil fuels, facilitating the reduction of fossil fuel exploration and resultant greenhouse gas emissions.[3]

Plasma-assisted methane pyrolysis for H_2 production combines the advantages of fast and cost-effective gas heating, along with CH_4 dissociation occurring at lower gas temperatures (induced by electron impact reactions) than those required for thermal pyrolysis. Also, it boasts low energy input demand and complete CO_2 neutrality, addressing major drawbacks of competing technologies (steam methane reforming and water electrolysis).[4,5] Nanosecond pulsed plasmas enable the generation of high electron densities and a strong non-equilibrium medium that stimulates CH_4 conversion under relatively mild conditions, typically resulting in a high energy efficiency.[6] Nonetheless, chemical and physical fundamental knowledge regarding CH_4 pyrolysis in these types of plasmas remains scattered, which limits the industrial uptake of the process. Thus, this work aims to bridge this knowledge gap in the plasma field and investigate various properties of nanosecond pulsed plasmas via a combination of both plasma diagnostics and 0D modelling techniques.

The experimental investigation was conducted in a pin-to-pin plasma reactor in a CH_4 atmosphere within a pressure range of 0.5 to 2.0 bar. Specifically, we performed electrical characterisation of the discharges, spectroscopic measurements of plasma volume, electron density, kinetics of gas heating and ground state species formation, while examining the effect of the applied pressure. For this purpose, time-resolved ICCD imaging, optical emission (OES), Rayleigh scattering, and laser-induced fluorescence (LIF) spectroscopies were employed. As displayed in Table 1, an increase in pressure causes a decrease in the peak electrical power and plasma volume. This decrease can be attributed to the higher gas density at elevated pressures, resulting in a lower specific energy input per CH_4 molecule, subsequently leading to lower peak electron density and gas temperature.

Table 1: Key experimental parameters measured at different applied pressures.

Pressure (bar)	Peak power (MW)	Plasma volume (mm^3)	Peak electron density (10^{17} cm^{-3})	Peak gas temperature (K)
0.5	7.6 ± 0.7	1.0 ± 0.1	8.72 ± 0.02	2868 ± 221
1.0	6.9 ± 0.3	0.8 ± 0.1	4.59 ± 0.01	1842 ± 172
1.5	5.3 ± 0.5	0.8 ± 0.1	2.10 ± 0.01	1410 ± 138
2.0	4.7 ± 0.2	0.7 ± 0.1	1.14 ± 0.01	920 ± 96

Furthermore, temporal gas temperature profiles have been compiled from three complementary spectroscopic techniques (OES of CH(X), OES of C_2 Swan and Rayleigh scattering, see Figure 1). These have revealed that the peak gas temperature is reached 1 µs after applying the pulse and sustained for ca. 4 µs. Subsequentely, the cooling process commences and lasts for ca. 30 µs (not shown in Figure 2), showing effective gas heating during the ns-pulsed plasma event.

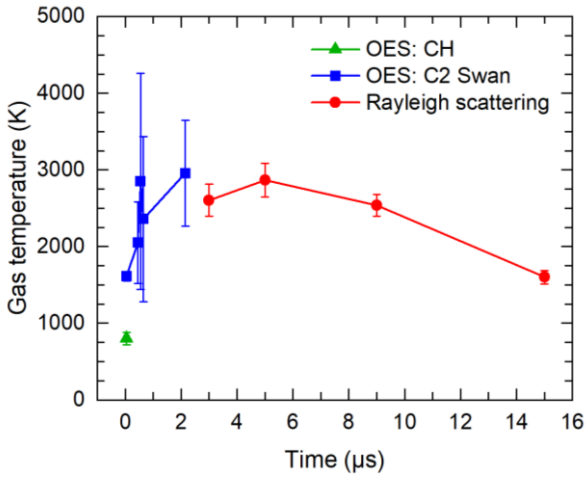

Figure 1: Gas temperature as a function of time measured by three techniques (OES of CH(X), OES of C_2 Swan band and Rayleigh scattering) at an applied pressure of 0.5 bar.

To reveal the plasma chemistry initiated in such pulsed plasma conditions, a 0D model (ZDPlasKin in tandem with Bolsig+) was developed with the goal of describing the chemical pathways that drive CH_4 plasma pyrolysis. The model comprises 81 species and 4483 reactions (ground-state, vibrationally and electronically excited molecules, radicals, ions and electrons). The electrical power was emulated by triangular pulses and experimentally proven gas temperature profiles were implemented in the simulations. While H_2 remains the main product, the model shows a correlation between rising pressures and reduced CH_4 conversions, alongside a shift in C_2 product selectivity from C_2H_2 (at lower pressure) to C_2H_6 (at higher pressure). Model validation was performed by comparison with experimentally recorded electron, CH(X), and H radical densities and kinetics.

This comprehensive approach, which integrates both modelling and experimental endeavours, converges towards important conclusions regarding the effect of pressure and gas temperature on CH_4 conversion and product selectivity, analysis of reaction pathways, and evaluation of the importance of electronic and vibrational excitation in the overall H_2 formation mechanisms.

References

(1) Liu, S.; Proudman, J.; Mitloehner, F. M. Rethinking methane from animal agriculture. *CABI Agriculture and Bioscience* **2021**, *2* (1), 1-13.
(2) Morais, E.; Delikonstantis, E.; Scapinello, M.; Smith, G.; Stefanidis, G. D.; Bogaerts, A. Methane coupling in nanosecond pulsed plasmas: Correlation between temperature and pressure and effects on product selectivity. *Chemical Engineering Journal* **2023**, *462*, 142227.
(3) Gautier, M.; Rohani, V.; Fulcheri, L. Direct decarbonization of methane by thermal plasma for the production of hydrogen and high value-added carbon black. *International Journal of Hydrogen Energy* **2017**, *42* (47), 28140-28156.
(4) Acar, C.; Dincer, I. Selection criteria and ranking for sustainable hydrogen production options. *international journal of hydrogen energy* **2022**, *47* (95), 40118-40137.
(5) Abbas, H. F.; Daud, W. W. Hydrogen production by methane decomposition: a review. *International journal of hydrogen energy* **2010**, *35* (3), 1160-1190.
(6) Taghvaei, H.; Jahanmiri, A.; Rahimpour, M. R.; Shirazi, M. M.; Hooshmand, N. Hydrogen production through plasma cracking of hydrocarbons: Effect of carrier gas and hydrocarbon type. *Chemical engineering journal* **2013**, *226*, 384-392.

Macroscopic parameterization of positive streamers in air: velocity, radius, field etc.

Ute Ebert[1,2,*], Dennis Bouwman[1], Jannis Teunissen[1]

[1] *Group Multiscale Dynamics, Centrum Wiskunde & Informatica (CWI) Amsterdam, The Netherlands*
[2] *Dept. Applied Physics, Eindhoven Univ. Technol., Eindhoven, The Netherlands*
[*] Ute.Ebert@cwi.nl

Streamer heads are essential building blocks of multi-streamer processes. They determine the growth of streamer trees or bursts. But velocity v and radius R of streamer heads can vary by orders of magnitude, and other macroscopic parameters vary as well, such as the background electric field $E_{\rm bg}$, the background electron density $n_{\rm bg}$, the maximal electric field $E_{\rm max}$, the charge content Q of the streamer head, the conductivity of the streamer channel $n_{\rm ch}$ and the degree of chemical activation of the medium.

We present a new axial model to approximate streamer heads:
We start from the fluid streamer model:

$$\begin{aligned} \text{Electron density:} \quad & \partial_t n_e = \nabla\cdot(\mu\mathbf{E}\, n_e) + \alpha\,\mu E\, n_e + S_{ph}, \\ \text{Ion density:} \quad & \partial_t n_+ = \alpha\,\mu E\, n_e + S_{ph}, \\ \text{Poisson equation:} \quad & \nabla\cdot\mathbf{E} = \frac{\rho}{\epsilon_0}, \qquad \rho = e\,(n_+ - n_e). \end{aligned}$$

In a coordinate system moving with the streamer velocity v, the operator ∂_t is replaced by $-v\partial_z$.
The electric field E consists of background field $E_{\rm bg}$ plus field enhancement generated by the charge layer. The layer is approximated as spherically symmetric with the unknown charge $q(r)$ where r is the radial coordinate:

$$E = E_{\rm bg} + \frac{q(r)}{4\pi\epsilon_0\, r^2}, \quad q(r) = \int_0^r 4\pi\, r'^2\, dr'\, \rho(r'), \quad q(r) = \begin{cases} 0 & \text{for } r = 0 \\ Q & \text{for } r > R \end{cases}$$

With background ionization, this model can be rewritten as **three first order ordinary differential equations (ODEs)** for $n_e(z)$, $n_+(z)$ and $q(z)$ on the streamer axis, and easily solved.
When photo-ionization is included, some implicit equation needs to be solved iteratively.

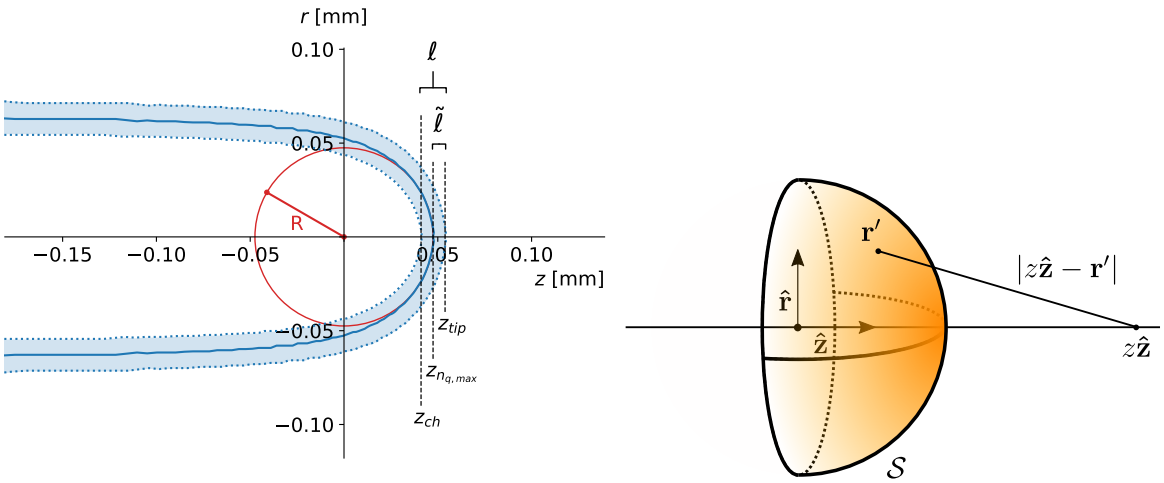

Fig. 1: **How to build an axial model for a streamer head:**
Left: Parameterization of a streamer head derived from a fluid streamer simulation in [1]. The maximal charge density as a function of z is indicated by a blue line. The red circle with radius R is fitted to this line.
Right: Calculation of photo-ionization on the streamer axis ahead of the charge layer.

The new ODE-model approximates the full 3D fluid model well, it largely relaxes computational demands, it relates macroscopic parameters to each other, and it allows for convenient parameter sweeps.

For example, we get relations between v, R, $E_{\max}$ and n_{ch} that depend on the transport and reaction coefficients of the gas in question. For air with photo-ionization, the relations are shown in Fig. 2.

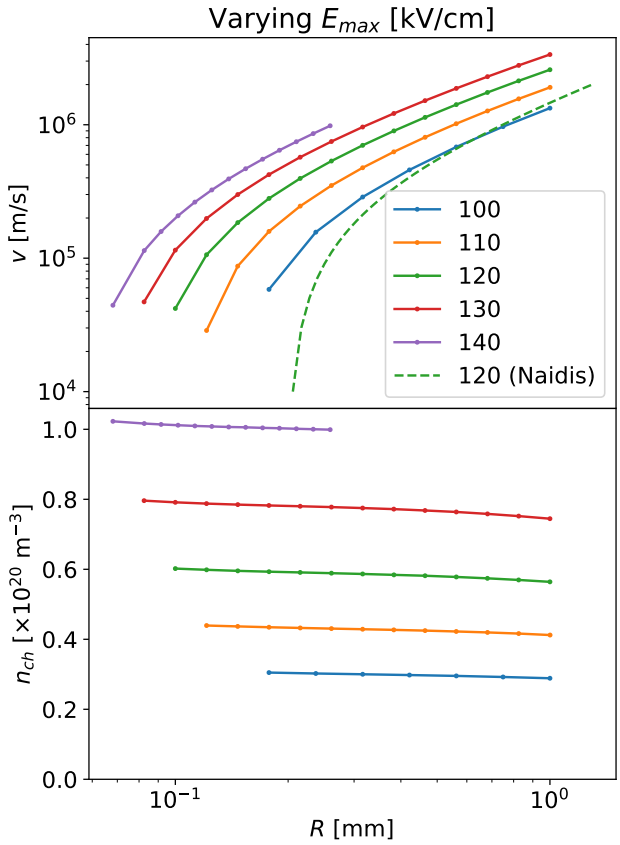

Fig. 2: **Relations between v, R, $E_{\max}$ and the generated channel conductivity** n_{ch} for steadily propagating streamer heads with photo-ionization in air under normal conditions. The colors indicate the values of the maximal electric field. The label [Naidis] indicates an earlier, less systematic approximation by Naidis [2].

How to read:
If radius R and velocity v of a streamer head are measured, the maximal electric field $E_{\max}$ can be read from the upper plot, and in a next step the channel conductivity n_{ch} can be read from the lower plot. It can be seen as well, that n_{ch} strongly depends on the maximal field $E_{\max}$ and little on the streamer radius R.

The results of ODE-approximation and macroscopic parameterization can be used
1. to construct computationally efficient multi-streamer models, and
2. to extract experimental data that are difficult to measure, as $E_{\max}$ in the example above.

[1] Dennis Bouwman, Hani Francisco and Ute Ebert, *Plasma Sources Sci. Technol.* **22** (2023) 075015.
[2] G.V. Naidis, *Phys. Rev. E* **79** (2009) 057401.

Influence of voltage waveform and repetition frequency on atmospheric-pressure barrier discharges in argon

MM Becker(*)[1], AP Jovanović[1], L Kusýn[2], T Hoder[2]

[1] *Leibniz Institute for Plasma Science and Technology (INP)*
Felix-Hausdorff-Str.2, 17489 Greifswald, Germany

[2] *Department of Plasma Physics and Technology, Masaryk University*
Kotlářská 267/2, 61137 Brno, Czech Republic

(*) markus.becker@inp-greifswald.de

Gas discharges operated at atmospheric pressure are an established method for generating non-thermal plasmas and are used in a wide range of applications. These include, for example, air and water purification, food processing and wound treatment [1]. Barrier discharges in particular are widely utilised atmospheric pressure plasma sources due to their robustness and scalability, and ongoing research aims to control the discharge properties in order to enhance the effectiveness and efficiency of applications [2]. A very important physical quantity is the electric field, which is influenced by the geometry, external power supply and space charge in the plasma. For this reason, research activities are currently focused on determining the electric field in atmospheric pressure discharges by means of experiments, simulations and a coupling of both [3]. For a correct interpretation of experimentally determined electric field strengths and – depending on the method used – for its determination, it is important to know to what extent space charge and shielding effects caused by charge carriers in the plasma influence the electric field for different operation conditions.

In order to provide a basis for this and to support data analysis and method development, this paper presents the results of a systematic study of the influence of waveform and repetition frequency of the applied voltage in a single filament barrier discharge in argon at atmospheric pressure. A time-dependent and spatially one-dimensional fluid Poisson model was used to simulate the spatiotemporal evolution of the discharge for sinusoidal voltages, bipolar rectangular pulses and positive nanosecond pulses in the frequency range from 5 kHz to 1 MHz (see Figure 1). It was investigated how the spatiotemporal distribution of the electric field and essential plasma parameters change under the influence of the applied voltage in the given parameter range. In addition, the gain and loss processes of excited argon atoms in the 2p states (in Paschen notation), which can be used and are recently investigated to determine the electric field using the so-called intensity ratio method [4], were analysed.

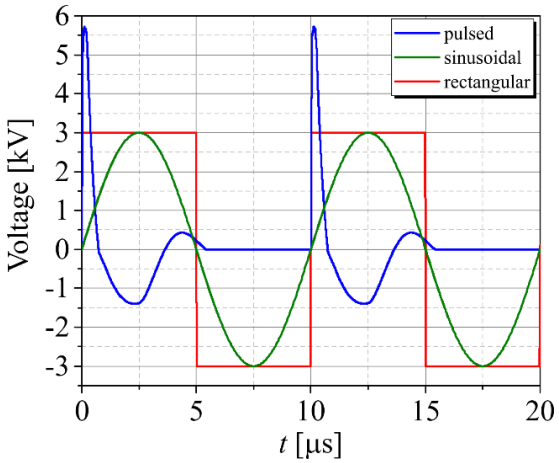

Fig. 1: Voltage waveforms used in the modelling for the example of f = 100 kHz.

The results show that for voltage repetition frequencies above 5 kHz, preionisation effects influence the discharge dynamics and lead to a weakening of the electric field during the streamer-driven discharge breakdown. In the case of a sinusoidal power supply, a mode transition to a discharge with low field strength and electron density in the discharge volume occurs at frequencies above 100 kHz (see Figure 2), with a periodic discharge only observed in the cathode layer (transition from typical barrier discharge mode with transient glow discharge to a mode with continuous plasma bulk). In general, it can be observed that the population processes of the 2p argon levels become more complex with increasing repetition frequency, i.e. stepwise processes, superelastic collisions and quenching of higher levels increasingly contribute to their population. The results thus represent an essential basis for the further development of the intensity ratio method for determination of the electric field in transient atmospheric pressure discharges.

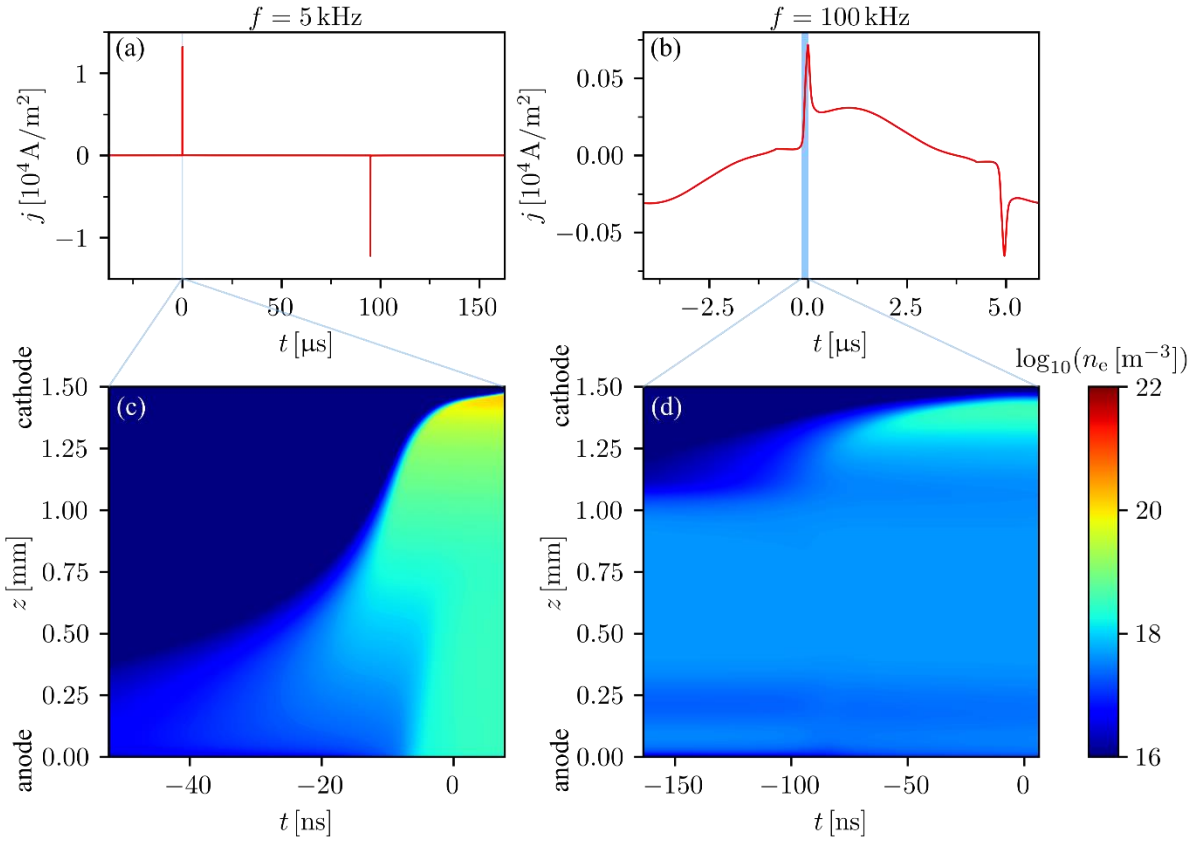

Fig. 2: Temporal evolution of the discharge current density during one period (a, b), and spatiotemporal evolution of the electron number density during the breakdown (c, d) for sinusoidal voltages with $f = 5$ kHz (a, c) and $f = 100$ kHz (b, d). The blue-coloured areas in (a) and (b) represent the time ranges shown in panels (c) and (d). The time $t = 0$ is set to the respective moment of maximum current.

The work was partly funded by the Deutsche Forschungsgemeinschaft (DFG) – project number 466331904 and the Czech Science Foundation under contract no. 21-16391S and supported by the project LM2023039 funded by the Ministry of Education, Youth and Sports of the Czech Republic.

[1] I. Adamovich *et al.*, *J. Phys. D: Appl. Phys.* **55** (2022) 373001.
[2] R. Brandenburg *et al.*, *Plasma Chem. Plasma Process.* **43** (2023) 1303–1334.
[3] B. Goldberg, T. Hoder, R. Brandenburg, *Plasma Sources Sci. Technol.* **31** (2022) 073001.
[4] L. Kusýn, D. Prokop, Z. Navrátil, T. Hoder, *Plasma Sources Sci. Technol.* **32** (2023) 045006.

Numerical investigation of stability of low-current point-to-plane negative corona in air

N G C Ferreira[1,2], P G C Almeida[1,2], A E Taher[1,2] , G V Naidis[3], M S Benilov[(*)1,2]

[1] *Departamento de Física, FCEE, Universidade da Madeira, Largo do Município, 9000 Funchal, Portugal*

[2] *Instituto de Plasmas e Fusão Nuclear, Instituto Superior Técnico, Universidade de Lisboa, 1049-001 Lisbon, Portugal*

[3] *Joint Institute for High Temperatures of the Russian Academy of Sciences, Moscow, Russia*

[(*)] benilov@staff.uma.pt

Negative corona discharges occur when the electric field is enhanced in the cathode, e.g. due to its sharpened form. Although a stationary glow corona discharge with very low-current is mentioned in the literature, the most commonly referred discharge in negative corona is the Trichel pulse regime, where periodic pulses in current of high amplitude appear. It is usually believed that this regime follows immediately the corona inception. In some works experiments were performed to reveal the mechanism of formation of such pulses, e.g. [1], and in other works simple and detailed numerical models were used, e.g. [2]. In principle, the stationary glow corona can evolve into the Trichel pulse regime by applying a certain perturbation (e.g., by increasing the voltage).

This paper reports modelling of low-current negative corona, in a point-to-plane discharge configuration at atmospheric-pressure air. In a previous work [3], results of simulations have shown that immediately after ignition the stationary negative corona discharge is stable, but as the voltage increased, it lost stability and pulses appeared. As the voltage was increased further, at higher currents, the discharge regained stability. This work focuses on the study of the discharge regimes occuring before and after the limit of stability, and on the effect that certain perturbation characteristics have on those regimes. For this purpose, a numerical model of low-current discharges in high-pressure air will be used, comprising equations of conservation and transport of charged species and the Poisson equation. A 'minimal' kinetic model of plasmachemical processes in low-current discharges in high-pressure air is used, which takes into account electrons, an effective species of positive ions, and three species of negative ions (O_2^-, O^-, and O_3^-). This model was validated in previous works with different purposes: a) comparison of the computed inception voltage of corona discharges with several sets of experimental data on positive and negative glow coronas between concentric cylinders, with good agreement in a wide range of pressures and diameters of the cylinders; b) investigation of the saturation of the breakdown voltage with increasing pressure in weakly non-uniform electric fields in compressed air, with qualitative agreement with the experiment in all the studied cases being achieved for protrusion heights of the order of 50 μm; and c) investigation of time-averaged characteristics of DC corona discharges in ambient air, in both concentric cylinders and point-to-plane, with good agreement between modelling and experimental data [4].

The simulated point-to-plane geometry has a 10 mm gap with a needle tip radius of 20 μm in atmospheric air. This configuration yields an inception voltage of 2314 V, which corresponds to the discharge voltage that is just sufficient for the electron impact ionization to compensate losses of the charged particles, initiating of a self-sustaining gas discharge. Stability of the negative corona discharge was studied against finite perturbations: perturbations in the form of small increments of the applied voltage (1V or above) were imposed and the evolution of the discharge over time was followed by means of a time-dependent solver. The limit of stability was in this case 2338 V, corresponding to a current of approximmately 32 nA.

Results of simulations have shown the following general trend: when the applied voltage is below the limit of stability, a single Trichel pulse appears (one single pulse rather than a periodic sequence, with amplitude of the same order of magnitude as classic Trichel pulses), followed by small damped oscillations. The amplitude of these oscillations is significantly lower than that of the Trichel pulse. This can be seen in Fig. 1(a) by the dotted red line. When the applied voltage exceeds slighly the limit of stability, a single Trichel pulse appears followed by weak periodic oscillations (rather than damped). These periodic oscillations are still not classic Trichel pulses. This scenario can be seen in Fig. 1(a) by the solid blue line. Finally, when the applied voltage clearly exceeds the limit of stability, classic Trichel pulses appear, as seen in Fig. 1(b).

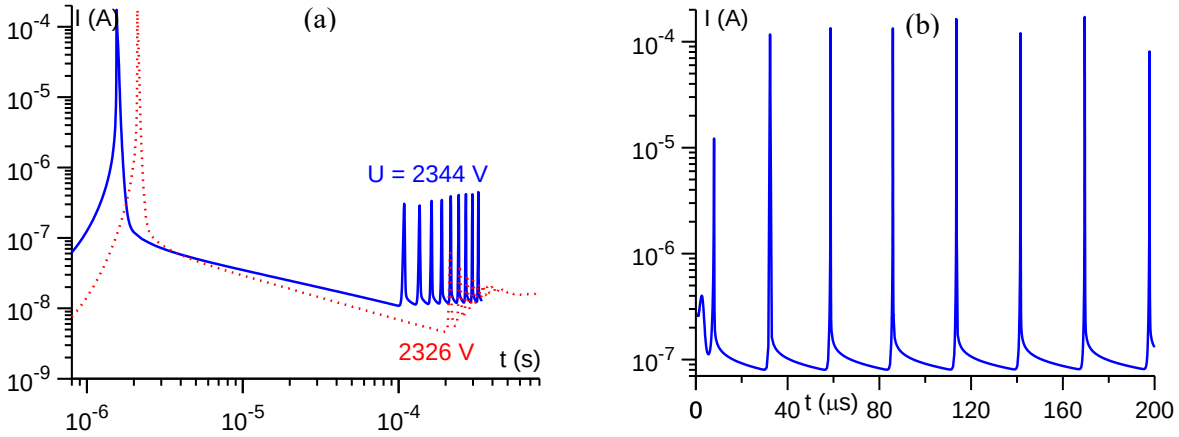

Fig. 1: Time evolution of current for an applied voltage below and slightly above the limit of stability (a), and significantly exceeding that limit (b).

In comparison with an instantaneous perturbation (constant applied voltage from t = 0), a step voltage perturbation (with finite growth rate) produces a peak of current (due only to displacement current) before the single Trichel pulse, and the single Trichel pulse appears slightly later when compared to the one produced by an instantaneous perturbation. For a perturbation amplitude of 2V, the single Trichel pulse is not present (there is a local maximum in current but the amplitude is much smaller than a typical Trichel pulse), whereas for perturbation amplitudes of 5V or higher the single Trichel pulse is present and has the same magnitude; the lower the perturbation amplitude the later the single Trichel pulse appears. When comparing different rise times of the step voltage perturbation, it can be seen that smaller rise times (0.2 μs – 1 μs) cause the sooner appearance of the single Trichel; if the rise time is big enough (e.g., 100 us) the single Trichel pulse is not present.

The activities at the IPFN Hub of Universidade da Madeira were supported by FCT - Fundação para a Ciência e Tecnologia, I.P. by project reference UIDB/50010/2020, by project reference UIDP/50010/2020 and by project reference LA/P/0061/2020.

[1] V. Tarasenko et al., *JETP Letters* **115** (2022).

[2] W. Salah et al., *AIP Advances* **12** (2022) 105123.

[3] A. E. Taher et al., *Proc. XXXV Int. Conf. Phenom. Ionized Gases (ICPIG)* (2023) p. 236.

[4] M. S. Benilov et al., *J. Appl. Phys.* **130** (2021) 121101.

Three-Dimensional Charged Particle Tracing of E×B Plasma Discharge in Hall Thrusters

Eduardo Calvo[1], Tiago Santos[2], J. Henriques[3], Mario J. Pinheiro[2,3], Paulo Sá [(*)1]

[1] *Centro de Estudos de Fenómenos de Transporte e Departamento de Engenharia Física, Faculdade de Engenharia da Universidade do Porto, Rua Doutor Roberto Frias s/n, 4200-465 Porto, Portugal*

[2] *Department of Physics, Instituto Superior Técnico-IST, University of Lisbon, Avenida Rovisco Pais, 1049-001, Lisboa, Portugal*

[3] *Instituto de Plasmas e Fusão Nuclear, Instituto Superior Técnico, University of Lisbon, Avenida Rovisco Pais, 1049-001, Lisboa, Portugal*

[(*)] paulosa@fe.up.pt

Hall thrusters (HTs) are recognized as a pivotal technology in electric propulsion for space missions, owing to their remarkable efficiency and versatility. Offering high specific impulse values ranging from 1000 to 3000 seconds, these devices significantly outperform traditional chemical propulsion engines. HTs can operate across a wide range of power inputs, from 10 W to 100 kW, and can use noble gases such as xenon and krypton as propellants, making them fitting for a variety of space missions. These thrusters can generate thrust levels from a few millinewtons (mN) to between 1 and 5 newtons (N), making them suitable for both small and large-scale missions that require quick deep-space travel. The working principle of HTs revolves around creating a powerful electric field within the plasma chamber. To achieve this, a transverse magnetic field is introduced to reduce electron conductivity. However, the longitudinally applied electric field introduces a perpendicular drift (E×B drift) in the azimuthal motion of the electrons [1]. The magnetic field is designed to strongly magnetize electrons, effectively trapping them along the magnetic field lines, while ions remain mostly unmagnetized. This configuration ensures electrons are collisional and confined by the magnetic field, whereas ions remain largely collisionless. For this cross-field discharge it is essential to have a continuous supply of electrons. This requirement is met by positioning an external hollow cathode device adjacent to the Hall discharge chamber. Typically, a hollow cathode comprises a durable tube made of refractory material, along with an insert designed to emit electrons efficiently due to its low work function. It also includes a heating mechanism, a plate positioned downstream, and an anode keeper to facilitate operation. The heating process, often initiated by coiling heaters around the cathode, raises the temperature, which in turn starts the discharge process. Subsequently, the electric field plays a crucial role in propelling the released electrons toward the anode, which operates at a high voltage [2].

In this simulation study, the HT was design based on the *Stationary Plasma Thruster-100* with a magnetic shielding configuration. In general, it consists of five copper coils in total (four outer with 1750 turns and one inner with 1440 turns), a boron nitride dielectric chamber, a stainless-steel anode, a magnetic circuit with low carbon steel, and a hollow cathode made of tungsten [3]. To efficiently simulate the vast number of particles typically involved in such systems, the study assumed each macroparticle represents 10^6 individual particles. Neutral Xenon (Xe) particles are expelled from the anode, while electrons are emitted from the hollow cathode. The movement and interaction with the electromagnetic fields were governed by the Lorentz force for the electrons and electric force for the Xe ions, whereas for the interaction between macroparticles, it was assumed a Monte Carlo collision model with elastic scattering, excitation, ionization, and double ionization collisions, using the Charged Particle Tracing module from COMSOL Multiphysics. The magnetic field was computed through a stationary Flexible Generalized Minimum Residual (FGMRES) solver using the Magnetic Field module by applying 2.5 A in the outer coils and -5 A in the inner coil, the electric field was computed through a stationary Conjugated Gradients solver using the Electrostatics module, by applying 300 V in the anode, 0 V on the hollow cathode and -25 V on the top of the magnetic structure,

corresponding to the floating potential that exists near the thruster's exit [4]. A time-dependent Generalized Minimum Residual (GMRES) solver was used to capture the motion of particles from 0 μs to 3 μs in 10^{-11} s time intervals. Overall, the simulation time was 22.5 days.

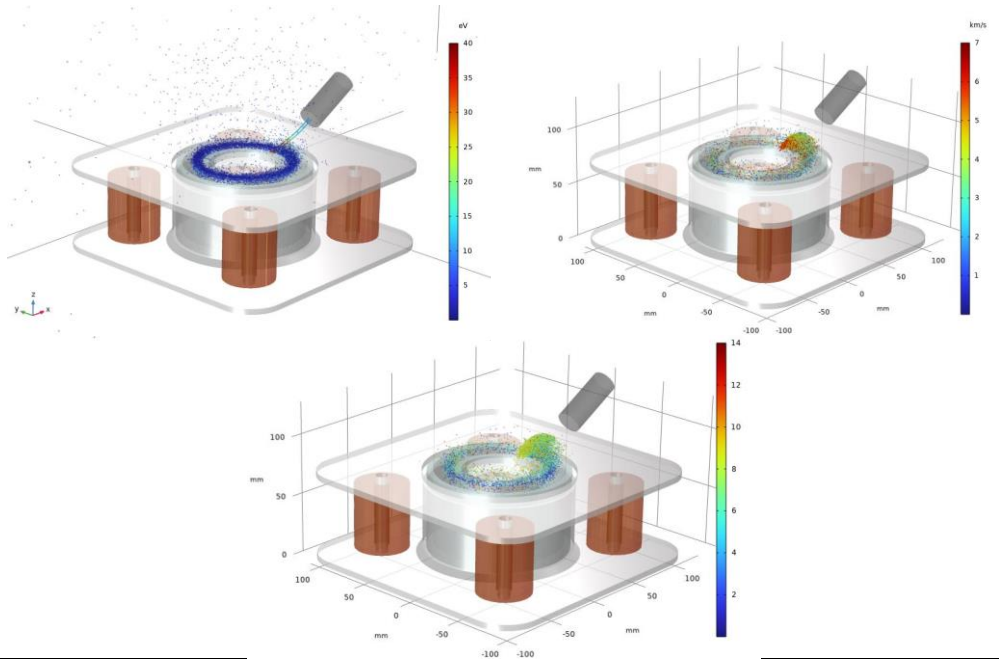

Fig. 1: Hall thruster plasma discharge at 3 μs (a) depicting electron behaviour, (b) depicting Xe^{+} ions behaviour, (c) depicting Xe^{2+} ions behaviour.

This model can output electric and magnetic fields, electric potential, particle trajectories, particle velocities, and particle densities. Figure1 presents the preliminary results of a three-dimensional charged particle tracing HT model [5]. Fig1(a) shows the electrons being emitted from the hollow cathode towards the chamber. The different colours represent the electronic temperature from each macroparticle. Here, we observe that most electrons are trapped in areas of higher magnetic field strength (20 mT), with temperatures ranging from 10 to 20 eV. It is also shown that electrons with higher temperatures tend to escape this pattern, moving towards the anode and in some cases colliding with it, highlighting the electron anomalous transport phenomena. Fig1(b) and Fig1(c) shows the motion of single charged Xe^{+} and Xe^{2+} ions that are ionized inside the chamber. The different colours represent the velocity from each macroparticle. Here, most ions are observed in this high magnetic field zone, being accelerated towards the thruster's exit by the electric field and reaching speeds up to 11 km/s for Xe^{+} and 22 km/s for Xe^{2+}. Meanwhile, some ionization occurs inside the chamber due to high-energy electrons escaping the magnetic field and moving towards the anode [1,3]. This comprehensive simulation opens new possibilities for future space research missions and contributes to our understanding of E×B plasma discharge dynamics in Hall thrusters. It also sets the way for the development of more efficient and scalable electric propulsion systems.

[1] I. D. Kaganovich et al., Physics of E × B discharges relevant to plasma propulsion and similar technologies. *Phys. Plasmas* 2020; 27 (12)

[2] D. Goebel et al., Plasma hollow cathodes. Journal of Applied Physics 2021; 130 (5)

[3] J. Boeuf; Tutorial: Physics and modelling of Hall thrusters. J. Appl. Phys. 2017; 121 (1)

[4] J. Walker et al. Electrical characteristics of a Hall effect thruster body in a vacuum facility testing environment. J. Electr. Propuls. 2022. 1, (18)

[5] COMSOL Multiphysics Users' Guide: n.p.

Solving steady and unsteady multi-physics problems using a hybridized discontinuous Galerkin solver

Peter Burda(*)[1], Nicolas Corthouts[2], Georg May[2], Zdeněk Bonaventura[1], Thierry Magin[2]

[1] *Department of Plasma Physics and Technology, Faculty of Science, Masaryk University, 611 37 Brno, Czech Republic*

[2] *von Karman Institute for Fluid Dynamics, Rhode-Saint-Genèse, 1640 Rhodes-Saint-Genèse, Belgium*

(*) peterburda2@gmail.com

Inductively coupled plasma (ICP) facilities possess unique properties such as accurately replicating the thermodynamic conditions of atmospheric reentry and enabling the examination of thermal shields for rockets and satellites. One of the most powerful ICP facility in the world is the plasmatron at von Karman Institute for Fluid Dynamics in Belgium, boasting a power output maxing out at 1200 kW and temperatures reaching 10000 K. The behaviour of reentry plasma in atmospheric conditions can be highly complex, featuring various strongly coupled physical phenomena. This complexity of the ICP facility needs to be predicted in the most accurate way to enhance the quality of the testing which led to the need of employing numerical methods. The development of the numerical method for ICP can be found for instance in [1] and [2]. ICP simulation codes are traditionally based upon the finite volumes method (FVM). The primary drawback of the FVM is that capturing high-temperature gradients near the wall region requires a high number of elements (cells) in that specific area. Another inherent limitation of the FVM is its low-order nature, making it challenging for studying the unsteadiness of the flow, including hydrodynamic instability or turbulence. In this contribution we will discuses an alternative approach providing high-order methods based upon the family of discontinuous Galerkin (DG) methods.

One of challenges in the description of ICP simulations is in managing multi-physics aspects involving calculation of flow, temperature and electric fields. In the language of mathematical physics, we simulate different physics over separate domains which are interconnected with specific interface conditions. One can approach multi-domain simulations using two distinct strategies. The first strategy is staggered, where individual solvers handle the domains, and these solvers only exchange data. The staggered approach can be either strongly or loosely coupled. In case of strongly coupled it is subiterated until the steady state solution is reached. In case of loosely coupled approach one forward step is performed successively for each of the domains. In both approaches, the information collected by one domain at its boundary is considered as a known quantity, although it is the result of the computations performed in another domain. However, these strategies may lead to instabilities, and there is a substantial body of literature on stability analysis of coupled methods (*e.g* [3]). Second possible strategy is a monolithic one. In this case the system is solved as a whole. The monolithic approach is allowing for faster and stable convergence to the solution. Additionally, this strategy has a profound impact on the system structure as it links the unknowns from distinct domains. In our work, a monolithic strategy is devoted for the hybridized discontinuous Galerkin (HDG) method [4], [5].

In this contribution we discusses two studies to demonstrate the capability of solving both steady and unsteady multi-physics problems using the HDG solver and further developing it for subsequent implementation in the ICP modelling. The first study solves steady conjugated heat transfer (CHT) problem, where the analytical solution is used as a benchmark for numerical solutions. In the CHT scenario, full problem is divided into the two subdomains. In the first subdomain, we solve heat transfer in the solid material, with governing equation being the heat diffusion equation (4). The second subdomain is representing fluid domain and is governed by Navier-Stokes equations (1) - (3).

Fluid

$$\frac{\partial u_x}{\partial x} = 0, \tag{1}$$

$$-\frac{\partial p}{\partial x} + \mu \frac{\partial^2 u_x}{\partial y^2} = 0, \tag{2}$$

$$\mu \left(\frac{\partial u_x}{\partial y} \right)^2 + k_f \frac{\partial^2 T_f}{\partial y^2} = 0. \tag{3}$$

Solid

$$\frac{\partial^2 T_s}{\partial y^2} = 0. \tag{4}$$

where k_s is the thermal conductivity coefficient for the solid, k_f is the thermal conductivity coefficient for the fluid, μ is the dynamical viscosity, u_x is the x-component of the velocity, p is the pressure, T_f is the temperature of the fluid and finally T_s is the temperature of the solid. Multi-physics sketch can be seen in the Fig.1.

In the second case, an unsteady CHT problem is solved. Formulation of the governing equations and domains the assignment is the similar to the steady state case, while a time dependent boundary condition is used for the solid domain, incorporating the time integration through the diagonally implicit Runge-Kutta method (DIRK) [6]. These two test cases are fundamental building blocks for implementation Kelvin-Helmholtz hydrodynamic instabilities of ICP hot jets within HDG solver.

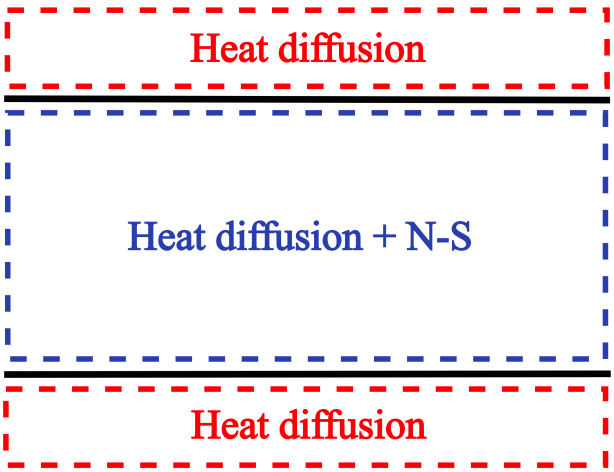

Fig. 1: Decomposition of domain in CHT problem. In the flow channel heat diffusion equation and the Navier-Stokes equations are solved. On the domains interface the only shared variable is the temperature, consequently only the heat diffusion equation is solved in the solid part.

[1] Magin, T., "A Model for Inductive Plasma Wind Tunnels," Ph.D. thesis, von Karman Institute for Fluid Dynamics, 2004.

[2] Lani, A., Villedieu, N., Bensassi, K., Kapa, L., Vymazal, M., Yalim, M. S., and Panesi, M., "COOLFluiD: An open computational platform for multi-physics simulation and research," 21st AIAA Computational Fluid Dynamics Conference, 2013.

[3] Giles, M. B., "Stability analysis of numerical interface conditions in fluid-structure thermal analysis," International Journal for Numerical Methods in Fluids, Vol. 25, No. 4, 1997, pp. 421–436.

[4] Nguyen, N. C., Peraire, J., and Cockburn, B., "An implicit high-order hybridizable discontinuous Galerkin method for linear convection-diffusion equations," Journal of Computational Physics, Vol. 228, No. 9, 2009, pp. 3232–3254.

[5] Nguyen, N., Peraire, J., and Cockburn, B., "Hybridizable Discontinuous Galerkin Methods," Spectral and High Order Methods for Partial Differential Equations, edited by J. Hestaven and R. E.M., Springer, 2011, lecture no ed., pp. 63–84.

[6] Kennedy, C. A., & Carpenter, M. H. (2016). Diagonally implicit Runge-Kutta methods for ordinary differential equations. A review (No. NF1676L-19716).

The electric potential in high power magnetron discharges: A toy model

K. Köhn[1], D. Krüger[1], L. Vogelhuber[1], D. Eremin[1], L. Xu[2], R.P. Brinkmann[(*)1]

[1] *Electrical Engineering and Information Technology, Ruhr University, 44780 Bochum, Germany*

[2] *Physical Science and Technology, Soochow University, Suzhou 215006, China*

[(*)] ralf-peter.brinkmann@tet.rub.de

Partially magnetized plasmas, as employed in high power impulse magnetron sputtering (HiPIMS) and various other technological applications, often exhibit the spontaneous formation of "spokes", dynamic ionization zones correlated with heightened plasma density and elevated electric potential. Conventional wisdom posits that accurately representing these phenomena requires moving beyond the assumption of quasineutrality, necessitating the inclusion of Poisson's equation. This study addresses the issue using a physically and geometrically simplified setup, amenable to transparent solutions.

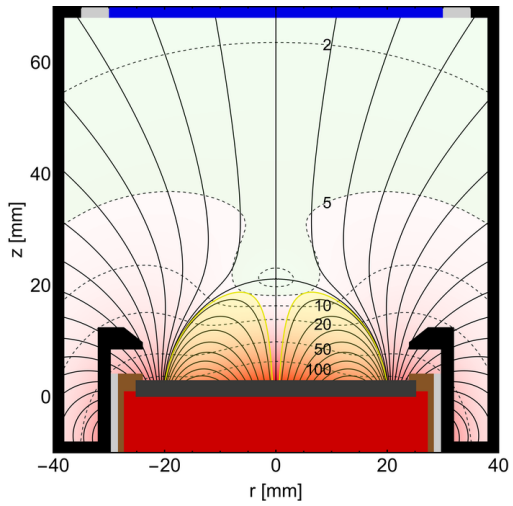

(a) Cross section of a circular planar magnetron and its magnetic field topology $\boldsymbol{B}(r, z)$ (to scale), mounted in a plasma chamber (not to scale).

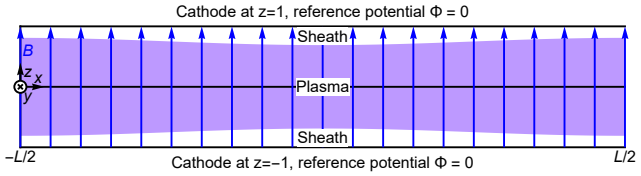

(b) Simplified magnetron geometry with doubled cathode and constant magnetic field. The distribution of the plasma and the electric potential are invariant in y-direction.

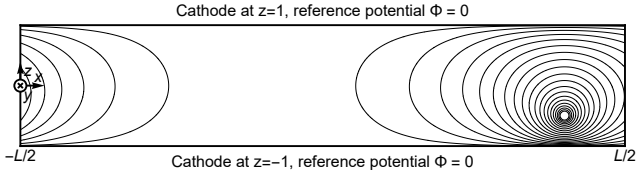

(c) Two-dimensional Green's function $G(x', z', x, z)$ which illustrates the reaction of the electric potential $\Phi(x, z)$ to a unit charge located at (x', z').

Fig. 1: Magnetron modeling: From a realistic device to a simplified toy model.

Starting from a planar magnetron as shown in Fig. 1(a), we focus on the ionization zone where the magnetic field lines run from cathode to cathode. The geometry is simplified to be Cartesian, Fig. 1(b). The field lines are straightened and the field strength is set to be constant. The cathode is doubled. Invariance in y direction is assumed. The relation of the potential $\Phi(x, z)$ to the charge density $\rho(x, z)$ is given by Poisson's equation. In dimensionless notation, it reads as follows, where the parameter ε denotes the ratio of the Debye length λ_D to the field line half length H:

$$-\varepsilon^2 \left(\frac{\partial^2 \Phi}{\partial x^2} + \frac{\partial^2 \Phi}{\partial z^2} \right) = n_\mathrm{i}(z) - n_\mathrm{e}(x, z), \qquad (1)$$

$$\Phi(x, z)\big|_{z=\pm 1} = 0.$$

The x-invariant ion density $n_\mathrm{i}(z)$ is taken from an external model and considered fixed in this context. The electrons are bound to their field lines so that the integrated number density $N_\mathrm{e}(x)$ is a given. However, they can freely move along the field lines and relax to Boltzmann equilibrium:

$$n_\mathrm{e}(x, z) = \exp\left(\Phi(x, z) - V(x)\right) = N_\mathrm{e}(x) \frac{\exp\left(\Phi(x, z)\right)}{\int_{-1}^{1} \exp\left(\Phi(x, z')\right) \, \mathrm{d}z'}. \qquad (2)$$

If the number density per field line is constant, $N_\mathrm{e}(x) = \bar{N}_\mathrm{e}$, the solutions of the model assume a typical discharge structure with quasineutral plasma and electron-depleted sheaths of thickness s:

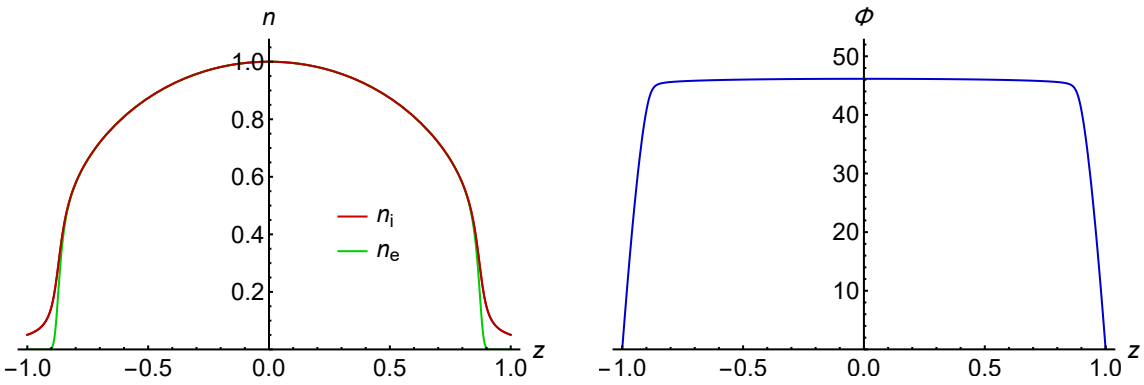

Fig. 2: Charge carrier densities (left) and potential (right) for a situation that is x-invariant.

The situation gets interesting when the number densities are perturbed, $N_\mathrm{e}(x) = \bar{N}_\mathrm{e} + \delta\tilde{N}_\mathrm{e}\cos(kx)$. Our primary question: Will the extra charges accumulate in the sheath and keep the plasma quasineutral, or will they accumulate in the plasma and violate quasineutrality? It turns out that the answer depends on how the wavelength compares to the geometric mean of the field line length and the sheath thickness. Note that this scale is independent of the Debye length and thus not of a thermal nature.

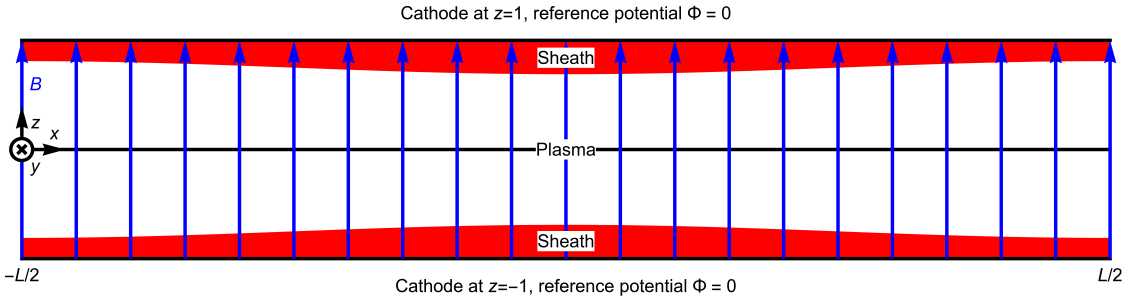

(a) Long wavelength: Additional charges tend to accumulate in the boundary sheath.

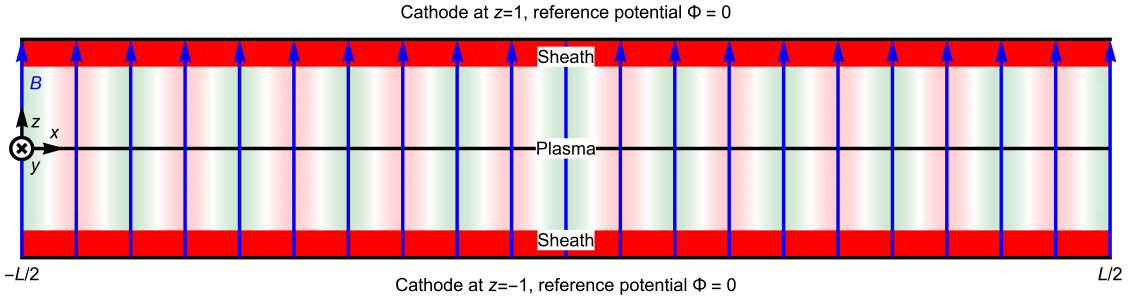

(b) Short wavelength: Additional charges tend to accumulate in the plasma and violate quasineutrality.

Fig. 3: Response of the electron density $n_\mathrm{e}(x, z)$ on perturbations $\delta N_\mathrm{e}(x)$ of different wavenumbers k.

Thus, Poisson's equation is indeed important for the modeling of high power magnetron discharges; the assumption of quasineutrality alone does not suffice. This fundamental insight extends beyond the simplified model explored in this study.

[1] K. Köhn, D. Krüger, D. Eremin. L. Xu, R.P. Brinkmann, *Plasma Sources Sci. Technol.* **32** (2023) 055012.

[2] K. Köhn, D. Krüger, E. Kemaneci, L. Xu, D. Eremin, R.P. Brinkmann, *Plasma Sources Sci. Technol.* **30** (2021) 105014.

Fast Calculation Tool for Breakdown Voltage in a setup with a Dielectric Surface

Rui Almeida[1,2], Pedro Almeida[1,2], Helena Kaufmann[3], Mikhail Benilov[(*)1,2]

[1] *Departamento de Física, FCEE, Universidade da Madeira, Largo do Município, 9000 Funchal, Portugal*

[2] *Instituto de Plasmas e Fusão Nuclear, Instituto Superior Técnico, Univ. de Lisboa, 1041 Lisboa, Portugal*

[3] *Siemens Energy, 10553 Berlin, Germany*

[(*)] benilov@staff.uma.pt

1 Introduction

At a setup's breakdown voltage (BDV), a transient non-stationary discharge will develop, where a high current flows between the electrodes. It is of considerable interest to be able to estimate, in a simple, fast and reliable way, the minimum voltage that causes breakdown for any given setup. It is a common engineering practice to evaluate the BDV resorting to the Townsend criterion, which only requires the specification of the ionization coefficient, the cathode emission coefficient and evaluating path integrals in the electrostatic field distribution. This criterion actually gives the self-sustainment voltage (SSV) of the discharge, i.e. the minimum voltage at which particle gain and loss mechanisms are balanced. Though in some cases this criterion can be extended[1] it isn't generally applicable, namely when diffusion, or photoimission are important. Furthermore, in setups which are more complicated than plane to plane the general relation between SSV and BDV is unknown.

In this work we present a quite accurate and fast tool to calculate the BDV of a generic setup based on the resonance method[2]. The tool is applied to a setup consisting of a dielectric disc spacer of 4 mm height close-stacked between two disc electrodes of 7.5 mm radius in air at 1 atm.

2 The Tool

The tool is described in detail in previous work [2]. It is based on a drift-diffusion description of the gas employing numerical modeling of transport and conservation of one positive species, electrons and three negative ions. The Poisson equation and equations for photoionization source terms are also solved. The tool employs only stationary calculations and follows a 5-step flowchart for the determination of the setup's SSV/BDV, 6-step in the case a dielectric is present.

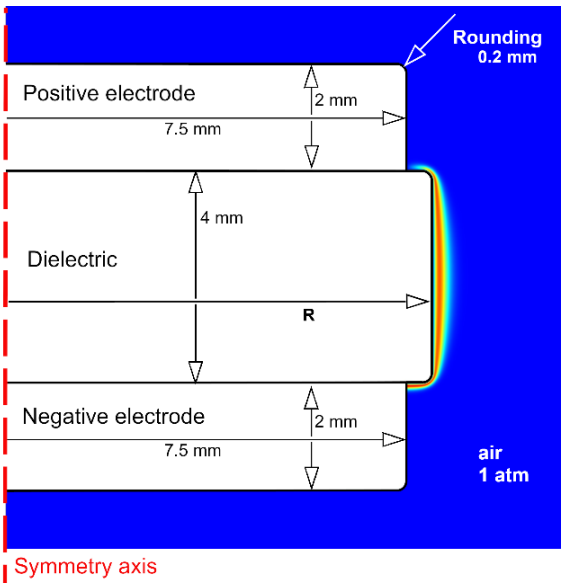

Figure: Schematic of setup. Calculations were performed for R=3mm, R=7.5mm and R=8.2mm.

3 Results and Discussion

In the studied setup, shown in the figure, the electric field distribution has a weak non-uniformity at ignition. Calculation of the BDV starting from a given initial state and using the drift-diffusion equations for its time-evolution, will be called the standard tool. Results for the BDV calculated using the new and the standard tool are given in the following table for three dielectric radii, two permittivities and two boundary/initial conditions. An experimental value of 10kV[3], confirms the calculated values for the case R=3mm. Calculations with the standard tool were actually 'informed' by the new tool's results regarding the tried initial voltages and the initial surface charge distribution (case j_n=0).

R (mm)	ε_D	**Tool's stationary calculations**		**Standard non-stationary calculations**	
		Self-Sustainment Voltage, Diel. BC		Breakdown Voltage, initial σ_s from	
		σ_s=0	j_n=0	σ_s=0	j_n=0
3	1	9.9kV	9.9kV	10.0kV	10.0kV
3	12				
7.5	1	9.4kV	6.8kV	9.5kV	6.9kV (+2%)
7.5	12	11.9kV		12.0kV	
8.2	1	14.0kV	11.5kV	14.2kV	11.6kV
8.2	12	8.3kV		8.7kV (+5%)	

Table: Comparison of the new tool's calculated SSV versus the standard tool's calculated BDV. Shown are results for the dielectric radii (R) of 3mm, 7.5mm, and 8.2mm, for the dielectric constants (ε_D) of 1 and 12 and for two dielectric surface boundary/initial conditions used in the new/standard tool. σ_s=0 means no surface charge in both tools; j_n=0 means no normal current density in the new tool, while in the standard tool it means that the initial surface charge is that of the steady state as calculated by the new tool with boundary condition(BC) on diel. j_n=0.

The standard tool was seen to lead to discharge extinction at the SSV as calculated by the new tool, this voltage was then successively increased by 1% until the standard tool produced breakdown (cases where an overvoltage of more than 1% was needed, are indicated in the table). In the columns for boundary/initial condition σ_s=0, the SSV/BDV is seen to increase with the dielectric radii and with the dielectric constant. A notable exception occurs for the protruding dielectric with higher permittivity, this was seen to be due to the strong electric field generated close to the cathode triple junction. When the boundary condition, in the new tool, is that of zero current density across the dielectric surface (steady-state case j_n=0), or when for the initial surface charge, in the standard tool, the surface charge distribution of the steady-state is used (last column j_n=0), results confirm that breakdown is facilitated when close to the active discharge path there is a dielectric. The reason why the voltages in the columns for boundary/initial condition j_n=0 don't depend on the dielectric constant, is related to the fact that the surface charge on the dielectric screens the effect of the dielectric, resulting on the gas side in near-parallel electric fieldlines along the dielectric surface. With the stated exception, the BDV of the pre-stressed setup(j_n=0) was generally lower than the unstressed setup(σ_s=0).

4 Conclusion

The developed tool for calculating BDVs based on stationary numerical modeling, has produced results to within 5% of those obtained through standard non-stationary modeling. Unlike the standard tool, where the BDV has to be obtained by a very computationally intensive and time-consuming trial and error procedure, the new tool provides a systematic procedure to calculate the SSV, which is seen to be very close to the BDV as calculated by the standard tool. It should be clear that, for the purpose of evaluating the performance in calculating BDVs, the here employed new and standard tools, cannot be compared. No other tools with the same general scope of application were found for comparison with this new tool.

IPFN activities were supported by FCT - Fundação para a Ciência e Tecnologia, I.P. by project references UIDB/50010/2020, UIDP/50010/2020 and LA/P/0061/2020 and by European Regional Development Fund through the Operational Program of the Autonomous Region of Madeira 2014-2020 under project PlasMaM1420-01-0145-FEDER-000016.

[1] Almeida, R. M. S. et al., *Plasma Sources Sci. Technol.* **32** (2023) 105014–105025.
[2] Benilov, M. S. et al., *J. Appl. Phys.* **130**, (2021) 121101–121123.
[3] Pillai, A. S. Et al., *J. Appl. Phys.* **58**, (1985) 146–153

Multi-physics simulation of microwave capillary discharge in Argon: towards comprehensive power balance

R. Brunovský[1], A. Obrusník[1,2], Z. Bonaventura[1], G. D. Stancu[3]

[1] *Department of Plasma Physics & Technologies, Masaryk University, Brno, Czech Republic*
[2] *PlasmaSolve s.r.o., Brno, Czech Republic*
[3] *Laboratoire EM2C, Centrale Supélec, L'Université Paris-Saclay, France*
rbrunovsky@mail.muni.cz

With growing environmental concerns, modern science increasingly focuses on processes that offer high efficiency in power conversion and usage. Microwave capillary plasma is notable for its high power densities (up to 10^5 W cm^{-3}) achieved with relatively low input powers [1]. In this work, we simulate Argon plasma generated in a surfatron, i.e., an electromagnetic wave-heated capillary discharge. One of the advantages of surfatron discharge is in its electrodeless configuration, which offers a great flexibility in operation conditions [1].

The microwave capillary discharge is simulated using the *COMSOL Multiphysics*. The multi-physics model comprises:

1. the microwave electromagnetic field,
2. an ambipolar plasma model for Argon including plasma chemistry processes,
3. the neutral Argon gas flow simulated by using fluid module.

The model is solved in 2D axisymmetric geometry. In fluid flow module, Navier-Stokes equations together with continuity equation are solved for velocity vector and density of the fluid [2]

$$\rho\frac{\partial \boldsymbol{u}}{\partial t} + \rho\left(\boldsymbol{u}\cdot\nabla\right)\boldsymbol{u} = \nabla\cdot\left(-p\boldsymbol{I} + \boldsymbol{K}\right), \tag{1}$$

$$\frac{\partial \rho}{\partial t} + \nabla\cdot\left(\rho\boldsymbol{u}\right) = 0, \tag{2}$$

where $\boldsymbol{u}$ is the flow velocity, ρ is the density of the liquid, p is pressure, $\boldsymbol{I}$ is the unit matrix and $\boldsymbol{K}$ is the stress tensor defined as

$$\boldsymbol{K} = \mu\left(\nabla\boldsymbol{u} + \left(\nabla\boldsymbol{u}\right)^{\mathrm{T}}\right) - \frac{2}{3}\mu\left(\nabla\cdot\boldsymbol{u}\right)\boldsymbol{I}, \tag{3}$$

where μ is the fluid viscosity. The pressure and velocity obtained from these equations serve as input parameters for the plasma module. In solving of the capillary flow, the flow is considered to be weakly compressible.

The electric field is solved by microwave module of *COMSOL Multiphysics* using the equation [2]

$$\nabla\times\mu^{-1}\nabla\times\boldsymbol{E} = \left(\omega^2\varepsilon_0\varepsilon_{\mathrm{r}} - j\omega\sigma\right)\boldsymbol{E}, \tag{4}$$

where ω is the angular frequency, ε_0 is permittivity of vacuum, ε_{r} is the relative permittivity and σ is conductivity. Within this context, it is also assumed that the ion motion can be neglected relative to the electron motion, due to the short timescale of microwave oscillations.

The evolution of electron density n_{e} is described by continuity equation [2]

$$\frac{\partial n_{\mathrm{e}}}{\partial t} + \nabla\cdot\boldsymbol{\Gamma}_{\mathrm{e}} = R_{\mathrm{e}}, \tag{5}$$

where $\boldsymbol{\Gamma_{\mathrm{e}}}$ represents electron flux and R_{e} denotes the electron source term accounting for electron gain and loss processes considered. Moreover, equation for energy density is solved [2]

$$\frac{\partial n_\epsilon}{\partial t} + \nabla\cdot\boldsymbol{\Gamma}_\epsilon + \boldsymbol{E}_{\mathrm{a}}\cdot\boldsymbol{\Gamma}_{\mathrm{e}} = S_\epsilon + Q_{\mathrm{rh}}/e, \tag{6}$$

where $\mathbf{\Gamma}_\epsilon$ represents energy flux density, $\boldsymbol{E}_\mathbf{a}$ is ambipolar electric field, S_ϵ is energy source term due to electron collision processes and [2]

$$Q_{\mathrm{rh}} = \frac{1}{2}\mathrm{Re}\left(\boldsymbol{J}\cdot\boldsymbol{E}^*\right), \tag{7}$$

is the electron heating by the microwave field with $\boldsymbol{J}$ representing the density of the electron current and * denotes the complex conjugate.

The geometry used in the simulation is shown in Fig. 1. Note that the geometry is similar to the one specified in [3]. The electron density distribution in the capillary for the pressure of 2000 Pa, and the absorbed microwave power of 61 W is shown in Fig. 2. Experiment results from [1] show that that only a low fraction of power, ranging between 4% to 20% is actually absorbed in the discharge itself. While the majority of the input power is, in fact, dissipated by other means. In this contribution we will study in detail the power balance in the microwave capillary discharge in various physical conditions. The ultimate goal is to compare the simulation results with experimental power balance determined by precise measurements that were published in [1].

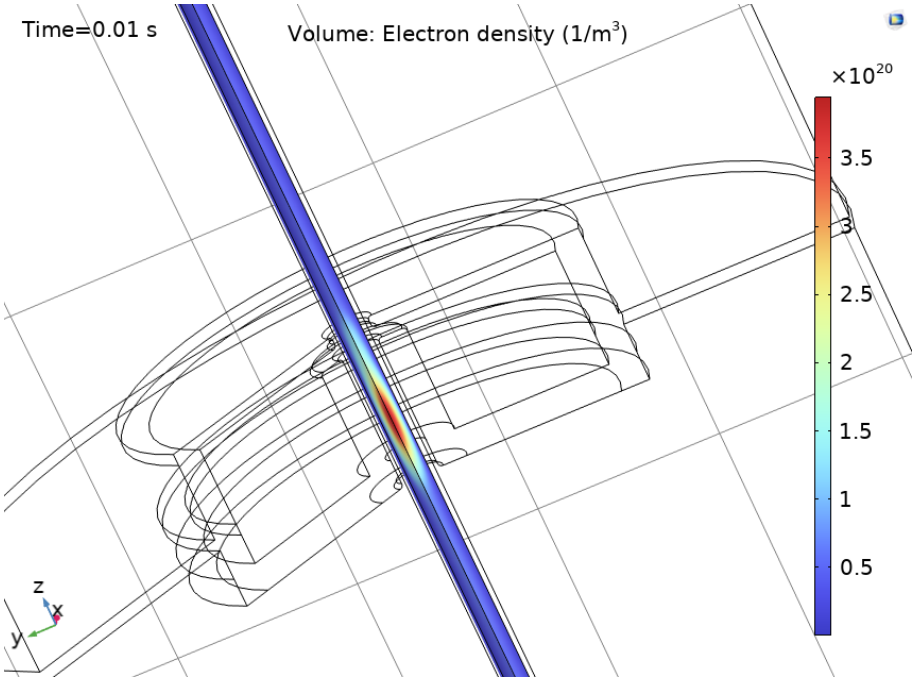

Fig. 1: Electron density in capillary at $p = 2000\,\mathrm{Pa}$ and absorbed power $P_{\mathrm{abs}} \approx 61\,\mathrm{W}$ visualised in 3D with entire surfatron geometry.

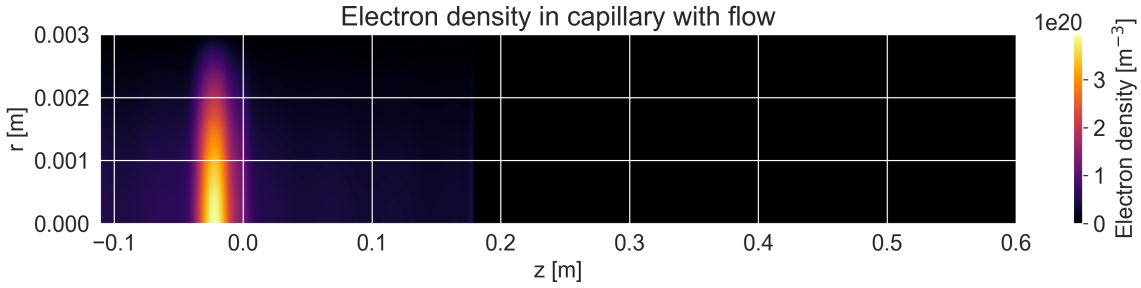

Fig. 2: Electron density in capillary at $p = 2000\,\mathrm{Pa}$ and absorbed power $P_{\mathrm{abs}} \approx 61\,\mathrm{W}$.

[1] F Coquery et al, *Plasma Sources Sci. Technol.* **31** 055003 (2022).
[2] COMSOL Inc. Plasma module user's guide, version 6.1., www.comsol.com, (2022).
[3] M Jimenez-Diaz et al, *J. Phys. D: Appl. Phys.* **45** 335204 (2012) .

Magnetic Enhancement of the Electrical Asymmetry Effect in Capacitively Coupled Plasmas

S. J. Doyle[1(*)], R. W. Boswell[2], C. Charles[2], J. P. Dedrick[3]

[1] *Department of Physics, School of Natural & Computing Sciences, University of Aberdeen, King's College, Aberdeen, AB24 3FX*

[2] *Space Plasma, Power and Propulsion Laboratory, Research School of Physics and Engineering, The Australian National University, ACT 2601, Australia*

[3] *York Plasma Institute, School of Physics, Engineering and Technology, University of York, Heslington, York, YO10 5DD, UK*

(*) *scott.doyle@physics.org*

The development of real-time control strategies for key discharge parameters, such as densities, fluxes, and energy distributions, is of fundamental interest to many plasma sources. Over the last decade, multi-harmonic `tailored' voltage waveforms have been successfully employed to achieve enhanced control of key parameters in a wide range of radio-frequency (RF) plasma sources through application of the electrical asymmetry effect (EAE)[1]. More recently, the analogous magnetic asymmetry effect (MAE) has been numerically and experimentally demonstrated to achieve a notable degree of control in parallel plate RF plasma sources. The MAE is achieved via selectively magnetising the charged species adjacent to one electrode, altering the charge flux to the surface and enforcing a DC self-bias to maintain quasineutrality[2]. This study addresses the degree of control achieved by the MAE in a non-planar geometry via 2D fluid/kinetic simulations of a magnetised RF capacitively coupled plasma (RF-CCP) source[3] employing two different magnetic topologies. The simultaneous application of the EAE and MAE is then presented for the same geometry, demonstrating a degree of non-linear behaviour dependant upon the applied magnetic topology.

Control of the DC self-bias voltage η_{dc} is demonstrated for a single 600 Vpp, 13.56 MHz discharge in both 'convergent' (maximum on-axis field strength) and 'divergent' (minimum on-axis field strength) magnetic topologies. MAE induced modulations of η_{dc} = 0.13 Vpp and η_{dc} = 0.03 Vpp are achieved for each magnetic topology, respectively, for magnetic field strengths between 50 - 1000 G.

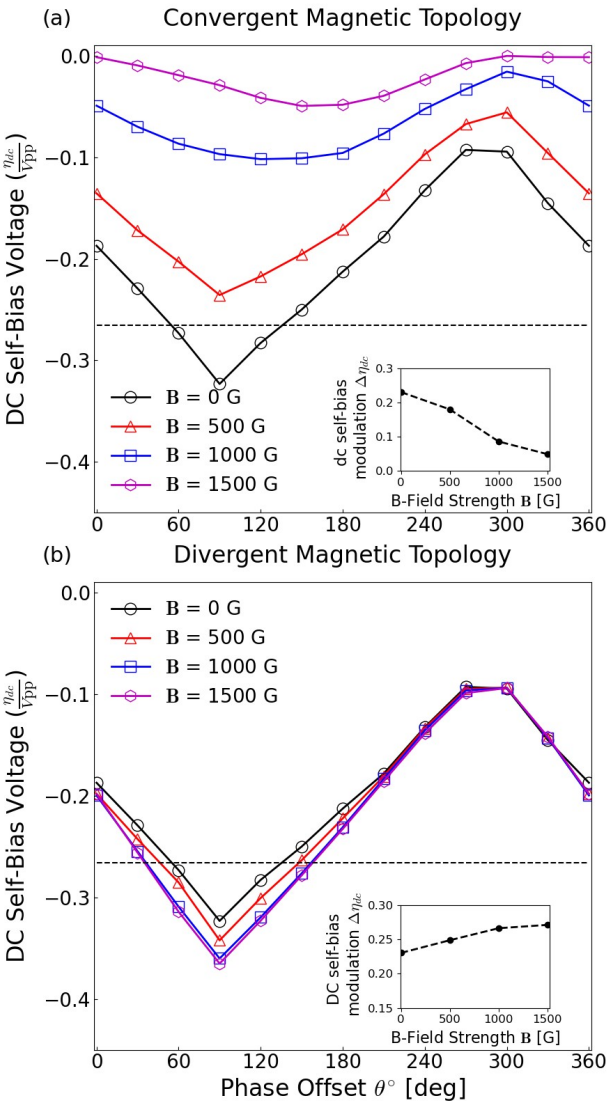

Fig. 1: Normalised DC self-bias voltages η_{dc}/V_{pp} , calculated via the RF phase-averaged alumina surface charge, at the alumina surface adjacent to the powered electrode for four 600 V_{pp}, 5 harmonic peak-type waveform discharges, with phase offsets in the range $0^o < \theta < 360^o$, employing (a) convergent and (b) divergent magnetic topologies. Inlay: DC self-bias modulation $\Delta\eta dc$, for each magnetic field strength.

Simultaneous application of an EAE and MAE is achieved through a multi-harmonic 'peak'-type tailored voltage waveform employing varying harmonic phase offsets between $0^o < \theta < 360^o$. The degree to which the DC self-bias voltage is modulated by the applied EAE is mediated by the orientation and magnitude of the applied magnetic field. The EAE induced DC self-bias modulations exhibit non-linear behaviour in response to a superimposed MAE, such that the resulting DC self-bias differs from an additive combination of the two effects alone Simultaneous application of the electrical and magnetic asymmetry effects offers the possibility of further decoupling ion and electron dynamics in RF plasma sources, and represents an improvement over each approach in isolation.

Acknowledgements:

The authors gratefully acknowledge Prof. M. J. Kushner, and Dr. A. R. Gibson for insightful discussions. This work was supported by the UK Engineering and Physical Sciences Research Council (EPSRC), grant reference number: EP/m508196/1.

References:

[1] B. G. Heil, et. al., "On the possibility of making a geometrically symmetric RF-CCP discharge electrically asymmetric", *Journal of Physics D: Applied Physics*, **41**, 165202, (2008).

[2] S. Yang, et. al., "Magnetical asymmetric effect in geometrically and electrically symmetric capacitively coupled plasma", *Plasma Processes and Polymers*, **14**, 1–9, (2017).

[3] S. J. Doyle, et. al., "Decoupling ion energy and flux in intermediate pressure capacitively coupled plasmas via tailored voltage waveforms", *Plasma Sources Science and Technology*, **29**, 124002, (2020).

Understanding NO formation and destruction by non-thermal effect in the quenching process of microwave air plasma

Q. Shen[1], A. Pikalev[1,2], J. Gans[1], M. C. M. van de Sanden[(*)1,3]

[1] *Dutch Institute for Fundamental Energy Research, Eindhoven, The Netherlands*

[2] *Instituto de Plasmas e Fusão Nuclear, Instituto Superior Técnico, Universidade de Lisboa, Lisboa, Portugal*

[3] *Department of Applied Physics, Eindhoven Institute of Renewable Energy Systems, Eindhoven University of Technology, Eindhoven, The Netherlands*

[(*)] M.C.M.vandeSanden@differ.nl

Plasma-based nitrogen fixation driven by renewable electricity holds promise to counteract the substantial CO_2 emission and energy consumption associated with the Haber-Bosch (HB) process [1]. Microwave plasma is gaining increasing interest worldwide due to its high operation flexibility, but a better performance in terms of energy efficiency is still required. An important step in this plasma-based gas conversion is the quenching of the dissociated air flow, which, next to the desired product NO, also contains atomic oxygen and nitrogen. Since most of the recombination energy released in the quenching process by these atomic fragments ends up in vibrational modes, the state of the gas could be non-thermal with the vibrational temperatures different from the gas temperature.

To explain the underlying mechanisms, we introduce a time-dependent multi-temperature quenching model coupling chemical and vibrational kinetics at different pressures, which gains insights into the pathways of NO formation and destruction. Relaxations of the vibrational and gas temperatures during the forced cooling trajectory are shown in this work. A new method, different from the theoretical-informational method [2], to calculate chemical reaction rate enhancement by vibrational excitation is proposed. A series of energy transfer channels including vibrational-vibrational (V-V) and vibrational-translational (V-T) energy transitions [3], together with chemical processes and heat conduction are tracked in the quenching process (Fig 1).

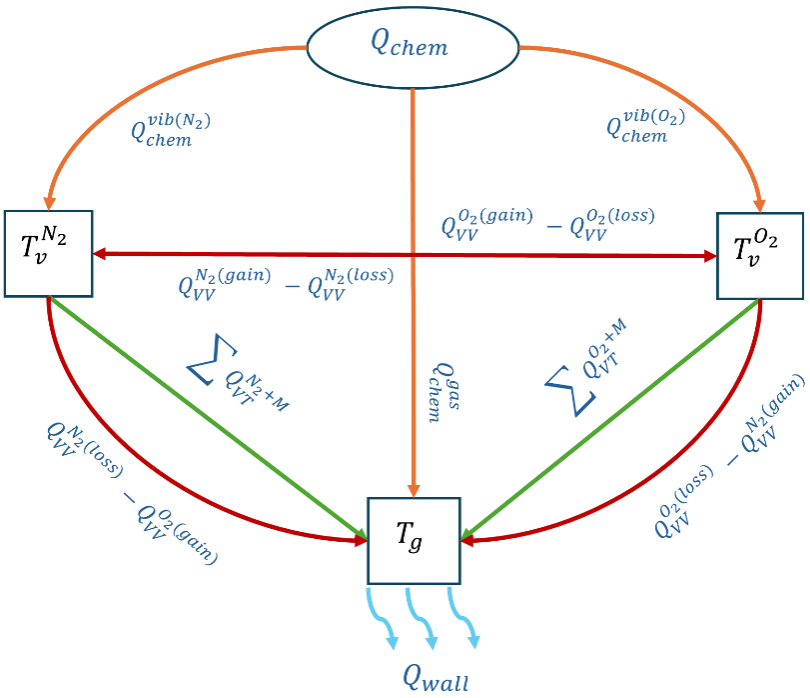

Fig. 1: Overview of the energy transition scheme in the quenching process.

Through manipulation of the cooling rate and the gas temperature in the plasma region, our model elucidates the effect of vibrational kinetics on NO production for different conditions. The predominant factor limiting the vibrational non-equilibrium is the V-T relaxation of N_2 and O_2 molecules due to collisions with oxygen atoms. The model also predicts that accelerating the oxygen atom recombination process in the quenching region is beneficial to preserve NO concentration from the plasma region, especially at high temperatures. This research establishes a foundation for the further advancement and optimisation of plasma reactors for the efficient production of nitrogen oxides.

The authors appreciate the help from all colleagues of the PSFD group in DIFFER. The authors also thank Professor Vasco Guerra and his group for the help with energy transition calculation. This work is financially supported by the China Scholarship Council Grant No. CSC202106240037. The work of A. Pikalev is financially supported by the European Space Agency under Project I-2021-03399.

[1] S. Kelly, & A. Bogaerts, *Joule* **5** (2021) 3006–3030.

[2] A. Fridman, *Cambridge university press* (2008).

[3] V. Guerra, & J. M. A. H. Loureiro, *Journal of Physics D: Applied Physics* **28** (1995) 1903–1918.

Numerical simulation of a low-pressure electrodeless ion source intended for air-breathing electric propulsion

Marek Šťastný[1,2], Kryštof Mrózek[2,3,4], Karel Juřík[1], Lukáš Havlíček[2], Michal Novotný[2], Adam Obrusník[3]

[1] *Department of Theoretical and Experimental Electrical Engineering, Faculty of Electrical Engineering and Communication, Brno University of Technology, Brno, Czech Republic*
[2] *SpaceLabEU, Brno, Czech Republic*
[3] *PlasmaSolve s.r.o., Brno, Czech Republic*
[4] *Department of Plasma Physics and Technology, Faculty of Science, Masaryk University, Brno, Czech Republic*

mailto:stastny@plasmasolve.com

Air Breathing Electric Propulsion (ABEP) systems offer a promising solution to extending the lifetime of Very Low Earth Orbit (VLEO) missions by using residual atmospheric particles as a propellant. Such systems would operate in very low-pressure environments where plasma ignition and confinement prove challenging. We employed advanced numerical simulations to explore the capability of our laboratory ion source in overcoming these challenges.

In this contribution, we present results of a Global Plasma Model (GPM) of a plasma burning in very low-pressure air mixture. The results are validated by experimental measurements acquired using a laboratory electrodeless ion source utilizing a resonator for plasma ignition. The device is specifically designed to operate within low-pressure environments as it holds potential applications in ABEP systems for Very Low Earth Orbit (VLEO) missions. Parametric studies were carried out via GPM to investigate the resonant behavior and its implications. The possibility of the model serving as a predictive tool is assessed through experimental validation against measured data, mainly the extracted ion current.

Parametric studies of resonant plasma are conducted using the GPM, which can describe plasma systems with complex physics and reaction kinetics. Since the GPM calculates volume-averaged quantities, it can serve as a fast and efficient tool for computing plasma properties. The numerical results are compared to experimental measurements while changing the operational pressure in the discharge chamber, input power and the external magnetic field. Our model includes a kinetic scheme, which contains over 600 reactions and processes. The model can replicate the resonant behavior with respect to varying magnetic field observed in the experimental data, as seen in the following figure:

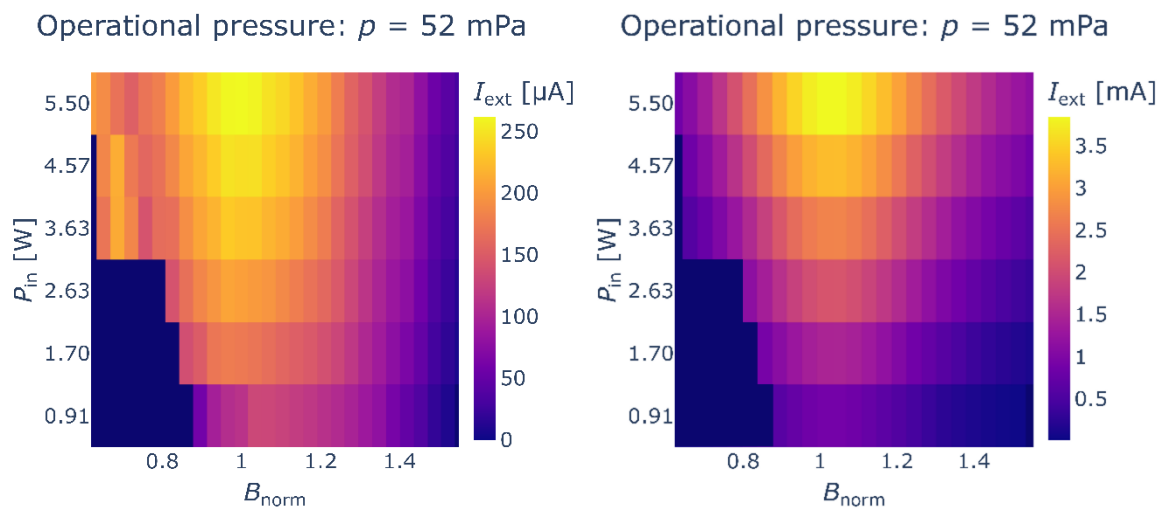

Fig. 1: Comparison between 2D graphs of extracted ion dependencies on normalized magnetic field (where $B_{\mathrm{norm}} = 1$ represents resonance) and input power.
(left: experimental results, right: GPM, $p = 52$ mPa).

The experimental values of extracted ion current differ from the predicted results by an order of magnitude, signaling potential for improvement. Using the GPM, we stand to better understand the underlying plasma processes and use this knowledge to improve the extraction efficiency of the device.

The verified model is further utilized in extrapolating additional information about the plasma such as ion composition, mean mass of ions or a degree of ionization.

The improved ion extraction in our prototype directly translates into producing larger thrust, which is imperative for VLEO operation due to significant drag. Deciding whether the thrust is net positive by direct comparison of the two variables should lead to better understanding the feasibility of the ABEP concept. Apart from further improving the device, our current research gravitates towards ensuring reliable thrust estimation as well as conducting additional plasma diagnostics.

Acknowledgement:

This work was supported by the SILAS project awarded by the Technology Agency of the Czech Republic (grant no. FW06010622)

The LisbOn KInetics LoKI-B+C simulation tool

A. Tejero-del-Caz[2], D. Simões[1], T.C. Dias[1], V. Guerra[1], M. Lino da Silva[1], L. Marques[1,3], N. Pinhão[1], C.D. Pintassilgo[1,4] and L.L. Alves[(*)1]

[1] *Instituto de Plasmas e Fusão Nuclear, Instituto Superior Técnico, Universidade de Lisboa, Portugal*

[2] *Departamento de Física, Facultad de Ciencias, Universidad de Córdoba, Campus de Rabanales, Spain*

[3] *Centro de Física das Universidades do Minho e do Porto, Universidade do Minho, Braga, Portugal*

[4] *Departamento de Engenharia Física, Faculdade de Engenharia, Universidade do Porto, Portugal*

[(*)] *llalves@tecnico.ulisboa.pt*

The LisbOn KInetics LoKI-B+C [1] is a simulation tool for plasma chemistry that couples two main calculation blocks: a Boltzmann solver (LoKI-B) [2,3] and a Chemical solver (LoKI-C), developed / consolidated resorting to the well-grounded scientific foundations of the Portuguese group N-PRiME. LoKI-B+C has been originally developed with flexible and upgradable object-oriented programming under MATLAB, to benefit from its matrix-based architecture, adopting an ontology that privileges the separation between tool and data.

LoKI-B (released as open-source code [4] licensed under the GNU GPL v3.0) solves the space independent form of the two-term electron Boltzmann equation for non-magnetised non-equilibrium low-temperature plasmas, excited by DC/HF electric fields or time-dependent (non-oscillatory) electric fields from different gases or gas mixtures. The tool addresses glow plasmas, using a stationary description for DC fields, a Fourier time-expansion description for HF fields, and a time-dependent description for time-varying fields. LoKI-B handles the electron kinetics in any complex gas mixture, describing first and second-kind electron collisions (with anisotropic effects for elastic and rotational encounters) with any target state, characterized by any user-prescribed population.

LoKI-C solves the system of zero-dimensional (volume average) rate balance equations for the most relevant charged and neutral species in the plasma, receiving as input the kinetic schemes for the gas/plasma system under study. LoKI-C uses several modules (i) to describe the mechanisms (collisional, radiative and transport) controlling the creation/destruction of species, namely various transport models for charged and neutral particles; (ii) to self-consistently calculate the gas temperature, by solving a gas/plasma thermal model; and (iii) to fully couple volume and surface kinetics, namely by solving a set of deterministic "rate-balance like" equations [5,6], accounting for different plasma-surface interaction processes, yielding the coverage of available/occupied sites at the surface while describing the interplay between surface and volume kinetics.

The solution of LoKI-B+C follows a workflow embedding four iterative cycles: (i) over the initial mixture composition, to obtain the user-prescribed *pressure*; (ii) over the reduced electric field, to satisfy the plasma *neutrality*, for an user-prescribed electron density (or some equivalent parameter, see below); (iii) over the densities of the most relevant excited states afecting the electron Boltzmann equation, to *globally* converge over the electron energy distribution function (EEDF) and the electron macroscopic parameters; and (iv) over the electron density, to obtain the user-prescribed *discharge current* (or *power density*). As output, LoKI-B+C self-consistently calculates the EEDF and the associated electron macroscopic parameters, the densities of species, the reaction creation/destruction rates, and the reduced electric field.

This contribution presents a status report of the LoKI-B+C simulation tool, and is intended to also receive comments and suggestions from the low-temperature plasmas community, in preparation of its release as open-source code. Presently, evolutions of LoKI-B+C under the supervision of the N-PRiME group, comprise mostly: (i) the development of LoKI-B++, the C++ version of LoKI-B; (ii) the inclusion

of an additional heating operator in LoKI-B, describing the combined ohmic-stochastic interaction of electrons with the applied electric field; (iii) the inclusion in LoKI-B of a DC magnetic field, at arbitrary angles; (iv) the time-dependent coupling between LoKI-B and LoKI-C; (v) the use of the hdf5 format to write output results; and (vi) the optimization of the iterative calculation cycles.

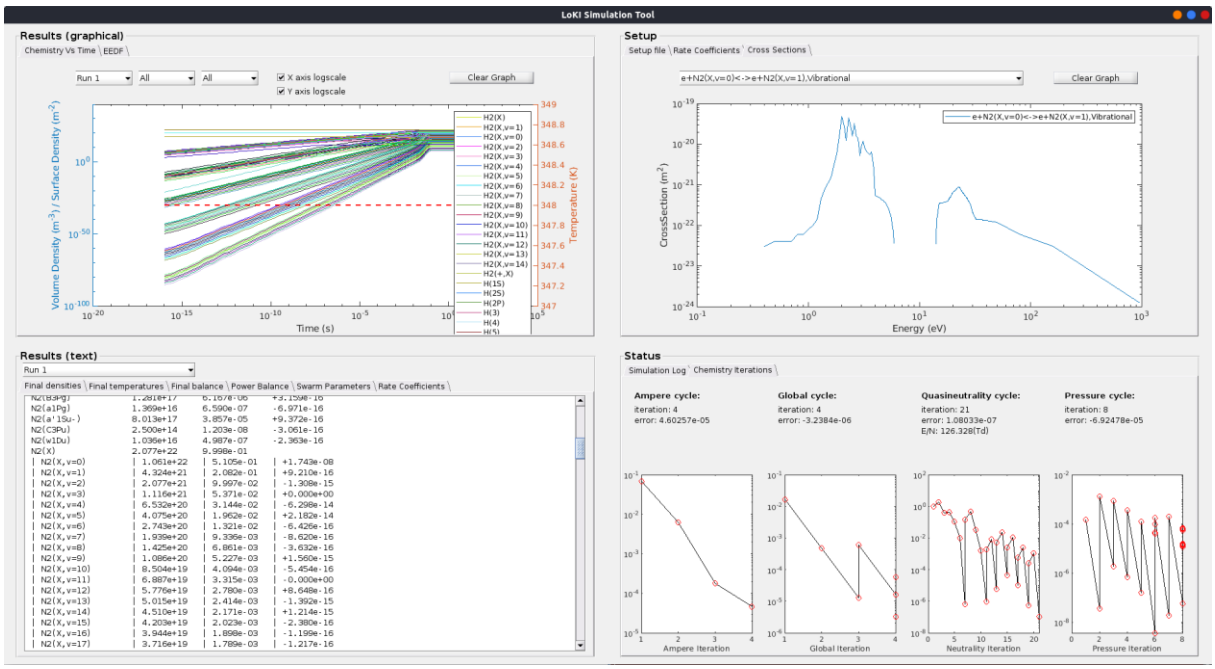

Fig. 1: Example of the Graphical User Interface display after a complete LoKI-B+C simulation.

Figure 1 presents an example of the Graphical User Interface (GUI) display after a complete LoKI-B+C simulation, for a situation where the working conditions impose the discharge current. The updated version of the GUI shows: in the lower-right corner, the four convergence cycles, from right to left, for the pressure, the neutrality, the global densities, and the discharge current; in the lower-left corner, the summary of the output results, in text format (the figure shows the results for the densities of species); in the upper-left corner, the summary of the output results, in graphical format (the figure shows the results for the densities of species, as a function of the calculation time); and in the upper-right corner, the summary of the input data (the figure depicts a vibrational cross section used in the calculations).

The current efforts in the development of LoKI-B+C are focused on replacing the pressure cycle by a different handling of the in/out-flows, and on generalizing the neutrality cycle so that it iterates over the reduced electric field to directly obtain the electron density, the discharge current or the power density imposed by the user.

Acknowledgements

This work was funded by Fundação para a Ciência e a Tecnologia under projects UIDB/50010/2020 (https://doi.org/10.54499/UIDB/50010/2020),UIDP/50010/2020(https://doi.org/10.54499/UIDP/50010/2020), LA/P/0061/202 (https://doi.org/10.54499/LA/P/0061/2020) and 2022.04128.PTDC (https://doi.org/10.54499/2022.04128.PTDC).

References

[1] nprime.tecnico.ulisboa.pt/loki/
[2] A. Tejero-Del-Caz *et al.*, *Plasma Sources Sci. Technol.* **28** (2019) 043001.
[3] A. Tejero-del-Caz *et al.*, *Plasma Sources Sci. Technol.* **30** (2021) 065008.
[4] github.com/IST-Lisbon/LoKI/
[5] D. Marinov *et al., Plasma Processes and Polymers* **14** (2017) 1600175.
[6] D. Simões *et al.*, *Plasma-surface coupled modelling of ammonia production in DC discharges,* ESCAMPIG XXVI, Brno, Czech Republic (2024).

Plasma model for high power impulse magnetron sputtering (HiPIMS) with helium

Z. Belkaid(*)[1], E. Morel[1], A. Revel [1], T. Minea[1]

[1] *Laboratoire de Physique des Gaz et des Plasmas, UMR 8578 CNRS, Université Paris Saclay, 91405 Orsay Cedex, France*

(*) zakaria.belkaid@universite-paris-saclay.fr

The use of helium as a working gas in High power impulse magnetron plasma (HiPIMS) is being considered as an alternative to the heavier gases commonly used such as argon. HiPIMS plasma in helium has interesting properties. The most striking is a much higher operating current densities (6 $\mathrm{A\,cm^{-2}}$) [1, 2] than the conventional pulses (typically 2 $\mathrm{A\,cm^{-2}}$). Moreover, when using a molybdenum target, the peak discharge current increases with the pulse voltage [2]. The peak current is characterised by a very fast rise time (< 5 μs) followed by a decay and a plateau (see fig.1(a) solid line).

To better understand this specific current pulse shape, the ionization region model (IRM) has been used for HiPIMS with helium instead of Ar/O_2 as before [3]. Cross sections [4, 5] and rate coefficients of inelastic collisions in helium HiPIMS were implemented in the model. IRM uses current and pulsed voltage measurements as inputs and replicates the waveform of the discharge current. As outputs, IRM gives the time evolution of plasma species and electron temperature. As a global model, the physical quantities obtained are averaged over the volume of the ionisation region (IR).

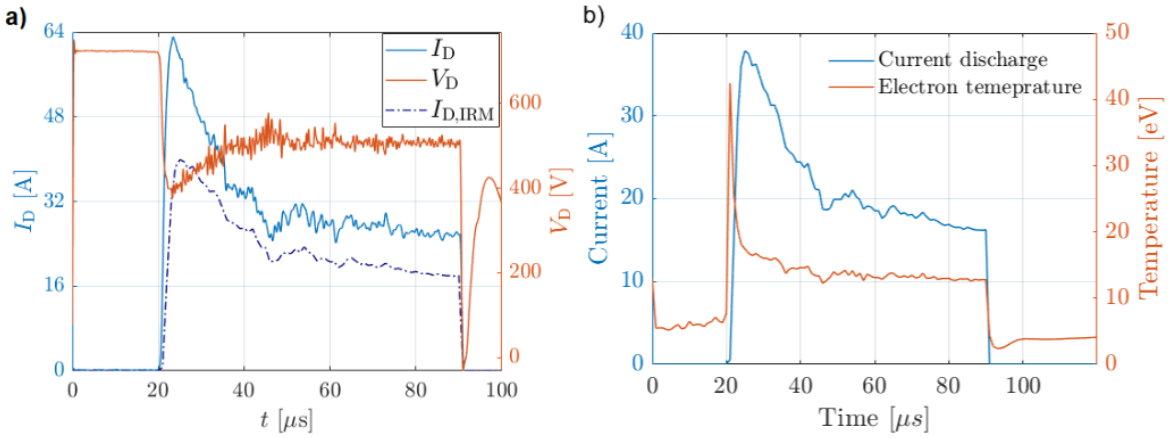

Fig. 1: (a) Measured discharge current (I_D) for a 700 V voltage pulse (V_D), with modeling result $I_{D,IRM}$ for a typical He/Mo HiPIMS pulse. (b) IRM current and electron temperature. evolution during the HiPIMS pulse.

One of the main fit parameters for the IRM is the voltage drop across the IR, which is set as a constant value during the pulse discharge. The equation for this voltage drop writes:

$$V_{IR} = f \times V_D : 0 < f < 1 \tag{1}$$

For Helium-Molybdenum IRM (He/Mo-IRM), f was modified to vary during the pulse by multiplying (1) with the ratio $I_D(t)/I_{Peak}$, which provides a better fit in case of helium and required by the sharp and fast variation of the discharge current. Fig.1(b) reports the time evolution of the current and electron temperature. The model accurately reproduces the rapid rise time of the peak and the subsequent decrease to a plateau. However, the IRM peak current is smaller than in experiments. Figure 1(b) shows that the peak current follows a peak in the cold electron temperature. The temperature increases from 10 eV to 40 eV, significantly surpassing the ionization energy of the ground state helium for a short time (< 5 µs). This spike in T_e has already been reported but using the PIC modeling [6].

Furthermore, the model provides the current composition of the discharge. As can be seen in fig.2, the peak current is carried solely by helium ions, while the current associated with metal ions is comparably

low due to the low sputtering yield of helium. At the beginning of the discharge, only helium can be ionized by the secondary electrons, which gain enough energy to ionize the ground state (24.58 eV). After the current peak, the He metastable states (19.6 eV) formed simultaneaously with the first peak current, will start to play via a two-steps ionization, which requires much less energy (4.76 eV and 3.96 eV). Consequently, the electron temperature decreases and so does the discharge current.

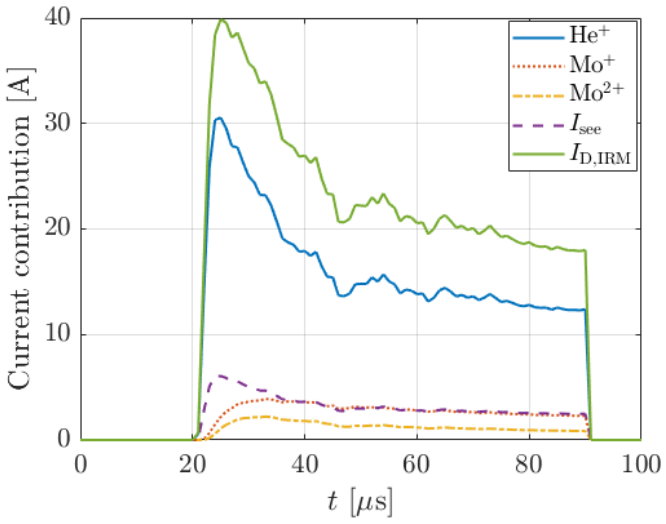

Fig. 2: Current composition of the IRM current for a 700 V HiPIMS discharge

The results of He/Mo-IRM will be presented in more detail, discussing the other fit parameters that have been adjusted to match the helium HiPIMS kinetics. The experimental results, including peak currents, the decrease to a plateau, weak current contributions from metal ions, and the cooldown of the electron temperature, will also be explained.

[1] E.Morel, Y.Rozier, C.Ballages, R.Bazinette, T.Forchard, C.Creusot, A.Girodet, and T.Minea, "Behavior of high current density pulsed magnetron discharge with a graphite target," Plasma Sources Sci. Technol.30(12), 125001(2021). https://doi.org/10.1088/1361-6595/ac3341

[2] E.Morel, Y.Rozier, A.El-Farsy, T.Minea,(2023). Impact of self-sputtering in High power impulse magnetron sputtering (HiPIMS) with helium. Journal of Applied Physics. 133. 10.1063/5.0145547.

[3] J T Gudmundsson et al 2016 Plasma Sources Sci. Technol. 25 065004 DOI 10.1088/0963-0252/25/6/065004

[4] S.F. Biagi FORTRAN code Magboltz, version 8.97, Sept 2011.www.lxcat.net/Biagi

[5] TRINITI database Napartovich A. P. and Drs. Dyatko N. A., Kochetov I. V., Sukharev A. G. from The State Science Center Troitsk Institute for Innovation and Fusion Research,Russia. www.lxcat.net/TRINITI

[6] A. Revel et. al. 2D PIC-MCC simulations of magnetron plasma in HiPIMS regime with external circuit, 2018, PSST, 27, 105009. doi :10.1088/1361-6595/aadebe

Macroscopic Model of Non-thermal Plasma Filament Based on Probabilistic Approach

Filip Zmeko[1], Eva Müllerová[1], Zdeněk Bonaventura[2],

[1] *Department of Power Engineering, Faculty of Electrical Engineering, University of West Bohemia, Pilsen, Czech Republic*

[2] *Departemnt of Plasma Physics and Technology, Faculty of Science, Masaryk University, Brno, Czech Republic*

Mathematical models that are based on kinetic and fluid approximations are traditionally used to evaluate various phenomena in non-thermal plasmas. However, the computational complexity of these models can be often very demanding [1], or even prohibitive in situations where it is necessary to resolve large spatial and extensive temporal scales to achieve convergent and physically consistent results.

We use a macroscopic probabilistic approach, see for example [2, 3, 4, 1], to model the propagation and branching of ionization waves, specifically focusing on predicting breakdown voltages in macroscopic electrode configurations. This approach enables direct comparison of statistically evaluated simulation results with experiments conducted under standardized conditions, such as defined in [5].

The macroscopic model used is based on the so-called Laplacian-growth-probability discharge model. This approach couples Laplace equation for electric potential φ

$$\Delta\varphi = 0, \tag{1}$$

with a probability for channel propagation

$$p_i = \frac{\varphi_i^\eta}{\sum_{j=1}^{n} \varphi_j^\eta}, \tag{2}$$

where φ_i represents the electric potential at location i, and η is the electric discharge branching parameter, for further details on the Laplacian growth model, see [6, 7].

The discharge channel is treated as a conductor with finite conductivity, and its propagation dynamics can be adjusted by varying several input parameters, such as the electric channel conductivity, or rate of discharge channel quenching.

By adjusting a set of these parameters, a macroscopic discharge model can be calibrated to mimic the desired macroscopic properties.

The probabilistic model combines the Finite Element Method (FEM) solver to solve the Laplace equation for the electric field and an iterative process for discharge channel propagation that consists of:

1) probability p_i evaluation along already grown discharge tree,

2) cumulative probability calculation, i.e., sum(p_i),

3) choice of propagation direction,

4) boundary condition implementation according to the electrode system and discharge tree morphology for the FEM solver, and

5) the electric potential φ_i calculation.

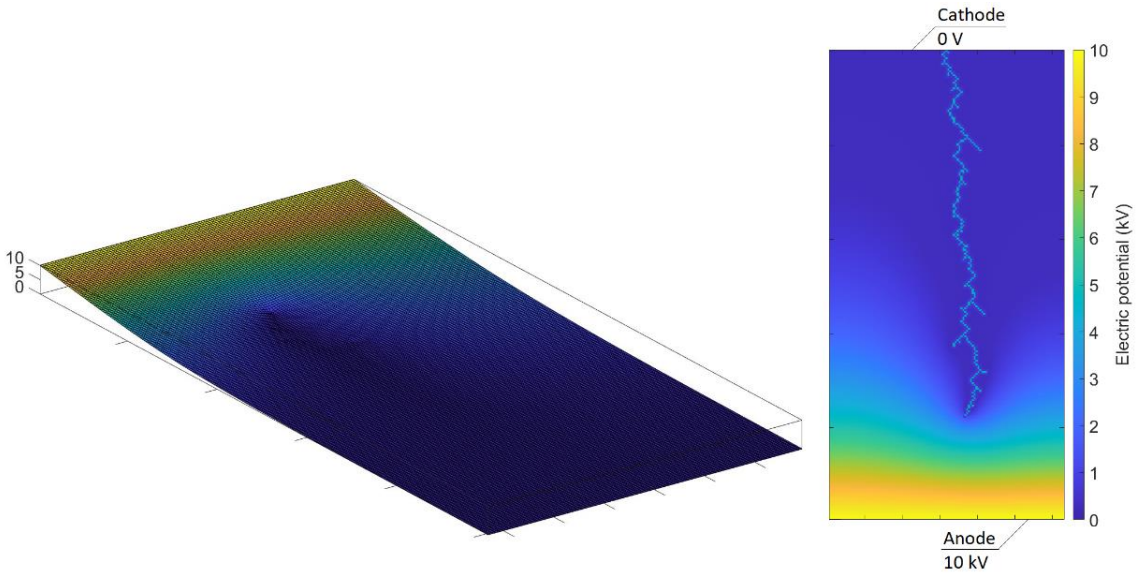

Fig. 1: The electrostatic potential (kV) for the zero-electric-channel-resistance approximation (left) and corresponding electric discharge path in 2D planar electrode system (right), created using [8].

Figure 1 shows a result of a discharge path obtained by the probabilistic model implemented in Matlab [8] for Cartesian 2D geometry. A zero channel conductivity is considered here with an applied voltage of 10 kV and a computational domain size of 1/6 cm by 1/3 cm.

This contribution will investigate the fine-tuning of the probabilistic discharge model parameters for the propagation of ionization waves in air at atmospheric and higher pressures. Our goal is to predict and statistically evaluate macroscopic parameters that are of crucial importance for electrotechnical applications, such as the probabilities of electrical breakdown under specific applied voltage waveforms.

Sweet spots and limitations of the macroscopic probabilistic approach will be discussed.

[1] M B Teixeira-Gomes et al 2023 Plasma Sources Sci. Technol. **32** 095010.

[2] M González et al 2019 Plasma Sources Sci. Technol. **28** 115007.

[3] A Luque and Ute Ebert 2014 New J. Phys. **16** 013039.

[4] A Luque et al 2017 Plasma Sources Sci. Technol. **26** 125006.

[5] International Electrotechnical Commission, "IEC 60060-1:2010, High-voltage test techniques - Part 1: General definitions and test requirements," 2010.

[6] T Kim, J Sewall, A Sud, MC Lin 2007 IEEE Comput Graph Appl. **27** 68-76.

[7] B Bickel, M Wicke, M Gross 2006 Computer Graphics Laboratory, ETH Zurich: *Adaptive Simulation of Electrical Discharges*.

[8] MATLAB, 2023. MATLAB Version: 9.8.0.1359463 (R2020a). Natick, Massachusetts: The MathWorks Inc.

[9] S Chen, F Wang, Q Sun, R Zeng 2018 IEEE Transactions on Dielectrics and Electrical Insulation **25** 2112-2121.

Obtaining of silicon nanoclusters by the PECVD method

S.S Ussenkhan[1,2], A.T. Zhunisbekov[1], Y. Yerlanuly,[2] A.U. Utegenov[2], *S.A. Orazbayev[2], T.S. Ramazanov[1,3], L. Boufendi[1], H.Vach[4]

[1] *Al-Farabi Kazakh National University, 71/23 Al-Farabi ave., 050040, Almaty, Kazakhstan*

[2] *Institute of Applied Sciences and Information Technologies, 280 Bayzakov str., 050038, Almaty, Kazakhstan*

[3] *Kazakh Physical Society, Almaty, 050040, Kazakhstan*

[4]*Laboratoire de Physique des Interfaces et des Couches Minces, CNRS, École Polytechnique, IP Paris, 91128 Palaiseau, France*

(*) sagi.orazbayev@gmail.com

Currently, due to the intensive development of nanotechnology, there is an increased interest in the study of nano-sized objects such as quantum wells, quantum wires, quantum dots, *etc*. In such nanoscale objects, the de Broglie wavelength of the electron is commensurate with the size of the object in one or more dimensions, which causes quantum mechanical effects in contrast to bulk materials. These effects are well manifested in the optical, electronic, and magnetic properties [1] of semiconductor materials. Consequently, they find many applications in microelectronics, medicine, solar energy, *etc*. Silicon is the most widely used semiconductor material in modern electronics and microelectronics. Therefore, research on the formation and modification of the parameters of silicon nanostructures is a very urgent task. Silicon nanoparticals exhibit quantum properties at temperatures up to room temperature, which is of practical interest [2] in the implementation of devices based on these materials.

In the present work, silicon nanocrystals were obtained in a pulsed dust-forming plasma generated in a high-frequency capacitive Ar + SiH_4 discharge at low pressure (figure 1). The experimental setup includes a vacuum reactor, a high-frequency generator, a matching device, and DC power supplies for the generation of an electric field during deposition. The obtained results were analyzed using AFM, SEM, TEM, XPS, UPS, and UV-VIS spectroscopy. The self-bias voltage was used to control the orientation of the nanoparticles just before their deposition. The dependence of the work function of the resulting substrate material on the size of the deposited nanoparticles will be discussed in detail during our presentation.

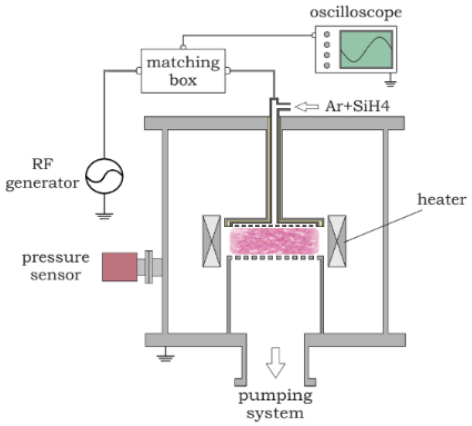

Fig. 1: Schematic of an experimental setup for the obtaining of silicon nanoclusters

[1] Fatme Jardali at all. *J. ACS Applied Nano materials* 2021 4 (11), 12250-12260.

[2] S. Ussenkhan at all. *Heliyon* 10 (2024) e23844

[3] Jardali, F.; Tran, J.; Liège, F.; Florea, I.; Leulmi, M.E.; Vach, H. *J. Nanomaterials* 2023, 13, 2169.

Influence of discharge kind on processes in Titan like atmosphere

F. Krčma, Z. Kozáková, F. Zbytek, M. Moravčík

Brno University of Technology, Faculty of Chemistry, Brno, Czech Republic

krcma@fch.vut.cz

The aim of the presented work is the comparison of chemical processes initiated by different discharges (glow and spark) in the same gaseous mixtures at fixed geometric conditions. The nitrogen-methane gaseous mixture at atmospheric pressure was used at different methane concentration (0–2 %). The specially designed stainless-steel reactor [1, 2] operating in the flowing regime (200 Sccm of nitrogen) allowed simultaneous measurements of emission spectra emitted by the discharge and *in situ* acquisition of proton transfer reaction time of flight mass spectra of discharge products. The electrode system consisted of two stainless steel hemispheric electrodes (diameter of 10 mm) with the interelectrode distance of 1 mm. The DC and audiofrequency (10 kHz, rectangular pulses) power supplies were used for the discharge generation at similar applied energies. All arrangements were kept exactly the same for both discharges to be able fully compare discharge conditions as well as discharge produced compounds. Experiments were done in two series, for each power supply separately. The whole system was purged by nitrogen flow of 30 Sccm overnight to obtain oxygen free conditions (like in the Titan atmosphere). The background PTR-TOF spectrum was collected for 1 minute in pure nitrogen without the discharge. After that, the discharge was ignited and stabilized for 20 minutes. Then OES spectra of selected species (CN, N_2, N_2^+, C_2, H) were collected and simultaneously, the average PTR-TOF spectrum was evaluated for 5 minutes. The same cycle was repeated for added methane flows of 1, 2, 3, and 4 Sccm. Finally, the discharge was stopped and the whole reactor was cleaned by the pure nitrogen flow of 200 Sccm for 8 hours to remove all generated species.

The optical emission spectra showed huge difference between the used discharges. The main difference was that the emission of iron lines was observed in case of the pulsed AC discharge while nearly no emission of the C_2 Swan system was visible. Further, the CN systems emission was much weaker in this case (see Fig. 1-left) and its intensity was decreasing with the methane presence increase (in contrary to the DC discharge). On the other hand, a strong H-alpha line broadening was observed (see Fig. 1-right).

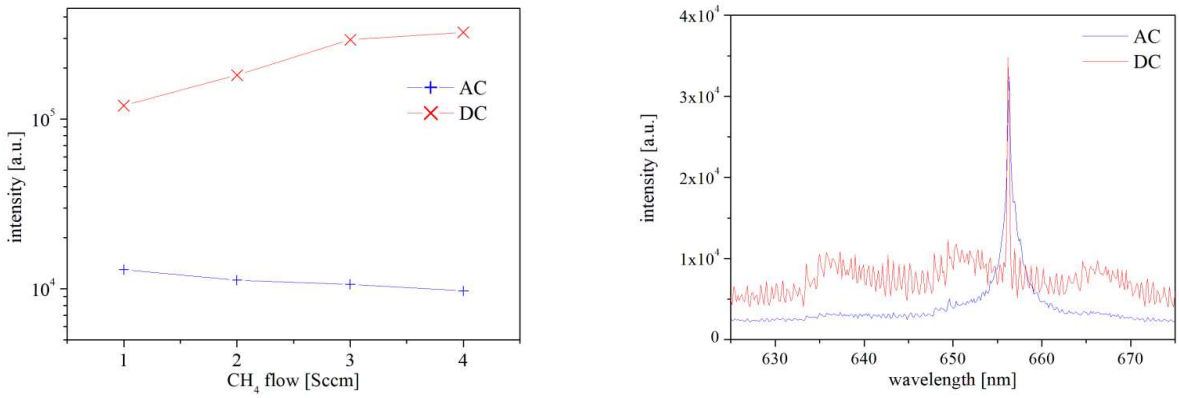

Fig. 1: Comparison of CN violet 0-1 band head intensity in both discharges (left); H-alpha line profile and CN red system emission in both discharges at methane flow of 4 Sccm (right, DC intensity was divided by factor 5).

The nitrogen second positive system intensity was the same in pure nitrogen, but it was increasing in DC and decreasing in the AC discharge. Hydrogen emission was increasing in both discharges, but its dependence on the methane concentration was much sensitive in the DC discharge.

Similar compounds with masses up to about 150 amu were formed by both discharges and majority of them has been already identified recently [1, 2]. In general, much higher products concentrations were observed in case of the DC discharge. Examples of obtained concentrations are shown in Fig. 2. It is necessary to note, that concentrations in the DC discharge with the higher methane addition were underestimated because the ionization precursor (H_3O^+) was consumed too much by the discharge products.

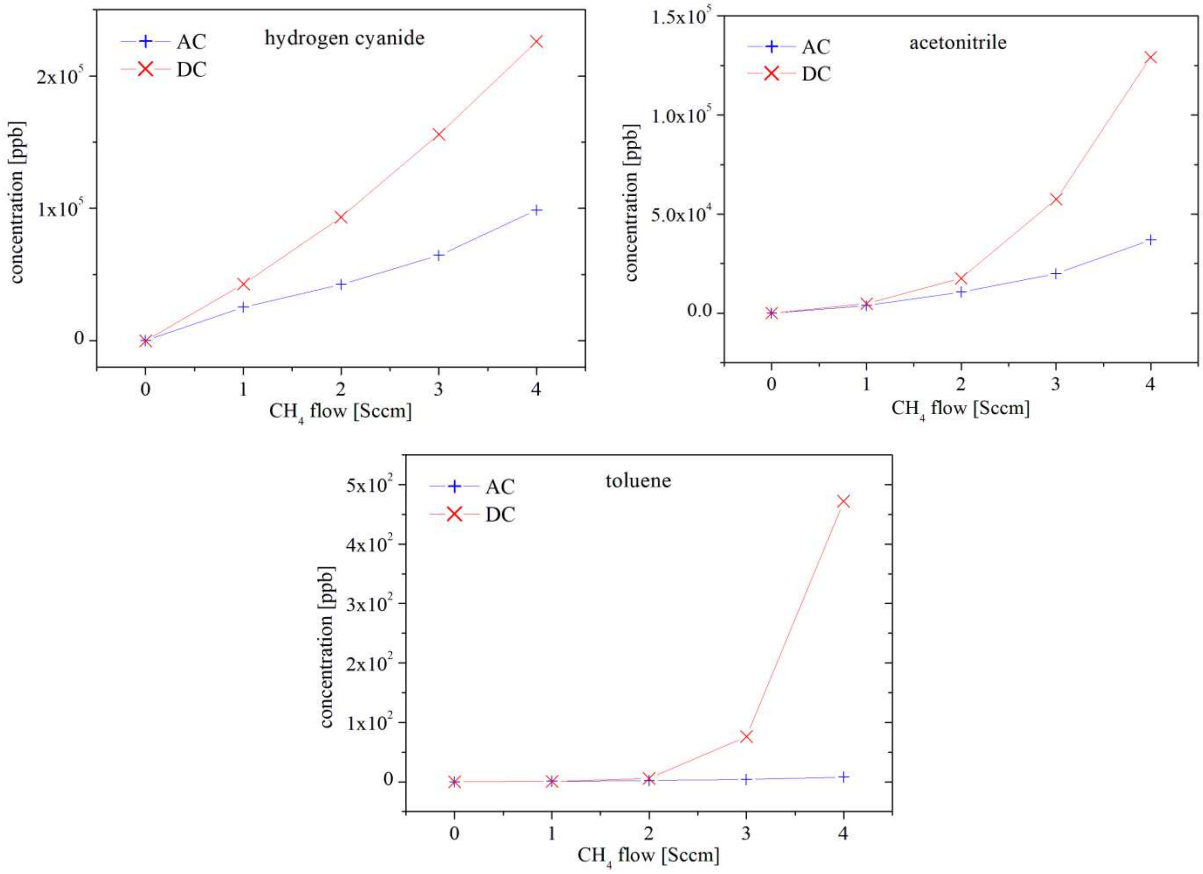

Fig. 2: Concentrations of selected compounds in dependence on methane addition in both discharges.

The presented results show a strong dependence of the synthetic processes in the Titan like atmosphere on the discharge kind. Next experiments will be focused on the DBD discharge under the same conditions; however, a modified electrode geometry will be used because the same geometry will be impossible to keep.

References

[1] S. Chudják, Z. Kozáková, F. Krčma, *ACS Earth Space Chem.*, **5** (2021) 535-543

[2] S. Chudják, Thesis, FCH BUT 2023

Influence of water vapor on electrical discharge-initiated processes in prebiotic atmospheres

M. Moravčík, F. Krčma

Brno university of technology, faculty of chemistry, institute of physical and applied chemistry, Brno, Czech Republic

The aim of the presented work is study of chemical process in extraterrestrial atmosphere and the synthesis of organic compounds formed in electrical discharges in gaseous mixtures at the atmospheric pressure and ambient temperature in the flowing regime. This study focuses on the influence of water molecules on chemical processes initiated by electrical discharges in probiotic atmospheres. This work is focused on the simulation of nitrogen-methane atmosphere and carbon dioxide atmosphere. These gases were chosen because they represent the main components of some known extraterrestrial atmospheres. The atmosphere of Titan, second largest moon of solar system, was mimicked by the gaseous mixture of methane (2-4 sccm) in 200 sccm of nitrogen. The second studied atmosphere was atmosphere of Mars that is based on the carbon dioxide. It was further enriched by small addition of nitrogen (2- 4 sccm) in 200 sccm of carbon dioxide. Water vapor with a flow rate of 0, 5,10, 15 and 20 sccm was gradually introduced into every gaseous mixture. A DC glow discharge was generated in a special reactor at atmospheric pressure [1].

The discharge formed products were analysed *in situ* using proton ionization mass spectrometry with a time-of-flight analyser. Huge number of simple aliphatic hydrocarbons, alcohols, aldehydes, and ketones was successfully identified. With increasing number of additives, more complex mainly aromatic substances were also formed as it can be seen in Figs. 1 and 2. In case of nitrogenous gaseous mixture, the most dominant detected gas products were ammonia, followed by hydrogen cyanide and acetonitrile. In case of carbon dioxide gaseous mixture, the most dominant detected species were ammonia or methanimine, with other additives high presents was confirmed for hydrogen cyanide or acetonitrile. Water and water dimer at molecular mass 37 are contamination, that were present in pure CO_2.

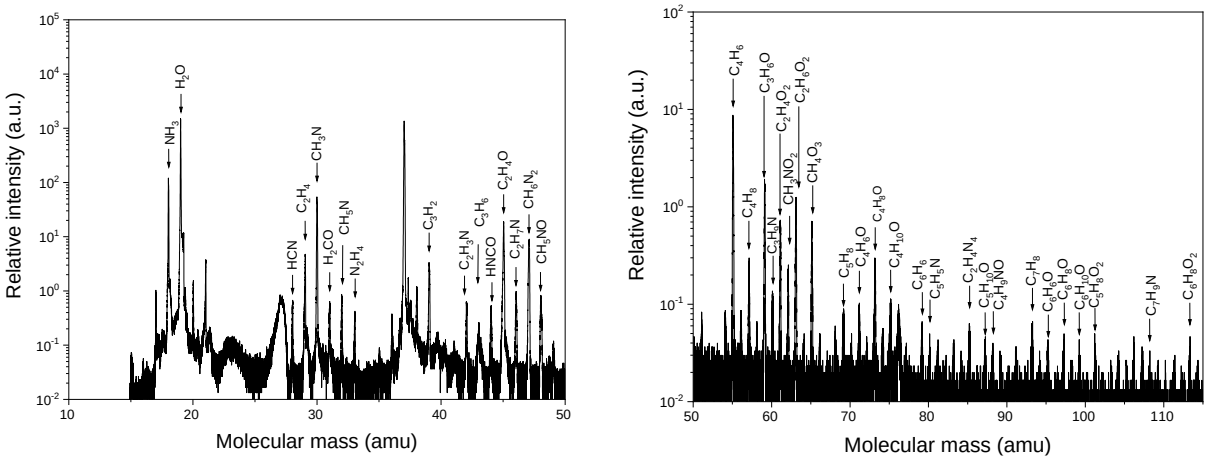

Fig. 1: The identified PTR-TOF mass spectrum of gaseous product in the discharge at nitrogen flow 4 sccm and water vapor flow 20 sccm in 200 sccm of carbon dioxide.

Simultaneously with PTR-TOF spectra acquisition, plasma diagnostics was carried out using optical emission spectroscopy. The lines of C and O together with CO Angstrom bands were identified in the pure CO_2, Hydrogen lines and bands of N_2, CN, CH and OH were identified with all admixtures. All

these groups were also presented in the compounds identified by PTR-TOF. Their changes in intensity were corresponding to the intensities of the mass spectrometry determined species.

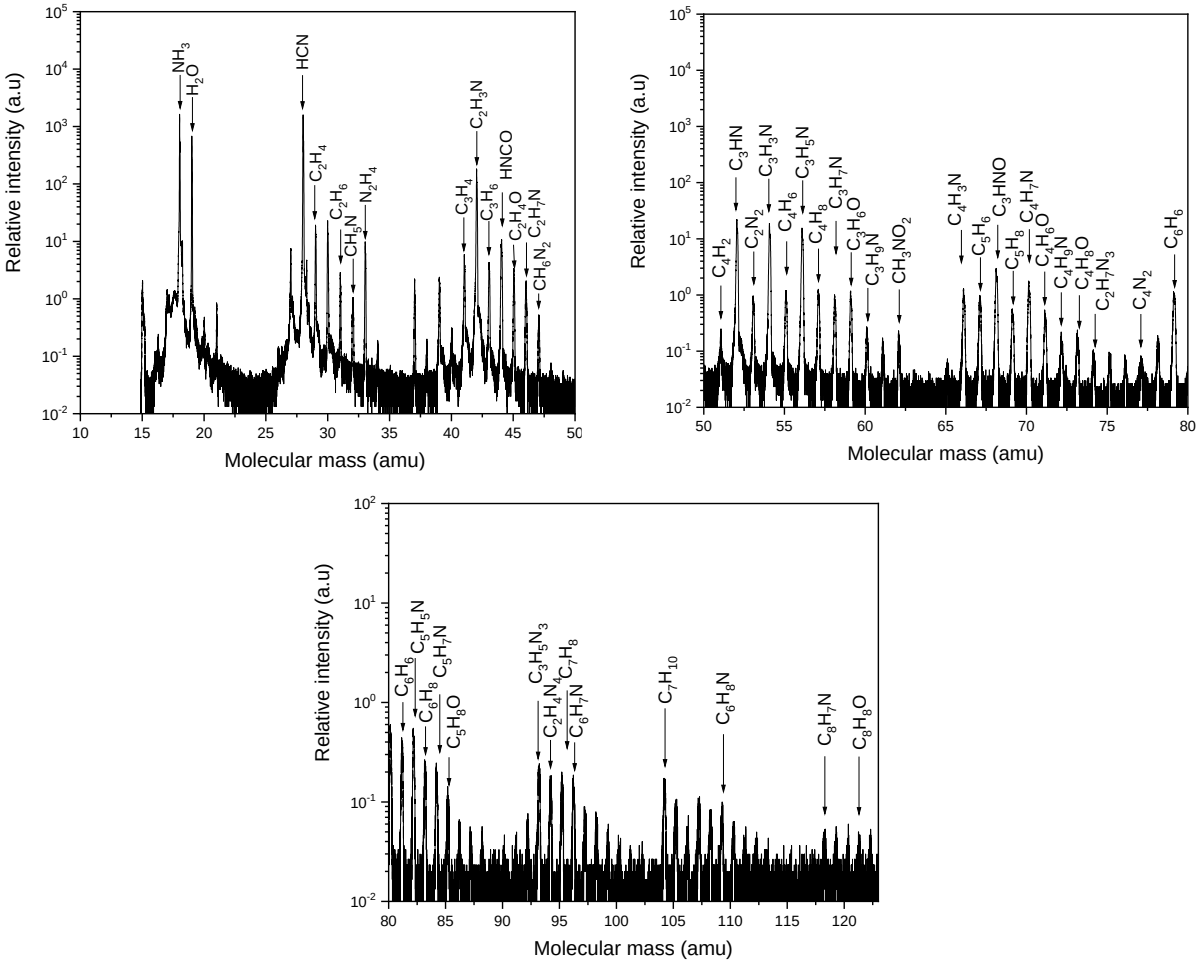

Fig. 2: The identified PTR-TOF mass spectrum of gaseous product in the discharge at methane flow 4 sccm and water vapor flow 20 sccm in 200 sccm of nitrogen.

In case of nitrogen-based mixture, the most dominant detected gas products were ammonia, followed by hydrogen cyanide, acetonitrile [2]. Significant increase of oxygen containing compounds was observed if water was added. One of the most important compounds formed is such case was formamide that is known as a precursor of uracil formation. This molecule is one of the nuclear acids bases. The OES spectra confirmed presence of C and H lines and CN, CH, NH, C_2 and N_2 spectral bands, if water was added also oxygen lines and OH bands were detected.

The substances detected in this work agree with the available literature and also with substances detected *in situ* in Mars's and Titan's atmospheres.

References

[1] S. Chudják, Z. Kozáková, F. Krčma, *ACS Earth Space Chem.,* **5** (2021) 535-543

[2] S. Chudják, Thesis, FCH BUT 2023

A Comprehensive Analysis of Optical Emissions in Exposed Lightning Channels

F. J. Pérez-Invernón(*)[1], J. F. Ripoll[2,3], F. J. Gordillo-Vázquez[1], P. Camino-Faillace[1], T. Neubert[4], O. Chanrion[4], N. Østgaard[5]

[1] *Institute of Astrophysics of Andalusia, Consejo Superior de Investigaciones Científicas, Granada 18008 Spain*

[2] *CEA, DAM, DIF, Arpajon, France*

[3] *UPS, CEA, LMCE, Bruyères-le-Châtel, France*

[4] *Space and Earth Science and Technology, Technical University of Denmark, Kongens Lyngby, Denmark*

[5] *Department of Physics and Technology, University of Bergen, Bergen, Norway*

(*) fjpi@iaa.es

The Atmosphere Space Interactions Monitor (ASIM) was installed on the International Space Station (ISS) on April 13, 2018. The ASIM included the Modular Multispectral Imaging Array (MMIA), designed to study the optical signals of atmospheric electrical phenomena [1]. The ASIM-MMIA's photometers, with their unprecedented high-sampling frequency of 100 kHz, and its high spatial resolution cameras, offering 400 × 400 meters per pixel, provide a unique opportunity to analyze light emissions from lightning-induced plasmas from space. ASIM photometers operate in the near UV line at 337 nm ± 2 nm (PH1), the UV band at 180–230 nm (PH2), and the neutral atomic oxygen multiplet at 777.4 nm ± 2.5 nm (PH3). Additionally, the MMIA instrument features two filtered cameras operating at 12 frames per second, one in the near UV (CHU1, 337 nm ± 2 nm) and the other in the neutral atomic oxygen multiplet (CHU2, 777.4 nm ± 2.5 nm).

In this study, we examine the optical signal from exposed lightning flashes that reaches the MMIA without interference from cloud scattering. We combine an electrodynamical model of hot air plasmas in lightning discharges [2,3] with computations of synthetic spectra of lightning-like discharges [4]. The electrodynamical model calculates the temporal and radial evolution of plasma parameters and chemical species. We ran different simulations of lightning-like discharges between 0 km and 16 km altitude, varying input energy, initial radius, initial mass, and humidity. We use a simplified model to estimate the peak current corresponding to each input energy. We then post-process the output of the electrodynamical model following the method in [4], providing the temporal evolution of the emitted spectra. In particular, we calculate the synthetic emissions of a 1 km portion of a flash propagating at the velocity of an intra-cloud burst at 12 km in the 777.4 nm and the 337 nm channels. Finally, we compare the simulated peaks in the photon fluxes with the observations of exposed flashes provided by ASIM-MMIA.

Preliminary results are shown in Figure 1. The first panel of Figure 1 shows the 777.4 nm simulated photon flux peak (black stars) and the photon flux peak of exposed lightning observed by ASIM-MMIA (red dots) versus the lightning flash peak current. A positive relationship between the photon flux peak and the peak current can be observed in both the simulations and observations. The second panel of Figure 1 shows the results at the 337 nm spectral line. Our results indicate that the thermal (due to ions, black stars) 337 nm optical emission of hot plasmas in exposed lightning can only be detected by ASIM-MMIA if the electric peak current is approximately above approximately 40 kA (about 76 J/cm input energy). Our electrodynamic model for the hot lightning plasma does not consider streamers in lightning so that the computed 337 nm optical emissions (black stars in bottom panel of Figure 1) that are thermal (due to ions) 337 nm emissions take values different that those observed by ASIM-MMIA. We hypothesize that the 337 nm photon flux detected by ASIM-MMIA from lightning discharges with a peak current below 40 kA is exclusively emitted by streamers, while

more energetic lightning flashes can produce detectable emissions in the 337 nm line from the excitation of ions (OII and NIII) [4].

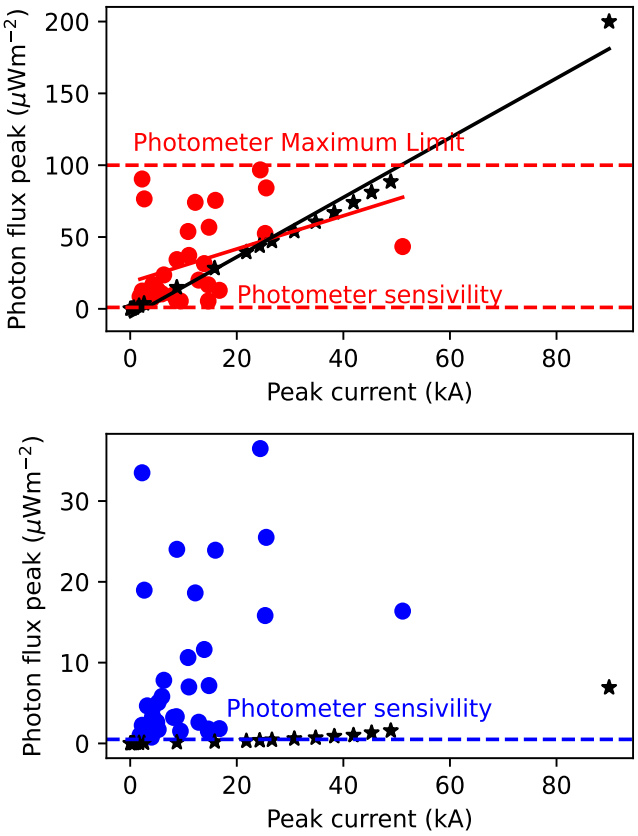

Figure 1: The first panel shows the 777.4 nm simulated photon flux peak (black stars) and the photon flux peak of exposed lightning observed by ASIM-MMIA (red dots) versus the lightning flash peak current. The red line represents a linear fit to the red dots, whereas the black line represents a linear fit to the black stars. The second panel shows the 337 nm simulated photon flux peak (black stars) and the observed photon flux peak of exposed lightning (blue dots). The peak current in the observations is provided by a ground-based lightning location system.

[1] Chanrion, O., Neubert, T., Lundgaard Rasmussen, I., Stoltze, C., Tcherniak, D., Jessen, N. C., ... & Lorenzen, M. (2019). The modular multispectral imaging array (MMIA) of the ASIM payload on the international space station. *Space Science Reviews*, **215**, 1-25.

[2]: Ripoll, J. F., Zinn, J., Jeffery, C. A., & Colestock, P. L. (2014). On the dynamics of hot air plasmas related to lightning discharges: 1. Gas dynamics. *Journal of Geophysical Research: Atmospheres*, **119**(15), 9196-9217.

[3]: Ripoll, J. F., Zinn, J., Colestock, P. L., & Jeffery, C. A. (2014). On the dynamics of hot air plasmas related to lightning discharges: 2. Electrodynamics. *Journal of Geophysical Research: Atmospheres*, **119**(15), 9218-9235.

[4]: Pérez-Invernón, F. J., Gordillo-Vázquez, F. J., Passas-Varo, M., Neubert, T., Chanrion, O., Reglero, V., & Østgaard, N. (2022). Multispectral optical diagnostics of lightning from space. *Remote Sensing*, **14**(9), 2057.

Toroidal Plasma Sources for Remote and Isotropic Processing

Scott J. Doyle and Mark J. Kushner

Electrical Engineering & Computer Science, University of Michigan, Ann Arbor, MI 48109-2122 USA

mjkush@umich.edu

In plasma materials processing for semiconductor fabrication, requirements for etching range from high aspect ratio anisotropic to highly selective isotropic. The latter, which includes chamber cleaning, is typically performed with remote plasma sources capable of producing large fluxes of halogen or oxygen radicals. The remote nature of the plasma source is intended to minimize the fluxes of charged particles or UV photons onto the wafer. Toroidal plasma sources (TPS) represent a class of devices that are capable of sustaining high powers in highly attaching gases [1]. A TPS typically consists of a ferrite core with a primary winding located outside the plasma reactor [2]. The plasma reactor is configured to provide a closed plasma loop that acts as the secondary winding to the ferrite core. Typical operating conditions are up to several kW power deposition, flow rates of up to several slm and pressures of up to 10 Torr with gas mixtures containing halogen donors such as NF_3.

In this paper, results from a computational investigation will be discussed of the fundamental properties of toroidal plasma sources sustained in Ar and Ar/NF_3 mixtures. These investigations were performed using the Hybrid Plasma Equipment Model (HPEM) [3]. In conventional inductively coupled plasmas, the induced electric field in the plasma is in the azimuthal direction. For 2-dimensional models this electric field is perpendicular to the plane of interest, and so typically appears only as a heating source. In a TPS, the induced electric field is in the plane of interest. To facilitate these conditions, a new capability was developed to represent the transfer of magnetic fields through the ferrite core from the primary and to secondary, and propagation of the secondary induced electric field in the x-y plane.

The base case operating conditions are 1 Torr of Ar/NF_3 mixtures flowing at 500 sccm with a power deposition of 1 kW at 500 kHz. Typical plasma conditions are shown in Fig. 1 for Ar and NF_3 only gas mixtures. To enable high power deposition beyond the capabilities of a single ferrite core, dual ferrite cores are used. Although the ideal TPS has closed-loop symmetry for power deposition in the x-y plane, when using dual sources this close-loop symmetry is broken. The end result is two parallel regions of power deposition. This distribution of power produces two lobes of electron density of approximately 2×10^{13} cm^{-3}. When operating in NF_3, the asymmetric power deposition produces sub-sustaining

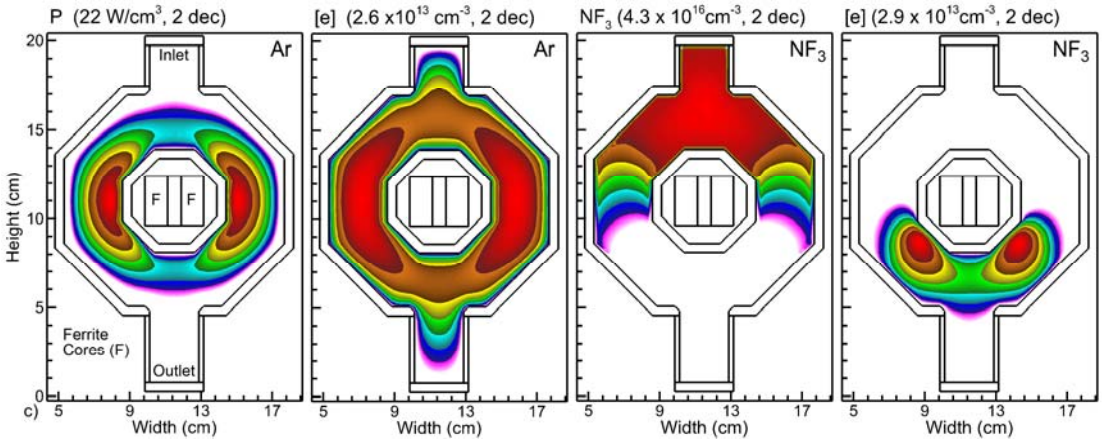

Fig. 1 : Properties of a dual-ferrite, remote toroidal plasma source with 1 kW power deposition at 500 kHz (left) Ar plasma: power and electron density. (right) NF_3 plasma: NF_3 density and electron density

electric fields near the inlet where the highly attaching NF_3 enters into the chamber. After a start-up transient, the plasma stabilizes lower in the reactor where the NF_3 dissociation has produced a less attaching environment. In this case the NF_3 is fully dissociated to produce dominantly a stream of NF, F and N. The gas temperature is several thousand degrees, resulting in a significant fraction of the dissociation being thermal. Results will be discussed for parametric studies for power, gas mixture and frequency.

This work was supported by MKS Instruments and the Department of Energy Office of Fusion Energy Sciences (DE-SC0020232).

[1] H. Li, Y. Zhou, and V. M. Donnelly; J. Vac. Sci. Technol. A **38**, 023011 (2020).
[2] S P Gangoli et al J. Phys. D: Appl. Phys. **40** 5140 (2007).
[3] T. Piskin et al., J. Appl. Phys. **133**, 173302 (2023).

Emission properties of low-pressure low-current DC discharge in freons of new generation

J Marjanović(*)[1], D Marić[1], Z Lj Petrović[2,3]

[1] *Institute of Physics, University of Belgrade, Pregrevica 118, 11080 Belgrade, Serbia*

[2] *Serbian Academy of Sciences and Arts, Kneza Mihaila 35, 11001 Belgrade, Serbia*

[3] *School of Engineering, Ulster University, Jordanstown, County Antrim BT37 0QB, United Kingdom*

(*) sivosj@ipb.ac.rs

Fluorocarbons, widely used in plasma-based technologies, find applications in the semiconductor industry for etching, cleaning, surface functionalization, deposition of fluorocarbon films, and carbon nanostructures [1,2]. Notably, tetrafluoroethane (HFC-134a) and its low Global Warming Potential (GWP) and low Ozone Depletion Potential (ODP) substitute gas, tetrafluoropropene (HFO-1234yf), serve not only as refrigerants in vehicles and household appliances but also in radiation particle detectors, high and medium voltage gas insulation systems, and polymer film deposition [3,4]. Understanding the electrical characteristics of these fluorocarbons when exposed to electric fields is crucial for developing new applications and enhancing existing ones. Our research focuses on acquiring data on fundamental processes that influence breakdown and gas discharge behavior in fluorocarbon gases under electric fields, aiding in the modeling of gas discharge applications. In our steady-state Townsend experiment (SST), we ignite discharges within a system consisting of two plan-parallel electrodes housed in a quartz tube. The electrodes, with a diameter of 5.4 cm, are positioned 1.1 cm apart. Here, we present a comparison of the results of our DC breakdown measurements for HFC-134a and HFO-1234yf. These results include optical emission spectra, spatially and spectrally resolved distribution of discharge emission, and Paschen curves, providing breakdown voltage and data that could be the basis for modelling and understanding the operation of the discharge.

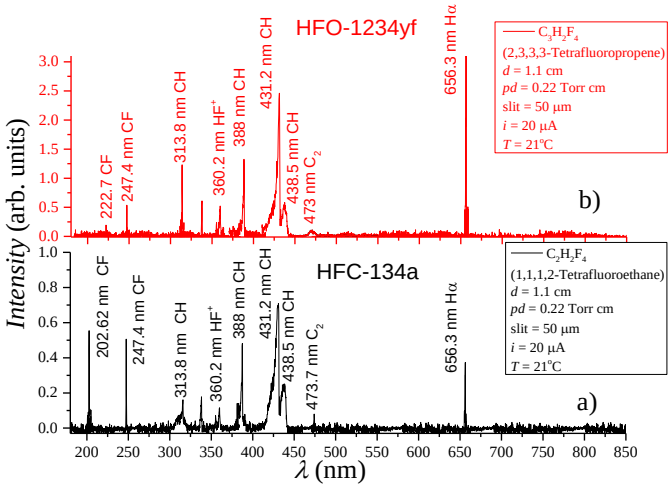

Fig. 1: Optical emission spectra of discharges in a) HFC-134a and b) HFO-1234yf obtained at *pd*=0.22 Torr cm (pressure times electrode distance) and *d*=1.1 cm. The width of the spectrograph slit was 50 µm.

Optical emission spectra of discharges in HFC-134a and HFO-1234yf (as shown in Fig. 1a) and b)) were recorded at low current in the Townsend regime within the 200-900 nm spectral range. Detected emissions include CF, CH, HF^+, C_2, and H_α. These emissions likely arise from excited species resulting from dissociative excitation of the parent molecules [5,6]. Analyzing emission spectra allows identification of possible excited species and proper selection of optical filters for spectrally resolved recordings of axial emission profiles (examples shown in Fig. 2a) and b)). The recorded data includes spatial profiles of total emission within the entire visible spectral range and the spatial distribution of

emission in narrow wavelength intervals centered around the most intense lines (at 431 nm and 656 nm). Axial emission profiles, obtained for different *pd* values, illustrate how changes in *E/N* (*pd*) impact the discharge structure and basic processes. Despite operating in the low-current Townsend regime, where space charge density is negligible and the electric field between electrodes is nearly uniform [7], spatial emission peaks in front of the cathode for both freons. This phenomenon is primarily attributed to heavy-particle excitation near the cathode [8]. Additionally, the CH emission (dashed lines in Fig. 2a) and b)) follows the integrated profiles (solid lines), while H_α emission (open circles in Fig. 2a) and b)) exhibits a distinct shape with a more pronounced peak in front of the anode (at these *E/N*). Axial profiles of emitted light in these two freons highlight the substantial contribution of heavy particles to breakdown across a wide range of *pd* values (i.e., the corresponding *E/N* values). In addition to the axial emission profiles, we present the Paschen curves (Fig. 2c)) measured for discharges in HFC-134a and HFO-1234yf, covering a range from 0.05 Torr cm to 1.2 Torr cm. HFO-1234yf has significantly higher breakdown voltages at the same *pd* as compared to HFC-134a.

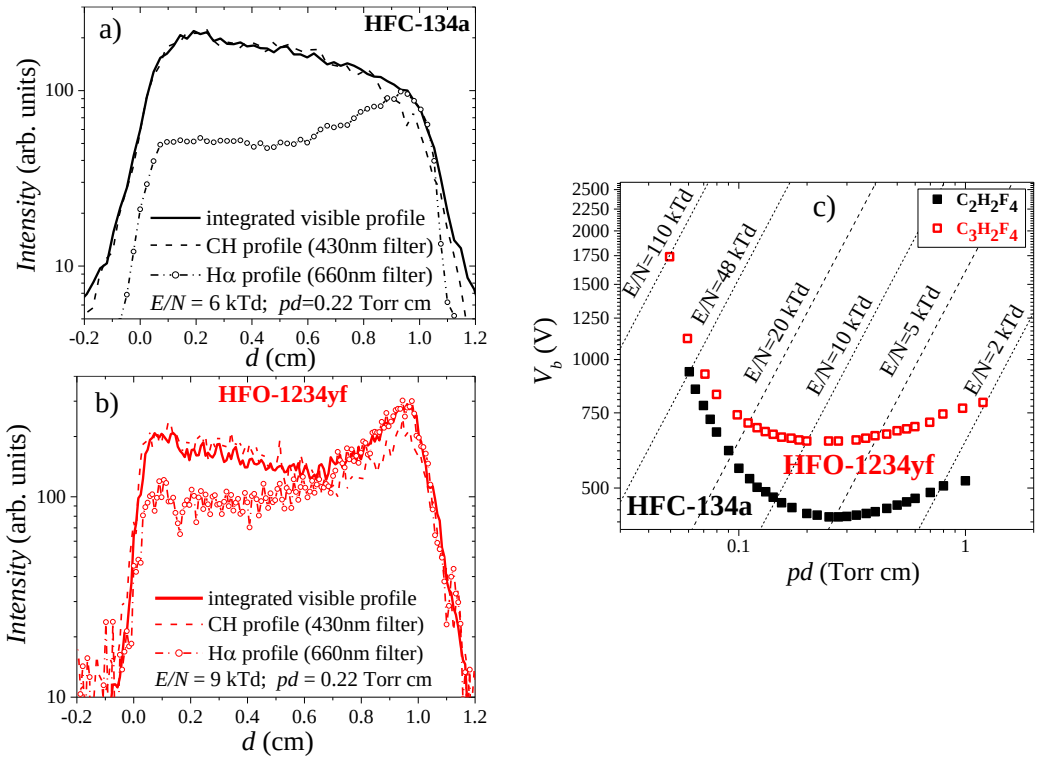

Fig. 2: Axial profiles of emission from discharges in a) HFC-134a and b) HFO-1234yf recorded at *pd*=0.22 Torr cm and *d*=1.1 cm; c) Paschen curves for discharges in HFC-134a and HFO-1234yf at *d*=1.1 cm, at various reduced electric field (*E/N*) indicated by dashed lines [1Td=10^{-21} Vm^2 and 1Torr=133.32 Pa].

Our experimental studies on low-pressure DC discharges in these two freons, combined with optical measurements, enable the identification of elementary processes and provide a complete set of breakdown data. Gaining a better understanding of these processes through data collection and analysis is important for modeling gas plasmas, which can effectively reduce pollutant densities.

This research was supported by the Science Fund of the Republic of Serbia, Grant No. 7749560, project EGWIn. Zoran Lj. Petrović is grateful to the SASA project F155.

[1] S. Vizireanu, M.D. Ionita, G. Dinescu et al., *Plasma Processes Polym*. **9** (2012) 363-370.
[2] S. Guruvenket, G. R. S. Iyer et al., *Applied Surface Science*, **254**(18) (2008) 5722-5726.
[3] M. Abbrescia, *Nucl. Phys. B Proc. Suppl.* **293** (2008) 177–178.
[4] M. Koch and C. M. Franck, *IEEE Trans. Dielec. and Elect. Insula*. **22**(6) (2015) 3260-3268.
[5] J. Pereira-da-Silva, et al., *Jour. Amer. Soc. for Mass Spect.* **32**(6) (2021) 1459-1468.
[6] V.S.A. Bonfim, L. Baptista, D.A.B Oliveira, et al., *J. Mol. Model*. **28** (2022) 309.
[7] S. Živanov et al., *Eur. Phys. J. Appl. Phys*. **11** (2000) 59–69.
[8] Z. Lj. Petrović, B. M. Jelenković, A. V. Phelps, *Phys. Rev. Lett*. **68** (1992) 325.

Effects of argon pulsed injection on a surface-wave plasma column at low pressures

Veronica Orlandi[1,2,3], Marguerite Dion[1,4], Jules Brochier[1,4], Alexis Paillet[2], Myrtil L. Kahn[3], Luc Stafford[4], Richard Clergereaux[1(*)]

[1] *Laboratoire Plasma et Conversion d'Energie, Laplace, Université Paul Sabatier, Toulouse, France*

[2] *Spaceship FR, CNES, Toulouse, France*

[3] *Laboratoire de Chimie de Coordination, LCC, CNRS, Toulouse, France*

[4] *Département de Physique, Université de Montréal, Montréal, Québec*

(□) *richard.clergereaux@laplace.univ-tlse.fr*

A widely-spread method for the deposition of functional coating deals with aerosol assisted processes [1], [2], [3]. The procedure includes introducing micrometre-sized droplets into the gas phase directly within the downstream plasma process. In this type of injection, employing pulsed aerosol spraying into the plasma is preferred over continuous injection [4]. This arises from the fact that an equilibrium state is re-established between each pulse, facilitating a better control over the deposition process [5]. However, the effects of pulsed injection on the plasma behaviour are not further documented in the literature.

This work focuses on the study of the behaviour of a plasma under the pulsed injection of gas. For their versatility and stability, a surface-wave plasma is used [6],[7]. It consists in a high-frequency, self-sustained discharge, that allow the creation of stable plasma columns over a wide range of operating conditions. For example, it works in a stationary state on a wide range of pressure from a few mTorr to atmospheric pressure [8]. The aim of this work is to characterize the surface-wave plasma characteristics with a pulsed gas injection and lay the groundwork for studying pulsed-aerosol injection.

This study focuses on the results obtained from investigating an argon (Ar) plasma sustained by a 915 MHz electromagnetic wave launched by a Surfatron and propagating along a dielectric tube with a 30 mm diameter. An injection system operating in a pulsed mode from Kemstream (Montpellier, France) was connected to the upper limit of the dielectric tube, so that the gas was sprayed downstream directly into the plasma. The pulsed injection introduced a temporal evolution of pressure determined by the injection time and frequency. Here, we set these parameters to 4 ms Ar pulse at 0.1 Hz. The latter induced a relatively weak pressure increase of approximately 50 mTorr from the base pressure at 1 mTorr. To characterize the dynamic behaviour of the plasma column, rapid imaging (12000 fps) was performed using a FASTCAM APX RS Photron.

Fig. 1-left reports snapshots of the plasma along a pulsed injection: it can be seen that the plasma column varies along the pulsed gas injection period. In stationary state, the latter is directly controlled by the balance between the power injected and the collisions. For example, from 10^{-5} to 10^{-1} Torr, the electron density and, consequently, the plasma length increases as described in the literature [9].

However, in the pulsed mode, the response is more complex (Fig. 1-right): the length sharply decreases with the pulsed injection, just before increasing and finally going back to equilibrium. Considering the balance between power deposition and collisions, one would expect that this behaviour varies with the injection conditions. However, independently of the injection parameters, and consequently, the pressure drop, the plasma column follows the same behaviour.

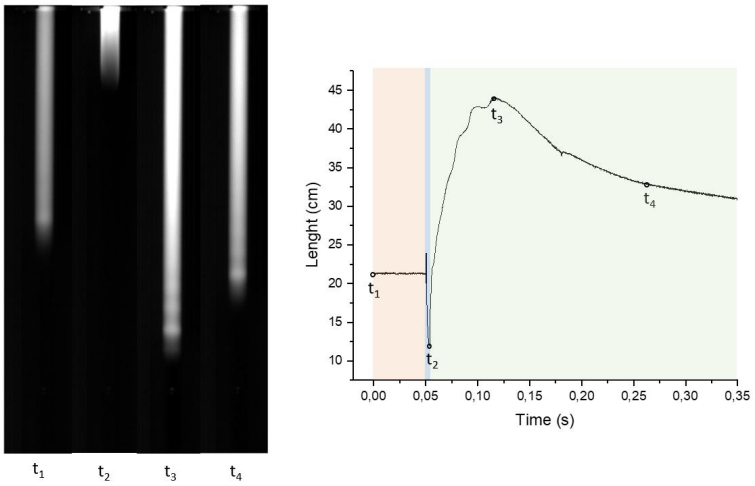

Fig. 1: Effects of argon pulsed injection along the pulse period with an injection time of 4 ms and frequency of 1 Hz – the discharge was obtained with 60 W. Rapid imaging enable to a) image the plasma column at different times along the pulse and b) plot its time evolution. The pulses are reported at different times t, in the the moments before (red), during (blue) and after the pulse (green).

As the pressure increase is relatively small, the behaviour of the plasma was hypothesized to be related to the pressure gradient or the gas flow rate rather than to the pressure difference. This hypothesis is confirmed by further experiments performed by introducing a diaphragm (2 mm in diameter) between the injection head and the plasma column to reduce the flow rate. With a head loss of 99.6%, the plasma column now varies directly with the gas pressure.

Hence, surface-wave plasmas sustained in the presence of pulsed gas injection are highly controlled by the gas flow rate. This can be attributed to the flow dynamics of the gas entering the tube and causing instabilities to the equilibrium of the self-sustained plasma.

[1] G. Carnide *et al.*, « Secured Nanosynthesis–Deposition Aerosol Process for Composite Thin Films Incorporating Highly Dispersed Nanoparticles », *Adv. Sci.*, vol. 10, n° 5, p. 2204929, févr. 2023, doi: 10.1002/advs.202204929.

[2] A. Stancampiano *et al.*, « Plasma and Aerosols: Challenges, Opportunities and Perspectives », *Appl. Sci.*, vol. 9, n° 18, p. 3861, sept. 2019, doi: 10.3390/app9183861.

[3] K. Takenaka et Y. Setsuhara, « Droplet-vaporization behavior during plasma-assisted mist chemical vapor deposition of zinc oxide films », *Plasma Sources Sci. Technol.*, vol. 28, n° 6, p. 065015, juin 2019, doi: 10.1088/1361-6595/ab2703.

[4] G. Carnide *et al.*, « Pulsed-aerosol assisted low-pressure plasma for thin film deposition », In Review, preprint, juin 2023. doi: 10.21203/rs.3.rs-3011018/v1.

[5] S. Chouteau, M. Mitronika, A. Goullet, M. Richard-Plouet, L. Stafford, et A. Granier, « Kinetics driving nanocomposite thin-film deposition in low-pressure misty plasma processes », *J. Phys. Appl. Phys.*, vol. 55, n° 50, p. 505303, déc. 2022, doi: 10.1088/1361-6463/ac9ac2.

[6] C. M. Ferreira et M. Moisan, Éd., *Microwave Discharges: Fundamentals and Applications*, vol. 302. in NATO ASI Series, vol. 302. Boston, MA: Springer US, 1993. doi: 10.1007/978-1-4899-1130-8.

[7] M. Moisan et J. Pelletier, *Physique des plasmas collisionnels: application aux decharges haute frequence*. Les Ulis, France: EDP Sciences, 2006.

[8] S. Boivin, X. Glad, J. P. Bœuf, et L. Stafford, « Analysis of the high-energy electron population in surface-wave plasma columns in presence of collisionless resonant absorption », *Plasma Sources Sci. Technol.*, vol. 27, n° 9, p. 095011, sept. 2018, doi: 10.1088/1361-6595/aadb61.

[9] M. Moisan *et al.*, « Properties and applications of surface wave produced plasmas », *Rev. Phys. Appliquée*, vol. 17, n° 11, p. 707-727, 1982, doi: 10.1051/rphysap:019820017011070700.

Ammonia production in a low- to mid-pressure microwave discharge

V. Wolf(*)[1], R. Friedl[1], U. Fantz[1,2]

[1] *AG Experimentelle Plasmaphysik, Universität Augsburg, 86135 Augsburg, Germany*
[2] *Max-Planck-Institut für Plasmaphysik, Boltzmannstraße 2, D-85748 Garching, Germany*
(*) vinzenz.wolf@physik.uni-augsburg.de

Ammonia (NH_3) is an important chemical, widely used for fertilizer production and in the chemical industry, also showing potential as a storage for energy from renewable sources and for hydrogen [1]. Recently, plasma-catalytic synthesis of NH_3 has attracted great interest as plasma reactors allow for intermittent operation and an efficient scale down as compared to the thermal-catalytic Haber-Bosch process, allowing for an easier use of electricity generated by renewable energy sources [2]. By providing ions, photons, radicals and metastable states, the plasma yields additional activation of the precursor molecules hydrogen and nitrogen, thereby lowering the activation energy needed for the generation of ammonia [3].

In order to link plasma parameters to the ammonia output, the experimental setup shown in Fig. 1 is used. A H_2 - N_2 mixture is introduced into a quartz glass tube with the length of $1\,\mathrm{m}$ and an inner diameter of $17\,\mathrm{mm}$. The setup is pumped by a rotary vane pump on the other side, leading to a directional gas flow at pressures between 10 - $1000\,\mathrm{Pa}$. Using a waveguide-based launcher (surfaguide) [4], a plasma column is generated in the quartz tube by a $2.45\,\mathrm{GHz}$ microwave generator with a power of $600\,\mathrm{W}$. Downstream of the plasma, a movable package made of stainless steel mesh containing a commercial Ruthenium catalyst ($2\,\mathrm{wt}\%$ Ru on γ-Al_2O_3 pellets) is located. Before measurements, the catalyst is pre-treated by in-situ heating to $620\,\mathrm{K}$ for two hours in a $20\,\mathrm{sccm}$ Ar gas stream in order to allow for sufficient desorption of adsorbates (water etc.) from the surface.
For detecting the composition of the output gas mixture, a residual gas analyzer (RGA) is located on the downstream side of the experiment. The system is calibrated using different calibration gases allowing to determine the concentrations of H_2, N_2, NH_3 and H_2O in the gas mixture. To further enhance accuracy for the determination of the NH_3 concentration ($m/z = 17$), the influence of the dissociative ionisation of H_2O molecules (cracking pattern, leading to a signal by OH^+ at $m/z = 17$) is also accounted for.
Optical emission spectroscopy (OES) is used to correlate the ammonia output and plasma parameters. For detecting the emission of the plasma in near UV to NIR range, a spectrometer with a FWHM $\Delta\lambda = 0.018\,\mathrm{nm}$ at a wavelength of $650\,\mathrm{nm}$ is used. By fitting the $\Delta\nu = -2$ sequence of the electronic $C^3\Pi_u \rightarrow B^3\Pi_g$ transition of molecular nitrogen at $360\,\mathrm{nm}$ - $380\,\mathrm{nm}$ using MassiveOES [5], the rotational and vibrational temperatures of the C state $T_{\mathrm{rot,C}}$ & $T_{\mathrm{vib,C}}$ can be determined. The Franck-Condon principle is utilized to translate the vibrational temperature to the ground state, $T_{\mathrm{vib,X}}$. The rotational temperature in the ground state ($T_{\mathrm{rot,X}}$) is obtained by considering the rotational constants of the ground and excited states [6].

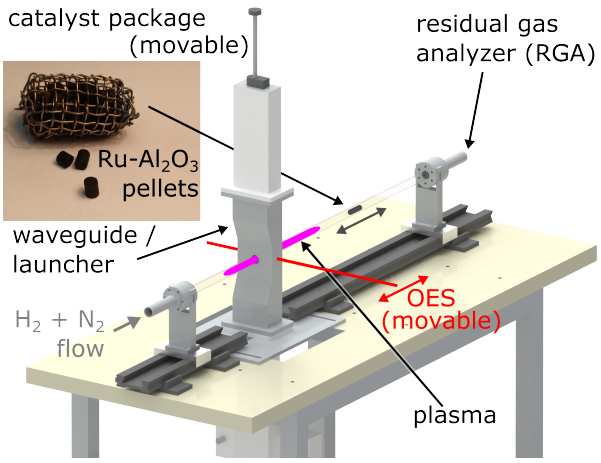

Fig. 1: Setup of the Surfaguide Gas Conversion Experiment (SurGE) with an image of the catalyst pellets used. Optical emission spectroscopy (OES) is available at a movable line of sight perpendicular to the quartz tube. A residual gas analyzer (RGA) is used to measure the gas composition.

The effects of pressure in the range of $15\,\mathrm{Pa}$ to $1000\,\mathrm{Pa}$, the hydrogen-nitrogen gas composition from $10\,\%$ to $90\,\%$ N_2, and the presence and position of the Ru-Al_2O_3 catalyst on ammonia production are investigated. Fig. 2 shows the concentration of H_2O and NH_3 obtained with the RGA over time can be seen for a microwave power of $600\,\mathrm{W}$, a pressure of $85\,\mathrm{Pa}$, a feed gas mixture of $\sim$50 % N_2 and $\sim$50 % H_2, and a fresh catalyst sample (after pre-treatment). Before the plasma is

switched on the catalyst package is far from the envisaged plasma region at the end of the quartz tube, and water, desorbed from the experiment walls and catalyst pellets, is dominant with a contribution of less than 0.5 ‰. As soon as the plasma is switched on at $t = 8\,\mathrm{min}$, NH_3 becomes dominant. After circa one minute plasma on time, the ammonia concentration reaches 7.5 ‰ due to ammonia generation in the bulk plasma and on the surface of the quartz tube. At the same time, water concentration reaches 1.8 ‰ due to desorption from surfaces heated by the plasma. At $t \approx 10\,\mathrm{min}$ (dashed line in the graph), the catalyst is moved to a position 3 cm behind the end of the plasma column. This leads to a sudden increase in the detected ammonia signal with the ammonia concentration reaching 15.0 ‰ at $t = 15\,\mathrm{min}$. As the catalyst is now heated by the plasma, also more water is desorbed. After reaching a maximum of 3.1 ‰ at 11 min, the H_2O amount slowly decreases again to 0.4 ‰ while the NH_3 concentration increases to a stable plateau of 17.5 ‰. This shows the importance of the presence of a catalyst, which in this case doubles the NH_3 concentration as obtained with the RGA. Apart from that, a time scale for an initial stabilization of the system of 15 to 20 min can be observed.

From measurements along the axis of the plasma column using OES and a thermocouple it could be derived that the gas temperature at the position of the catalyst package is in the range of $\sim$ 550 K. When moving the package into contact with the end of the plasma column, the temperature rises to $\sim$ 780 K and the ammonia yield decreases to 16.8 ‰. If the catalyst package is moved 3 cm further into the plasma, this leads to a shortening of the plasma column, whereas the catalyst is in range of even higher temperatures of $\sim$ 1100 K and the detected ammonia decreases to 10.0 ‰. This suggests a detrimental effect of high gas temperatures for ammonia generation, as is expected from literature [7].

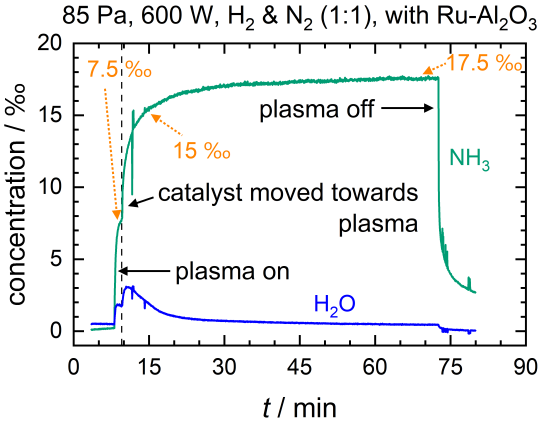

Fig. 2: NH_3 and H_2O concentration as determined with the RGA over time.

With a constant catalyst-plasma distance of 3 cm during an increase in pressure over two orders of magnitude, the ammonia concentration decreases by one order of magnitude. Simultaneously, $T_{\mathrm{vib,X}}$ and $T_{\mathrm{rot,X}}$ as determined by OES near the edge of the plasma column show a gradual equilibration, with $T_{\mathrm{rot,X}}$ increasing from $\sim$ 600 K to $\sim$ 1300 K and $T_{\mathrm{vib,X}}$ decreasing from 7000 K to 2500 K. A T_{vib} decrease goes along with decreased population of highly vibrationally excited N_2 molecules and hence, indicates less available activated precursor molecules and thus less NH_3 production. On the other hand a T_{rot} increase again indicates a possible contribution of increased NH_3 destruction. The next steps include further investigations with reference to plasma parameters like atomic densities (N & H), electron temperature and density, and the correlation between NH emission and NH_3 output as a measure of a precursor molecule.

[1] K. Rouwenhorst et al., *Renewable and Sustainable Energy Reviews* **114** (2019) 109339.
[2] A. Bogaerts et al., *ACS Energy Lett.* **3** (2018) 1013.
[3] A. Bogaerts et al., *J. Phys. D: Appl. Phys* **53** (2020) 443001.
[4] M. Moisan et al., *IEEE Transactions on Plasma Science* **12.3** (1984) 203.
[5] J. Vorac et al., *Rev. Sci. Instrum.* **90** (2019) 123102.
[6] P. Bruggeman et al., *Plasma Sources Sci. Technol.* **23** (2014) 023001.
[7] R. Antunes et al., *International Journal of Hydrogen Energy* **47** (2022) 14130.

Novel microwave plasma source for wastewater treatment and prevention of chemical pollution in the environment

T Bogdanov(*)[1], E Benova[2], P Marinova[3]

[1] *Faculty of Medicine, Medical University—Sofia, "St. Georgi Sofiyski" St. No. 1, 1431 Sofia, Bulgaria*

[2] *Clean & Circle CoC, Sofia University, 8 Dragan Tsankov Blvd.., 1164 Sofia, Bulgaria*

[3] *Faculty of Forest Industry, University of Forestry, 10 Kliment Ohridski Blvd., 1797 Sofia, Bulgaria*

(*) t.g.bogdanov@gmail.com

This paper introduces a pilot investigation into a novel microwave plasma source, the Ar plasma torch at 2.45 GHz, designed for wastewater treatment and the mitigation of chemical pollution, with a primary focus on combatting the proliferation of per- and poly-fluoroalkyl substances (PFAS) in the environment. The utilization of plasma torch technology originates from its exceptional capacity to generate an array of reactive species including charged particles, hydrogen, and oxygen radicals, coupled with the emission of ultraviolet radiation and the establishment of a microwave field. These unique characteristics render plasma torches highly effective in degrading organic contaminants present in wastewater.

The research methodology encompasses a comprehensive characterization of the plasma torch system, particularly identifying and optimizing key operational parameters such as microwave power and gas flow rate. Through systematic experimentation, the plasma torch's performance in producing reactive species crucial for pollutant degradation will be rigorously evaluated. Furthermore, the study aims to elucidate the mechanisms underlying the interaction between the plasma torch and PFAS compounds, shedding light on the efficacy of this innovative technology in mitigating PFAS contamination. The presented plasma source is based on Utility model registration with certificate № 4602/2023 from the Patent Office of Republic of Bulgaria for „DEVICE FOR CREATING LOW-TEMPERATURE PLASMA TORCH". A diagram of the plasma source is presented in Fig. 1.

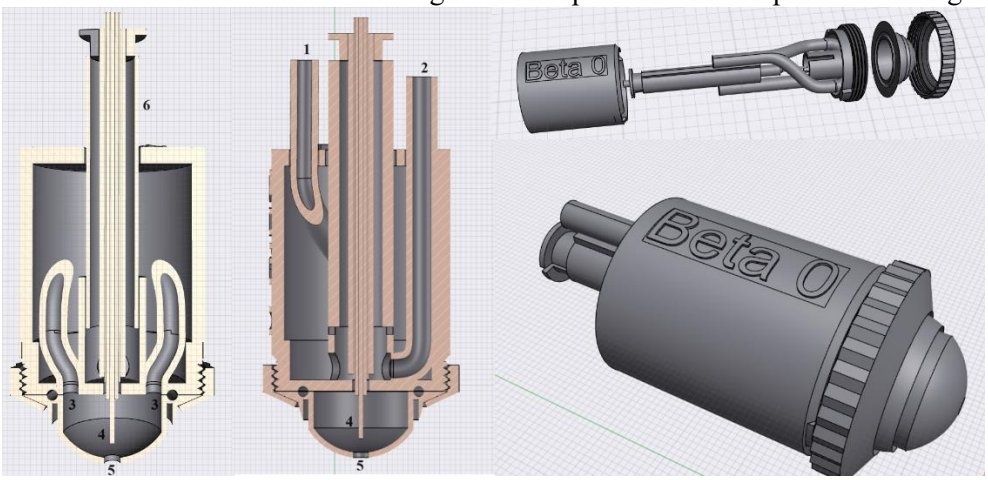

Fig. 1. Diagram of the plasma source in two projections, assembled and axially disassembled. 1 – working gas input; 2 – cooling gas input; 3 – working gas output; 4 – antenna; 5 – plasma torch gap; 6 – antenna guide.

The device is designed to operate efficiently with either argon (Ar) or other inert gases, as well as gas mixtures, offering versatility in its application for wastewater treatment. To enhance the device's performance and stability, additional cooling of the antenna has been integrated, particularly crucial for ensuring reliable operation even at high input microwave power levels. Moreover, the flexibility of the device allows for the adjustment of the antenna depth, enabling the creation of optimal conditions to

align the plasma torch with the radiated wave power while minimizing reflected wave power, thereby enhancing overall efficiency.

Furthermore, this research endeavors to conduct a systematic investigation into fundamental plasma torch characteristics. Parameters such as torch length and temperature will be meticulously studied across varying input wave power levels, gas velocities, and antenna positions. This comprehensive analysis aims to provide insights into the intricate interplay between these parameters and their impact on plasma torch performance. By elucidating these relationships, the study seeks to optimize the device's operational parameters to maximize its efficacy in wastewater treatment and PFAS decontamination applications.

The study will comprehensively present the results of wastewater treatment alongside the investigation into plasma characteristics. This integrated approach allows for a holistic understanding of the plasma torch's performance in both pollutant degradation and fundamental plasma torch behavior. By juxtaposing the outcomes of wastewater treatment with the corresponding plasma characteristics studies, a comprehensive analysis of the device's efficacy and operational parameters can be achieved. This unified presentation ensures that insights gained from plasma torch characterization directly inform and enhance the efficiency of wastewater treatment processes, thereby advancing the development of sustainable solutions for environmental remediation. Images from the treatment process are presented in Fig. 2, providing visual context to complement the analytical findings.

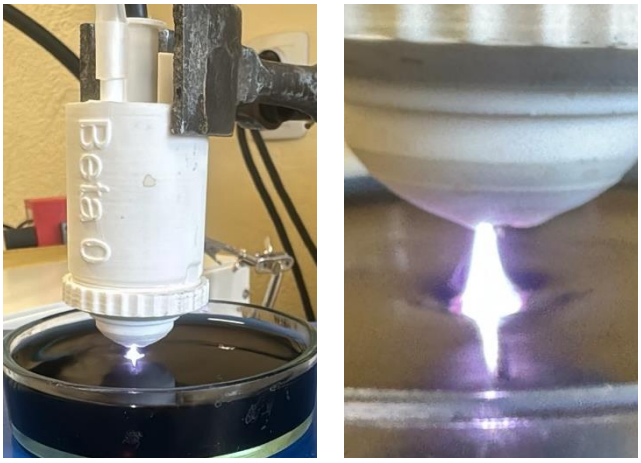

` Fig. 2. Operating plasma source treating wastewater

The outcomes of this research hold immense potential in advancing sustainable wastewater treatment strategies, especially in addressing the pressing challenge of PFAS pollution. By harnessing the capabilities of plasma torch technology, this study paves the way for the development of efficient and environmentally friendly solutions for wastewater treatment and chemical pollution prevention based on plasma devices, contributing to the preservation of water quality and ecosystem health.

Acknowledgement:

This work is supported by the PROMISCES (Preventing Recalcitrant Organic Mobile Industrial chemicalS for Circular Economy in the soil-sediment-water System) project which has received funding from the European Union's Horizon 2020 research and innovation program under Grant Agreement No 101036449.

Iron oxide reduction in a high-performance microwave argon-hydrogen plasma

J. Thiel(*), S. Kreuznacht, M. Böke, A. von Keudell

Experimental Physics II - Reactive Plasmas, Ruhr University Bochum, 44801 Bochum, Germany
(*) jonas.thiel-n4w@rub.de

Global steel production accounts for a substantial part of man-made CO_2 emissions. The utilization of green hydrogen in future industry processes has the potential to render iron ore reduction nearly climate-neutral [1, 2]. Microwave-sustained thermal hydrogen plasmas can be employed for iron oxide reduction, with the end products being H_2O and Fe. For instance, the advantages are faster reduction rates and lower energy consumption than existing methods. Using plasmas also enables the production of various reactive species like atomic hydrogen, hydrogen ions, and excited H_2 molecules. The effects of especially vibrationally-excited H_2 molecules and hydrogen ions on the reduction process at the interface between the plasma and an iron/iron oxide surface have already been investigated in a global equilibrium model [3]. Further experiments focusing on microscopic process parameters and non-equilibrium surfaces processed during the reduction are not sufficiently addressed. This study is intended to follow up on these research questions and to investigate the interface between iron oxide and hydrogen.

Therefore, an argon-hydrogen microwave plasma is used for iron ore reduction by either injecting an iron oxide powder into the gas flow or exposing defined solid samples to the plasma. The samples primarily consist of hematite (Fe_2O_3). The main reaction equation is then:

$$Fe_2O_3 + 3H_2 \longrightarrow 2Fe + 3H_2O.$$

The plasma is generated in a resonator and is sustained by a 6 kW-capable microwave source. The combination of an axial as well as two tangential gas inflows generates a swirl-like gas flow pattern, which stabilizes the plasma on the central axis and ensures steep radial temperature gradients to protect the wall of the discharge tube. Furthermore, this swirl flow shall prevent the iron oxide particles from adhering to the tube's surface. Without the presence of the swirl flow, the plasma would burn directly on the surface of the tube. Below the resonator, the plasma subsequently enters a water-cooled double-walled reactor chamber where solid samples can be treated on a substrate holder by the plasma-produced reactive species. Alternatively, iron oxide particles can be added to the axial gas flow. A specially designed particle feeder is employed to ensure defined admixtures. Fig. 1 shows a schematic of the experimental setup for the two different operation modes.

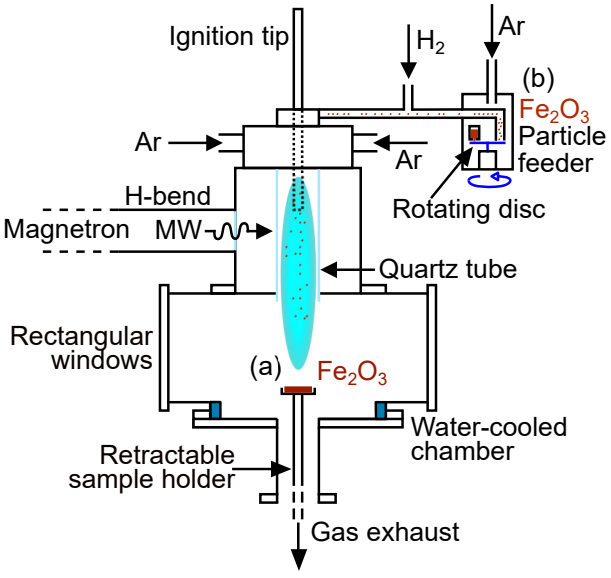

Fig. 1: Schematic of the experimental setup of the microwave discharge for the two operation modes: (a) – using a defined solid sample of hematite (Fe_2O_3) and (b) – injecting a defined amount of hematite particles into the gas flow.

A design study is performed to view the motion, residence time, and location of melting/evaporation of injected particles in the presence of the swirl flow for the microwave discharge compared with a cylindrical ICP discharge. Particle size, gas flow, and temperature profiles are being varied. The degree of particle addition into the gas flow continuously transforms the plasma into a metal plasma, making optical diagnostics, especially laser diagnostics, rather challenging due to the strong scattering background.

Thus, for in-situ investigations, optical emission spectroscopy is used to examine the influence of metal particles on the properties of the plasma. Furthermore, a major focus lies in determining the gas temperature, as it is a crucial parameter for both analytical considerations and simulations of physical or chemical reactions. As ex-situ diagnostics, XRD depth profiling, XPS, and SEM are employed to characterize the interaction surface between the hematite sample and the hydrogen and quantify the degree of reduction.

A similar setup using a high-performance microwave discharge is already operated for hydrogen production via plasma methane pyrolysis [4]. There, optical emission spectroscopy has been conducted to measure the emission of black body radiation from hot carbon particles and of the dicarbon Swan bands. The evaluation revealed a gas temperature of around $4.500\,\mathrm{K}$ in the center below the resonator, as seen in Fig. 2, where spatial-resolved profiles of the gas temperature are depicted [5].

In conclusion, this study investigates the microscopic interface between iron oxide samples and reactive hydrogen species produced by a high-performance microwave plasma by applying spectroscopic and material-characterizing diagnostics. Thereby, the treatment of solid samples as well as of powders of hematite is considered. A major focus lies in determining the gas temperature as a crucial variable for the iron ore reduction process.

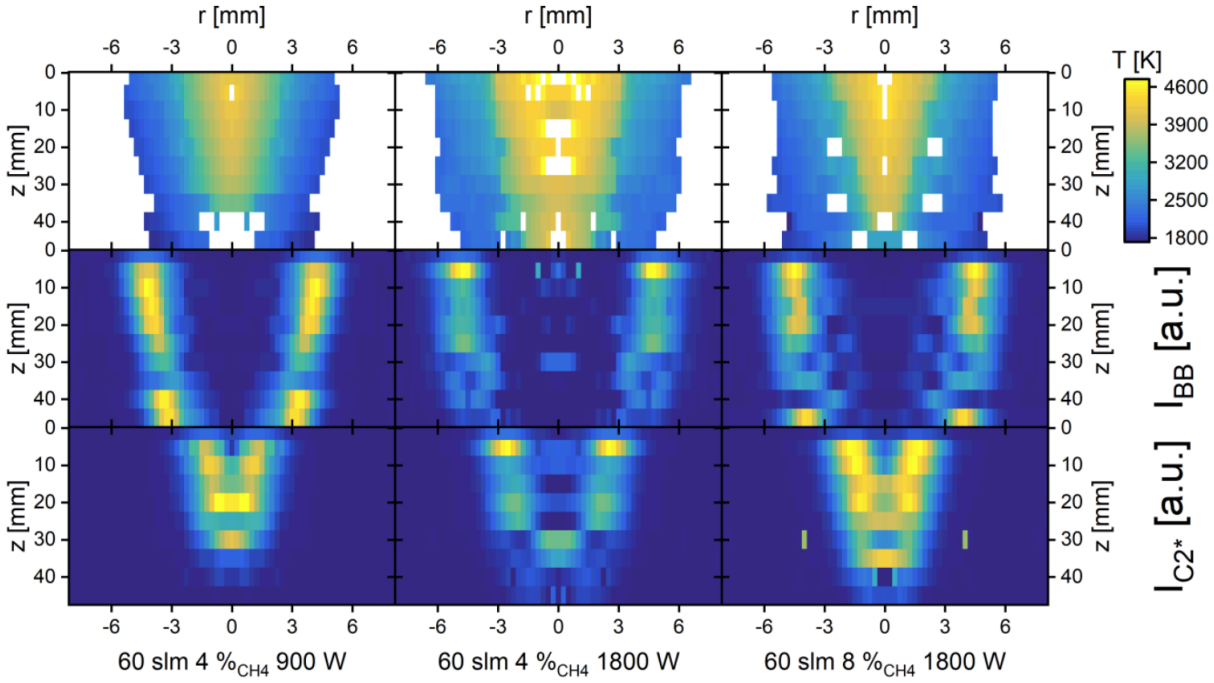

Fig. 2: Space resolved profiles of the gas temperature (T), the emission of the black body radiation (I_{BB}) and the emission of the dicarbon Swan bands (I_{C2^*}) as a function of the radial and axial position for three different sets of operating parameters in an Ar/CH_4 microwave plasma. Retrieved from [5].

Acknowledgment

This project is supported by the International Max Planck Research School for Sustainable Metallurgy.

[1] S. Kumar, Z. Xiong *et al.*, *Chem. Eng. J.* **472** (2023) 145025.
[2] P. Rajput *et al.*, *Ironmak. Steelmak.* **41** (2015) 721–731.
[3] K. Sabat and A. Murphy, *Metall Mater Trans B* **48** (2017) 1561–1594.
[4] S. Kreuznacht *et al.*, *Plasma Processes Polym.* **20** (2022) 202200132.
[5] S. Kreuznacht *et al.*, *ISPC 25 – Conf. Proc.*, Kyoto (2023), 4-P-303.

Investigation of emission spectra of atmospheric CO_2 plasmas sustained with microwave pulsation in a high Q resonator

Lucas Silberer(*)[1], Sergey Soldatov[1], Guido Link[1], Alexander Navarrete[3], Roland Dittmeyer[3], John Jelonnek[1,2]

Karlsruhe Institute of Technology (KIT), [1]IHM, [2]IHE, [3]IMVT, 76131, Karlsruhe, Germany

(*) lucas.silberer@kit.edu

With rapidly growing renewable energy capacity from seasonal fluctuating resources like wind and solar energy, the demand for technologies to store the surplus of renewable energy is increasing [1]. Power to liquid technologies can be used to convert surplus renewable energy into liquid fuels. The extended storage time and the high energy density per volume surpasses alternative storage solutions like flywheels, batteries or comppressed air storage [2]. Liquid fuels can be produced from syngas by use of the Fischer-Tropsch process. The use of green hydrogen and CO that was produced by reduction of CO_2 (eq. 1), captured from industrial processes or from air will finaly result in a carbon neutral liquid fuel production process [3].

$$CO_2(g) \rightarrow CO(g) + 1/2\ O_2 + 283\ kJ/mol, \quad (1)$$

For this reduction process microwave plasmas have shown the highest conversion efficiency (over 80 %) at low pressure conditions [4]. Atmospheric pressure plasma systems are much more suitable for industrial applications, however, the efficiency of the process decreases with increasing presure beacause of excessive heating of the reaction gas. At atmospheric pressure, the mean gas temperature can be lowered by modulating the supplied microwave power with times shorter than the residence time of the gas in the reactor. This was demonstrated in experiments with a coacial plasma torch [5]. Moreover, it was experimentally proven that after plasma ignition in the coaxial torch within the first two microseconds a transient non-equilibrium regime with $T_{vib}/T_{rot} \sim 2$ can be reached. This was desmonstrated to be beneficial for the CO_2 conversion and efficiency. Because of the limited power handling capabilities (< 300 W @ 2.45 GHz) of the plasma torch, the approach of microwave power modulation was also investigated in a surface wave reactor called Surfaguide, which can be operated with a power of several kilowatts [6]. Yet as compared with continuous wave operation, for the investigated pulse regimes only limited improvement in conversion and efficiency of the CO_2 splitting process was measured. For a given maximum peak power of 4 kW at 2.45 GHz the plasma inside the reactor destinguished for power off times above a certain threshold time. Therefore the electric field strength was too low to re-ignite the plasma in the Surfaguide with the next pulse. Thus to sustain the plasma with microwave modulation in the Surfaguide, the intervals between the microwave pulses had to kept below 11 µs at 4 kW microwave power. Through the concentration of electromagnetic energy in a high Q microwave resonator a surface-wave plasma re-igntion regime can be enabled. To investigate that, a reactor based on a TM_{01} cylindrical resonator with a high quality factor (Q = 2500) was designed and built to operate with microwave power modulations in a broad parameter range from 200 ns to 400 ms. The microwave cavity (see Fig. 1) is designed to ignite a CO_2 plasma at atmospheric pressure with a microwave power of 4 kW. With high resolution optical emission spectroscopy the emission spectra of pulsed CO_2 plasmas in the cavity were recorded. The latest results will be presented a the conference and carfully compared with the results reported for the pulsed CO_2 plasma sustained in the coaxial plasma torch.

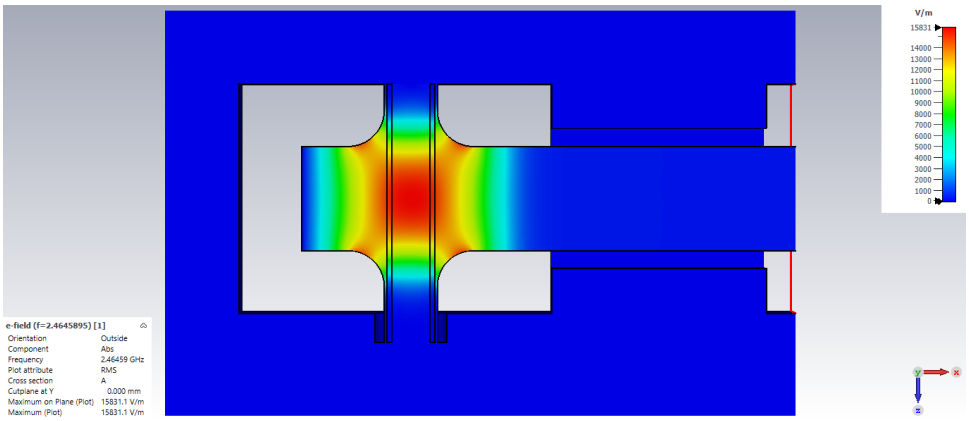

Fig. 1: Simulated electric field (RMS) in the cross-section of the self-igniting microwave cavity. CST Studio Suite was used for the simulation. The microwave input port is on the right edge and the reaction gas travels through the center of the resonator guided by a quarz tube in the maximum electric field zone.

[1] IEA (2019), More of a good thing – is surplus renewable electricity an opportunity for early decarbonisation? *IEA*, Paris. https://www.iea.org/commentaries/more-of-a-good-thing-is-surplus-renewable-electricity-an-opportunity-for-early-decarbonisation

[2] T. Schaaf, J. Grünig, M. R. Schuster, T. Rothenfluh, A. Orth, Methanation of CO_2 - storage of renewable energy in a gas distribution system. *Energ Sustain Soc* **4** (2014) 2. https://doi.org/10.1186/s13705-014-0029-1

[3] A. Navarrete, G. Centi, A. Bogaerts, A. Martin, A. York, G. D. Stefanidis, Harvesting Renewable Energy for Carbon Dioxide Catalysis. *Energy Technol-Ger* **5** (2017) 796. https://doi.org/10.1002/ente.201600609

[4] R. Snoeckx, A. Bogaerts, Plasma technology - a novel solution for CO2 conversion? *Chem. Soc. Rev.* **46** (2017) 5805, https://doi.org/10.1039/C6CS00066E

[5]S. Soldatov, et al, ACS Energy Lett. 2021, 6, 124−130. https://doi.org/10.1021/acsenergylett.0c01983

[6] S. Soldatov , L. Silberer, G. Link , A. Navarrete, R. Dittmeyer, J. Jellonnek (23.05.2023). CO2 conversion in a pulsed surfaguide microwave plasma at atmospheric pressurel [conference proceedings]. ISPC 25, Kyoto, Japan. https://www.ispc-conference.org/ispcproc/ispc25/pdf/2-P-213.pdf

Optimization of gas quenching of atmospheric CO_2-plasma sustained in microwave reactor by application of water-cooled nozzles

Sergey Soldatov(*)[1], Lucas Silberer[1], Guido Link[1], Alexander Navarrete[3], Roland Dittmeyer[3], John Jelonnek[1, 2]

Karlsruhe Institute of Technology (KIT), [1]IHM, [2]IHE, [3]IMVT, 76131, Karlsruhe, Germany

(*) sergey.soldatov@kit.edu

In the last decade, the increasing application of renewable energy sources, particularly based on wind and solar power, enabled the gradual replacement of fossil fuels that is necessary for the decarbonization of industry. At the same time, the inherent intermittency of these sources urges technologies to store the surplus of renewable electricity [1]. One of the most advanced technologies is the synthesis of liquid fuels, which thanks to its high energy density and extended storage time, surpasses alternatives like flywheels, batteries, or compressed air storage [2]. A particularly promising approach involves the endothermic reduction of carbon dioxide (see eq. 1) from industrial emissions, which not only serves to energy storage but can also contribute to the mitigation of greenhouse gas [3].

$$CO_2(g) \rightarrow CO(g) + 1/2\ O_2 + 283\ kJ/mol, \quad (1)$$

The characteristic times of natural fluctuations of wind and solar energy can scale down to several minutes and to follow these fluctuations the conventional chemical reactors are often too slow. Plasma reactors allow to start/stop the gas activation process within seconds and is therefore well suited for the intermittent availability of electricity [4]. So far, plasma reactors driven by microwave energy have demonstrated the highest efficiency (over 80%) for the conversion of CO_2 to CO at low pressure conditions [5]. In general, atmospheric systems are more robust and cheaper and therefore are more appropriate for future industrial applications as compared with vacuum ones. At the same time, the efficiency of the process gets worse when the pressure increases that urges the temperature quenching in plasma afterglow. A promising approach for quenching is the application of a water-cooled metallic nozzle in the afterglow region which serves both for effective gas cross-mixing and gas cooling [6]. Very earlier experiments in 1980s with supersonic acceleration of gas in the nozzle at vacuum conditions have shown an energy efficiency up to 90% [7]. In last 5-7 years, the nozzle configurations again have drawn new attention, particularly for atmospheric CO_2 plasmas sustained with microwave [8-11]. It was shown that fast quenching with water cooled nozzle promotes both efficiency and conversion [9-11]. Despite of very promising results, the authors claim that the design of quenching system is far from optimum and there is a room for optimization [11].

In present work, we report on the optimization of gas quenching in the afterglow of atmospheric CO_2-plasma sustained in a Surfaguide microwave reactor by means of water-cooled nozzle constructions. In COMSOL Multiphysics, the flow dynamics of a gas mixture is modeled, whose effective heat capacity, heat conductivity, viscosity and density is a result of contribution of different gas species for a given temperature. The gas supplied through a helical injector flows through the reactor tube which included an effective heat source (< 1.6 kW) and further through the nozzle construction. To optimize the nozzle the taper angle (and correspondingly its length) as well as the nozzle diameter and nozzle length were varied (see Fig. 1 left). For practical reasons, two nozzles were fabricated for validation in the experiment: with a taper angle of 45° and 78° that corresponds to a difference in a gas-to-metal heat flux of a factor of 3.3. Experiments have demonstrated that the improvement through the application of nozzles compared to the no-nozzle reference case is of a factor of 4 and 2.5 for conversion and efficiency, respectively. As for the difference between two nozzle configurations, the “short” nozzle (45°) has shown some better performance as compared with the “long” (78°) nozzle (see Fig. 1 right).

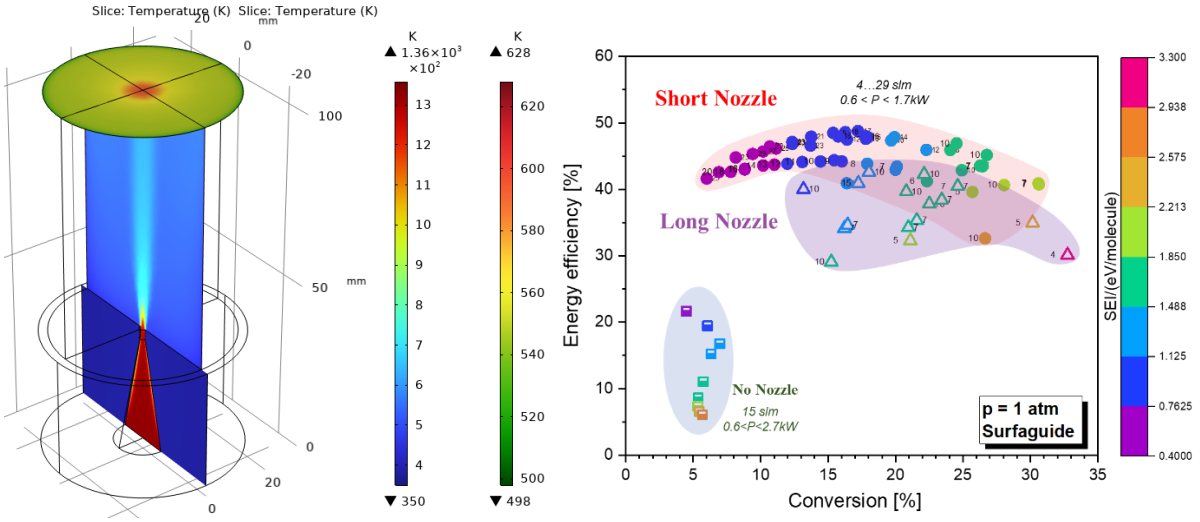

Fig. 1: (**left**) Simulated gas temperature distribution for in- and after-nozzle domains. Left scale represents the temperature in axial cut plane, and right scale corresponds to temperature in cross plane which is 70 mm away from nozzle end.
(**right**) Energy efficiency vs. conversion for no-nozzle configuration (15 slm, power scan) against the two nozzle geometries: 45° („short“) and 78° („long“) where both gas flow rate and power are varied. SEI is color coded.

[1] IEA (2019), More of a good thing – is surplus renewable electricity an opportunity for early decarbonisation? *IEA*, Paris https://www.iea.org/commentaries/more-of-a-good-thing-is-surplus-renewable-electricity-an-opportunity-for-early-decarbonisation
[2] T. Schaaf, J. Grünig, M. R. Schuster, T. Rothenfluh, A. Orth, Methanation of CO_2 - storage of renewable energy in a gas distribution system. *Energ Sustain Soc* **4** (2014) 2. https://doi.org/10.1186/s13705-014-0029-1
[3] A. Navarrete, G. Centi, A. Bogaerts, A. Martin, A. York, G. D. Stefanidis, Harvesting Renewable Energy for Carbon Dioxide Catalysis. *Energy Technol-Ger* **5** (2017) 796. https://doi.org/10.1002/ente.201600609
[4] J. A. Martens, A. Bogaerts, N. De Kimpe, P. A. Jacobs, G.B. Marin, K. Rabaey, M. Saeys, S. Verhelst, The Chemical Route to a Carbon Dioxide Neutral World. *ChemSusChem* **10** (2017) 1039. DOI: 10.1002/cssc.201601051
[5] R. Snoeckx, A. Bogaerts, Plasma technology - a novel solution for CO2 conversion? *Chem. Soc. Rev.* **46** (2017) 5805, https://doi.org/10.1039/C6CS00066E
[6] S. Van Alphen, A. Hecimovic, Ch. K. Kiefer, U. Fantz, R. Snyders, A. Bogaerts, Modelling post-plasma quenching nozzles for improving the performance of CO2 microwave plasmas, *Chemical Engineering Journal* **462** (2023) 142217, https://doi.org/10.1016/j.cej.2023.142217
[7] R. I. Asisov, A. K. Vakar, V. K. Jivotov, M. F. Krotov, O. A. Zinoviev, B. V. Potapkin, A. A. Rusanov, V. D. Rusanov, A. A. Fridman, Non-Equilibrium Plasma-Chemical Process of CO2 Decomposition in a Supersonic Microwave Discharge, *Proc. USSR Acad. Sci.* **271** (1983) 94–98
[8] V. Vermeiren and A. Bogaerts, Supersonic Microwave Plasma: Potential and Limitations for Energy-Efficient CO2 Conversion, *The Journal of Physical Chemistry C* **122(45)** (2018) 25869-25881, DOI: 10.1021/acs.jpcc.8b08498
[9] E.R. Mercer et al, Post-plasma quenching to improve conversion and energy efficiency in a CO2 microwave plasma, *Fuel* **334** (2023) 126734, https://doi.org/10.1016/j.fuel.2022.126734
[10] A. Hecimovic, F. A. D'Isa, E. Carbone, U. Fantz, Enhancement of CO2 conversion in microwave plasmas using a nozzle in the effluent, *Journal of CO2 Utilization* **57** (2022) 101870, https://doi.org/10.1016/j.jcou.2021.101870
[11] A. Hecimovic, C. K. Kiefer, A. Meindl, R. Antunes, U. Fantz, Fast gas quenching of microwave plasma effluent for enhanced CO2 conversion, *Journal of CO2 Utilization* **71** (2023) 102473, https://doi.org/10.1016/j.jcou.2023.102473

Reaction of lithium-6 with thermal neutrons as a source of nuclear-induced plasmas of gas mixtures

M. Khasenov(*)[1], K. Samarkhanov[1,2], E. Batyrbekov[3], Yu. Gordienko[1], Yu. Ponkratov[1], V. Bochkov[1], E. Saparbek[1], A. Sluyanov[1], S. Tolmachev[1]

[1] Institute of Atomic Energy Branch of the National Nuclear Center of the Republic of Kazakhstan, Kurchatov 071100, Kazakhstan
[2] Sarsen Amanzholov East Kazakhstan University, Oskemen 070000, Kazakhstan
[3] National Nuclear Center of the Republic of Kazakhstan, Kurchatov 071100, Kazakhstan
(*) mendykhan845@gmail.com

The study of optical (laser and spontaneous) radiation of nuclear-excited plasma is of interest for the development of a method of energy output from a nuclear reactor, as well as for the control and regulating of nuclear reactor parameters [1]. Direct pumping of active media generally performed by nuclear reaction products such as $^{3}He(n,p)T$, $^{10}B(n,\alpha)^{7}Li$, $^{235}U(n,f)F$, or others using thermal neutrons from a nuclear reactor. The laser's active medium needs to include ^{235}U, ^{3}He, or ^{10}B, or a combination of these isotopes applied to the laser chamber's walls. The laser chamber's size and the nuclear reaction products' path length in the gas mixture define the degree of spatial inhomogeneity while utilizing a surface pump source. The use of lithium-6 as a surface source of excitation of the gas medium, due to the long path length of tritium nuclei in the gas (see Table 1), makes it possible to excite large volumes of gas in comparison with the use of uranium-235 or boron-10. Table 1 shows the path length for helium and argon gas, which most often serve as buffer gases in laser mixtures.

Isotope, isotopic distribution	Reaction cross section for thermal neutrons, barns	Products of reaction	Kinetic energy of reaction products, MeV	Path length of the products at pressure of 1 atm, cm [1]	
				He	Ar
^{10}B, 19.6%	3800	^{4}He	1.5	4.1	0.8
		^{7}Li	0.85	2.6	0.53
^{235}U, 0.72%	580	Light fission fragments	99	7.3	2.5
		Heavy fission fragments	68	6.2	2.2
^{6}Li, 7.5%	945	^{4}He	2.05	6.3 [*]	1.2 [*]
		^{3}H	2.73	35.0 [*]	6.7 [*]

* - this work

Table 1: Particle path length in helium and argon.

Studies of luminescence of gas mixtures under excitation by following nuclear reaction products:

$$^{6}Li + n \rightarrow {}^{4}He + {}^{3}H \quad (1)$$

were performed at the IVG.1M nuclear reactor with thermal neutron flux density up to $3 \cdot 10^{14}$ m/cm^{2}s. In the first experiments, lithium was applied by wetting liquid lithium with a layer thickness of about 50 μm on the surface of the chamber, and later capillary-porous structures (CPS) were used. The irradiation chamber was filled with the investigated gas mixture and loaded into the central experimental channel of the nuclear reactor. The emission spectra were recorded using a compact spectrometer QE65Pro (Ocean Optics). The results of studies of noble gas luminescence within a chamber with a lithium layer are given in [2, 3].

The present paper presents the results of investigations of the emission of argon-nitrogen mixture. The pressure at 300 K was 91 kPa for Ar and 2.4 kPa for N_2, and the thermal neutron flux density was $2.9 \cdot 10^{13}$ n/cm^{2}s. The lines of atomic argon and the bands of the second positive nitrogen system predominate in the spectra at 300-400 K. Upon increasing the temperature of the lithium layer up to ≈ 520 K, the lithium lines appear in the spectra, as well as the lines of sodium and potassium impurities (Figure 1).

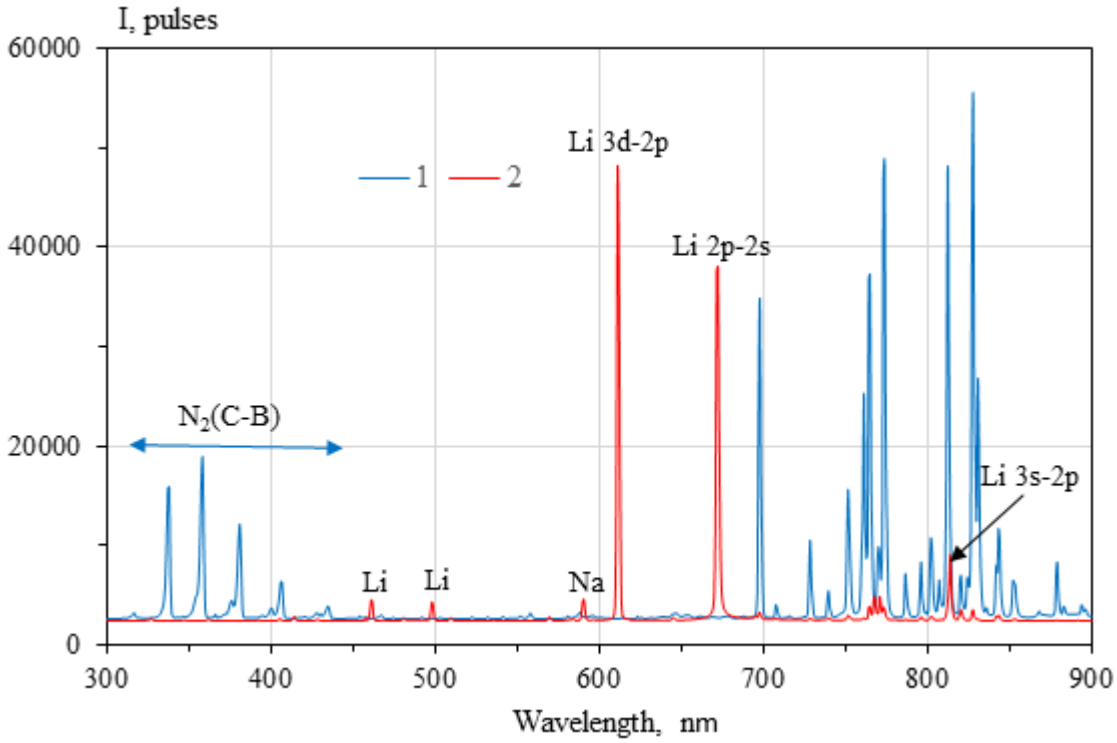

Fig. 1: Emission spectra of Ar-N_2 mixture at 375 K (1) and 720 K (2). The integration time of the spectrometer was 300 ms (1) and 10 ms (2).

The rapid increase in luminescence intensity at higher temperatures is well approximated by the following expression:

$$I \sim \exp(-A/kT) \tag{2}$$

where A - activation energy of this process. For the 610.4 nm lithium line, a value of A=1.68 eV was obtained. These values agree well with the lithium vaporization (sublimation) energy equal to 1.63 eV (156.9 kJ/mol) [4]). Since the saturated vapor pressure of lithium is low ($4 \cdot 10^{-6}$ Pa at 520 K and 0.08 Pa at 720 K), the emission process cannot be associated with the usual thermal evaporation of lithium. The lithium vapor density different from the saturated vapor density is formed in the gas excitation area by the nuclear reaction products.

Acknowledgments: This research is funded by the Science Committee of the Ministry of Science and Higher Education of the Republic of Kazakhstan (Grant No. AP 23490367).

References

[1] S.P. Mel'nikov et al., *Lasers with Nuclear Pumping*. Springer, 2015, 455 p.
[2] G. A. Batyrbekov et al., *J. of Luminescence* **220** (2020) 116973.
[3] Yu. N. Gordienko et al., *Laser and Particle Beams* **37** (2019) 18-24.
[4] D. Henriquesa et al., *ECS Transactions* **46** (1) (2013) 303-312.

Synthesis of metal/polymer nanocomposite thin film through interaction of a gold salt solution aerosol with a Dielectric Barrier Discharge

Elène Bizeray[1], Antoine Belinger[1], Simon Dap[1], Fiorenza Fanelli[2], Nicolas Naudé[1]

[1] *LAPLACE, Université de Toulouse, CNRS, INPT, UPS, Toulouse, France*

[2] *National Research Council (CNR), Institute of Nanotechnology (NANOTEC), Bari, Italy*

(*) nicolas.naude@laplace.univ-tlse.fr

Low-temperature atmospheric pressure plasma technologies offer unique opportunities for the synthesis of hybrid nanocomposite thin films consisting of inorganic nanoparticles (NPs) embedded into an organic matrix. Some studies have shown that it is possible to deposit them by combining plasma processes with an aerosol of either a dispersion of preformed gold NPs or a solution of a gold precursor in a suitable solvent. [1] . In our work, as suggested in a previous publication [2], a dielectric barrier discharge (DBD) in nitrogen is associated with an aerosol of solution of gold salt (tetrachloroauric(III) acid trihydrate, $HAuCl_4 \cdot 3H_2O$) in a polymerizable solvent (isopropyl alcohol). The process is schematically shown in Fig 1. The novelty of this process mainly resides in the fact that it enables the synthesis of the NC thin films in a single step, avoiding the direct handling of NPs.

Fig. 1: Overview of the nanocomposite thin film synthesis process

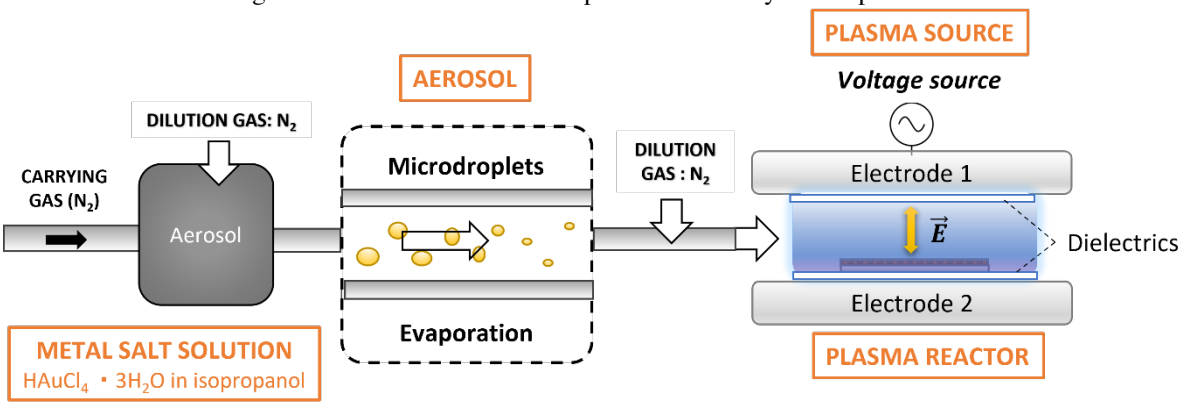

For synthesis of nanocomposite layers with a DBD at atmospheric pressure, a dual-frequency excitation is typically used to control independently the growth of the matrix and the transport of the nanoparticles [2,3]. In our study, a high frequency excitation (above 10 kHz) is necessary for the gold salt reduction to form gold NPs and the organic matrix growth, while a low-frequency excitation (typically below 1 kHz) is needed to avoid nanoparticles being trapped in the gas gap and, therefore, to favor their transport to the surface of the substrate.

Preliminary results have shown that we are able to synthesize nanocomposite thin films with the inclusion of gold nanoparticles in an organic matrix, deriving from plasma polymerization of isopropyl alcohol. Chemical composition, morphology and optical properties of the resulting nanocomposite layers have been investigated using various characterization techniques, such as Fourier-transform infrared spectroscopy, X-ray photoelectron spectroscopy, scanning electron microscopy and UV-visible absorption spectroscopy (Fig. 2).

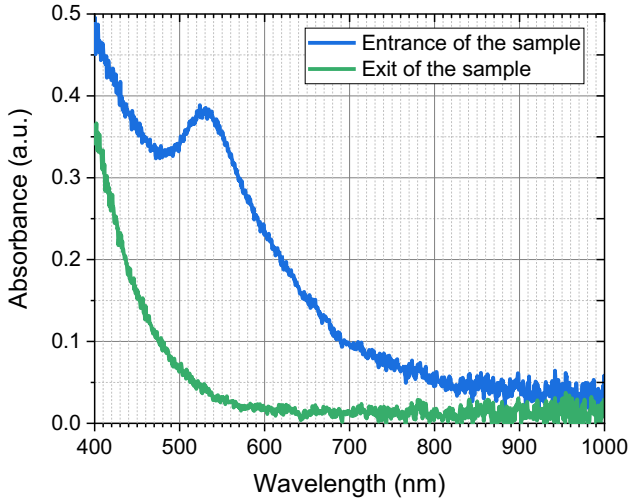

Fig. 2: UV-visible spectroscopy spectrum of a nanocomposite coating

Overall, these results provide new insights into the possibility of using a single-step aerosol-assisted plasma process based on a dielectric barrier discharge at atmospheric pressure to deposit hybrid nanocomposite coatings.

[1] A. Uricchio and F. Fanelli, Processes 9, 2069 (2021).
[2] E. Nadal *et al*., Nanotechnology 32, 175601 (2021).
[3] P. Brunet *et al*., Langmuir 34, 1865 (2018).

Characterization and optimization of 3-pin atmospheric pressure plasma jet system for water treatment

N Škoro(*)[1], O. Jovanović[1], G. Malović[1], N. Puač[1]

[1] *Institute of Physics, University of Belgrade, Pregrevica 118, 11080 Belgrade, Serbia*

(*) nskoro@ipb.ac.rs

Cold plasma-based treatment processes are eco-friendly because they operate without any additional chemicals at atmospheric conditions. Contact of plasma with water generates a rich mixture of Reactive Oxygen and Nitrogen Species (RONS) (e.g. $HO^{\cdot}$, $O^{\cdot}$, O_3, H_2O_2, $NO^{\cdot}$, ONOOH, NO_3^-, NO_2^-, …) that are deposited in the water making Plasma Activated Water (PAW). Treatment of water for production of PAW has been studied extensively in the last decade [1]. This led to development of various electrode geometries for atmospheric pressure plasma sources and new generation of power supply units. Increase number of investigations of different plasma systems led to a discovery of some new phenomena like Pulsed Atmospheric Plasma Streamer (PAPS) [2]. But still the biggest obstacle in the field is the volume of these discharges i.e. their upscaling so that they can be used in water treatments for industry, agriculture, medicine etc. Usually the water treatment is done by atmospheric discharge positioned above the water surface or with discharge inside the water sample. In case of discharge positioned above the water the effective surface that is in direct contact with the discharge is small. The increase of contact surface can be done by increasing the plasma area or by introducing recirculation of water in the system.

In this work we present the results of water treatment by 3-pin Atmospheric Pressure Plasma Jet (APPJ) (shown in Fig. 1) which was utilized in a system for PAW production. Two options of the system were investigated: without and with the recirculation system for water samples [3]. 3-pin APPJ was made by using syringe needles as powered electrodes connected to a high voltage power supply. The inner diameter of needles is 1 mm and the outer diameter 1.8 mm. Each needle is placed in the glass tube and the distance between the tip of the needle and the edge of the tube is 5 mm. During treatments the water sample was positioned at the distance of 20 mm from the needle tips. The plasma was driven by an RF power supply with a frequency of 320 kHz. Argon gas with a total flow rate of 2 slm was used as a feed gas throughout the experiments.

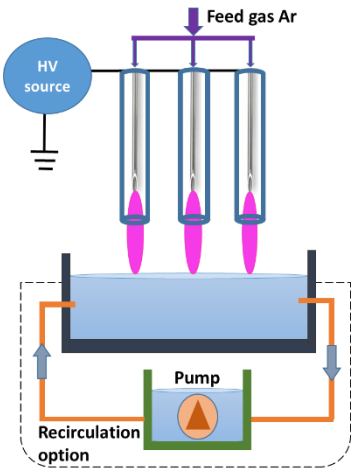

Figure 1. Experimental setup of the 3-pin APPJ for water treatments

A dielectric vessel holding a water sample was placed under the plasma source. Water in the vessel could be stationary (in case of smaller sample volumes) or it could be connected in a recirculation loop with an additional vessel, increasing the total volume of the water sample up to 600 ml. The idea was to test if we could increase the volume of obtained PAW while keeping similar properties, i.e. pH and RONS concentrations. In case of sample recirculation, a water pump (Atman AT-300) in the external vessel was used to run the water sample under the plasma jet and to adjust the flow of the sample in the system. Due to the capacity of the pump in some cases we had to use additional chokers to additionally reduce the water flow. In our experiments we have used volumes from 100 ml up to 600 ml of water.

The treatment times were from 10 min up to 90 min depending on the volume and if the water recirculation was used. After treatments, we measured pH using a probe while the presence of RONS was measured by using strips and spectrophotometrically.

For stationary water sample case we treated volume of V_0=100 ml of distilled water. After the treatment time of 20 mins we measured pH of 3.5 while concentrations of H_2O_2, NO_2^-, and NO_3^- were around 10 mg/l, 20 mg/l and 10 mg/l respectively. By addition of the recirculation system we were able to treat volumes of 400 ml and 600 ml of distilled water. For these measurements the input power to the pin-jet was kept the same as for the stationary case.

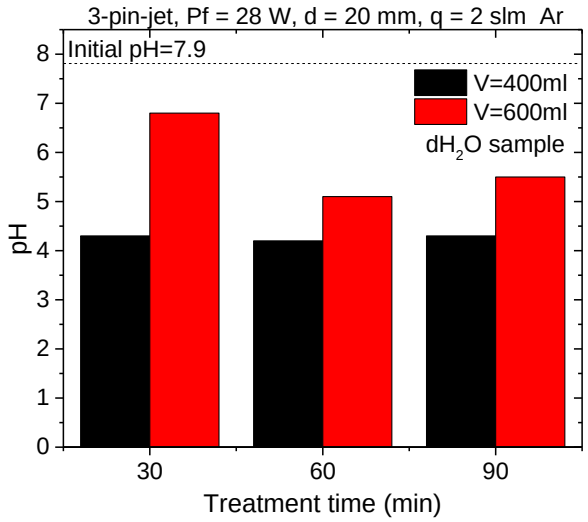

Figure 2. Measurements of pH of water samples treated for 30 mins, 60 mins and 90 mins using the recirculation system for two sample treatment volumes.

Since the volume sample was increased, we increased also the treatment time. In Figure 2 we show measurements of pH values after 30 mins, 60 mins and 90 mins of treatment. In case of V_0=400 ml pH values were almost constant despite the increased duration of treatment and stayed around 4. For V_0=600 ml of sample, pH was reducing more slowly in time with respect to 400 ml case. After 60 mins of treatment pH was further reduced and the final value stayed around 5. However, increased sample volume affected creation of reactive species. So even after 90 mins of treatment concentrations of H_2O_2, NO_2^-, and NO_3^- were not reaching the values obtained with 100 ml of sample and were below 5 mg/l, 10 mg/l and 5 mg/l respectively for 400 ml volume and all below 5 mg/l for 600 ml of water sample.

So, on one side we obtained smaller reduction of pH by increasing the amount of the water sample treated. Generating PAW with less acidic conditions can be beneficiary for some applications where low pH can induce negative effects (e.g. application related to seeds and plants). Nevertheless, increasing the amount of the water sample reduces production of long-lived reactive species in PAW. This reduction cannot be compensated by just increasing the treatment time even if going to extreme duration such as 90 minutes. Therefore, when scaling up the system keeping target RONS concentration and their tuning has to involve changing more parameters so the optimization presents a complex and entangled task.

Acknowledgments: *This work was supported by Science Fund of the Republic of Serbia, 7739780, APPerTAin-BIOM project and MSTDI of Republic Serbia grant number 451-03-66/2024-03/200024.*

References

[1] P. J. Bruggeman et al., Plasma Sourc. Sci. Techn. **25** (2016) 053002.
[2] N Puač et al., Appl. Phys. Lett. **101** (2012) 024103.
[3] A. Kumar et al., Sci. Total Environ. **864** (2023) 161194.

Non-thermal plasma treatment of landfill leachate for detoxification of hazardous pollutants

P. Marinova[1,3*], T. Bogdanov[2,3], E. Benova[3], M. Kirilova[3,4], Y. Todorova[3,4], I. Yotinov[3,4], I. Schneider[3,4], Y. Topalova[3,4]

[1] *Faculty of Forest Industry, University of Forestry, 1756 Sofia, Bulgaria*

[2] *Medical University of Sofia, Faculty of Medicine, 1431 Sofia, Bulgaria*

[3] *Clean & Circle Center of Competence, Sofia University, 1164 Sofia, Bulgaria*

[4] *Sofia University "St. Kliment Ohridski", Faculty of Biology, 1164 Sofia, Bulgaria*

(*) plamena_dragozova@ltu.bg

Novel plasma sources find their place from industry to biomedicine – including ecology and environmental protection, sustainable agriculture, food processing and safety, microbiological control, etc. Low-temperature plasma has made a significant impact on society over the past half-century. The development of low-temperature plasma technologies presents a new opportunity to improve the quality of life and open new areas for advanced research. A new opportunity for the application of plasma technology appears in the efforts on waste and wastewater management. One of the main problems of long-term storage of solid waste from urban daily activities is the production of leachate – a highly concentrated organic and nitrogen-rich liquid [1]. The leachate from solid waste landfills contains high concentrations of various organic and inorganic recalcitrant compounds, most of which are highly toxic. The treatment of this complex mixture of contaminants of environmental concern, including per- and polyfluoroalkyl substances (known as PFAS) is a challenge for waste/wastewater management and conventional technologies usually have low efficiency. Cold atmospheric plasma (CAP) sources of various types operating at atmospheric pressure usually produce a non-equilibrium plasma that can be used for the successful degradation of complex organic compounds [2].

This study is focused on the possibility of reduction in PFAS concentrations in model water and leachate contaminated with Perfluorooctanoic acid (PFOA) after treatment with plasma. In the treatment of wastewater and sludge with a high content of various pollutants, it is of particular interest how the additional contaminants affect the degradation of PFAS. The competitive reactions to the PFAS defluorination occurring during the treatment need to be investigated. Determining the dependence between the concentrations of contaminants such as NOx and the suppression in degradation of persuasive compounds will not only help to increase the degradation ratio but also to understand the mechanisms of PFAS degradation. It was previously reported that the process was strongly impacted by the presence of NO_2 and NO_3 due to scavenging of H and e-aq [3].

Three plasma sources (Surface-wave-sustained Argon plasma torch, underwater discharge and dielectric barrier discharge) operating at various discharge conditions have been used to produce the plasma in order to describe the effect of the plasma treatment of model water contaminated with PFOA and leachate contaminated with PFAS. In surface-wave-sustained Argon plasma torch, the plasma is produced by a microwave plasma torch sustained by an electromagnetic surface wave at 2.45 GHz in Argon at atmospheric pressure and input wave power of 100 W. The microwave plasma torch can operate in two treatment regimes – the designed experimental setup allowed the achievement of a continuous flow process of treatment (flow rate of 1.127 mL/min) and a batch treatment. The dielectric barrier discharge (DBD) with liquid electrode generates plasma discharge above water surface at high frequency power supply with frequency of 11 kHz which operates at voltage of 16 kV and mean power is 36 W. The underwater diaphragm discharge used in this study consist of camera separated by a dielectric membrane in two containers. The high frequency (15 kHz) voltage of 5 kV is applied to the electrode in the camber denoted by "+" and the electrode denoted by "–" is grounded. The obtained concentrations of reactive oxygen and nitrogen species in the treated water in the presence of PFOA

have been investigated, as well as changes in the concentration of PFOA during plasma treatment depending on the presence of other pollutants in variable concentrations. The case of obtaining shorter chain PFAS as a consequence of the treatment is considered.

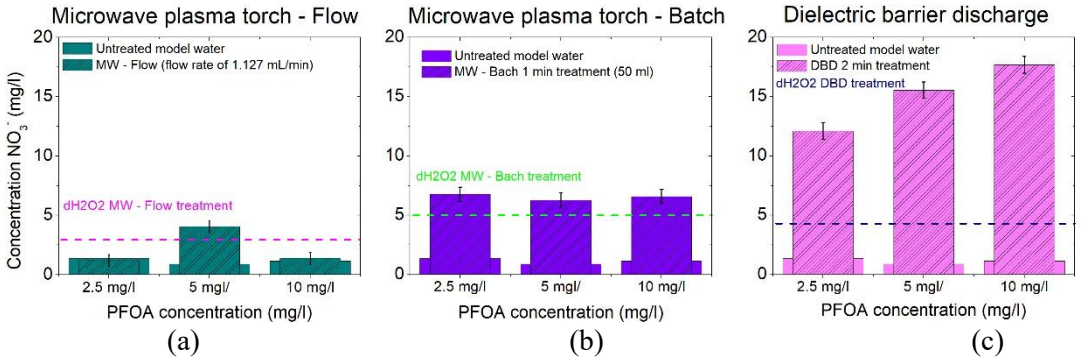

Fig. 1: Concentration of NO_3^- in model water contaminated with PFOA treated by microwave plasma torch in water flow configuration (a), microwave plasma torch in batch configuration and treatment time 1 min (b) (MW power 100 W, Argon flow 3 l/min) and dielectric barrier discharge and treatment time 2 min (c). The dashed lines correspond to NO_3^- concentration in treated distilled water without added contaminants.

When dealing with multicomponent systems, such as highly polluted wastewater together with the plasma as a complex system of reactive species, electrons and UV, changes in the concentration of the various constituents must be carefully monitored. The possibility of reducing toxic pollutants during plasma treatment is promising, but obtaining new no less toxic compounds in high concentration as products of PFAS degradation is also a possible outcome.

Acknowledgments

This work is supported by the PROMISCES (Preventing Recalcitrant Organic Mobile Industrial chemicalS for Circular Economy in the soil-sediment-water System) project which has received funding from the European Union's Horizon 2020 research and innovation program under Grant Agreement No 101036449. The equipment used in the investigation is from the Clean&Circle Center of Competence, Grant № BG05M2OP001-1.002-0019: "Clean Technologies for Sustainable Environment - Waters, Waste, Energy for a Circular Economy", financed by the Science and Education for Smart Growth Operational Program (2014-2020) and co-financed by the EU through the ESIF.

[1] Zhang M., X. Zhao, D. Zhao, T.-Y. Soong, S. Tian, Poly- and Perfluoroalkyl Substances (PFAS) in Landfills: Occurrence, Transformation and Treatment, *Waste Management*, Volume 155, 2023, Pages 162-178, https://doi.org/10.1016/j.wasman.2022.10.028.

[2] Vesel, A., Zaplotnik, R., Primc, G., Mozetiˇc, M., Katan, T., Kargl, R., Mohan, T., Kleinschek, K.S. Non-Equilibrium Plasma Methods for Tailoring Surface Properties of Polyvinylidene Fluoride: Review and Challenges. *Polymers* 2021, 13, 4243, https://doi.org/10.3390/polym13234243.

[3] Umar, M. Reductive and Oxidative UV Degradation of PFAS—Status, Needs and Future Perspectives. Water 2021, 13, 3185., https://doi.org/10.3390/w13223185

Modifying atmospheric pressure surface-wave-sustained plasmas with silicon plates for discharge stability

G. Regodon[1], H. Acosta-Rivera[2], R. Alvarez[2,3], V. Rico[2], A. Palmero[2], M.C. García[4,*]

[1] *Departmento de Física, Campus Rabanales, Edificio C2, Universidad de Córdoba, 14071 Córdoba, Spain*

[2] *Instituto de Ciencia de Materiales de Sevilla (CSIC-US), Américo Vespucio 49, 41092 Sevilla, Spain*

[3] *Departamento de Física Aplicada I, Escuela Politécnica Superior, Universidad de Sevilla, c/Virgen de África 7, 41011 Sevilla, Spain*

[4] *Departmento de Física Aplicada, Radiología y Medicina Física, Campus Rabanales, Edificio C2, Universidad de Córdoba, 14071 Córdoba, Spain*

(*) fa1gamam@uco.es

Surfatron coupling devices can be used to maintain columnar microwave argon plasmas within dielectric tubes sustained by an azimuthally symmetric TM_{00} [1,2]. Typically, a part of the plasma column forms in the tube region inside the surfatron. At 2.45 GHz and under atmospheric pressure conditions, these plasma columns experience radial contraction and do not entirely fill the tubes containing them [3]. At elevated feed-gas flow rates, this phenomenon results in the splitting of the plasma column into two or more smaller-diameter filaments, rendering it highly unstable.

In this work, the changes experienced by these plasma columns when introducing small silicon pieces of different sizes and nature are studied as a mean to modify the propagation of the electromagnetic signal and the features of the plasma, aiming to avoid both, plasma formation inside the surfatron and the filamentation phenomenon. For this purpose, the plasma was generated inside a quartz tube (6-8 mm inner and outer diameters), using different microwave power levels (P = 100, 140, 180 W), and argon flow rates (F_{Ar} = 200, 400 sccm), while small rectangular silicon pieces of different lengths (4 mm × Length × 300 μm) were introduced to check their influence. Using the 3 cm long Si (intrinsic) piece, the original multi-filamented plasma transformed into just one stable plasma column at the region outside the surfatron (Fig. 1a). Remarkably, higher argon flows lead to the formation of a rather unstable plasma in the region inside the surfatron, whose instability was enhanced at higher powers (Fig. 1b). When using shorter Si pieces (L = 1 and 2 cm), the plasma only formed outside the surfatron if the outer end of the Si piece was placed at the surfatron gap (Fig. 1c), otherwise the plasma also appears at the back part of the piece inside the surfatron. Under the studied experimental condition, it was not possible to generate plasmas of this type using dielectric SiO_2 pieces (L = 1, 2, 3 cm long) (Fig. 1d). No differences were observed when using doped and intrinsic silicon pieces of the same geometry and size.

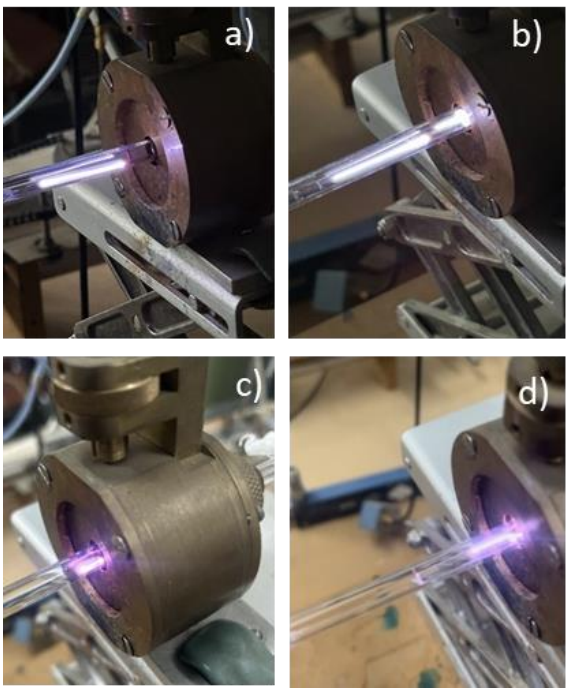

Fig. 1: (a) L = 3 cm, P = 140 W, FAr = 400 sccm; (b) L = 3 cm, P = 180 W, F = 600 sccm, (c) L = 2 cm, P = 100 W, F = 200 sccm

Optical Emission Spectroscopy techniques were used to diagnose the plasma and understand the changes experimented when introducing the Si pieces. A Czerny-Turner type spectrometer of 1 m focal length (with a 1200 grooves/mm holographic grating and a photomultiplier as a detector) was used for

the analysis of the plasma emission. From the collisional broadening of the Ar I 840 nm line [5], the gas temperature (T_g) was measured. On the other hand, the electron density (n_e) was measured from the collisional broadening of the H_β line [6].

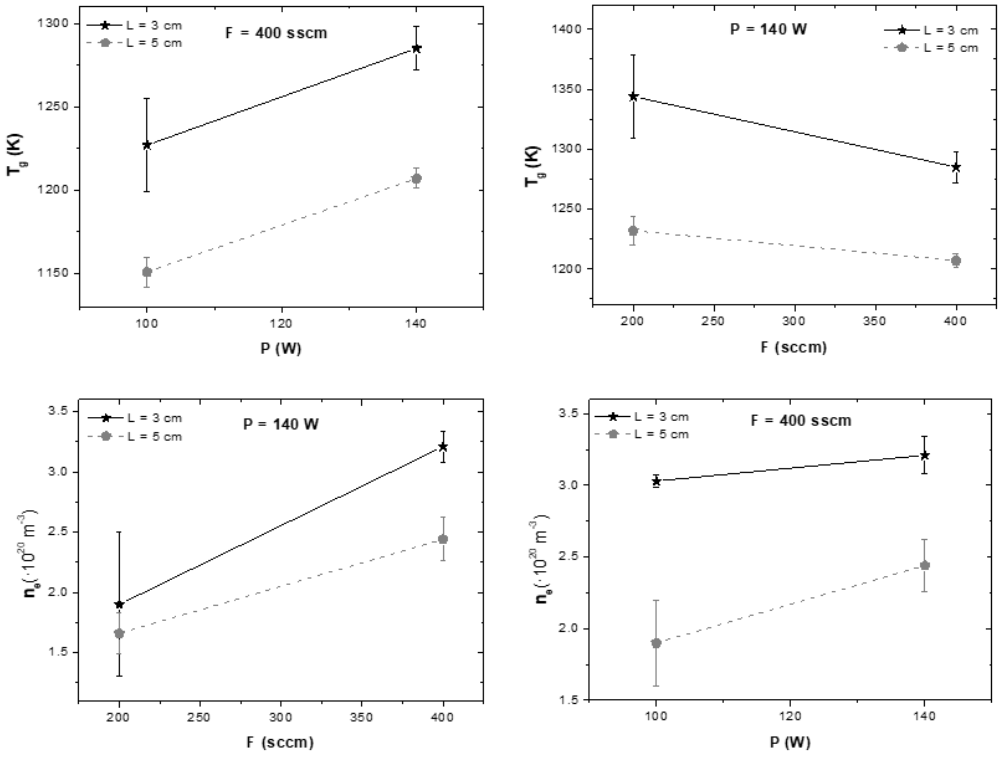

Fig. 2: Measured values of T_g and n_e with power (P) and argon flow rate (F), when using a 3 and 5 cm Si pieces.

In terms of electron density and gas temperature, these plasmas are different from classical surface wave-maintained discharges produced in the original (non-modified) configuration, which suggests that they do not likely fall within the same category, as the surface wave propagation is most likely disrupted by the Si plate. Actually, simulations with COMSOL Multiphysics show that the electric field can be more than doubled at the edge of the silicon piece during surfatron start up. This explains that the device start up is easier with the silicon piece in the dielectric tube, and that the plasma column starts beyond the silicon piece.

Acknowledgements.- The authors acknowledge projects PID2020-112620GB-I00 and PID2020-114270RA-I00 funded by MCIN/AEI/10.13039/501100011033 and project TED2021-130124A-I00 funded by AEI/10.13039/501100011033/Unión Europea Next Generation EU/PRTR

[1] C.M. Ferreira and M. Moisan, *Microwave Discharges: Fundamentals and Applications* (1993) NATO ASI Series B. Plenum Press, Springer Science & Business Media, New York.
[2] J. Henriques, E. Tatarova, F. Dias, C. Ferreira, *J. Appl. Phys.* **109** (2011) 023302.
[3] E. Castaños Martinez, Y. Kabouzi, K. Makasheva, M. Moisan, Phys. Rev. E **70** (2004) 066405.
[4] E. Castaños Martinez, M. Moisan, Y. Kabouzi, *J. Phys. D Appl. Phys.* **42** (2009) 012003.
[5] M.C. García, C. Yubero, A. Rodero, *Spectrochim. Acta B: Atomic Spectroscopy* **193** (2022) 106437
[6] C. Yubero, M.D. Calzada, M.C. Garcia, *J. Phys. Soc. Japan* **74** (2005) 2249–2254.

Inactivating *C.sphaerospermum* and its mechanism in atmospheric pressure plasmas with water mist

Tomoya Ohara[1], Shinano Kinoshita[1] Kazuo Takahashi[(*)2]

[1] *Department of Electronics, Kyoto Institute of Technology, Matsugasaki, Sakyo-ku, Kyoto 606-8585, Japan*

[2] *Faculty of Electrical Enginieering and Electronics, Kyoto Institute of Technology, Matsugasaki, Sakyo-ku, Kyoto 606-8585, Japan*

[(*)] takahash@kit.jp

Sterilization technology is crucial in many industries, and there are currently several methods used to achieve it. However, selecting the appropriate sterilization method is essential and depends on various factors such as toxicity, temperature, and other issues related to the object to be treated. Atmospheric pressure plasma sterilization is a promising general-purpose sterilization method that can overcome these issues and sterilize materials with low toxicity and low-temperature conditions.

In this study, we aimed to elucidate the mechanism of inactivation of *C.sphaeospermum* using atmospheric pressure plasmas with water mist. The inactivation system used in this study consisted of a mist generator and a discharge device. The mist generator used an ultrasonic transducer to convert liquid water in a tank into mist, and the discharge device consisted of two stages of two rows of copper wire covered with ceramic. It was connected to high voltage in an upper part and to the ground in a lower part to generate plasmas by applying an AC voltage of 13 kVpp. The water mist was carried by dry air at a flow rate of 1.0 L/min and blown through the plasma onto the object (*C.sphaeospermum*) to be treated. We examined the system's inactivation ability by counting the number of surviving cells after treatment on a plate medium coated with *C.sphaerospermum*. Additionally, the treatment was conducted with and without water mist in the gas, and the results were compared.

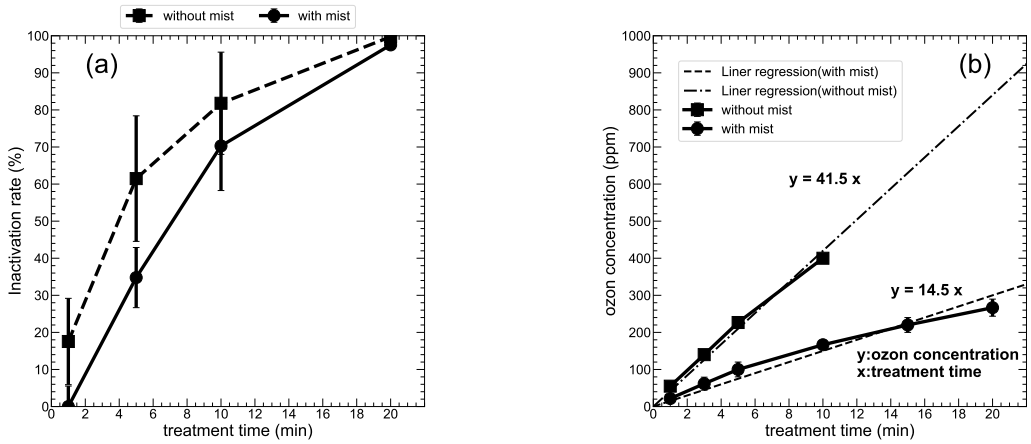

Fig. 1: (a) inactivation rates of *C.sphaerospermum* as a function of treatment time in the treatments without and with water mist, and (b) ozone concentration as a function of the time.

Figure 1 (a) depicts the relationship between the treatment time and the inactivation rate of *C.sphaerospermum*. It is indicated that with an increase in treatment time, the inactivation rate of *C.sphaerospermum* also increases. The graph also indicates that the inactivation rate of *C. sphaerospermum* reaches 99% within 20 minutes, regardless of whether mist is present or not. Figure 1 (b) shows ozone concentration versus treatment time. The graph shows that ozone concentration increases as the treatment time increases. However, the detector tube used to measure ozone concentration had a limit of 400 ppm, so it was not possible to measure the ozone concentration in the treatment without water mist after 10 minutes. Therefore, the ozone concentration after 20 minutes was estimated from the measurement result using a regression line. The graph reveals that the mist inclusion in the gas reduces the increase in ozone concentration by approximately one-third.

The OH radical, which has a strong oxidizing ability than ozone, is one of excited species produced by the plasma with water mist. The radical was detected by a chemical probe method. In this study, gels made from the fluorescent reagent NaTA solution were treated with the inactivation system and fluorescence was observed. Figure 2 shows the fluorescence intensity of treated and untreated NaTA gels. It is indicated that the fluorescence intensity of the gel was shown to be enhanced by treatment with mist-containing gases.

The results showed that *C. sphaerospermum* could be inactivated 99% by the treatment with an atmospheric pressure plasma for 20 min. In the treatment with the atmospheric pressure plasma without water mist, inactivation is considered to be caused by exposure to ozone generated from oxygen molecules. However, the plasma with water mist had the same inactivation rate while the ozone concentration was less than that of the plasma without water mist. We measured the OH radical and observed that the amount of the OH radical produced increased in the plasma with water mist. Therefore, the OH radical in addition to ozone is responsible for inactivation of *C.sphaerospermum* by the atmospheric pressure plasmas with water mist.

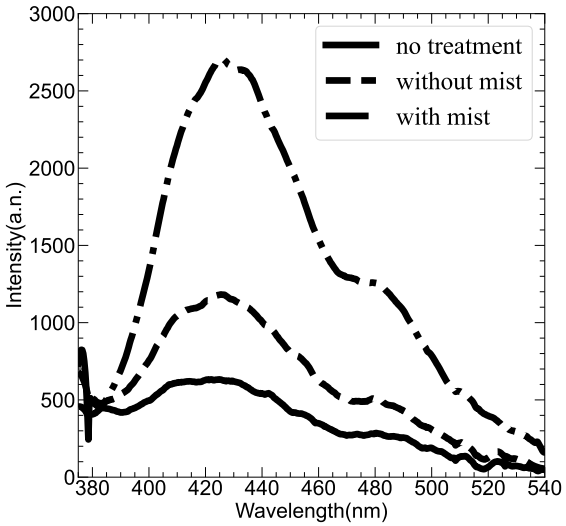

Fig. 2: Intensities of fluorescence from NaTA-containing gels in wavelength between 380 and 540 nm.

Tunable stability of microwave plasma synthesized few-layer graphene dispersion in water

O.Jašek(*)[1], J. Toman[1], P. Sťahel[1], J. Jurmanová[1], M. Stupavská[1]

[1] *Department of Plasma Physics and Technology, Faculty of Science, Masaryk University, Kotlářská 2, CZ-611 37, Brno, Czech Republic*

(*) *jasek@physics.muni.cz*

Formation of a stable dispersion of graphene in water is an important technological issue concerning both fundamental as well as applied research. Hydrophobic nature of graphene surface makes it very difficult to form stable dispersion of pure graphene, with high C/O atomic content ratio, in water without the use of surfactants. Up to now the most often used approach is the utilization of the graphene oxide (GO), oxidized formed of graphene with large quantities of carbon-oxygen/hydrogen related functional groups, which is well soluble in water/(surfactant) mixture. Such dispersion is applied to the selected surface and after liquid evaporation the reduction of the material to reduced graphene oxide is carried out. However, for the future large-scale applications, the use of dangerous chemicals as well as time and energy consuming processing steps should be minimized.

From this point of view, microwave plasma-based gas-phase synthesis of graphene [1] and its derivatives represents a simple, environmentally friendly, and easily scalable production method enabling emerging large-scale applications. Microwave plasma decomposition of organic precursors, hydrocarbons and alcohols, and subsequent formation of carbon nanostructures in the gas-phase is strongly dependent on the temperature and plasma plume stability of the environment formed by the plasma discharge [2]. Structure of the synthesized carbon material changes from graphitic nanoparticles to graphene nanosheets with increasing H/C atomic ratio of the precursor and delivered microwave power.

In our work, gas-phase synthesized few-layer graphene was prepared by high-temperature decomposition of ethanol in dual-channel microwave plasma torch at atmospheric pressure. Samples of few-layer graphene with different amount of structural disorder and oxygen content were prepared using variation of torch nozzle central channel gas flow (Qc = 500 – 920 sccm) and delivered microwave power (100-350 W). Ethanol flowrate was kept constant at 23 sccm carried out by 700 sccm of Ar. Lower power and increased flow rate of Ar in central channel led to the high-temperature environment instability (Figure 1) and structural and chemical changes of the material. More details can be found in our previous publications [2, 3]. After the synthesis, the nanopowder was scraped from the reactor walls and analyzed by electron microscopy, Raman and X-ray photoelectron spectroscopy (XPS). Plasma diagnostic was carried out by optical emission spectroscopy and ICCD camera imaging.

Fig. 1: Instability of torch discharge at high Qc.

Samples of graphene with different amount of disorder and oxygen related functional was used for preparation of dispersions in water. Dispersions were produced using deionized (DI) water containing 7.5 mg of graphene nanopowder in 500 ml of DI water. Three methods of preparation were compared: a) applying standard ultrasound for 10 minutes, b) applying more powerful cavitation technique and c) plasma treatment of nanopowder before ultrasonication. Plasma treatment of nanopowder was carried out in dielectric barrier discharge (DBD) using N_2 or N_2/propane-butane (N_2 – 6 slm /PB – 85 sccm) atmosphere for 120 s followed by ultrasonication in DI water for 10 minutes.

Prepared dispersions were left to settle down and regularly monitored (Figure 2). We can observe that graphene material exhibiting higher disorder – hdG type, as determined by higher D/G Raman band

ratio and lower sp^2/sp^3 bond ratio as well as higher oxygen content, 3 at% compared to 1 at% (G type sample), formed more stable dispersion and after the sedimentation phase of larger graphene clusters, 48 hours, the suspension became stable without any observable changes. We also observe positive influence of plasma treatment of the nanopowder in DBD, however according to the material analysis there were only small changes in the chemical composition of the material after plasma treatment.

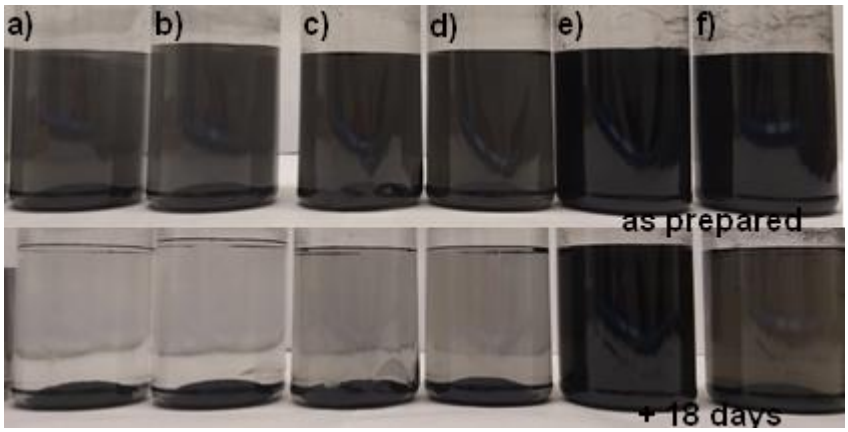

Fig. 2: Stability of few-layer graphene dispersion in water (type, preparation method): a) G, ultrasound b) hdG (ultrasound) c) G DBD N_2, d) G N_2/PB e) hdG N_2, f) hdG N_2/PB

In conclusion, direct control of structural and chemical properties of few-layer graphene during its synthesis using microwave plasma decomposition of ethanol at atmospheric pressure enabled us to control and improve graphene dispersion stability in water providing important insights into the formation mechanism of such dispersions and simplifying preparation process of such dispersions.

This work was supported by project LM2023039 funded by the Ministry of Education, Youth and Sports of the Czech Republic.

[1] A. Dato, *Journal of Materials Research* **34** (2019) 214–230.
[2] O. Jasek et al., *J.Phys D:Appl. Phys.* **54** (2021) 165201.
[3] J. Toman et al., *J.Phys D:Appl. Phys.* **52** (2019) 265205.

Experimental Evidence of TIAGO Torch Plasma as a Surface Wave Discharge and Identification of the Radiation Zone: Improving Graphene Synthesis.

F.J. Morales-Calero[1], A. Cobos-Luque[1], J.M. Blázquez-Moreno[2], A.M. Raya[1], R. Rincón(*)[1], J. Muñoz[1], A. Benítez[2], N.Y. Mendoza-González[1], J.A. Alcusón[1], A. Caballero[2], M.D. Calzada[1].

[1] *Laboratory of Innovation in Plasmas, Universidad de Córdoba, 14014 Córdoba, Spain.*

[2] *Dpto. Química Inorgánica e Ingeniería Química, Instituto Químico para la Energía y el Medioambiente (IQUEMA), Universidad de Córdoba, 14014 Córdoba, Spain.*

(*) rrincon@uco.es

Microwave plasma technology at atmospheric pressure arouses interest thanks to its remarkable performance in many challenging areas, such as green energy generation and graphene production by hydrocarbon decomposition. One of the most outstanding devices in this field is the TIAGO (Torche à Injection Axiale sur Guide d'Ondes) torch. It generates a plasma where two luminous regions can be distinguished: a bright filament (dart) and a fainter shell (plume). This dart has been experimentally demonstrated to be a Surface Wave Discharge (SWD) by the analysis of the axial distribution of electron density [1]. This kind of plasmas are usually enclosed in dielectric tubes. Thus, surrounding air must behave as a virtual dielectric cylinder to allow the propagation of the surface wave along the plasma column. Among other features, SWDs are characterized by the existence of a radiation zone previous to the formation of the surface wave, an increase of its length with the power supplied and a linear decrease of electron density along the discharge whose slope does not depend on applied power.

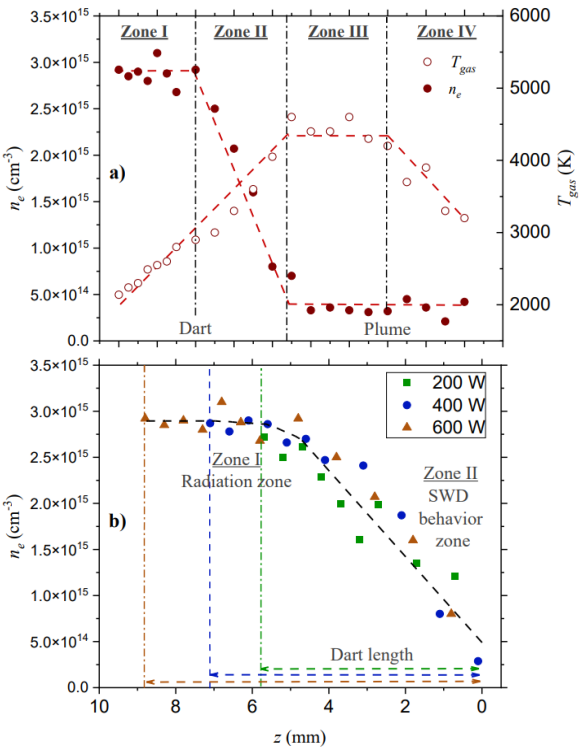

Fig. 1: a) Zones identified along the TIAGO torch (600 W) b) Axial distribution of the electron density with the origin of coordinates at the end of the dart, taking the positive direction towards the injector.

In Fig 1, an axial characterization of the main parameters—electron density and gas temperature—of the plasma generated at 600 W has been carried out [1]. Based on these parameters, four zones can be identified along the plasma (Fig 1a), with the first two corresponding to the dart and the next two corresponding to the plume. If the origin of coordinates is placed at the end of the dart and the data obtained for different microwave power supplied to the plasma are plotted together (Fig 1b), it is observed that the value of the electron density is independent of the applied power. It can be seen that there is a region where the electron density remains constant at its maximum value and then decreases linearly as we move away from the injector. This corresponds to the radiation zone (Zone I), which, as expected, is followed by the zone where the surface wave forms (Zone II), exhibiting SWD-type behavior. Zones III and IV (plume), are characterized by a reduced presence of electrons (Fig 1a), suggesting that the plume behaves as a postdischarge.

This research provides valuable information for the optimization of TIAGO torch applications, concretely the formation of graphene nanosheets, application for which this device has proven to be suitable [2]. In [1], and taking in account the numerical analyses of Nowakowska et *al*. [3], the unshielding of this plasma results in the radiation of electromagnetic energy into space (aproximately 43%), especially along positions closer to the nozzle exit, *i.e*. Zone I, the radiation zone. This energy, in consequence, is not being utilized during the graphene synthesis process. To optimize this process, a crucial step is to minimize energy loss through radiation to maximize the available microwave energy input. To this aim, a metallic shielding has been placed around the TIAGO reactor, essentially creating a Faraday cage (Fig 2). The shielding strategy prevents radiation losses and results in a remarkable increase in graphene formation up to 22.8%. This value, along with the emitted gases proportions and plasma volume increase, shows a correlation with conditions associated with higher input power [4], which demonstrates a greater utilization of the energy supplied to the plasma. The synthesized material undergoes a thorough examination, employing diverse techniques like Raman spectroscopy (Fig 3), X-ray photoelectron spectroscopy (Fig 4), and others. These analyses highlight that the quality of graphene remains consistent, even with the implementation of shielding. Therefore, the electromagnetic shielding of the TIAGO torch discharge significantly boosts solid material formation and energy yield without compromising the intrinsic properties and quality of the synthesized graphene.

Fig. 2: TIAGO torch shielded plasma during graphene synthesis

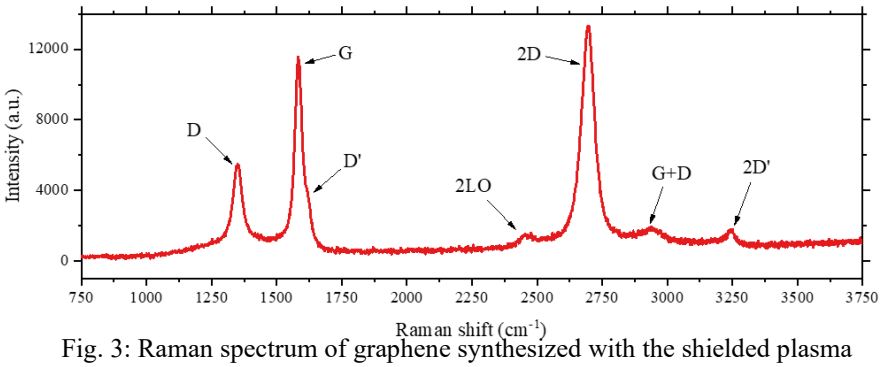

Fig. 3: Raman spectrum of graphene synthesized with the shielded plasma

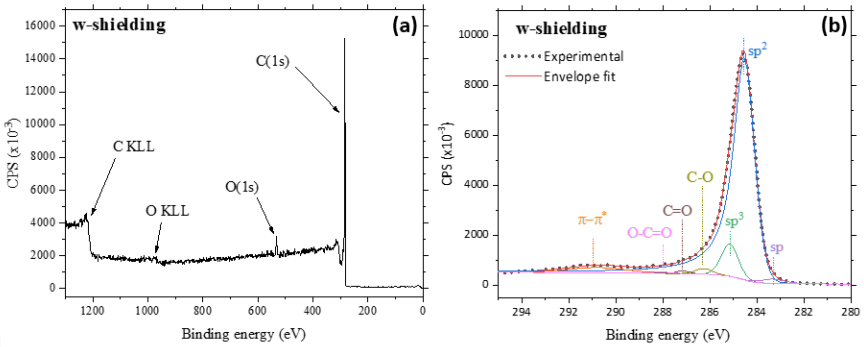

Fig. 4: XPS spectrum (a) and C(1s) peak deconvolution (b) of graphene synthesized with the shielded plasma

[1] F.J. Morales-Calero, *Plasma Sources Science and Technology,* **32** (2023) 065001
[2] R. Rincón, *Plasma Sources Science and Technology,* **24** (2015) 032005
[3] H. Nowakowska, *Plasma Sources Science and Technology*, **30** (2021) 095011
[4] J. Toman, *Fuel Processing Technology*, **239** (2023) 107534.

Aknowledgments: This work was partially supported by Grant TED2021129261AI00 funded by MCIN/AEI/ 10.13039/501100011033 and by the European Union NextGenerationEU/PRTR. The predoctoral contract of F.J. Morales-Calero was granted by a MOD-2.2 from Plan Propio de la Universidad de Córdoba (2020). Finally, the authors of the present work are greatly thankful to Prof Michel Moisan of the Groupe de Physique des Plasmas (University of Montreal) for the TIAGO torch donation.

Simulation of plasma, chemistry, and flow dynamics in flame-based and plasma-based hydride atomizers

Adam Obrusník[1], Martina Mrkvičková[1], Waseem Khan[1], Nima Boulouki[1], Tomáš Medek[1], Milan Svoboda[2], Jan Kratzer[2], Jiří Dědina[2], Pavel Dvořák[1]

[1] *Department of Plasma Physics and Technology, Faculty of Science, Masaryk University, Brno, CZ*

[2] *Czech Academy of Sciences, Institute of Analytical Chemistry, Brno, Czech Republic*

(*) adamobrusnik@physics.muni.cz

Atomic absorption and atomic fluorescence spectroscopy are typically employed for extremely sensitive element determination. Hydride generation based on a conversion of analyte from the liquid sample into volatile hydride is a very useful approach since the analyte is introduced to the spectrometer in gaseous form [1]. In this contribution, we focus on hydride atomizers, which aim is to convert an analyte hydride to analyte free atoms. Efficiency of their operation directly impacts the limit of detection of the whole analytical procedure [2]. It has been previously shown [3] that the key chemical specie which enables the process and positively correlates with the efficiency of atomizers is atomic hydrogen, H.

In conventional, flame-based, atomizers, atomic hydrogen is primarily produced in an oxyhydrogen flame retarded by argon gas and it was previously confirmed by a combination of (TA)LIF measurements and numerical simulation that the concentrations of atomic hydrogen e.g. in a miniature diffusion flame atomizer can reach as much as 10^{23} m^{-3} [4]. This is several orders of magnitude above typical concentration of analyte supplied to the atomizer.

For the reasons stated above, it shows promise to study low-temperature plasmas as an alternative to flame-based atomizers. Plasma is known to be very efficient in decomposition of molecules while maintaining low temperature of the background gas and it could also act as a potent source of hydrogen radicals.

In this contribution, we present a simulation study which combines 2D or 3D gas flow simulation with global plasma modeling of a DBD atomizer. The simulation data is also compared against (TA)LIF measurements to gain more confidence in the models. The primary aim of the work is to explain certain phenomena which were observed experimentally when developing plasma-based atomizers and also to shed some light on the different chemical dynamics of flame-based and plasma-based atomizers.

Acknowledgement

This research has been supported by the Czech Science Foundation under Contract 23-05974K and by the Project LM2023039 funded by the Ministry of Education, Youth and Sports of the Czech Republic.

References

[1] J. Dedina, D.L. Tsalev. Wiley and Sons Inc. Hydride generation atomic absorption spectrometry. 1995.

[2] S. Brandt et al. Spectrochim Acta B **126** (2016) 6

[3] P. Dvořák et al. Chemical Science **10** (2019) 3643

[4] A. Obrusnik et al. Journal of Analytical Atomic Spectrometry **35** (2020) 1464-1471

A different take on dry reforming of methane in DBD: combining sorbents and plasma for single-stage carbon capture and utilization

R Vertongen(*)[1], G De Felice[2], H van den Bogaard[2], F Gallucci[2], A Bogaerts[1], S Li[2]

[1] *Research group PLASMANT, Department of Chemistry, University of Antwerp, Universiteitsplein 1, 2610 Antwerp, Belgium*

[2] *Research group Inorganic Membranes and Membrane Reactors, Sustainable Process Engineering, Department of Chemical Engineering and Chemistry, Eindhoven University of Technology, De Rondom 70, Eindhoven 5612 AP, the Netherlands.*

(*)*rani.vertongen@uantwerpen.be*

In the transition to a more sustainable society, it is crucial to decarbonize the industry through electrification and carbon capture, utilization, and storage (CCUS) [1,2]. One way to reduce the overall cost is to apply single-stage CCU and circumvent process steps [3]. For example, with adsorption-based carbon capture, the CO_2 is first captured from a dilute source such as flue gas (~ 15 vol% CO_2) or direct air capture (DAC) [4]. Second, the adsorbed CO_2 is converted *in situ*, while simultaneously regenerating the adsorbent. Plasma technology is a promising candidate to realize single-stage CCU. The plasma enables the desorption of CO_2 from a sorbent and the simultaneous conversion to CO. Li et al. [5] demonstrated CO_2 capture with a hydrotalcite sorbent and plasma-based desorption and conversion in a dielectric barrier discharge (DBD) plasma reactor.

In this study, we explore the flexibility of such a plasma-sorbent system, specifically for sorption-enhanced dry reforming of methane (DRM). The combined reaction of CO_2 and CH_4 is interesting for producing value-added gas mixtures, such as syngas and hydrocarbons. In addition, variable input streams, such as biogas and landfill gas, can be easily coupled to the plasma when using a sorbent system. To the best of our knowledge, no previous research has investigated DRM with a plasma-sorbent system for single-stage CCU.

A cylindrical DBD reactor was packed with zeolite 5A pellets (size 250-355 µm) as the sorbent material and compared to non-adsorbing quartz particles as a control measurement. The sorbent selectively adsorbs CO_2 to filter CH_4, in line with the literature for zeolite 5A [6]. In the adsorption stage, CO_2 with Ar as carrier gas was fed to the reactor until the sorbent material was saturated (flow rate of 20/20 mL_n/min). To clear the lines and remove non-adsorbed CO_2, the reactor was flushed with a high flow rate of CH_4 and Ar (50/50 mL_n/min). This also ensures we only measured surface desorption and conversion in the desorption step. Finally, in the desorption step with a CH_4/Ar flow (20/20 mL_n/min), the plasma was switched on to induce CO_2 desorption. We applied a frequency of 45 kHz and a constant plasma power of ca. 30 W. The time-dependent concentrations were determined with FTIR (Agilent Technology, Cary 630). Additional samples were taken with an in-line gas chromatograph (GC, Thermo Scientific® Trace 1300) equipped with two thermal conductivity detectors and a flame ionization detector. To study the influence of water, a simple humidity meter (Extech Instruments Humidity Alert II 445815) was installed in the line.

Figure 1 presents the concentrations as a function of time during the desorption step when the Ar/CH_4 plasma is ignited. The concentrations of CO_2 and CO exhibit similar profiles, indicating that the CH_4/Ar plasma is suitable to desorb CO_2 and convert it to CO at the same time. The concentration of CH_4 drops within the initial 200 seconds, due to three primary factors: (1) CH_4 is consumed via non-oxidative coupling into higher hydrocarbons induced by the plasma, which also explains the drop observed in CH_4 concentration in the blank experiments; (2) dilution of the relative concentration due to CO_2 desorption from the sorbent into the gas phase; (3) CH_4 consumption as a result of reactions with desorbed CO_2. Due to the latter two reasons, the CH_4 concentration decreases to a lower level in the case of zeolite 5A compared to the blank experiment. Subsequently, it begins to increase and reaches a plateau, corresponding to the declining CO_2 desorption over time.

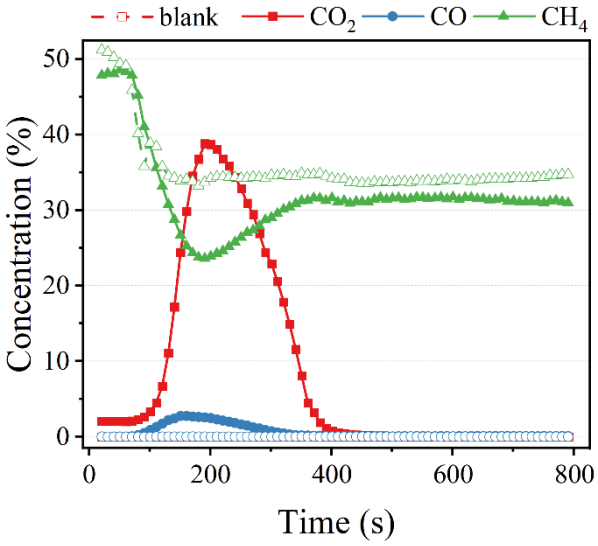

Figure 1 Concentration of CO_2, CO, and CH_4 in the outlet stream during the desorption stage when the Ar/CH_4 plasma is ignited.

Measurements with GC confirm the formation of H_2 and C_{2+} hydrocarbons, including C_2H_6, C_2H_4, C_2H_2, and C_{3+} products. Although most of these products (except CO) could also be formed by CH_4 non-oxidative coupling only, the presence of H_2O suggested possible DRM reactions. Notably, the zeolite showed potential for *in situ* removal of H_2O, shifting the equilibrium and possibly enhancing the conversion in the plasma. Material analysis revealed that the surface area and pore volume of zeolite 5A decreased after plasma exposure, caused by the carbon deposition on the sorbent. However, the material remained stable since we observed no significant morphological changes. Overall, this plasma-sorbent system is an interesting proof-of-concept for *in situ* CCU.

[1] C. Hepburn, E. Adlen, J. Beddington, E.A. Carter, S. Fuss, N. Mac Dowell, J.C. Minx, P. Smith, C.K. Williams, The technological and economic prospects for CO2 utilization and removal, Nature 575 (2019) 87–97. https://doi.org/10.1038/s41586-019-1681-6.

[2] IEA Global Energy and Climate Model, (2023). https://www.iea.org/reports/global-energy-and-climate-model (accessed December 12, 2023).

[3] S. Sun, H. Sun, P.T. Williams, C. Wu, Recent advances in integrated CO2 capture and utilization: a review, Sustain Energy Fuels 5 (2021) 4546–4559. https://doi.org/10.1039/D1SE00797A.

[4] M. Erans, E.S. Sanz-Pérez, D.P. Hanak, Z. Clulow, D.M. Reiner, G.A. Mutch, Direct air capture: process technology, techno-economic and socio-political challenges, Energy Environ Sci 15 (2022) 1360–1405. https://doi.org/10.1039/D1EE03523A.

[5] S. Li, M. Ongis, G. Manzolini, F. Gallucci, Non-thermal plasma-assisted capture and conversion of CO2, Chemical Engineering Journal 410 (2021) 128335. https://doi.org/10.1016/j.cej.2020.128335.

[6] M. Mofarahi, F. Gholipour, Gas adsorption separation of CO2/CH4 system using zeolite 5A, Microporous and Mesoporous Materials 200 (2014) 1–10. https://doi.org/10.1016/j.micromeso.2014.08.022.

Nanosecond plasmas generation of a chemical gradient for detonation initiation: O-TALIF and OES characterisation

V. Lafaurie (*)[1], Z. Shu[1], M. Sadauskaite[1], P. Vidal[2], S. M. Starikovkaia[1]

[1] *Laboratoire de Physique des Plasmas (LPP), UMR 7648 CNRS, Sorbonne Université, Université Paris-Saclay, École Polytechnique, Institut Polytechnique de Paris,Route de Saclay, Palaiseau, France*
[2] *Institut Pprime, UPR 3346 CNRS, ENSMA, Chasseneuil-du-Poitou, France*
(*) victor.lafaurie@lpp.polytechnique.fr

1 Introduction

To this day, combustion still represents over 90% of the energy produced in the world [1]. While serious efforts are being made to reduce our societies reliance on this method, it is apparent that no sustainable can be made without the chemical energy release that comes from burning fuels. The most common method for such energy production is the constant pressure (or Brayton cycle) combustion engine. This procedure has been used and optimised since the 18^{th} century and as such, little improvements remain to be made. There are, however, other methods of combustion. One such alternative is the pressure gain (or Ficket-Jacobs) cycle, which could theoretically allow up to 30% increase in efficiency. Such process implies combustion through detonation waves (often seen as the coupling between a shockwave and a flame) which are notoriously harder and more dangerous to work with than regular flames. This work focuses on one aspect of this, namely the instability of ignition of a detonation. One of the proposed methods for the ignition of a detonation wave is through acceleration of a flame through a chemical gradient known as the gradient mechanism of Zel'dovich [3]. Transient low-temperature plasmas, such as the nanosecond plasmas used here, can have significant effects on the chemistry of a mixture. This work introduces and characterizes a novel type of plane-to-plane discharge to generate a gradient of concentration of atomic oxygen along the span of the electrode.

2 Experimental setup and results

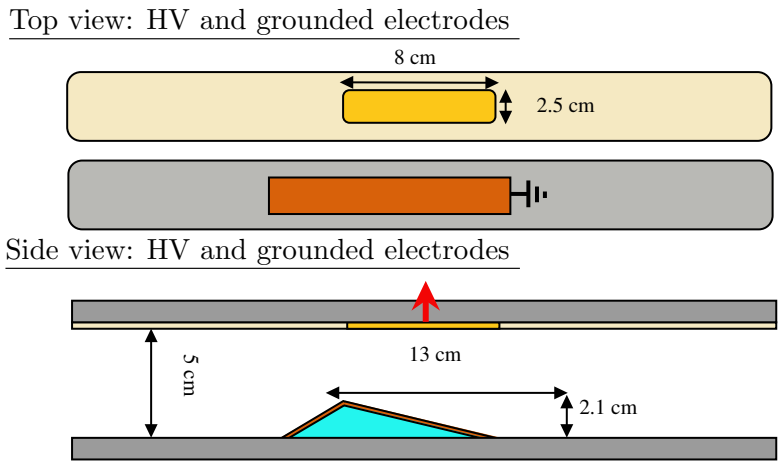

Fig. 1: Schematic of the electrode setup in top (HV electrode), side and bottom view (mass electrode). Red arrow indicates HV connection.

Using a 3D-printed piece secured on the bottom flange and covered with copper tape, a varying section from a 2.9 to a 5 cm gap was imposed (Fig. 1). This varying gap leads to varying plasma parameters in a single discharge.

The initial assessment of the plasma, performed with ICCD imaging (PI-MAX4 camera 200-800 nm, unfiltered, see Fig. 2), showed that this type of electrode generates a diffuse plasma. This plasma is clearly seen to produce a gradient of the intensity of emission along the axis of the widening of the

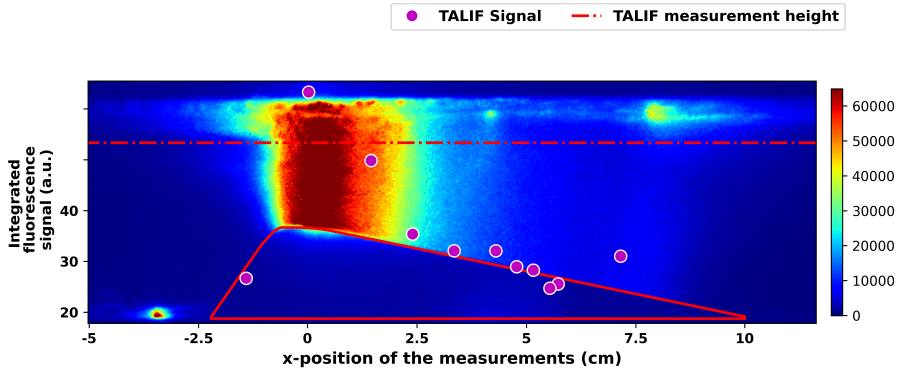

Fig. 2: ICCD imaging (20 ns gate) and O-TALIF signal intensity in 100 mbar of air.

gap. The observed trend, indicating fluctuations in energy deposition across the span, was validated through O-TALIF measurements (Fig. 2). Notably, there is a discernible gradient in atomic oxygen density, correlating with the gap width. Additional confirmation of varying electric field generation was obtained through optical emission spectroscopy (OES) using the line-ratio method, and capacitive probe measurements conducted along the x-direction of the electrode. These findings align with expectations of reduced electric field changes with the gap.

The discharge setup was evaluated in stoichiometric H_2:O_2 mixtures at 100 to 250 mbar pressure, successfully initiating a detonation wave across a wide range of deposited energies. Further investigations are planned to ascertain whether these results stem from Zel'dovich gradient mechanisms.

The work was partially supported by AID/CIEDS PPRINCE (3335) and PEPS ENERGIE 2024 ZEPhiR.

3 References

[1] Energy Institute - Statistical Review of World Energy (2023); Smil (2017) – with major processing by Our World in Data. "Direct primary energy from biofuels" (dataset). Energy Institute, "Statistical Review of World Energy"; Smil, "Energy Transitions: Global and National Perspectives" (original data). https://ourworldindata.org/grapher/global-primary-energy

[2] Wolański, Piotr 2013 *P COMBUST INST* **34.1** pp 125

[3] Y. B. Zeldovich 1980 *Combust. Flame* **39** pp 241

	Morning Session Chairman: Aranka Derszi		
9:15	Topical invited	L. Vialetto	Modelling molecular plasmas: from elementary processes to environmental applications
9:45	Hot topic	M. Baeva	DC arcs of short lengths in atmospheric pressure air: properties of the boundary layers and heat loads on the copper electrodes
10:05		Z. Kozáková	Interaction of cold microwave plasma torch with biopolymer surfaces: RONS distribution and decontamination effects
10:30	Coffee Break		
	Midday Session Chairman: Francesco Taccogna		
11:00	General Invited	L.L. Alves	Global modelling of non-equilibrium low-temperature plasmas
11:45	Topical invited	A. Gómez-Ramírez	Plasma Chemistry and Catalysis
12:15	Oral	C. Ionita	Combined effects of Dielectric Barrier Discharge plasma treatment and Ag nanoparticles on Triticum Durum seed germination
12:35		T. Osawa	Gas cylinder-free atmospheric steam plasma source for surface treatment sterilization
12:55	Lunch		
14:30	Excursions - Villa Tugendhat, Špilberk Castle, Brno Underground		
17:00		Lab tour MUNI	
18:00	**Garden Party** MUNI Kotlářská 2		
19:00			
21:30			

Challenges in plasma modelling for environmental applications: electron kinetics and transport

Luca Vialetto[1]

[1] *Department of Aeronautics and Astronautics, Stanford University, 496 Lomita Mall, Stanford, CA 94305, United States of America*
vialetto@stanford.edu

Computer models are a powerful tool for advancing scientific and technological investigation of plasmas for environmental applications. However, developing such tools is a great challenge due to the complex chemical network and multiple time scales. Moreover, these models are strongly dependent on the choice of atomic and molecular data, such as cross sections and rate coefficients. In this work, electron kinetics and transport in gases and plasmas is studied using different computational approaches. First, the importance of anisotropic scattering of electrons with molecules on calculations of electron transport parameters is investigated using Monte Carlo simulations. Finally, a 2-D fluid model is presented which is being developed to study electron kinetics and transport in surface dielectric barrier discharges for water treatment. As a result of the models, insights into optimization of electron impact cross sections which are used as input to the fluid model are derived.

Introduction

Atmospheric pressure plasma sources have been widely studied in recent decades for application in medicine, agriculture, aerospace engineering, and plasma processing of materials and surfaces [1, 2, 3]. As an example, the dielectric barrier discharge (DBD) is a practical and low-cost configuration, where the plasma is generated by a time-varying high voltage (several kVs) between two electrodes; the dielectric barrier is to prevent arcing between electrodes which could otherwise occur following electrical breakdown of the gas. Recently, surface DBDs in ambient air have found applications in agriculture for plasma indirect treatment of water [4, 5]. The uniqueness of this process is the adjustability of the pH with one system which can be used for sanitation purposes. Additionally, the technology can be used on-demand for production of nitric acid, and therefore nitrates, in a plant-usable form of water. However, despite an excellent capability, most of the currently available plasma sources for water treatment still have several shortcomings such as scalability, durability of the electrodes, and possible requirements for carrier gases or other chemicals [6]. Moreover, comprehensive understanding of the main physical and chemical mechanisms as a function of operational parameters is still limited [7]. Similar considerations for microwave discharges for CO_2 conversion are applicable.

Numerical modelling of atmospheric pressure plasmas operating with molecular gases is still challenging, mainly due to the complex chemical network and multiple timescales. So far, many studies have relied on lower-dimensional (0-D) models where a large number of species and chemical reactions are taken into account [8, 9]. The use of these models is also motivated by the large disparity of timescales, ranging from electron impact ionization ($1-10$ ns) to slower neutral reactions and gas-phase mass transport ($\sim$ s timescale), as shown in Fig. 1. However, 0-D models typically neglect the transport of charged and neutral species in the plasmas, the interactions of the plasma with surfaces, and the spatial non-uniformity of the discharge. Moreover, kinetic and fluid models are strongly dependent on the choice of atomic and molecular data, such as cross sections and rate coefficients. Such coefficients are usually calculated from collision cross-section data by solving numerically the electron Boltzmann equation (EBE). Requirements of accuracy, consistency, and completeness of such cross sections sets significantly affects the predictive capability of these models, not only in the estimation of macroscopic plasma parameters, but also in the determination of the main chemical mechanisms [10].

In this presentation, electron kinetics and transport in molecular gases and plasmas is investigated using different numerical methods. First, Monte Carlo simulations of electron swarm in gases are presented to assess the accuracy of the available sets of cross sections. The importance of anisotropic

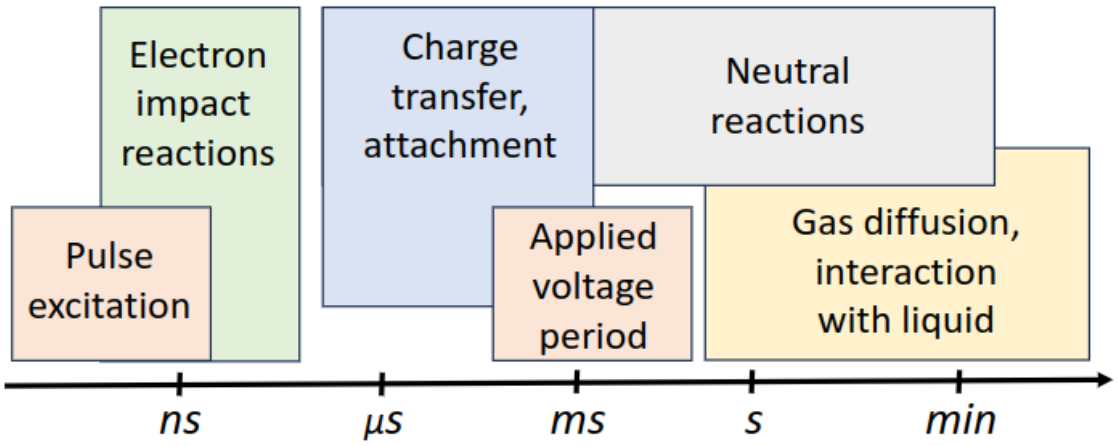

Fig. 1: Multiple timescales in surface DBDs for water treatment.

scattering of electrons is emphasized. Finally, an application for surface DBD for water treatment is given. The emphasis is on the fluid model development and assessment of the accuracy in the assumptions that are usually taken for description of electron kinetics and transport in atmospheric pressure plasmas.

Monte Carlo simulations of electron swarm in gases

The first part of the presentation focuses on several aspects of anisotropic scattering of electrons in gases. A Monte Carlo simulations code for electrons has been developed to study the effect of scattering dynamics in electron rate and transport coefficients [11]. First, the accuracy of the implementation and treatment of anisotropic scattering is assessed through benchmarking calculations of two-term, multi-term Boltzmann solver, and Monte Carlo simulations [14]. Fig. 2 shows results obtained with isotropic, forward, and screened Coulomb angular scattering models in electron-neutral collisions with the Lucas-Salee ideal gas model. The impact of scattering on electron swarm parameters is demonstrated in both conservative and non-conservative model gases using Monte Carlo simulations and 10-term solutions of the electron Boltzmann equation showing excellent agreement between the two codes.

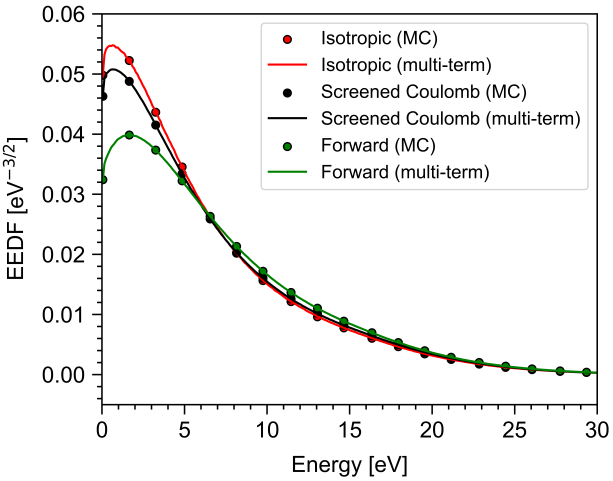

Fig. 2: Electron energy distribution function calculated at 100 Td with Lucas-Salee ideal gas model using Monte Carlo simulations (dots) and multi-term Boltzmann solver (lines) [14]. Three different angular scattering models have been used: isotropic (red), screened-Coulomb (black), and forward scattering (green).

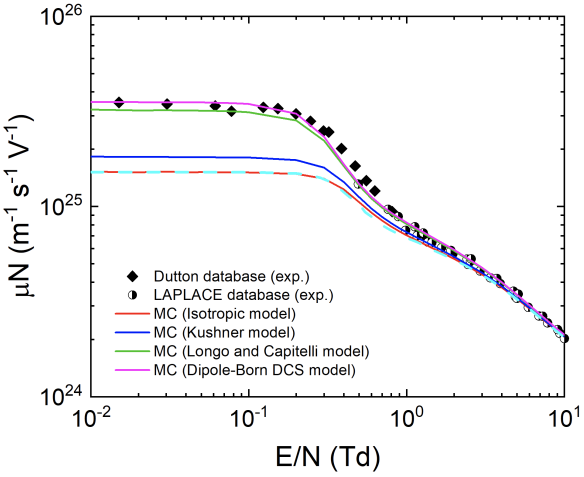

Fig. 3: Electron reduced mobility measured (dots) and calculated (lines) using Monte Carlo simulations in CO with different angular scattering models and Biagi's set of cross sections, as a function of the reduced electric field.

Then, the importance of anisotropic scattering of electrons in real gases is assessed. Specifically, an anisotropic scattering model for dipole rotational collisions of electrons has been derived based on the dipole-Born differential cross sections. Results of electron reduced mobility obtianed with Monte Carlo simulations using different angular scattering models is compared with measured transport parameters in Fig. 3. It has been found that the application of anisotropic scattering of electrons in rotational collisions affects significantly the calculated electron transport parameters in molecular gases, such as CO [11], NO [12], and H_2O [13]. The consequences in the electron swarm derived cross sections are also discussed. Finally, the application of Monte Carlo simulations of electrons in arbitrary mixture of gases is presented. As an example, electron transport parameters calculated in air with variable concentrations of H_2O vapor are presented and compared with experiments [15]. These results are important for estimation of three-body attachment cross sections of electrons in air with variable admixture of water vapor, which is often neglected in plasma chemistry models at atmospheric pressure [15]. It is demonstrated that insights provided by Monte Carlo simulations of electron swarms in gases are important for accurate optimization of electron impact cross sections that are used as input to fluid models of the plasma.

Fluid modelling of plasmas for environmental applications

A 2-D fluid model for surface DBDs is being developed to study the influence of operational parameters in plasma formation and production of reactive oxygen and nitrogen species. The model couples fluid discharge equations for a four fluid mixture including neutrals, electrons, positive ions, and negative ions, with the Poisson equation. The electron rate and transport coefficients are derived from Monte Carlo simulations of electrons. The transport of charged particles has been described using the drift-diffusion approximation. Results of the fluid model have been benchmarked against PIC/MCC simulations and Full-Fluid Moment Model results for a 1-D DC breakdown in Ar [16]. Furthermore, the correctness of the implementation has been tested against analytical and manufactured solutions. As an example, the model is applied to study discharge formation in surface DBDs operated with air. As a perspective, results obtained from the fluid model can be used to inform lower dimensional (0-D) chemistry models to accurately describe the gas heating, ion wind, and neutral species transport effects on the chemical reactions occurring in the plasma and gas phase.

Challenges and future outlook

Despite electron transport in gases has been studied since decades, we conclude that modelling and simulations of electrons in arbitrary mixture of gases are still challenging. This is mostly due to the lack

of experimental electron transport parameters and accurate cross sections of electron impact dissociation of molecules. Comparison between electron swarm measurements and calculations can provide valuable insights into the collision dynamics and cross sections magnitude and shape. Apart from electron swarm, modelling of surface DBDs with complex chemistry is still limited to timescales much shorter than the typical treatment time, that is in the order of minutes. Methods to bridge longer timescales and integrate experimental data into modelling frameworks is sought after for quantitative understanding of plasma formation and dynamics.

Acknowledgments

The results presented have been obtained in collaboration with colleagues from the Eindhoven University of Technology (J. van Dijk, M.C.M. van de Sanden), IST-Lisbon (V. Guerra, P. Viegas, L.L. Alves), Maastricht University (P. Diomede, G.J. van Rooij), Texas Tech University (M. Flynn, J. Stephens), and Stanford University (K. Hara) whose important contribution is acknowledged. This work was supported by the Stanford Energy Postdoctoral Fellowship through contributions from the Precourt Institute for Energy, Bits & Watts Initiative, StorageX Initiative, and TomKat Center for Sustainable Energy.

[1] M. Keidar, K.-D. Weltmann, S. Macheret, *J. Appl. Phys.* **130** (2021) 080401.
[2] M. Meyer, J. Foster, M. J. Kushner, *Plasma Sources Sci. Technol.* **32** (2023) 085001.
[3] J. P. Boeuf, L. C. Pitchford, *J. Appl. Phys.* **97** (2005) 103307.
[4] C. Sze, B. Wang, J. Xu, J. Rivas-Davila, M. A. Cappelli, *RSC Adv.* **11** (2021) 37886.
[5] R. Agus, F. Avino, L. Ibba, B. Myers, L. Zampieri, E. Martines, A. Howling, I. Furno, *Chem. Eng. J.*, *In press*.
[6] G. Neretti, M. Taglioli, G. Colonna, C. A. Borghi, *Plasma Sources Sci. Technol.* **26** (2017) 015013.
[7] L. Ibba, R. Agus, F. Avino, I. Furno, P. F. Ambrico, *Plasma Chem. Plasma Proc.* (2024) 1–21.
[8] Y. Sakiyama, D. B. Graves, H.-W. Chang, T. Shimizu, G. E. Morfill, *J. Phys. D: Appl. Phys.* **45** (2012) 425201.
[9] G. Pierotti, C. Piferi, A. Popoli, M. Cavedon, A. Cristofolini, E. Martines, C. Riccardi, *Plasma Sources Sci. Technol.* **32** (2023) 064005.
[10] I. Adamovich, *et al.*, *J. Phys. D: Appl. Phys.* **55** (2022) 373001.
[11] L. Vialetto, A. B. Moussa, J. van Dijk, S. Longo, P. Diomede, V. Guerra, L.L. Alves, *Plasma Sources Sci. Technol.* **30** (2021) 075001.
[12] V. Laporta, L. Vialetto, V. Guerra, L. L. Alves, *Plasma Sources Sci. Technol.* **31** (2022) 054001.
[13] M. Budde, T.C. Dias, L. Vialetto, N. Pinhao, V. Guerra, T. Silva, *J. Phys. D: Appl. Phys.* **56** (2023) 255201.
[14] M. Flynn, L. Vialetto, A. Fierro, J. Stephens, *Under revision*.
[15] J. de Urquijo, O. Gonzalez-Magana, E. Basurto, A.M. Juarez, *J. Phys. D: Appl. Phys.* **57** (2024) 125205.
[16] A. Mansour, L. Vialetto, Y. Yamashita, K. Hara, *In preparation*.

DC arcs of short lengths in atmospheric pressure air: properties of the boundary layers and heat loads on the copper electrodes

Margarita Baeva [(1).(*)], Ammar Najam [(1)], Petrus Pieterse [(1,2)], Dirk Uhrlandt [(1,2)]

[1] *Leibniz Institute for Plasma Science and Technology (INP), 17489 Greifswald, Germany*

[2] *Institute for Electrical Power Engineering, University of Rostock, 18051 Rostock, Germany*

[(*)] baeva@inp-greifswald.de

The behaviour of electric arcs of short lengths and low current levels generated between copper electrodes in atmospheric-pressure air is important to the understanding of the processes occurring during the contact separation in switching devices. Although a lot of modelling work on switching arcs has been carried out over the years, the processes related to the phase of contact separation have been left out of scope. The main reason can be probably seen in the non-equilibrium conditions that have to be taken into account.

In this work, we present the studies based on a one-dimensional unified chemical and thermal non-equilibrium model of dc electric arcs [1] between copper electrodes of 10 mm length each in atmospheric-pressure air, which from the best of authors' knowledge has not been reported so far. In experiments, the inter-electrode distance is varied from 20 µm up to 1 mm at a constant current of 0.88 A and the arc voltage has been measured. The main focus is set on the computed properties of the near-electrode boundary layers, which are spatially resolved. The plasma chemistry involves the 11-species reaction database by Dunn and Kang [2]. The emission of electrons from the non-refractory cathode is considered as a thermo-field emission and computed applying the TMM (transferred matrix method) [3] and an appropriate field enhancement factor. A description of the model in detail will be given in a forthcoming publication. Results from the model and experiment are summarized in what follows.

Figure 1 shows the arc voltage as a function of the arc length. A near-linear increase of the voltage is observed with the increase of the arc length. A value of about 13 V is found at miniscule arc lengths that indicates the value of the total voltage in the cathode and anode sheaths. The experimental course of the arc voltage was reproduced by the determination of the mean current density to be used in the model for a given arc length. The obtained mean current density decreases with the increase of the arc length that can be related to an increase of the arc attachment area.

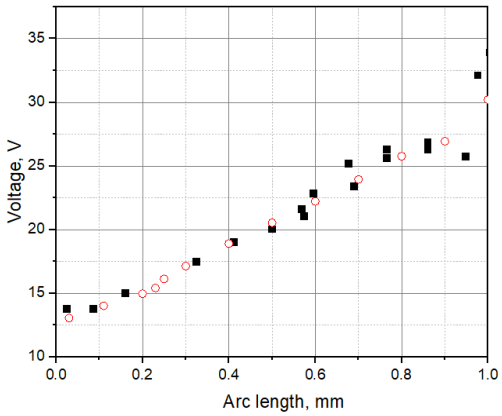

Fig. 1: Measured (solid) and computed (open symbols) arc voltage as function of the arc length.

The temperatures on the electrode boundaries in contact with the plasma and the corresponding heat fluxes from the plasma are shown in Figure 2a (subscripts "c" and "a" denote the cathode and the anode, respectively). Figure 2b shows the distribution of the electric potential along the inter-electrode distance (the position of the cathode is at the value of 0 and the position of the anode varies). The highest value (though still below the melting point) of the anode temperature T_a is reached for the shortest arc length. Notice the change in the T_a, Q_a-behaviour and the reversal of the anode fall for arc lengths beyond 0.2 mm.

Figure 3 shows the distribution of the gas and electron temperature (a), and the species number densities (b) along the inter-electrode distance for arc lengths of 0.03 (curves 1); 0.11(curves 2) and

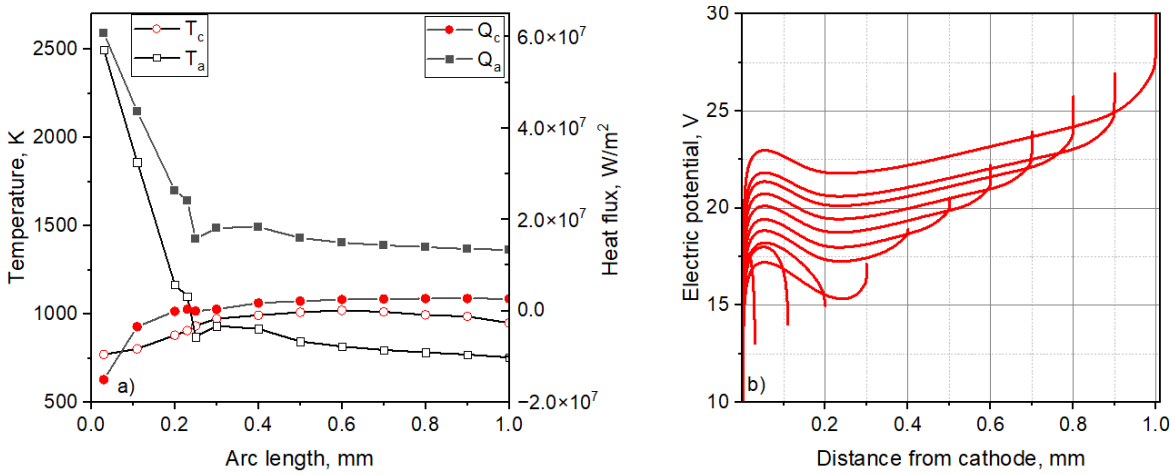

Fig. 2: Temperature and heat flux at the electrodes (a) and distribution of the electric potential between the electrodes (b) for various arc lengths.

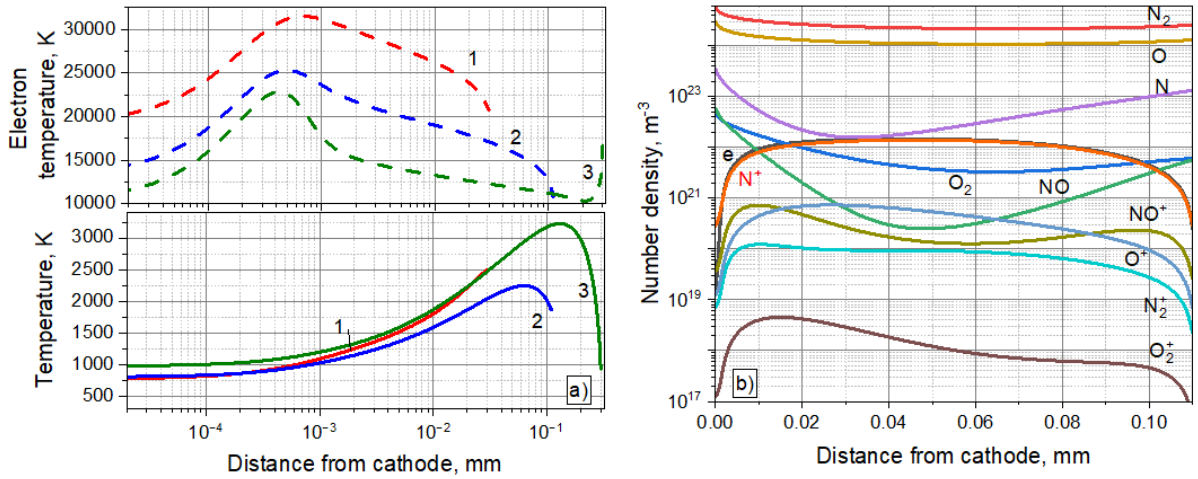

Fig. 3: Distribution of the temperatures of heavy particles and electrons for arc lengths of 0.03, 0.11, and 0.3 mm (a); distribution of species number densities for an arc length of 0.11 mm (b).

0.3 mm (curves 3). Maximum temperature is reached at the anode for the shortest arc length and shifts towards the cathode. The electron temperature reaches a maximum in the cathode sheath and drops towards the plasma bulk due to the processes of ionization and dissociation. With the reversal of the anode fall, an increase of the electron temperature is obtained in front of the anode. The results indicate conditions of a strong thermal non-equilibrium. The computed plasma composition (Figure 3b) shows the that N_2 and O are the dominant neutral species, while N^+ is the dominant ion. The deviation from quasi-neutrality is well pronounced in thin sheaths adjacent to the electrodes.

Acknowledgment

The work is funded by the German Research Foundation (DFG) Project number 524731006.
Radiation data is provided by Yann Cressault, LAPLACE Lab, Toulouse, France.

[1] M. Baeva, D. Loffhagen and D. Uhrlandt, *Plasma Chem. Plasma Process.* **39** (2019) 1359.
[2] P. A. Gnoffo, R. N. Gupta and J. L. Shinn, *Conservation Equations and Physical Models for Hypersonic Air Flows in Thermal and Chemical Nonequilibrium* (1989)Technical Paper 2867, NASA.
[3] M. Baeva, *AIP Advances* (2018) **8** 085322.
[4] A. Najam, P. Pieterse and D. Uhrlandt, *Energies* **13 (**2020) 6377.

Interaction of cold microwave plasma torch with biopolymer surfaces: RONS distribution and decontamination effects

Zdenka Kozáková(*)[1], Lucie Žlebková[1], Kristína Trebulová[1], Veronika Petrová[1], Magdaléna Kocianová[1], Todor Bogdanov[2], František Krčma[1]

[1] *Faculty of Chemistry, Brno University of Technology, 612 00 Brno, Czech Republic*

[2] *Faculty of Medicine, Medical University of Sofia, Dunav street 2, 1000 Sofia, Bulgaria*

(*) kozakova@fch.vut.cz

Interactions of various non-thermal plasma systems with various surfaces have been studied for many decades. But not only due to the increased resistance of microorganism to conventional antimicrobial drugs, special attention is given to different plasma jets or torches interacting with biological surfaces mainly during the last decade [1]. Although numerous studies are available on the diagnostics of selected reactive oxygen and nitrogen species (RONS) like ·OH, ·O, NO, NO_2, O_3 or H_2O_2 in the gaseous phase using optical emission and absorption spectroscopies or laser induced fluorescence [2], information about their distribution on the solid surfaces is still lacking. The presented contribution demonstrates the RONS distribution of the microwave plasma torch on the biopolymer surfaces and compares it with its decontamination effect on selected microorganisms.

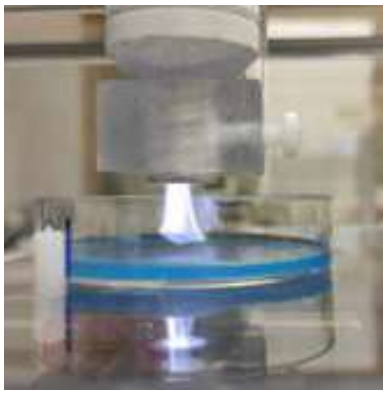

Fig. 1: Plasma treatment of biopolymer containing indigo dye by the microwave plasma torch.

The used plasma system was based on the microwave torch (surfayok) in argon [3]. Plasma was generated at atmospheric pressure with low power from 9 to 15 W, and the argon flow of 5 L/min. The treated biopolymer plates containing reagents for RONS determination or microorganism culture for decontamination effect observation were placed under the plasma torch so that the tip of the active plasma plume was positioned just 1.5 mm above the biopolymer surface ensuring the highest RONS spreading on the whole plate surface (Fig. 1). Petri dishes with the diameter of 50 mm were used for the agar-based biopolymer layer preparation (thickness of 5 mm). Following reagents were embedded into the biopolymer structure in order to determine particular reactive species by their colour change: indigo dye for ozone, potassium iodide with starch for non-specific ROS, and Griess reagent powder kits (Merck) for nitrates and nitrites. To observe decontamination effects visible as an inhibited growth area, bacteria *Escherichia coli*, *Staphylococcus epidermidis*, *Propionibacterium acnes* as well as yeast *Candida glabrata* were chosen. The prepared biopolymer layers were treated by the cold plasma torch at different treatment times and modes (static or scanning).

Formation and surface distribution of ozone during the static microwave plasma torch treatment in different distances of the active plasma tip from the biopolymer surface was evaluated by the indigo dye discoloration. Among three tested distances of 0, 1.5, and 10 mm, 1.5 mm was determined as the most suitable for the uniform static treatment of the whole biopolymer surface in the 50 mm Petri dish. Formation of nitrates and nitrites was confirmed by the brownish or pink colour of the commercial kit, respectively. Their distribution over the biopolymer surface was increased during the static torch treatment time from 30 to 300 seconds (Fig. 2). The same results were achieved for the non-selective ROS effects. The total ROS formation caused oxidation of potassium iodide to iodine which was determined by the blue colour in the reaction with starch. According to the colour intensity related to the RONS concentration, nitrites (pink colour) seemed to be the most effectively produced species in the microwave plasma torch. Comparing the results of RONS distribution during the static microwave

torch treatment to antimicrobial effects on microorganisms evaluated by the size of the inhibited growth area, we can state that they were in good agreement, even for highly resistant bacteria *P. acnes* (Fig. 2). I.e., the size of the inhibited growth area increased with the increasing treatment time and the affected area corresponded to the area of the highest RONS production.

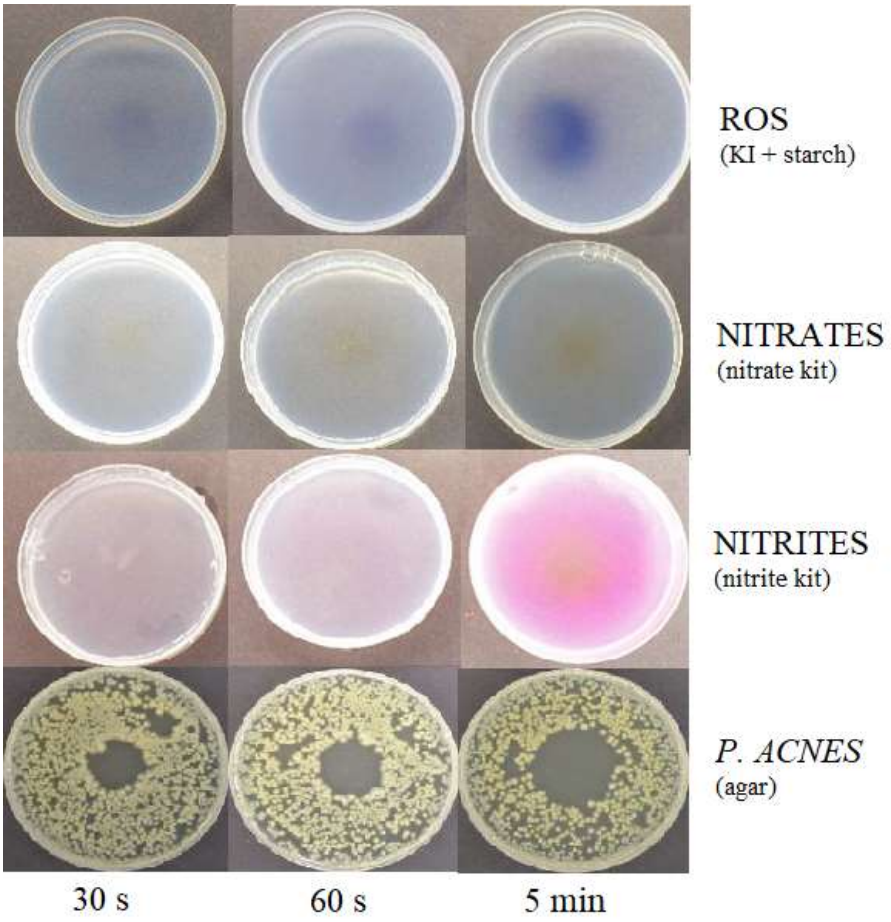

Fig. 2: Demonstration of RONS distribution and decontamination effects observed by inhibited growth area of *Propionibacterium acnes*. Biopolymer containing appropriate reagent kit was treated by the cold microwave torch in argon (power of 9 W; argon flow of 5 L/min) for 30 s, 60 s, and 5 min, respectively.

Besides the static mode of the cold microwave torch, two modified plasma regimes were applied for the biopolymer surface treatment to obtain homogeneous RONS distribution and higher decontamination effects. Employing the scan mode of the plasma torch in a "snake" shape, a uniform distribution of desired species was observed. Moreover, decontamination over 70 % was achieved for bacteria *E. coli* and yeast *C. glabrata* even after one run of such scanning treatment. Contrary to the scan mode, using the lid on the Petri dish during the treatment did not bring the expected impact of the increased RONS formation and antimicrobial decontamination, probably due to the argon accumulation under the lid preventing the supply of the surrounding air.

Acknowledgements. This research is a part of the COST CA20114 Action. The microwave plasma system was developed in the collaboration of both institutions.

[1] D. B. Graves, *Phys. Plasmas* **21** (2014) 080901.
[2] F. Krčma et al., J. Phys. D: Appl. Phys. **51** (2018) 414001.
[3] T. Bogdanov, E. Benova, System for the low temperature plasma torch generation *Protected construction* (2023) BG 4602 U1.

Global modelling of non-equilibrium low-temperature plasmas

Luís L Alves(*)[1]

[1] *Instituto de Plasmas e Fusão Nuclear, Instituto Superior Técnico, Universidade de Lisboa, Portugal*

(*)llalves@tecnico.ulisboa.pt

Global (zero-dimensional) models are very popular in the modeling of low-temperature plasmas, especially when the focus is on plasma chemistry. This talk will briefly introduce the LisbOn Kinetics LoKI-B+C simulation tool, highlighting some of the most recent simulation results obtained with the code. We will underline the importance of validation activities, comparing modelling results with experimental measurements, to unfold the full potential of modelling as a predictive tool.

The field of low-temperature plasma (LTP) science and engineering is driven by a dual focus on both fundamental scientific exploration and practical applications aimed at societal advancements. Fundamental research endeavors to delve into the underlying principles governing these plasmas, playing a pivotal role in achieving the scientific breakthroughs necessary for successful applications.

Modelling activities are a fundamental component in any research domain, complementing and/or aiding experimental diagnostics; providing predictions on the behaviour of significant quantities, especially when experimental acess is limited; and contributing to a deeper understanding of the field‘s fundamental knowledge. Modelling and simulation of LTP have been considered as requirements for advancing the field, and model-based design for plasma equipment and processes has been identified as a critical capability realizing industrial objectives [1]. The guidance offered by LTP models proves particularly valuable given the inherent complexity of the medium (often characterized by different material phases), composed by charged particles (electrons and ions) and by neutral species in different excited states, intrinsically in non-equilibrium as result of collisional, radiative and electromagnetic interactions.

Global (zero-dimensional) models are very popular in the modeling of LTP, especially when the focus is on plasma chemistry [2]. In these models, the dynamics of the plasma species *s* is described by particle rate balance equations, composed by production and destruction terms as defined by chemical reactions, in addition to a loss term due to transport writen under an algebraic form

$$\frac{dn_s}{dt} = \sum_j \left\{ \left(a_{sj}^{(2)} - a_{sj}^{(1)} \right) k_j \prod_l n_l^{a_{lj}^{(1)}} \right\} - \nu_{transp_s} n_s \ . \qquad (1)$$

Here, n_s is the density of the species; $a_{sj}^{(1)}$ and $a_{sj}^{(2)}$, are the stoichiometric coefficients of species *s*, as they appear on the left- and right-hand sides of a reaction *j*, respectively; k_j is the rate coefficient of reaction *j*; and ν_{transp_s} is the spatial-averaged loss frequency due to transport to the walls. The set of chemical reactions defining the kinetic scheme of interest should include both volume and surface mechanisms. The extension to a surface kinetics can be easily done by considering a mesoscopic description [2], including for example physical adsorption/desorption, chemical adsorption, surface transport, and Eley-Rideal and Langmuir–Hinshelwood recombination processes. The rate coefficients for electron-induced processes, such as ionisation, excitation/de-excitation and dissociation, are obtained by averaging the corresponding energy-dependent cross sections over the electron energy distribution function (EEDF), and for other chemical reactions, e.g. between the neutral species or the ions, they are typically calculated from temperature-dependent Arrhenius equations, obtained from literature. In non-equilibrium LTP, the EEDF should be calculated by solving the electron Boltzmann equation coupled to the rate balance equations. In this case, there is no need to solve the electron-energy balance equation to close the model, since the electron Boltzmann equation makes it possible to obtain

the electron mean energy (or an equivalent electron kinetic temperature) for a given value of the reduced electric field E/N (where E is the electric field and N is the density of the gaseous mixture), to be determined self-consistently.

The transport of charged particles is key to identify the operating point of a gas discharge, defined through a Schottky-like condition [2,3] that balances the net creation rate of electrons and ions due to kinetic mechanisms in the volume, with their loss rate to the walls. Satisfying this condition allows self-consistently determining as eigenvalue the reduced electric field that maintains the plasma, consistent with the required net creation-rate of charged particles, for given discharge parameters (e.g. gas density and plasma dimensions) that define the corresponding particle losses. In the end, a direct effect of this eigenvalue on the plasma chemistry is expected, via the electron excitation and ionization frequencies influencing the kinetics.

Global models can be solved using codes available in the LTP community: ZDPlasKin, a freeware code developed by Pancheshnyi *et al.* [4]; GlobalKin, developed by Kushner *et al.* [5, 6] and available upon request; Quantemol-P, developed with a graphical user interface [7], corresponding to a commercial application that extends GlobalKin to the automatic generation of a plasma chemistry from a set of userdefined species; and the global model within the PLASIMO commercial software, developed by van Dijk *et al.* [8]. In this work, we will use the LisbOn KInetics LoKI-B+C [9], a simulation tool for plasma chemistry (to be relased as open-source code), which couples two main calculation blocks: a two-term Boltzmann solver (LoKI-B) [10,11] (released as open-source code licensed under the GNU GPL v3.0) and a Chemical solver (LoKI-C), developed / consolidated resorting to the well-grounded scientific foundations of the Portuguese group N-PRiME.

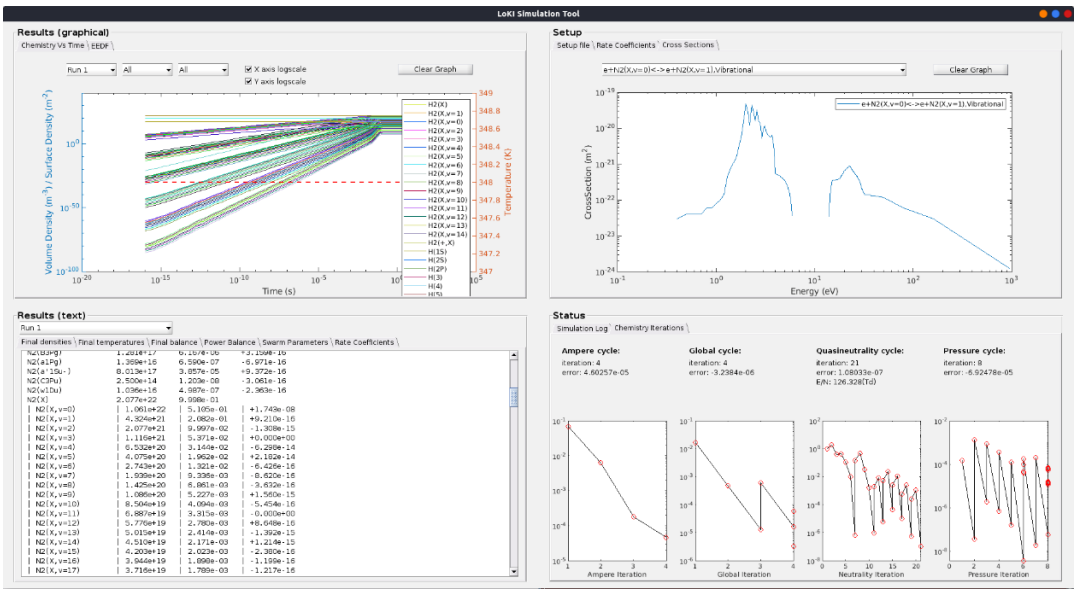

Fig. 1: Example of the Graphical User Interface display after a complete LoKI-B+C simulation.

LoKI-B+C has been developed to handle kinetic schemes in *any* complex gas mixture, describing *any* type of collisional encounter between *any* electron/neutral/ion species. In particular, LoKI-B considers first and second-kind electron collisions, including anisotropic effects for elastic and rotational collisions. The solution of LoKI-B+C follows a workflow embedding four iterative cycles: (i) over the initial mixture composition, to obtain the user-prescribed *pressure*; (ii) over the reduced electric field, to satisfy the plasma *neutrality*, for an user-prescribed electron density (or some equivalent parameter, see (iv)); (iii) over the densities of the most relevant excited states afecting the electron Boltzmann equation, to *globally* converge over the EEDF and the electron macroscopic parameters; and (iv) over the electron density, to obtain the user-prescribed *discharge current* (or *power density*). As output, LoKI-B+C self-consistently calculates the EEDF and the associated electron macroscopic parameters, the densities of species, the reaction creation/destruction rates, and the reduced electric field.

This talk will briefly introduce LoKI-B+C and its workflow. We will focus on the formulation used to describe electron anisotropic scattering in LoKI-B, and the flexibility of the code to parse I/O data,

adopting the standards of the future platform LXCat 3.0 [12]. And we will attempt to illustrate a simulation example (see Fig. 1), before highlighting some of our most recent simulation results obtained using LoKI-B+C.

The literature proposes several formulations to describe the transport of charged particles in the global modeling of LTP, and we will analyze the influence of several of these formulations using as testbeds DC discharges in oxygen and microwave discharges in helium [13].

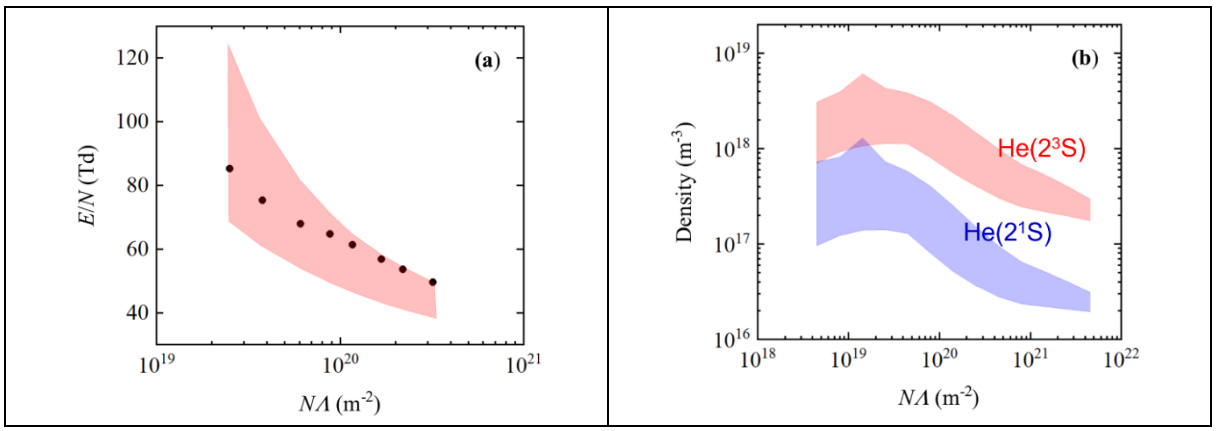

Fig. 2: Measurements (points) and calculations (bands), adopting various charged-particle transport models, of: (a) discharge characteristics of E/N vs. $N\Lambda$ in oxygen, for cylindrical DC discharges (1 cm radius and 52.5 cm length) at 10 mA current; (b) densities of metastables in helium, as a function of $N\Lambda$, for cylindrical microwave discharges (0.3 cm radius), at 2.45 GHz frequency, $5\text{x}10^{18}$ m^{-3} electron density, and 1000 K gas temperature.

Results show that (see Fig. 2) using different charged-particle transport models can result in uncertainties of 20% – 60% and 8% – 115% in the discharge characteristics of oxygen and helium, respectively, with larger dispersion at low pressure and low electron density. The spreading in the results is observed also in the densities of the main plasma species, corresponding to uncertainties up to 60% and within 50% – 150% in oxygen and helium, respectively.

The development of kinetics schemes for plasma chemistry is only meaningful when these schemes are validated by comparing simulation predictions with experimental measurements. The LTP community has been following this path for many years, but it is suggested that it should adopt a higher paradigm, defining *reaction mechanisms* validated against *benchmark experiments* [14]. The concept of reaction mechanism was introduced by the combustion community, and it corresponds to a set of experimentally validated reactions and corresponding rate coefficients. And in the present context, benchmark experiments represent a significant ensemble of experimental data, intended (or suited) for model validation, obtained in well defined and reproducible conditions, using established diagnostics, and assessing multiple quantities.

A recent effort in this direction involved the comparison of simulations made by the N-PRiME group in Lisbon with measurements made in benchmark experiments by a group from the *Laboratoire de Physique des Plasmas* (LPP) in Paris, in collaboration with a team from the Lomonosov Moscow State University (MSU), regarding oxygen plasmas produced by DC glow discharges for gas pressures of 30 – 1000 Pa and currents of 10 – 40 mA. The study comprised the densities of the main species in the discharge, $O_2(X^3\Delta_g^-)$, $O_2(a^1\Delta_g)$, $O_2(b^1\Sigma_{g+})$ and $O(^3P)$, and also the reduced electric field and the gas temperature, and it revealed new mechanisms for the creation / destruction of these species [14].

Figure 3(left) shows simulation results and measurements of the $O(^3P)$ density, as a function of pressure, for a discharge current of 30 mA. Measurements were obtained from radially averaged vacuum ultraviolet (VUV) and actinometry diagnostics, and from on-axis cavity ringdown spectroscopy (CRDS). There is good agreement between model and experiment, which is greatly due to the values used for the recombination probability, taken from experiment. The effect of the discharge current on the $O_2(a^1\Delta_g)$ density is shown in Fig. 3(right), for gas pressures of 50 and 400 Pa. As expected, an increase in current/electron density leads to larger densities of the metastable, which again agree well with VUV and optical emission spectroscopy (OES) measurements.

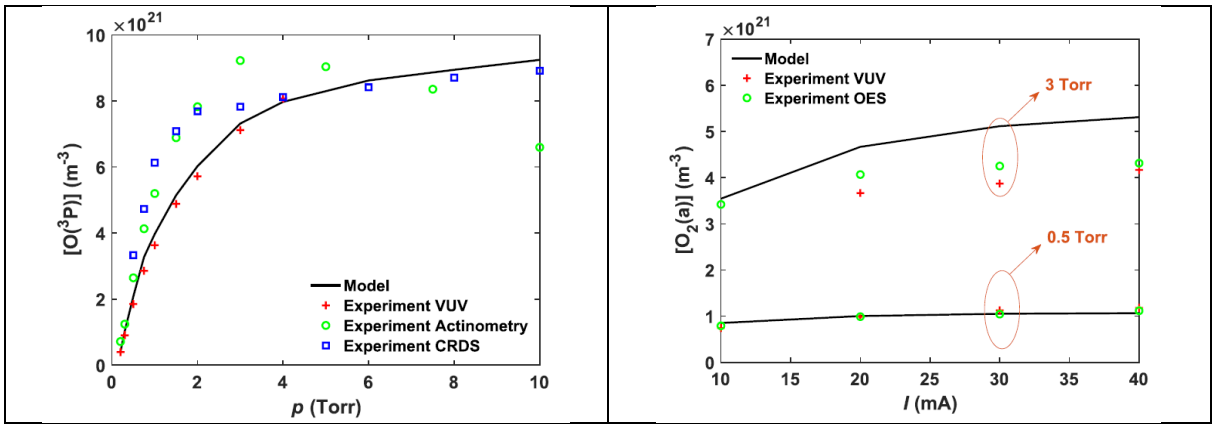

Fig. 3: Measurements (points) and calculations (curves) for cylindrical DC discharges in oxygen (1 cm radius and 52.5 cm length; wall temperature of 323.15 K): left, $O(^3P)$ density, as a function of pressure for 30 mA current; right, $O_2(a^1\Delta_g)$ density, as a function of discharge current, for 0.5 and 3 Torr gas pressures.

We will conclude presenting the results of our current efforts to model nitrogen-hydrogen plasmas produced in DC glow discharges with borosilicate glass walls [15], with low H_2 concentrations (< 5%), at 5 sccm continuous flow, 50 – 500 Pa pressures and 10 – 40 mA discharge currents. This involves a critical review of the rate coefficients adopted in the kinetic scheme, with a special focus on the wall reactions, the reactions leading to the production/destruction of mixed H/N species, and the electron-impact reactions that will mostly affect the trends as a function of current [16].

Modelling activities in the field of LTP are an essential and widely embraced research component for investigating fundamental processes, providing quantitative predictions on the behaviour of systems, guiding the design of experiments and diagnostics, and optimising devices. The potential of modelling as a predictive tool can only be achieved after a validation process, by comparing modelling results with experimental measurements, a step that requires an intense collaborative work within the community.

Acknowledgements
This work was funded by the Fundação para a Ciência e a Tecnologia under projects UIDB/50010/2020 (https://doi.org/10.54499/UIDB/50010/2020),UIDP/50010/2020(https://doi.org/10.54499/UIDP/50010/2020), LA/P/0061/202 (https://doi.org/10.54499/LA/P/0061/2020) and 2022.04128.PTDC (https://doi.org/10.54499/2022.04128.PTDC).

References
[1] I. Adamovich *et al.* 2022 *J. Phys. D: Appl. Phys.* **55** 373001.
[2] L. L. Alves *et al.* 2018 *Plasma Sources Sci. Technol.* **27** 023002.
[3] W. Schottky 1924 *Physica Z* **25** 635.
[4] S. Pancheshnyi *et al.* 2008 ZDPlasKin (www.zdplaskin.laplace.univ-tlse.fr).
[5] A. M. Lietz and M. J. Kushner 2016 *J. Phys. D: Appl. Phys.* **49** 425204.
[6] D. S. Stafford and M. J. Kushner 2004 *J. Appl. Phys.* **96** 2451.
[7] J. J. Munro and J. Tennyson 2008 *J. Vac. Sci. Technol. A* **26** 865.
[8] J. van Dijk *et al.* 2009 *J. Phys. D: Appl. Phys.* **42** 194012.
[9] nprime.tecnico.ulisboa.pt/loki/
[10] A. Tejero-Del-Caz *et al.*, *Plasma Sources Sci. Technol.* **28** (2019) 043001.
[11] github.com/IST-Lisbon/LoKI/
[12] github.com/LXCat-project/LXCat/
[13] L. L. Alves and A. Tejero-del-Caz 2023 *Plasma Sources Sci. Technol.* **32** 054003.
[14] T. C. Dias *et al.* 2023 *Plasma Sources Sci. Technol.* **32** 084003.
[15] A. Chatain *et al.*, *Plasma Sources Sci. Technol.* **32** 035002, 2023.
[16] D. Simões *et al.*, *Plasma-surface coupled modelling of ammonia production in DC discharges,* ESCAMPIG XXVI, Brno, Czech Republic (2024).

Plasma Chemistry and Catalysis

P. Navascués[1], J. Garrido-García[1], M. Oliva-Ramírez[1, 2], J. Cotrino[1, 2], A. González-Elipe[1], Gómez-Ramírez A.[1, 2,*]

[1] *Laboratory of Nanotechnology on Surfaces and Plasma. Instituto de Ciencia de Materiales de Sevilla (CSIC-Universidad de Sevilla), Avda. Américo Vespucio 49, E-41092 Seville, Spain*

[2] *Departamento de Física Atómica, Molecular y Nuclear, Universidad de Sevilla, Avda. Reina Mercedes, E-41012 Seville, Spain*

(*) anamgr@us.es

Since the discovery of the ozonizer by Siemens in 1857 [1], [2], plasma has been used to carry out several chemical processes of high interest, such as hydrocarbon reforming, synthesis of high-value-added chemicals (hydrogen, ammonia), and elimination of pollutants (VOCs, CO2). In the late 1990s and throughout the first two decades of the 21st century, many studies have been published incorporating classical catalysts into plasma reactors, leading to the establishment of the term "plasma catalysis" within the community [3]. The objective behind the inclusion of catalysts in plasma reactors is to enhance the energy efficiency and chemical yield of the processes, aiming to achieve synergies between plasma-assisted chemistry and the classical catalytic effect of catalysts in contact with plasma. Numerous studies have been conducted to analyze the synergistic effect of plasma catalysis in processes of significant environmental importance (such as CO_2 elimination, greenhouse gas conversion, NO_x and NH_3 synthesis, water decontamination, etc.) as well as those of energetic interest (including H_2 synthesis, CH_4 conversion, alcohol production, etc.).[4], [5] Different authors have analysed, both experimentally and theoretically, the possible mechanisms that take place in the plasma in the presence of catalysts, leading to an increase in process performance. For this purpose, operational parameters of plasma reactors are usually varied, among which temperature, operating voltages, gas flow and type of barrier materials stand out. Currently, numerous works are still being published on this topic, and it is an area of great interest in the field of plasma chemistry, with one of the highlights being the recent controversy over the real role of catalysts during plasma-assisted processes. [6], [7] Recent studies have demonstrated that the synergistic effect [5], [8] found is not due to a classical catalytic effect (or if so, it is of second order), but rather to the modifications that the inclusion of metallic particles has on the electrical properties of the discharge. Although those results would depend greatly on the type of process under study (they will not be the same for hydrocarbon reforming as for ammonia synthesis) they open a debate of great interest in the scientific community.

In this talk, we will focus on the ammonia synthesis process carried out in a packed-bed plasma reactor, including a classical ruthenium (Ru) catalyst -used in conventional thermal methods- in the ferroelectric packed-bed barrier, aiming to increase the yields and energy efficiencies of the process. We will analyse the ammonia synthesis process in the presence/absence of the Ru catalyst, and working at two different temperatures, ambient and 190°C (at which purely catalytic effects could be expected). We will address the study of the catalyst's effect on plasma properties, analysing current curves through the reactor, power consumption, energy efficiency, and simulating the possible effects of incorporating the metallic catalyst into the packed bed. Our results demonstrate, for the first time in the literature up to our knowledge, that the reported synergy is not due to a classical catalytic effect but rather to the modifications that the inclusion of metallic particles (classical catalysts) has on the plasma. Additionally, it is shown that purely chemical catalytic effects are negligible during plasma-assisted NH_3 synthesis. Our conclusions reveal that the use of classical metallic catalysts, which are highly expensive, is not a good strategy for increasing the energy efficiency of the plasma-assisted ammonia synthesis. These results are highly significant in the field of plasma catalysis, where it has traditionally been assumed that the found synergy is due to catalytic effects, implying that the catalytic effect is responsible for the increased reaction yield.

[1] W. Siemens, 'Ueber die elektrostatische Induction und die Verzögerung des Stroms in Flaschendrähten', *Ann Phys*, vol. 178, no. 9, pp. 66–122, Jan. 1857, doi: https://doi.org/10.1002/andp.18571780905.
[2] U. Kogelschatz, 'Dielectric-Barrier Discharges: Their History, Discharge Physics, and Industrial Applications', *Plasma Chemistry and Plasma Processing*, vol. 23, no. 1, pp. 1–46, 2003, doi: 10.1023/A:1022470901385.
[3] A. Bogaerts *et al.*, 'The 2020 plasma catalysis roadmap', *J Phys D Appl Phys*, vol. 53, no. 44, p. 443001, 2020, doi: 10.1088/1361-6463/ab9048.
[4] A. Bogaerts, E. C. Neyts, O. Guaitella, and A. B. Murphy, 'Foundations of plasma catalysis for environmental applications', *Plasma Sources Sci Technol*, vol. 31, no. 5, p. 053002, 2022, doi: 10.1088/1361-6595/ac5f8e.
[5] C. Yan *et al.*, 'Recent Advances in Plasma Catalysis', *The Journal of Physical Chemistry C*, vol. 126, no. 23, pp. 9611–9614, Jun. 2022, doi: 10.1021/acs.jpcc.2c03062.
[6] C. Ndayirinde *et al.*, 'Plasma-catalytic ammonia synthesis: Packed catalysts act as plasma modifiers', *Catal Today*, vol. 419, p. 114156, 2023, doi: https://doi.org/10.1016/j.cattod.2023.114156.
[7] P. Navascués, J. Garrido-García, J. Cotrino, A. R. González-Elipe, and A. Gómez-Ramírez, 'Incorporation of a Metal Catalyst for the Ammonia Synthesis in a Ferroelectric Packed-Bed Plasma Reactor: Does It Really Matter?', *ACS Sustain Chem Eng*, vol. 11, no. 9, pp. 3621–3632, Mar. 2023, doi: 10.1021/acssuschemeng.2c05877.
[8] A. Bogaerts, E. C. Neyts, O. Guaitella, and A. B. Murphy, 'Foundations of plasma catalysis for environmental applications', *Plasma Sources Sci Technol*, vol. 31, no. 5, p. 053002, 2022, doi: 10.1088/1361-6595/ac5f8e.

Acknowledgements

The authors acknowledge projects PID2020-114270RA-I00, and PID2020-112620GB-I00 funded by MCIN/AEI/10.13039/501100011033, project TED2021-130124A-I00 funded by AEI/10.13039/501100011033/Unión Europea Next Generation EU/PRTR and projects P18-RT-3480, US-1381045, and US-1380977 funded by Conserjería de Economía, Conocimiento, Empresas y Universidad de la Junta de Andalucía (PAIDI-2020) and Programa Operativo Feder 2014-2020.

Combined effects of Dielectric Barrier Discharge plasma treatment and Ag nanoparticles on Triticum Durum seed germination

E.G. Teodorescu-Soare[1], C. Ionita[(*)2], C.T. Konrad-Soare[2], I. Mihaila[3], B. Tatarcan[3], I. Topala[4], R. Schrittwieser[2]

[1]*Faculty of Agriculture, Ion Ionescu de la Brad Iasi University of Life Sciences, M. Sadoveanu Alley 3, 700490, Iasi, Romania*

[2]*Institute for Ion Physics and Applied Physics, University of Innsbruck, Technikerstr. 25, A-6020, Innsbruck, Austria*

[3]*Alexandru Ioan Cuza University of Iasi, Integrated Centre of Environmental Science Studies in the North-Eastern Development Region (CERNESIM), 11 Carol I Blvd., 700506, Iasi, Romania*

[4]*Alexandru Ioan Cuza University of Iasi, Faculty of Physics, Iasi Plasma Advanced Research Centre (IPARC), 11 Carol I Blvd., 700506, Iasi, Romania*

[(*)]codrina.ionita@uibk.ac.at

We present and discuss results of investigations on the influence of atmospheric-pressure plasma, created by a dielectric barrier discharge (DBD), on Triticum Durum wheat seeds, combined with the effect of different amounts of colloidal silver nanoparticles in aqueous solution, known for their antibacterial and antifungal properties. The plant germination rates along with plant root and stem growth have been monitored over two weeks and compared with plant features of reference seed batches.

Plasma treatments are currently intensively studied as seed processing technology for agricultural purposes [1]. Although atmospheric barrier plasma discharges are already widely used in agriculture, the collective influence concomitantly with secondary treatments still remains unknown. On the other hand, colloidal Silver nanoparticles are also extensively used in agriculture and other industries for decontamination purposes. These are widely known for their effect on microbiological organisms of various pathogenic bacterial strains [2-5]. Its addition to the germination water helps protecting the seed from the evolution of pests that can inhibit the germination process and further plant development. Several theories are proposed as to why Silver nanoparticles are highly effective in bacterial deactivation, including membrane thinning [6], acting on the respiratory chain [7] or directly on the DNA strains [8]. The toxicity of Ag nanoparticles also extends to living organisms such as aquatic life (fish) where prolonged exposure to NO_3Ag or Ag nanoparticles has a detrimental effect on overall health due to Ag particles accumulation in the lungs and liver [9,10] and must be applied with caution.

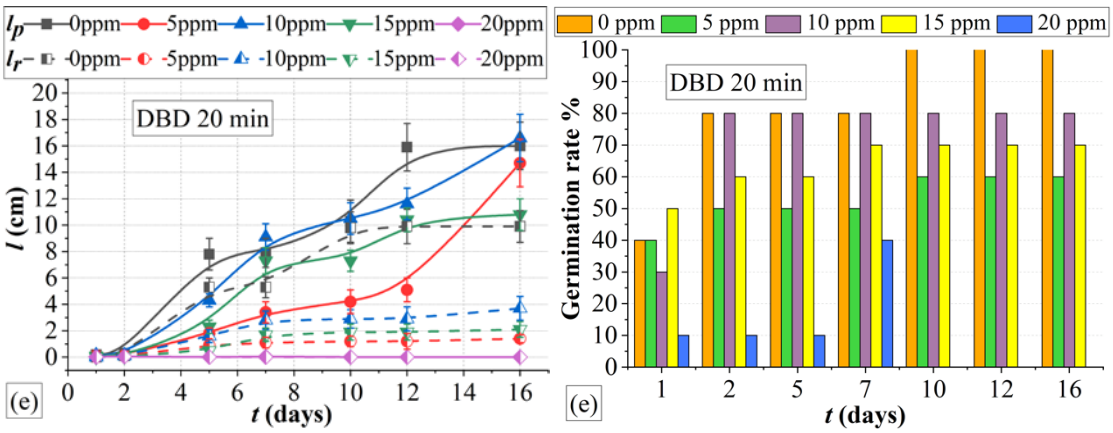

Fig. 1: Evolution rates of l_p - plant length and l_r - root length (left) and seed germination rates for 20 min DBD-treatment with increasing amounts of applied colloidal Ag concentrations (right).

Materials and Methods

A total number of 250 Triticum Durum seeds have been used in these experiments. A group of 50 untreated seeds have been kept and used as reference. The rest of 200 seeds were subjected to cold plasma treatment in a planar parallel DBD configuration with a 5 mm gap, an AC discharge at 50 Hz and 15,5 kV peak-to-peak amplitude for treatment durations of 3, 5, 10 and 20 min. In order to observe the dynamics of reactive O_2 and N_2 species in gas phase, we used the Fourier-transform infrared spectroscopy (FTIR) technique (JASCO 4700 series). During plasma exposure onto the wheat seeds, fresh air was circulated in the discharge gap and passed through the FTIR gas cell (with a light path of 100 mm). Spectra were acquired with a resolution of $r = 4$ cm^{-1}, with a wavenumber range between $n = 4400$ to 600 cm^{-1}.

Every seed batch, including the reference group, was then separated further into five equal quantities and placed into Petri dishes, where distilled water with different concentrations of colloidal Ag (0, 5, 10, 15 and 20 ppm) were added. The colloidal Silver nanoparticles with typical sizes between 20-60 nm were obtained by electrolysis in a commercial two-electrode configuration.

An JEOL JSM 6390 instrument, with a Schottky electron gun operated under 80 kV accelerating voltage at 10 μA emission current, was used in order to perform high-resolution SEM imaging and EDS spectroscopy analysis on the seeds. This allowed for both imaging and elemental mapping of the atomic species present on the seed surfaces.

Conclusion

Seed treatment by applying individual plasma treatment or in combination with different quantities of colloidal Ag have been monitored and evaluated. Generally, this has led to increased germination and higher plant size compared to reference untreated batch, where only 60% of the seeds have sprouted. The highest germination rate was recorded for a concentration of 20 ppm Ag nanoparticles with no applied DBD treatment. On the other hand, favourable for the sprouting process was also a shorter DBD treatment of 10 min cumulated with lower Ag nanoparticle concentrations of 5 to 10 ppm, where 90% germination rate was achieved. Longer DBD treatment together with high-concentration colloidal Ag has proven to inhibit plant growth, the two being not compatible.

The DBD treatment alone had a positive effect on monitored plant characteristics, while the addition of increasing amounts of colloidal Ag had an overall negative effect, due to its high toxicity.

[1] A. Waskow, *Plasma Processes and Polymers* **19** (2022) 2100152 1–22.

[2] D. Thuc, *Materials Letters* **181** (2016) 173–177.

[3] S. Sudheer Khan, *Colloids and Surfaces B: Biointerfaces* **87** (2011) 129–138.

[4] P. Logeswari, *Journal of Saudi Chemical Society* **19** (2015) 311–317.

[5] A. Miri, *Spectrochimica Acta Part A: Molecular and Biomolecular Spectroscopy* **141** (2015) 287–291;

[6] I. Sondi, *J. Colloid Interface Sci.* **275** (2004) 177–182.

[7] Q.L. Feng, *J. Biomed. Mater. Res.* **52** (2008) 662–668.

[8] J.R. Morones, *Nanotechnology* **16** (2005) 2346–2353.

[9] D Nayak, *Journal of Colloid and Interface Science* **457** (2015) 329–338.

[10] A. Bruneau, *Aquatic Toxicology* **174** (2016) 70–81.

Gas cylinder-free atmospheric steam plasma source for surface treatment/sterilization

Taiki Osawa[1], Kai Fukuchi[1], Akito Shirai[1], Akane Yaida[1], Akitoshi Okino(*)[1]

[1] *FIRST, Tokyo Institute of Technology, Yokohama, Japan*

(*) aokino@es.titech.ac.jp

Background

Currently, processing technologies for products with microstructures such as semiconductors are evolving year by year, and materials with various properties are used in products by bonding multiple materials like layers. To create this microstructure or as a pre-process for bonding materials, wet processes such as self-assembled organic monolayer formation[1] and dry processes such as plasma etching and chemical vapor deposition (CVD) are used. However, the wet process generates waste fluid, and the dry process needs large facility and complex process because it uses vacuum equipment.

In recent years, surface treatment technology using atmospheric plasma has been attracting attention. Atmospheric plasma does not require vacuum equipment and allows continuous treatment under atmospheric. In addition, since a large amount of chemically reactive species can be generated, hydrophilic treatment can be achieved in a short time[2]. As shown in Fig. 1, multi-gas plasma jet that can stably generate plasma at low temperatures below 50℃ under atmospheric pressure was developed our laboratory. And plasma generated by various gases has irradiated some materials such as fluoroplastic PFA sheets and heat-sensitive polyimide films. Even PFA sheets, which are considered difficult to hydrophilize, showed a high hydrophilic effect when irradiated with oxygen plasma for 10 seconds, reducing the contact angle of droplets from 85 degrees to 30 degrees. In oxygen plasma, hydroxyl radicals ($HO^{\cdot}$) can be generated by the reaction between oxygen plasma and surrounding air. I think that the fluoro group of PFA surface was replaced by hydroxy groups(-OH) as hydrophilic groups by reacting this $HO^{\cdot}$, resulting in hydrophilicity.

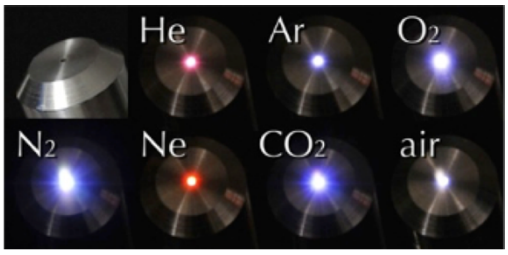

Fig. 1: Multi-gas plasma jet

Because of its high reactivity, $HO^{\cdot}$ is used not only for surface treatment but also in other fields. For example, $HO^{\cdot}$ also have high oxidizing power and contribute to bactericidal action. In particular, oxygen plasma has been shown to be highly effective in both the gas and liquid phases, and bactericidal effects can be achieved by the reaction of highly oxidizing reactive species with bacteria. Therefore, atmospheric plasma is also expected to be applied to the field of sterilization. However, multi-gas plasma jet use a various gases to generate plasma, and thus require gas cylinders. In recent years, the price of gas cylinders has skyrocketed, and since oxygen plasma generates a large amount of ozone, a simple and harmless plasma-generating medium is required. Therefore, the purpose of this study is to develop an atmospheric pressure plasma system using steam as a plasma generating gas in order to generate more hydroxyl radicals without using gas cylinders.

Steam plasma source

To generate more hydroxyl radicals, just steam was used as a plasma generation gas. As shown in Fig. 2, purified water was introduced at 10 mL/min using a peristaltic pump into a copper tube heated to about 200℃ by a ribbon heater. When the purified water touched the heated copper tube, it was

evaporated, generating 17 L/min of steam since the volume was increased more than 1,700 times. Steam plasma was generated by introducing the steam into the plasma jet, and applying an AC voltage of 9 $kV_{0\text{-}p}$ and 16 kHz to the electrodes in the plasma jet as shown right side of Fig. 2.

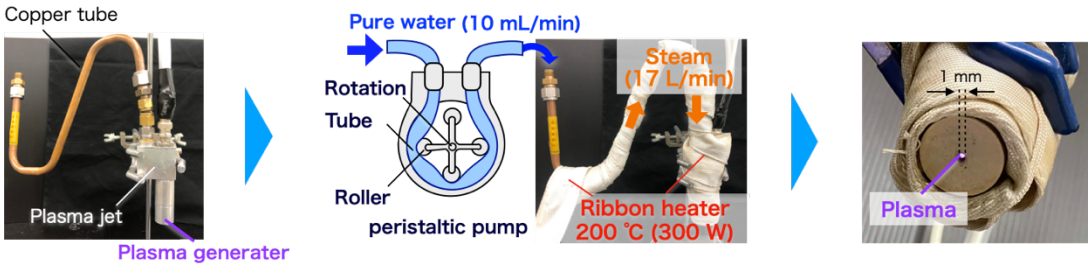

Fig. 2: Generation mechanism of steam plasma

Sterilization of *Staphylococcus aureus* by steam plasma irradiation

To investigate the bactericidal effect of steam plasma, a sterilization experiment was conducted in which *Staphylococcus aureus* was irradiated with steam plasma. The treated samples were prepared by dropping 1 mL of *Staphylococcus aureus* at $10^{4\text{-}5}$ CFU/mL onto agar medium and drying it. 10 mL/min water was introduced to generate steam plasma, and the treated samples were placed 10 mm from the irradiation port and irradiated with plasma for 10 and 30 seconds. The results are shown in Figure 3. It was found that even 10 seconds plasma treatment of *Staphylococcus aureus* could sterilize a wider area than the 1 mm diameter of the plasma irradiation port. Quantification of sterilization results will be reported in the presentation.

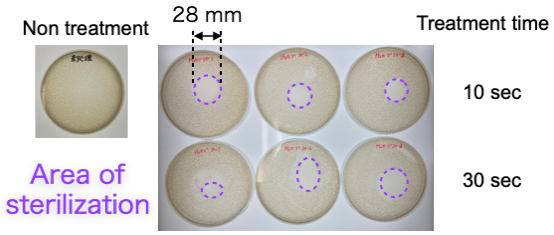

Fig. 3: Disinfection effect of *Staphylococcus aureus* by steam plasma irradiation

Design of steam plasma jet with built-in heater

It was found that the steam plasma jet introduced above can generate plasma and sterilize *Staphylococcus aureus*. However, water droplets were observed near the plasma port, probably due to the distance between the plasma port and the heating section. Since water droplets may prevent stable plasma generation, we considered that heating should be performed at a position closer to the plasma generator. Therefore, using 3D CAD, we designed a steam plasma jet with a built-in heater inside the plasma housing as shown in Figure 4. By integrating the heater into the plasma jet, we designed a device that can be heated close to the plasma generator and does not generate water droplets. In the presentation, we will report on the various characteristics of this device.

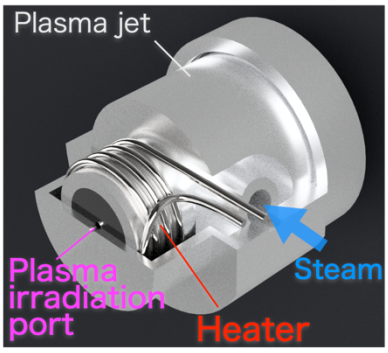

Fig. 4: Design of steam Plasma jet with built-in heater

[1] J. W. Schultze, A. Heidelberg, C. Rosenkranz, T. Schäpers and G. Staikov, *Electrochim. Acta*, **51,** (2005) 775.

[2] T. Takamatsu, H. Hirai, R. Sasaki, H. Miyahara, A. Okino, *IEEE Transactions on Plasma Science,* **41,** (2013) 119-125.

Detailed conference program Saturday 12th, 2024

Morning Session Chairman: Carlos Pintassilgo, František Krčma			
8:30	General invited	J. Országh	Measurements of electron cross sections of small molecules
9:15	Topical invited	F. Cichocki	PIC modeling challenges in diverse low temperature plasma scenarios
9:45	**Crookes Prize**	X.Tu	Plasma Catalysis for Sustainable Production of Fuels and Chemicals: Challenges and Perspectives
10:30	Coffee Break		
Midday Session Chairman: Carlos Pintassilgo, František Krčma			
11:00	Hot topic	J. de Urquijo	Electron drift velocity and longitudinal diffusion coefficients in H2O-He and H2O-Ar gaseous mixtures
11:20		F.J. Morales-Calero	Upscalling mesoporous graphene production through atmospheric pressure plasma technology for enhanced Li-based batteries
11:40	Oral	A. Cobos-Luque	Effect of nanoparticles on the material properties of graphene-based nanocomposites
12:00	Hot Topic	Q. Delaviere--Delion	Impact of axial instabilities on ion energy distribution function in Hall thruster: time-resolved RPA measurements
12:20	CLOSING - Carlos Pintassilgo, Zdeněk Bonaventura		
12:50			

Measurements of electron cross sections of small molecules

J Országh(*), B Stachová, Š Matejčík

Department of Experimental Physics, Faculty of Mathematics, Physics and Informatics, Comenius University in Bratislava, Mlynská dolina F2, 84248 Bratislava, Slovakia

(*) juraj.orszagh@uniba.sk

Low-energy electron interactions with molecules play an important role in many natural phenomena, laboratory and industrial applications which was shown by the increase of publications on the topic in last decades. The range of fields and topics where these processes need to be considered ranges from plasmas through focused electron beam-induced processing, radiation damage of DNA to atmospheric processes, astrophysics and astronomy. To understand the processes and to be able to utilize them it is necessary to characterize and evaluate them.

The internal energy of molecules is concealed within their degrees of motion, leading to quantized energy levels. For each type of motion, there exist corresponding energy levels: electronic state energy levels, vibrational energy levels, and rotational energy levels. The interaction of a molecule with another particle or an electromagnetic wave can induce a change in its motion, thereby altering the energetic level and the internal molecular energy. The probability of this change is known as the cross section, which is one of several parameters used to characterize the kinetics of the interaction process and depends on the collision energy [1]. Many environments in which electron-molecule interactions play a significant role are highly complex, with multiple concurrent processes influencing each other. Plasmas and atmospheres serve as excellent examples, where it is practically impossible to experimentally determine all parameters. This is where modelling comes into play, but even the simplest models require reliable input data that precisely characterize the processes. Probabilities of processes - cross sections, are crucial among these data. For models considering a wider range of interaction energies, cross sections must be defined for every energy value within the range. Currently, the lack of data is often a challenge, with cross sections either being unknown, or their values determined only for a few specific energies, necessitating estimation based on known processes for similar molecules or utilizing other forms of approximate data. Consequently, the reliability and precision of model results may be compromised. The cross section values for electron-molecule collisions span in a relatively large range of values. For example, according to Itikawa et al. [2] the values for low-energy electron impact on water reach the order of 10^{-13} cm^2 for rotational transitions and less than 10^{-18} cm^2 for some dissociative excitations.

The relatively wide range of expected values affects the possibilities of experimentally determining the cross sections. Nowadays, perhaps the most commonly used experimental setup is based on crossed beams of molecules and electrons, with some variations regarding the electron beam source and molecular source. The electron beam is typically generated by a relatively simple electron gun with a heated filament as a source of electrons. If a narrower distribution of kinetic energy of the electrons in the beam is desired, the gun can be accompanied by some kind of kinetic energy monochromator, such as a hemispherical or trochoidal type. The molecular source is often an effusive capillary, which creates the beam by restricting the motion of molecules in the direction perpendicular to the desired beam and allows for the thermal effusion of molecules into the reaction chamber. This setup enables conditions that ensure binary collisions, allowing the interactions to be studied almost one by one. The rest of the experimental setup is given by the kind of electron-molecule interaction that is supposed to be studied. For example, the detection method and detector will be determined by the products of the selected reaction. For ions it can be mass spectrometer, for photons spectrometer, for scattered electrons electron energy analyser, etc.

The results can vary from relative curves (Fig. 1.), which often depict the dependence of signal intensity corresponding to a specific product on the incident electron energy, to absolute cross section values for a range of conditions (Fig. 2.). The relative curves provide an overview of the relative process efficiency, and threshold value(s). Transitioning from relative to absolute results requires more sophisticated calibration methods. The simplest procedure assumes the availability of at least one cross section value from the measured range. Then it is possible to bootstrap the data to this value and determine the cross sections for other processes. While the first procedure is based on data processing, the second method is experimental and requires the use of calibration compound. The cross section value of the calibration compound is known, and it is introduced into the experimental system at a known ratio with the studied compound. The third, most sophisticated method involves the experimental determination of all parameters for the direct calculation of the cross section (i.e., molecule and electron concentration in the beams, angles and efficiency of collection, etc.).

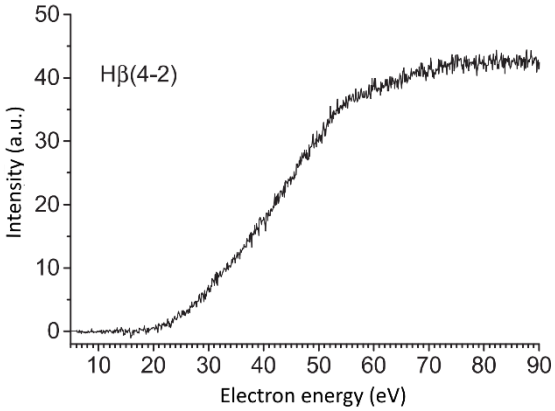

Fig. 1. Relative dependence of intensity for electron-impact induced production of excited hydrogen atom from the molecule of acetylene [3].

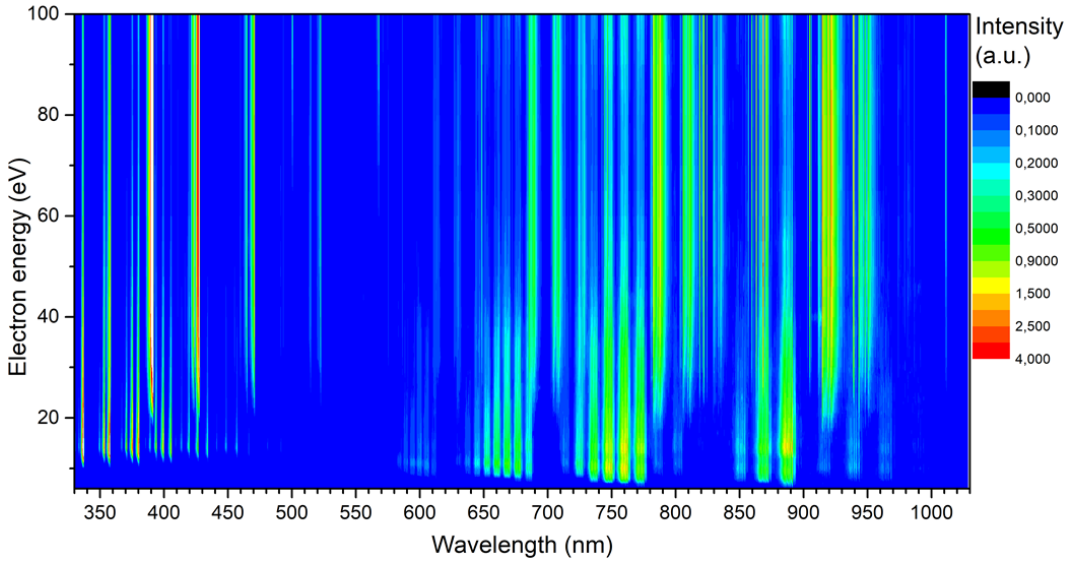

Fig. 2. Spectral electron energy map of electron impact induced emission of nitrogen from which the cross section for any detected process can be determined within the experimental energy and spectral limits [4].

This work was partially supported by the Slovak Research and Development Agency under grants nr. APVV-19-0386 and APVV SK-PL-23-0050 and by Slovak grant agency VEGA under grant No. 1/0489/21.

[1] M. J. Brunger, (2019). Molecular processes and techniques for measuring their scattering cross sections. In O. Ingólfsson (Ed.), *Low-Energy Electrons: Fundamentals and applications* (pp. 1-46). Pan Stanford Publishing Pte. Ltd.
[2] Y. Itikawa & N. Mason, *J. Phys. Chem. Ref. Data* **34**(1) (2005).
[3] J. Országh, M. Danko, P. Čechvala et al., *The Astrophysical Journal* **841**(1) (2017).
[4] J. Blaško, J. Országh, B. Stachová et al., *Eur. Phys. J. D* **77**:22 (2023).

PIC modeling challenges in diverse low temperature plasma scenarios

Filippo Cichocki[(*)1], Vittorio Sciortino[2], Pierpaolo Minelli[3], Francesco Taccogna[3]

[1] *ENEA, C.R. Frascati, Dipartimento "Nucleare" (NUC), Frascati, Italy*
[2] *Università "Aldo Moro", Dipartimento di Fisica, Bari, Italy*
[3] *Institute for plasma science and technology (ISTP), Bari, Italy*
[(*)] filippo.cichocki@enea.it

Particle-in-cell modeling is particularly appropriate to study the complex kinetics of low temperature plasmas. In this work, we present a few challenges in PIC modeling for low temperature plasmas, with a direct application in 3 different scenarios: the plasma discharge inside a negative ion source, the plasma interaction with a fusion reactor monoblock, and the collisionless expansion of a propulsive plasma within a magnetic nozzle. These examples will serve to highlight the high versatility of the PIC modeling approach and to illustrate the different solutions adopted in each case.

1 Introduction

The particle-in-cell method [1], complemented with Monte Carlo collisions algorithms for volumetric collisions and other phenomenological models to account for plasma-wall interaction phenomena, represents a very flexible and adaptable approach to deal with a large variety of low temperature plasma scenarios, and especially with those featuring a complex non-equilibrium kinetics. This work focuses on electrostatic PIC models, in which the set of considered Maxwell's equations reduces to Poisson's equation and a time-constant non-uniform magnetic induction field is assumed. The peculiarities and challenges of the PIC approach in 3 different application scenarios are then discussed in detail: (i) a negative ion source, where special care is given to the description of the collisional processes and of the electron energization, (ii) the simulation of the plasma-wall interaction at a fusion reactor monoblocks, where specific plasma-wall interaction models are implemented, and, finally, (iii) the expansion of a propulsive plasma within a magnetic nozzle with a focus on the correct outflow boundary conditions.

2 Simulation of a negative ion source

Negative ion sources [2] are characterized by a relatively low dense - low temperature plasma, with plasma densities in the order of $10^{18}\mathrm{m}^{-3}$ and electron temperatures of a few tens of eV. The magnetic filter used to prevent electrons from reaching the extraction region has the effect of enhancing their non-Maxwellian behaviour, so that a kinetic treatment is particularly needed. Here, we have applied the PICCOLO code ("PIC COde for LOw temperature plasmas") to model the plasma generation and transport within SPIDER [4], the negative ion source currently considered for the ITER fusion reactor. Two aspects are worth a special discussion: the electron energization, and the collisional processes.

Regarding the former, in SPIDER, the plasma is heated by 8 RF drivers with a cylindrical shape (see Fig. 1, which shows only 4 drivers, being a 2D $y-z$ simulation). Since the implemented PIC model is electrostatic, no direct interaction between electrons and RF fields is simulated, therefore an alternative energization algorithm is implemented to mimic the correct energy absorption [5]. At each PIC step, given the total absorbed power P_{abs} per driver, the heating RF frequency f_{RF}, the average kinetic energy $\langle E_{\mathrm{k}}\rangle$ of electrons and the total number of electron macro-particles $N_{\mathrm{mp,tot}}$ within each driver, a target heating temperature is computed as:

$$T_{\mathrm{heat}} = \frac{2}{3}\left(\langle E_{\mathrm{k}}\rangle + \frac{P_{\mathrm{abs}}}{eN_{\mathrm{mp,tot}}W_{\mathrm{mp}}f_{\mathrm{RF}}}\right), \tag{1}$$

where W_{mp} represents the number of elementary electrons per macro-particle. Then, if Δt_{PIC} is the PIC time step, a given number of electrons $N_{\mathrm{mp,heat}} = f_{\mathrm{RF}}\Delta t_{\mathrm{PIC}}N_{\mathrm{mp,tot}}$ inside each driver is randomly selected and their velocity resampled from a Maxwellian velocity distribution, with temperature T_{heat}.

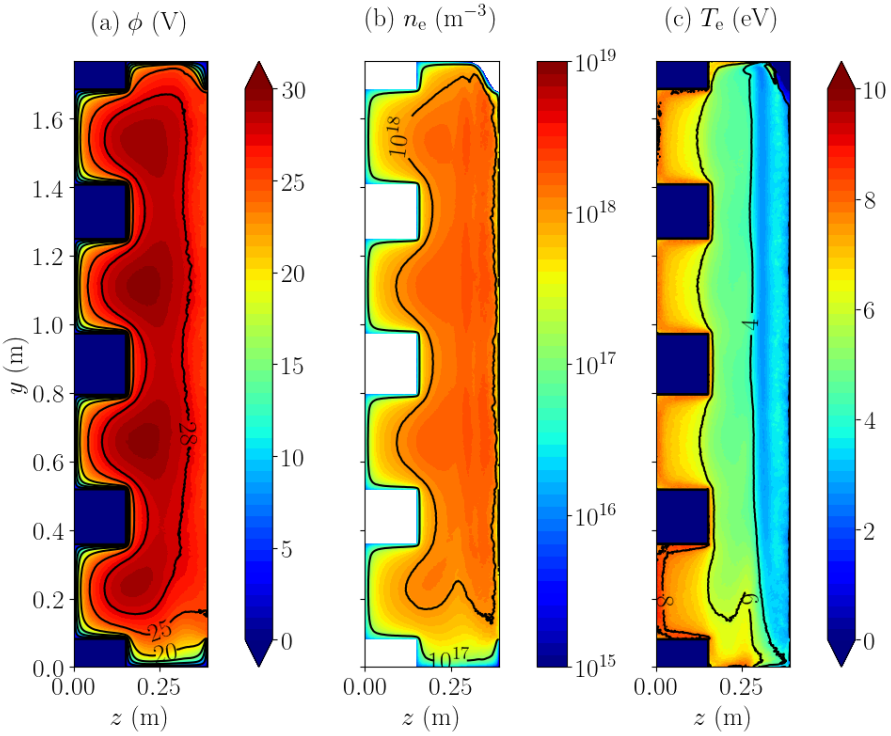

Fig. 1: (a) Plasma potential, (b) plasma density and (c) electron temperature in a 2D simulation of the SPIDER negative ion source. The domain is uniform in the direction normal to the page (x). The magnetic induction field is perpendicular to the page and peaks to 7 mT close to the extraction grid ($z_{\max}$).

Volumetric collisions are modeled with a Monte Carlo Collisions technique [3], based on the "Null Collisions" method. The neutral gas is considered here as a fixed uniform background and consists in a mixture of hydrogen molecular and atomic gas (of density around $2 \cdot 10^{19}$ m^{-3}). A large set of collisional processes are included, and namely ionization, elastic, and excitation collisions, but also (for the molecular gas) dissociation, dissociative ionization, and dissociative attachment (that leads to a negative hydrogen ion). For what concerns wall interaction, on the other hand, the simulation of the emitted negative ion current would require to model the emission of negative ions from the caesiated molybdenum extraction grid, due to both neutral atom and ion impacts [2]. However, this has not been included in the simulations where no negative ions are tracked.

Referring to Fig. 1, a simplified 2D geometry has been considered, with 4 drivers featuring $P_{\text{abs}} = 100$ kW and assumed to be uniform along the x direction. Homogeneous Dirichlet conditions are imposed at the drivers and expansion chamber walls ($\phi = 0$ V), while a slightly positive potential (25 V) is imposed at the extraction grid surface ($z = z_{\max}$). Finally, a vacuum permittivity ϵ_0 increased by a factor of 22500 is applied to reduce the computational cost. This has the effect of increasing the width of plasma sheaths by a factor of 150, however, the transport within the acceleration chamber and the collisional processes in the volume are correctly reproduced.

3 Plasma-wall interaction at the divertor monoblocks

Magnetic confinement tokamak reactors are designed to divert a significant fraction of the power exhaust towards a dedicated wall (named divertor) that is made of many small monoblocks (with a characteristic size of 1 cm and typically made of tungsten). The assessment of the energy and particle fluxes on the walls is therefore crucial, and it has already been attempted with a PIC model, considering a realistic monoblock geometry for the DTT reactor [6]. In this scenario, it is particularly relevant to include in the modeling (apart from collisional processes with the neutral background) also the physics of the plasma-wall interaction. In this respect, the most relevant phenomena are secondary electron emission (SEE)

from electron impacts (which is around 1 order of magnitude larger than that induced by ions), and, given the large operating monoblock temperatures (> 2000 K), also the thermionic electron emission. Here, the models presented in Ref. [7] have been considered, and SEE electrons are divided between backscattered electrons and true secondaries, since these two sub-populations can have very different emission energy and angle distributions.

Some preliminary results from the project PARADIGM ("PARametric Analysis of DIvertor Geometry considering Multiple kinetic effects") obtained with the DESPICCO code ("Divertor Edge Simulator of Plasma-wall Interaction with Consistent COllisions") are shown in Fig. 2. A Deuterium plasma and background gas are considered with real elementary particle masses, in a 2D domain extending along the toroidal direction y and the direction normal to an axisymmetric divertor z. Periodic conditions for both particles and fields are assumed at $y_{\min}, y_{\max}$ (see Ref. [7] for more details). The main goal is to assess the effect of the monoblock geometry and of the plasma and magnetic field conditions, on the energy fluxes to the walls. Fig. 3 shows the 2D potential and electron density maps in two scenarios featuring different monoblock geometries and magnetic field orientations. Electron surface emission (mainly due to thermionic emission) can be appreciated in subplot (a) close to the monoblock surface.

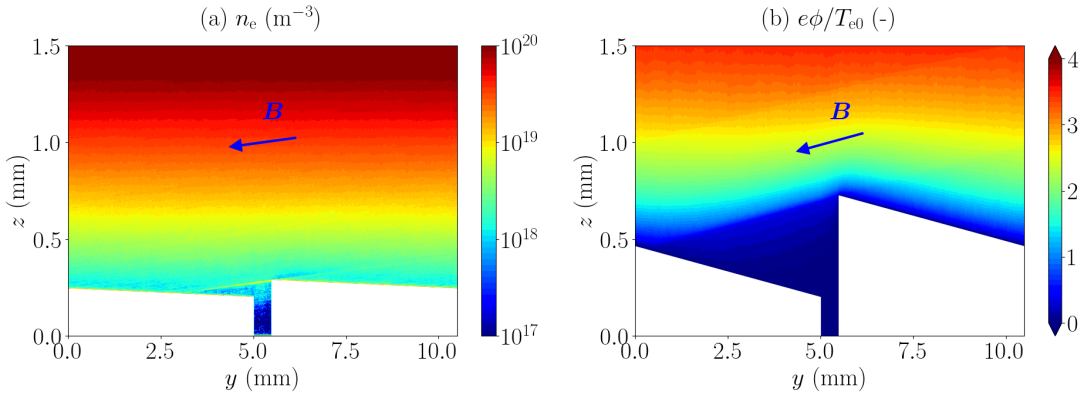

Fig. 2: (a) Electron density and (b) normalized electric potential ($T_{e0} = 40$ eV) for an angle of (a) 2 deg and (b) 6 deg between $\boldsymbol{B}$ (shown by a blue arrow) and the bevelled monoblock surface. Thermionic electron emission with a wall temperature of 3300 K is assumed here.

4 Magnetic nozzle simulation

Magnetic nozzles (MNs) are convergent-divergent magnetic field topologies used in electric thrusters to guide the plasma ions acceleration downstream. While the issue of the ion streamlines detachment appears to have been properly explained with a 2-fluids model [8], there are still many open aspects in the study of this technology that require a fully kinetic treatment, such as the non-equilibrium electron thermodynamics and the electron streamlines detachment.

A subtle and relevant topic in MNs simulation is that of the particle boundary conditions at the open outflow boundaries, a topic that has already been treated by several authors [9, 10]. Since electrons are much more mobile than ions, when the plume reaches the downstream boundary, a much larger number of electrons would get lost because of their much larger mobility, so that some of them must be reflected backwards to guarantee a globally ambipolar plume. Fig. 4 shows some preliminary results for a typical MN expansion obtained with the PICCOLO code, and assuming an artificially increased vacuum permittivity (by a factor of 1000) to limit the computational cost. In the simulation, we impose a fixed flux of electrons and Xe ions (with their real elementary masses) from the leftmost domain boundary ($z = 0$). Quasi-neutrality is automatically satisfied by refluxing all particles that cross the injection surface (at $z = 0$) towards the source plasma ($z < 0$). At the open boundaries $z_{\max}$ and $r_{\max}$, on the other hand, all ions are lost and electrons are either reflected or not, according to their mechanical energy E_{tot} (relative to infinity),

$$E_{\text{tot}} = \frac{1}{2} m_e v_e^2 - e\left(\phi_{\text{exit}} - \phi_{\text{infty}}\right), \tag{2}$$

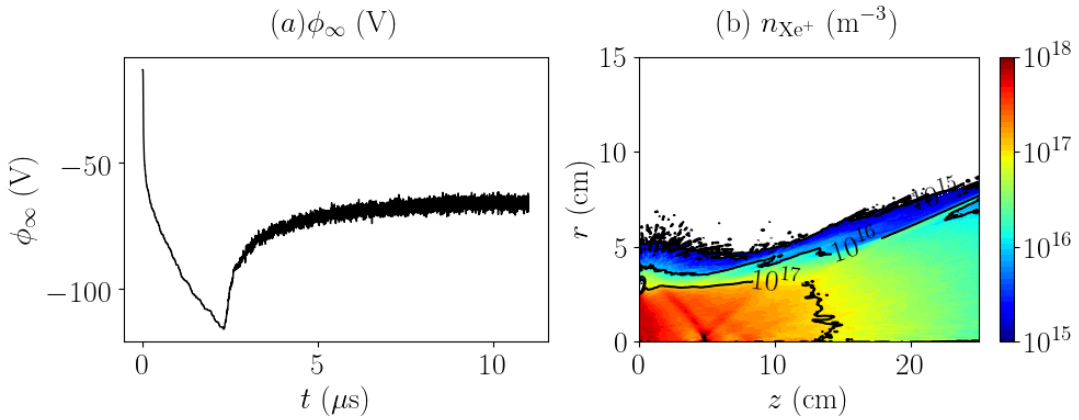

Fig. 3: (a) Time evolution of the infinity potential ($\phi = 0$ at $r = z = 0$), and (b) Xe ion density 2D map. The domain is cylindrical, with $r = 0$ corresponding to the plume centerline.

where m_e, v_e are the elementary electron mass and velocity, ϕ_{exit} is the local electric potential at the outflow position, and ϕ_{infty} is the potential at infinity. All electrons with $E_{tot} < 0$ are specularly reflected backwards toward the simulation domain, while all ions and electrons with $E_{tot} > 0$ are lost and charge up a virtual capacitor at infinity, according to:

$$\frac{d\phi_\infty}{dt} = \frac{I_i + I_e}{C_\infty}, \tag{3}$$

where I_i, I_e are the ion and electron currents that leave the domain, and C_∞ is an equivalent electric capacity. As shown in Fig. 4(a), the capacitor at infinity charges up negatively with respect to the plasma plume, and when it reaches a stationary value, current ambipolarity is guaranteed, with no boundary effects on the plasma plume properties, as shown in Fig. 4(b).

5 Conclusions

The increasing computational power of modern High Performance Computing clusters, makes the PIC modeling approach more and more convenient for an ever growing range of applications and scenarios. This work has highlighted such a high versatility by presenting and discussing three plasma scenarios featuring different numerical and physical challenges.

Acknowledgments

The simulations of Sec. 3 have been run as part of the PARADIGM Eurofusion HPC project, on the Marconi and LEONARDO HPC clusters.

Bibliography

[1] F. Taccogna, F. Cichocki *et al*, J. Appl. Phys. **134** (2023) 150901.
[2] M. Bacal, *Physics and applications of hydrogen negative ion sources*, Springer Nature **124**, 2023
[3] V. Vahedi and M. Surendra, Computer Physics Communications **87** (1-2) 179-198, 1995
[4] G. Serianni *et al*, Fusion Engineering and Design **146** 2539–2546, 2019
[5] G. Fubiani, L. Garrigues *et al*, New Journal of Physics, **19** 015002, 2017
[6] F. Cichocki, P. Innocente *et al*, Plasma Phys. Control. Fusion **66** 025015, 2024
[7] F. Cichocki, V. Sciortino *et al*, Nucl. Fusion **63** 086022, 2023
[8] M. Merino and E. Ahedo, Plasma Sources Sci. Technol. **23** 032001, 2014
[9] S. Andrews, S. Di Fede and M. Magarotto, Plasma Sources Sci. Technol. **31** 035022, 2022
[10] M. Li, M. Merino *et al*, Plasma Sources Sci. Technol. **28** 034004, 2019

Plasma Catalysis for Sustainable Production of Fuels and Chemicals: Challenges and Perspectives

X. Tu(*)

Department of Electrical Engineering and Electronics,University of Liverpool, UK

(*)*Xin.Tu@liverpool.ac.uk*

The conversion of inert molecules (e.g., CO_2, CH_4, and N_2) with strong chemical bonds for the synthesis of value-added synthetic fuels and platform chemicals has attracted significant interest. However, the activation of these molecules remains a great challenge due to their thermodynamical stable, requiring a substantial amount of energy for activation. Non-thermal plasma (NTP) has emerged as a promising technology for gas conversions into fuels and chemicals under ambient conditions. The combination of NTP with heterogeneous catalysis has great potential for achieving a synergistic effect through the interactions between the plasma and catalysts, which can activate catalysts at low temperatures, improve their activity and stability, and lead to a notable increase in conversion, selectivity, and yield of end-products, as well as enhance the energy efficiency of the process. Furthermore, plasma processes can be switched on and off instantly, offering great flexibility in decentralised fuel and chemical production using renewable energy sources, particularly intermittent renewable energy. This presentation will discuss the challenges and opportunities in plasma catalytic gas conversion to fuels and chemicals, including various chemical processes such as CH_4 activation, CO_2 conversion, and ammonia synthesis.

Electron drift velocity and longitudinal diffusion coefficients in H_2O-He and H_2O-Ar gaseous mixtures

J. de Urquijo[*1], O. González[1], L.G. Pérez-Romero[1,2], E. Basurto[3]

[1]*Instituto de Ciencias Físicas, Universidad Nacional Autónoma de Méixco, 04510, México*

[2] *IICBA, Universidad Autónoma de Morelos, 62210, Morelos, México*

[3]*Universidad Autónoma Metropolitana-Azcapotzalco, México*

[(*)] *jdu@icf.unam.mx*

We present the measurement of the flux electron drift velocity, W_F, and the flux longitudinal diffusion coefficient, $ND_{L,F}$, over a wide range of the density-normalised electric field intensity, E/N. The share of H_2O vapour in the H_2O-He and H_2O-Ar mixtures ranged from 0.5% to 70%. In this abstract we shall only present and discuss two cases. The whole set of measurements will be presented at the Conference. The measured transport coefficients were derived from the analysis of electron transients obtained from a Pulsed Townsend Apparatus which has been described thoroughly in [1,2].

We shall focus this presentation on the effects on both the electron drift velocity and the longitudinal diffusion coefficient over the E/N regions where the negative differential conductivity (NDC) effects are apparent. Explanations of this effect, consisting in a decrease of the electron drift velocity with increasing E/N, has been given in several papers, of which we single out that of Petrovic et al [3], who provide simple models of elastic and inelastic collision cross sections for electron scattering in which NDC can occur without the presence of a Ramsauer-Townsend minimum, as in the case of Ar and other gases.

Figure 1 shows the drift velocities, W_F, for the particular case of 5% content of H_2O in Ar and He and, for comparison in trends, those of He, Ar and H_2O. We see that the NDC effect in the 5% H_2O-Ar mixture is large since Ar has a very pronunced minimum in its momentum transfer cross section at 0.3 eV [4]. On the other hand, the momentum transfer cross section for electron scattering in He has no such minimum [4], but the drift velocity curve does show the NDC effect very clearly. H_2O has a shallow minimum in its momentum transfer cross section at a much larger collision energy around 6 eV [5]. Thus, a better explanation may be given with one of the NDC models presented in [3], with a He rising cross section, together with comparatively small inelastic cross sections (a factor of 100 is considered for Model 1 in Ref. [3], which in the case of H_2O would correspond with the rotational cross sections.

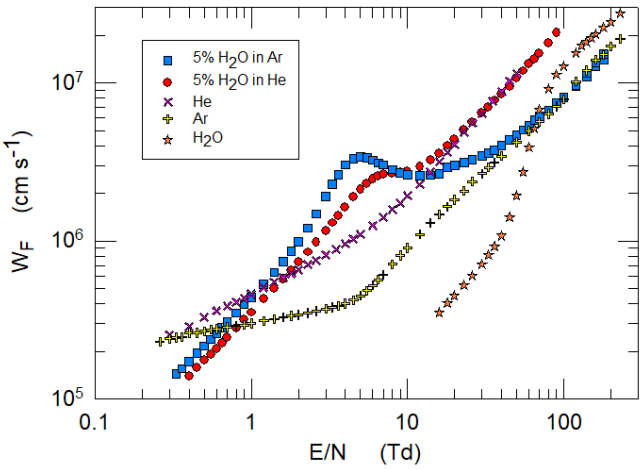

Fig. 1: Electron drift velocity (Flux) in 5% H_2O-He and 5% H_2O-Ar mixtures, and their comparison with the coresponding curves for He, Ar and H_2O

To the best of our knowledege no other data have been presented for W_F nor for $ND_{L,F}$ in these mixtures before.

The case for the longitudinal diffusion coefficient is also very interesting and is shown in Fig. 2, where one can see a very large NDC effect for the 2% H_2O-Ar curve, with a sharp decay starting at a maximum located at E/N=1.4 Td and ending at a minimum at 3.5 Td, with a difference in values of nearly two orders of magnitude. Past this minimum, the curve grows and merges those of Ar and H_2O. On the other hand, the case for the 2% H_2O-He curve is modest in comparison with the former, although very interesting also, and it is concomitant with the effect shown for the corresponding drift velocity. Again, past the minimum, the curve rises and merges with that of He.

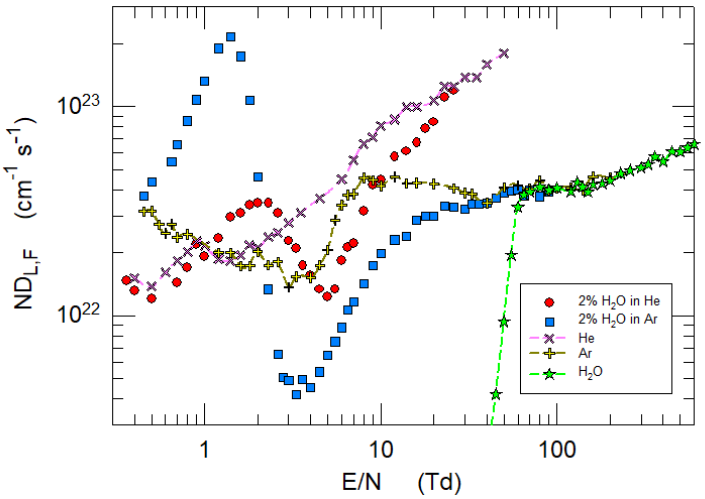

Fig. 2: Density-normalised longitudinal diffusion coefficient (Flux) in 2% H_2O-He and H_2O-Ar mixtures, and their comparison with the coresponding curves for He, Ar and H_2O

We believe that these measurements, derived over a wide range of E/N and for mixtures between 0.5% and 70% H_2O, may be useful for improving the still incomplete cross section set of H_2O, as dicussed by Song et al [6] and Budde et al [7,8].

Acknowledgements.

The authors are grateful to A. Bustos, G. Bustos and H. Hinojosa for their technical assistance. This project was supported by PAPIIT-UNAM 112223.

References

[1] de Urquijo J. et al *J. Phys D: Appl. Phys*. **57** (2024) 125205
[2] Hernández-Àvila et al *J. Phys D: Appl. Phys*. **35** (2002) 2264-69
[3] Z. Lj. Petrovic, R. W. Crompton and G. N Haddad *Aust, J. Phys.* **37** (1984) 23-34
[4] Zecca A. *Nuovo Cimento* **19** (1996) 1-146
[5] Zecca A. *Nuovo Cimento* **24** (2001) 1-118
[6] Song M. Y. et al *J. Phys. Chem. Ref. Data* **50** (2021) 023103
[7] Budde M et al J. *Phys D: Appl. Phys*. **55** (2022) 445205
[8] Budde M et al *J. Phys. D: Appl. Phys.* **56** (2023) 255201

Upscalling mesoporous graphene production through atmospheric pressure plasma technology for enhanced Li-based batteries.

F.J. Morales-Calero[1], A. Cobos-Luque[1], J.M. Blázquez-Moreno[2], R. Rincón[(*)1], A.M. Raya[1], J. Muñoz[1], A. Benítez[2], N.Y. Mendoza-González[1], J.A. Alcusón[1], A. Caballero[2], M.D. Calzada[1].

[1] *Laboratory of Innovation in Plasmas, Universidad de Córdoba, 14014 Córdoba, Spain.*

[2] *Dpto. Química Inorgánica e Ingeniería Química, Instituto Químico para la Energía y el Medioambiente (IQUEMA), Universidad de Córdoba, 14014 Córdoba, Spain.*

[(*)] rrincon@uco.es

Since it was discovered in 2004, graphene has been hailed as *"the material of the future"* due to its remarkable properties and fascinating applications, including energy storage and innovative battery design [1,2]. Different methods have emerged for graphene synthesis, being the Hummers method the most fundamental approach. This method produces a low-quality product through a harmful process to the environment. More recent methods have enabled the production of high-quality graphene from highly oriented pyrolytic graphite (HOPG) by techniques such as mechanical exfoliation or laser ablation. However, these techniques lack of scalability, limiting their potential for meeting industrial requirements. Nevertheless, several methods have been developed to generate high-quality graphene that allows scalability, although they show different drawbacks. Among them, liquid phase exfoliation (LPE) and chemical vapor deposition (CVD) stand out. Therefore, none of this methods offers a single-step, low-cost approach for obtaining high-quality graphene powder.

Plasma technology represents a significant advance in this field. Microwave plasma torches (Fig. 1) exhibit high reactivity, making them capable of inducing decomposition reactions with a high efficiency (~100%), surpassing traditional chemical processes. Organic molecules are broken into atomic components, leading to the formation of compounds different from the original ones when the atoms recombine at the plasma outlet. At atmospheric pressure, the numerous collisions between electrons and heavy particles favor the nucleation process of materials, such as graphene as it has been reported using ethanol as a carbon precursor [3]. It is an eco-friendly, cost-effective and scalable method for high-quality graphene generation in a single-step process. So, it is deeply engaging to optimize the technique. To enhance the quantity of synthesized graphene, a process refinement has been conducted based on two key parameters: the amount of ethanol considered [4] and the applied power [5]. It was discovered that microwave power proves to be the optimal parameter for upscaling the process, resulting in an increase in graphene production rate from 79.3 mg/h to 111.3 mg/h when the power was raised from 350 W to 500 W [5]. This increase also enhances energy yield, as a 40% increase in graphene production rate was achieved with just a 30% increase in power. Moreover, it is achieved without compromising material properties: physicochemical characteristics of graphene powder have been analyzed using different analysis techniques: Raman spectroscopy, X-ray photoelectron spectroscopy, electron microscopy, thermogravimetry, and X-ray crystallography. No significant modifications were detected due to changes in applied power. Additionally, nitrogen adsorption/desorption tests as well as pore size distribution measurements of graphene obtained with both 350 and 500 W were carried out (Fig. 2). In both cases, isotherm curves show a type IV behavior, related to mesoporous materials, and a similar pore size

Fig. 1: Microwave plasma torch during graphene synthesis process.

distribution. Their porosity fits a bi-modal distribution, with a first zone of small mesoporosity (3-18 nm), and a second zone with large mesopores and some macropores (30-70 nm). The absence of microporosity is confirmed by t-plot method.

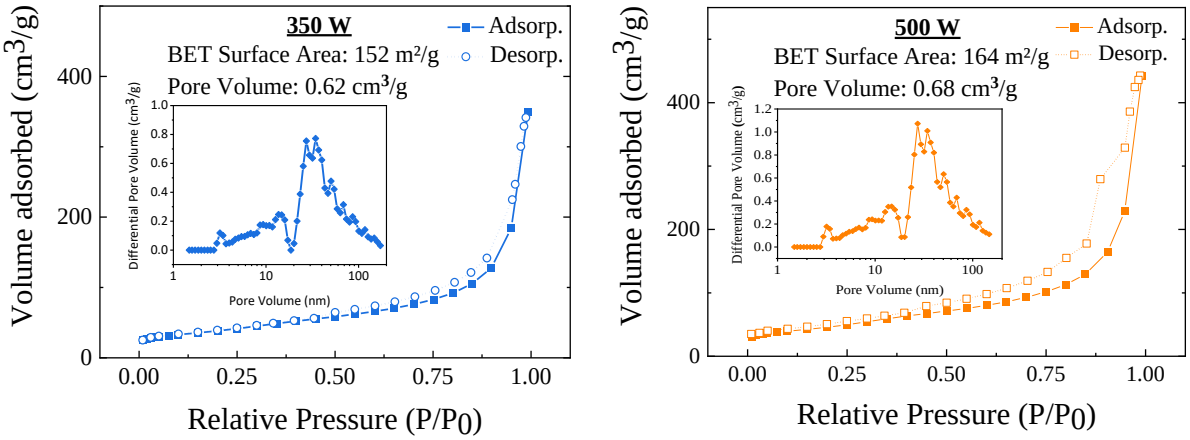

Fig. 2: Nitrogen adsorption/desorption curves and pore size distributions.

Once upscalled graphene yield, graphene synthesized through microwave plasma technology is found to be of particular interest for applications in the energy storage field, specifically in the design of high-performance Lithium-Sulfur (Li-S) batteries. During discharge, the lithium metal anode undergoes oxidation, releasing lithium ions and electrons that migrate to the sulfur cathode. However, during the electrochemical reactions at the positive electrode, the cyclic sulfur molecule (S_8) is reduced, leading to the formation of a series of polysulfides (Li_2S_n), some of them in solution. Here lies one of the main drawbacks of these batteries: the shuttle effect [6], which involves the migration of polysulfides during charge and discharge cycles. This causes the formation of polysulfide deposits on the lithium electrode, which results in a loss of battery capacity and faster degradation of performance over time, diminishing energy efficiency and reducing lifespan. However, the porosity properties of graphene can fight the shuttle effect, capturing polysulfides in solution as shown in Fig. 3. The first picture depicts the dissolution of Li_2S_6 polysulfide in a dioxolane (DOL) and dimethoxyethane (DME) mixture (DOL:DME, 1:1) to mimic the electrolyte environment used in batteries. The yellow color characteristic of high-order polysulfides is clearly visible. In the subsequent image, graphene powder is incorporated. After two hours, it is observed that the solution has become colorless, indicating the adsorption of these polysulfides by the graphene matrix. So, to improve Li-S batteries performance, we propose the integration of a sulfur-graphene composite that acts as a highly-efficient positive electrode.

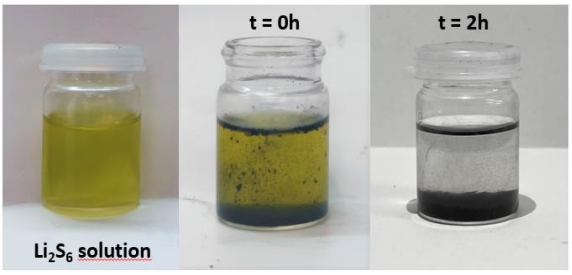

Fig. 3: Polysulfides capturing by graphene

[1] A. Dias, *Chemical Engineering Journal,* **430** (2022) 133153.
[2] F.J. Soler-Piña, *J Colloid Interface Sci,* **640** (2023) 990-1004.
[3] C. Melero, *Plasma Phys Control Fusion*, **60** (2018) 014009.
[4] A. Casanova, *Fuel Processing Technology*, **212** (2021) 106630.
[5] J. Toman, *Fuel Processing Technology*, **239** (2023) 107534.
[6] A. Benítez, *Renewable and Sustainable Energy Reviews*, **154** (2022) 111783.

Aknowledgments: This work was partially supported by Grant TED2021129261AI00 funded by MCIN/AEI/ 10.13039/501100011033 and by the European Union NextGenerationEU/PRTR. The predoctoral contract of F.J. Morales-Calero was granted by a MOD-2.2 from Plan Propio de la Universidad de Córdoba (2020). Finally, the authors of the present work are greatly thankful to Prof Michel Moisan of the Groupe de Physique des Plasmas (University of Montreal) for the TIAGO torch donation.

Effect of nanoparticles on the material properties of graphene-based nanocomposites.

A. Cobos-Luque[1], F.J. Morales-Calero[1], O. Jasek[2], A.M. Raya[(*)1], R. Rincón[1], J. Muñoz[1], M.D. Calzada[1].

[1] *Laboratory of Innovation in Plasmas, Universidad de Córdoba (Spain).*

[2]*Department of Plasma Physics and Technology, Faculty of Science, Masaryk University, Kotlářská 267/2, 611 37 Brno, Czech Republic*

[(*)] *f32rabea@uco.es*

Graphene-based nanocomposites (NCs) consist of a matrix -graphene- in which nanometer-size particles are included. These particles should not compromise the intrinsic properties of graphene but rather enhance the overall characteristics of the NC. Such nanostructures are of special interest in the field of energy storage. For example, using graphene-Cu, graphene-TiO_2 or graphene-Au nanocomposites as electrode materials has improved the performance of batteries [1]. Among other NC production techniques, microwave plasmas at atmospheric pressure stands out. This process offers numerous benefits in contrast to chemical methods, making it a compelling option for industrial-scale nanostructures production: does not require vacuum equipment since it can operate at atmospheric pressure and no hazardous or contaminating products are produced during the synthesis process. Furthermore, surplus products from various industries or pollutant emissions can serve as precursors, which are substances that could be introduced into plasma and used for synthesis of nanostructures and/or formation of nanocomposites.

In this research, graphene and graphene-Cu NCs are synthesized by using a TIAGO (*Torche à injection Axiale sur Guide d'Ondes*) and the effect of Cu NPs on graphene properties is deeply studied by Raman spectroscopy, X-ray photoelectron spectroscopy, Transmission electron microscopy (TEM) and thermal-gravimetric analysis. As reported in [2-4], graphene and graphene-Cu NCs can be obtained by introducing ethanol molecules into an argon plasma and acting on input microwave energy. Since the discharge is generated on the tip of the field applicator, which is made of copper, Cu NPs can be sputtered during the synthesis the graphene thus resulting in the formation of graphene-Cu NCs. Low-magnification TEM image of graphene sample (Figure 1a) shows the distinctive structure of graphene in the absence of any other nanostructured carbon material or carbonaceous particles. Furthermore, the structure exhibits homogeneity, evident in transparent zones representing extended sheets and darker zones indicating folded graphene sheets. In contrast. Low-magnification TEM image of graphene-Cu NC (Figure 1b) shows graphene sheets with the presence of few nanometer units Cu NPs, as evidenced in the compositional analysis (Figure 1c) with C (marked in red) and Cu (marked in green) signals originating from graphene and the particles observed in the TEM image, respectively.

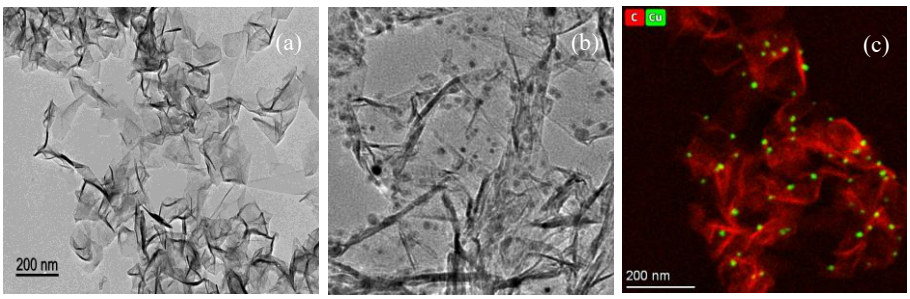

Fig. 1: Low-magnification TEM images of (a) graphene and (b) graphene-Cu NC samples. (c) compositional analysis of graphene-Cu NC by energy dispersive spectroscopy.

To assess the influence of larger Cu NPs on graphene properties, Raman spectra of both graphene and graphene-Cu NCs were measured and are shown in Figure 2.

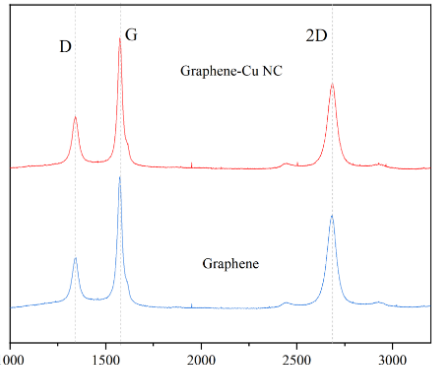

Fig. 2: Raman spectra of graphene and graphene-Cu NCs.

Regardless of the presence of Cu NPs, G and 2D bands characteristic of graphene are observed. Indeed, similar I_D/I_G and I_{2D}/I_G ratios from the Raman spectra indicate similar number of defects and thickness in both samples, *i.e.*, graphene quality remains uncompromised when larger Cu NPs are included. Nevertheless, as it was reported previously in [4], the presence of Cu NPs on graphene has an impact on graphene oxidation resistance as evidenced by thermogravimetric analysis (TGA). The graphene sample exhibits exceptional thermal stability (Figure 3), peaking at ~700°C, which is typical for graphene materials. This stands in contrast to graphene-Cu NC, where copper (Cu) may serve as a catalyst for oxidative reactions during thermal stability assessments. The first derivative of the TGA curve (dTG curve) and its characteristics varied significantly between the two materials, with graphene showing typical GNS behavior and graphene-Cu NPs displaying a fast onset of oxidation followed by a gradual decrease in oxidative reaction speed.

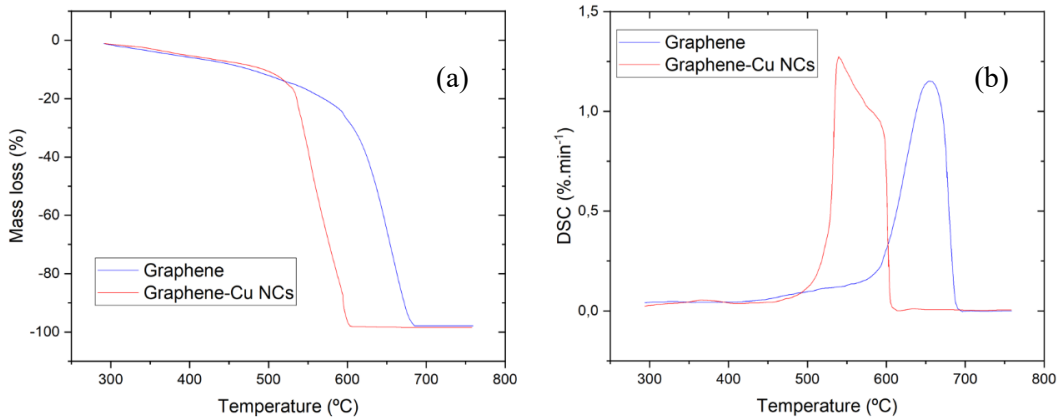

Fig. 3: TGA (a) and dTGA (b) analyses of prepared Graphene and Graphene-Cu NPs

In conclusion, using microwave plasmas at atmospheric pressure, graphene-based NCs can be synthesized which might exhibit different characteristics while keeping high quality graphene properties.

Aknowledgments: This work was partially supported by Grant TED2021129261AI00 funded by MCIN/AEI/ 10.13039/501100011033 and by the European Union NextGenerationEU/PRTR the project LM2023039 funded by the Ministry of Education, Youth and Sports of the Czech Republic. Finally, the authors of the present work are greatly thankful to Prof Michel Moisan of the Groupe de Physique des Plasmas (University of Montreal) for the TIAGO torch donation.

[1] S. Ghosh, *J. Phys. D: Appl. Phys.*, **55** (2024) 13001.
[2] C. Melero, *Plasma Phys. Control. Fusion*, **60** (2018) 014009.
[3] A. Casanova, *Fuel Processing Technology*, **212** (2021) 106630.
[4] J. Toman, *Fuel Processing Technology*, **239** (2023) 107534.

Impact of axial instabilities on ion energy distribution function in Hall thruster: time-resolved RPA measurements

Q. Delavière--Delion[(*)1], F. Gaboriau[1], G. Fubiani[1], L. Garrigues[1]

[1] *LAPLACE - Université Paul Sabatier - CNRS - INPT, Toulouse, 31062, France*

[(*)] quentin.delaviere@laplace.univ-tlse.fr

Hall thrusters are low-pressure cross-field plasma devices in which numerous instabilities can develop, making it challenging to track ion energy distribution functions (IDFs) over time. To overcome this issue, a technique based on the detection of similar events has been developed. The results presented at ESCAMPIG 2024 will show an experimental finding that reveals an evolution of the IDFs on two distinct time scales: firstly, a deceleration of the ions at the frequency of the breathing mode (BM) oscillations (≈ kHz), and secondly, an oscillation of the ion energy associated with the ion transit time oscillations (≈100 kHz).

In a Hall thruster (HT), an axial electric field **E** and a radial magnetic field **B** are imposed through an annular ionisation channel. Only electrons are magnetised, heavy ions are not. So, the application of these two fields perpendicular to each other generates an electron current in the **E**×**B** direction (the azimuthal direction). This important electronic current results from an efficient ionization of the gas, but is also a source of energy for the instabilities development in the plasma.

BM (~kHz) is described as an instability resulting from an enhanced ionization efficiency within the magnetic barrier [2], causing a violent ionization of the entire gas. The ionization front then moves down the channel towards the gas source, away from the magnetic barrier, reducing the efficiency of trapping and ionization. This allows neutrals to repopulate the channel, perpetuating the process.

Ion transit time oscillations (ITTO) are faster oscillations with a period equal to the ion transit time in the acceleration zone. They manifest as potential variations in the thruster channel and in the first few centimeters of the plume (plasma outside the channel) at frequencies around 100 kHz [3], [4], [5], These electric field fluctuations significantly impact ion acceleration, altering the ion energy distribution function (IDF), the ion current I_i and consequently the discharge current ($I_d = I_i + I_e$, where I_e represents the electron current from the cathode crossing the magnetic barrier). Figure 1 shows the temporal evolution of the IDFs over a time period corresponding to a BM oscillation. Oscillations in the hundreds of kHz are also visible, appearing as zig-zag patterns. These oscillations are characteristic of the ITTOs in the plasma and reflect a periodic variation in the ion energy at the ITTO frequency. This time-resolved IDF was obtained from simulations conducted using a hybrid model in which the electrons and neutrals are described as fluids, and the ions are described using the PIC method.

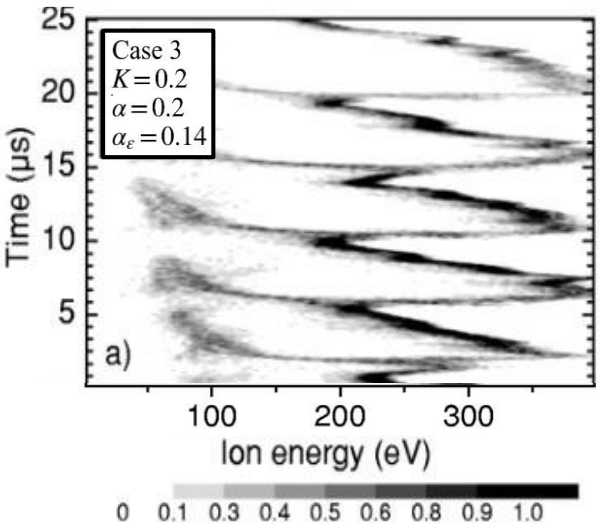

Fig. 1 Temporal IDF obtained for a simulated case with empirical anomalous transport and energy loss coefficients from Ref. [1].

In the literature, various techniques have been used with varying degrees of success to establish the TIDF. Techniques based on FFT, Empirical Transfer Function, and Shadow Manifold Interpolation [6], either require a huge amount of data and high regularity or are not robust against noise and discharge

irregularities. One solution can be to stabilize the discharge by externally forcing BM oscillations. However, even if the discharge becomes more regular, it is not perfect, and we are no longer under the plasma's "natural" conditions. Although averaging the discharge (acquisitions) allows us to begin to discern the evolution of the IDF associated with BM, the irregularities of ITTO average out the faster evolutions than those attributable to BM. To our knowledge, there is no experimental evidence demonstrating ion energy variation at the ITTO scale.

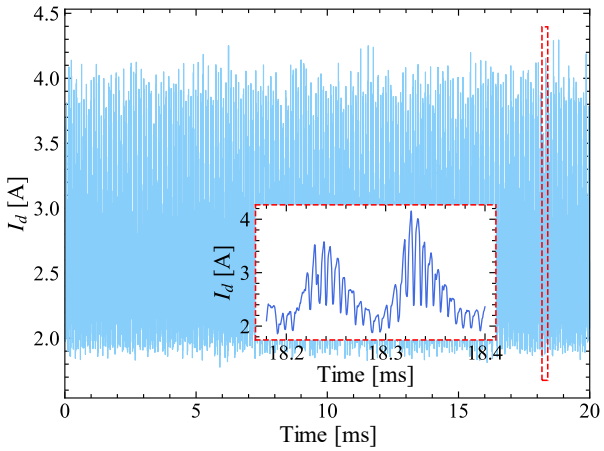

Fig. 2: Evolution and zoom on the discharge current.

Since the discharge always exhibits a certain degree of irregularity (amplitude, frequency, shape, number of sub-oscillations), as can be observed in *Fig.2*, we propose to identify, on a reference signal of the discharge (which does not vary with the modification of RPA settings), the oscillations that are most similar to each other. Here, the discharge current is chosen as the reference signal. This approach assumes that over a sufficiently long time, certain patterns repeat with a satisfactory degree of similarity.

Therefore, for each RPA ion filter voltage, the collected ion current and the corresponding discharge current are acquired over time. Once the pattern search has been performed on each series of discharge currents, families of oscillations with the most similar patterns can be created. The ion currents associated with the time coordinates of these most similar oscillations are then recovered. Subsequently, for each time, the corresponding IDF is calculated. Finally, the data can be assembled to reconstruct a time-resolved IDF. We will present with more details this process and a particularly compelling result at the ESCAMPIG 2024 conference in Brno.

Q. DD has benefited from a PhD funding from the French Ministry of Research. This work is supported by the CNES agency.

[1] J. Bareilles, G. J. M. Hagelaar, L. Garrigues, C. Boniface, J. P. Boeuf, and N. Gascon, 'Critical assessment of a two-dimensional hybrid Hall thruster model: Comparisons with experiments', *Phys. Plasmas*, vol. 11, no. 6, pp. 3035–3046, Jun. 2004, doi: 10.1063/1.1719022.

[2] J. P. Boeuf and L. Garrigues, 'Low frequency oscillations in a stationary plasma thruster', *J. Appl. Phys.*, vol. 84, no. 7, pp. 3541–3554, Oct. 1998, doi: 10.1063/1.368529.

[3] J. Vaudolon and S. Mazouffre, 'Observation of high-frequency ion instabilities in a cross-field plasma', *Plasma Sources Sci. Technol.*, vol. 24, no. 3, p. 032003, Jun. 2015, doi: 10.1088/0963-0252/24/3/032003.

[4] G. J. M. Hagelaar, J. Bareilles, L. Garrigues, and J.-P. Boeuf, 'Two-dimensional model of a stationary plasma thruster', *J. Appl. Phys.*, vol. 91, no. 9, pp. 5592–5598, Apr. 2002, doi: 10.1063/1.1465125.

[5] F. Petronio, 'Plasma instabilities in Hall Thrusters: a theoretical and numerical study', PhD thesis, École Polytechnique, Palaiseau, 2023. [Online]. Available: https://theses.hal.science/tel-04401336

[6] A. Thomas and K. Lemmer, 'Time-resolved ion energy measurements using a retarding potential analyzer for electric propulsion applications', *Rev. Sci. Instrum.*, vol. 95, no. 2, p. 023505, Feb. 2024, doi: 10.1063/5.0176167.

Conference participants and Author Index

Surname	Name	Affiliation	Page
Aceto	Domenico	CNR - ISTP, Bari, Italy	166
Adamovich	Igor	Ohio State University, USA	31
Akashi	Haruaki	N.D.A., Yokosuka, Japan	95
Almeida	Rui	UMa, Funchal, Portugal	129, 304
Almeida	Pedro	UMa, Funchal, Portugal	279
Alomari	Lara	Institut PPRIME, Université de Poitiers, France	174
Alves	Luís	IPFN/IST, Lisbon, Portugal	126, 314, 373
Arellano	Fatima Jenina	OU, Osaka, Japan	66
Babucic	Neda	IPB, Belgrade, Serbia	224
Baeva	Margarita	INP Greifswald, Germany	369
Baghel	Shubham Singh	IPFN-IST, Lisboa, Portugal	126
Baikaliyev	Akdaulet	Al-Farabi KazNU, Almaty, Kazakhstan	
Bajon	Corentin	LAPLACE, Toulouse, France	160
Balo	Kristof	OIPT, Bristol, United Kingdom	
Bannert	Peter	Heinzinger, Rosenheim, Germany (**SPONSOR**)	
Becker	Markus	INP Greifswald, Germany	294
Beilis	Isak	Tel Aviv University, Israel	180
Belinger	Antoine	LAPLACE, Toulouse, France	156
Belkaid	Zakaria	LPGP, Orsay, France	316
Benilov	Mikhail	UMa, Funchal, Portugal	52
Benova	Evgenia	UNISOFIA, Bulgaria	170
Bente	Nicolas	LAPLACE, Toulouse, France	176
Bílek	Petr	Institute of Plasma Physics, Prague, Czech Republic	158
Bogdanov	Todor	Clean & Circle CoC, Sofia, Bulgaria	335
Bonaventura	Zdeněk	Masaryk University, Brno, Czech Republic	45, 124
Booth	Jean-Paul	LPP-CNRS, Palaiseau, France	88, 133, 281
Brandenburg	Ronny	INP, Greifswald, Germany	
Brinkmann	Ralf Peter	RUB, TET, Bochum, Germany	302
Bruggeman	Peter	UMN, Minneapolis, USA	20
Brunovský	Radoslav	Masaryk University, Brno, Czech Republic	306
Burda	Peter	Masaryk University, Brno, Czech Republic	300
Calvo	Eduardo	FEUP-DEF, Porto, Portugal	111, 113, 298
Carbone	Emile	INRS, Varennes, Canada	222
Cartry	Gilles	Aix Marseille University, France	232
Cichocki	Filippo	ENEA, Fracati, Italy	386
Cobos-Luque	Antonio	UCO, Córdoba, Spain	395
Cró	Camila	UMa, Funchal, Portugal	54
Cunha Dias	Tiago	University of Michigan, Ann Arbor, USA	60, 243
Čech	Jan	Masaryk University, Brno, Czech Republic	162
da Silva	Caitano	New Mexico Tech, Socorro, USA	191
de Urquijo	Jaime	UNAM, Cuernavaca, Mexico	391

Conference participants and Author Index

Surname	Name	Affiliation	Page
Delavière--Delion	Quentin	LAPLACE, Toulouse, France	397
Derzsi	Aranka	Wigner RCP, Budapest, Hungary	141
Dogariu	Arthur	Texas A&M, USA	203
Donko	Zoltan	Wigner RCP, Budapest, Hungary	143
Dvořák	Pavel	Masaryk University, Brno, Czech Republic	209
Ebert	Ute	CWI Amsterdam and TU/e, Netherlands	292
Eremin	Denis	Ruhr Uni Bochum, Germany	109
Fantz	Ursel	MPI IPP, Garching, Germany	67, 164, 333
Fatima	Areej	Masaryk University, Brno, Czech Republic	129
Ferreira	Nuno	UMa, Funchal, Portugal	296
Flores Alfaro	Gabriel	LIST, Alzette, Luxembourg	81
Foddis	Roberto	BNC, San Rafael, USA (**SPONSOR**)	
Fubiani	Gwenael	LAPLACE, Toulouse, France	121
Gans	Jonas	DIFFER, Eidhoven, Netherlands	43
Garcia	Maria C.	UCO, Cordoba, Spain	168, 351
Gerakis	Alexandros	LIST, Esch-sur-Alzette, Luxembourg	205
Gómez-Ramírez	Ana	Universidad de Sevilla, Spain	377
Graef	Wouter	Plasma Matters, Eindhoven, Netherlands (**SPONSOR**)	222
Guerra	Vasco	Universidade de Lisboa, Portugal	22, 103
Guo	Yihao	TU/e, Eindhoven, Netherlands	189
Hartmann	Peter	Wigner RCP, Budapest, Hungary	85
Hnilica	Jaroslav	Masaryk University, Brno, Czech Republic	87
Hoder	Tomáš	Masaryk University, Brno, Czech Republic	154, 249, 255
Hopkins	Matthew	Sandia, Albuquerque, USA	251
Hübner	Gerrit	AEPT, Bochum, Germany	119
Inagaki	Yoshinobu	Hokkaido University, Sapporo, Japan	41
Ionita-Schrittwieser	Codrina	Univ. Innsbruck, Austria	379
Jankes	Erik	Platit a.s., Šumperk, Czech Republic (**SPONSOR**)	
Jansky	Jaroslav	UNOB, Brno, Czech Republic	283
Janssen	Jesper	Plasma Matters, Eindhoven, Netherlands (**SPONSOR**)	
Jasek	Ondrej	Masaryk University, Brno, Czech Republic	355
Jiménez-Redondo	Miguel	MPE, Garching, Germany	195
Jovanovic	Olivera	Institute of Physics Belgrade, Serbia	257
Jüngling	Elia Johannes	Ruhr University Bochum, Germany	145
Juřík	Karel	DTEEE FEEC BUT, Brno, Czech Republic	90
Kadlec	Stanislav	Eaton, Czech Republic (**SPONSOR**)	
Kawaguchi	Satoru	Muroran I. T., Japan	218
Kersten	Holger	CAU Kiel, Germany	9
Khan	Waseem	Masaryk University, Brno, Czech Republic	62
Kiefer	Christian	IPP, Munich, Germany	164
Kolev	Stanimir	Sofia University, Bulgaria	228

Conference participants and Author Index

Surname	Name	Affiliation	Page
Kozak	Tomas	University of West Bohemia, Pilsen, Czech Republic	64
Kozáková	Zdenka	BUT FCH, Brno, Czech Republic	371
Krčma	František	BUT FCH, Brno, Czech Republic	321
Kreyder	Geoffrey	LPP, Polytechnique Paris, France	83
Kudrle	Vit	Masaryk University, Brno, Czech Republic	45
Kuijpers	Lex	DIFFER, Eindhoven, Netherlands	223
Kumari	Priyanka	FMFI UK, Bratislava, Slovakia	226
Kushner	Mark	University of Michigan, Ann Arbor, USA	327
Kutasi	Kinga	Wigner RCP, Budapest, Hungary	193
Labenski	Robin	Ruhr-University Bochum, Germany	263
LaCombe	Grayson	UMN, Minneapolis, USA	247
Litch	Evan	NERS, Ann Arbor, USA	115
Liu	Yang	IST-ID, Lisbon, Portugal	288
Luo	Lan-Yue	THU, Beijing, China	286
Malagón-Romero	Alejandro	CWI, Amsterdam, Netherlands	128
Maletić	Dejan	IPB, Belgrade, Serbia	75
Malovic	Gordana	Institute of Physics Belgrade, Serbia	75, 245, 347
Marinova	Plamena	Clean & Circle CoC, Sofia, Bulgaria	349
Marjanovic	Jelena	Institute of Physics Belgrade, Serbia	329
Masheyeva	Ranna	HUN-REN Wigner RCP, Budapest, Hungary	235
Maťaš	Emanuel	FMPH CU, Bratislava, Slovakia	79
Maťašová	Mária	FMPH CU, Bratislava, Slovakia	151
Mazankova	Vera	UNOB, Brno, Czech Republic	239
Mechielsen	Thomas	TNO, Delft, Netherlands	153
Meindl	Arne	IPP, Munich, Germany	67
Mihailova	Diana	Plasma Matters, Eindhoven, Netherlands (**SPONSOR**)	
Miyazaki	Toshiaki	Hokkaido University, Sapporo, Japan	137
Mohr	Sebastian	Quantemol, London, United Kingdom	35
Moore	Chris	SNL, Albuquerque, USA	93, 105
Morales-Calero	Francisco Javier	UCO, Córdoba, Spain	230, 393
Moravčík	Marek	BUT FCH, Brno, Czech Republic	323
Mrkvičková	Martina	Masaryk University, Brno, Czech Republic	253
Mrozek	Krystof	PlasmaSolve, Brno, Czech Republic	90, 284, 312
Naudé	Nicolas	LAPLACE, Toulouse, France	345
Navrátil	Zdeněk	Masaryk University, Brno, Czech Republic	273
Nelson	Anna	Quantemol, London, UK	
Nijdam	Sander	Eindhoven University of Technology, Netherlands	189
Nikic	Dejan	UNM, Albuquerque, USA	107
Nonaka	Tomoyuki	Samco, Kyoto, Japan	237
Obrusnik	Adam	Masaryk University, Brno, Czech Republic	359
Orlandi	Veronica	LAPLACE, Toulouse, France	331

Surname	Name	Affiliation	Page
Orszagh	Juraj	CU, Bratislava, Slovakia	384
Osawa	Taiki	TITech, FIRST, Yokohama, Japan	381
Panarese	Antonio	CNR - ISTP, Bari, Italy	97
Papamichou	Kleopatra	TNO, SEL, Delft, Netherlands	47
Pascual Fort	Carmen	EM2C CNRS CentraleSupelec Université Paris-Saclay, France	69
Pawłat	Joanna	LUT, Lublin, Poland	48
Pazderka	Michal	Masaryk University, Brno, Czech Republic	249
Perez-Invernon	Francisco Javier	IAA - CSIC, Granada, Spain	325
Pikalev	Aleksandr	DIFFER, Eindhoven, Netherlands	39
Pintassilgo	Carlos	IPFN, Lisboa, Portugal	101
Polášková	Kateřina	CEITEC BUT, Brno, Czech Republic	261
Prokop	David	Masaryk University, Brno, Czech Republic	71, 255
Puac	Nevena	Institute of Physics Belgrade, Serbia	224, 245, 257
Puač	Marija	Institute of Physics, Belgrade, Serbia	12
Rincón	Rocío	UCO, Córdoba, Spain	357
Robertson	Colin	HIDEN ANALYTICAL LTD, Warrington, England (**SPONSOR**)	
Robledo-Martinez	Arturo	UAM, Mexico City, Mexico	139
Rutigliano	Maria	CNR-ISTP, Bari, Italy	199
Saab	Ghina	USJ-ESIB, Beyrouth, Lebanon	147
Saito	Atsushi	AGC Inc., Yokohama, Japan	50
Santos	Diego	UMa, Funchal, Portugal	58, 277
Sasaki	Koichi	Hokkaido University, Sapporo, Japan	91, 267
Selaković	Nenad	IPB, Belgrade, Serbia	245
Shen	Qinghao	DIFFER, Eindhoven, Netherlands	310
Shetty	Sanath	CU, Bratislava, Slovakia	178
Schmid	Marvin	Hoschule Furtwangen University, Germany	
Schreuder	David	TU Dresden, Germany	73
Schrittwieser	Roman	Univ. Innsbruck, Austria	265
Silberer	Lucas	IHM, Eggenstein-Leopoldshafen, Germany	339, 341
Skácel	Jan	Masaryk University, Brno, Czech Republic	124
Skopal	Petr	Masaryk University, Brno, Czech Republic	259
Skoro	Nikola	IPB, Belgrade, Serbia	345
Sobczuk	Franciszek	Jagiellonian University, Krakow, Poland	16
Stamate	Eugen	Technical University of Denmark, Kongens Lyngby	
Stancampiano	Augusto	GREMI, Orléans, France	21
Stancu	Gabi Daniel	CentraleSupélec, EM2C-CNRS, Gif-sur-Yvette, France	183
Starikovskaia	Svetlana	LPP (CNRS, Ecole Polytechnique), Palaiseau, France	362
Šimek	Milan	IPP CAS, Prague, Czech Republic	269
Šťastný	Marek	SpaceLab, Brno, Czech Republic	312
Taccogna	Francesco	CNR-ISTP, Bari, Italy	117
Takáčová	Alica	Masaryk University, Brno, Czech Republic	154

Conference participants and Author Index

Surname	Name	Affiliation	Page
Takahashi	Kazuo	KIT, Kyoto, Japan	353
Tarvainen	Olli	STFC-ISIS, Didcot, United Kingdom	18
Teunissen	Jannis	CWI, Amsterdam, Netherlands	191
Thiel	Jonas	Ruhr University Bochum, Germany	149, 337
Tomanková	Kristína	PlasmaSolve, Brno, Czech Republic	284
Tsonev	Ivan	PLASMANT, Antwerp, Belgium	122
Tu	Xin	Univ Liverpool, United Kingdom	390
Tungli	Jan	Eaton, Roztoky u Prahy, Czech Republic	281
Ussenkhan	Sultan	Al-Farabi KazNU, Almaty, Kazakhstan	320
Utegenov	Almasbek	LLP "IASIT", Almaty, Kazakhstan	135
van Helden	Jean-Pierre	INP, Greifswald, Germany	211
Van Rompaey	Stijn	PLASMANT, Antwerpen, Belgium	290
van "t Veer	Kevin	Plasma Matters,Eindhoven, Netherlands (**SPONSOR**)	
Vertongen	Rani	PLASMANT, Antwerp, Belgium	360
Vialetto	Luca	Stanford University, USA	365
Viegas	Pedro	IPFN, IST-UL, Lisboa, Portugal	60,243
Vitelaru	Catalin	INOE, Marguele, Romania	186
Wagenaars	Erik	York Plasma Institute, United Kingdom	24
Wolf	Vinzenz	Uni Augsburg, EPP, Germany	333
Yamashita	Yuya	Tokyo Tech, Japan	271
Yamazaki	Yuka	Nitto, Duesseldorf, Germany	
Zajíčková	Lenka	CEITEC, Brno, Czech Republic	233
Zarzeczny	Dawid	LUT, Lublin, Poland	56
Zavadil	Milos	HIDEN ANALYTICAL LTD, Warrington, England (**SPONSOR**)	
Zhan	Shu	LPP, Palaiseau, France	275
Zielke	Dominikus	Zeiss SMT, Oberkochen, Germany	
Zmeko	Filip	FEE UWB Pilsen, Czech Republic	318

Emails of conference participants and sponsors can be found in the abstracts and advertisements.

ESCAMPIG 2024 Statistics

Program highlights:

- **14,5** hours of conference talks (6 general invited talks + 7 topical invited talks, 8 + 7 Hot topic talks and oral contributions)
- **2** Prize talks (William Crookes prize and IUPAP Early carrier prize)
- **154** Posters – 2 Best student poster awards, 11/12 ESCAMPIG Topics covered
- **2** Workshops

Participants:

- **26** countries
- **191** science program participants: ~ 1/3 students, ~ ¼ women
- **17** sponsors

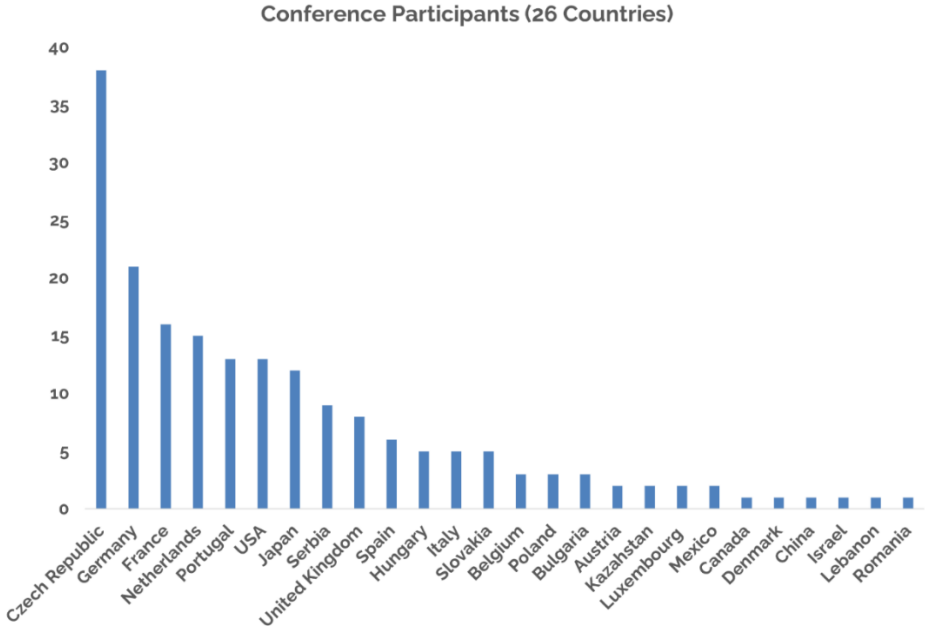

Fun facts:

- **1083** beers consumed during the conference
- **3** hours of coffee breaks (**F** coffees + **U** kg sweets + **N** l water)
- **Everyday** ESCAMPIG Herald including **5** ciphers!
- **10+** hours of social program including **Stormy** lab tour
- EMPs by Lightnings, Rockets and Students in the Farraday cages **presented by CdS!**

ESCAMPIG 2024 conference photo

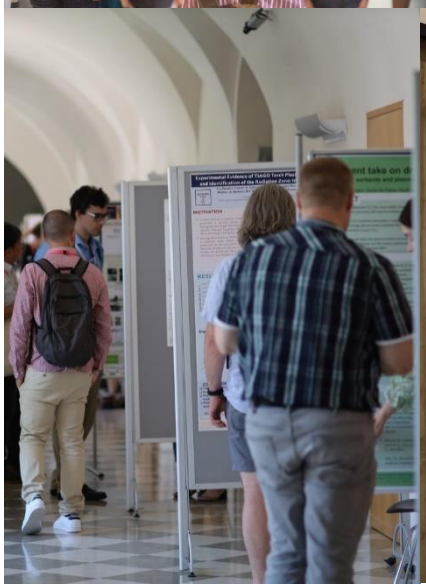

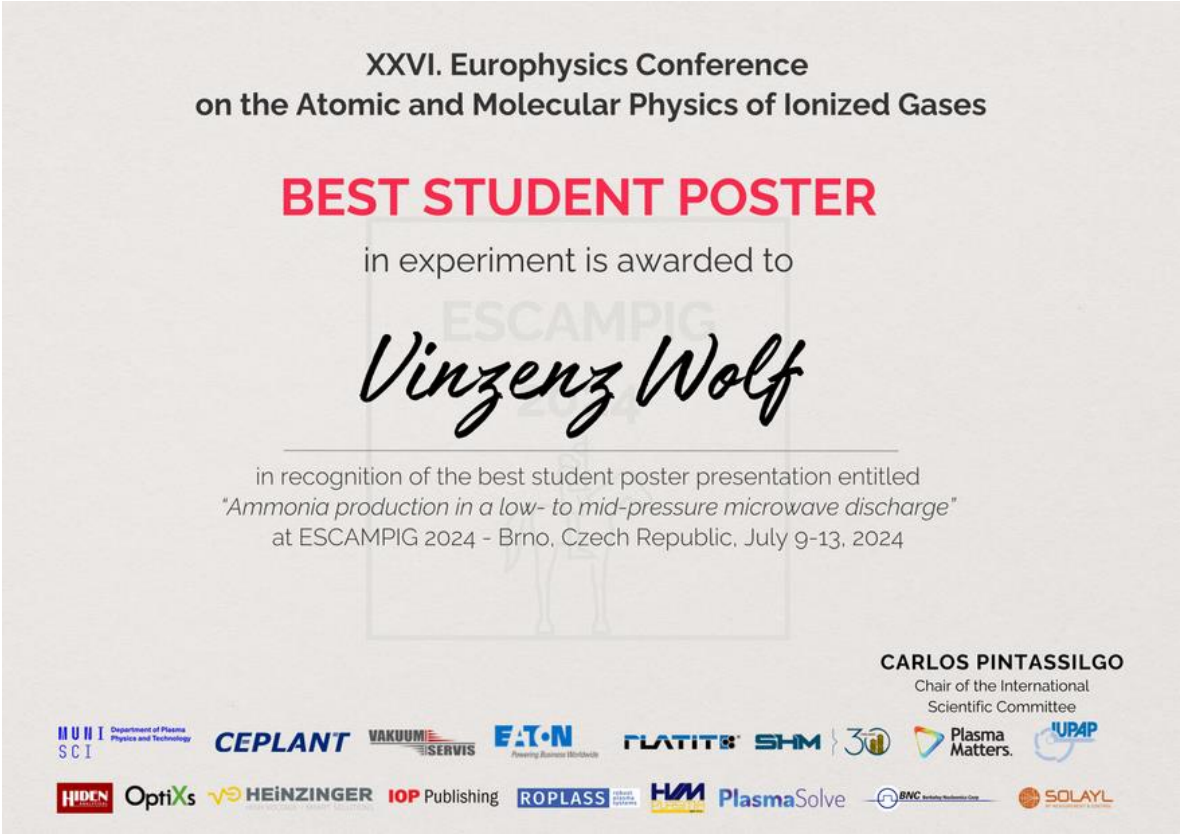

XXVI. Europhysics Conference
on the Atomic and Molecular Physics of Ionized Gases

BEST STUDENT POSTER

in experiment is awarded to

Vinzenz Wolf

in recognition of the best student poster presentation entitled
"Ammonia production in a low- to mid-pressure microwave discharge"
at ESCAMPIG 2024 - Brno, Czech Republic, July 9-13, 2024

CARLOS PINTASSILGO
Chair of the International
Scientific Committee

XXVI. Europhysics Conference
on the Atomic and Molecular Physics of Ionized Gases

BEST STUDENT POSTER

in modelling is awarded to

Marek Šťastný

in recognition of the best student poster presentation entitled
*"Numerical simulation of a low-pressure electrodeless
ion source intended for air-breathing electric propulsion"*
at ESCAMPIG 2024 - Brno, Czech Republic, July 9-13, 2024

CARLOS PINTASSILGO
Chair of the International
Scientific Committee

ESCAMPIG HERALD

Welcome to ESCAMPIG 2024!

Each conference day, there will be an edition of the ESCAMPIG HERALD. It will be available at the reception desk. We aim is to lighten the packed scientific and social schedule. Enjoy the conference!

VENUE

www.hrady.cz

The conference takes place at the historical complex Královo Pole Monastery. The complex of the former carthusian monastery is protected as a cultural monument of the Czech Republic.

Except for the parish house and the Holy Trinity Church, the complex has been a part of the Faculty of Information Technology of the Brno University of Technology since the 1960s.

The Margrave John Henry issued the founding document of the new charterhouse in Královo Pole on 13th August 1375. It was the very first one in Moravia. The monastery was named Cella Trinitas.

In 1782 the monastery was dissolved during the religious reforms of Emperor Joseph II. To the present form, it was rebuilt at the beginning of the 21st century.

CHESS

CHECKMATE INSIGHTS

Do you play chess? This chess piece puzzle was prepared by Petr Bílek according to Lev Milman vs Joseph Fang, 2005.

Checkmate is the essence of chess and involves coordination among your pieces. No single piece can deliver checkmate alone. Can you find the forced checkmate in 3 moves? White is on the move.

TODAY'S CIPHER

WHAT ON EARTH AM I SUPPOSED TO DO WITH THESE NUTS?

Cipher games are logic and brain-teasing puzzles that are very popular in Czechia. We established the ESCAMPIG cipher team and prepared a game especially for our physical audience. The event was meant to be one of the options in the Friday afternoon social program.

Only a few participants chose the cipher game over getting lost in the Brno underground or other city sights. Instead of canceling, we decided to give them to everyone to solve!

We will bring you those puzzles daily in the conference newspaper.

For the first cipher of the conference, you will need to find a pencil, a ruler, and a pack of three nuts in your ESCAMPIG conference bag. Then, look at the picture to the right of this text. The solution to the cipher is one English word. Are you up to the challenge?

The procedure for solving each cipher will be available later on the conference website.

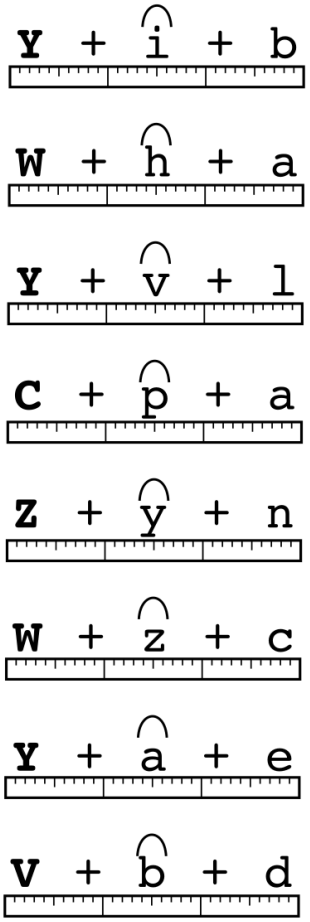

9TH JULY 2024 **ESCAMPIG HERALD** BRNO

WELCOME PARTY

The first social event of ESCAMPIG 2024 starts at 18:00. Enjoy a buffet-style meal with soft and alcoholic drinks. The summer evening at the conference venue will be accompanied by live cimbalom music and a folklore dance school.

PAVEL'S BIG PAN

16 kg turky breast
5 kg Wallachian smoked sausages
2,5 kg smoked bacon
10 kg potatoes
3 kg onion
0,2 kg czech garlic
7 kg mix color bell peppers
oil, salt, pepper, cumin, paprika

Our chef Pavel prepares his special big pan for us. To replicate at home, first, prepare your largest pan. Cut vegetables to bite sizes. Chop the meat, sausages, and bacon. Light up your fire, fry the meat first, and cook with rest of ingridients with care.

CIMBALOM MUSIC

Pol'ana Brno provides live music this evening. Pol'ana has a 75-year-old tradition of preserving the Slovakian folklore culture in Brno. It was established by a group of Slovakian university students and now has more than 80 members. **Fun fact:** Rado Brunovský, a violist in the ensemble, is a PhD student of plasma physics.

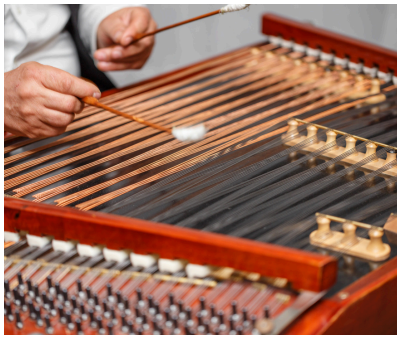

The cimbalom is a large hammered string instrument traditionally used in local folklore music.

Why Slovakian folklore? Even though Czechia and Slovakia are independent, the history, language, and familiarity make us more cohesive than other neighbors.

WINE

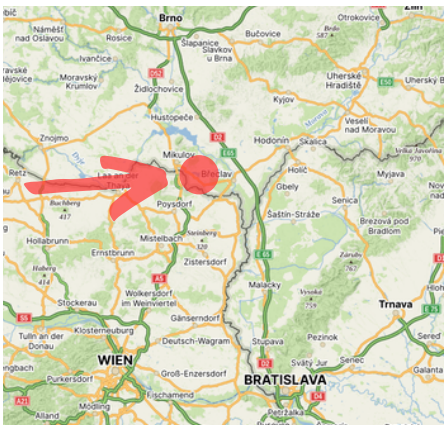

ESCAMPIG wine comes from private wine maker Jan Michalica from Hlohovec near Břeclav at Czech, Austria and Slovakia boundaries.

We offer you a selection of two red wines:
Cabernet Moravia is a local cross-breed between Zweigeltrebe and Cabernet Franc.
Merlot is a very old variety of red wines grown across the globe.

We offer you a selection of four white wines:
Hibernal was developed in 1944 and is pest- and fungus-resistant and strong against frosts.
Chardonnay is an old and well-known variety originating in France.
Kerner was bred in 1929 by crossing Trollinger and Riesling.
Pálava is a wine grape developed in 1953 in Moravia, and it stays local. It is full-bodied, aromatic, and sweet with a golden-yellow color.

TOMORROW EARLY START

Conference Opening by ISC Chair Carlos Pintassilgo and LOC Chair Zdeněk Bonaventura at 08:20.

Remember to check the conference program! If you have any questions or encounter unexpected problems, feel free to contact the organizers at the reception.

ESCAMPIG HERALD

ONLINE

ESCAMPIG HERALD

LIQUEFACTION OF HELIUM ANNIVERSARY

On 10th July 1908, around 7 p.m., Heike Kamerlingh Onnes in Leiden, the Netherlands, succeeded in helium liquefaction. Today is the 116th anniversary of his historical achievement.

He utilized a five-stage cooling cascade: He used chloromethane (boiling point 249 K) to liquefy ethene (b.p. 170 K), ethene to liquefy oxygen (b.p. 90 K), and oxygen to liquefy air (b.p. around 79 K).

He used liquid air to precool hydrogen before its liquefaction (b.p. 20 K) and hydrogen to precool helium (a scarce gas back then), further cooled by the Joule-Thomson expansion.

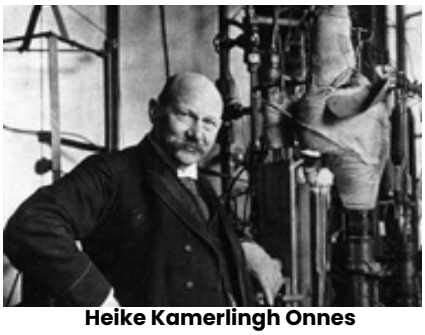

Heike Kamerlingh Onnes
www.espacotempo.com.br

After 13 hours of cooling, the measured temperature of helium reached a constant value. It refused to decrease further as if the thermometer was in a liquid. At that moment, Onnes illuminated the vessel with helium and saw the surface of liquid helium "standing out sharply defined like the edge of a knife."

The work was so intensive that day that Onnes had no time to eat. His wife had to feed him. The long-term preparation of the experiment was so exhausting that after the successful liquefaction of helium, Onnes fell ill for several months.

Onnes later studied the behavior of matter at such low temperatures. He discovered superconductivity and opened the door to the discovery of superfluidity and a further journey into an even much cooler world.

As luck would have it, yesterday was also the 130 anniversary of Pyotr Kapitsa's birthday in 1894. He was a famous soviet physicist researching the world of extra-low temperatures.

WANTED

HOLGER KERSTEN
08:35

MARIJA PUAČ
09:20

PETER BRUGGEMAN
11:00

AUGUSTO STANCAMPIANO
11:45

HAUNTED

BY THE FOLLOWING QUESTIONS?

- What are the latest trends in plasma simulation research?
- What are the challenges in multi-physics plasma models?
- How does high-performance computing enhance plasma simulations?
- What uncertainties impact plasma model accuracy?
- How are plasma simulations applied in the industry?

WORKSHOP
PREDICTIVE AND PRACTICAL SIMULATIONS OF PLASMA SYSTEMS AND PLASMA PROCESSES
17:00 - 19:00

Find the answers you seek and put your restless mind at ease in the panel discussion with world-leading experts.

Featuring: Anna Nelson, Vasco Guerra, Markus Becker, and Mark Kushner, chaired by Adam Obrusník.

10TH JULY 2024 **ESCAMPIG HERALD** BRNO

TODAY'S CIPHER

Today enigma draws on the wisdom of several generations of renowned physicists. It was prepared by Petr Bílek.

To solve it, you need to pick up a full version of the cipher, containing three printed sheets, from the reception.

Can you crack the cipher and reveal the English password?

Werner von Siemens	Enrico Fermi	Erwin Schrödinger	Wolfgang Pauli	Ernest Rutherford	Isaac Newton
Ludwig Boltzmann	Archimedes	Stephen Hawking	Lev Landau	Michael Faraday	Niels Bohr
Galileo Galilei	Marie Curie	Albert Einstein	Werner Heisenberg	Lord Kelvin	Richard Feynmann
Paul Dirac	James C. Maxwell	Blaise Pascal	Nikola Tesla	Aristotle	Max Planck

I have never met a man so ignorant that I could not learn something from him.	Before I came here, I was confused about this subject. Having listened to your lecture, I am still confused -- but on a higher level.	I do not think you can name many great inventions that have been made by married men.	Most important part of doing physics is the knowledge of approximation.	Thoroughly conscious ignorance is the prelude to every real advance in science.	Nothing is more practical than a good theory.
A physical law must possess mathematical beauty.	If I have seen further it is by standing on the shoulders of Giants.	One never notices what has been done; one can only see what remains to be done.	Give me a place where I can stand —and I shall move the world.	Truth is so obscure in these times, and falsehood so established, that, unless we love the truth, we cannot know it.	An alleged scientific discovery has no merit unless it can be explained to a barmaid.
The roots of education are bitter, but the fruit is sweet.	Stop telling God what to do with his dice.	Not only is the Universe stranger than we think, it is stranger than we can think.	If a man never contradicts himself, the reason must be that he virtually never says anything at all.	Physics is like sex: sure, it may give some practical results, but that's not why we do it.	Ideas alone have little value. An innovation's importance lies in its practical implementation.
Can you measure it? Can you express it in figures? Can you make a model of it? If not, your theory is apt to be based more upon imagination than upon knowledge.	God made the bulk; the surface was invented by the devil.	A new scientific truth does not triumph by convincing its opponents and making them see the light, but rather because its opponents eventually die, and a new generation grows up that is familiar with it.	God does not play dice with the universe.	A man who is certain he is right is almost sure to be wrong.	Not only does God play dice but... he sometimes throws them where they cannot be seen.

ESCAMPIG HERALD

TYCHO BRAHE (*1546 †1601): GOLDEN EYE

wikipedia.org

Tyge Ottesen Brahe was born the first of eleven children on 14 December 1546 in Knudstrup, Denmark. Tycho, raised by his uncle, initially set on a path to becoming a lawyer.

On 21st August 1560, a partial solar eclipse ignited his passion for astronomy, leading him to pursue his true interests despite his uncle's disapproval.

After his uncle's death in 1565, Tycho inherited substantial property, enabling him to travel to universities and expand his knowledge.

In 1566, Tycho's observations of the conjunction of Jupiter and Saturn revealed inaccuracies in the existing astronomical tables. Thus, he constructed highly accurate metallic instruments and develop a new targeting system, making his measurements 20 times more precise than any other of the time.

In November 1572, Tycho identified a newly appeared object in Cassiopeia constelation as a star, challenging the prevailing beliefs of the time.

King Frederick II of Denmark funded two observatories that became the world's leading centers for astronomical observation.

In 1597, Tycho's fortunes changed when Danish King Christian IV ceased funding. The following conflict resulted in Tycho's expulsion from Denmark. He traveled across Europe for two years until Emperor Rudolf II invited him to the royal court in Prague.

www.oldmapsonline.org

Tycho became the emperor's principal astronomer with a generous salary and the new observatory at Benátky nad Jizerou.

From there he collaborated with Johannes Kepler. Tycho had vast observational data, and Kepler excelled in its analysis. Their collaboration lasted only a year due to their strong personalities and ensuing arguments.

In October 1601, during a personal meeting with Emperor Rudolf II, Tycho was tasked with creating new astronomical tables, a project completed by Kepler in 1623.

WANTED

GABI DANIEL STANCU
08:30

CATALIN VITELARU
09:15

KINGA KUTASI
11:00

MIGUEL JIMÉNEZ REDONDO
11:45

WORKSHOP

ADVANCEMENTS IN NON-EQUILIBRIUM PLASMA LASER DIAGNOSTICS

17:00 - 19:00

Laser diagnostics remain essential to the advancement of plasma knowledge and engineering. The workshop will expose recently achieved progress.

Discuss with Jean-Pierre van Helden, Alexandros Gerakis, Arthur Dogariu, and Pavel Dvořák with Gabi Daniel Stancu as a chairman.

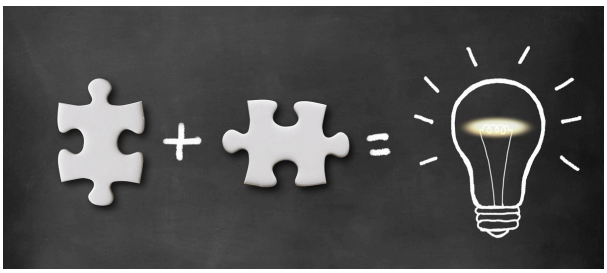

TODAY'S CIPHER

We bring you a new puzzle. The puzzle was prepared by Vít Kudrle and it is only a play with words. We found an ancient plasma physics textbook. However, some statements seem quite suspicious. Maybe a code is hidden somewhere. The solution is one English word.

- The magnetic part of the Lorentz force is independent of the particle velocity vector.
- For a wave frequency higher than the plasma frequency, the plasma reflects the wave.
- Absorption spectroscopy is an experimentally simpler technique than its counterpart.
- For tokamak plasma stability, particle trajectories should be open.
- Particle velocities after a collision can be easily calculated using momentum conservation and basic geometric formulae in a rectangle.
- Plasma simulations are easiest using a hexagonal mesh.
- A high probability of photon reabsorption increases the transparency of the plasma.
- To the outside observer, the bulk plasma is charged.

CONFERENCE DINNER

The renovated Poupě Brewery House continues the quality beer tradition in the Brno center. The restaurant with its brewery on Dominikánská Street is based on the best tradition of Czech beer culture and offers up to 350 seats.

The Brno City Brewery near Mendel Square brewed its first batch of beer on 12th September 1545. Its best period so far was in 1798-1805 thanks to one of the most important personalities of the Czech brewing industry, a brewer František Ondřej Poupě. The Poupě Brewery House in the city center is named after this famous brewmaster.

www.pivovar-poupe.cz

LIVE MUSIC

Dinner ambient music ís provided by **Jazz Baía,** a jazz band based in Brno. The guitar and bass duo will play jazz standards, Brazilian bossa nova and samba, and jazz versions of songs you might not expect to hear from a jazz band.

Dance to the early hours with **Byznys Time,** a band that has been entertaining audiences for many years at various parties, weddings, and balls. Their repertoire includes both modern and old-school songs that are sure to entertain and energize everyone. Whether you're looking for the latest hits or classic tunes, Byznys Time has something for everyone to enjoy.

CHESS CORNER

CARLSEN'S QUEEN SACRIFICE

This chess piece puzzle was prepared by Petr Bílek. It is linked to the World Chess Championship 2016.

It was a chess match between the reigning world champion Magnus Carlsen and the challenger Sergey Karjakin. Carlsen finished the game with a beautiful checkmate in two. Can you find it as White?

ESCAMPIG HERALD

IVO BABUŠKA(*1926 †2023)

THE INFINITE MATHEMATICIAN WITHIN FINITE ELEMENT

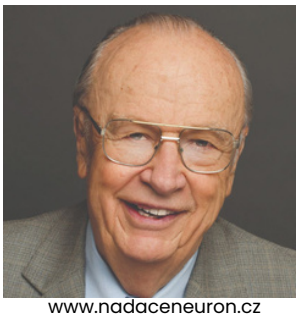

www.nadaceneuron.cz

Ivo Babuška was a mathematician known worldwide. He was born on 22nd March 1926 in Prague, Czechoslovakia. His father, Milan Babuška, was a famous architect who designed many buildings, e.g., the National Technical Museum and the National Museum of Agriculture in Prague.

After World War II, in 1949, he graduated in civil engineering at the Czech Technical University in Prague. In 1955, he received a PhD in Mathematics, and in 1960, he became a research professor.

Ivo Babuška belonged among the most influential mathematicians in the Institute of Mathematics at the Czech Academy of Science. He worked there as the leader of a numerical mathematics group.

His group analyzed the technology of constructing the 91-meter-high gravitational dam Orlík on the Vltava River in south Bohemia. The mathematical problem was to solve a nonlinear heat conduction partial differential equation describing the solidification of concrete. All the computations (about 3*10^6 arithmetic operations) were carried out by a team of people on mechanical desk calculators.

Ivo Babuška established the Czechoslovakian journal Applications of Mathematics back in 1956. He was also one of the founders of the series of the international scientific meetings EQUADIFF.

The first EQUADIFF Conference on Differential Equations was held in Prague in 1962. It was an exceptional forum where mathematicians from the East and the West could meet.

In 1968, after the Soviet army invasion, Babuška and his family hastily departed for a planned one-year stay at the University of Maryland in College Park, USA. The university offered him a prolongation of the contract. Ivo Babuška declined the order from the Czechoslovak authorities to return and due to the turn in the political situation in Czechoslovakia and the normalization period after 1969, he had stayed in the USA ever since.

Professor Babuška substantially influenced the theoretical development of numerical mathematics and computational mechanics. He is also known for his theoretical results in the theory of partial differential equations.

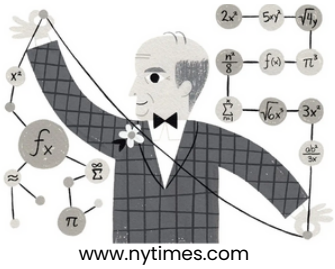

www.nytimes.com

Together with Rheinboldt, he founded the field of a posteriori error analysis and adaptive methods.

His famous contribution is a generalization of the famous Lax–Milgram theorem, which gives conditions under which a bilinear form can be "inverted" to show the existence and uniqueness of a weak solution to a given boundary value problem. The result bears his name: Babuška–Lax–Milgram theorem.

BTW: Today is also the anniversary of the passing of Boris Galerkin, known for his contributions to applied mathematics and finite element method.

WANTED

LUCA VIALETTO
09:15

LUÍS ALVES
11:00

ANA GÓMEZ-RAMÍREZ
11:45

12TH JULY 2024 **ESCAMPIG HERALD** BRNO

TODAY'S CIPHER

We bring you a new puzzle. The puzzle made by Pavel Dvořák looks like the constellations, see below.

To solve it, you need to look at the true version of this cipher, which is located on three windows of the conference building. The solution is again one word.

AQUILA, CASSIOPEIA, CENTAURUS, DELPHINUS, ORION, SAGITTARIUS

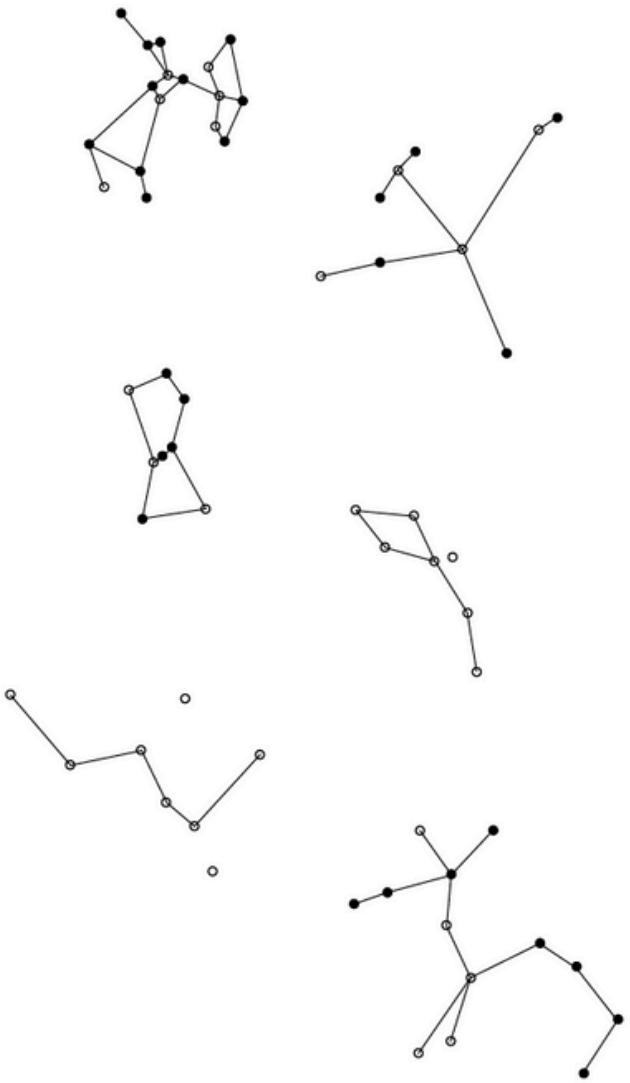

EXCURSIONS

Please check the instructions that you have received at the registration. If you were assigned a specific time, be punctual!

Villa Tugendhat – An architectural gem from 1929 that was ahead of its time. Even today, you can still get inspired by the unique design.
Špilberg castle – One of Brno's dominant features was once the harshest prison in the Austro-Hungarian Empire.
Water Tanks – Brick water tower systems from the 19th century were decommissioned in 1997 and changed into a unique space.
LabTour (CEPLANT and Department of Plasma Physics and Technology) – Starting from 16:30 with 15-minute intervals, you can tour the laboratories and get acquainted with the directions of plasma research at SCI MUNI.

GARDEN PARTY

SCI MUNI BOTANICAL GARDEN

Enjoy the small barbecue party from 18:00 to 21:30. You can look forward to grilled sausages and the Czech version of camembert (Hermelín).

Explore the beauty of the well-kept plants and greenhouses and browse through the newly installed exhibition of sculptural works of students from the Faculty of Fine Arts, BUT.

CHESS CORNER

This chess piece puzzle was again prepared by Petr Bílek. It is linked to the famous game played by Albert Einstein in 1913.

Einstein sets up a brilliant trap in the Italian Game, one of the most popular chess openings.

EINSTEIN = MAGNUS C^2ARLSEN

At a critical moment, Einstein sacrificed his rook to gain the initiative and attack hisopponent's king. He won the game with a beautiful tactical combination that resulted in a forced checkmate.

Can you find, just as Einstein did, a checkmate in six moves for white?

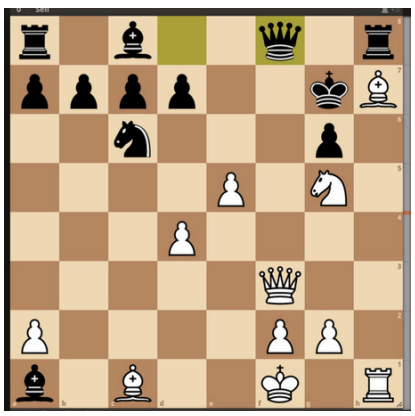

ESCAMPIG HERALD

ERNST MACH(*1838 †1916) LORD OF THE SOUND

Ernst Waldfried Joseph Wenzl Mach was a famous physicist born on 18th February 1838 in Chrlice. Nowadays, Chrlice is part of Brno. He studied at a high school in Kroměříž and graduated at the age of 17.

In 1855, he enrolled at the University of Vienna and graduated with his work on electric discharges and induction. He stayed at the University of Vienna as an assistant to Albert von Ettingshausen. He became an associate professor with a habilitation thesis on the Doppler effect.

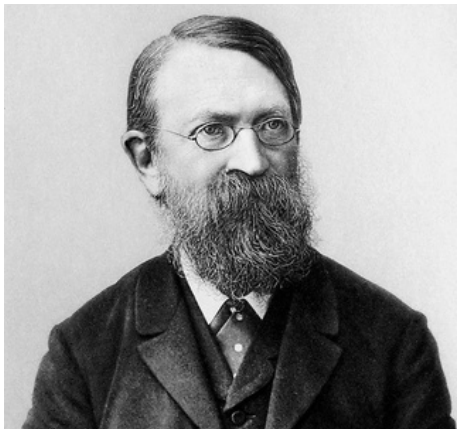

wikipedia.org

Mach became a professor of experimental physics at Charles University in Prague in 1867. At that time, it was called Karl-Ferdinand University.

His lectures, accompanied by well-premeditated experiments, soon gained a reputation for their excellence and pedagogical brilliance. Mach was elected as a rector of the university two times. However, during his second rectorship, he resigned after disapproving of the administrative procedures of the statutory division of the university into Czech and German parts in 1882.

In Prague, he worked on acoustic and optical experiments and invented new experimental methods in stroboscopy and photography. His advanced development led him to manufacture a device capable of photographing a flying bullet. It made the visualization of the sound waves of a supersonic bullet flight possible.

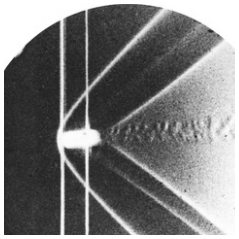

1888 photography of a supersonic bullet
wikipedia.org

Mach determined the angle of the wavefront relative to the direction of projectile motion by the ratio of the projectile's velocity to the speed of sound propagation in the environment. Since 1929, this ratio has been referred to as the Mach number.

One of his most significant scientific achievements was the experimental proof of the Doppler effect. He also wrote a renowned book on mechanics entitled 'Die Mechanik in ihrer Entwicklung,' published in 1883, where he criticized the foundations of Newtonian mechanics. He refused to accept the general theory of relativity and the concept of the molecular and atomic structure of substances.

WANTED

JURAJ ORSZÁGH
08:30

FILIPPO CICHOCKI
09:15

CROOKES PRIZE TALK

Plasma Catalysis for Sustainable Production of Fuels and Chemicals: Challenges and Perspectives

XIN TU 09:45

Xin Tu is a Chair Professor of Plasma Catalysis in the Department of Electrical Engineering and Electronics at the University of Liverpool, UK.

He has published over 220 research papers. He is the inventor of 5 PCT patents and is the Co-Founder of Plasma2X Ltd. (https://p2xinnovations.com).

THE LAST CIPHER

A wheel and a crocodile are two symbols of Brno, which remind us of two local legends. The second - the crocodile - resembles a dragon, which is said to have once terrorized Brno and its wide surroundings.

The dragon was defeated by a clever man, who fed dragon with a fake cow - a burnt lime was sewn into a cowhide. After the dragon gobbled the cow up and drank water from the Svratka river, the exothermic reaction of the burnt lime and water killed the dragon.

To say goodbye to Brno, show that you are as smart as the bygone savior of Brno and solve the following puzzle. The very last ESCAMPIG 2024 enigma was prepared by Pavel Dvořák.

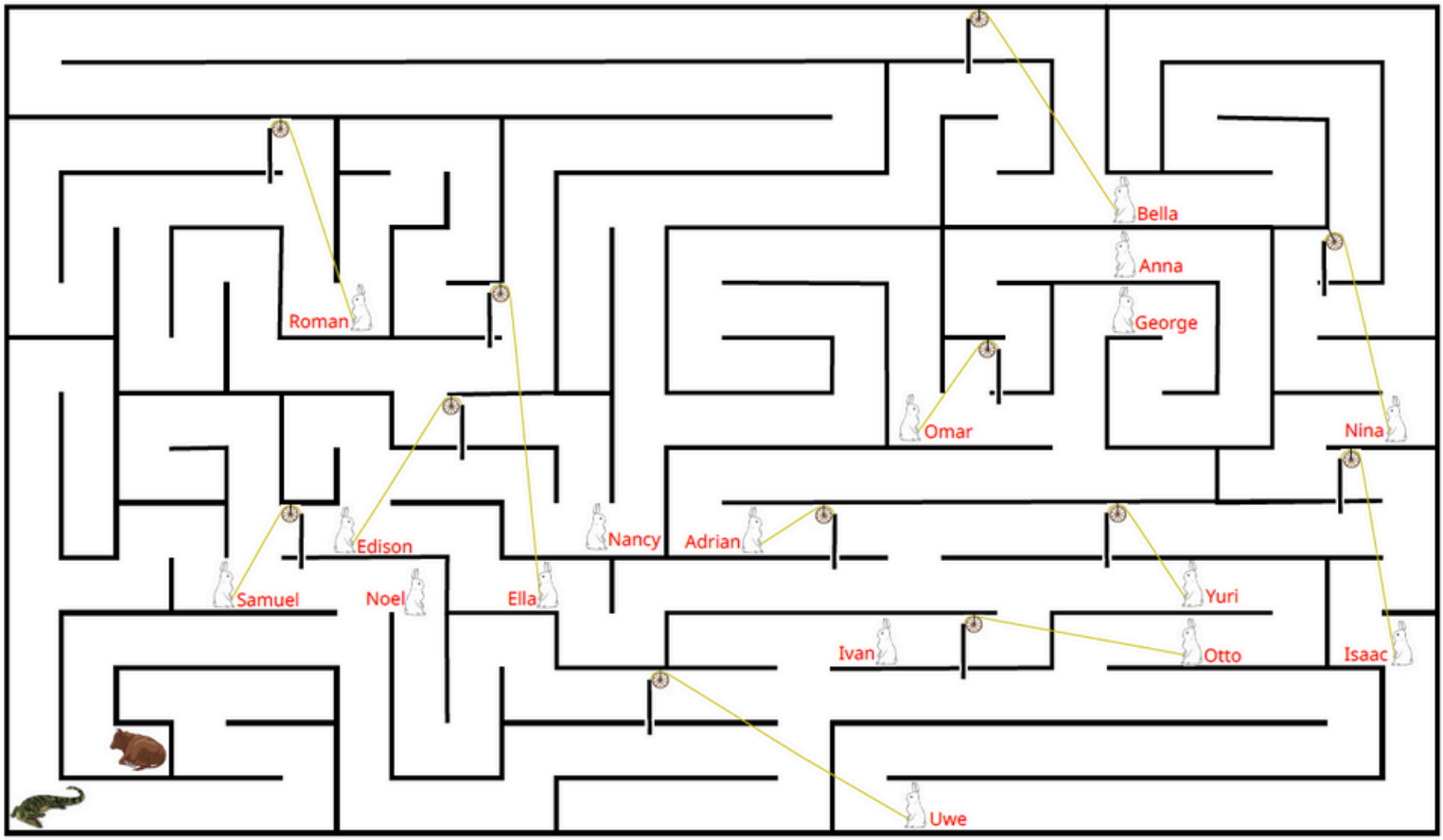

CHESS CORNER

CAN YOU OUTTHINK THE ENGINE?

Computers are incredibly good at chess. It is unlikely that any human will ever beat a top computer in chess again. Even achieving a draw would be a tremendous achievement.

However, in special cases, a human can still play chess better than a computer.

In this position, White can probably win by force with a beautiful concept; the main line results in a checkmate in ten moves. However, Stockfish, the best chess engine in the world, can't find it.

Will you find it? Hint: the key is a beautiful queen and rook sacrifice. This chess piece puzzle was again prepared by Petr Bílek.

SPECIAL EDITION **BRNO**

ESCAMPIG HERALD

CIPHER'S SOLUTIONS

TUESDAY – NUTS CHALLENGE

The first cipher was an elementary mechanics problem. The text in the newspaper said to use the pencil, the ruler, and the package of three nuts from your ESCAMPIG conference bag. But what to do with them?

Each line of the cipher consists of three letters standing on a ruler. Each letter represents a nut - a big, fat one (extension nut), a crowned one (crown nut), and a normal one. Place these nuts on the letters on your ruler.

What to do next? There is a little help hidden in the picture. The third column of letters says 'balanced'. The physical objects will remain in a balanced position if we support them below their center of mass. Your task is to find a center of mass for each set of nuts staying on the ruler.

To find it, it is helpful to use the last tool recommended in the newspaper. Place your ruler on the pencil (perpendicularly), scroll the pencil under the ruler, and find the position where the ruler is balanced on the pencil. The position of the intersection of the ruler and pencil gives you a letter. Solving this for each row gives the answer **POSITRON**.

WEDNESDAY – PHYSICISTS

Solving this puzzle give you the answer **FLUX**.

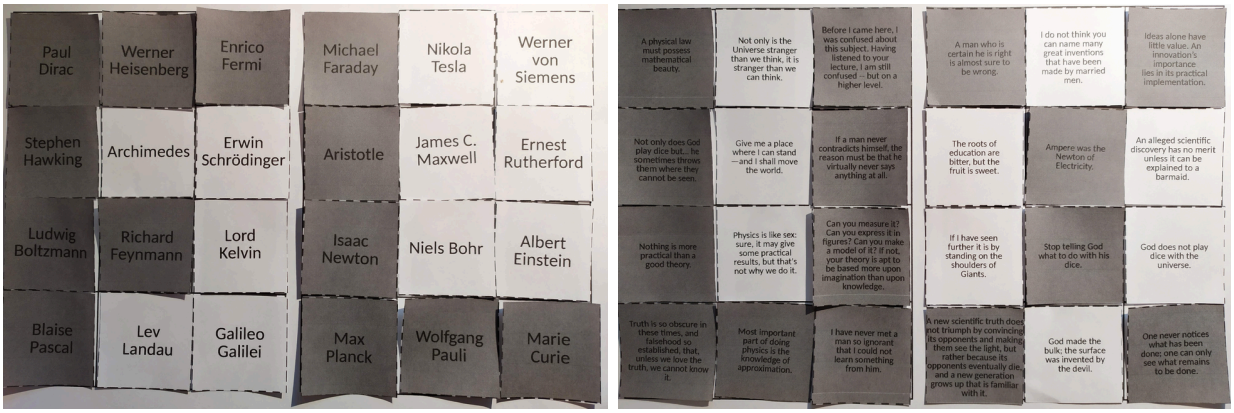

THURSDAY – TEXTBOOK

The statements were faulty. Negating the verb would correct them, but that would be trivial and not reveal any hidden code. Let's try a different approach – changing nouns, adjectives, or adverbs. There are many possibilities, but the correct words are the most obvious ones. Look at the first letters of the corrected words, and suddenly, the most important plasma particle is revealed. The answer is **ELECTRON**.

1. MAGNETIC – ELECTRIC
2. HIGHER – LOWER
3. ABSORPTION – EMISSION
4. OPEN – CLOSE
5. RECTANGLE – TRIANGLE
6. HEXAGONAL – RECTANGULAR
7. TRANSPARENCY – OPACITY
8. CHARGED – NEUTRAL

ESCAMPIG HERALD

FRIDAY – CONSTELLATIONS

The constellation cipher was not our idea. A cipher based on the same principle was made by Monika Spasovová in a cipher game made during a holiday camp in 2023. We guess the original idea came from a popular Czech cipher game called “Tmou.”

The cipher had two parts: a polarization filter and a paper sheet with six constellations, where some of the stars were only drawn by black color, while holes in the paper reprented others. So they transmitted light and “radiated.” However, some of the holes were filled with a polarization foil. So if you observed the constellations through the polarization filter, you saw only some of the stars “radiate.” The number of the radiating stars gave you the order of the letter from the constellation’s name, which was a part of the solution.

If you had a bad luck and you started with horizontal polarization, you read **TURN IT**.

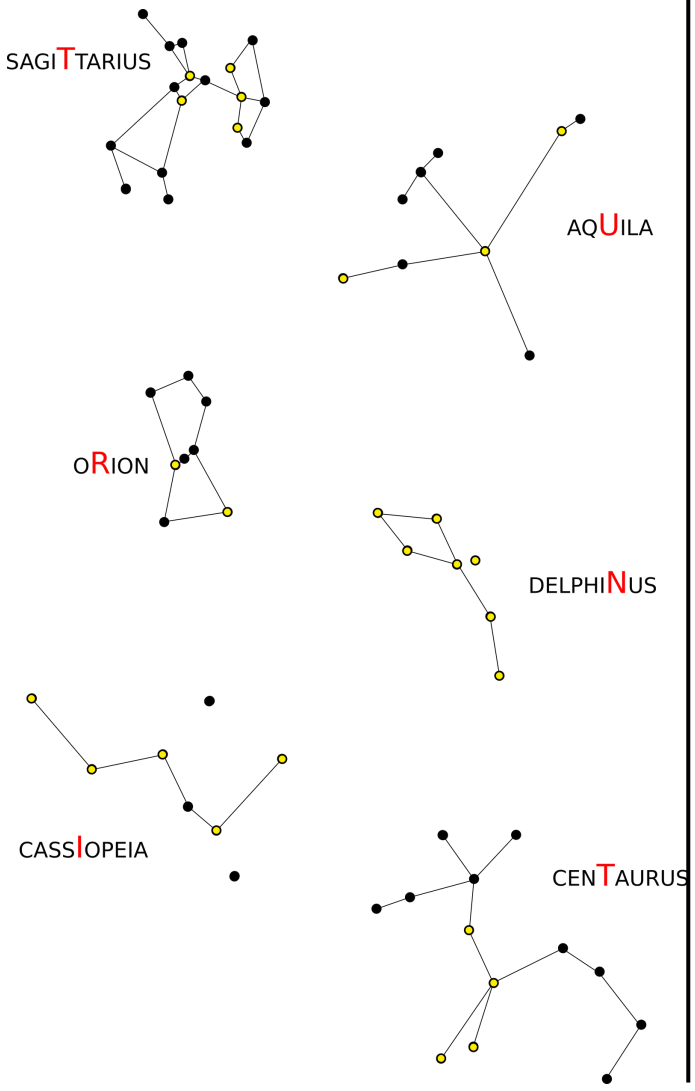

If you turned the filter to the vertical polarization, you would read the solution **GARDEN**, which should have draw your attention to the garden party, that was unfortunately cancelled due to the weather.

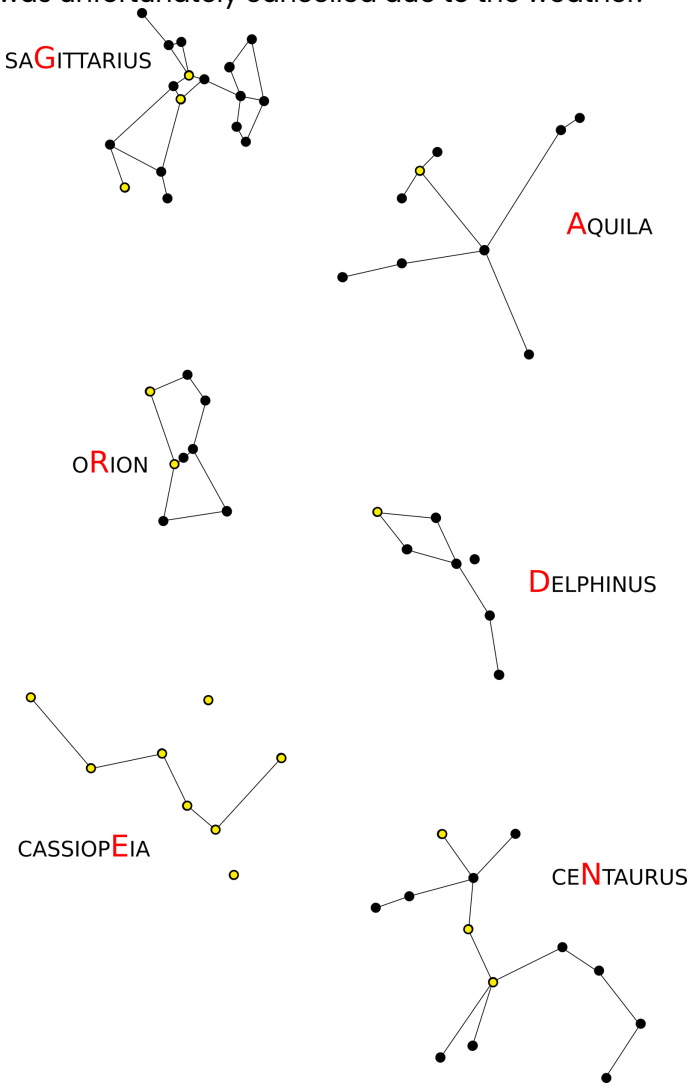

ESCAMPIG HERALD

SATURDAY - MAZE

The hungry dragon from the legend travels through the maze to the cow, but it eats each rabbit it meets on its way. Most rabbits are attached by a rope to an obstacle. When a rabbit is eaten, the corresponding obstacle falls to the maze's lower floor, causing a change in the maze layout.

In the end, the dragon finally finds its way to the cow, and the first letters of the devoured rabbits' names give you the solution to the farewell cipher: **SEE YOU IN BRNO AGAIN**.

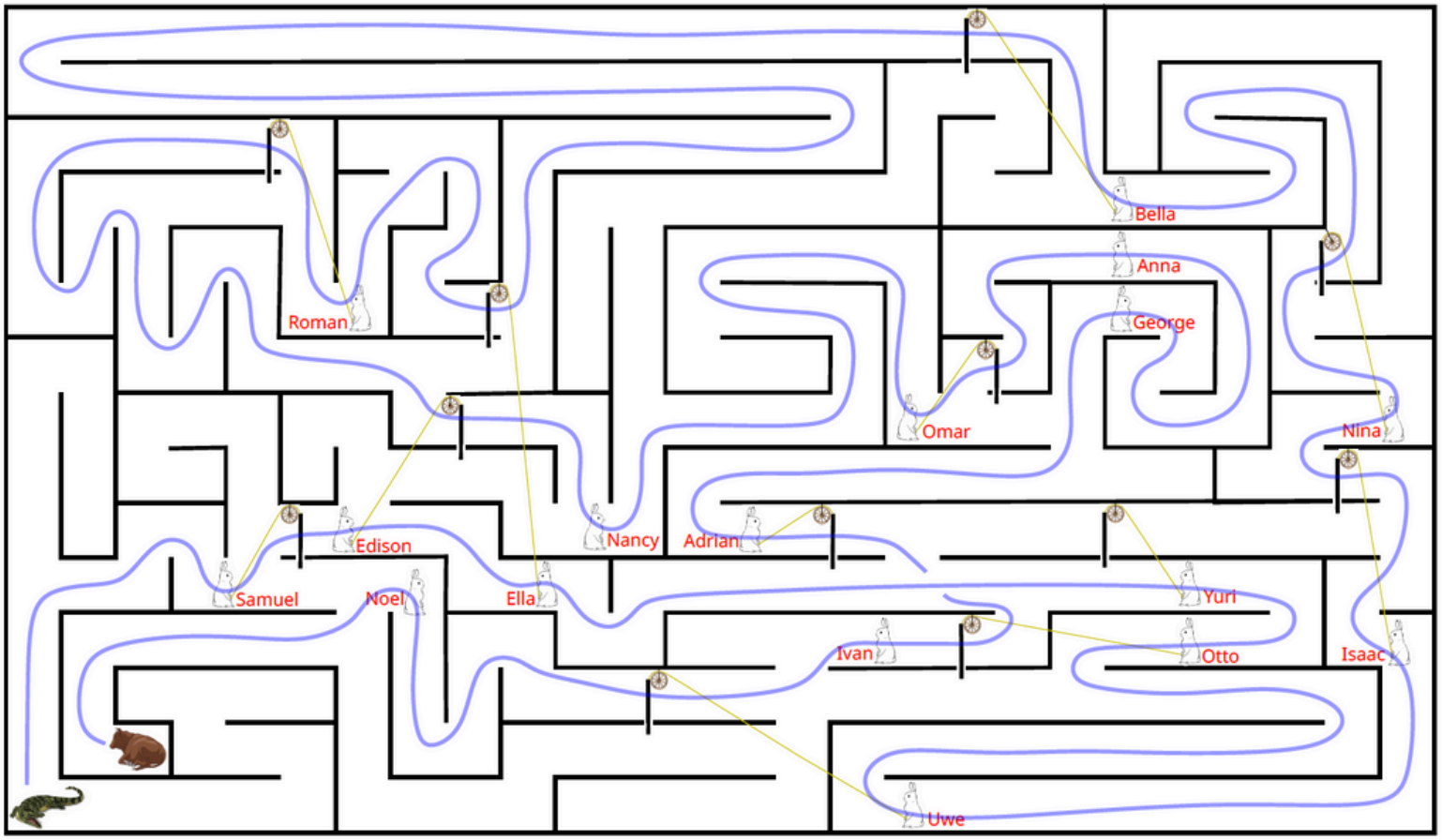

CEPLANT

Research & Development Centre for Plasma and Nanotechnology Surface Modifications

We introduce plasma-based solutions for surface and material engineering aiming for technology transfer and application industry.

Large Research Infrastructure

CEPLANT is an open facility for R&D institutions and researchers to explore new topics of plasma physics.

Key Enabling Technology Centre

CEPLANT provides services for R&D performing companies in European Union to implement advanced plasma technologies.

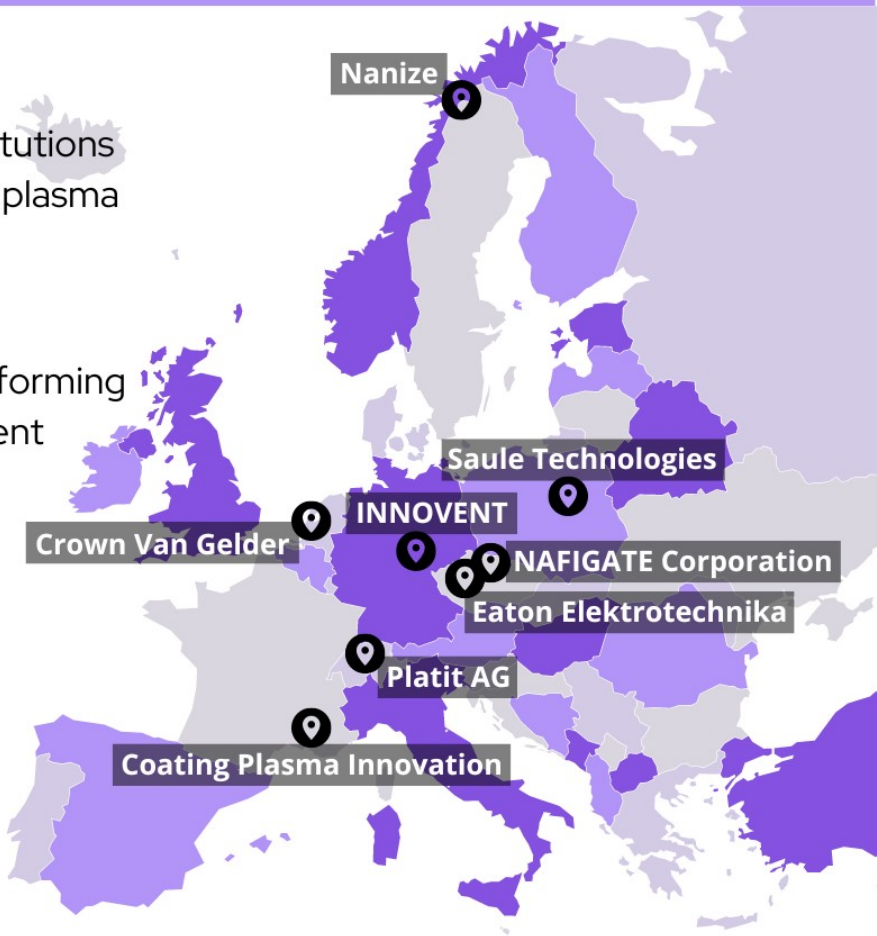

Keypoints

- open access research and analyses
- big fleet of high-end equipment
- eco-friendly technologies
- low-cost technologies
- solution to your specific problems and needs

Services

- low-temperature (cold), atmospheric plasma surface treatment of various materials
- optimisation and customisation of proprietary plasma technologies according to demand
- deposition of functional coatings and nanostructures
- plasma diagnostics and simulations
- unique facilites for complex material surface and volume analysis

MUNI SCI Department of Plasma Physics and Technology

info@ceplant.cz

www.ceplant.cz

Kotlarska 267/2 | 602 00 Brno | Czech Republic

Industrial utilisation

- Textile and Nanofibres
- Polymers
- Glass processing
- Automotive
- Composite materials
- Mechanical engineering
- Solar energy
- Plasma agriculture

Core facilities

- proprietary unique DCSBD plasma technologies
- various commercial plasma sources
- industrial systems for PVD magnetron sputtering
- surface mechanical properties analyses
- surface analytics (XPS, SIMS, MALDI, SEM, AFM, XRD)
- optical measurement of thin films

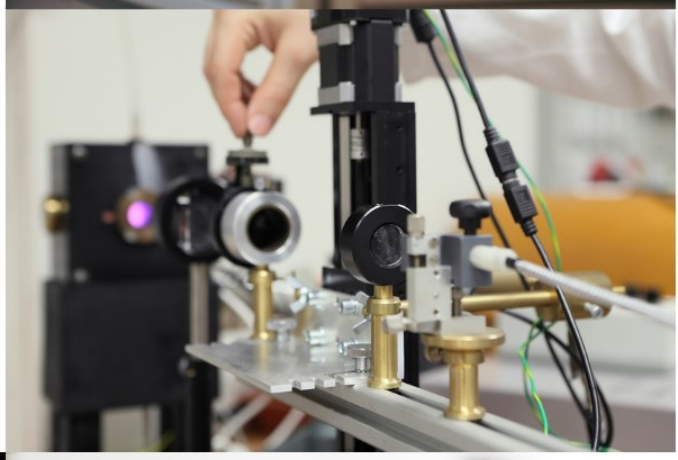

We offer our equipment for other scientists.

We perform the necessary analyses for your research.

We explain fundamental plasma processes.

We send you the price list on request.

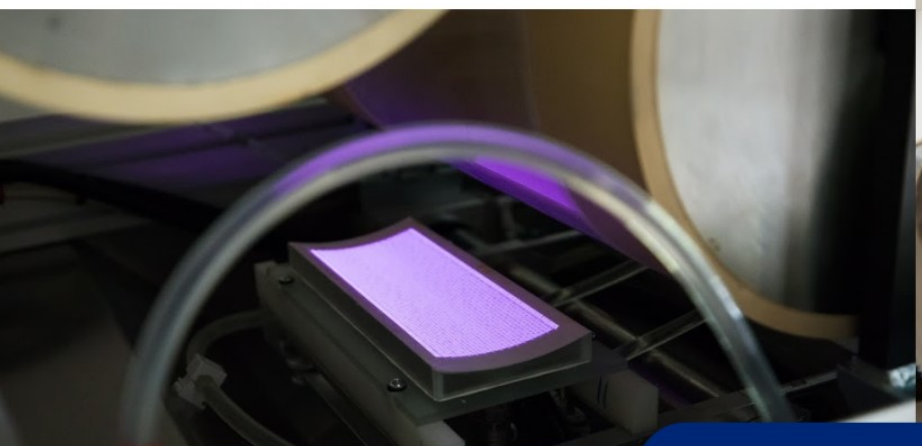

info@ceplant.cz
www.ceplant.cz
Kotlarska 267/2 | 602 00 Brno | Czech Republic

INTERNATIONAL UNION OF PURE AND APPLIED PHYSICS

IUPAP Centenary YEARS 1922 - 2022

Advancing physics across international boundaries for the past 100 years

INTERNATIONAL COMMISSIONS

C1: Commission on Policy and Finance
C2: Commission on Symbols, Units, Nomenclature, Atomic Masses and Fundamental Constants
C3: Statistical Physics
C4: Astroparticle Physics
C5: Low Temperature Physics
C6: Biological Physics
C8: Semiconductors
C9: Magnetism
C10: Structure and Dynamics of Condensed Matter
C11: Particles and Fields
C12: Nuclear Physics
C13: Physics for Development
C14: Physics Education
C15: Atomic, Molecular, and Optical Physics
C16: Plasma Physics
C17: Laser Physics and Photonics
C18: Mathematical Physics
C19: Astrophysics
C20: Computational Physics

AFFILIATED COMMISSIONS

AC1: International Commission for Optics
AC2: International Commission on General Relativity and Gravitation
AC3: International Commission for Acoustics
AC4: International Commission on Medical Physics

WORKING GROUPS

WG1: International Committee for Future Accelerators (ICFA)
WG2: Communication in Physics
WG5: Women in Physics
WG7: International Committee on Ultrahigh Intensity Lasers (ICUIL)
WG9: International Cooperation in Nuclear Physics (ICNP)
WG10: Astroparticle Physics International Committee (ApPIC)
WG11: Gravitational Wave International Committee (GWIC)
WG12: Energy
WG13: Newtonian constant of Gravitation
WG14: Accelerator Science
WG15: Soft Matter
WG16: Industry
WG17: Centenary

AIMS

- To stimulate and promote international cooperation, communication, research and education in physics;
- To foster inclusiveness and diversity in physics;
- To uphold openness, honesty and integrity in the practice, application and promotion of physics;
- To support the free circulation of scientists;
- To promote international agreements on symbols, units and nomenclature; and cooperating with other organizations on disciplinary and interdisciplinary problems.
- To help in the application of physics toward solving problems of concern to humanity.

2022

The yearlong CENTENARY celebrations will:

- Increase awareness of physics discoveries and the close ties among physicists at research centres globally.
- Stimulate worldwide interest in physics and science, as a tool for education and a motor of innovation, technology & economic development.
- Reach out to the global physics community, national science organisations, policy-makers, societies, students, families and the general public.

Inter Union Relations

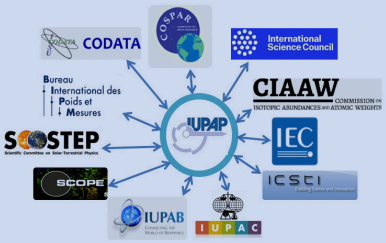

Conference Sponsorship

Each year, IUPAP sponsors and endorses ~ 50 conferences annually with special attention given to those held in developing countries.

Young Scientist Awards & Commission Awards

~200 prizes have been awarded in the last 10 years

Contact Us

IUPAP Singapore Nanyang Technological University, Nanyang Executive Centre #04-09, 60 Nanyang View, Singapore 639673
Tel: +65 6592 7784 • Email: IUPAP.Admin@ntu.edu.sg • Website: www.iupap.org

Vakuum Servis s.r.o., Hasičská 2643, 756 61 Rožnov p. R.
office@vakuum-servis.cz

RGA 160 testing system

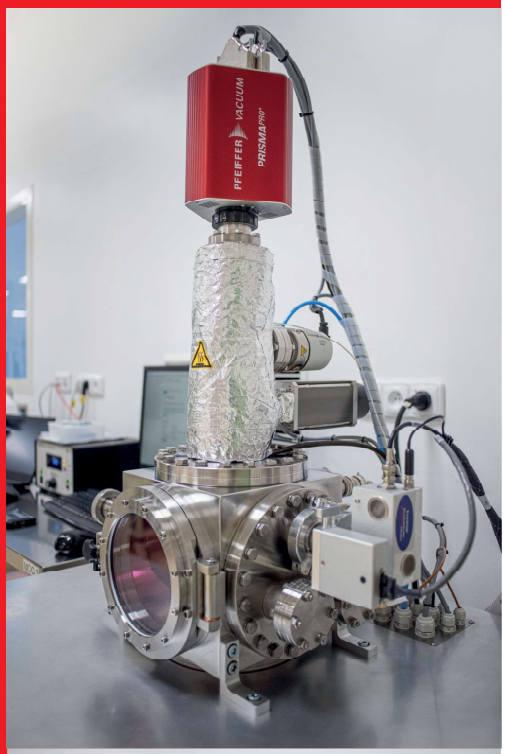

Main characteristics

- Multipurpose testing device for RGA analysis of UHV components
- Quantitative outgassing analysis for hydrocarbons, water vapour and other specific chemicals, based on customer needs
- Measurement method based on ASML standard GSA 07 2221
- Dedicated control software with fully automated measurement cycle with final acceptance protocol in pdf form
- Possibility of final plasma cleaning and vacuum bakeout of vacuum components before measurement

Technical details – standard version

- Oil-free vacuum pumping system with turbomolecular pump and primary scroll pump
- UHV DN160 CF cubical chamber with internal volume of 7 litres
- All-metal vacuum valves
- Quadrupole mass spectrometer Pfeiffer Prisma Pro, mass range 0-200 amu, Faraday + C-SEM detector, open type ion source with Y2O3 iridium filaments
- Calibration gas mixture included
- Integrated heating for automated system bakeout, (temperature can be adjusted up to 130°C)
- Ultimate pressure up to < 5e-9 mbar (for empty chamber, after 24 hrs bakeout)
- Minimal detectable leakrate < 5e-7 mbar.l.s^{-1} for H2O; < 5e-10 mbar.l.s^{-1} for CxHy
- Footprint 850 x 750 mm

Customization possibilities:

- Enlargement of a specimen chamber up to 40 liters
- Dedicated pumping system for quadrupole analyzer – better stability of measurement performance
- Plasma cleaning unit – helps to keep the system in pristine condition free from hydrocarbons

MEOPTA - RGA200 29. 4. 2022 0:19:30

Outgas Values

	Qmeasured [mbar*l/s]	Qbackground [mbar*l/s]	Qbatch [mbar*l/s]	Qspec [mbar*l/s]	Acceptance factor *)	Qbatch/A [mbar*l/(s*cm)]	t spec [h:mm]	t LDL [h:mm]
H_2O	1.85E-6	1.18E-6	1.18E-6	✓ 2.00E-6	0.59	Inf	31:28	29:09
CxHy v	7.32E-10	2.31E-9	2.31E-9	✓ 2.00E-6	< 0.01	Inf	29:09	29:09
CxHy nv	3.28E-10	2.32E-10	2.32E-10	X 0.00E+0	****.**	Inf	-	29:09
N_2	1.72E-7	2.35E-7	2.35E-7	✓ 2.00E-6	0.12	Inf	29:09	29:09
O_2	9.35E-8	1.45E-7	1.45E-7	X 0.00E+0	****.**	Inf	-	29:09
Ar	1.08E-8	1.09E-8	1.09E-8	X 0.00E+0	****.**	Inf	-	29:09

A factor 2 out of specification is accepted to avoid 'false Negative' conclusions

ICtot	Sum of Ion Current in the RGA
Ptot	Total Pressure within the Chamber
EM	Electron Multiplier
Q	Outgas rate
t spec	The time between the start of the pump down and the third outgas value in a row lower then the specification value
t LDL	The time between the start of the pump down and the third outgas value in a row lower then the LDL value
LDL	Low Detection Limit is two times of background level

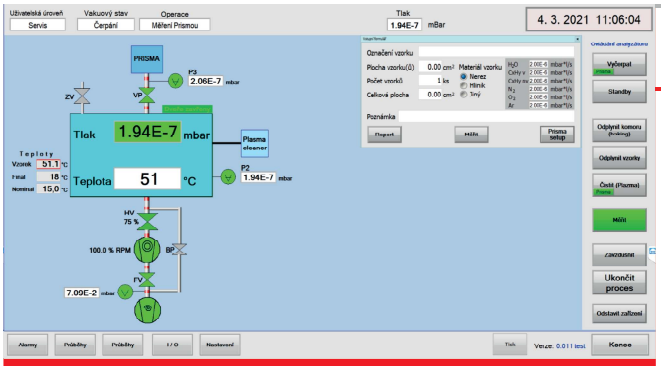

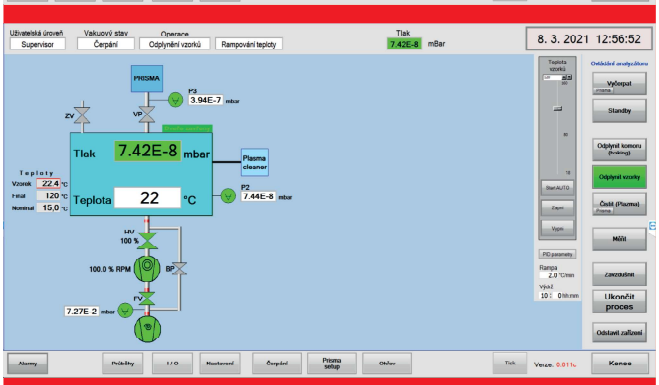

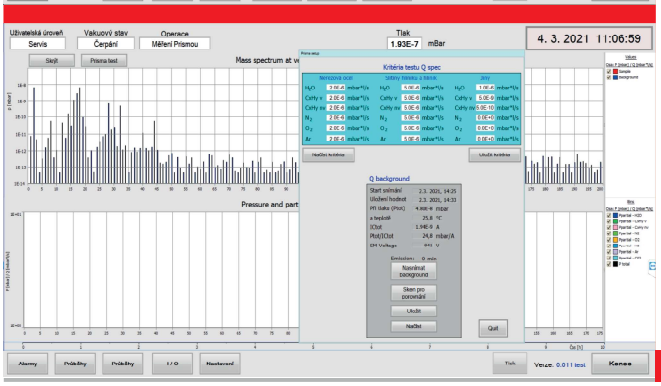

MEOPTA - RGA200 29. 4. 2022 0:19:30 VAKUUM SERVIS

Batch information

Marked as: Test vak

Note: pred testem peaky pritomne, perioda cca 50min

Quantity: 1 pcs

Surface 1 pc: 0 cm^2

Total Surface: 0.00 cm^2

Device information

QMG 250 PRISMA PRO

Serial number of Electronics: 44529302

Serial number of Senzor: 44529276

Pump speed: 95 l/s

RESULT SUMMARY

Sample(s) analyze

Start Pump 27.4. 2022, 9:28

Start RGA time: 28.4. 2022, 14:23

Qualification time: 29.4. 2022, 0:19 (9:55)

Report: Test vak peaku_prazd-2022_04_28-14:23

ICtot: 1.52E-8 A

Ptot: 4.46E-8 mbar

Ptot / ICtot: 2,9 mbar/A

EM Voltage: 1320 V

Temperature: 25,5 °C

Background information

Start Pump 2.3. 2022, 6:45

Start RGA time: 2.3. 2022, 7:00

Qualification time: 2.3. 2022, 16:58 (9:57)

ICtot: 1.99E-8 A

Ptot: 3.44E-8 mbar

Ptot / ICtot: 1,7 mbar/A

EM Voltage: 1320 V

Temperature: 25,6 °C

MEOPTA - RGA200 29. 4. 2022 0:19:30 VAKUUM SERVIS

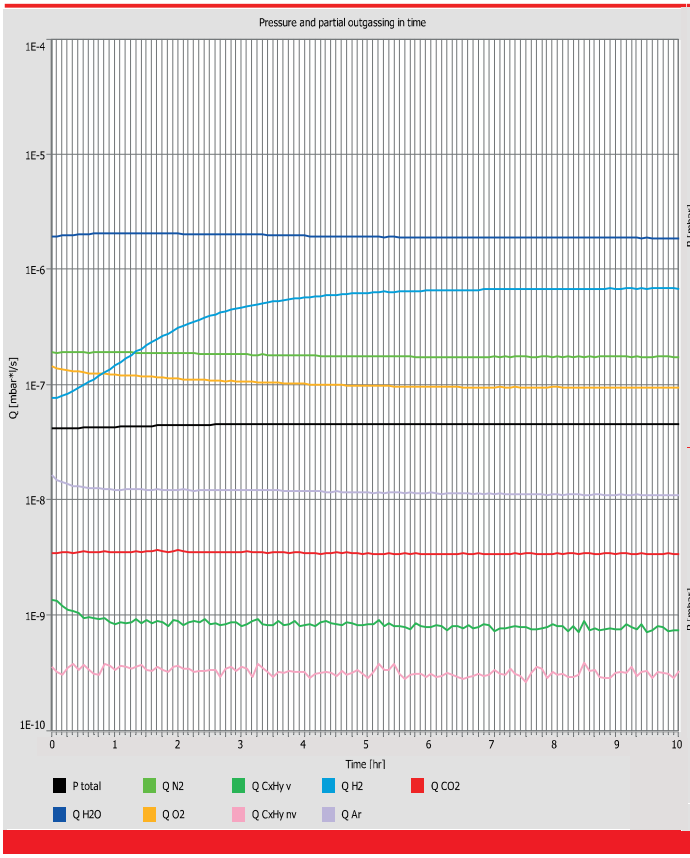

MEOPTA - RGA200 29. 4. 2022 0:19:30 VAKUUM SERVIS

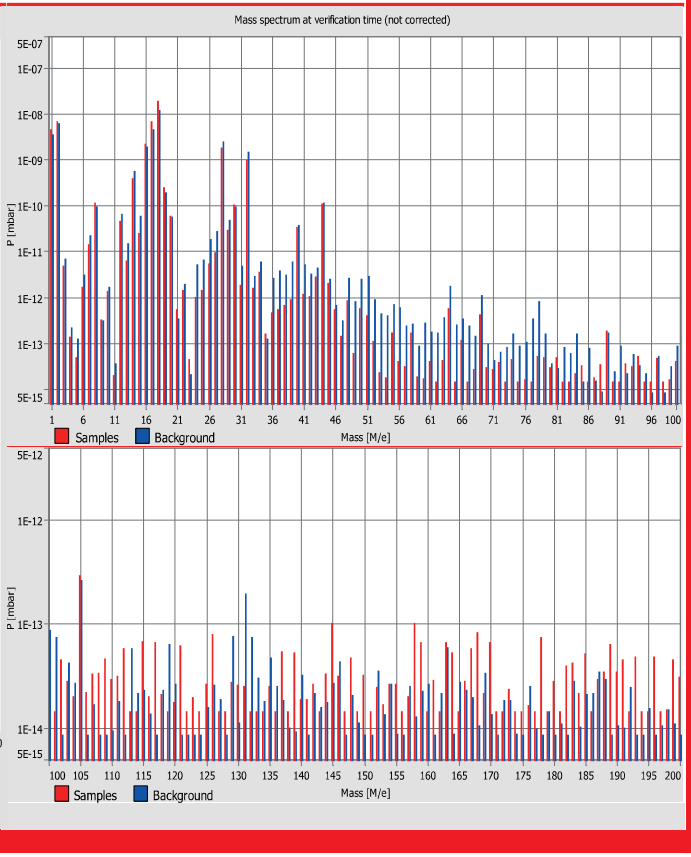

SHM

SUPER HARD MATERIALS

www.shm-cz.cz

INDUSTRIAL
PVD COATINGS

Custom Systems OptiXs

Do you have an idea for a project but...

- lack the capacity to implement it?
- cannot find a suitable commercial product for your application?
- lack a student to get it off the ground?

Get in touch with us!

- Laser technology
- Optics
- Vacuum
- Electronics
- Programming
- 3D printing

...and much more

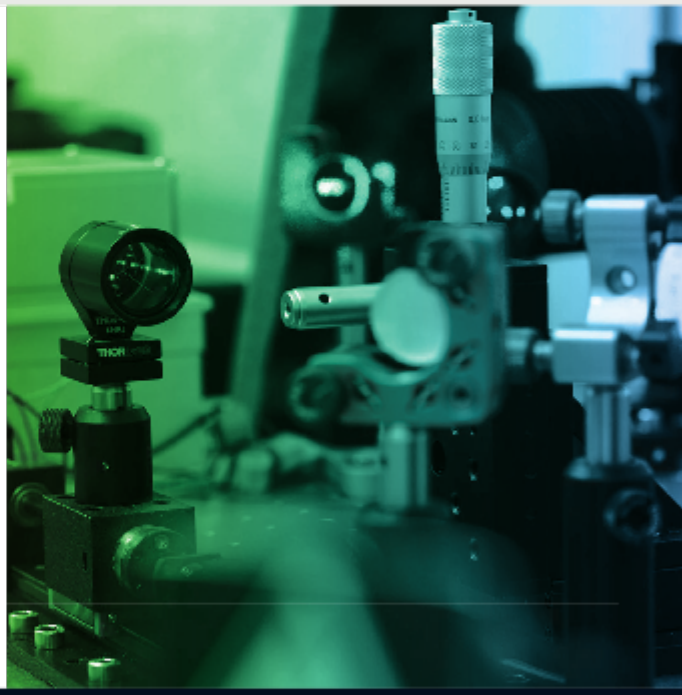

Check out our case studies and find out more at:

www.optixs.cz/en/custom-systems-521

Contact us

www.optixs.cz
info@optixs.cz
+420 910 920 610

OptiXs

SOLAYL
RF MEASUREMENT & CONTROL

Products & Services for RF Plasma Applications

Matching Networks

- Standard or customized
- For CCP, DBD or ICP reactors
- LF, HF and VHF

Vacuum Capacitors

- Refurbished capacitors
- Certified compliance with the original or derated specifications
- Tested properties: torque, vacuum, capacitance, high voltage rating up to 6kV

Consulting Service

- Troubleshooting of technical issues
- Design & build of RF systems
- RF modeling of your system
- On-site or remote consulting

Equipment Rental

Cesar® RF Power Generators

- 400kHz / 2, 13.56 & 40.68MHz
- Up to 1kW
- Matchers also available

Power Inductors

- Standard or customized
- Variable or fixed
- Air-cooled or water-cooled

RF Probes

- In-line RF voltage current sensors
- Customized to your application
- High power rating

Phone: +33 (0)9-70-90-20-20 www.solayl.com Email: contact@solayl.com
SOLAYL SAS, 4 Impasse Agrippa d'Aubigné, 28000 Chartres, France

PLATIT®

Advanced Coating Systems

SWISS QUALITY

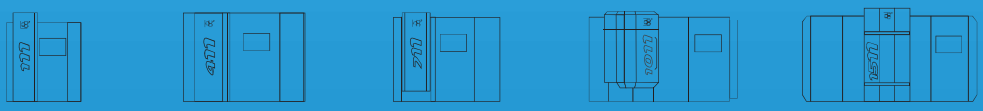

PLATIT® π - Series

PLATIT AG • Headquarters • Eichholzstrasse 9 • CH-2545 Selzach • info@platit.com • + 41 32 544 6200

PLATIT®

platit.com

A LEADING MANUFACTURER OF HIGH-TECH PVD AND PECVD COATING UNITS FOR TOOLS AND COMPONENTS

PLATIT offers a wide range of high-tech standard and custom coating solutions for PVD coating, which are characterized by a modular design, high flexibility and maximum user-friendliness. As a Swiss company with service, support and saleslocations in Europe, North America and Asia, we are always there where our customers need us. Our own sites are complemented by a broad network of distributors and partners.

We have already installed over 650 coating units for our customers worldwide and maintain a close partnership with them. Our customers benefit from our many years of experience in the field of cathodic arc coating, sputter coating and HiPIMS technology. Based on our know-how, we use these technologies for different applications and can also integrate them in hybrid processes.

In addition to coating units, we also design and build complete turnkey systems for coating processes. These complete solutions include all upstream and downstream process steps of hard coating such as decoating, edge pre-treatment, cleaning, post-treatment and quality control. This make our systems ideal for seamless integration into tool manufacturing and regrinding process.

We maintain an open-source philosophy, allowing our customers to customize PVD coatings to their specific requirements and individual needs. We enable our customers to differentiate themselves from the market standard in dedicated application fields with the highest coating performance and competitive advantages.

As part of the BCI Blösch Group, we are a family-owned company.

PLATIT®

www.hidenanalytical.com
info@hiden.co.uk

HIDEN ANALYTICAL

Instruments for Plasma Characterisation

Mass spectrometers for vacuum, gas, plasma and surface science

Molecular Beam Mass Spectrometer

Analyse atmospheric plasma and reactive gas phase intermediates with the HPR-60.

HPR-60 MBMS – for Analysis of Neutrals, Radicals & Ions

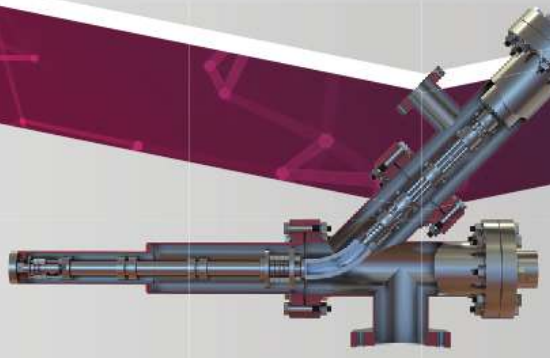

Plasma Ion Analyser

Measure key plasma parameters with EQP mass and energy analysers.

EQP Series – Systems for Plasma Research

Residual Gas Analyser

Rapidly analyse gas and vapour species with the HPR-30.

HPR-30 Series – for Vacuum Process Analysis

Langmuir Probes

Extrapolate critical plasma parameters in real-time with ESPion Langmuir probes.

ESPion – Advanced Langmuir Probe for Plasma Diagnostics

DIFFUSE COPLANAR SURFACE BARRIER DISCHARGE PLASMA

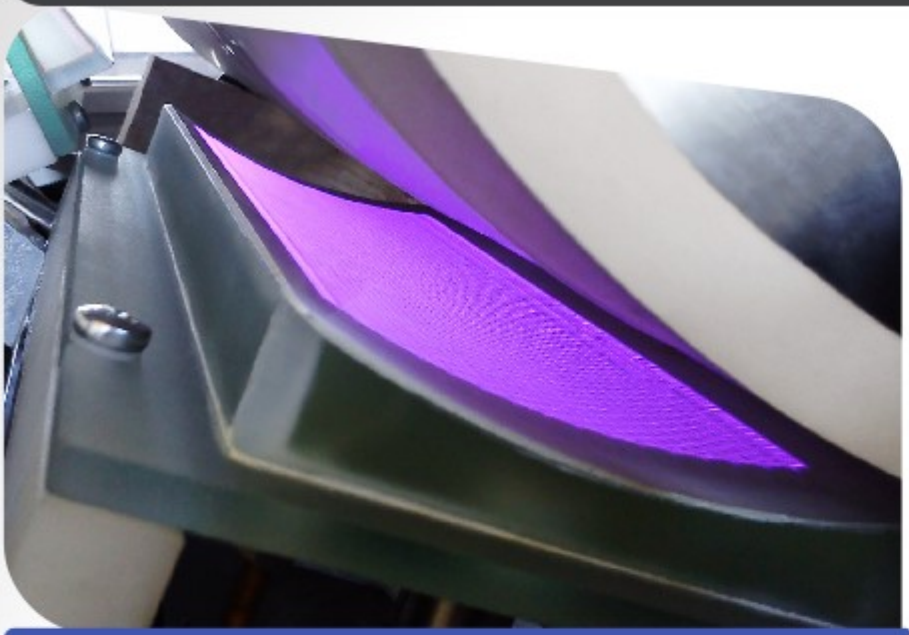

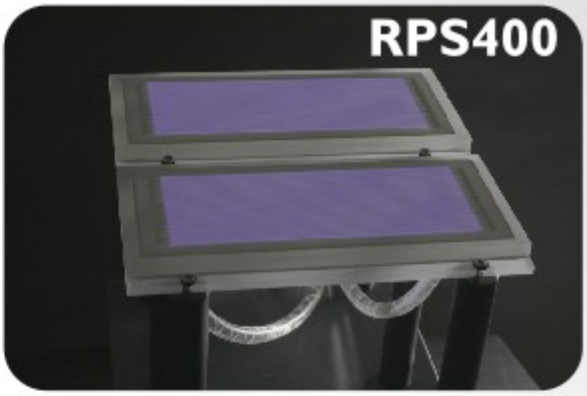

- ***Ambient air diffuse plasma***
- ***Planar and curved geometry***

- Plasma area of one unit: 19 cm × 8 cm
- Power of one plasma unit > 400 W
- High plasma power density ~ 100 W/cm³
- Permanent hydrophilization
- Treatment speed: 3 – 100 m/min
- Suitable for inline treatment of rigid and flexible polymeric and metallic foils, flexible glass, paper, nanomaterials

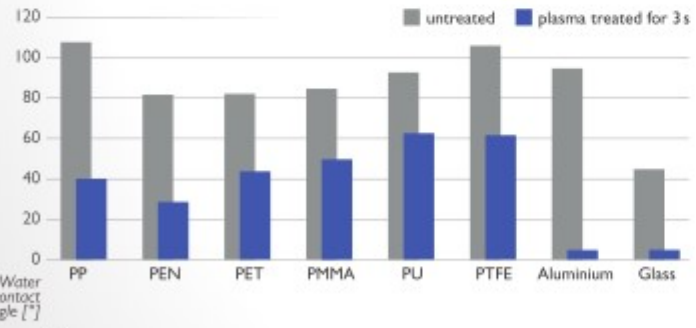

Biodecontamination chamber

We offer

- Consultation and proposal for a solution to a customer's specific problem using the most modern plasma technologies
- Comparative studies of plasma treatment with various commercially available systems at CEPLANT with your samples (rigid or flexible)
- Hand-held or continuous plasma treaters
- Integrated roll-to-roll plasma treatment lines

Robust Plasma Systems (ROPLASS), *Masarykova 118, 664 42 Modřice, Czech Republic*
www.roplass.cz, info@roplass.cz

ROPLASS robust plasma systems

PLASIMO modules

Plasma

- LTE: Equilibrium Thermodynamics
- Quasi-LTE: Elemental Diffusion
- Non-LTE: Drift-Diffusion-Inertia, Quasi-Neutrality
- Non-thermal: Monte-Carlo/Hybrid

Electromagnetic

- Electrostatic and Magnetostatic
- Inductive: Frequency and Time Domain
- Microwaves

Temperature and Flow Fields

- Subsonic and Supersonic
- Compressible and Incompressible

Radiation Transport

Builtin Boltzmann Solvers: BOLSIG+ and LoKI-B

Chemistry

- Global Model, Collisional Radiative Model
- Chemical Reduction Tools: PA, ILDM

- Created for modeling of plasmas with various degrees of equilibrium
- Designed as a flexible and user friendly modeling toolbox
- Available for Windows, macOS and Linux/Unix

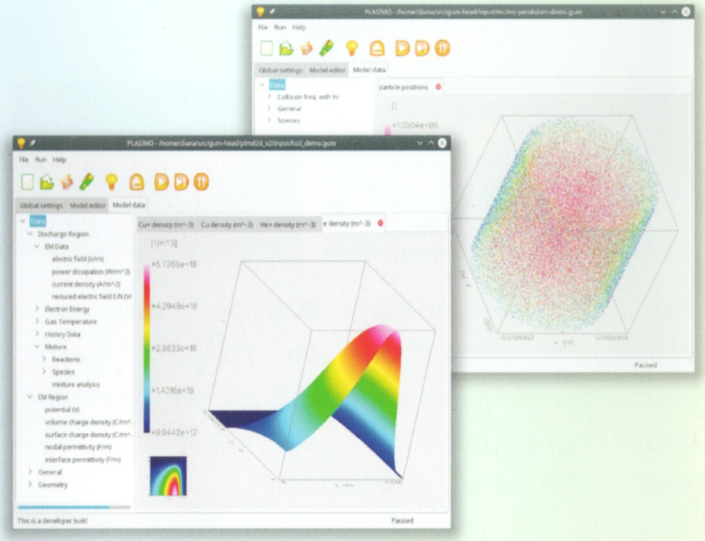

P.O.Box 6336, 5600 HH Eindhoven, The Netherlands
info@plasma-matters.com
www.plasma-matters.com

Plasma Matters.

TU/e EINDHOVEN UNIVERSITY OF TECHNOLOGY

The Plasma Simulation Software

PLASIMO

for research, education, industry and innovation

Plasma Matters

www.plasma-matters.com

Assorted PLASIMO applications

Complex mixtures

PLASIMO has been used to model very complex mixtures, such as CO_2-CH_4, H_2-N_2-O_2, and O_2-$SiCl_4$. PLASIMO provides a number of chemical reduction tools, such as Pathway Analysis and Intrinsic Low Dimensional Manifold.

Transport and radiation in complex mixtures

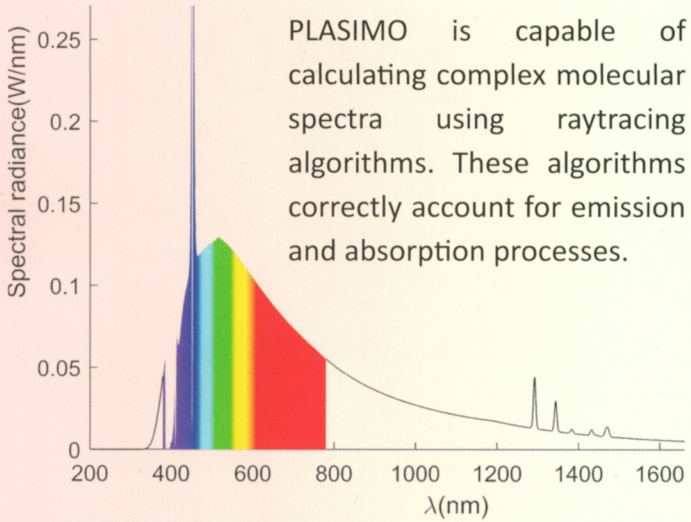

PLASIMO is capable of calculating complex molecular spectra using raytracing algorithms. These algorithms correctly account for emission and absorption processes.

Cascaded arc

PLASIMO has been used for simulating a plasma source for material research under fusion-relevant conditions (Magnum-PSI). PLASIMO successfully handles the challenging combination of the transonic flow field and magnetic confinement.

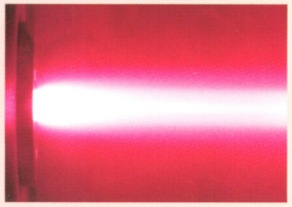

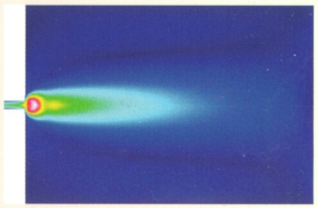

Capacitively coupled plasmas

PLASIMO has been widely used for CCP plasmas in various configurations and for a large range of operating parameters.

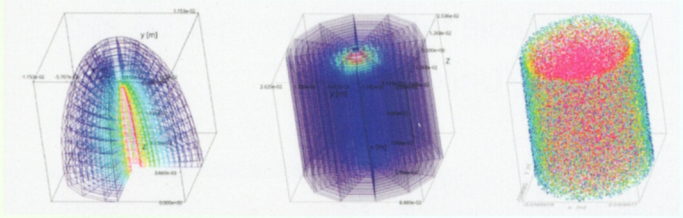

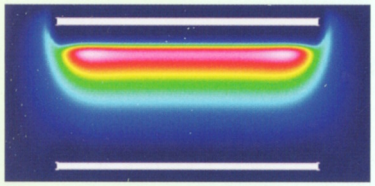

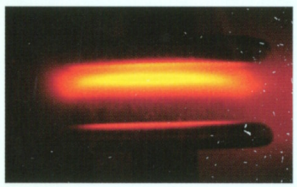

PLASIMO has helped research on micro-plasmas for biomedical applications, on dielectric barrier discharges for air cleaning and surface treatment, sputtering plasmas for laser applications, and reactors for surface modification.

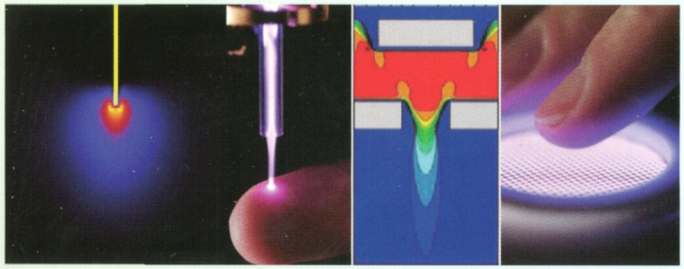

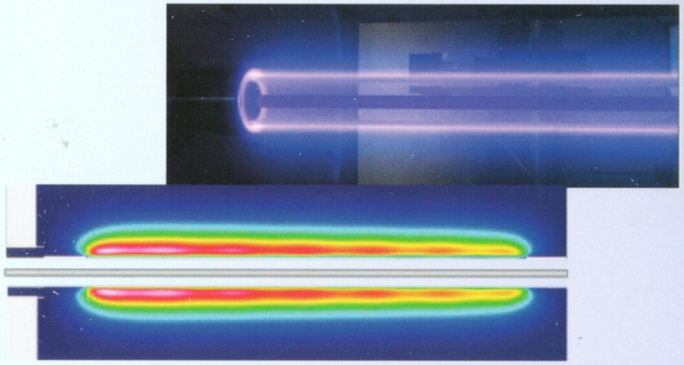

Microwave plasmas

PLASIMO self-consistently describes the interaction between the electromagnetic and plasma aspects of the microwave discharges. PLASIMO has helped research on surfatron plasmas, coaxial waveguides, microwave plasma torches, and surfaguides.

Inductively coupled plasmas

PLASIMO offers two different approaches for solving the ICP fields: frequency and time domain modeling. This makes it applicable to ICP plasmas in various regimes, including low frequency and low pressure.